RTO-EN-020

NORTH ATLANTIC TREATY ORGANISATION

RESEARCH AND TECHNOLOGY ORGANISATION
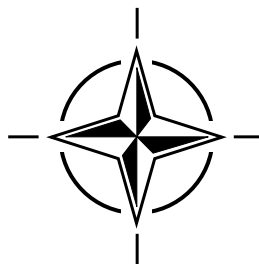
BP 25, 7 RUE ANCELLE, F-92201 NEUILLY-SUR-SEINE CEDEX, FRANCE

RTO EDUCATIONAL NOTES 20

Active Control of Engine Dynamics
(Le contrôle actif pour la dynamique des moteurs)

The material in this publication was assembled to Support a RTO/VKI Special Course under the sponsorship of the Applied Vehicle Technology Panel (AVT) and the von Kármán Institute for Fluid Dynamics (VKI) presented on 14-18 May 2001, in Brussels, Belgium.

Distribution and Availability on Back Cover

This page has been deliberately left blank

_____

Page intentionnellement blanche

NORTH ATLANTIC TREATY ORGANISATION

RESEARCH AND TECHNOLOGY ORGANISATION

BP 25, 7 RUE ANCELLE, F-92201 NEUILLY-SUR-SEINE CEDEX, FRANCE

RTO EDUCATIONAL NOTES 20

Active Control of Engine Dynamics
(Le contrôle actif pour la dynamique des moteurs)

The Research and Technology Organisation (RTO) of NATO

RTO is the single focus in NATO for Defence Research and Technology activities. Its mission is to conduct and promote cooperative research and information exchange. The objective is to support the development and effective use of national defence research and technology and to meet the military needs of the Alliance, to maintain a technological lead, and to provide advice to NATO and national decision makers. The RTO performs its mission with the support of an extensive network of national experts. It also ensures effective coordination with other NATO bodies involved in R&T activities.

RTO reports both to the Military Committee of NATO and to the Conference of National Armament Directors. It comprises a Research and Technology Board (RTB) as the highest level of national representation and the Research and Technology Agency (RTA), a dedicated staff with its headquarters in Neuilly, near Paris, France. In order to facilitate contacts with the military users and other NATO activities, a small part of the RTA staff is located in NATO Headquarters in Brussels. The Brussels staff also coordinates RTO's cooperation with nations in Middle and Eastern Europe, to which RTO attaches particular importance especially as working together in the field of research is one of the more promising areas of initial cooperation.

The total spectrum of R&T activities is covered by the following 7 bodies:

- AVT   Applied Vehicle Technology Panel
- HFM   Human Factors and Medicine Panel
- IST   Information Systems Technology Panel
- NMSG   NATO Modelling and Simulation Group
- SAS   Studies, Analysis and Simulation Panel
- SCI   Systems Concepts and Integration Panel
- SET   Sensors and Electronics Technology Panel

These bodies are made up of national representatives as well as generally recognised 'world class' scientists. They also provide a communication link to military users and other NATO bodies. RTO's scientific and technological work is carried out by Technical Teams, created for specific activities and with a specific duration. Such Technical Teams can organise workshops, symposia, field trials, lecture series and training courses. An important function of these Technical Teams is to ensure the continuity of the expert networks.

RTO builds upon earlier cooperation in defence research and technology as set-up under the Advisory Group for Aerospace Research and Development (AGARD) and the Defence Research Group (DRG). AGARD and the DRG share common roots in that they were both established at the initiative of Dr Theodore von Kármán, a leading aerospace scientist, who early on recognised the importance of scientific support for the Allied Armed Forces. RTO is capitalising on these common roots in order to provide the Alliance and the NATO nations with a strong scientific and technological basis that will guarantee a solid base for the future.

The content of this publication has been reproduced
directly from material supplied by RTO or the authors.

Printed by St. Joseph Print Group Inc.
(A St. Joseph Corporation Company)
1165 Kenaston Street, Ottawa, Ontario, Canada K1G 6S1

Active Control of Engine Dynamics
(RTO EN-020 / AVT-083)

Executive Summary

Active control presents the opportunity to mitigate future challenges associated with design constraints and operational requirements in gas turbines, including control of compressor system and combustion system instabilities. Several programs are exploring this technology to address issues related to higher pressure and temperature operation for improved performance, volume reduction for increased thrust-to-weight ratio, and operation near lean blowout limits for reduced emission. The aim of the course was to present the state-of-the-art of this emerging technology, including the experimental and theoretical understanding of the control processes and control issues, and to describe the latest developments for its practical implementation.

The course started with an introduction into fundamental stability characteristics and active control approaches, followed by a lecture on control theory with special consideration of robustness and fundamental limits of controllers.

For combustion systems, fundamental flow and combustion processes that determine the behavior of system dynamics was described and different physics-based active and passive control approaches were developed. Subsequently, theory associated with the application of standard control laws and strategies to linear combustor dynamics was discussed, using the spatial averaging method to construct reduced-order models of the dynamics. In addition, models of the control processes and its application to active control were reviewed. The practical application to power gas turbines was described, including control approach, design issues, results from long-term experiments, and assessment of active control compared to passive control methods.

For compression system dynamics, analysis of hydrodynamics models for multi-mode pre-stall dynamics of axial compression systems was described, which include non-linear coupling between surge and stall. This was followed by the description of analytical and experimental techniques for diagnostics and control of compression instabilities. Different sensor and actuator architectures were discussed together with linear and non-linear techniques to optimize closed-loop performance and robustness. The course was concluded with R&D needs and an assessment of future prospects for active control.

In summary, the course has shown for combustion systems, that progress in actuator and sensor technologies and the increased understanding of the physical control processes associated with flow, combustion, and acoustics has made the active control approach a viable option even at full scale. The successful implementation of instability suppression in heavy duty power gas turbines and its continuing evaluation related to reliability, lifetime, and performance will enhance confidence for other applications such as aeroengines, for which active control needs have been established. Current efforts focus on reducing pattern factor and suppression of combustion instability associated with performance increases and emission reduction. To minimize the risk of implementing active control on aeroengines, life extension of combustors maybe the first practical application in conjunction with implementation of diagnostics and information technologies for health monitoring. For airbreathing missiles propulsion, suppression of combustion instabilities and extension of lean blowoff limits are viable options for active control applications. For future developments of "smart combustors" active control will play an enabling role when combined with distributed wireless sensors and distributed actuators.

For compression systems, significant progress has been made of coupling the actuation mechanism with the physics. A variety of actuation schemes have been developed and successfully demonstrated in systems ranging from low-speed, single stage rigs to full-scale engines, however active control has not been implemented in a practical system. One of the difficulties is obtaining low-weight and highly reliable actuators with sufficient control authority and frequency response. Given the difficulty in controlling stall and surge behavior on practical systems, diagnostic systems for detecting abnormal operational conditions may be the more important early application.

Le contrôle actif pour la dynamique des moteurs
(RTO EN-020 / AVT-083)

Synthèse

Le contrôle actif offre le moyen de réduire l'impact des futurs défis représentés par les contraintes de conception et les besoins opérationnels associés aux turbomoteurs, y compris le contrôle des instabilités des compresseurs et des systèmes de combustion. Ces technologies sont actuellement étudiées par le biais de différents programmes de recherche, ayant pour objectif d'examiner la possibilité de faire fonctionner les turbomoteurs à des températures et à des pressions plus élevées afin d'améliorer leurs performances, de réduire leur volume pour améliorer le rapport poussée-poids, et de fonctionner aux limites de l'extinction pauvre afin de réduire les émissions. Le cours a eu pour objectif de présenter l'état actuel des connaissances de ces technologies émergentes, y compris les connaissances théoriques et expérimentales dans le domaine du contrôle et de ses processus, et de décrire les derniers développements en ce qui concerne sa mise en œuvre concrète.

Le cours a commencé par une introduction aux caractéristiques fondamentales de stabilité et aux différentes approches du contrôle actif, suivi d'un cours sur la théorie du contrôle, qui a mis l'accent sur la robustesse et les limites intrinsèques des contrôleurs.

En ce qui concerne les systèmes de combustion, les processus fondamentaux de flux et de combustion qui déterminent le comportement de la dynamique du système ont été décrits, et différentes approches du contrôle actif et passif basées sur la physique ont été examinées en détail. Par la suite, la théorie associée à l'application de lois et de stratégies de contrôle normalisées à la dynamique des chambres de combustion linéaires a été discutée, en faisant appel à la méthode de moyenne spatiale pour construire des modèles réduits de la dynamique. Un certain nombre de modèles des processus de contrôle et leurs applications au contrôle actif ont été étudiés. Les applications pratiques aux turbomoteurs ont été décrites, y compris les approches du contrôle, la conception, certains résultats d'expériences à long terme et une évaluation du contrôle actif par rapport aux méthodes du contrôle passif.

En ce qui concerne la dynamique des systèmes de compression, l'analyse de modèles hydrodynamiques de la dynamique multi-mode de systèmes de compression axiale en prédécrochage a été présenté, y compris le couplage non-linéaire entre le pompage et le décrochage. Cette présentation a été suivie de la description de techniques analytiques et expérimentales pour le diagnostic et le contrôle des instabilités de compression. Différentes architectures de capteurs et d'actionneurs ont été discutés, ainsi que des techniques linéaires et non-linéaires permettant d'optimiser les performances en boucle fermée et la robustesse. Le cours a conclu par un tour d'horizon des besoins en R&D et une évaluation des perspectives futures en matière de contrôle actif.

En conclusion, le cours a démontré que grâce aux progrès réalisés dans le domaine des technologies des actionneurs et des capteurs, ainsi qu' aux nouvelles connaissances des processus physiques de contrôle des flux, de la combustion et de l'acoustique, le contrôle actif est une option valable, même en grandeur réelle. L'élimination des instabilités dans les grands turbomoteurs et son évaluation continue en ce qui concerne la fiabilité, le cycle de vie et les performances permettra de rehausser le niveau de confiance en vue d'autres applications telles que les moteurs d'avion, pour lesquels les besoins en contrôle actif ont été établis. Les efforts actuellement consentis dans ce domaine concernent principalement la réduction des écarts de température et l'élimination des instabilités de combustion, associées à l'amélioration des performances et la réduction des émissions. Afin de réduire au minimum les risques associés à l'application du contrôle actif aux moteurs d'avion, la première application concrète pourrait être le prolongement du cycle de vie des chambres de combustion, en parallèle avec la mise en œuvre des technologies du diagnostic et de l'information pour le contrôle de l'état de fonctionnement des moteurs. En ce qui concerne la propulsion des missiles aérobies, l'élimination des instabilités de combustion et l'extension des limites de l'extinction pauvre représentent des options valables pour d'éventuelles applications du contrôle actif. Le contrôle actif, associé à des capteurs sans fil et à des actionneurs répartis, est appelé à jouer un rôle habilitant dans le développement futur des «chambres de combustion intelligentes».

En ce qui concerne les systèmes de compression, des progrès appréciables ont été réalisés en couplant le mécanisme actionneur avec des aspects ayant trait à la physique. Diverses configurations d'actionneurs ont été développées et démontrées avec succès pour des systèmes allant de bancs d'essai basse vitesse à un seul étage à des moteurs réels, mais le contrôle actif n'a pas été mis en œuvre dans un système particulier. L'une des difficultés consiste à obtenir des actionneurs légers et hautement fiables dotés de suffisamment de contrôle et de réponse en fréquences. Etant donné les difficultés rencontrées pour contrôler le pompage et le décrochage dans des systèmes en service, il se pourrait que l'application prioritaire soit la détection de conditions de fonctionnement anormales.

Contents

List of Authors/Lecturers

Special Course Directors:

Prof. R.A. Van den Braembussche
von Kármán Institute
72, Chaussee de Waterloo
1640 Rhode-Saint-Genese, Belgium

Dr. K. C. Schadow
Strategic Analysis, Inc.
2896 Calle Heraldo
San Clemente, CA 92673
United States

Authors/Lecturers

FRANCE
Prof. S. Candel
EM2C Lab. Ecole Central Paris
Grande Voie des Vignes
92295 Chatenay Malabry

Mr. S. Ducruix
EM2C Lab. Ecole Central Paris
Grande Voie des Vignes
92295 Chatenay Malabry

Mr. D. Durox
EM2C Lab. Ecole Central Paris
Grande Voie des Vignes
92295 Chatenay Malabry

Mr. D. Veyante
EM2C Lab. Ecole Central Paris
Grande Voie des Vignes
92295 Chatenay Malabry

GERMANY
Mr. J. Hermann
IfTA GmbH
Industriestrasse 33
82194 Groebenzell

Mr. A. Orthmann
IfTA GmbH
Industriestrasse 33
82194 Groebenzell

UNITED STATES
Dr. A. Banaszuk
United Technologies Research Center
411 Silver Lane, MS 129-15
East Hartford, CT 06108

Mr. R. L. Behnken
Control and Dynamical Syst. 107-81
California Institute of Technology
Pasadena, CA 91125

Dr. F. Culick
205 Guggenheim, Mail Stop 205-45
California Institute of Technology,
Pasadena, CA 91125

Dr. C. Jacobson
United Technologies Research Center
411 Silver Lane, MS 129-15
East Hartford, CT 06108

Mr. R. M. Murray
Control and Dynamical Syst. 107-81
California Institute of Technology,
205 Guggenheim, Mail Stop 205-45
Pasadena, CA 91125

Mr. J.D. Paduano
M.I.T.
Room 31-265
Cambridge, MA 0219-4307

Mr. Yong Wang
Control and Dynamical Syst. 107-81
California Institute of Technology,
205 Guggenheim, Mail Stop 205-45
Pasadena, CA 91125

Prof. V. Yang
Dept. of Mechanical Engineering
The Pennsylvania State University
104 Research Building East
University Park, PA 16802

Mr. S. Yeung
Control and Dynamical Syst. 107-81
California Institute of Technology,
205 Guggenheim, Mail Stop 205-45
Pasadena, CA 91125

Prof. K. Yu
Dept. of Aerospace Engineering
University of Maryland
College Park, MD 20742

LOCAL COORDINATOR

Prof. R. Van den Braembussche
von Kármán Institute for Fluid Dynamics
Chaussee de Waterloo, 72
1640 Rhode-Saint-Genese
Belgium

Introductions – Stability Characteristics and Control Approach[*]

V. Yang
Department of Mechanical Engineering
The Pennsylvania State University
University Park, PA 16802, USA
Email: vigor@psu.edu

Summary

This lecture provides an overview of various fundamental aspects of active control of gas-turbine combustion dynamics. The physical mechanisms and practical means for modulating flow and combustion processes are discussed.

1. Introduction

The quest for enhanced performance, service reliability, maintainability, and availability has been the thrust of gas turbine engine research since its invention in 1905. While traditional approaches yielded profound improvement over the years and require further optimization, intelligent control of gas turbines offers a radically new avenue for advancing the state-of-the-art. By synthesizing novel control strategies at the component, substystem, and system levels, realization is possible of desired engine characteristics previously limited by phenomena such as compressor surge and stall, lean blow out limit, and combustion instabilities. Even relatively modest improvements in a design can result in substantial payoffs. For example, only a 5-10% improvement in stall pressure ratio is required to lead to a 2-5% reduction in gross takeoff weight of an engine, a 2-5% improvement in range, and up to a 3% decrease in cost. Such data exemplifies the strong impetus for pursing active control in gas turbines for fuel economy and augmented performance.

In contrast to passive control, the term 'active control' implies control of a system involving expenditure of energy from a source external to the system. Generally, the purpose is to minimize the difference or 'error' between the instantaneous desired and actual behavior of the system. Control may be exercised with feedback of information about the actual response of the system (closed-loop control) or without feedback (open-loop control). The field of active control of combustion is concerned both with control of dynamics, notably combustion instabilities, and with various forms of the 'regular' problem, for example maintaining operation to optimize some property of the performance.

Although the earliest proposals for active feedback control of combustors, and the initial experiments, were motivated by the intention to control combustion instabilities in rockets, ramjets, and afterburners, subsequent work has demonstrated other possible applications. Thus one can now conceive of situations in which the purpose of introducing active combustion control (ACC) may be one or a combination of two or more of the following: (1) improve the performance of a combustor (e.g., reduce pollutant and/or noise emissions, reduce specific fuel consumption, increase combustion efficiency, improve pattern factors in gas turbine combustors, etc.); (2) permit modification of combustor design (e.g., reduce its length); (3) damp combustion instabilities; (4) increase combustor reliability; (5) extend operational limits of combustors (e.g., permit stable operation at lower equivalence ratios); and (6) improve performance of other military combustion processes such as shipboard incineration, and power and heat generation in the field. Because the practical problem of suppressing combustion instabilities has been the chief motivation for investigating ACC, it is useful to explain some broad aspects of the subject by considering feedback control of unsteady motions in a combustor. The essential reason for the presence of instabilities in a combustion system is the existence of internal feedback such that energy may be transferred to a fluctuation at a rate dependent on the fluctuation itself. Passive control involves changes of design, (e.g., in the composition or types of reactants, injection system, chamber geometry) either (1) to reduce the rate at which energy

---

[*] Part of the materials presented in this chapter were excerpted from the AGARD Report 820, entitled "Active Combustion Control for Propulsion Systems," authored by K. Schadow, V. Yang, F. Culick, T. Rosfjord, G. Sturgess and B. Zinn.

is transferred to the unsteady motions or (2) to increase losses of energy, for example by the use of suitable resonators to introduce a dissipative process. Use of active control may be effective by causing either (1) or (2) to occur by sensing the instabilities and then using a feedback control loop to modify one or more input parameters. What may be possible, or what actually happens in a particular case, can be established only by understanding the system in question.

In the experimental work reported to date, relatively simple laboratory burners are typically used, having relatively large length/diameter ratios, although demonstration has been made in two full-scale land-based gas turbine applications. The undesirable oscillations often have motions largely in the axial direction. Control has been exercised, or at least the levels of oscillations have been reduced, by applying several methods of actuation, the most common being: forcing the motion of a portion of the boundary, for example of the inlet; injecting acoustic waves with a loudspeaker; and modulating the primary or a secondary fuel supply. A typical arrangement for active control of combustion instabilities in a dump combustor is sketched in Figure 1 involving actuation, A(t), achieved by modulating the flow through a fuel injector. The actual performance of the system is monitored by two pressure sensors, for the real-time, s(t), and time-average, $\bar{s}$ (t), condition monitoring, respectively . Three different levels of ACC are shown. The first (marked 1) shows an open-loop operation in which the actuator is used without any feedback. The second (marked 2) adds a fast sensor to provide real-time feedback for control of the actuator signal. The third (marked 3) employs an additional sensor to detect the overall performance in a time-averaged sense. This sensor output is used to adjust the controller parameter to adapt to changes in operating conditions. In general more than two sensors could be used, distributed in space and measuring several properties of the motions, for example velocity and radiation in addition to the pressure.

For the control circuit 2 shown in Figure 1, the information acquired by the sensor must be processed and used within the feedback loop to activate a controller whose output drives the actuator according to a control law. Most demonstrations to date have used simple control laws which dictate oscillatory actuation at some phase relative to the sensed response of the system, and at some amplitude found to give best results, i.e., lowest amplitude of oscillations. That approach is a special form of classical PID (proportional/integral/derivative) control in which the control signal is proportional to the error itself, its time-integral, and/or its derivative. The conditions for optimal control influence have always been obtained experimentally with little preparatory design work, a consequence of the lack of knowledge of the systems under investigation.
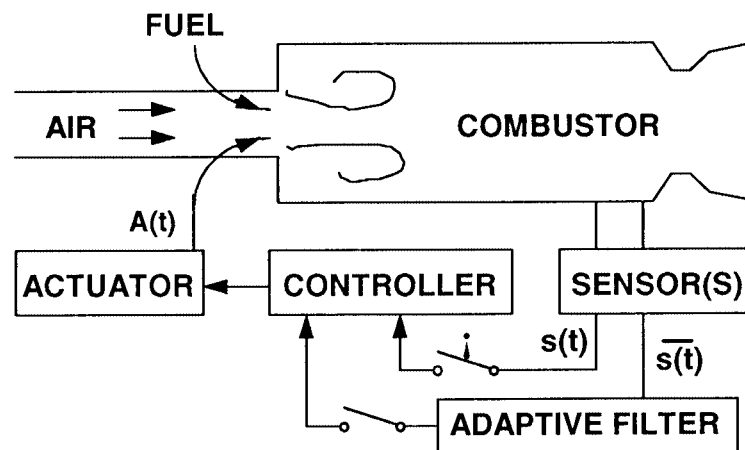

Fig. 1 Active Control Arrangement to Suppress Combustion Instabilities in Dump
Combustor.

According to the preceding remarks, there are broadly four areas in which research and development must proceed to form a firm basis for practical applications of ACC: sensing, actuation, formulation of control laws, and understanding of the systems to be controlled. As part of the progress required, it is essential to acquire understanding of the scaling laws, particularly with respect to the power density of a combustor. This short course covers a broad range of issues ranging from future requirements of combustion systems to topics of basic research that must be addressed to realize the promise of active control of combustion.

2. Background

Although active feedback control had been posed and investigated for a restricted class of problems in the early 1950s for reasons cited in the preceding section, the idea was not pursued experimentally until the 1980s. It seems fair to recognize that the work at Cambridge University, supported by Rolls Royce with a view to application to afterburners, marked the beginning of the recent considerable activity in this area (see References 14 through 19). Indeed, the sequence of increasingly more elaborate experimental projects within the program introduced many of the novel ideas which have subsequently been vigorously pursued by a large number of research groups throughout the world. In particular, many of the types of sensing and actuation now being investigated were first used at Cambridge.

The general notion of active feedback control of combustion dynamics has recently attracted considerable interest of customers and manufacturers, mainly those producing systems for propulsion and stationary power generation. The chief reasons for this attention include: the trend toward higher combustor pressure (particularly in the past twenty years or so) not only for higher performance in some sense, but also for smaller size, improved efficiency, and reduced emissions of pollutants. While overall efficiency of a system has in the past been largely a matter of gaining a competitive advantage, independent of any regulatory practices, that is no longer the case. Increasingly stringent specifications on pollutant generation will likely be met not only by reducing the amount of pollution produced in combustion of a unit mass of fuel, but also by requiring less fuel to generate a unit of power output or thrust. Those requirements and the traditional methods of achieving desired improvement are discussed in Section 3. An implication of that discussion is that the customary methods of design changes (a strategy of 'passive' control) seem to be approaching their limits. Hence the interest in active control is a direct consequence of widespread practical motivations.

On the other hand, the subject of active control of combustion remains primarily a matter of research. Apart from a small number of relatively recent observations of emission levels, practically all work on ACC has been concerned with control of coherent pressure oscillations, i.e. combustion instabilities. The general reasons why research on active control of combustion dynamics has concentrated on control of combustion instabilities are easy to understand. First, it is generally true that as designs of combustors are pressed to give higher performance – normally a matter of raising power density – the likelihood is also raised that combustion instabilities will occur. Many examples exist for rockets, ramjets, and afterburners. Second, in the past several years, instabilities have become a serious problem in gas turbine combustors under quite different circumstances. In order to reduce production of nitrogen oxides, it is desirable to consume much of the fuel with lean burning to reduce the temperature. That implies operating a combustor as close to lean blow-out as possible. But then the global combustion process – the flame – tends to become unstable. The consequent unsteady motions can couple to global motions in the chamber, producing combustion instabilities.

Finally, there is a class of practical applications including heaters and incinerators of waste, for which intentionally pulsed combustion is effective for improved efficiency. Active control of pulsed combustion is attractive to ensure optimum operating conditions, avoiding, for example, inadvertent operation when the pulsations can cause unacceptable rates of surface heat transfer or reduced efficiency.

3. Requirements for Future Combustors

Active combustion control is a technology that requires basic research and development for all components of an active control system – sensor, actuator and controller. It is therefore appropriate to identify the projected needs and challenges for future combustors when determining the application opportunities for active control. This section provides a brief assessment of the requirements for future combustors as used in aeroengine and surface gas turbines.

Gas turbine engines have been developed for either aeroengine propulsion or surface power/propulsion. The aeroengine device, which is used for both military and commercial aircraft, always uses direct fuel injection in the combustor. That is, the liquid fuel is injected (often by an airblast fuel nozzle) into the combustor, where the physical processes of atomization, vaporization and fuel-air mixing occur. In contrast, surface power/propulsion devices, which can be used for ground power generation or ship propulsion, may utilize either direct-fuel-injection or fuel-air premixing. The former is identical to aeroengine combustors, but in the premixed arrangement, the aforementioned physical processes are essentially completed prior to entering the combustor. One consequence of fuel-air premixing is that the heat release is more concentrated. Because of the differences in fuel preparation, the requirements for aeroengines and premixed surface power/propulsion gas turbine combustors may be different.

3.1 Aeroengine Gas Turbines

Aeroengine gas turbines provide propulsion for aircraft, both military and commercial. In addition to requirements on performance and emissions that accompany any powerplant, there is a premium on achieving them in a compact, light-weight device that is very fuel efficient and highly reliable. These demands are projected to become increasingly severe for future aeroengine gas turbines. It is important to determine enabling technologies that might mitigate these challenges.

The basic performance trends for aeroengine gas turbines have been toward increasing thrust-to-weight ratio for military devices, and lower specific fuel consumption (i.e. fuel flow rate per pound of thrust) for commercial devices. The former is sought to increase maneuverability, while the latter supports reduced operating costs. Among the consequences common to both goals is the trend toward higher pressure ratios, with higher temperatures at both the combustor inlet and exit.

Based on these performance trends and mission-driven engine configuration studies, it is concluded that operating conditions for combustion systems will continue their historical trends toward increasing stringency. With long-term goals of doubling thrust-to-weight ratio and reducing specific fuel consumption by 25 to 50 pct, overall pressure ratios in the range of 50 to 75 are virtually certain, and values up to 100 are possible. For commercial applications, bypass ratios could increase to as high as 25 using gear-driven fans. For military applications bypass ratios will be more modest, but turbine inlet temperatures will increase significantly to values associated with combustor equivalence ratios of 0.5 - 0.7. These targets reflect the range of set-point operation over the power curve. The desire for military systems with shorter acceleration/deceleration response times imposes additional demands for more rapid transients between the set-point conditions. At times, the static stability of the combustor, and its adjacent components, will be exceeded.

These projected performance trends will impact the combustor design. Burning-length-to-dome-height ratios will approach 1.5, with a mean radius in the range of 216 to 250 mm (8.5 to 10 in.), regardless of engine airflow; dome heights will be in the range of 50 - 150 mm (2 to 6 in.) depending on the core engine airflow. Combustion intensities will range from 100 to 160 MW / m^3/ bar (10 to 16 MBtu / hr / ft^3/ atm). While the general combustor configuration will likely remain annular, the combustor inlet section diffuser may be changed for overall engine pressure ratios above 70. Specifically, passage heights in axial-flow compressors at very high pressures can become so small (depending on core engine airflow) that losses due to secondary flow begin to dominate, preventing final high efficiencies from being achieved. Under such circumstances, the final stages of compression might necessarily be done through one or more centrifugal-flow stages. This could have severe impacts on combustor configuration. At high pressures, secondary flow losses might also present difficulties for feeding shower-head cooling schemes in the leading edges of turbine inlet guide vanes. Therefore, shower-head cooling requirements might preclude the use of ultra-low pressure loss combustors in engines with very high overall pressure ratios. Also, the high fuel turndown ratio associated with high temperature turbines will make fuel-staged combustion systems common.

In order to cope with the requirements for future combustors, enabling technologies must be identified. For the demands discussed above, advances in high pressure fuel pumps, high temperature combustor liner materials, and fuel systems capable of handling super-critical fuels are required. Furthermore, in order to preserve and improve the combustor performance at these severe conditions, means are required for promoting the mixing of fuel, air, and combustion products in the burner, and for preserving stable operation under both steady-state and transient conditions. That is, the critical requirement for achieving the high combustion intensities associated with high pressure conditions, in reduced-size devices, is improved mixing of fuel and air inside the burner. Fuel-air premixing, such as used in some surface power/propulsion gas turbines, is precluded because of the very short autoignition time associated with very high pressure ratio cycles. While adequate mixing and an extremely high combustion efficiency is readily achieved for very fuel-lean operation, efficiency could become mixing-limited for higher equivalence ratios. Improved mixing is also necessary to minimize undesirable emissions of NOx, CO, and smoke at higher equivalence ratios. Further, the increased combustion intensity at any set-point may increase the likelihood of coupling with acoustic waves, promoting combustor dynamics problems. Such problems may also be exacerbated by faster transient responses.

The chemical reactions that determine energy release and pollutant formation occur on the molecular scale. However, the flow in a combustor is turbulent, and the mixing process must cascade down to the smallest eddy before molecular processes can become significant. The minimum turbulent length scale (Kolmogorov) determines the smallest mixing length scale. At atmospheric conditions, this scale is approximately 0.4 mm (0.015 in.) and decreases by three-orders-of-magnitude at 100 atm. In contrast, the dimension of the flow field structures are of

the same order as the combustor geometry, which are on the order of 100 mm (4 in.). Hence, the mixing process must progress through an enormous dynamic range before molecular reactions can occur in significant amounts. While a wide range of eddies always exists in the combustor, achieving the stringent standards for efficiency and emission control requires that this mixing cascade occurs quickly and efficiently. That is, to achieve worthwhile improvements in mixing at fixed pressure loss will demand dramatic reduction in the characteristic "integral" turbulent length-scale associated with combustors. Radical geometric changes, such as reducing the combustor characteristic length scale by an order of magnitude, or greatly increasing the number of active shear layers to promote many length scales, appear to be essential.

3.2 Premixed Surface Power/Propulsion Gas Turbines

Surface power/propulsion gas turbines provide either ground power or propulsion for ships. Among the critical requirements for these gas turbines is high power density (power per occupied volume), high durability, and extremely low emissions. The latter is distinctively different than for aeroengine gas turbines, with allowed emission levels more than an order-of-magnitude lower. While this standard may not be required of all surface gas turbines (e.g. emission goals for ship propulsion are currently less strict than for ground power gas turbines), economics should drive manufacturers to develop only one surface gas turbine design. Since the lowest levels of emissions are obtained through the flame temperature control achieved with premixed combustion, and ground power gas turbines must strive for the lowest emissions levels to be competitive, the industry standard for new surface gas turbines is premixed combustion. The trend in development of surface gas turbines is toward lower emissions levels and higher cycle efficiencies. The former is driven by (real and anticipated) air quality regulations, while the latter affects operating cost (i.e. "cost of electricity"). Currently, many ground power gas turbines guarantee NOx and CO exhaust concentrations limited to 25 ppm @ 15 pct oxygen (i.e. parts per million at a standard exhaust flow dilution to achieve 15 mole pct oxygen). Future products will strive for "single digit" (e.g. 9 ppm) guarantees. Depending on the application, such emission goals may result in engine cycles other than the "simple (Brayton) cycle" – cycles which, for example, extract heat of compression (i.e. "intercool") between two compressors.

The lowest level of emissions is achieved by employing a premixed combustion strategy. Generally, a fixed distribution of effective flow area divides the combustor airflow and delivers the greatest fraction to the set of premixing fuel nozzles. The maximum airflow fraction, or leanest fuel-air mixture, is limited by the lean blowout (LBO) mixture, which is the leanest mixture which will sustain combustion. If the premixing airflow fraction is increased (starting from a high fuel-air ratio), then the fuel-air ratio, the flame temperature, and the formation rate of NOx all decrease. However, as the fuel-air ratio approaches the LBO level, the flame temperature will not support sufficiently fast CO oxidation rates and its concentration in the combustor exhaust increases. That is, CO acts as a precursor to marginal stability, reflecting either globally reduced oxidation or the presence of sub-LBO fuel-air pockets which have extinguished. Hence, as depicted in Figure 2, there is a "window" of fuel-air ratio, and of corresponding flame temperature, that will simultaneously result in low NOx and CO. The width of the window will depend on both the inherent combustor stability characteristics and the level of desired emissions control. The figure shows the window width for sub-25 ppm levels; the window is clearly narrower for lower limits. Generally, homogeneous (i.e. non-catalytic) combustion systems do not provide a window width covering the full mixture (or temperature) range experienced from low to baseload gas turbine power. Hence, to preserve ultra-low emissions over a wide power range will require shifting the premixing airflow fraction as the overall fuel-air ratio changes to remain within the desired flame temperature window. It is also true that as the fuel-air mixture approaches the LBO limit, thermoacoustic instabilities become more prevalent. Indeed, premixed combustion with its intense heat release gradients provides greater opportunities for coupling with the acoustics and fluid mechanics, and remedies to combustion instabilities are a common development challenge.
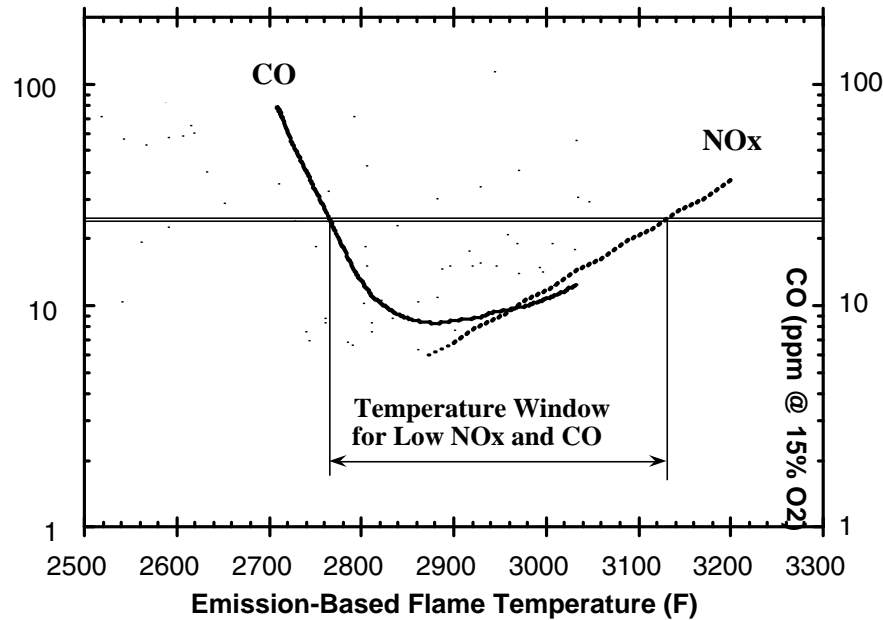
Fig. 2 Flame Temperature Window for Both Low NOx and CO from Premixed Combustion.

4. Classification of Instability Modes and Driving Mechanisms

Because instabilities arise from sources entirely internal to the system, an external observer perceives the result as the dynamical behavior of a self-excited system capable of exciting and sustaining oscillations over a broad range of frequencies. Typically, the oscillations grow out of a re-enforcement between the noise inherent in the combustion process and the acoustic modes of the feed-system/combustion chamber combination without benefit of any other external influence. The prevalence of instabilities in gas turbine engines is primarily due to two fundamental reasons:

1) combustion chambers are almost entirely closed and the internal processes tending to attenuate unsteady motions are weak; and
2) the energy required to drive unsteady motions represents an exceedingly small fraction of the heat released by combustion.

These underlying causes are present in any combustion chamber, but are especially consequential for gas turbine engines in which the energy intensity is extremely high, typically on the order of $100 \, MW/m^3/bar$. In typical instances, less than 0.1% of the chemical energy release rate is sufficient to generate pressure oscillations having peak amplitudes equal to the mean chamber pressure. This striking result leads to two immediate conclusions. First, the possibility of instabilities in an engine must be recognized and anticipated from the beginning of a development program. Second, the existence and severity of combustion instability can be sensitive to very minor changes in the system. Without enhanced understanding, the occurrence of potential combustion instability problems must be regarded as part of the price for the development of any new system. Basic research into understanding, bypassing, and controlling the mechanisms responsible for the initiation and growth of combustion instabilities is a crucial step toward minimizing the delays and costs of solving these problems during the development process.

Current solutions to occurrences of combustion instability in gas turbine engines involve three approaches: (1) use of prescribed air/fuel ratio variations among individual elements of injectors, (2) systematic introduction of a pilot flame, (3) use of acoustic dampers to suppress specific acoustic modes, and/or (4) implementation of active control techniques. One or more of these approaches may be introduced, depending on the severity of the combustion instability problem, and typically empirical engineering approaches must be applied.

Several modes of oscillations have been commonly observed. They are often classified according to their spatial structures and driving mechanisms as low, intermediate, and high frequency instabilities. Low frequency

instabilities, also known as 'buzz', received much attention in many gas-turbine development programs. Characteristically, this mode corresponds to the vibrations of a Helmholtz resonator, with a frequency range between a few and several hundred Hz. Two sources may give rise to its occurrence. The first is associated with the interactions between the unsteady combustion in the chamber and a specific portion of the fuel feed system. The second arises from the coupling between entropy waves and acoustic motions in the chamber. It is well established that, fluctuations of the reactant mixture ratio (i.e., fuel/air unmixedness) may lead to entropy waves, which then interact with the nonuniform mean velocity field in the chamber to generate acoustic waves.

High frequency instabilities, often called 'screeching' or 'screaming,' are the most common and vexatious, and are characterized by reinforcing the interactions between acoustic oscillations and combustion processes inside the combustion chamber. Depending upon the response of combustion processes to chamber oscillations, energy can be fed into acoustic waves such that their amplitude grows. The most destructive result of these large amplitude pressure excursions is the increased heat transfer to the chamber walls and excessive vibration. Burn-throughs can occur in a few seconds or less, causing complete failure of the engine. This type of instability is usually characterized by well defined frequencies and mode shapes that correspond closely to the classical acoustic modes of the chamber. Fundamental modes of high frequency instabilities are thus categorized as longitudinal and transverse, according to the spatial character of unsteady motions within the combustion chamber. Longitudinal modes propagate along in the axial direction of the chamber, with no variation in the transverse plane and are usually observed in chambers with large length-to-diameter ratios. Transverse modes exhibit no axial variation in oscillatory behavior, but propagate radially and tangentially along planes perpendicular to the chamber axis. For contemporary engine designs in which the chamber aspect ratio and nozzle contraction ratio are relatively small, pure transverse modes of oscillations dominate because of the effective damping of the longitudinal oscillations by the nozzle and the distribution of the combustion along the chamber. Combined modes comprised of the superposition of longitudinal and transverse modes are often observed in annular combustors.

Each transverse mode may exist in three forms: radial, standing tangential, and spinning tangential waves. The differences between standing and spinning tangential modes can be visualized by plotting particle trajectories for these two modes of oscillations. Particles move back and forth for the standing mode of oscillation, but have an epicyclic trajectory around the chamber in the tangential direction for the spinning mode of oscillation. The standing mode particle trajectory can be explained by the fact that the acoustic velocity varies oppositely in consecutive cycles with respect to the fixed pressure nodal surface. The situation is similar for the spinning modes of oscillation, except now the pressure nodal surfaces rotate with angular frequency corresponding to the model frequency; therefore, particles move in a net circular fashion as time elapses. Spinning wave motions seem to be usually more detrimental because of their effectiveness in agitating gas molecules in transverse directions, thus enhancing heat transfer to the chamber walls. However, spinning waves may also be accompanied by an increase in combustion efficiency, presumably due to accelerated mixing processes. This phenomenon of increased efficiency accompanied by decreased stability is a common trade-off in engine designs, and the ability to design for both efficiency and stability simultaneously represents one potential payoff for instability research.

Several possible mechanisms have been proposed that may be responsible for driving combustion instability. Of the various intermediate processes occurring during the combustion, atomization, vaporization, droplet interaction, mixing of the vaporized propellants and chemical kinetics are the most sensitive processes to the oscillations of velocity and pressure. For discussion purposes, the non-steady effects considered here can be divided into two groups: effects associated with atomization and vaporization, and effects related to the mixing process.

The atomization and jet breakup process, and its relationship to spray formation through pressure, temperature and velocity perturbations, can affect the energy release characteristics of the gas phase, and thus the stability of the combustor. The vaporization process that is directly related to the local pressure, temperature, and velocity, will be affected by oscillations in these quantities. Furthermore, there can be mixture ratio gradients in the vapor because of the stratification of the liquid spray in the injector. If the transverse acoustic field is imposed on such a spray, the vapor will be displaced relative to the droplet, causing mixture ratio oscillations in the vicinity of each vaporizing droplet. Hence, there will be an oscillation in the burning rate, which can couple with the acoustic field to produce a spinning mode of combustion instability.

When the vaporization rate becomes extremely high, it is possible that a droplet is heated rapidly through its critical temperature. With droplet shattering, clouds of the very fine secondary droplets are rapidly gasified. In such cases, the burning rate could be controlled by the rate of gas-phase mixing. Again, this oscillation of the burning rate is coupled with the acoustic field to generate flow oscillations.

5. Stability Analysis

To begin to understand the essential characteristics of combustion instabilities, it is best first to distinguish linear and nonlinear behavior. Linear behavior presents only one general problem, linear instability, which received widespread attention during the 1950s and 1960s; see, e.g., the monograph by Crocco and Cheng[71] and the comprehensive compilation of works edited by Harrje and Reardon,[7] and Yang and Anderson.[72] Any disturbance may be synthesized as an infinite series of harmonic motions. An approximate analysis developed over many years (see Culick[33] and Culick and Yang[44]) allows one to use classical acoustic modes as the terms in the series and to compute the perturbations of the complex wave number for each mode due to various contributing processes in a combustion chamber. The real part of the wave number gives the frequency shift, and the imaginary part gives the growth (or decay) constant associated with each mode. Vanishment of the imaginary part determines the formal condition for linear stability, whose dependence on the parameters characterizing the system is then known.

Two basic nonlinear problems arise when dealing with combustion instabilities: determining the conditions for the existence and stability of limit cycles for a linearly unstable system and finding the conditions under which a linearly stable system may become unstable to a sufficiently large disturbance. In the language of modern dynamical systems theory, these two problems are identified as supercritical and subcritical bifurcations, respectively. The term bifurcation refers to the characteristic that the character of the steady behavior of the system suffers a qualitative change abruptly as a parameter of the system is varied continuously. This may at first seem an unnecessarily formal description of the phenomenon. In fact, the framework provided by the approximate analysis and application of some of the ideas of dynamical systems theory forms a widely useful and convenient basis for understanding combustion instabilities.

Figure 3 is a schematic diagram suggesting the commonly accepted point of view of combustion instabilities. A measurement of pressure at a fixed location shows, roughly, a time dependence similar to the for the displacement of a simple mechanical oscillator. Hence, it is natural to suppose that the fluctuation of pressure from its mean
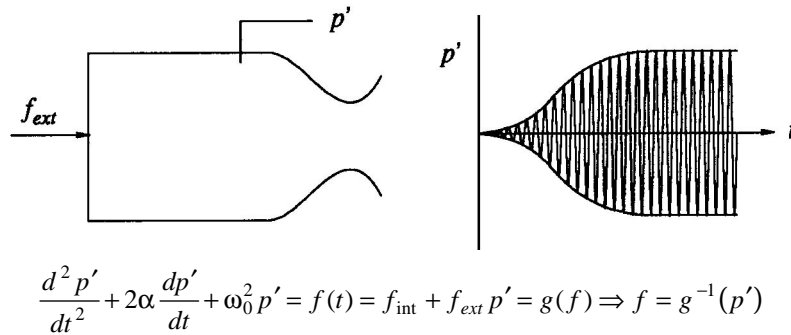

$$\frac{d^2 p'}{dt^2} + 2\alpha \frac{dp'}{dt} + \omega_0^2 p' = f(t) = f_{\text{int}} + f_{ext} \quad p' = g(f) \Rightarrow f = g^{-1}(p')$$

Fig. 2 Pressure oscillations in a combustion chamber.

value satisfies the oscillator equation with damping constant α, natural frequency ω_0, and forcing $f(t)$,

$$\frac{d^2 p'}{dt^2} + 2\alpha \frac{dp'}{dt} + \omega_0^2 p' = f(t) = f_{\text{int}} + f_{ext} \tag{1}$$

Usually there are no significant external forces acting on the flow in a combustion chamber: it is a good approximation to neglect f_{ext}. Then the internal force represents those processes not typically accounted for in α and ω_0, notably combustion and, in some formulations, nonlinear behavior.

For the moment, we confine attention to linear behavior exhibited as the exponentially growing amplitude in Fig. 3. It is convenient to assume that the terms $2\alpha \, dp'/dt + \omega_0^2 p'$ contain all linear processes except those associated with combustion. Thus, the internal forcing f_{int} contains the mechanisms tending to excite the instability. Although a priori determination of f_{int} is not always feasible, the following heuristic form may be assumed as a physically useful representation:

$$f_{\text{int}} = q(p') = 2\alpha_c \frac{dp'}{dt} + \omega_c^2 p' \tag{2}$$

With a view to later remarks on active control of combustion instabilities, we interpret the preceding model with the block diagram drawn in Fig. 4. The equation of motion, Eq. (1), is abbreviated by the relationship $p' = g(f)$ between the input (sum of internal and external forcing) and the output. The internal forcing (i.e., combustion response) depicted in Fig. 3 appears as a feedback path. Because the system is linear, the Laplace transform may be applied to present the system in the frequency domain. The transfer function relating the pressure to the external force is

$$\frac{P(s)}{F_e(s)} = \frac{G(s)}{1 - Q(s)G(s)} \tag{3}$$

[Note that the force f_{int} is fed back positively to correctly represent the system defined by Eq. (1); hence, the minus sign, rather than the more familiar plus sign, appears in the denominator of Eq. (3).] The natural motions, possible when no external force is acting, are defined by equating the denominator of the transfer function to zero.

$$Q(s) G(s) - 1 = 0 \tag{4}$$

For the simple example here, with Eqs. (1) and (2) we find

$$G(s) = \frac{1}{s^2 + 2\alpha s + \omega_0^2} \qquad \text{and} \qquad Q(s) = 2\alpha_c s + \omega_c^2 \tag{5}$$

Substitution in Eq. (4) gives

$$s^2 + 2(\alpha - \alpha_c)s + \left(\omega_0^2 - \omega_c^2\right) = 0 \tag{6}$$

The roots of this equation are

$$s = -(\alpha - \alpha_c) \pm i\sqrt{\left(\omega_0^2 - \omega_c^2\right) - (\alpha - \alpha_c)^2} \tag{7}$$

Hence, as earlier argued, s has a possible positive real part, and the natural motion is unstable is $\alpha_c > \alpha$, assuming both α and α_c to be positive.

The condition $\alpha - \alpha_c = 0$ defines neutral stability; motions neither grow nor decay. When $\alpha - \alpha_c$ is expressed in terms of the parameters characterizing the system, the locus $\alpha - \alpha_c = 0$ in the space of parameters is called the stability boundary. In the literature of combustion instabilities, the stability boundary is normally computed in a quite different fashion but, as we shall see later, the results are equivalent.

A continuum, such as the gaseous environment inside a combustion chamber, is basically an infinite degree of freedom system. For time-harmonic behavior of the (linear) unsteady motions, however, the chamber boundary conditions allow solutions only at discrete modal frequencies. Each mode can basically be treated as a one-degree-of-freedom oscillator, demonstrating the utility of Eq. (1). It is with frequency. Therefore, the degree to which combustion destabilizes a mode depends on the frequency of the mode itself. If the energy gain due to combustion response is greater than energy damping, then an instability of the particular mode results. Mathematically, this condition is equivalent to having a positive real part of an eigenvalue in Eq. (7).

Although practical situations are profoundly more complex than the simplified system in Fig. 4, the preceding remarks summarize the basis for treating, and if possible eliminating, combustion instabilities in practice. Beginning with an unstable mode, there are clearly several ways to achieve the desired result that the modes should be stable. First, damping might be increased with the addition of attenuating devices, such as small resonant cavities or acoustic liners, a common practice in liquid-propellant rocket engines. This tactic will cause a small frequency shift, but a second method of stabilization involves changes of geometry to displace the resonant peaks sufficiently in frequency so that no peak is lower than the driving curve. That is one consequence of using baffles: breaking the chamber into effectively smaller compartments introduces new internal boundary conditions, causing the normal modes to occur at lower frequencies. On the other side of the energy balance, the strategy consists in reducing the driving in the vicinity of the unstable resonance. That is, generally, a more time-consuming and
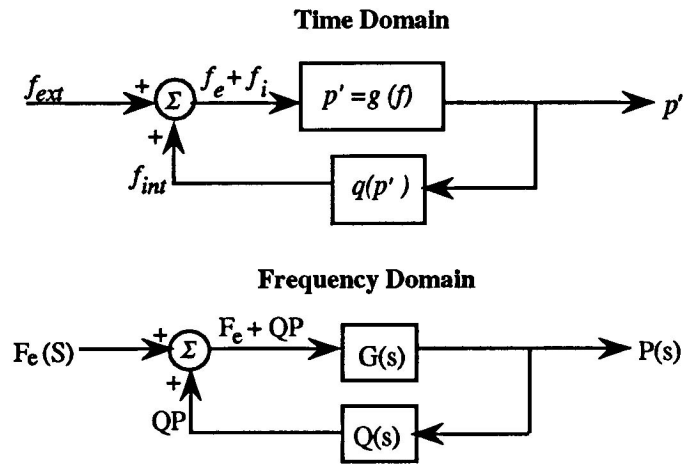
Time Domain

Frequency Domain

Fig. 4 Feedback loop of unsteady motions in a combustion chamber.

expensive procedure but is commonly a necessary approach when it is not possible to introduce sufficient damping to stabilize the system. Work to change injector design or the entry conditions of the injected propellants, in some sense never thoroughly understood, produces favorable effects on the driving curve.

6. Implementation of Active Combustion Control

The concept of active combustion control has appeared in several forms over the past four decades. The first attempt was made by Tsien[11] in an effort to apply control theories to suppress the chugging instability in a liquid-propellant rocket engine. His analysis was based on a combustion model which considered a pressure-dependent time lag between the instants of propellant injection and burning. Stabilization of the combustion conditions was achieved by modulating the propellant injection rate through a capacitor controlled by a servomechanism with pressure feedback. The problem of intrinsic stability was studied using the Nyquist plot to determine the suitable servo coefficients. Similar approaches were used by Marble and Cox[12] and Lee et al.[13] to control the low-frequency instabilities in bipropellant liquid rocket engines. However, no experimental results based on this "servo-stabilization" concept have been published, primarily because of the limitations of instrumentation at that time.

With recent developments in fast-response sensors and actuators, some interesting studies on the active control of various problems have been reported. Ffowcs-Williams[14] described the concept of "anti-sound" — the elimination of unwanted oscillations in an acoustic field by means of acoustic interference. The basic idea is to first determine the characteristics of a given acoustic field, and then to use that information to manipulate a secondary source of sound which serves as an acoustic actuator. Control is achieved by producing waves out of phase with the unwanted oscillations. In principle, this wave-cancellation technique is applicable to combustion systems; however, implementation to a full-scale combustor is quite unlikely because the energy density of the oscillatory flow field may well exceed that which can be matched by such acoustic actuators as loudspeakers. Furthermore, as a result of the intrinsic richness of the thermo-acoustic interactions, implementation of a control system in a combustion chamber is much more complicated than for normal temperature and pressure environments.

Practical applications of the active control of combustion instabilities have been demonstrated in several research experiments. At Cambridge University, Dine[15] showed that the instabilities of a flame burning on a gauze in a Rijke tube can be eliminated as follows. First, the light emitted from CH free radicals was monitored as a measure of the unsteady heat-release rate from the flame. This information was then processed and fed back to a loudspeaker placed near one end of the tube to increase the acoustic energy dissipation from the boundary. The same problem was studied by Heckl.[16,17] However, instead of a photo-multiplier, a microphone was used as the sensor to excite the loudspeaker. Results indicated that instabilities can be suppressed over a wide range of phase difference between unsteady oscillations and actuating pressure waves, provided the control gain is sufficiently large. This observation clearly demonstrated that the control of combustion instabilities can not be explained simply by the principle of anti-sound, which requires that the control excitation be precisely out of phase with existing oscillations.

More recently, Bloxsidge et al.[18,19] reported the control of low-frequency combustion instabilities in a laboratory jet-engine afterburner. The mass flow into the combustion chamber was varied by oscillating a center body inserted in the choked inlet nozzle, thereby exerting the necessary modifications on the unsteady flow fields. The system was partially successful in suppressing the instabilities, with the amplitude of the fundamental mode reduced by fifty percent.

Lang et al.[20] and Poinsot et al.[21,22] explored the active control of instabilities in a small laboratory burner, using a loudspeaker as the control actuator. Both experiments used the same gaseous reactants, but with two different types of flame holders: a multiple orifice plate with 80 holes placed in a premixed propane-air stream; and an array of three rearward-facing steps through which fuel was injected into the air flow. Acoustic pressure was measured by a microphone located upstream of the chamber. The signal was then filtered, phased-shifted, amplified, and sent to a loudspeaker attached to the burner. In addition to the demonstration of instability control, their work showed that the active control technique can be used effectively to study the initial transient behavior of instabilities.

One feature common to the above approaches is that they all used mechanical means, such as loudspeakers or moving bodies, to suppress instabilities. For practical systems containing high energy density, implementation of these means may not be feasible due to the relatively large amount of power required to drive control actuators. It appears that the most direct method of control should be based on the manipulation of energy sources of oscillatory flow fields. Langhorne et al.[23] reported that pressure oscillations in a laboratory afterburner can be reduced significantly by a controlled secondary supply of fuel which is effective in generating the energy necessary for instability control. This method offers a promising solution to problems of low-frequency oscillations in full-scale combustors. Sivasegaram et al.,[24] Billoud et al.,[25] Wilson et al.,[26] and Schadow et al.[27] have all demonstrated experimentally the effectiveness of this technique. The theoretical study of Yang et al.[28] and Fung et al.[29] and the numerical simulations of Menon,[30] Shyy et al.,[31] and Neumeier and Zinn[32] have also demonstrated the viability of controlled fuel injection. For detailed reviews of active control of combustion instabilities, see Culick,[33] Candel,[2] McManus et al.,[1] and Zinn and Neumeir.[68]

In addition to its applications for propulsion systems, active control technology has been used to enhance mixing in incinerator afterburners and to increase the DRE (destruction and removal efficiency) for waste materials. Parr et al.[9] have conducted a detailed study of the concept of utilizing vortex combustion for incineration in a small-scale gaseous fuel system and an extension to a more practical system using liquid fuels. Acoustic excitation was used to stabilize coherent vortices in the air flow, with the fuel modulated and introduced into the air vortex exactly at the instant of vortex formation. This concept has demonstrated its effectiveness in improving waste destruction. The DRE for liquid benzene exceeded 99.999% for a afterburner/incinerator of 56 kW energy release, even when the waste surrogate constituted 17% of the total fuel content. The controller also reduced emissions: CO dropped from 2900 ppm to as low as 2 ppm and NOx was reduced to 12 ppm. Parameters critical to the controller performance were the forcing level of the fuel injection, the fraction of the circumferentially entrained air, and the phase angle of the fuel injection with respect to the air vortex roll-ups.

The most common sensor used in ACC is the pressure transducer. For controlling combustion instability this is a natural choice, as the instability is characterized by the chamber pressure oscillations. Experimentally, photomultipliers have also been successfully used, since their signals can give a measure of the unsteady heat release which is at the root of the instability. The placement of either type of sensor is important. For example, the shapes of the chamber acoustic modes should be sufficiently well-known to avoid placing a pressure sensor at a pressure node point. Also, a photomultiplier's signal could be misleading if the sensor is positioned so that its field of view does not completely cover the entire range of motion of a spatially varying reaction zone. Recent advances in machine vision applied to an array of optical sensors may offer a solution, and also provide the controller with information regarding the global distribution of unsteady heat release. Of course, optical access (including interference by sooty flames) is another problem. Other optical sensors, such as laser-induced fluorescence for species measurement and LDV for velocity sensing are probably unfeasible for practical applications, but may be useful in experimental control systems. Optical sensors may be key in pattern factor control, since the temperature distribution throughout the cross section of a chamber is desired.

For combustion instability control, most ACC actuators attack either the acoustics (directly with mechanical acoustic actuation or indirectly through controlled fuel flow), or the hydrodynamics of a reacting shear layer in a dump combustor (by fluid dynamic forcing near the origin of the shear layer). The former approach is sensible in that chamber acoustics play a defining role in the energy feedback loop which causes high-frequency instabilities. The latter approach also has intuitive merit since the spatial and temporal unsteadiness of the heat release (source of energy for the instability) is strongly tied to the turbulent hydrodynamics of the shear layer. Both actuators have demonstrated varying degrees of success in closed-loop control, and shear layer actuation has exhibited positive influence in open-loop mode. Perhaps tandem acoustic and hydrodynamic actuation could accomplish more than either one alone.

7. Controller Design

A variety of feedback-control techniques, summarized in Table I, have been used for suppressing combustion instabilities. The most primitive type is the proportional (P)-controller in a single-input and single-output (SISO) setting, in which stability and performance are achieved only by an operational amplifier between the sensor and actuator. The P-controller can be extended to form a proportional-integral-derivative (PID) control system, in which the I-control is used for achieving zero steady error, since it integrates the error in time, and the D-control serves to enhance the transient response, since it regulates the tendency of motion.[35] Conceptually, there are only three control parameters in a single PID controller module, so that the controller design is greatly simplified. However, for high-order plant dynamics, such a low-order controller may not satisfy various performance requirements. For linear systems, a PID controller can be extended to accommodate a filter with phase compensation in the frequency domain, or to form an integral state-feedback controller in the time domain. If all states cannot be measured, an observer is needed for output-feedback control.[8,28] It is not difficult to design an observer for a finite-dimensional linear time-invariant (FDLTI) system, but it is much more challenging to design one for a time-varying or nonlinear system.

In the frequency domain, the open-loop dynamics of an FDLTI system can be conveniently represented by the Bode plot, through either physics-based modeling or system identification, or a combination of the two. The representation of system dynamics in the frequency domain simplifies the filter design, and the stability analysis can be based on the Nyquist criterion. The robustness of a controller is traditionally predicted in terms of phase and gain margins for single-input single-output (SISO) systems. When uncertainties are simultaneously present in both phase and gain, the issue of robustness can be expressed by the H_∞-based structured singular value (μ) of the closed-loop system.

Among the various time-domain tools for controller design, the linear quadratic regulator (LQR) controller appears to be the most robust, with its gain margin in the range of $[1/2, \infty)$ and at least 60° phase margin. However, the LQR controller can be applied only if all the states can be measured without any appreciable noise contamination. Otherwise, a state estimator is needed to meet this requirement. The resulting output-feedback control system is known as the linear quadratic guassian (LQG) controller, if a Kalman filter is used as the state estimator. The scheme may be further extended for nonlinear systems using an energy method in terms of the Lyapunov function. The major deficiency of the LQG technique lies in its failure to guarantee any gain and phase margin. The H_∞-based structured singular value (μ) approach allows for quantification of robust stability and performance for bounded uncertainties.

Non-model-based controllers, such as least mean square (LMS) and artificial neural network back-propagation adaptive controllers, employ iterative approaches to update control parameters in real time. However, those methods often encounter difficulties of numerical divergence and local optimization, and consequently may not guarantee stability and performance. In addition, most adaptive algorithms do not accommodate a physical model of plant dynamics. It is often risky to establish general rules for performance improvement and fault diagnostics based on approximate reasoning, such as fuzzy logic. Moreover, formulation of fuzzy logic rules requires an extensive physical understanding and operations experience that is not usually available for combustion dynamics.

While the control schemes summarized in Table I have been employed in various combustion problems with some success, direct implementation of these techniques on practical propulsion systems may not be feasible, due to lack of robustness, reliability, and operationability. Compared with mechanical devices, a combustion chamber with feedback control of fuel burning exhibits several distinct features:

- distributed actuation arising from the burning of injected fuel;
- time lag associated with the complex chain of fuel injection-atomization-ignition-combustion processes;
- intensive noise due to intrinsic fluid dynamic and combustion unsteadiness;
- time variation of mean flow conditions due to transient operation of the chamber; and
- model uncertainties and parametric errors resulting from physical assumptions and mathematical approximations employed for simulating system dynamics.

In view of the above, this paper uses the H_∞ theory may provide a reasonable solution for the design of a robust feedback control scheme for suppression of combustion instabilities. The controller provides robust stability and performance relative to specified bounds of model uncertainties, parametric errors and exogenous disturbances (e.g., chamber perturbations and sensor noise). The control law can be extended over a wide range of operating conditions.

Table I. Survey of Active Combustion Control Techniques

Control Technique	Application	References	Remarks
PID design	• Nonlinear generic combustion instability	• Fung and Yang [35]	1. easy to adjust control parameters. 2. may not fulfill various performance requirements.
Bode-Nyquist frequency domain design and Root locus	• Generic combustion instability • Low frequency combustion instability • Low frequency combustion instability • Coaxial dump combustor • Longitudinal combustion instability in premixed combustor • Thermoacoustic instability in premixed laminar combustor • Liqid-fueled combustion systems	• Bloxsidge, et al. [19] • Langhorne, et al. [23] • Fung, et al. [29] • Schadow, et al. [27] • Gulati and Mani [69] • Annaswamy and Ghoniem [70] • Hantschk, et al. [67]	1. easy to identify systems and design controller in frequency domain. 2. fail in time-varying and nonlinear systems. 3. only for SISO, can be more general in H_∞ and μ control. 4. controllability and observability can not be predicted. 5. easy for filter design. 6. can serve as the basis of phase-lead and phase-lag compensator design.
Observer-based design: Adaptive observer and Model-based observer	• Thermoacoustic instability in rocket motor • Longitudinal combustion instability	• Yang, et al. [28] • Neumeier and Zinn [8]	1. nominal model-based observer can be extended to optimal LQG regulator. 2. adaptive observer has no guarantee of convergence; its algorithm is one branch of the gradient iterative rules.
LQR and LQG control	• Thermoacoustic instability in premixed laminar combustor	• Annaswamy, et al. [70]	1. LQR control has optimal and robust properties of gain and phase margins, but requires measurements of all states. 2. LQG control has no robust property and is used only for rejection of intensity-known noise.
LMS adaptive and Neural Network back propagation	• Generic combustion instability • Boiler combustion systems • Dump combustor • Large scale solid rocket motor	• Billoud, et al. [25] • Allen, et al. [72] • Kemal and Bowman [74] • Koshigoe, et al. [37]	1. sensitive to initial conditions and gradient dynamic parameters. 2. has similar algorithm in System ID. 3. may be replaced by off-line ID plus Bode-Nyquist or observer-based controller.
Fuzzy logic control	• Longitudinal combustion instability	• Menon and Sun [75]	1. only effective when many states can be sensored. 2. need experience to set up logic rules and scales. 3. not used solo.
Lyapunov-based design	• Generic combustion instability	• Krstic [28]	1. need more generalized control algorithms. 2. nonlinear H_∞ control is based on Lyapunov design, but with general algorithms.

8. References

1. McManus, K. R., Poinsot, T. and Candel, S. M., "A Review of Active Control of Combustion Instabilities," *Progress in Energy and Combustion Sciences,* 1993, Vol. 19, pp. 1-29.

2. Candel, S. M., "Combustion Instabilities Coupled by Pressure Waves and Their Active Control," 24th Symposium (International) on Combustion, Sydney, July 1992.

3. Nelson, P. A. and Elliott, S. J., "*Active Control of Sound*," Academic Press, 1990.

4. Wang, K. W., von Flotow, A. H., Shoureshi, R., Hendricks, E. W. and Farabee, T. M., "Active Control of Vibration and Noise," ASME DE-Vol. 75, 1994.

5. Badmus, O. O., Chowdhury, S., Eveker, K. M., Nett, C. N. and Rivera, C. J., "A Simplified Approach for Control of Rotating Stall Part 1: Theoretical Development," AIAA 93-2229, 1993.

6. Epstein, A. H., Ffowcs Williams, J. E., and Greitzer, E. M., "Active Suppression of Compressor Instabilities," AIAA 86-1994, 1986.

7. Harrje, D. T. and Reardon, F. H., "Liquid Propellant Rocket Combustion Instability," NASA SP-194, 1972.

8. Neumeier, Y. and Zinn, B. T., "Experimental Demonstration of Active Control of Combustion Instabilities Using Real Time Modes Observation and Secondary Fuel Injections," 26th International Symposium on Combustion, Naples, Italy, July 28, 1996.

9. Parr, T. P., Gutmark, E. J., Wilson, K. J., Yu, K., Smith, R. A., Hanson-Parr, D. M. and Schadow, K. C., "Compact Incinerator Afterburner Concept Based on Vortex Combustion," 26th International Symposium on Combustion, Naples, Italy, July 28, 1996.

10. Yu, K., Wilson, K. J., Parr, T. P. and Schadow, K. C., "Active Combustion Control Using Multiple Vortex Shedding," AIAA 96-2760, 1996.

11. Tsien, H. S., "Servo-Stabilization of Combustion in Rocket Motors," *ARS Journal*, Vol. 22, 1952, pp. 256-263.

12. Marble, F. E., and Cox, D. W. JR., "Servo-Stabilization of Low-Frequency Oscillations in a Liquid Bipropellant Rocket Motor," *ARS Journal*, Vol. 23, 1953, pp. 63-74.

13. Lee, Y. C., Gore, M. R., and Ross, C. C., "Stability and Control of Liquid Propellant Rocket Systems," *ARS Journal*, Vol. 23, 1953, pp. 75-81.

14. Ffowcs-Williams, J. E., "Anti-Sound," *Proceedings of Royal Society of London*, Vol. A395, 1984, pp. 63-88.

15. Dine, P. J., "Active Control of Flame Noises," Ph.D. Thesis, Cambridge University, Cambridge, England, 1983.

16. Heckl, M. A., "Heat Sources in Acoustic Resonators," Ph.D. Thesis, Cambridge University, Cambridge, England, 1985.

17. Heckl, M. A., "Active Control of the Noise from a Rijke Tube," *IUTAM Symposium on Aero- and Hydro-Acoustics, Lyon 1985*, Springer-Verlag, 1986, pp. 211-216.

18. Bloxsidge, G. J., Dowling, A. P., Hooper, N., and Langhorne, P. J., "Active Control of Reheat Buzz," AIAA Paper 87-0433, 1987.

19. Bloxsidge, G. J., Dowling, A. P., Hooper, N., and Langhorne, P. J., "Active Control of an Acoustically Driven Combustion Instability," *Journal of Theoretical and Applied Mechanics*, Vol. 6, 1987, pp. 161-175.

20. Lang, W., Poinsot, T., and Candel, S., "Active Control of Combustion Instability," *Combustion and Flame*, Vol. 70, 1987, pp. 281-289.

21. Poinsot, T., Bourienne, F., Candel, S., Esposito, E., and Lang, W., "Suppression of Combustion Instabilities by Active Control," *Journal of Propulsion and Power*, Vol. 5, No. 1, 1987, pp. 14-20.

22. Poinsot, T., Veynante, D., Bourienne, F., Candel, S., Esposito, E., and Surget, J., "Initiation and Suppression of Combustion Instabilities by Active Control," *Proceedings of the 22nd Symposium (International) on Combustion*, 1988, pp. 1363-1370.

23. Langhorne, P. J., Dowling, A. P., and Hooper, N., "Practical Active Control System for Combustion Oscillations," *Journal of Propulsion and Power*, Vol. 6, No., 3, 1990, pp. 324-333.

24. Sivasegaram, S., Tsai, R. F., and Whitelaw, J. H., "Control of Combustion Oscillations by Forced Oscillation of Part of the Fuel Supply," *Combustion Science and Technology,* Vol. 105, 1995, pp. 67-83.

25. Billoud, G., Galland, M. A., Huynh, C., and Candel, S., "Adaptive Active Control of Combustion Instabilities," *Combustion Science and Technology*, Vol. 81, 1992, pp. 257-283.

26. Wilson, K. J., Gutmark, E., Schadow, K. C., and Smith, R. A., "Feedback Control of a Dump Combustor with Fuel Modulation," *Journal of Propulsion and Power*, Vol. 11, 1995, pp. 268-274.

27. Schadow, K. C., Gutmark, E., and Wilson, K. J., "Active Combustion Control in a Coaxial Dump Combustor," *Combustion Science and Technology*, Vol. 81, 1992, pp. 285-300.

28. Yang, V., Shinha, A., and Fung, Y. T., "State-Feedback Control of Longitudinal Combustion Instabilities," *Journal of Propulsion and Power*, Vol. 8, 1992, pp. 66-73.

29. Fung, Y. T., Yang, V., and Shinha, A., "Active Control of Combustion Instabilities with Distributed Actuators," *Combustion Science and Technology*, Vol. 78, 1991, pp. 217-245.

30. Menon, S., "Active Combustion Control in a Ramjet Using Large-Eddy Simulations," *Combustion Science and Technology*, Vol. 84, 1992, pp. 51-79.

31. Shyy, W., Thakur, S., and Udaykumar, H. S., "A High Accuracy Sequential Solver for Simulation and Active Control of a Longitudinal Combustion Instability," *Computing Systems in Engineering*, Vol. 4, 1993, pp. 27-41.

32. Neumeier, Y., and Zinn, B. T., *Active Control of Combustion Instabilities with Real Time Observation of Unstable Combustor Modes*, AIAA 96-0758, 1996.

33. Culick, F. E. C., *Combustion Instabilities in Liquid-Fueled Propulsion Systems*, AGARD-CP-450, Vol. 1, 1989, pp. 1-73.

34. Fung, Y. T., "Active Control of Linear and Nonlinear Pressure Oscillations in Combustion Chambers," Ph.D. Thesis, Dept. of Mechanical Engineering, Pennsylvania State University, University Park, PA, 1991.

35. Fung, T., T., and Yang, V., "Active Control of Nonlinear Pressure Oscillations in Combustion Chambers," *Journal of Propulsion & Power*, Vol. 8, 1992, pp. 1282-1289.

36. Padmanabhan, K.T., Bowman, C.T., and Powell, J.D., "An Adaptive Optimal Combustion Control Strategy," *Combustion and Flame*, Vol. 100, 1995, pp. 101-110.

37. Koshigoe, S., Komatsuzaki, T., and Yang, V., "Active Control of Combustion Instability with On-line System Identification," AIAA Paper 96-0759, 1996.

38. Cohen, J.M., and Anderson, T.J., "Experimental Investigation of Near-Blowout Instabilities in a Lean, Premixed Step Combustor," AIAA Paper 96-0819, 1996.

39. Gutmark, E., Parr, T. P., Hanson-Parr, D. M. and Schadow, K. C., "Synchronized Acoustic Excitation of Fuel and Oxidizer for Efficient Combustion," AIAA Aeroacoustics Conference, 1995.

40. Reuter, D., Hegde, U. G, Daniel, B. R. and Zinn, B. T., "Flame Driving of Longitudinal Instabilities in Dump Type Ramjet Combustors" *Combustion Science and Technology,* Vol. 55, pp. 125-138, July 1987.

41. Poinsot, T. J., Trouve, A. C., Veynante, D. P., Candel, S. M. and Esposito, E. J., "Vortex-driven Acoustically Coupled Combustion Instabilities," *Journal of Fluid Mechanics,* 177, pp. 265-292, 1987.

42. Low, H. C., Wilson, C. W., Abdel-Gayed and Bradley, D., "Evaluation of Novel Igniters in a Turbulent Bomb Facility and a Turbo-Annular Gas Turbine Combustor," AIAA-89-2944, 1989.

43. Powell, E. A. and Zinn, B. T., "Nonlinear Combustion Instability in Liquid Propellant Rocket Engines," Proceedings of the 13th Symposium (International) on Combustion. The Combustion Institute, pp. 491-503, 1971.

44. Culick, F. E. C. and Yang, V., "Overview of Combustion Instabilities in Liquid-Propellant Rocket Engines," in *Liquid Rocket Engine Combustion Instability*, Progress in Astronautics and Aeronautics, Vol. 169, 1995.

45. Menon, S., "A Numerical Study of Secondary Fuel Injection Techniques for Active Control of Combustion Instability in a Ramjet," AIAA 92-0777, 1992.

46. Furlong, E. R., Baer, D. S. and Hanson, R. K., "Combustion Control and Monitoring Using a Multiplexed Diode-Laser Sensor System." AIAA 96-2763, 1996.

47. Langhorne, P. J., "Reheat Buzz: An Acoustically Coupled Combustion Instability. Part 1. Experiment," *Journal of Fluid Mechanics*, Vol. 193, pp. 417-443, 1988.

48. Brouwer, J., Ault, B. A., Bobrow, J. E. and Samuelson, G. S., "Active Control Application to a Model Gas Turbine Combustor," ASME 90-GT-326, 1990.

49. Matta, L. M., Zhu, C. and Jagoda, J. I., "Mixing by Resonant Acoustic Driving in a Closed Chamber," *Journal of Propulsion & Power*, Vol. 12, No. 2, pp. 366-370, March-April 1996.

50. Wiltse, J. M. and Glezer, A., "Manipulation of Free Shear Flows Using Piezoelectric Actuators," *Journal of Fluid Mechanics*, Vol. 249, pp. 261-285, 1993.

51. Ogata, K., *Modern Control Engineering,* 2nd Edition, Prentice-Hall Pub., 1990.

52. Gutmark, E., Parr, T.P., Hanson-Parr, D.M., and Schadow, K.C., "Active Control of a Premixed Flame", AIAA 90-2448, 1990.

53. Schadow, K.C., Gutmark, E.J., Parr, T.P., Wilson, K.J., and Yu, K., "Vortex Combustion with Synchronized Fuel Injection", presented at Twelfth International Symposium on Airbreathing Engines, _September 10-15, 1995, Melbourne, Australia.

54. Yu, K., Wilson, K.J., Parr, T.P., Smith, R.A., and Schadow, K.C., "Characterization of Pulsating Spray Droplets and Their Interaction with Vortical Structures", presented at 34th Aerospace Sciences Meeting and Exhibit, January 15-18, 1996, Reno, NV.

55. Parr, T.P., Gutmark, E.J., Wilson, K.J., Hanson-Parr, D.M., K. Yu, Smith, R.A., and Schadow, K.C., "Compact Incinerator Afterburner Concept Based on Vortex Combustion", presented at Twenty-Sixth International Symposium on Combustion, July 28-August 2, 1996, Naples, Italy.

56. Yang, V., Santavicca, D.A., and Ray, A., "Intelligent Control of Gas Turbine Combustion Dynamics for Performance and Emission Improvement," Proceedings of the Ninth ONR Propulsion Meeting, 1996, pp. 286-292.

57. Knoop, P., Culick, F.E.C., and Zukoski, E.E., "Extension of the Stability of Motions in a Combustion Chamber by Nonlinear Active Control Based on Hystersis," submitted to *Combustion Science and Technology*.

58. Sterling, James, Combustion Science and Technology, Vol. 89, pp. 167-179, 1993.

59. Burkhardt ,H. and Strubenhoff, V., "Multispectral Vision-Guided Flame Control", presented at ECAPT '93: Karlsruhe 25-27 March 1993, Second Meeting of BRITE-EURAM Concerted Action on Process Tomography, Workshop on "Process Monitoring & Control".

60. Tao, W. and Burkhardt, H., "Application of Fuzzy Logic and Neural Networks to the Control of a Flame Process". In Proceedings of the 2nd IEE Conference on "Intelligent Systems Engineering", Hamburg, September 1994.

61. Delabroy, O., Haile, E.. Veynante, D., Lacas, F., and Candel, S. (1996) Revue Generale de Thermique, 35, 475-489. Reduction de la production des oxydes d'azote (Nox) dans une flamme de diffusion a fioul par excitation.

62. Delabroy, O., Lacas, F., Poinsot, T., Candel, S., Hoffmann, T., Hermann, J., Gleis, S., and Vortmeyer, D., "A Study of Nox Reduction by Acoustic Excitation in a Liquid Fueled Burner," *Combustion Science and Technology*, Vol. 119, pp. 397-408.

63. Haile, E., Delabroy, O., Lacas, F., Veynante, D., and Candel, S., "Structure of Acoustically Forced Spray Flame", 26th Symposium (International) on Combustion. The Combustion Institute, Pittsburgh, 1996.

64. Gutmark, E.J., Schadow, K.C., Nina, M.N.R., and Pita, G.P., "Suppression of Combustion Instability by Geometrical Design of the Bluff-Body Stabilizer", Journal of Propulsion and Power, Vol. 11, No. 3, pp. 456-463, 1995.

65. Gleiss, S., Vortmeyer, D., and Rau, W., "Experimental Investigations on the Transition from Stable to Unstable Combustion by Means of Active Instability Control," AGARD CP 479, pp. 22.1-22.7, 1990.

66. Hermann, J., Gleis, S., and Vortmeyer, D., "Active Instability Control (AIC) of Spray Combustors by Modulation of the Liquid Fuel Flow Rate," Combustion Science and Technology, Vol. 118, pp. 125, 1996.

67. Hantschk, C., Hermann, J., and Vortmeyer, D., "Active Instability Control with Direct Drive Servo Valves in Liquid-Fueled Combustion Systems, 26th International Symposium on Combustion, Naples, Italy, 1996.

68. Zinn, B.T., and Neumeir, Y., "An Overview of Active Control of Combustion Instabilities," AIAA Paper 97-0461, 1997.

69. Gulati, A., and Mani, R., "Active Control of Unsteady Combustion - Induced Oscillations," *Journal of Propulsion and Power*, Vol. 8, 1992.

70. Annaswamy, A.M., and Ghoniem, A.F., "Active Control in Combustion Systems," *IEEE Control Systems Magazine*, Vol. 15, 1995, pp. 49-63.

71. Crocco, L., and Cheng, S.I., *Theory of Combustion Instability in Liquid Propellant Rocket Motors*, AGARD Monograph, No. 8, Butterworths, London, 1956.

72. Yang, V., and Anderson, W.E., *Liquid Rocket Engine Combustion Instability*, Progress in Astronautics and Aeronautics, Vol. 169, AIAA, 1995.

73. Allen, M.G., Butler, C.P., Johnson, S.A., Lo, E.Y., and Russo, F., "An Imaging Neural Network Combustion Control System for Utility Boiler Applications," *Combustion and Flame*, Vol. 94, 1993, pp. 205-214.

74. Kemal, A., and Bowman, C.T., "Real-Time Adaptive Feedback Control of Combustion Instability," *Proceedings of The Combustion Institute*, Vol. 26, 1996, pp. 2803-2809.

75. Menon, S., and Sun, Y., AIAA Paper 96-2759, 1996.

This page has been deliberately left blank

_____

Page intentionnellement blanche

Active Control of Engine Dynamics: Lectures on Control Theory

Clas A. Jacobson
United Technologies Research Center,
MS15, 411 Silver Lane,
East Hartford, CT 06108,
860 610 7652, `jacobsca@utrc.utc.com`

Andrzej Banaszuk
United Technologies Research Center,
MS15, 411 Silver Lane,
East Hartford, CT 06108,
860 610 7381 , `banasza@utrc.utc.com`,
`http://abanaszukresearch.homestead.com/homepage_research.html`

Executive Summary

Thermoacoustic instability develops in gas turbine engines when acoustic modes in the combustor couple with unsteady heat release in a positive feedback loop. The instability causes unacceptably high levels of pressure oscillations and often leads to catastrophic hardware failure. It develops in lean premix gas turbines for industrial power er, military thrust augmentors, and rocket engines. Active control using fuel modulation is an effective way to reduce the pressure oscillations. In this lecture we present application of control theory to analyse limits of achievable reduction of the level of pressure oscillations in combustors.

Abstract

In this lecture we present application of control theory of single-input single output systems to analysis of control of combustion instability. We examine effect of control feedback loops on pressure oscillations. The modeling framework is linear and nonlinear frequency domain description of controlled combustion dynamics. In particular, we investigate what determines achievable reduction of the level of pressure oscillation in combustors. We apply analytical methods using experimentally obtained combustion models. Standard results of linear control theory apply to linear combustion process models with proportional actuators. Random input describing function analysis allows extension of fundamental limits studies to nonlinear models of combustion process. The results of analysis are supported by results of experiments and model simulations. In particular, we reproduce in model simulations and explain analytically the peak-splitting phenomenon observed in combustion experiments.

1 Introduction

Emphasis on reducing the levels of pollutants created by gas turbine combustors has led to the development of premixed combustor designs, especially for industrial applications. Premixing large amounts of air with the fuel prior to its injection into the combustor greatly reduces peak temperatures within the

combustor and leads to lower NOx emissions. However, premixed combustors are often susceptible to so-called thermoacoustic combustion instabilities which arise due to the destabilizing feedback coupling between acoustics and heat release. These instabilities lead to large pressure oscillations in the combustor which cause increased environmental noise and decreased combustor durability [1]. Experiments show that active control using fuel modulation is an effective way of reducing the level of pressure oscillations in combustors [1] [2] [3] [4] [5] [6] [7] [8] [9]. However, it has been observed that the achieved reduction of pressure oscillation varied between experiments from 6dB to 20dB. Moreover, in some cases the attenutation of oscillations at the primary frequency was accompanied by excitation of oscillations in some other frequencies [2] [3] [4] [6] [9]. This phenomenon was refered to as *secondary peaks* or *peak splitting*. A satisfactory explanation of different attenuation levels and peak-splitting phenomena has not been presented in the literature. One of the reasons was that most of the studies used nonlinear limit-cycling models of combustion processes which limited mathematical tools available for analysis.

In this paper we investigate the factors that determine achievable reduction of the level of pressure oscillation in combustors using fuel control. We apply analytical methods based on experimentally obtained combustion models. The results of analysis are supported by results of experiments and model simulations. In particular, we reproduce in models and explain analytically the peak-splitting phenomenon observed in combustion experiments.

To explain the combustion instability to control engineers not familiar with combustion physics, we begin with description of a simple physics-based model of combustion process. The model describes the coupling of the bulk acoustic mode of the combustor cavity with heat release. It has the form of a feedback interconnection of a lightly damped linear system (modeling acoustic pressure and velocity in combustor) with a heat release model involving transport delay and a saturating nonlinear function. Analysis shows that the delay can introduce a destabilizing positive feedback in the thermoacoustic loop. This can lead to loss of damping in the system up to linear destabilization (where a pair of eigenvalues crosses over into the right half plane). In the event of destabilization, the saturated nonlinearity in the heat release model causes the system to settle into a limit-cycle.

Turbulent velocity perturbations can be modeled as a broad-band noise driving the system. Thus, even if the heat release feedback does not cause instability, low damping and high disturbance level can result in high pressure oscillation level. This description is only qualitative, as the model has several unknown parameters. A quantitative analysis is performed in the paper using empirically obtained models of combustion process.

Next, we present results of combustion experiment in a single nozzle rig operating at high equivalence ratios (rich fuel) conditions controlled with proportional actuators. We show that data observed at high equivalence ratio (rich fuel) conditions is well fitted by a stable, noise driven model and nonlinear effects are not apparent. For this condition, we use linear control theory methods to explain the peak-splitting phenomenon observed in the single nozzle rig experiments. We also study the limits of achievable performance using standard fundamental limits results.

The linear analysis framework is appropriate for combustion at a high equivalence ratio condition where the actuator being used for the purposes of control is a proportional unsaturated hence a linear actuator. However, if either the combustion or the control path is nonlinear, the linear analysis breaks down and a nonlinear analysis must be carried out to adequately explain the phenomenon.

Even in the case of high equivalence ratio condition where the combustion process can be described by a linear model, a nonlinear analysis is required if on-off valves, which are typically cheaper and more reliable than the proportionalvalves, are used as actuators. A nonlinear analysis is also required if proportional valve actuators work in a saturated condition.

In the second half of the paper, we employ a nonlinear framework for studying the results from experiments in a sector rig controlled with three on-off actuators. Peak splitting is again observed in the experiments. To provide a model-based explanation we consider a linear model of the plant,

nonlinear model of the actuators and include effects of a strong wide-bandwidth noise disturbance. Model simulations closely match the experimental results.

We show that in the presence of strong disturbance the standard sinusoidal input describing function analysis is not satisfactory. Instead, we use a *random input describing function* analysis and show it to be an appropriate tool for dealing with oscillatory nonlinear systems with a high noise level. In particular, the peak splitting phenomenon observed in UTRC sector rig controlled with on-off valves [8] and in experiments conducted at Cambridge University [2] [3] [4] is explained. The use of random input describing functions allows us to analyse nonlinear combustion models in the presence of strong driving broad-band disturbance. In particular, it is possible to extend the studies of limits of achievable performance in this context and gain valuable intuition.

We conclude the paper with interpretation of the meaning of the results in the context of combustion technology.

2 Physics-based model of combustion process

In this section, a low-order physics-based model which describes the coupling between the bulk acoustic mode in combustor and heat release is presented. The model parameters have not yet been tuned to match the experimental frequency responses. Therefore, the experimental data interpretation in this paper will be done using the linear models obtained by fitting the experimentally obtained frequency responses. However, we present the UTRC combustion model in this section to introduce the physical variables that are believed to play the most important role in reduced order modeling of the combustion instability seen in UTRC combustion rigs.

The UTRC model does not pretend to be a universal model of combustion instability. Unsteady fluid dynamics and flame area variations that could influence the heat release have been neglected. The reason for this simplifying assumption is that these phenomena were determined to be steady and stable during combustion experiments at UTRC [10]. The fluctuations of the equivalence ratio (normalized fuel/air ratio) was determined to be the major effect responsible for coupling the pressure fluctuations with heat release.

The abstraction of the physical problem is shown in Figure 1. The combustor volume is modeled as
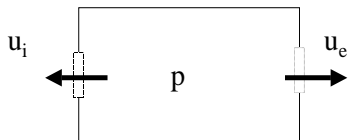

Figure 1: Schematic For Bulk Model Modeling of Combustion Chamber

M_i	Inlet Mach Number
M_e	Exit Mach Number
c_i	Inlet Sound Velocity
c_e	Exit Sound Velocity
V	Combustor Volume
l_i	Effective Length of Inlet Orifice
l_e	Effective Length of Exit Orifice
ρ_i	Inlet Gas Density
ρ_e	Exit Gas Density

a lumped acoustic capacitance. The thermoacoustic model equation is given as

$$\frac{d}{dt}\begin{bmatrix} \rho c u_i \\ \rho c u_e \\ p \end{bmatrix} =$$

$$\begin{bmatrix} -M_i c_i/l_i & 0 & c_i/l_i \\ 0 & -M_e c_e/l_e & c_e/l_e \\ -A_i c/V & -A_e c/V & 0 \end{bmatrix}\begin{bmatrix} \rho c u_i \\ \rho c u_e \\ p \end{bmatrix} +$$

$$\begin{bmatrix} 0 \\ 0 \\ H\left(u_i(t-\tau)+u_t(t), w(t-\tau)\right) \end{bmatrix}. \tag{1}$$

The state variables are the combustor chamber pressure p, the upstream nozzle mass velocity $\rho c u_i$ and the downstream exit mass velocity $\rho c u_e$. The combustion process is controlled by variable $w(t)$ representing the fuel mass flow. A stochastic input to the system is lumped in the variable $u_t(t)$ representing the turbulent velocity component in the nozzle. This component is assumed to be a broad-band white noise. The addition of the heat release (expressed as the forcing term $H\left(u_i(t-\tau)+u_t(t), w(t-\tau)\right)$ in (1)) results in a feedback system by changing the local density of the fluid thereby affecting the acoustic variables. The presence of parameter τ (which models the time delay associated with primarily convective lag together with some chemical and nozzle mixing time lag from the nozzle to the plane of heat release) turns the dynamics that govern the thermoacoustic system into that of a delay equation. For additional details on the model and explicit characteristics of the forcing term, see [11].

The parameters in the model equation (1) are described in Table 2. Note that the assumption that the heat release can be expressed as a function of the form $H\left(u_i(t-\tau)+u_t(t), w(t-\tau)\right)$ is just a simplifying assumption, and an exact formula for the function $H(\cdot, \cdot)$ cannot be easily derived from basic physical assumptions. However, it is reasonable to assume that in the lean condition fuel/air ratio condition $H(\cdot, \cdot)$ is decreasing in the first argument and increasing in the second argument. Under this assumption one can easily see that for some values of delay the heat release term will provide a positive feedback that can lead to reduction of effective damping of the system up to destabilization. In most references [12] [13] [9] [5] pressure oscillations in combustors are attributed to self-excitation of coupled acoustics and heat release system resulting in a limit-cycling behavior. However, the addition of the broad-band disturbance term representing the tubulence allows explanation of high level of pressure oscillations using a model of the combustor as a lightly damped, linearly stable system driven by noise. Note that there are important differences between behavior observed in small laboratory combustion control experiments and full-scale industrial combustors. Laboratory combustors have typically lower damping than industrial combustors. At the same time, laboratory combustors may have lower turbulence levels than larger, more complex

devices. With low damping and low noise levels, it is likely that significant pressure oscillations will only occur due to self-excited limit-cycle oscillations [9] [5]. Industrial combustors can exhibit noticeable pressure oscillations in a stable, noise-driven regime. In the present paper we are considering the latter case. More discussion of the effect of noise on pressure oscillations in combustors in linearly stable and unstable regime can be found in [14] [15] and [16].

An actuation system model (valve and the piping) relating the fuel mass flow to the electrical valve command input should be included to obtain the control model. After including the actuation effects, a realistic physics-based control oriented model which includes the bulk acoustic mode and actuator dynamics valid in the range where the valve modulating fuel has some effect is a nonlinear 4-th order model including heat release delay. Nonlinearities represent the heat release function, the area of the valve and the injection orifice. Due to the limited actuator bandwidth and lightly damped acoustic mode, the model can be simplified for the purposes of actual control design.

In the following sections, system identification techniques are used to identify a second order linear model with a delay to describe the dynamics from electrical valve input to the combustor pressure. Such a model, though attractive for control design purposes fails to capture the nonlinearities present in the real combustor experiment. A more elaborate version of UTRC physics-based model of combustion described in [16] includes quadratic jet dump losses at the orifices [17] [18] which gives a nonlinear damping mechanism and uses certain nonlinear model to capture nonlinearities present in the combustion process (nonlinear dependence of heat release on equivalence ratio). This results in an additional nonlinear damping mechanism.

The above discussion captures some of the tensions in modeling and controlling combustion instabilities. If the linear model equation is believed to capture the physics for the purposes of the control - and this hypothesis is validated by the experiments for certain combustor conditions - then the control design and analysis is easy and can be carried out within the framework of the linear control theory. This is done in the first part of the paper. However, if the linear model is not validated by the experimental data or if the control path contains nonlinearities (such as with use of on-off or saturating actuators), nonlinear control design and analysis tools have to be applied.

3 UTRC combustion instability experimental setup

The UTRC Combustion Dynamics and Control team investigated the feasibility of attenuating combustion instabilities using active control techniques. A cost-effective alternative to the engine (full annular combustor with many fuel nozzles) testing is to test a sector cut out from the full combustor annulus containing one or more fuel nozzles. This paper presents experimental results in a full scale single-nozzle combustor and in a three-nozzle sector combustor using fuel modulation for control.

The experimental setup consists of a 4 MW single-nozzle combustor (see Figure 2) and a three-nozzle sector combustor, using full-scale engine fuel nozzle at realistic operating conditions (see Figure 3). In the experiments, between 10% to 17% of the net fuel was modulated for control purposes using linear proportional or nonlinear on-off valves. For more details on the experiments in the sector rig see [7] [8].

4 Identification and validation of a linear model from a frequency response experiment

Models of combustion instability dynamics in UTRC single nozzle and sector (three-nozzle) rigs operating at various equivalence ratio conditions have been identified by fitting the experimentally obtained frequency responses from fuel valve command input to the pressure sensor output. In the frequency
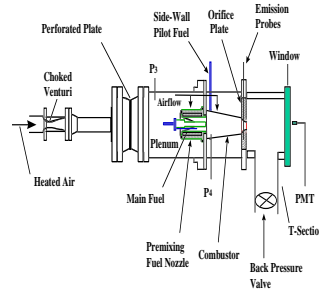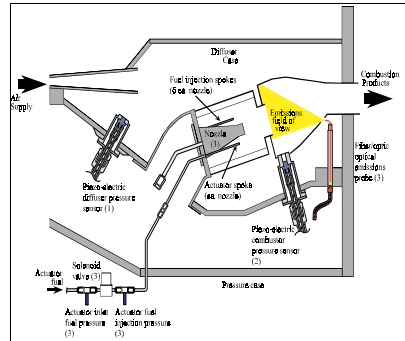
Figure 2: UTRC single-nozzle combustion rig

Figure 3: UTRC three-nozzle sector rig

range around the resonant peak, the responses are well fitted by a stable lighly damped second order system with (large) delay. This model agrees well with the structure of the physics-based model. In fact, we anticipate that the parameters of the physics based model can be chosen to match the identified model, at least for a high equivalence ratio condition, where no strong effects of nonlinear phenomena have been observed in the experimental data. As tuning of the parameters of the physics-based model to match the experimentally obtained frequency response has not yet been done, we will rely on the experimentally obtained models to explain phenomena observed in closed-loop experiments.

At the high equivalence ratio condition, the pressure oscillations seen in the UTRC single nozzle rig are relatively small and the proportional actuator used for control operates in the linear range and does not saturate. Therefore, a linear plant model and a linear controller model were used to analyze the behavior of the controlled system. Figure 4 shows the structure of the model. Figure 5 shows an experimentally obtained frequency response of the pressure to proportional fuel valve command. A second order system with delay was chosen to fit the experimentally obtained frequency reponse. Delay $\tau = 4.4$ ms was chosen to match the phase response in $300 - 400$ Hz frequency range. The phase lag $360ft$ due to delay has been subtracted from the experimental phase response. The phase response obtained in this way resembled roughly that of a 2nd order system. A 2nd order stable system was chosen to fit to the frequency response obtained by factoring out the delay. The identified resonant frequency of the plant was $f_r = 233$ Hz and the identified damping coefficient was $\xi_r = 0.0671$. In the actual experiment, pressure time-series data is available from which the power spectral density (PSD) can be evaluated. In this paper, all pressure PSD plots actually display the square root of PSD (a
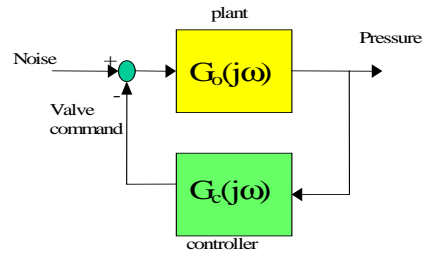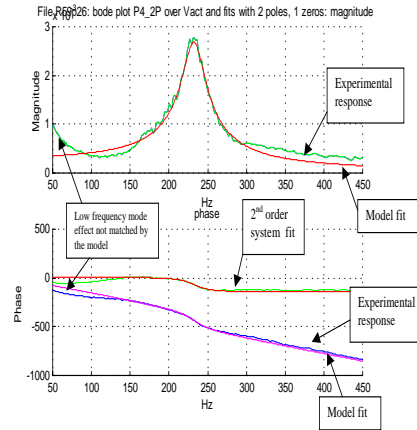
Figure 4: Linear model structure

Figure 5: Linear model identification from a frequency response experiment in the single nozzle rig

quantity proportional to the magnitude of the transfer function from noise to pressure if the noise is white). Since, the noise driving the combustion dynamics is not available, a white noise model is built at the plant input (see Figure 4) to match the experimentally obtained uncontrolled pressure PSD. The disturbance noise model does not necessarily represent any particular physical phenomena and it should be interpreted as an equivalent disturbance input that allows us to match the experimentally obtained pressure PSD with the results of the model simulations. In the actual combustion experiment, wide band turbulent air velocity fluctuation in the nozzle is one of the sources for the presence of disturbance.

By the nature of the identification, the identified plant includes the actuation dynamics and the thermoacoustic process (acoustic mode with the heat release feedback coupling). The frequency response of the actuation system is effectively flat over a wide band of frequencies around the resonant frequency representing the combustion process and can be modeled as a complex gain. This explains why no dynamics are needed in the model (which fits the experimentally observed response in the frequency band around the resonant frequency ω_r) to represent the actuation dynamics.

An observer-based phase-shifting controller has been tested in experiment and in the model. Figure 7 compares the experimentally obtained pressure PSD with the PSD obtained from running the simulation (using a white noise disturbance input model) with various phase-shifting controllers. (The open-loop PSD is shown in Figure 6). The fact that these are in close agreement shows that the linear stable model including a broad band disturbance is capable of reproducing the results of closed-loop control and it is suitable to use the identified model in interpreting experimental results.
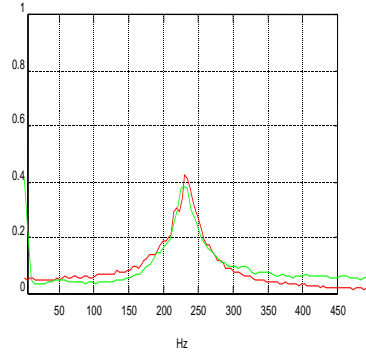
Figure 6: Square root of PSD of pressure from experiment and from model simulation

5   Sensitivity function analysis of peak-splitting phenomenon

Figure 7 shows that the largest attenuation of pressure oscillations at the high equivalence ratio condition is achieved for control phase shift value of $\theta = -60$. However, the attenuation of the pressure oscillations in a narrow frequency band around the frequency corresponding to the uncontrolled resonant peak is accompanied by excitation of oscillations in the frequency bands on both sides of the central attenuation band. In the active control of combustion literature, this phenomenon is referred to as the peak-splitting phenomenon.

The active combustion control performance objective (reduce the amplitude of the pressure time-series) can be posed in frequency domain as bounds on the sensitivity function

$$S(j\omega) = \frac{1}{(1 + G_0(j\omega)G_c(j\omega))}, \tag{2}$$

where $G_0(j\omega)$ and $G_c(j\omega)$ denote the plant and the controller transfer functions respectively (see Figure 4). The closed-loop transfer function from noise to pressure signal is

$$\frac{p(j\omega)}{n(j\omega)} = G_0(j\omega)S(j\omega). \tag{3}$$

Therefore, the sensitivity function gives the difference between the open loop $(G_c(j\omega) = 0)$ pressure PSD $|G_0(j\omega)n(j\omega)|^2$ and the closed loop pressure PSD $|G_0(j\omega)S(j\omega)n(j\omega)|^2$, in decibels given by

$$
\begin{aligned}
20log(|S(j\omega)|) &= 10log(|G_0(j\omega)S(j\omega)n(j\omega)|^2) \\
&- 10log(|G_0(j\omega)n(j\omega)|^2).
\end{aligned}
\tag{4}
$$

The goal of the control design is to shape the sensitivity function so that the original performance specification of reducing the amplitude of the pressure time-series is met. As expressed by equation (4), the magnitude of the sensitivity function determines whether the controller attenuates or magnifies the effect of noise at any given frequency.

A convenient way to visualize the attenuation and excitation frequency bands is the Nyquist diagram, i.e., the parametric plot of the product $G_0(j\omega)G_c(j\omega)$ in the complex plain. It is easy to see that the points of the plot of $G_0(j\omega)G_c(j\omega)$ outside the unit circle centered at the point (-1,0) correspond to frequencies at which the pressure oscillations are attenuated ($|S(j\omega)| < 1$) with control, whereas the point inside the circle correspond to points where the pressure oscillations are magnified ($|S(j\omega)| > 1$).

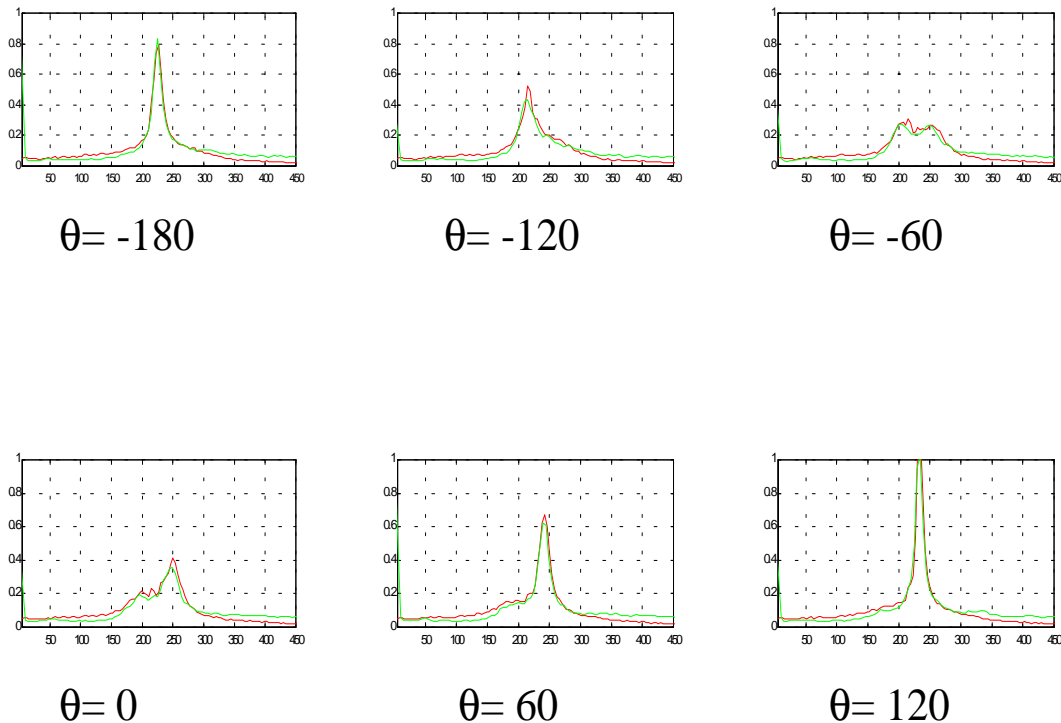# PSD of pressure from model simulation and experiment

Figure 7: Effect of a phase-shifting controller on pressure PSD in experiment and simulation

Without control, the power spectrum of the pressure oscillations shows a peak centered at the resonant frequency ω_r of the lightly damped open-loop plant. Thus, in order to reduce oscillations in this band, the controller must be designed such that $|(1 + G_0(j\omega)G_c(j\omega))| >> 1$ ($|S(j\omega)| << 1$) in this band. An observer-based controller (see [19] [20] [21] for more details) used in UTRC combustion experiments inis (roughly) a 2nd order, highly damped, band-pass controller with the central frequency close that of the plant. The effect of this controller is to simply rotate the Nyquist diagram so that the distance of the point $G_0(j\omega_r)G_c(j\omega_r)$ from the point (-1,0) is maximized, as is seen in the Figure 8. As a result, the controller is referred to as a phase-shifting controller. For a 2nd order plant with small delay, the phase-shifting controller shapes the loop such that $G_0(j\omega)G_c(j\omega)$ lies almost entirely outside the unit circle centered at the point (-1,0). Such a controller attenuates oscillations in a wide band of frequencies centered at the resonant frequency ω_r of the open-loop plant.

Unfortunately, large delay in the plant makes it much more difficult to achieve broad band attenuation of pressure oscillations. Because of the presence of large delay, the plant phase characteristic changes rapidly for frequencies between 180Hz to 270Hz where the plant has a considerable gain due to the resonance. The fast roll-off in the phase due to the presence of delay results in an "in-phase" feedback control signal on both sides of an attenuation band centered at ω_r. On the Nyquist diagram it is represented by the two branches of the plot of $G_0(j\omega)G_c(j\omega)$ inside the unit circle. Closing the loops results in pressure oscillation in these two frequency bands resulting in the "peak-splitting phenomenon":

pressure PSD with two peaks on both sides of the open-loop pressure PSD, as shown in Figure 9.
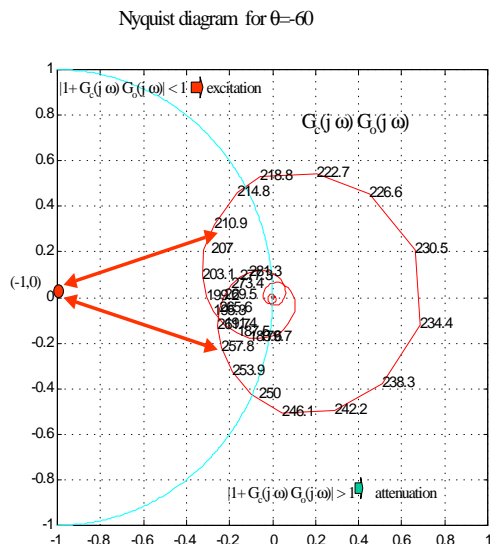

Figure 8: Nyquist diagram for the phase-shifting controller with optimal phase shift.

The peak splitting phenomenon observed in the sector rig motivated us to study the fundamental limitations assosciated with the use of active control in the linear control of combustion instabilities. The goal of the study was to better understand the effect of delay, limited actuator bandwidth and authority and unstable open loop poles on the achievable performance.

6 A framework for studying limits on achievable performance

The purpose of this section is to investigate the fundamental limitations imposed upon closed-loop sensitivity due to the presence of right half plane poles, delay and limitations on actuator bandwidth. The fundamental limitations yield controller independent upper bounds on the achievable performance. The utility of studying the fundamental limitations is two-fold. First, they allow one to obtain control design independent conclusions on the performance limits. Second, they allow the trade-offs inherent in any control design to be seen more clearly.

The sensitivity function is used to model the performance objective because its magnitude at any frequency gives the attenuation or amplification factor for the sinusoidal noise at that frequency. Moreover, if one were to view the action of control as damping augmentation of the open-loop dynamics, the closed-loop damping ratio ζ equals the damping ratio of the poles of the sensitivity transfer function. In frequency domain, the damping ratio ζ is related to the performance bandwidth $\Delta\omega_1$ (where $|S| < 1$) by

$$\zeta \approx \frac{\Delta\omega_1}{2\omega_r} \tag{5}$$

where ω_r denotes the resonance frequency.

We use the linear second order model with the time-delay identified in section 4 as a model for the combustion process. The reasons for neglecting the actuator dynamics and the higher order plant dynamics are :
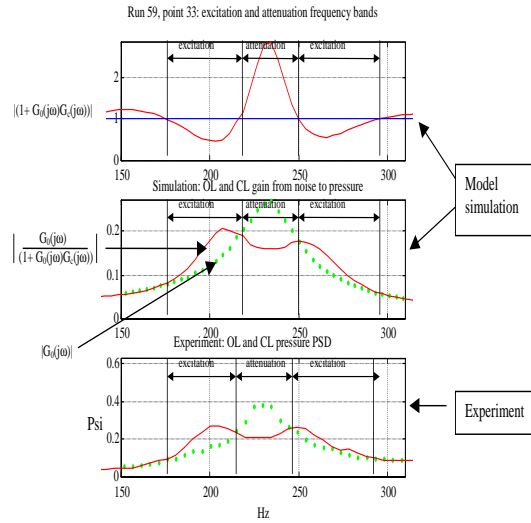
Figure 9: Explanation of peak-splitting phenomenon.

1. Any stable minimum phase dynamics are invertible in the controller. In fact, any infinite bandwidth controller *always* inverts these dyanmics. These dynamics do not affect conservation equations - which determine the performance limits.

2. The higher-order plant dynamics are *gain stabilized* - on account of robustness considerations - by rolling-off the control gain at higher frequencies. Thus, the effect of these higher order dynamics is not important once control bandwidth restrictions are imposed.

Performance (stability) trade-offs can be carried out using certain conservation laws that govern the area under the sensitivity (complementary sensitivity) curve. These laws yield bounds on stability and obtainable performance with *any* LTI controller, i.e., the approach is controller independent. As an example, consider the Bode integral formulae for the sensitivity function. It states that if the open-loop system is a stable rational function with relative degree at least two (or one if there is delay present in the loop) then, provided the closed-loop system is stable, the sensitivity function must satisfy the integral constraint [22]

$$\int_0^\infty log \mid S(\jmath\omega) \mid d\omega = 0. \tag{6}$$

As a result, noise attenuation ($\mid S(\jmath\omega) \mid < 1$) over a certain frequency band is always accompained by noise amplification ($\mid S(\jmath\omega) \mid > 1$) over some other frequency range. The situation is worse if the plant has unstable poles. The sensitivity integral then is given by

$$\int_0^\infty log \mid S(\jmath\omega) \mid d\omega = 2\pi\sigma_r. \tag{7}$$

where σ_r is the real part of the resonant unstable pole-pair. Thus, in the presence of unstable poles, a larger *penalty* is paid in terms of sensitivity amplification. Figure 10 gives a graphic interpretation of the area formula - sensitivity reduction is always accompanied by sensitivity amplification.

The frequency domain performance objective for active control of combustion is to shape the sensitivity function so that the it is small at and near ω_r, i.e.,

$$|S(j\omega)| < \epsilon \tag{8}$$
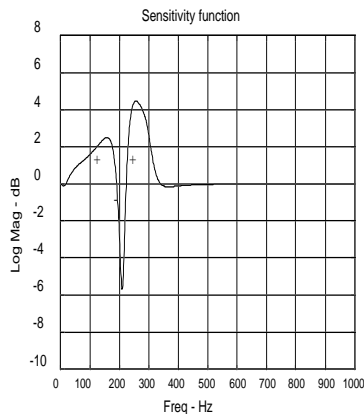
Sensitivity function

Figure 10: A typical sensitivity function showing positive and negative areas

for $\omega \in \Delta\omega_1$ where $\Delta\omega_1$ is a frequency band centered at ω_r (see Figure 11 for a graphical representation of this performance specification).

The equalities (6) and (7) show that negative area under the sensitivity curve ($|S(j\omega)| < 1$) must be balanced by positive area ($|S(j\omega)| > 1$). Thus, attenuation ($|S(j\omega)| < 1$) in one frequency band must be accompanied by amplification ($|S(j\omega)| > 1$) at other frequencies. If the control bandwidth is infinite, the positive area may be distributed over a wide frequency range so amplification at any given frequencies may be designed to be arbitrarily small. However, if the control bandwidth is finite (so the loop rolls off beyond certain low and high frequencies), the positive area would have to be accommadated in a smaller band (where loop gain is high) and this would necessarily results in peaking of the sensitivity function.

To model the effect due to finite control bandwidth, we require the open loop gain to satisfy the inequality

$$\mid L(\jmath\omega) \mid \leq \delta\left(\frac{\omega_c}{\omega}\right)^{1+k} \tag{9}$$

for high frequencies $\omega > \omega_c$. Here, it is assumed that $\delta < \frac{1}{2}$ and $k > 0$ (relative degree of at least two). We impose a similar constraint on the loop gain

$$\mid L(\jmath\omega) \mid \leq \delta\left(\frac{\omega}{\omega_b}\right)^{1+k} \tag{10}$$

for low frequencies $\omega < \omega_b$. We define the frequency band

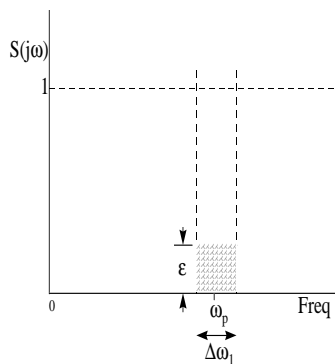$$\Delta\omega_2 = \omega_c - \omega_b \tag{11}$$

Figure 11: Performance specification for sensitivity function : $|S(j\omega)| < \epsilon$ for $\omega \in \Delta\omega_1$ where $\Delta\omega_1$ is a frequency band centered at ω_r.
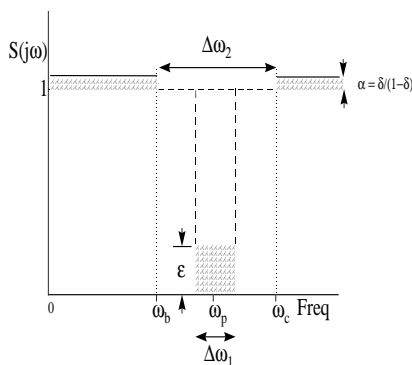

Figure 12: Performance specification for finite bandwidth control : $| L(j\omega) | \leq \delta(\frac{\omega_c}{\omega})^{1+k}$ for frequencies $\omega > \omega_c$. $\delta < \frac{1}{2}$ and $k > 0$ (relative degree of at least two) and $| L(j\omega) | \leq \delta(\frac{\omega}{\omega_b})^{1+k}$ for frequencies $\omega < \omega_b$.

as the control band. Figure 12 illustrates the finite bandwidth performance specification with $\Delta\omega_1$ as the performance bandwidth and $\Delta\omega_2$ as the control bandwidth. The restriction of the loop gain at high (equation (9)) and low (equation (10)) frequencies imposes additional constraints on the sensitivity function. Now, in addition to the performance specification - $|S(j\omega)| \leq \epsilon$ for $\omega \in \Delta\omega_1$, a control bandwidth specification - $|S(j\omega)| \leq \alpha = \frac{\delta}{1-\delta}$ for $\omega > \omega_c$ and $\omega < \omega_b$ must also be met.

7 Area formulae based sensitivity tradeoffs for a second order unstable system with a delay

In this section, we compute the performance limitations as peaking in the sensitivity function magnitude. The area formula for 2nd order right-haft plane pole pair with real part σ_r and a time-delay τ is given by equation (7). If the plant is open-loop stable, $\sigma_r = 0$. It is important to note that the delay τ does not affect the area formulae. This is true as long as no restriction on control bandwidth is placed. As we
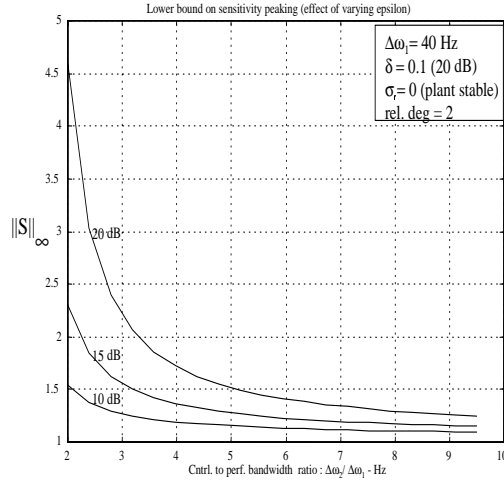
Figure 13: $\parallel S \parallel_\infty$ - effect of varying ϵ

shall see momentarily, the delay starts to play an important role as restrictions on control bandwidth comes in to play.

The infinite control bandwidth case in the absence of any right half plane zeros is not interesting, because area formula does not imply a peaking phenomenon, only an area conservation. On the other hand, waterbed effect (which is present in non-minimum phase systems - by using Poisson integral equation) leads to peaking for the systems with right-half plane zeros - even with infinite control bandwidth [22], [23].

We wish to investigate the behavior of sensitivity subject to the loop bandwidth restriction in (9) and performance requirement at the resonant pole frequency ω_r; see Figure 12 for the performance chart. The area formula together with the constraints in Figure 12 and high frequency roll-off characteristics can be manipulated (as in [22] [24]) to show that

$$
\begin{aligned}
log \parallel S \parallel_\infty \quad \geq \quad & \frac{1}{\Delta\omega_2 - \Delta\omega_1}(2\pi\sigma_r + \Delta\omega_1 log\frac{1}{\epsilon} \\
- \quad & (\omega_b)log\frac{1}{1-\delta} - \frac{3\delta\omega_c}{2k}(1 - \frac{1}{(1 + \frac{\pi}{\tau\omega_c})^k})),
\end{aligned}
\tag{12}
$$

where

$$
\parallel S \parallel_\infty = \sup_{\omega \in [0,\infty)} |S(j\omega)|.
\tag{13}
$$

For a stable plant ($\sigma_r = 0$), the desired performance bandwidth product $\Delta\omega_1 log\frac{1}{\epsilon}$ directly determines the the amount of sensitivity peaking. The inequality (12) shows that a large performance bandwidth product is necessarily accompanied by a large peaking in the sensitivity function.

Using the inequality (12), Figures 13, 14 and 15 plots bounds on sensitivity peaking. Figure 13 depicts the effect of varying the performance requirement (ϵ) while Figure 14 compares the sensitivity bounds for different values of the delay (τ). Figure 15 plots the peaking $\parallel S \parallel_\infty$ as a function of damping ratio ζ_r of the unstable pole pair. The plots show that as the ratio of the control bandwidth to the performance bandwidth ($\frac{\Delta\omega_2}{\Delta\omega_1}$) decreases, the sensitivity peaking becomes more and more severe. Further, the peaking is accentuated by increase in the delay (τ), increase in the performance requirement
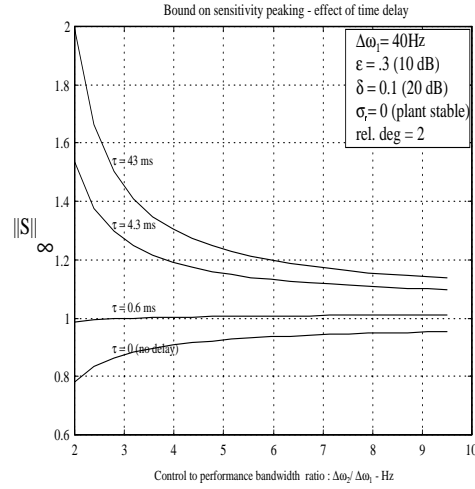
Figure 14: $\parallel S \parallel_\infty$ - effect of varying delay τ

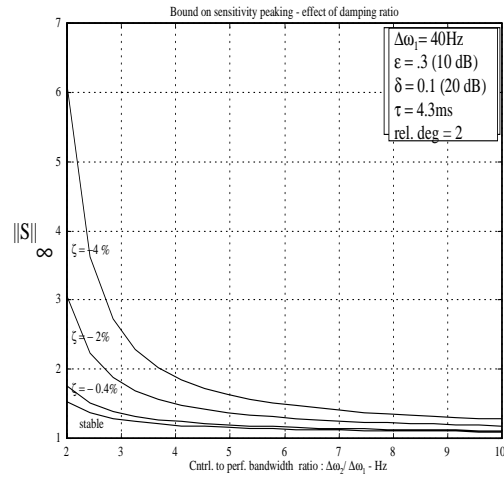Figure 15: $\parallel S \parallel_\infty$ - effect of varying damping ratio of resonant poles.
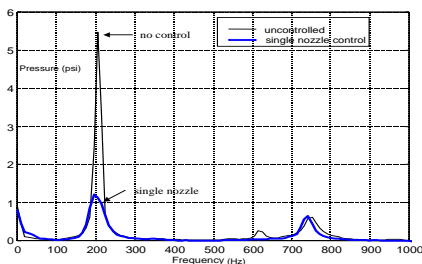
Figure 16: PSD shows 15dB reduction of pressure oscillations with control in UTRC single-nozzle rig. An on-off valve was used. No peak-splitting observed.
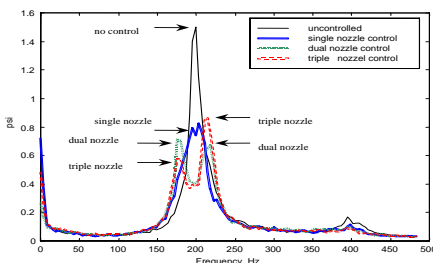

Figure 17: PSD shows 6.5dB reduction of pressure oscillations with control in UTRC sector (three-nozzle) rig. on-off valves were used. Peak-splitting limited effectiveness of closed-loop control.

(ϵ) or increase in the real part of the unstable pole of the open-loop plant σ_r. For an open-loop stable plant the inequality (12) is still valid with $\sigma_r = 0$.

8   Peak splitting phenomenon in sector rig experiments

In early experiments with combustion instability in a UTRC single-nozzle rig at low equivalence ratio conditions, a phase shifting controller modulating liquid fuel was very effective [7]. Pressure oscillations were reduced by 15dB (6 times), as shown in Figure 16. However, in the sector rig control experiments [8], the effect of phase-shifted control in the sector rig using on-off valves resulted in peak splitting as seen in the Figure 17 (with one, two and three nozzles). The identification of the model of the plant in the form of second order system with delay from frequency reponse using the method described in Section 4 was performed. The delay value $\tau = 7$ ms was obtained. (Note that the delay in the sector rig was larger as compared to the single nozzle rig.) The identified resonant frequency of the plant was $f_r = 208.9$ Hz and identified damping coefficient was $\xi = 0.0229$.

In Section 5 we showed how large delay could lead to larger peaking in the sensitivity function (see Figure 14) for the linear case. In the sequel we use the describing function framework to explain the observed phenomenon with the on-off actuators. The principal difficulties arise because of the non-linearity and the presence of the strong driving noise. The feedback block diagram of the controlled combustion process in the sector rig is shown in Figure 19. A plant model was obtained (as described in the first part of the paper) by fitting a 2nd order system with delay to an experimentally obtained transfer function between one valve command input and the pressure signal output (see Figure 18). A driving disturbance noise model (a broad-band Gaussian noise with the level adjusted to match the uncontrolled pressure oscillations) was also obtained in the way that has already been described in
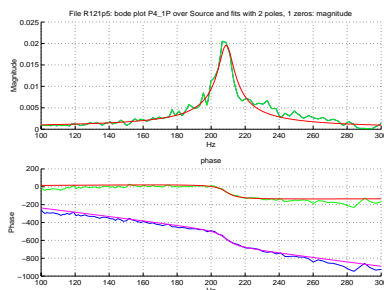
Figure 18: Frequency responses of pressure to valve command in UTRC sector rig experiment.
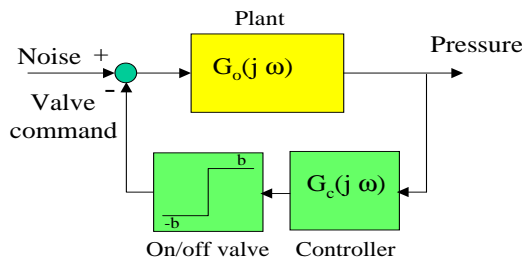

Figure 19: Model of the controlled combustion process with on-off valves.

the first part of the paper . The simulations of the model with on-off actuators and a phase-shifting controller (with one to three on-off valves) were performed and Figure 20 compares the square root of PSD of pressure in controlled and uncontrolled case from experiment and from model simulation. Assymetric peak splitting was observed in sector rig experiment when the third valve was turned on. This was attributed to longer fuel line for the thrid valve than for the first two, which resulted in a larger phase lag and lower authority. To match the asymmetry in the simulation, the relay blok in Figure 19 was splitted into two and an extra delay was added in series with one of the relays. Note that the simulation results match well the qualitative and quantitative features of the experimental results.

We claim that the peak splitting effect seen in sector rig experiments (see Figures 17 and 20) is caused by a large delay (larger than in the case of single nozzle rig). A purely linear analysis of peak-splitting presented in Section 5 has to be modified however, because of the on-off valves which cause the loop to be nonlinear. A describing function analysis will be used instead.

9   Sinusoidal input describing function analysis

A first order harmonic balance can give a prediction of the magnitude and frequency of possible limit cycles in the closed-loop systems if the disturbance input is neglected. The equation to be solved is

$$G_0(j\omega)G_c(j\omega) = -\frac{1}{N(A)}, \tag{14}$$

where $N(A)$ is the describing function (see [25]) of the relay representing the on-off valve given as

$$N(A) = \frac{4b}{\pi A}, \tag{15}$$

and b denotes the relay output magnitude. Figure 21 illustrates a graphical way of determining existence of solutions of this equation for a controlled case at which peak splitting can be observed. Intersections

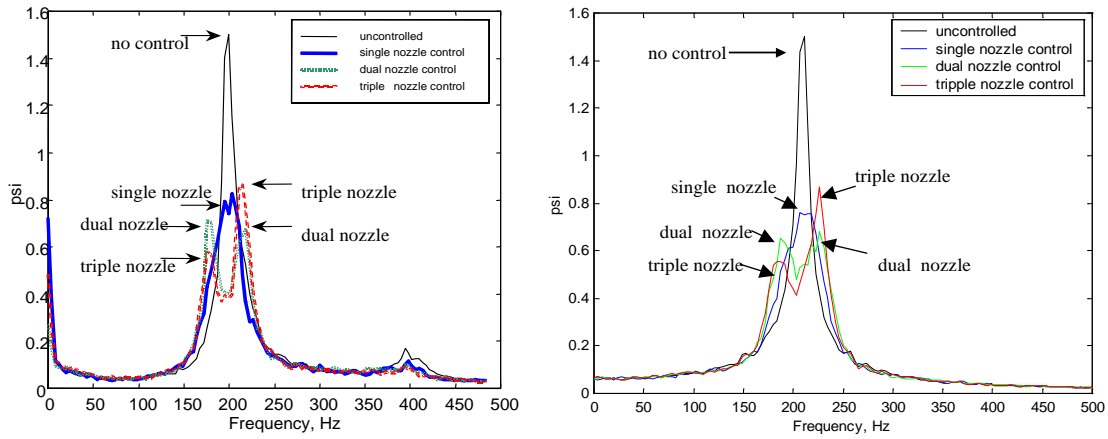**Experimental results**   **Simulation**

Figure 20: PSD of pressure signal with on-off control of one, two, or three liquid fuel nozzles The peak splitting phenomenon observed in experiment and simulation.

of the plot of the transfer function $G_0(j\omega)G_c(j\omega)$ with the plot of $-\frac{1}{N(A)}$ indicates the possibility of two limit cycles with frequencies 183 Hz and 238 Hz. The predicted value of the pressure magnitude in the two limit cycles was about 1 psi for three actuated nozzles and a third of that value for one actuated nozzle. Simulations of the model show that in the closed-loop system without noise, the two limit cycles - at the frequencies close to the ones predicted by the describing function analysis, i.e., 183 and 238 Hz - coexist. Figure 22 shows time traces, phase-portraits, and PSD corresponding to both attractors. The phase portraits are obtained from time shifts of the pressure signal by 0, 3, and 7 sample periods of .5ms. Next, the disturbance model is included in the simulations. Figure 23 shows a comparison of the pressure PSD with the nominal level of noise and without noise for one to three actuated nozzles. The two PDS's are vastly different. In particular, the shapes of power spectra, the frequencies of the peaks, and the values of pressure PSD at the peaks strongly depend on the presence of noise and on the number of actuated nozzles.
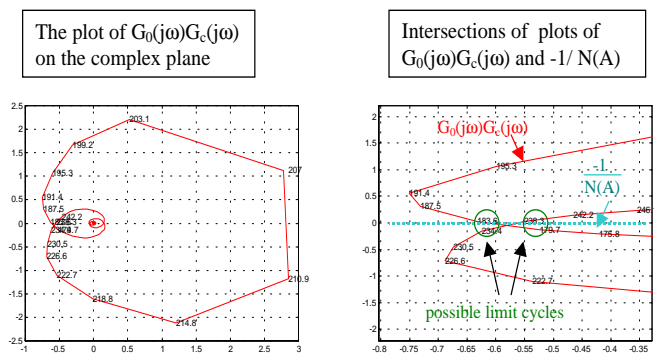

Figure 21: Graphical determination of the amplitude and frequencies of the possible limit cycles for a controlled liquid fuel model with a describing function method.
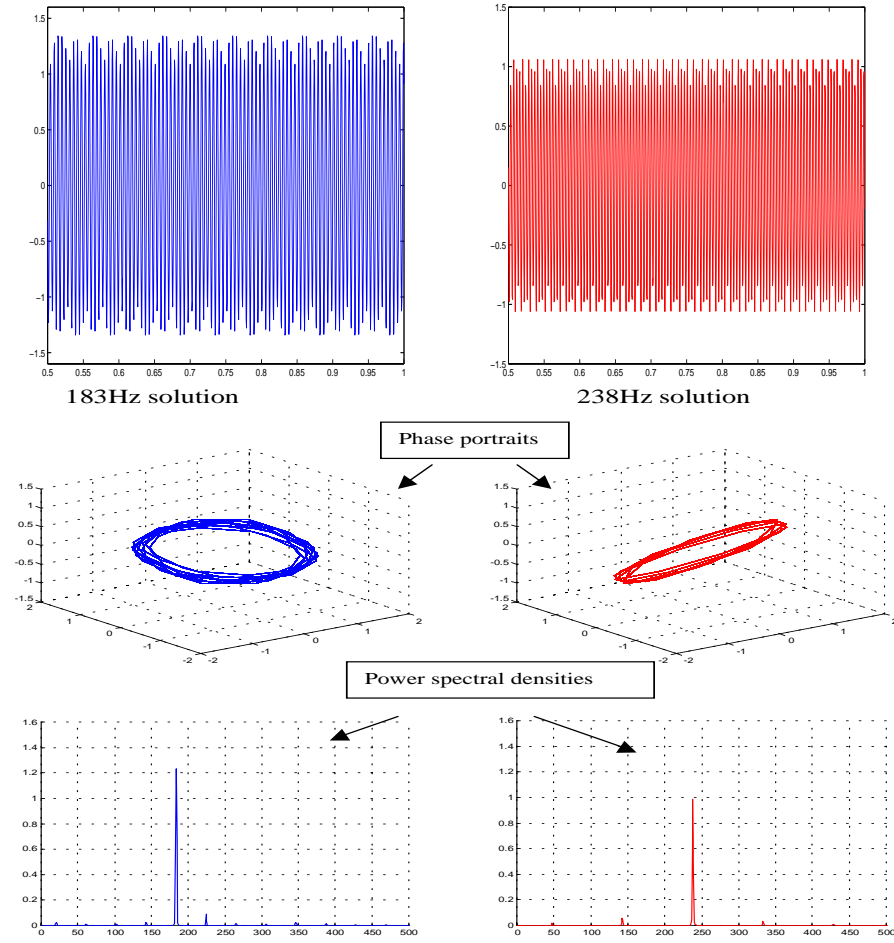
Figure 22: The coexisting attractors of the closed-loop system with three actuated nozzles without noise from simulation. Time traces, phase-portraits, and PSD.

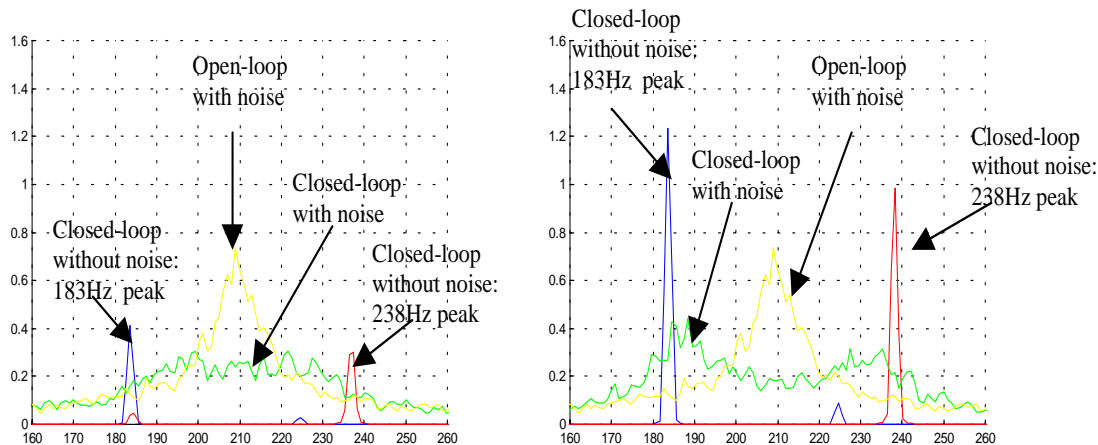One actuated nozzle   Three actuated nozzles

Figure 23: Model simulation: effects of noise and actuator authority on the pressure power spectra under closed-loop control with on-off valve.

Here is an interpretation of the observed effect of noise in a language of dynamical systems. The no-noise attractors are relatively small in size. The presence of large levels of noise causes the state of the system to visit regions in the phase-space far away from the attractors where the dynamics are not affected by saturated control but in fact are similar to the open-loop dynamics. The power spectra represent an average statistics of the motion of the state of the system. In the case when noise is large relative to the saturated control, one observes more of the spectral characteristics of the open-loop plant in the closed-loop spectra.

Another interpretation of the effect of the noise (using the language of control theory) is analogous to the explanation to the effective linearization of a relay characteristic by a control dither [26] [27]. The strong noise propagates through the loop and provides a bias for the periodic signal resulting from a limit cycle condition driving the on-off valve. This reduces the effective gain of the valve for the periodic signal. This gain reduction causes the on-off valve to work effectively as a proportional saturated valve with a low gain.

Our inability to analytically predict the frequencies and levels of pressure PSD peaks using standard sinusoidal describing function analysis in the presence of noise indicates a need for a new analysis tool that would explicitly take the noise into account. Such an analysis tool is introduced in the next section.

As we mentioned in the Introduction, the peak-splitting has been previously observed in combustion control experiments at Cambridge University [2] [3] [4]. In particular, in the experiments described in [4] on-off fuel injectors were used. The effect of control on the pressure oscillations was analyzed with sinusoidal-input describing function method, assuming that the closed-loop system dynamics is in a small magnitude limit cycle. The analysis in [4] faces the limitations described in this section and hence does not satisfactorily explain the peak-splitting. As we argued above, the driving noise is needed for model-based explanation of peak-splitting in the case of on-off actuators in a feedback loop is the driving noise.

10 Random input describing functions

In this section, the random input describing function framework as described in [25] is introduced to analyze the feedback system in the presence of the noise. Assume that a nonlinear static element described by a function $f(.)$ is driven by a signal

$$u(t) = B + A\sin(\omega t + \theta) + r(t), \tag{16}$$

where B is a constant, $r(t)$ is a zero-mean Gaussian (normal) random variable with standard deviation σ, and $A\sin(\omega t + \theta)$ is a sinusoidal signal with a random phase θ uniformly distributed over $[0, 2\pi]$. Introducing a sinusoid with a random phase allows a uniform treatment of the familiar sinusoidal input describing function and the random input describing function. In fact, one can show that ([25]) averaging the response of the sinusoidal process with uniformly distributed random phase is equivalent to averaging of the response due to deterministic sinusoid over one period and the resulting sinusoidal input describing functions (deterministic and stochastic) are actually identical.

Using a random input describing function analysis, the output of the nonlinear element $y(t) = f(u(t))$ is approximated by

$$y_a(t) = N_B B + N_A A\sin(\omega t + \theta) + N_R r(t), \tag{17}$$

where the individual gains N_B, N_A and N_R depend on all three quantities B, A, and σ. The gains are chosen to minimize the mean square error between the output of the nonlinear element and its approximation. The form of the best approximation in the mean square error sense does not have to be prescribed from the onset. In fact, it is possible to show that an optimal linear filter approximation of a static nonlinear element results in the static gains being the best filters [25].

The optimal gains are given by the following formulas (from [25], p. 371):

$$N_B(B, A, \sigma) = \frac{1}{B} E[f(u(0))] = \\ \frac{1}{(2\pi)^{\frac{3}{2}}\sigma B} \int_0^{2\pi} d\theta \int_{-\infty}^{\infty} dr f(B + A\sin(\theta) + r)\exp(-\frac{r^2}{2\sigma^2}), \tag{18}$$

$$N_R(B, A, \sigma) = \frac{1}{\sigma^2} E[f(u(0))r(0)] = \\ \frac{1}{(2\pi)^{\frac{3}{2}}\sigma^3} \int_0^{2\pi} d\theta \int_{-\infty}^{\infty} dr f(B + A\sin(\theta) + r)r\exp(-\frac{r^2}{2\sigma^2}), \tag{19}$$

$$N_A(B, A, \sigma) = \frac{2}{A} E[f(u(0))\sin(\theta)] = \\ \frac{2}{(2\pi)^{\frac{3}{2}}\sigma A} \int_0^{2\pi} d\theta \int_{-\infty}^{\infty} dr f(B + A\sin(\theta) + r)\sin(\theta)\exp(-\frac{r^2}{2\sigma^2}). \tag{20}$$

The gains will be referred to as the describing functions of the nonlinear element. If $r(t) = 0$ and $B = 0$, the last formula reduces to the usual sinusoidal input describing function. Note that the describing functions can be explicitly calculated for the case where $f(.)$ is a polynomial or a sinusoidal function.

Consider now a feedback interconnection of a linear system and nonlinear static nonlinear function $f(.)$ driven by a sum of a constant, sinusoidal signal, and a Gaussian process $B_i + A_i\sin(\omega t) + r_i(t)$ as shown in Figure 24. One can attempt to find a stationary solution of the feedback system by replacing the nonlinear element by the collection of the describing functions. It is reasonable to assume that the component $r_i(t)$ of the driving disturbance is Gaussian, however the same can not be said of the component $r(t)$ because it is affected by non-Gaussian process $y(t)$ at the output of the nonlinear element. of the loop signal $x(t)$ which forms the input to the nonlinear element (see Figure 24). However, since in the case of combustor the linear transfer function in the loop has poles close to the imaginary
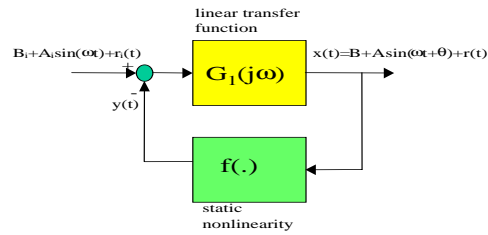
Figure 24: Structure of the feedback interconnection
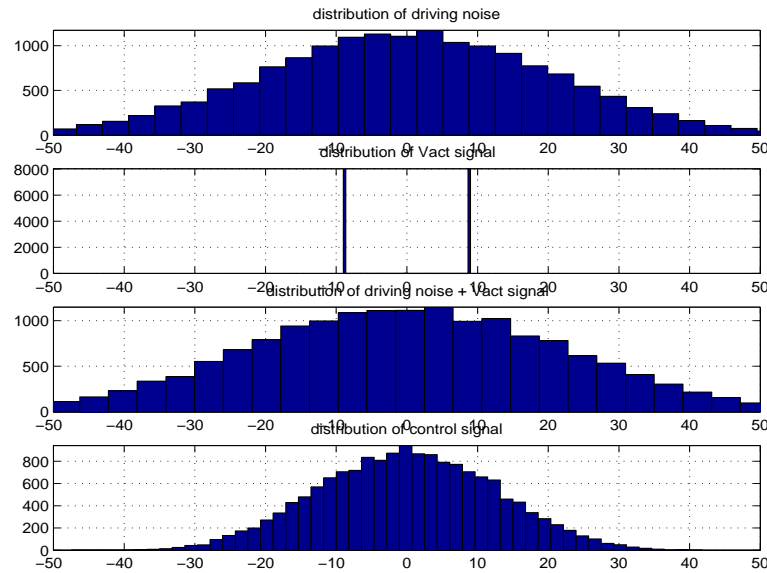
Figure 25: Distribution of signals in the loop from the simulation.

axis, its output is a convolution of the past non-Gaussian inputs with the slowly decaying impulse response of the linear plant. Since the convolution averages many identically distributed stationary input processes, one might expect that $r(t)$ too has approximately Gaussian distribution. We do not have a precise formulation of a result in this direction. Hence, the crucial assumption about Gaussian distribution of the random component $r(t)$ at the input to the nonlinear element is only verified by the simulations (see Figure 25).

The constant, sinusoidal, and Gaussian component of the solution at every point of the feedback loop can be calculated using a quasi-linear description. One can then look for forced response either as a stable driven system or as self-excited oscillations. Assuming that the Gaussian component $r_i(t)$ of the disturbance has Power Spectral Density $\Phi_{ii}(j\omega)$, the corresponding equations are as follows (σ is variance of the signal $r(t)$):

1. Stable driven system

$$B = \frac{G_1(0)}{1 + N_B(B, A, \sigma)G_1(0)}B_i \tag{21}$$

$$A = \frac{G_1(j\omega)}{1 + N_A(B, A, \sigma)G_1(j\omega)}A_i \tag{22}$$

$$\Phi_{xx}(j\omega) = |\frac{G_1(j\omega)}{1 + N_R(B, A, \sigma)G_1(j\omega)}|^2 \Phi_{ii}(j\omega) \tag{23}$$

$$\sigma^2 = \frac{1}{2\pi} \int_{-\infty}^{\infty} \Phi_{xx}(j\omega)d\omega. \tag{24}$$

2. Self-excited oscillations with driving noise

$$B = \frac{G_1(0)}{1 + N_B(B, A, \sigma)G_1(0)}B_i \tag{25}$$

$$1 + N_A(B, A, \sigma)G_1(j\omega) = 0 \tag{26}$$

$$\Phi_{xx}(j\omega) = |\frac{G_1(j\omega)}{1 + N_R(B, A, \sigma)G_1(j\omega)}|^2 \Phi_{ii}(j\omega) \tag{27}$$

$$\sigma^2 = \frac{1}{2\pi} \int_{-\infty}^{\infty} \Phi_{xx}(j\omega)d\omega. \tag{28}$$

11 Random input describing function analysis of the nonlinear sector rig model

Consider the simplified plant model of controlled combustion process in UTRC sector rig illustrated in Figure 19. One or three actuated nozzles is considered, represented by the value of valve saturation equal to 3 and 9, respectively. The plant model (2nd order system with delay) was identified from a frequency response as described earlier in this paper. In the simulation the system is driven by a broad band noise with Power Spectral Density $\Phi_{ii}(j\omega)$. Figure 26 presents the Nyquist plot of $G_1(j\omega)$ - denoting the product of the plant and controller transfer functions. The graphical sinusoidal describing function analysis (ignoring Gaussian noise) predicts possibility of two limit cycles with frequencies 187Hz and 242Hz. The frequencies do not change as the number of actuated nozzles changes. With on-off relay actuators, the random input describing function framework allows one to incorporate the effects of Gaussian noise. In the absence of noise, the closed loop system exhibits a limit cycle with amplitude A_0. The presence of Gaussian noise driving the system has the effect of supressing the self-excited
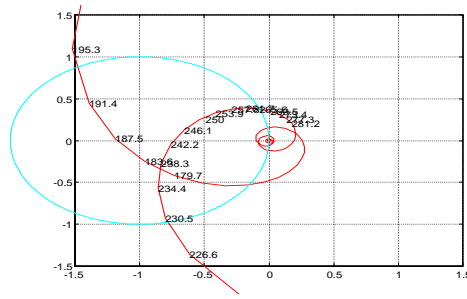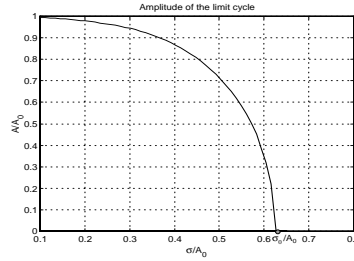
Figure 26: Nyquist diagram for the plant

x

Figure 27: The amplitude of the limit cycle in the presence of the Gaussian noise

oscillations. In particular, with a relay nonlinearity, the amplitude of the self-excited oscillations is easily shown to satisfy the equation

$$A(\sigma) = \int_{-A/\sigma}^{+A/\sigma} \sqrt{1 - \frac{\sigma^2 s^2}{A^2}} e^{-s^2/2} ds \frac{A_0}{\sqrt{2\pi}}. \tag{29}$$

One can show that $A(\sigma) \leq A_0$. Figure 27 plots the numerically computed solution of the integral equation (29). Thus, the presence of noise ($\sigma > 0$) leads to a reduction in the amplitude of this limit cycle and at a critical positive value of $\sigma = \sigma_0$, the limit cycle disappears ($A(\sigma_0) = 0$) and the random input describing function gain

$$N_R = \sqrt{\frac{2}{\pi}} \frac{b}{\sigma} \qquad \forall \sigma > \sigma_0. \tag{30}$$

For the values of $\sigma < \sigma_0$, the gain $N_R(\sigma)$ was numerically computed using the relationships (19) and (20). Figure 28 plots the gains $N_R(\sigma)$ and $N_A(\sigma)$. N_A is a step function with values

$$
\begin{aligned}
N_A^- &= -\frac{1}{G_1(j\omega)} \quad for\ \sigma < \sigma_0, \\
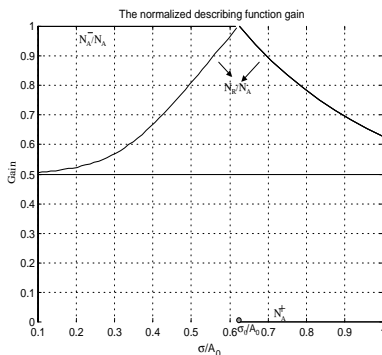N_A^+ &= 0 \quad for\ \sigma > \sigma_0
\end{aligned}
\tag{31}
$$

Figure 28:

and transition at σ_0, the critical σ where the limit cycle ceases to exist. N_R monotonically increases between 0 and σ_0 and decreases for values of $\sigma > \sigma_0$. We have

$$
\begin{aligned}
N_R(0, A(0), 0) &= \frac{N_A^-}{2}, \\
N_R(0, A(\sigma_0), \sigma_0) &= N_A^-, \\
N_R(0, A(\sigma), \sigma) &< N_A^- \qquad \forall \sigma \neq \sigma_0.
\end{aligned}
\tag{32}
$$

The last inequality ensures that the feedback interconnection of $G_1(j\omega)$ and $N_R(0, A(\sigma), \sigma)$ is linearly stable for all $\sigma \neq \sigma_0$. The second equality in (32) implies that the largest loop gain occurs at the critical value σ_0 where the loop is arbitraily close to destabilization (eigenvalues on the imaginary axis). For values of σ away from σ_0, the eigenvalues move in to the LHP thereby ensuring asymptotic stability for all $\sigma \neq \sigma_0$. For the critical value, the linear analysis is inconclusive in predicting the stability of the loop.

Therefore, in the presence of a *large* Gaussian noise (such that $\sigma > \sigma_0$), limit cycle is absent and the Gaussian processes balance alone explains the power spectra observed in the simulation. The Gaussian input describing function for the relay in the absence of constant bias and sinusoidal function is

$$
N_R(0, 0, \sigma) = \sqrt{\frac{2}{\pi}} \frac{b}{\sigma}.
\tag{33}
$$

The equation for the standard deviation σ at the input of the relay element (with saturation value b) is

$$
\sigma = \sqrt{\frac{1}{2\pi} \int_{-\infty}^{\infty} \left| \frac{G_1(j\omega)}{1 + \sqrt{\frac{2}{\pi}} \frac{b}{\sigma} G_1(j\omega)} \right|^2 \Phi_{ii}(j\omega) d\omega}.
\tag{34}
$$

For a given noise characteristics Φ_{ii}, this equation may be solved for σ graphically or by the method of successive iterations. While in general the latter method is not guaranteed to converge, in our case it indeed converges for Figures 29 and 30 plots the results of the method for the cases $b = 3$ (one nozzle actuated) and $b = 9$ (three nozzles actuated) respectively. In either case, the computed solutions for σ agree well with the result from the simulation.

One actuated nozzle, b=3.
1. Graphical solution for σ :
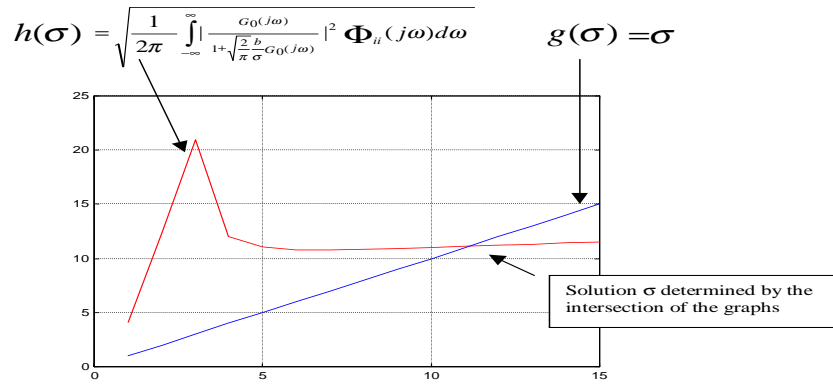
$$h(\sigma) = \sqrt{\frac{1}{2\pi} \int_{-\infty}^{\infty} |\frac{G_0(j\omega)}{1+\sqrt{\frac{2}{\pi}\frac{b}{\sigma}}G_0(j\omega)}|^2 \, \Phi_{ii}(j\omega)d\omega} \qquad g(\sigma) = \sigma$$

Solution σ determined by the intersection of the graphs

2. Iterative solution for σ: shown 15 iterations for σ (dots) starting at σ=1 and the value of σ from a simulation (continuous line).

Figure 29: Solution for σ

Three actuated nozzles, b=9.
1. Graphical solution for σ :

$$h(\sigma) = \sqrt{\frac{1}{2\pi} \int_{-\infty}^{\infty} |\frac{G_0(j\omega)}{1+\sqrt{\frac{2}{\pi}\frac{b}{\sigma}}G_0(j\omega)}|^2 \, \Phi_{ii}(j\omega)d\omega} \qquad g(\sigma) = \sigma$$

Solution σ determined by the intersection

2. Iterative solution for σ: shown 15 iterations for σ (dots) starting at σ=1 and the value of σ from a simulation (continuous line).

Figure 30: Solution for σ
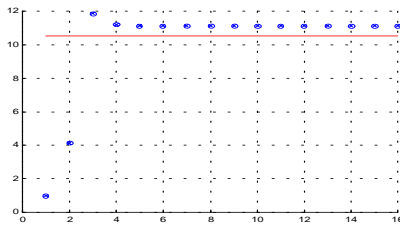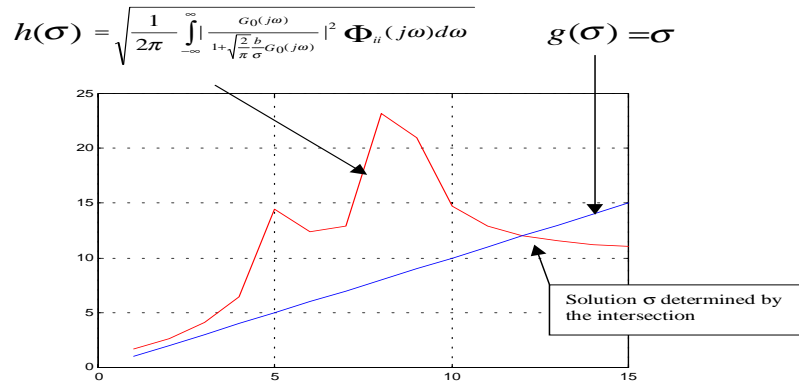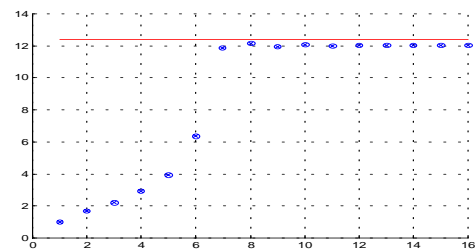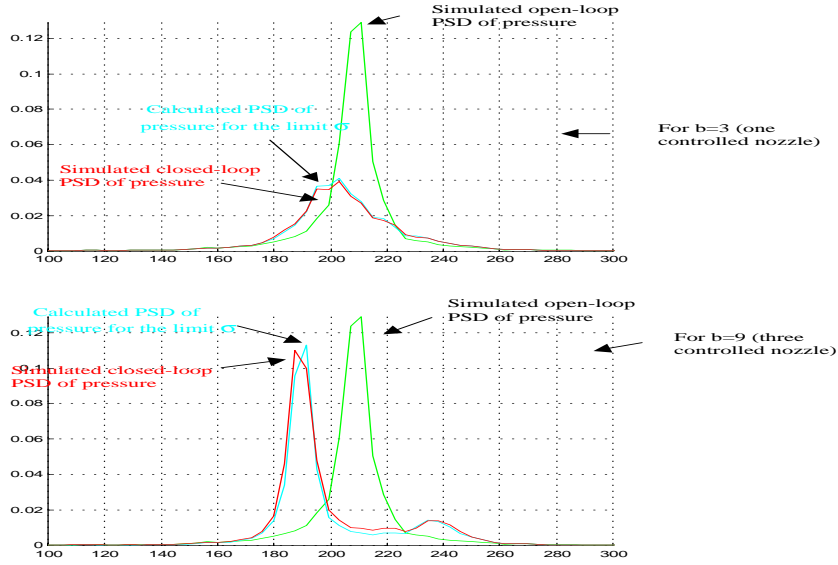
Figure 31: Pressure PSD from the Random Input Describing Function calculation and from the simulation

12 Limitations of achievable control performance with on-off actuators

Note that the analysis presented in the previous section shows that, except for a critical $\sigma = \sigma_0$, the Fourier transform of the Gaussian component of combustor pressure is well approximated by the formula

$$p_g(j\omega) = G_0(j\omega)S(j\omega, A, \sigma)n_i(j\omega), \tag{35}$$

where $n_i(j\omega)$ is the Fourier transform of the driving disturbance and

$$S(j\omega, A, \sigma) = \frac{1}{1 + G_0(j\omega)N_R(0, A, \sigma)G_c(j\omega)} \tag{36}$$

is a *modified sensitivity function* that depends on the magnitude of the limit cycle A and standard deviation σ of the Gaussian component at the input of the relay nonlinear element. In fact, we have shown that indeed there are values of σ and A for which the limit cycle and Gaussian process balance is achieved in the control loop. We are now in a position to extend the linear analysis presented in the first part of the paper to the case of control with on-off actuators. The only difference is that the controller transfer function $G_c(j\omega)$ needs to be replaced by the product $N_R(0, A, \sigma)G_c(j\omega)$. Note that for any *fixed* value of σ and A *all* the results of the linear analysis, including interpretation of peak splitting and analysis of fundamental limits, are applicable.

13 Practical implication for combustion process control

Analysis provided in this paper indicates that the peaking phenomenon defined as excitation of oscillations with closed-loop control is to a large extent inevitable for combustion processes with large delay controlled with actuators of limited bandwidth. This is reflected in the fact that the sensitivity for the linear actuator case and modified sensitivity function to the on-off actuator case function will achieve
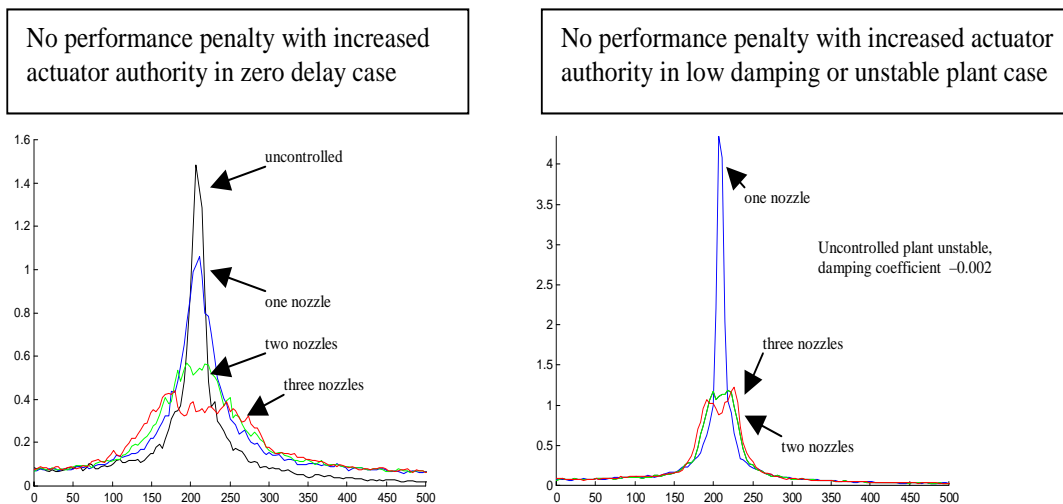
Figure 32: Model simulation: effects of delay and damping on pressure power spectra under closed-loop control for a nominal noise level.

values exceeding 1. However, note that the peaking in the sensitivity function *does not* always imply the peak splitting in closed-loop PSD of pressure. It is the product $G_0(j\omega)S(j\omega)$ or $G_0(j\omega)S(j\omega, A, \sigma)$ that determines whether or not the peak splitting will be seen. In the high equivalence condition the damping of the combustion plant is relatively large. This means that the plant transfer function $G_0(j\omega)$ has a significant gain in the frequency bands where the sensitivity function is peaking. Thus, peak splitting is likely to occur. On the other hand, in the low equivalence ratio regime the plant damping is low. In this case the peaking will not occur, as the plant transfer function $G_0(j\omega)$ has a very small gain in the frequency bands where the sensitivity function is peaking. This explains why there was no significant peak splitting observed in experiments with control in some low equivalence ratio conditions.

Reducing the plant delay would extend the band of frequencies in which attenuation of the pressure oscillations is achieved. The excitation bands would occur where the plant has very small gain, and hence no peak splitting would be observed. Similarly, decreasing the plant damping would have a beneficial effect on peak splitting due to two effects. Firstly, reducing the plant damping would reduce the frequency band $\Delta\omega_1$ shown in Figure 11 in which the sensitivity function is small. This would reduce the peaking implied by formula (12). Secondly, decreasing the plant damping would lower the plant gain in the excitation frequency bands.

The figure 32 shows that in both these cases there is relatively smaller performance penalty (in terms of peak splitting). The results have been computed for large noise standard deviation σ.

We are now in a position to explain the difference between the experimental results in single-nozzle rig shown in Figure 16 and sector rig shown in Figure 17. We can attribute the higher uncontrolled oscillations level in the single nozzle rig to a lower damping of the plant. Moreover, the plant delay identified from the frequency responses was higher in the sector rig than in the single-nozzle rig. As we have argued above, a low damping factor and a low delay value would prevent the peak splitting.

Practical implications of this analysis are as follows. Even though peaking in the sensitivity function is unavoidable in current combustion process control due to large process delay and small actuator bandwidth, it leads to serious limitation of achievable control performance (peak splitting) only in the case of large plant delay and large plant damping, like in the case of high equivalence ratio condition.

In this case the open-loop pressure oscillations are relatively small and control objectives are modest, so that the required level of pressure oscillations could be met even in the presence of performance limiting factors described in this paper. In the case when the performance specification cannot be met, an actuation mechanism that involve smaller value of process delay has to be developed. This could be achieved by fuel injection closer to the flame area or by an increased mixing rate.

Conclusion

In the first part of this paper, we conducted linear analysis of combustion instability in UTRC rigs with control. It was experimentally determined that linear analysis was applicable for the high equivalence ratio and large delay in the feedback loop and limited actuator bandwidth are major factors that limits the effectiveness of the active control. An intuitive Nyquist based analysis was used to analyze the performance characteristics of the simple phase-shifting controller. In order to study the fundamental limitations imposed upon performance due to the presence of delay, unstable dynamics and limited controller bandwidth, a more sophisticated controller independent analysis was carried out with in the framework of linear control theory. In particular, the peak-splitting phenomenon observed in our experiment and reported by other researchers was explained with the aid of this analysis. In the second part of this paper it has been shown that random input describing function analysis is an appropriate tool to study effect of the strong driving disturbance in a nonlinear model. The describing function analysis predicts that for sufficiently large levels of disturbance, the loop effectively behaves linearly with the feedback gain dependent upon the variance of the Gaussian noise. As a result, the fundamental limitations studied in the the first part of this paper can be used to explain the peak splitting phenomenon even in the nonlinear case.

Acknowledgement

References

[1] J.R. Seume, N. Vortmeyer, W. Krause, J. Hermann, C.-C. Hantschk, P. Zangl, S. Gleis, D. Vortmeyer, and A. Orthmann, "Application of active combustion instability control to a heavy duty gas turbine," in *ASME Paper 97-AA-119, Proc. of ASME Asia '97 Congress and Exhibition, Singapore, October 1997.* 1997, ASME.

[2] G.J. Bloxsidge, A.P. Dowling, N. Hooper, and P.J. Langhorne, "Active control of acoustically driven combustion instability," *Journal of Theoretical and Applied Mechanics*, vol. 6, pp. 161–175, 1987, special issue, supplement to Vol. 6.

[3] G.J. Bloxsidge, A.P. Dowling, N. Hooper, and P.J. Langhorne, "Active control of reheat buzz," *AIAA Journal*, vol. 26, pp. 783–790, 1988.

[4] P.J. Langhorne, A.P. Dowling, and N. Hooper, "Practical active control system of combustion ocsillations," *Journal of Propulsion*, vol. 6, pp. 324–333, 1988.

[5] J.P. Hathout, A.M. Annaswamy, M. Fleifil, and A.F. Ghoniem, "A model-based active control design for thermoacoustic instability," *Combustion Science and Technology*, vol. 132, pp. 99–105, 1998.

[6] M. Fleifil, A.M. Annaswamy, J.P. Hathout, and A.F. Ghoniem, "The origin of secondary peaks with active control of thermoacoustic instability," in *Proceedings of the AIAA Joint Propulsion Conference, Seattle 1997*, 1997.

[7] J. M. Cohen, N. M. Rey, C. A. Jacobson, and T. J. Anderson, "Active control of combustion instability in a liquid fueled low NOx combustor," in *1998 ASME Gas Turbine and Aerospace Congress*. 1998, ASME.

[8] J.R. Hibshman, J.M. Cohen, A. Banaszuk T.J. Anderson, and H.A. Alholm, "Active control of combustion instability in a liquid-fueled sector combustor," in *1998 ASME Turbo Expo*. 1999, ASME.

[9] W.R. Saunders, M.A. Vaudrey, B.A. Eisenhauer, U. Vandsburger, and C.A. Fannin, "Perspectives on linear compensator designs for active combustion control," in *AIAA paper 2000-0717, 37th AIAA Aerospace Sciences Meeting, Reno, January 1999*. 1999, AIAA.

[10] T. J. Anderson, W.A. Sowa, and S.T. Morford, "Dynamic flame structure in a low nox premixed combustor," in *1998 ASME Gas Turbine and Aerospace Congress*. 1998, ASME.

[11] A.A. Peracchio and W. Proscia, "Nonlinear heat release/acoustic model for thermoacoustic instability in lean premixed combustors," in *1998 ASME Gas Turbine and Aerospace Congress*. 1998, ASME.

[12] F.E.C. Culick, W.H. Lin, C.C. Jahnke, and J.D. Sterling, "Modeling for active control of combustion and thermally driven oscillations," in *Proceedings of the 1991 American Control Conference*. 1991, pp. 2939–2948, IEEE.

[13] R.M. Murray, C.A. Jacobson, R. Casas, A.I. Khibnik, C.R. Johnson Jr., R. Bitmead, A.A. Peracchio, and W.M. Proscia, "System identification for limit cycling systems: A case study for combustion instabilities," in *Proceedings of 1998 American Control Conference*, 1998.

[14] V. Burnley, *Nonlinear Combustion Instabilities and Stochastic Sources*, Ph.D. thesis, California Institute of Technology, Pasadena, CA, 1996.

[15] T.C. Lieuwen and B.T. Zinn, "Investigation of limit cycle oscillations in an unstable gas turbine combustor," in *AIAA paper 2000-0707, 38th AIAA Aerospace Sciences Meeting, Reno, January 2000*. 2000, AIAA.

[16] C. A. Jacobson, A. I. Khibnik, A. Banaszuk, J. Cohen, and W. Proscia, "Active control of combustion instabilities in gas turbine engines for low emissions. part i: Physics-based and experimentally identified models of combustion instability," in *Applied Vehicle Technology Panel Symposium on Active Control Technology*, Braunschweig, Germany, May 2000.

[17] U. Ingard and S. Labate, "Acoustic circulation effects and the nonlinear impedance of orifices," *J. Acoustical Soc. America*, vol. 22, no. 3, March 1950.

[18] U. Ingard, "Acoustic nonlinearity of an orifice," *J. Acoustical Soc. America*, vol. 42, no. 1, 1967.

[19] A. Banaszuk, Y. Zhang, and C.A. Jacobson, "Active control of combustion instabilities in gas turbine engines for low emissions. part ii: Adaptive control algorithm development, demonstration and performance limitations," in *Applied Vehicle Technology Panel Symposium on Active Control Technology*, Braunschweig, Germany, May 2000.

[20] A. Banaszuk, Y. Zhang, and C.A. Jacobson, "Adaptive control of combustion instability using extremum-seeking," in *2000 American Control Conference*, Chicago, June 2000.

[21] A. Banaszuk, K.B. Ariyur, M. Krstic, and C.A. Jacobson, "An adaptive algorithm for control of combustion instability," *Automatica*, 2000, submitted.

[22] M.M. Seron, J.H. Braslavsky, and G.C. Goodwin, *Fundamental Limitations in Filtering and Control*, Springer, New York, 1997.

[23] J. Doyle, B.A. Francis, and A. Tannenbaum, *Feedback Control Theory*, MacMillan, New York, 1992.

[24] J.S. Freudenberg and D.P. Iooze, "A sensitivity tradeoff for plants with time delay," *IEEE Trans. Automatic Control*, vol. AC-32, pp. 99–104, February 1987.

[25] A. Gelb and W.E. Vender Velde, *Multiple–Input Describing Functions and Nonlinear System Design*, McGraw–Hill, 1968.

[26] G. Zames, "Dither in nonlinear systems," *IEEE Trans. Automatic Control*, vol. AC-21, pp. 660–667, 1976.

[27] C.A. Desoer and S.M. Shahruz, "Stability of dithered non-linear systems with backlash and hysteresis," *Int. J. Control*, vol. 43, pp. 1045–1060, 1986.

[28] Andrzej Banaszuk, Clas A. Jacobson, Alex I. Khibnik, and Prashant G. Mehta, "Linear and nonlinear analysis of controlled combustion processes. part i: Linear analysis," in *1999 Conference on Control Applications*, Hawaii, August 1999.

[29] Andrzej Banaszuk, Clas A. Jacobson, Alex I. Khibnik, and Prashant G. Mehta, "Linear and nonlinear analysis of controlled combustion processes. part ii: Nonlinear analysis," in *1999 Conference on Control Applications*, Hawaii, August 1999.

[30] A. Banaszuk, P.G. Mehta, C.A. Jacobson, and A.I. Khibnik, "Limits of achievable performance of controlled combustion instability," *IEEE Transactions on Automatic Control*, 2001, submitted.

This page has been deliberately left blank

_____

Page intentionnellement blanche

Active Control of Engine Dynamics: Fundamentals and Fluid Dynamics – Experiments

K.H. Yu

Department of Aerospace Engineering
University of Maryland
College Park, MD 20742, USA
E-mail: yu@eng.umd.edu

Summary

Combustion reactions in a confined system are very difficult to predict as they involve unsteady flow dynamics, non-equilibrium chemical kinetics, and additional complexity introduced by potential interaction between them. Dynamic response of the reactants feed systems, vibration characteristics of the structure, and the enclosed fluid may also interact with the heat release processes making it difficult to assess the relative importance of various mechanisms. In the first part of this lecture, fundamental flow and combustion processes that determine the behavior of combustion system dynamics will be briefly discussed. Also, while experiments on combustion system dynamics and control have been performed for centuries, the modern-day combustion-control experiments involving a fast-response dynamic feedback loop have been conducted only in the last 15 years. Depending on the particular application and design, several different active control approaches have been utilized. Different approaches of actively controlling combustion will be summarized and the essential features as well as the new insight obtained in those experiments will be discussed. The second part of this lecture will provide a brief review of recent experimental studies, categorized by applications. While earlier studies were motivated mainly by instability suppression in propulsion applications, recent research and developments on active combustion control have considered a large variety of applications involving a wide range in scope. Some of the new interests have come from power generation and incineration industries as well as more traditional propulsion industry. The scope and the hardware considered in these investigations vary widely, stemming from, for instance, the use of simple Rijke tube for control algorithm development to full-scale implementation into an industrial gas turbine.

1. Active Control Classification

Active combustion control (ACC) is an emerging art of regulating combustion performance using a dynamic hardware component that rapidly modifies combustion input. ACC is an attractive idea because it relies on proper timing of fuel injection rather than spatial changes of flowfield as required in passive approaches. Since timing adjustment is simpler than the potential geometry modifications associated with passive control, ACC provides flexibility in performance and eliminates costly design changes. With the recent advances in electronics, it is becoming a very popular technology in propulsion and power industries.

The relative performance of active control action can only be defined within the context of the applications. Such performance is also closely correlated with the sensors and actuators as well as the controllers. Furthermore, there are usually more than one performance parameters that are important, and the practical problem of active control implementation often takes a form of a constrained optimization of a coupled system output. Consequently, the research and development of active combustion control technology have taken vastly different approaches and forms.[1-3] Thus, a lot of work that have been done until now are rather unique in certain elements, and it is difficult to classify them into standard categories. Nevertheless, in the following, an attempt is made to create a general classification for much of the experimental, numerical, and control-oriented analytical works as well as component related research.

1.1 Hierarchy of Active Control

First, much of the experimental research, which has been conducted to date, can be grouped into three general categories that indicate the degree of system complexity. Figure 1 shows a schematic of an active control component diagram. It shows three essential sub-components of an active control system -- actuator, controller, and sensor.
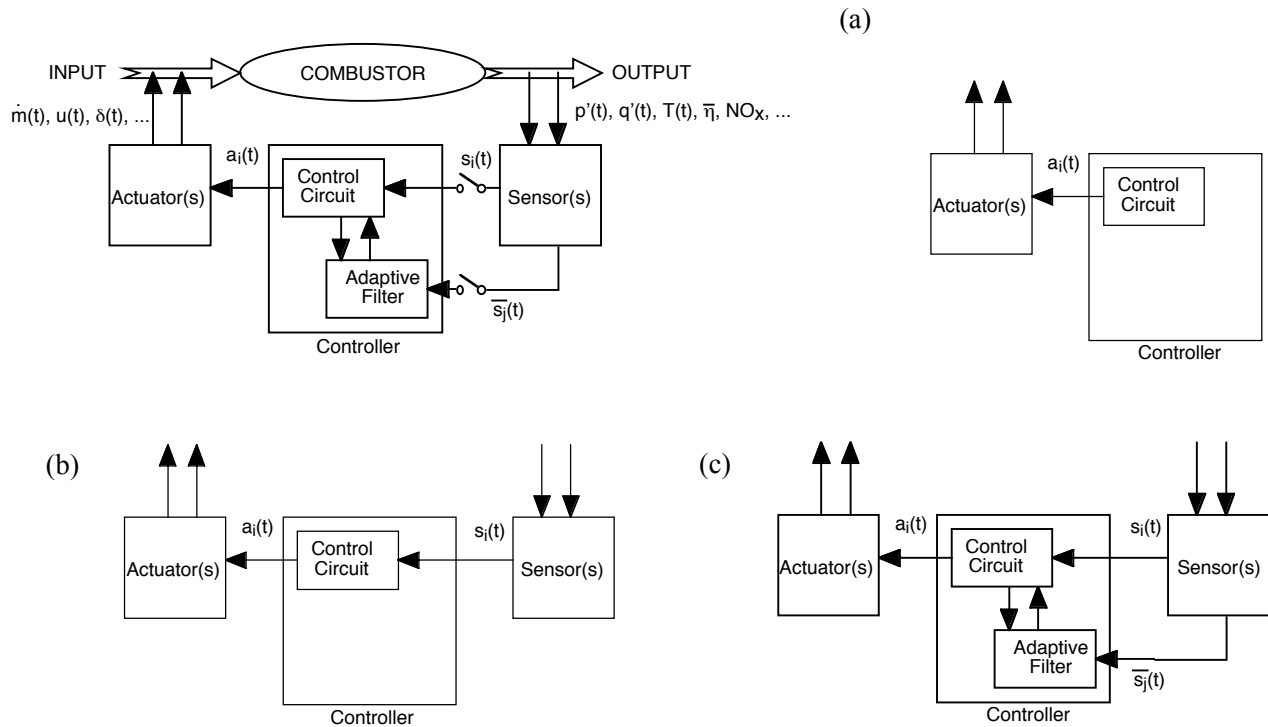

Figure 1. Schematic of an active control system
(a) Open-loop control, (b) Closed-loop control, and (c) Adaptive control

OPEN-LOOP CONTROL

An open-loop control system consists of only actuator and controller, as shown in Fig. 1a. Because the controller output is pre-programmed, there is no need for a sensor. This is a simplest form of active control, and it relies on perturbing the input to the combustor enough to obtain the desired output. In order to be of practical use, the input action of the actuator may need to be amplified by the flow structure or coupled with other physical processes.

The useful actuator must be able to alter sufficiently the combustion process or those processes that closely affect the combustion process, given the proper control action. Some of the more common actuators include fuel injectors, acoustic drivers, and mechanical shakers. Typical control action consists of generating oscillatory inputs having sufficient amplitude and frequency to obtain the desired outcome.

Due to its inherent simplicity, an open-loop system is very easy to implement. To determine whether this approach is adequate for a given system, an open-loop transfer function of the combustor is required. While such transfer function can be obtained not just by experimental method but also by analytical or numerical approaches, this step is considered most critical as the optimized performance depends on the fixed control action.

Some of the examples of open-loop control include not only instability suppression but also combustion enhancement and emission reduction. The details of these experiments will be discussed in the ensuing sections.

CLOSED-LOOP CONTROL

A closed-loop control adds a sensor element to the open-loop control. Figure 1b shows the schematic of a closed-loop control. The role of the sensor is to monitor the combustor output in real time and actively modify the control action accordingly. Since a feedback action is required with the close-loop control, it is desired that the frequency response of the closed-loop sensor exceed the operating frequency of the actuator and the controller.

For dynamic feedback consideration, desirable parameters for sensing are pressure fluctuations, heat release fluctuations, and temperature fluctuations. In earlier investigations, pressure and lumination sensors were most commonly used as temperature sensing via a thermocouple yielded rather slow frequency response. With proliferation of diode lasers, however, sensing temperature fluctuation and product species concentration has also become a viable option. In fact, sensor development has been one of the key areas that helped the renewed interest in the technology.

Also, employing a closed-loop system placed an added importance to the control algorithms. The control algorithm can be as simple as a given phase lag between sensor and actuator to some that may require extensive control logic. Some of the more notable control techniques are summarized in Section 1.4. In a closed-loop control, because of the feedback design, one of the key elements a controller designer must consider is the stability characteristic of the controller. Also, the robustness of the controller to parameter variation needs to be considered.

ADAPTIVE CONTROL

Adaptive control refers to a self-adjusting controller that can modify the controller action depending on the transient external circumstance. In a simple closed-loop control as defined in Fig. 1b, the optimum control action may change over time depending on the other output that are not being sensed. For instance, such output may amount to the altitude or the speed of vehicle in a propulsion system, and for a power generation device, it may amount to the overall power output level. In any rate, having an extra layer of control allows one to adjust the closed-loop filter in such a way that the control action is optimized for all conditions.

Figure 1c shows a schematic of an adaptive controller. Typically, the parameter that requires a change in the controller setting varies much more slowly than the closed-loop controller of Fig. 1b. Consequently, the adaptive filter may not need to operate at the same frequency response as the primary controller. In the same token, an open-loop adaptive control filter may also be used if the slow change in time-averaged parameters is already known. However, a typical adaptive filter may require an additional sensor that provides transient response of the short-time averaged output.

A more extended view of an adaptive control system is a control system that provides a "self-calibration." In that sense, any of the closed-loop controller which allows an on-line system identification may be considered an adaptive control system. Thus, in this expanded definition, most of the closed-loop controller, except those that require an off-line system identification, would be considered an adaptive controller. The real distinction, then, is how fast the system identification and implementation of the modified control action can be implemented in the controller. Some of the earlier experiments that incorporated an adaptive technique used a single sensor and adaptive numerical filters that updated the controller action at the same sampling rate by averaging the signal over a short time period.[4]

1.2 Actuators

In any practical application, actuators and sensors are the key components that enable the use of the active control approach. In that sense, combustion response to actuators is the single most important characteristic that determines the potential of the active control approach and sets the boundaries of the control ability. This is evident from the fact that an actuator is an essential part in all three control systems classified in Fig. 1. The characteristics of actuated combustion performance is what sets active control approach apart from other passive methods.

Some of the ACC actuators that have been used to date include (1) compression drivers that add acoustic energy at particular frequencies, (2) small flow injectors that add secondary mass flux at particular timing, (3) large flow valves that modulate the total mass flux, (4) mechanical devices that either trip the transient boundary layers or change the shear layer mixing, (5) fluidic devices that add momentum to the flow without changing the mass flux, and (6) special electrodes that initiates current-stabilized electric discharge[5,6]. Also, some of the recent actuator development work have considered utilizing various material properties including piezoelectric and magnetostrictive characteristics as well as electro-mechanical behavior. Also, other physical mechanistic characteristics such as atomization modulation and electrostatic potential have been explored for actuator consideration with mixed results.
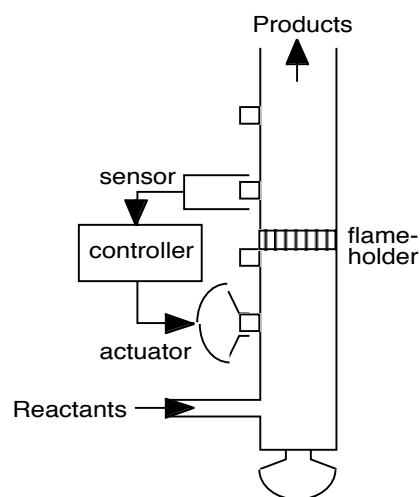
Figure 2. Typical active control demonstration experiments using a simple tube combustor.

ACOUSTIC DEVICES

Acoustic devices create pressure waves, which influence the combustion performance in several different ways. One way is a direct interaction between acoustics and combustion via Rayleigh criterion, which changes the amount of acoustic energy gain. Joos and Vortmeyer[7] showed the importance of combustion-acoustic interaction by recording simultaneously self-sustained oscillations of the acoustic pressure, acoustic velocity, and combustion via OH- radical emission. They showed that oscillation amplitude was suppressed when pressure and energy oscillations became out of phase.

In many earlier experiments involving active combustion control, loud speakers were used to control pressure oscillation phase. They were widely used because of the easy availability and good frequency response characteristics. Figure 2 shows a schematic of a typical set-up employed in some of these experiments, which demonstrated suppression of combustion instabilities.[8-10] Lang et al.[8] employed a 10-W loudspeaker system to suppress longitudinal instability using a simple, constant-gain, phase-shift controller with very little energy consumption. Gleis et al.[10] proposed the use of active control system to study the onset of self-sustained instability in simple premixed laboratory burners.

Another way that acoustics alter the combustion performance is by generating large coherent structure that affect the large-scale mixing process. Jets, wake flows, and shear layers are particularly sensitive to acoustic forcing at certain frequencies, which create large vortices. For instance, such flow features amplify initial excitation with a relatively small amplitude, thus allowing manipulation of the mixing between fuel-and-air or reactants-and-products.

Figure 3 shows a premixed combustor at Ecole Centrale Paris, where some of the early active control experiments were conducted. Yu et al.[11] used a pair of loudspeakers to organize large coherent vortices in the wake of the V-gutter flameholder. The volumetric heat release was increased by up to 50% depending on the frequency. Figure 4 shows a comparison of flame structures with and without acoustic excitation. The observed heat release pattern in that experiment closely followed the vortex motion which was responsible for combustion enhancement. The increase in volumetric heat release was a function of the vortical structures with the highest increase observed when the Strouhal number, based on the inlet velocity and flameholder dimension, was between 0.4 and 1.6. The flame structures in Fig. 4b and 4c caused 40% and 30% increase in volumetric heat release respectively compared to that in Fig. 4a. Phase-lock-averaged C2 chemiluminescence image in Fig. 4c also shows the nature of periodic heat release associated with the vortical structure.

Acoustic devices can also be used to change the turbulence intensity directly. For instance, large-amplitude excitation can increase the turbulent transport property sufficiently to enhance molecular-level mixing, which in turn increases the turbulent flame speed. This approach, however, would require a substantial amount of acoustic energy to be effective.
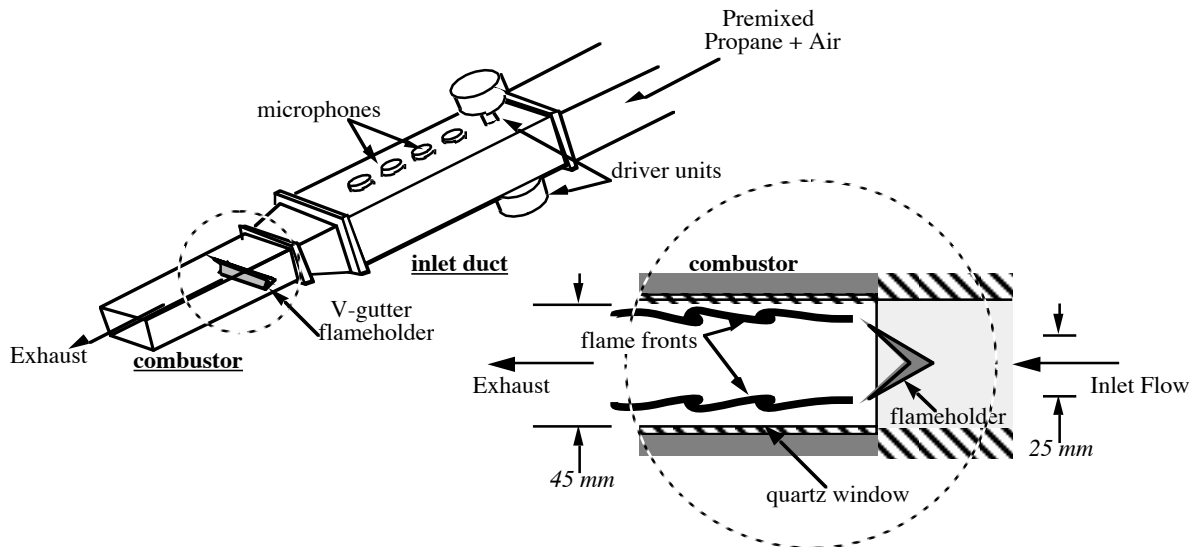
Figure 3. Open-loop active control experiment at Ecole Centrale Paris. [Yu et al 1991]

The compression drivers are effective in controlling certain type of combustion devices, particularly those in which the burner is not pressurized or the initial turbulence intensity is low. Gulati and Mani[9] ran a similar experiment as that of Lang et al.[8] and reported that the control performance deteriorated at higher output conditions. While they suggested a need for a better controller, the results also indicated the deterioration in actuator effectiveness. If the difference in turbulence intensities between flows with and without actuation became less significant, the potential performance benefit associated with active combustion control action would also be reduced.

Another way an acoustic device can be utilized as an actuator is by focusing acoustic energy to a localized area. McManus et al[12] used acoustic devices to acoustically force the boundary layer just upstream of the flow separation. In contrast to setting up a global acoustic field inside a combustor, they attempted to localize the actuation where the local disturbance can easily be amplified. Later, such idea led to the development of "zero-mass-flux" actuator, also know as synthetic jets. Typically, these actuators utilize piezoelectric mechanism to obtain very high frequency response.

MASS FLUX MODULATION

Mass flux modulation can be considered an extension of localized acoustic oscillations but with net flow rate. Choudhury et al.[13] used a series of pulsed jets whose flowrates were controlled by a rotating valve to affect the flowfield just upstream of the rearward-facing-step flame holder. Poinsot et al.[14] successfully implemented a closed-loop pulsed-fuel-injection strategy in a bluffbody flameholder combustor and demonstrated about 20 dB reduction in oscillation amplitude.

Gutmark et al.[15,16] studied acoustically forced jet flame characteristics using a loudspeaker mounted in the plenum chamber and found that the stability characteristics were affected if the forcing frequencies were close to the Kelvin-Helmholtz frequency or preferred mode frequency. A similar system was later installed in a fuel line to modulate the fuel flux in a controlled fashion.[17,18]

Fuel flux modulation, especially that involving liquid fuel, can be obtained via high-frequency-response fuel injectors and servo valves. Langhorne et al.[19] used an automotive fuel injector to obtain on-off modulation of fuel flux. The modulated fuel flux was pre-vaporized before being injected into the combustor. Yu et al.[20] utilized a swirl atomizer which was close-coupled to an automotive fuel injector to obtain finely atomized pulsed fuel sprays. Such sprays were injected directly into the self-sustained vortex structure in the combustor to minimize the controller fuel consumption. The same authors later utilized air-assisted atomization of pulsed fuel sprays to further reduce the controller fuel droplet size.[21,22]
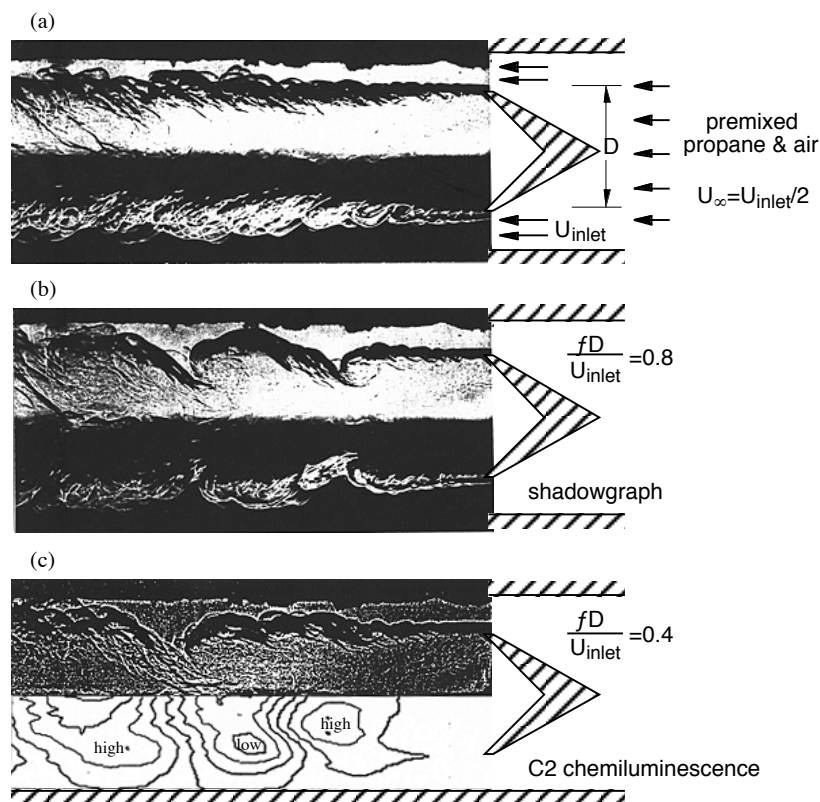
(a)

(b)

(c)

Figure 4. Flame structures associated with open-loop combustion control. Reynolds No. = 60,000, u'/U~0.1 (a) Baseline case with Strouhal No., fD/U =0, (b) Strouhal No. = 0.8, and (c) Strouhal No. = 0.4. [Yu et al. 1991]

Typical fuel injectors suffer from limited frequency response. This is due to the fact that the displacement amplitude of electromechanical actuation decreases with frequency. Consequently, performance of a typical actuation device, designed for certain displacement amplitude, deteriorates at high frequencies. Neumeier & Zinn[23] developed a high frequency actuator that takes advantage of a special material property using magnetostrictive device. Under actuation, such a device produces a small change in material length but with relatively large actuation force suitable for liquid flow modulation.

For actuating large mass flux such as in air flow modulation, electro-pneumatic transducers and electro-hydraulic servo valves can be employed. These valves typically contain a vibrating mechanical device that restricts the orifice size within a certain frequency range, typically reaching an upper limit of several hundred Hertz. Parr et al.[24] and Gutmark et al.[25] used such devices to create periodic vortical structures in air flow and actively controlled vortex combustion effectively reducing an incinerator size. While one drawback of the large capacity drivers is their high cost, Wilson et al.[26] developed a more affordable actuator using a piezoelectric wafer, that can be implemented in a similar system.

HEAT FLUX MODULATION

In most cases involving instability suppression, the end goal of actuation is to bring about controlled modulation in heat release. While the previously considered actuation approaches utilize either combustion-acoustic interaction or modulation of reactant flow rate to achieve this, there are other actuation approaches that try to control heat release directly. One such approach is to generate electric plasma. Afanasiev et al.[5] utilized electric arc discharge to add electric energy to the combustion system. While the arc discharge also produced acoustic emission, the net effect was to produce unsteady heat addition. Because the electric resistance of the flowfield was a function of the ionized combustion products, the amount of electric energy added became a function of transient combustion energy release.

Schadow et al.[27] used periodically generated flame kernels as an actuation device. The transient flame kernels were generated by igniting a flowrate-matched premixed flow with periodic sparks. Hermann et al.[28] used a pilot burner as an actuator. The flow rate of pilot gas was modulated with a direct drive servo valve and the associated heat release modulation from the pilot burner was then used for actuation of the main burner. The flow rate for pilot burner ranged between 5 % to 10 % of the main fuel flux.

MOVING SURFACES

Unlike acoustic devices which utilize vibrating diaphragm to generate acoustic waves that propagate at sound speed, moving surface devices oscillate in such a fashion to create local disturbances that propagate at convection velocity of the flow. This would be due to either high damping characteristics of the moving mass or because the oscillation frequency is outside the range that favors acoustic energy propagation in the ducted system. As a result, the actuation from a moving surface devices amounts to the modification in the boundary condition or the change in convective mass flux.

Bloxsidge et al.[29,30] utilized an actively controlled moving plug to suppress low frequency instability typically referred to as reheat buzz phenomenon. The plug was oscillated using a mechanical shaker device at relatively low frequencies using a band-pass filtered feedback circuitry. The instability frequency was at 88 Hz with substantial cyclic deviation. According to the authors, the primary mechanism was the change in acoustic boundary conditions. A similar shaker device was applied to a V-gutter flameholder by Trouve et al.[31] The flameholder was oscillated in a rocking motion in an effort to create organized vortices that would affect volumetric heat release. However, the limited frequency response of such devices made it difficult to produce significant changes in the reacting flowfield. The combustor flowfield, which was actuated at frequencies substantially different from the characteristic flow frequency and the system acoustic frequency, behaved in a quasi-steady fashion.

Piezoelectric film and shape memory alloy actuators can produce oscillations in high and low frequency ranges respectively. These materials are the type of smart structure module, and are being considered for flow control applications. Although there has not been any reported use of these materials in combustion control applications as of yet, these actuators could also be useful if the frequencies of application interest matches the range of actuators.

1.3 Sensors

Sensors with the proper time-response characteristics are needed in closed-loop feedback control applications. While it is important that the ACC sensors provide a timely response of the result due to actuation, they do not have to directly monitor the particular system property that the control approach is trying to optimize. It is sufficient that the sensor provides the information that is a precursor to the system property that the controller wants to optimize. Sensors with two different response time-scales may be considered. The sensor for direct feedback application requires sufficiently short time response consistent with the ACC goals. On the other hand, a slow-response sensor could still be used for the use with the outer adaptive loop.

The availability of sensors is closely linked to the diagnostic capability as well as the manufacturing practices. With the proliferation of compact diode lasers and micromachining technology, new sensors are being developed at a fast pace. This in turn will enable better optimization of combustor performance. Like actuators, sensor characteristics determine the boundary of controllable performance such as frequency range and instability amplitude. However, unlike actuators, sensors are not a "show-stopper"; instead, they simply enhance the potential for control-performance optimization.

While the specification required for sensors depends on the particular application and the environment at which the sensors are to be used, general consideration of the approach demands that the sensors be rugged, suitable for high temperature, and have good frequency response.

PRESSURE AND HEAT RELEASE

Some of the performance parameters that active control approach often addresses include pressure oscillations and heat release characteristics. Therefore, conventional sensors typically include measurements on dynamic pressure or instantaneous heat release. For dynamic pressure measurements, piezoresistive-type or piezoelectric-type transducers are often employed because of their high sensitivities and high natural frequencies. Leadless sensors for pressure measurements in hostile environment are also being considered recently.[32] For heat release measurements, optical techniques are often preferred over conventional thermometry or heat flux transducers, because of the cost consideration as well as the frequency response.

Microphones or dynamic pressure transducers have been used to provide rapid response feedback to actuation output. Pressure measurements have often been associated with combustion instability suppression. In such a case, the sensor signal provides the direct information on the parameter that is being controlled. Depending on the type of performance being controlled, pressure measurement may be made at any location. However, for longitudinal instability suppression, the pressure sensor should not be mounted at acoustic node location.[14]

Photodiodes and photomultipliers have also been widely used in earlier experiments.[4,33] Such luminosity sensors can be combined with a narrow-band intereference filter to provide information on chemiluminescence. The most widely used radical species are CH, C2, and OH radicals, as the chemiluminescence from these radicals appear almost exclusively in the reaction zone. Depending on the flame characteristics and flow conditions, radiation intensity within certain wavelengths, corresponding to the chemiluminescence from those radicals, can be used as an indicator of heat release. The wavelengths typically chosen are 431.5 nm, 516.5 nm, and 306.5 nm for CH, C2, and OH radicals, respectively.[34]

Chemiluminescence is often used in lean premixed flame environments, such as in gas turbines. The intensity of chemiluminescence decreases at higher pressure due to the dominant effect of quenching rate, but the increase in volumetric reaction rate and higher concentration of radical species partly compensate for the adverse pressure dependence. As a result, the decline in radical chemiluminescence intensity at higher pressure is rather gradual and it would still be possible to use chemiluminescence as an indicator of reaction dynamics. However, chemiluminescence measurements would not be a good indicator in the presence of soot or any other blackbody radiation that can interfere with the chemiluminescence intensity in the selected bandwidths.

CONCENTRATION AND TEMPERATURE

Flue gas analyzers are often used to measure the chemical composition of combustion products, such as NOx, CO, or unburned hydrocarbons.[24,35] Most gas analyzers utilize electrochemical sensors or a chromatographic system to measure concentration of certain species, but typically a steady sampling of subject gas is required. Consequently, the response time, associated with in-situ sampling, is limited, usually on the order of 10 sec. Thus, while the output of conventional gas analyzers can be used as a slow sensor for the adaptive loop in emissions monitoring, it is not appropriate for a fast-response feedback sensor.

For in-situ monitoring as required in a fast-response, close-loop-control application, optical techniques are again gaining a popularity. Also, the optical techniques are no longer limited to emission spectroscopy, as active laser diagnostic techniques have been made more practical in the last few years. In particular, the advancement in small, affordable diode lasers has contributed significantly to the sensor development. Some of the diode-laser-based sensors have already been field tested with active control loop using either in-situ or fast extractive sampling approach. Furlong et al.[36,37] demonstrated the use of diode-laser sensors in more practical environment by successfully implementing the sensor in a compact waste incinerator[35] which was closed-loop controlled.

For active control sensor application, absorption techniques, which provide measurements averaged over a path, are most widely used.[38] For determining vibrational gas temperature and species concentration, absorption measurements at multiple wavelengths have been used.[39] Typical wavelengths, used for such absorption measurements, have been in the near-infrared or in the infrared ranges. Hanson & Baer[38] and co-workers at Stanford[36,37,40] have developed diode-laser absorption sensors for number of combustion-related species, including H_2O, CO, CO_2, NO, NO_2, N_2O, as well as O_2 and various hydrocarbon species. Some of the specific wavelengths that have been successfully tested are 1.34 μm and 1.39 μm for H_2O, 1.5 μm and 2.3 μm for CO, and 1.5 μm and 2.0 μm for CO_2.

MEMS ACTUATORS AND SENSORS

Some of the interest in MEMS (Micro-Electro-Mechanical-System) devices come from the facts that the micromachining technology is rapidly emerging and it provides potential reduction in cost. With potential reduction in size, it may also be possible to further enhance performance by considering an

option of a large-scale distributed control system. Along the same line, it may be possible to extend active combustion control to miniaturized combustion systems being considered for various applications such as micro-UAV or micro power generation systems.

While MEMS actuators and sensors are not yet practical enough to be used in hostile combustion environment, there are still much interest in research and development community for the inherently fast time response associated with their sizes. Ho & Tai[41] reviewed the MEMS devices suitable for flow control applications. There has been much effort on concept demonstration by building micro sensors and actuators such as micro flap actuators[42,43] and micro pressure sensors.[44] However, most of these systems are still too fragile for rugged applications. More research is needed to make them practical.

1.4 Control Algorithm

While actuator is the component that enables the use of active combustion control approach in a target system, control algorithm is the part which can make the technique successful. Thus, the optimization of performance is closely linked to the characteristics of the control algorithm. In the same context, the role of sensor is to extend the capability of control algorithm by providing pertinent system response data on controller's action.

In the simplest form of ACC, the controller executes a pre-determined control action without the help of sensors. An open-loop controller, if it can be implemented effectively, is a preferred choice over a closed-loop controller which is more complex. However, the applicability of an open-loop controller is somewhat restricted because it is generally not possible to determine the transient response of the system to actuation. Unless such information is known a priori, it would be difficult to determine a proper course of control action. Thus, a use of feedback loop is often employed out of necessity to gain understanding on system response characteristics.

In actively controlling combustion through the use of a feedback loop, a number of different control algorithms have been implemented over the years with various results. However, unless these algorithms were applied to the same system under the same conditions, it is not fair to draw any conclusions based on system-specific controller response. For the same token, one controller may work better under certain situation than others further complicating their comparison. In the following, some of the different control algorithm approaches are described and the corresponding results are examined where applicable.

PROPORTIONAL CONTROL

Proportional control describes the simplest type of closed-loop control algorithms, which has also been most widely used. This type of algorithms can be further classified into P-controller (proportional), PI-controller (proportional-integral), PID-controller (proportional-integral-derivative), and other similar varieties depending on the second-order correction.[45,46] In the simplest form, there are one input from the sensor and one output to the actuator. The sensor signal is transformed into a proportional output using an operational amplifier. In PI-control, an adjustment can be made to the baseline value by integrating the errors in time, while the derivative portion in PID-control can resolve the time response more precisely.

Fung & Yang[47] provided a theoretical analysis describing various proportional control approaches applied to nonlinear combustion instabilities. They established an optimization procedure for gain selection. Most of the control algorithms used in earlier experiments belong to this category. While the controller is very flexible in term of control parameter adjustment, it may not be sophisticated enough to respond to other performance challenges.

NEURAL NETWORK

Neural network describes an adaptive logic system which is modeled after the structure of the brain. In a simple neural network, various inputs from different sensors are multiplied by respective weighting function. A transfer function is used to convert the combined results, which are then used as the input to the actuators. Because of the apparent adaptation to different operating conditions, neural network

belongs to a class of controllers that are termed adaptive control. A potential problem associated with neural networks occurs during the training period when the controller is learning the response to various actuation. Clearly, this type of control algorithm would be more appropriate in cases where improper actuation never cause drastic failure. For added safety, a control algorithm utilizing a neural network can be pre-trained using simulation data. This would help setting up safety margins for final training of the neural network via direct experiments.

Gutmark et al.[33] first applied such an algorithm in active combustion control system using multiple input signals. The authors used a neural network filter consisting of seven hidden neurons to transform the two input signals to one output signal. Flame emulator was trained using the back propagation method.. Blonbou et al.[48] applied two neural networks to suppress instabilities in a Rijke tube. Liu & Daley[49] used neural networks to develop a mode observer and output model, which was used to drive acoustic actuation system. Vaudrey & Saunders[50] described the neural network training process which was used to predict the frequency response of a tube combustor.

FUZZY LOGIC

Fuzzy logic describes a multi-valued logic which allows conventional evaluation of the combustor response using so called fuzzy sets, that are constructed on the basis of expert knowledge either pre-programmed or obtained through training. The controller works in a similar fashion as in neural networks except the actual sensor nodes in neural networks are replaced by fuzzy functions and fuzzy rules. By reducing the infinite number of possibilities into a finite number of combinations, the control response for a given situation can be simplified. If the response for many of the combination states can be formulated by expert knowledge, fuzzy logic can effectively reduce the training requirement. Furthermore, because of the simplified logic, controller response can be enhanced. Fuzzy logic can be a powerful tool if extensive physical understanding and operational experience are available. It is especially useful if the control process is very complex and is difficult to model. However, depending on the resolution of the fuzzy subsets, the controlled state may not be fully optimized.

The use of fuzzy logic in active combustion control is rather limited. Menon & Sun[51] applied fuzzy logic rules to suppress longitudinal mode instability in a numerical experiment. Also, recently, a fuzzy logic controller was successfully tested in a liquid-fueled dump combustor experiment at Naval Air Warfare Center in China Lake.

MODEL-BASED CONTROL

Model-based control describes a wide variety of adaptive control approaches in which physically based models were used. Some of the physical processes that can be modeled include not only system acoustics, flow dynamics, reaction dynamics, actuators and sensors, but also prevalent coupling between these processes.

In some of the control-oriented investigations, the system dynamics were represented in the frequency domain using the Bode plot.[46,52] This made it convenient to design the control filter for stability consideration, based on the Nyquist criterion. While this approach can serve as the basis for determining the proper phase delay, it may not work with nonlinear systems or in an unsteady, transient operation.[53]

Annaswamy et al.[54] conducted a model-based control design using the linear quadratic Gaussian (LQG) method, and showed that the LQG controller performed better than proportional controllers in a bench-top combustor similar to those from earlier experiments (Fig. 2). The LQG design is similar to linear quadratic regulator (LQR) controller, but uses a Kalman filter to estimate the states. While the LQG controller is robust in gain and phase, it does not guarantee the gain and phase margins when uncertainties in the states are present.[55] Robustness of such control could be an issue.

OTHER ADAPTIVE CONTROL

There are many adaptive algorithms that are not based on physical models. Some of them have employed an adaptive filter and a least mean squared (LMS) algorithm to update control coefficients.[4,55-57] However, the convergence of coefficients may be sensitive to initial conditions. If all states are not

known, an observer-based approach can be considered to provide a real-time identification of the unstable modes.[58,59] Although a model-based observer can be extended to the LQG controller, designing an observer with a wide robustness range for a nonlinear system can be a challenge.[53]

2. Combustion Oscillations and Control Mechanisms

Combustion instabilities in propulsion systems occur as some disturbances in pressure or velocity are amplified by combustion heat release and generate acoustic energy in a periodic manner. The acoustic energy reinforces the disturbances continually, making the cycles self-sustained. As the increased level of thermal and mechanical loads from combustion instabilities can present serious problems to the performance and structures of the systems, some types of combustion controls may be needed. Passive approaches of changing the system design, such as fitting baffles, resonators, or acoustic liners into the combustors, usually require costly modification and often prove to be impractical because of narrow range of frequencies that can be controlled. In comparison, active control is a very attractive solution. Culick[60] provided theoretical review of combustion instabilities and discussed the pertinent issues associated with actively controlling nonlinear acoustics in combustion chambers.

In suppressing combustion instabilities, one can damp the oscillation amplitude with an out-of-phase combustion-acoustic coupling. This is done by introducing secondary heat release oscillations at a proper phase with respect to the pressure oscillations, which are monitored. By maintaining a proper phase difference, a negative coupling which lowers acoustic energy density is sought. Since this mechanism is governed by Rayleigh's criterion[61], the approach may be described as a Rayleigh suppression method.

Another possible approach of active control is to directly remove the sources of heat release oscillations. When the sources of heat release oscillations which sustain the instabilities are known, the sources may be broken up directly. If the source is related to the large-scale coherent vortical structures in the shear layers, a direct shear layer control may be attempted to disrupt the coherency in the shear layers.

2.1 Rayleigh suppression

Combustion-acoustic interactions may become either a source or a sink of acoustic energy depending on their phase difference. Mathematically, the equation for the acoustic energy balance can be derived from the standard governing equations (Appendix) and can be expressed as the following:

$$\Delta \varepsilon \approx \frac{\gamma - 1}{\gamma} \int_t^{t+T} \frac{p' \, q'}{\overline{p}} d\tau + \text{smaller terms}$$

where $\Delta \varepsilon$ is the change in acoustic energy density after one cycle, p' the acoustic pressure, $\overline{p}$ the mean pressure, q' the fluctuating component of energy release, and T the oscillation period. This relation, commonly known as Rayleigh's criterion in literature, shows that acoustic energy density may increase or decrease in time depending on the phase of q' with respect to that of p'. Chu and Kovasznay[62] discussed higher order source terms stemming from linear disturbances, while Culick[60,63,64] established the foundation for approximate analysis of nonlinear acoustics using Galerkin's approach.

Thus, given a proper phase difference, oscillations in combustion heat release can effectively damp the instabilities. In many active control studies, total fuel flow into the combustors is modulated in order to induce heat release oscillations at a desired phase. Poinsot et al.[14] used loudspeakers as the actuator in imposing acoustic modulations to the upstream flow. As the heat release modulations followed the fuel flow modulations, the instability amplitude would either grow or decay depending on the phase relation with the pressure. Thus, a feedback system was used to maintain a proper phase difference between the pressure signal and the actuator signal. Langhorne, Dowling, and Hooper[19] sought a more practical approach by using solenoid valves instead of loudspeakers. The valves directly regulated the amount of secondary fuel injection into the combustor. Gutmark et al.[18] also used loudspeakers to generate fuel flow modulation. Using a phase-lock controller, they were able to lock into the instability frequency and shift the actuator phase accordingly. The combustor pressure or chemiluminescence signal was used as the

reference signal in this study. In all three experiments, significant reductions in sound pressure level were observed with the control.

The success of fuel flow modulation techniques depend on their ability to induce heat release modulation in a timely fashion. For example, heat release modulation follows fuel mass modulation with a certain delay time, which is associated with atomization, fluid mixing, and/or chemical reaction processes. Unless this delay time is orders of magnitude smaller than the instability period, it must be taken into account to correctly determine the proper phase of modulation. In many cases, experimental measurements are the only sure way of obtaining the correct values of time delay as it depends on many parameters and specific operating conditions. As the phase information on heat release is *a posteriori*, the implementation of fuel modulation techniques usually requires experimental testing procedures.

2.2 Direct shear layer control

As the combustion instabilities are sustained by acoustically coupled heat release oscillations which amplify acoustic energy, de-coupling of combustion process can also lead to suppression of combustion instabilities. Unlike the previous approach in which acoustic energy is damped by out-of-phase combustion-acoustic coupling, the direct shear layer control is an approach to remove the source of heat release oscillations by suppressing the development of large-scale coherent structures in the shear layer.

A number of recent studies, using combustors with either rearward facing steps[34,65-67] or bluff body flame holders[68], revealed that coherent structures in shear layers play the dominant role in modulating the heat release. Schadow et al.[69] identified these structures as drivers of combustion instabilities in their dump combustor. By comparing phase-resolved spatial chemiluminescence pictures with vortex structure visualizations, Yu, Trouve, and Candel[11] showed that heat release oscillations closely follow the vortex trajectories. Since the oscillations in heat release rate is responsible for sustaining the instabilities, controlling the shear layers may be the key to combustion instability control.

The physical mechanisms of the combustion instabilities that are in consideration are illustrated in Fig. 5. The instability cycles consist of a series of linked events that are coupled by combustion-acoustic interactions[34]: acoustic oscillations at the flame-holder sheds vortical structures, burning of these structures provides heat release modulations, and more acoustic energy is generated from combustion-acoustic coupling interactions balancing the intrinsic losses. The link between acoustic oscillations and heat release may be broken up not only by inducing out-of-phase coupling interactions but also by disrupting the coherency in shear layers.
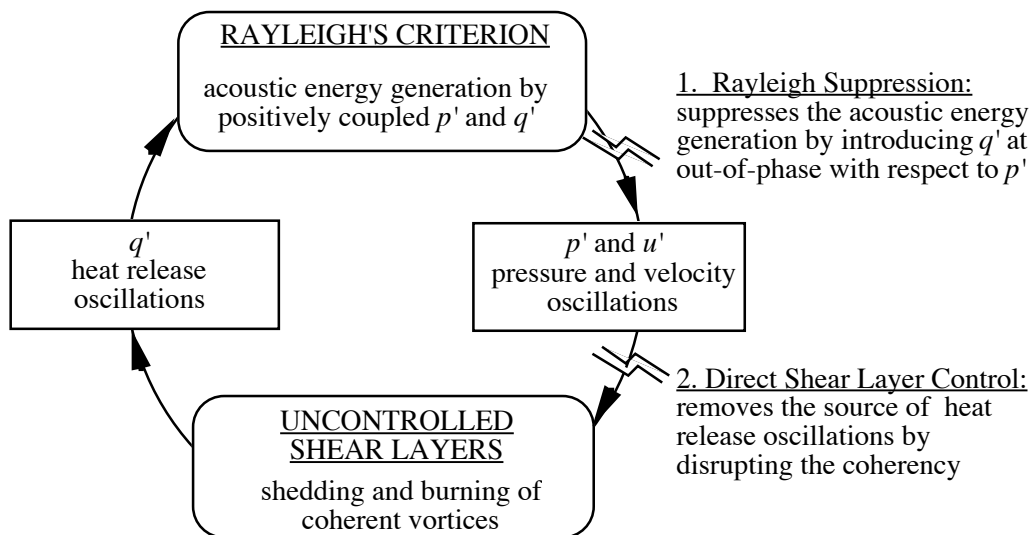

Figure 5. Self-sustained combustion instability cycles and possible controlling mechanisms. The combustion instability in consideration is driven by large-scale coherent structures in the shear layers.

Some encouraging results were shown in earlier experiments. In passive control experiments, using nonstandard inlet duct cross sections, Schadow and Gutmark[70] showed that changing the initial shear flow conditions can be very effective. Taking more active approaches, McManus, Vandsburger, and Bowman[12] were able to change combustor performances by directly exciting the shear layer using a loudspeaker-driven cavity. Yu, Trouve, and Candel[11] obtained similar results by acoustically forcing the upstream inlet flow.

3. Suppression of Combustion Instability

Combustion instability refers to the occurrence of unwanted pressure oscillations with a large amplitude. Any ducted system featuring a source of heat release is susceptible to combustion instabilities. Combustion instabilities may cause significant practical problems by producing excess vibrational or thermal loads to a subjected system. Over the years, excessive amplitude pressure oscillations have been found responsible for causing structural failure, performance degradation, and equipment damage in propulsion systems.[71] Many different approaches have been adopted to study physical mechanisms for such phenomena.[72] Recent interest from the industrial gas turbine industry stems from the desire to operate the gas turbines at very lean fuel-air ratios for NOx reduction consideration. However, it is well known that a lean premixed combustion system is especially susceptible to combustion instabilities.

Combustion instability suppression has been a subject of focused research efforts in recent years and has been the dominant driving force for ACC studies. As a result, the bulk of ACC literature is related to instability suppression. In the following, some of the more recent efforts for actively suppressing combustion instabilities are surveyed.

3.1 Aeroengines

Since the genesis of closed-loop active combustion control work was for instability suppression in aeroengines in the late 1980's, much effort has been focused in this area. While a lot of progress has been made, there are still a lot of work left to be done. One such challenge is to use liquid fuel for control and minimize the fuel amount by directly pulsing it into the combustion chamber. Because of the combustion delays associated with liquid-fuel atomization, droplet heating, vaporization and burning processes, it has been difficult to perform fast-response in-situ control using liquid fuel. Such a challenge is currently being addressed by a coordinated research effort in U.S., which seeks to increase the operational capability of future advanced air-breathing propulsion systems using actively controlled JP-10 fuel management.[73]

RAMJET DUMP COMBUSTOR

Low frequency instabilities associated with longitudinal mode were the subject of numerous earlier investigations. Many experimental[34,67,68,74-76] and computational studies[77,78] have shown the critical role of large coherent vortical structures in driving these instabilities and the importance of combustion-acoustic interaction. The initial attempt to suppress these instabilities used the passive approaches.[70] However, with the emergence of ACC demonstration experiments[14,17,33], much attention has shifted to more flexible ACC technology. Computational efforts for actively controlled ramjet soon followed.[79,80]

The earlier investigation on ACC for ramjet used gaseous fuel which is not practical for application. The renewed research effort in this area stems from the desire to extend ACC to liquid-fueled combustors and explore the use of ACC approach in practical liquid-fueled ramjets. Recent progress in liquid-fuel actuator technology and enhanced understanding of the combustor dynamics provided an ideal background to further advance ACC technology to liquid-fueled ramjets. The typical strategy is to inject a small amount of secondary fuel flux in a periodic fashion and actively adjust its timing with respect to the combustor processes.[20,81,82]

In this type of approach, the timing of fuel injection follows the similar consideration as that stated by Rayleigh's criterion.[61,83] However, one must utilize an additional strategy to effectively supply a two-phase flow into a desired location. The interaction of small droplets with large flow features is sensitive to flow Strouhal number. Recent experiments[84-86] and computations[87-89] suggested that only those
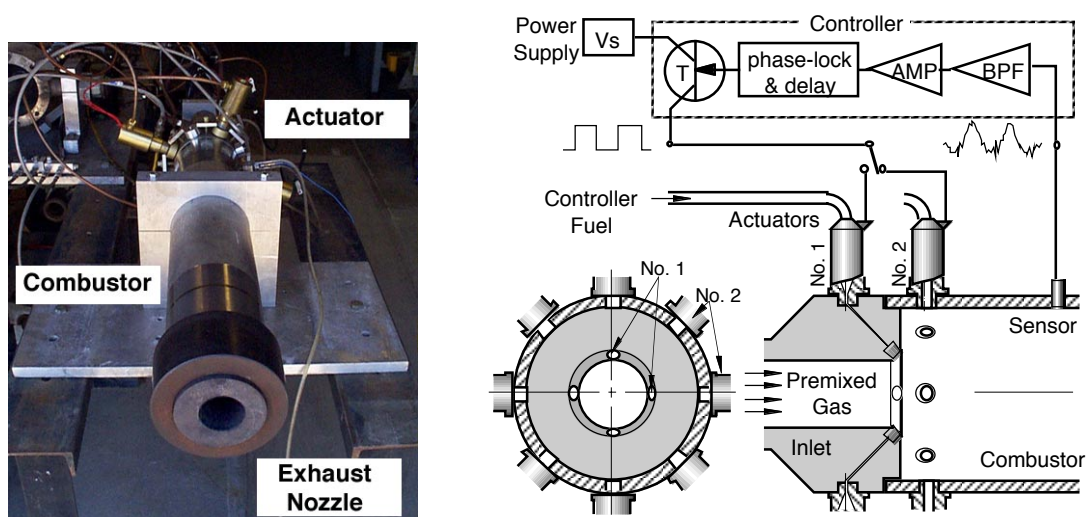
Figure 6. A model ramjet dump combustor for liquid-fueled ACC study at NAWC, China Lake.

droplets with Stokes number on the order of unity are affected by fluid motion and yet have enough momentum to be dispersed further outside the carrier fluid path.

Yu et al.[20] showed that vortex-droplet interaction mechanism could be utilized to control the fuel droplet dispersion inside an axisymmetric ramjet combustor, shown in Fig. 6. Figure 7 shows the spatial and temporal distribution of fuel droplets in the combustor as a function of pulsed injection timing. The vortex shedding process was used as a reference for fuel injection timing. Subsequent experiments revealed that instability was suppressed when the controller fuel was injected in advance of the vortex shedding or synchronized with the vortex shedding event. Adjusting the fuel injection timing to follow the vortex shedding, on the other hand, resulted in higher amplitude oscillations.
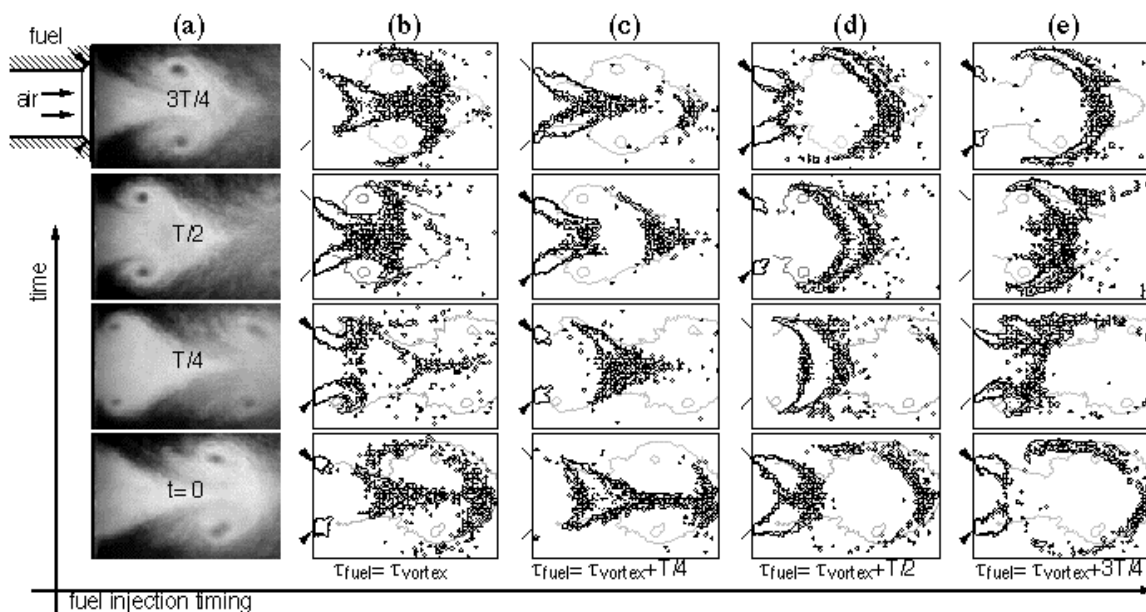
Figure 7. Spatial dispersion of controller fuel droplets with respect to the vortex location in a ramjet dump combustor. The location of fuel droplets was obtained by phase-lock averaging Mie-scattering flow visualization images. (a) vortex shedding cycle associated with the instability, (b) closed-loop controlled fuel injection at timing $t = \tau_{vortex}$, (c) $t = \tau_{vortex} + T/4$, (d) $t = \tau_{vortex} + T/2$, (e) $t = \tau_{vortex} + 3T/4$ [Yu & Scahdow 1999]

While the precise timing for proper fuel injection must be rig-dependent, the above experiments shed new light on the physical mechanism. As was shown in Fig. 4, heat release oscillation in a premixed combustor goes through the low cycle in the leading part of the vortex and the high cycle in the trailing part of the vortex. This is caused by the entrainment of the fresh reactants by vortex action, which initially lowers the temperature in the leading part of the vortex. As the entrained reactants mix with the high temperature products in the trailing part of the vortex, the local heat release cycle goes up. Then, the strategy for active fuel injection is to deliver additional fuel in the leading part of the vortex, where the heat release oscillation tends to be in the low cycle without the additional supply. This would reduce the amplitude of heat release fluctuation, thus leading to potential instability suppression.

Figure 8 shows the onset of liquid-fueled active instability suppression, which was obtained by shifting the fuel injection timing from a quarter cycle after the vortex shedding (corresponding to Fig. 7c) to the synchronized fuel injection phase (Fig. 7b). The oscillation amplitude attained with the vortex-synchronized fuel injection is much lower. The sketch in Fig. 9 illustrates the desired spatial distribution of secondary (controller) fuel droplets with respect to the vortex.
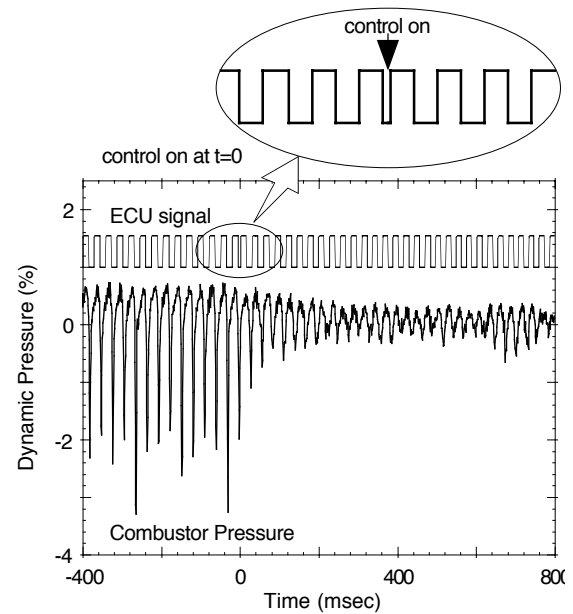

Figure 8. Onset of active instability suppression by adjusting the timing of pulsed fuel injection from $\tau_{vortex} + T/4$ to τ_{vortex} at time t=0. [Yu & Scahdow 1999]

AEROENGINE GAS TURBINES

Use of liquid fuel is also an important consideration in typical gas turbines for aircraft or marine applications. While the presence of swirl may introduce additional complexity in gas turbine flow field, the overall ACC approach is quite similar to that of dump combustor. Cohen et al.[90] demonstrated active instability suppression using a full-scale engine nozzle at realistic operating conditions. The instability was a result of operating the gas turbine at lean premixed conditions for low NOx purpose. Since there is a tradeoff between low thermal NOx and increased CO emission at very lean conditions, the desirable operating band for a lean premixed combustor is very narrow and often falls within the unstable combustor regime. By incorporating a simple fuel actuator and ACC strategy into a full-scale engine fuel nozzle, the authors were able to demonstrate a substantial reduction in instability amplitude without compromising NOx and CO emission levels. McManus et al.[91] implemented a pulse-width-modulation technique in an evaluation study geared toward liquid-fueled gas turbines. Przybylko[92] discusses some of the challenges associated with active combustion control in gas turbines including pattern-factor control and high-cycle fatigue as well as emission control.
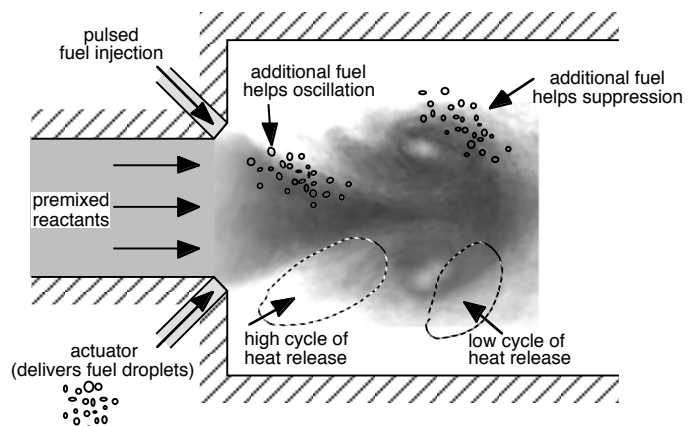

Figure 9. Illustration of liquid-fueled active instability suppression in a ramjet dump combustor using timing-controlled secondary fuel injection.

AFTERBURNERS

Afterburner geometry is somewhat similar to a Rijke tube, with a straight duct and a heat release source. The instabilities are often of two types - relatively high frequency "screech" associated with transverse mode oscillations and a low frequency "rumble" related to longitudinal-mode oscillations. While the transverse instabilities can be attenuated with passive devices such as acoustic liner or flameholder geometry, the longitudinal mode is difficult to alleviate. Langhorne et al.[19] used a secondary fuel injection scheme to suppress low frequncy instabilities in a model afterburner. This technique has become a standard model for practical active control approach.

3.2 Industrial Gas Turbines

Because of the increasing concern on pollutant emissions such as NOx and CO, much of the recent interest in ACC technology has come from power generation industry. Because the thermal mechanism is responsible for the bulk of the NOx formation, the standard approach is to lower the combustion temperature by lean premixed operation. As reviewed previously, combustion instability is a concern for lean premixed combustion systems, because the premixing reduces the margin of combustor stability and thus system operability.

RESEARCH AND DEVELOPMENT

The earlier attempt on closed-loop feedback control utilized a slow adjustment of the average flow rate. Brouwer et al.[93] used a closed-loop modulation of the swirl airflow to modify the fuel injection characteristics in a can-type model combustor. The characteristic time response appeared to be on the order of a second. This approach, which may not be considered a dynamic control under the current definition, was used to optimize the combustion performance. Jackson and Agrawal[94] also applied a slow control using a cost-minimization approach to optimize the combustion temperature and NOx. Richards et al.[95] utilized an open-loop cyclic fuel injection to change the transient equivalence ratio outside the instability band thereby achieving suppression of oscillations. The success of such an approach, however, would be tied closely with the dynamics of the combustor and pollutant generation mechanism.

Fast-response, dynamic actuation of secondary fuel injection is now being widely used in gas turbine burners. The physical mechanism and the extent at which controlled oscillations lead to a better emission performance were investigated by Poppe, Sivasegaram, and Whitelaw[96] using a sector of gas turbine. Their results suggested that the effect of oscillations on the degree of premixedness may play an important role in NOx reduction mechanism. Jones et al.[97] applied a closed-loop controlled secondary fuel injection at subharmonic frequencies to suppress longitudinal mode instability. Also, much progress has been made on model-based control approaches. Annaswamy et al.[98] investigated the performance of optimal control designs including LQG-LTR and H_∞ methods in a 1 kW tube combustor.

PRACTICAL IMPLEMENTATION

One distinguishing feature of gas turbine flowfield is the presence of swirling flow. Depending on the flameholder design, the presence of swirl can change the instability characteristics. Sivasegaram & Whitelaw[99] reported a reduction in oscillation amplitude with swirl for a disk-stabilized flame and an increase for a sudden-expansion dump. Paschereit et al.[100] studied both the axisymmetric mode and the helical mode oscillations in a swirl-stabilized burner, and applied a closed-loop control to suppress the instabilities.

Seume et al.[101] developed a fast-response feedback active control system as an insurance measure for unpredictable occurrence of combustion instability in practical gas turbines. Sattinger et al.[102] describes the successful implementation of an observer-based control algorithm in a sub-scale combustor. Hermann et al.[103] described the implementation of fast-response closed-loop ACC system in the Siemens type V94.3A stationary gas turbine. The ACC system was implemented in a 260 MW Siemens gas turbine along with other passive measures to maximize the performance and to suppress any unwanted self-excited oscillations that may occur in the annular combustion chamber under certain operating conditions. Figure 10 shows the schematic of the Siemens ACC set-up.
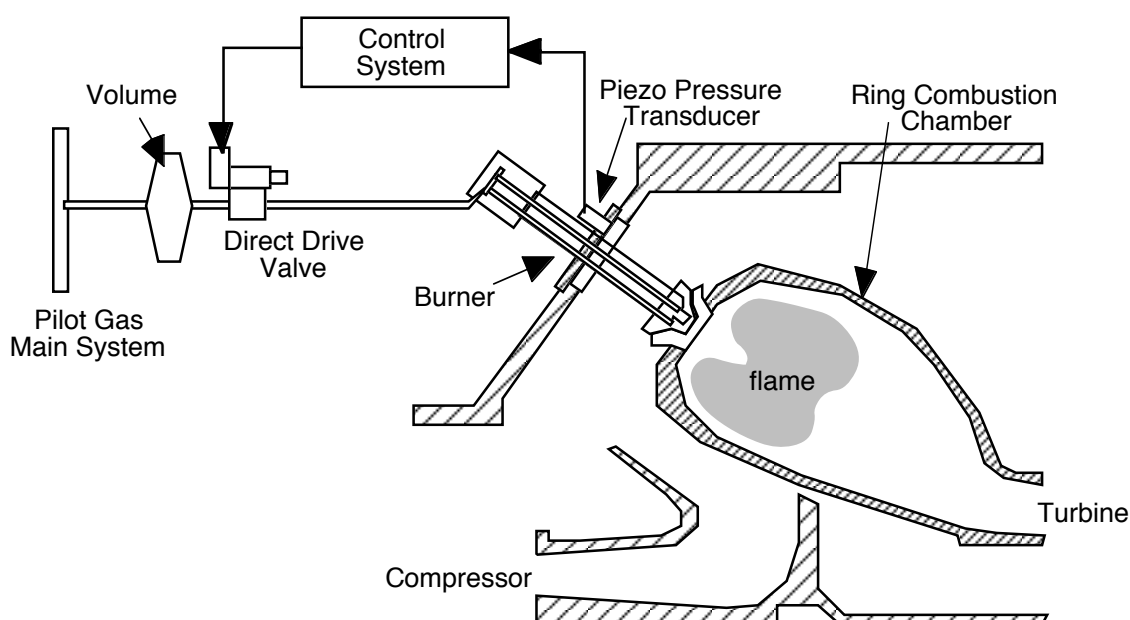
Figure 10. Schematic representation of ACC setup for the Siemens Model Vx4.3A heavy duty gas turbine.
[Hermann et al. 2000]

3.3 Rockets

Combustion instabilities are major concerns in solid-propellant rockets as well as liquid rockets. Analytical approach addressing the problems of rocket combustion instabilitiess goes back many decades. Sirignano and Crocco[104] used the method of characteristics to study the longitudinal mode combustion and flow oscillations. Also, the oscillations in transverse modes were theoretically examined by Zinn[105] for liquid-propellant rockets. Zinn and Powell[106] applied Galerkin's method to describe liquid rocket instabilities. In solid-rocket problems, Culick[60,63,64] established the approximate analysis also using Galerkin's approach.

Experimentally, passive control requiring geometry modification is very expensive and time consuming in rockets. Thus, ACC has received an increasing amount of attention, particularly for larger motors where the instability frequency is low. For such a case, modulated injection of mono-propellant could be considered. However, partly due to the hostile motor environments in which traditional actuators do not function properly, experimental work in this area has been rather limited. Some of the recent approaches have considered the use of CO2 lasers for actuation.

Recent modeling work for ACC has been expanded to include rocket applications. Mohanraj et al.[107] developed a heuristic combustor model which was applied to a gas rocket for instability suppression. Some of the control strategies being discussed for rockets include not only the heat flux modulation effect but also mass injection approach. Mettenleiter et al.[108] described the recent development in the numerical simulation of ACC applied to solid rocket motors. The primary effect considered was the modulation in mass loading.

4. Increase in Volumetric Heat Release

For limited-volume applications such as in propulsion systems or ship-board equipment, increasing the volumetric heat release is an important consideration. A fast open-loop control was shown to be an effective tool in increasing the combustion performance. Typically, acoustic forcing or periodic fuel injection approaches are utilized to organize coherent structures or large vortices, which are then manipulated to obtain desired mixing characteristics. For diffusion flames, the mixing between fuel and oxidizer can be controlled in an active manner, while for premixed flames, the mixing between the reactants and the products are targeted.

4.1 Generation of Coherent Structure

The interest in coherent structure generation stems from the potential of controlling combustor performance. In a typical combustion system, reacting shear layers and their dynamic features are sensitive to flow excitation. Small amount of excitation, typically less than a few percent of the mean flow velocity, can dramatically alter the flow field increasing the entrained volume significantly.[109] The change is produced by organized vortical structures which become highly dispersive under certain wavelength conditions. The most interesting conditions occur when forcing is applied at a Strouhal frequency, which is based on the jet diameter, ranging between 0.24 and 0.64.[110]

Acoustic forcing of combustor inlet flow has been used to control shear layer mixing through vortex dynamics and optimize combustion performances. The key to such a control approach is to modify turbulent mixing between fuel and air or between the reactants and the products by exciting the large coherent vortices. McManus et al.[111] excited the vortical structures in a dump combustor through periodic forcing of the boundary layer that led up to the mixing layer. This affected the flow separation behavior and drastically altered combustion characteristics, with the data suggesting up to 15% increase in volumetric heat release. The results appeared to be related to the increase in turbulent transport property due to large coherent structures that were generated.

Yu et al.[11] showed that acoustic forcing in the proper frequency range, accelerated the small-vortex growth in the initial shear layers, creating large-scale vortical structures. The early entrainment by faster growing vortices broadens the reaction zone, and the continued entrainment by propagating large-scale vortical structures improves the mixing between fresh reactant and hot gases in the reaction zone. They further showed that the optimum frequency for enhancing the volumetric heat release was related to the hydrodynamic features in the reaction zone. The increase in volumetric heat release, deduced from time-averaged C2 emission measurements, was nearly 50 %.

4.2 Control of Vortex Dynamics

Since turbulent jets are highly responsive to acoustic forcing which organizes coherent vortex structures in the shear layers, the dynamics of organized vortices can be further modified by controlling the timing between various vortex generation mechanisms. Yu et al.[112] injected secondary periodic jets directly into the shear layers that were excited with acoustic forcing. This allowed a complex interaction between the vortices, which could be controlled by changing the timing and duration of the vortex shedding.
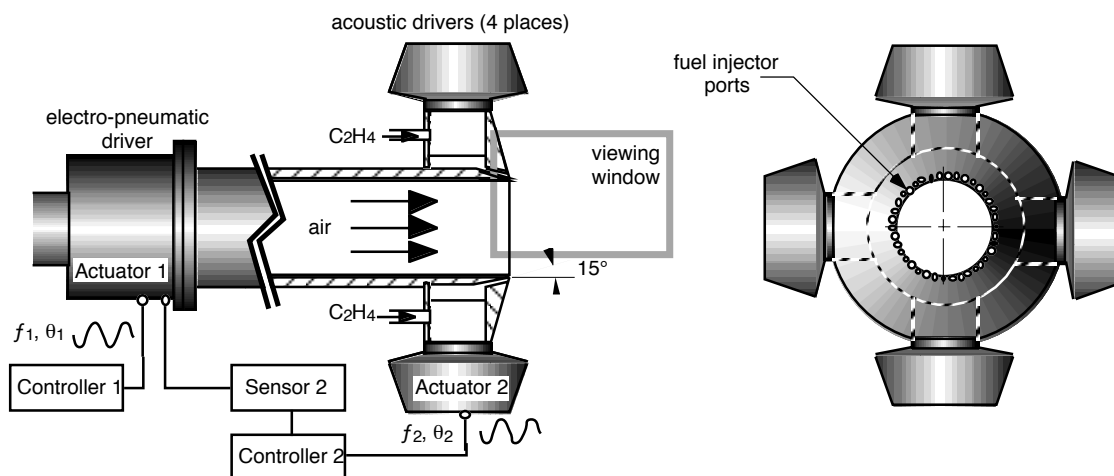

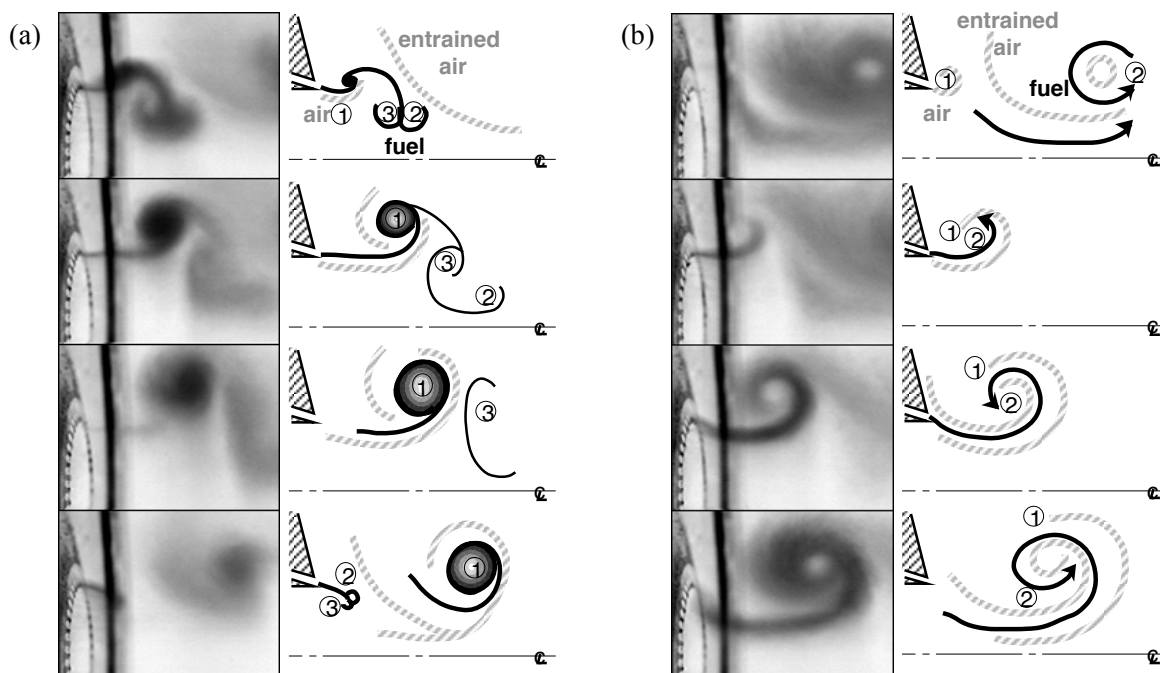Figure 11. 50 kW diffusion flame burner at NAWC, China Lake.

Figure 12. Phase-lock averaged fuel flow visualization and illustration of vortex dynamics. The timing of pulsed fuel injection was such that (a) fuel injection led the air vortex shedding by $\pi/2$, and (b) fuel injection trailed the air vortex shedding by $\pi/2$.

The vortex dynamics and growth behavior can be optimized by the use of closed-loop control. Figure 11 shows the 50 kW diffusion flame burner used in the experiments by Yu et al.[113] Figure 12 shows the sequence of phase-lock averaged Mie-scattering images showing the concentration of fuel injected in a periodic fashion. The timing of fuel injection was closed-loop controlled with respect to the air vortex shedding. Figure 12a shows a condition in which the pulsed fuel jet was started prior to the air vortex shedding. A pair of counter-rotating vortices (labeled 2 and 3 in the illustration) associated with fuel jet starting was observed to be pulled into the low-pressure central region between the air vortices. The main part of the fuel was, however, injected into the core of the subsequently shed air vortex, 1, forming a concentrated lump of fuel. The fuel lump stayed in the core and propagated with the air vortex, preventing further mixing. On the other hand, fuel jet, which was injected just after the air vortex shedding, evolved differently, as shown in Fig. 12b. First, the fuel flow was observed to be strained by the high-velocity air flow following the air vortex, 1. The starting fuel vortex 2, then, interacted with the air vortex 1, intensifying the surrounding flow entrainment.
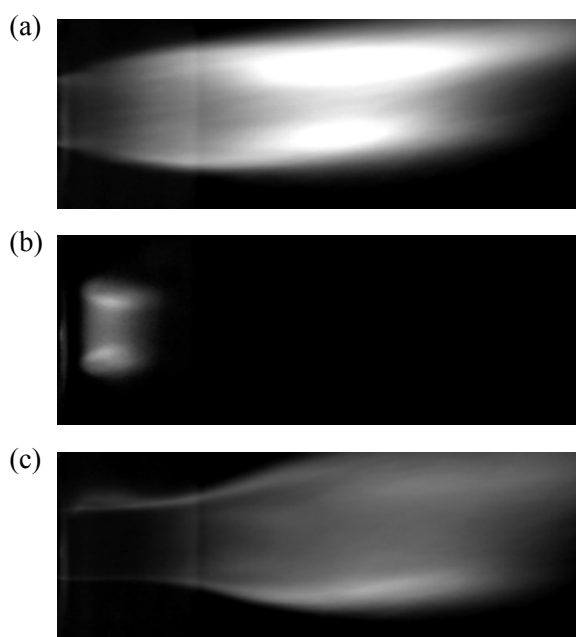

Figure 13. Chemiluminescence and incandescence from the diffusion flames of Fig. 12. (430±5 nm)

(a) inefficiently controlled, long flames with high soot production corresponding to Fig. 12a,

(b) efficiently controlled, short flames that are free of soot, corresponding to Fig. 12b, and

(c) uncontrolled flames with a moderate amount of soot production

Figure 13 shows the time-averaged flame structures associated with each condition corresponding to Figure 12 conditions. They revealed that the latter condition corresponding to Fig. 12b resulted in much more efficient flames with most of the heat release occurring close to the vortex path. The condition of Fig. 12a, as well as the uncontrolled fuel injection, produced inefficient burning with much longer flame lengths. Their results indicated that the flame length could be shortened by an order-of-magnitude by applying a proper closed-loop control.

5. Reduction of Hazardous Emissions

With increasing concerns on environmental issues, there is a growing urgency for industry to address reduction of hazardous emission. ACC has an enormous potential as an enabling technology in the area of pollutant reduction. Because the chemical processes that lead to the formation of pollutants are sensitive to the rate coefficients and the concentration of other intermediate species, temporal control of quasi-equilibrium concentration or local temperature will have a significant impact on the overall reaction products. The difficulty is that many of the chemical processes have the characteristic time scales that are well below the characteristic actuator response time.

Consequently, one often tries to convert the problem into another one that may be more practical to handle. For instance, the present interest in lean premixed combustion comes from the fact that it generates very low levels of NOx emission, compared to more widely used diffusion flame processes. While this reduces the combustor operating margin by introducing the problem of combustion instabilities, ACC may be used to suppress instabilities and extend the operating margins. Typically, the most problematic instabilities have a time scale that is comparable to available actuator response.

5.1 NOx Reduction

Some of the standard approaches for reducing the level of NOx in gas turbines include lean premixed combustion, steam injection, staged combustion, and rich-quench-lean-type combustion.[114] Lean premixed combustion, as stated before, is susceptible to combustion instabilities that may be suppressed by ACC approaches that were reviewed in Section 3.2. In non-premixed combustion or premixed combustion at high temperature, NOx formation can be discouraged by minimizing the time the flow is exposed to high temperature. This also favors the notion of active flow control processes such as vortex-stabilized combustion which can provide large variation in flow temperature. Also, active injection of coolant to quench the products of vortex combustion can be considered for NOx reduction purpose. Haile et al.[115] conducted open-loop control experiments on a 25 kW domestic boilers and on a 850 kW furnace obtaining substantial reduction in NOx levels.

5.2 Soot Reduction

Many power generation and propulsion systems use hydrocarbon fuels that have high propensity to soot. Excessive emission of soot is undesirable not only for environmental consideration but it also contributes to plume signature and reduces combustion efficiency. Soot control technologies are somewhat similar to those for NOx consideration as sooting process is readily affected by the mixing process. An example of soot reduction using vortex dynamic control can be seen in Fig. 13. The conditions of Fig. 13b not only produced more concentrated flames but the flames became blue and free of soot. This can be contrasted with the uncontrolled flames of Fig. 13c that resulted in substantial production of soot.

One additional mechanism that may be considered for ACC of soot is the hydrodynamic path of the reactant streams. Lin & Faeth[116,117] showed that soot production was suppressed if the flow conditions were made such that the flow streamlines crossed the flame sheets from the fuel side to the oxidizer side. This encouraged the oxidation of soot and prevented soot particle growth from nucleation. While it may be possible to actively control the flow velocities and direction to take advantage of this effect, it may be difficult to control the streamlines in highly turbulent flows.

5.3 Incinerator

One example of successful transition of laboratory results to practical implementation can be found in compact waste incinerator being developed by NAWC scientists. Parr et al.[24] conducted a systematic scale-up of their vortex-stabilized emission reduction concept and applied to an afterburner of a ship-board compact waste incinerator. In a typical incinerator, the combustion products from a primary kiln where the waste is first incinerated still contain a substantial amount of incompletely burnt pollutants and must be treated further. While an afterburner can be used to reduce the emission of harmful pollutants into the stack, existing afterburners require a relatively large volume to ensure complete reaction at relatively low combustion temperature for thermal NOx consideration. To reduce the size of an afterburner per given capacity, one may consider a dynamic control of the secondary pyrolysis processes. Parr et al.[24] used an open-loop control to actively stabilize coherent vortices inside the afterburner and properly timed injections of additional fuel, surrogate waste, and air flow to control the local mixture ratio and the residence time. The physical understanding was acquired in a 5 KW laboratory burner using simultaneous PLIF images of air, fuel, and intermediate species corresponding to various destruction and removal efficiencies of a waste surrogate. The initial experiment was then scaled up to 50 kW and eventually to 1.2 MW conditions.[35]

6. Other Potential Benefits

The advantages of ACC techniques in combustion instability suppression have been well documented. There are also clear evidences of improved performance regarding volumetric heat release and pollutant reduction. While potential benefits of ACC processes are inherently huge, the practically attainable limits have not been properly quantified in most cases. Since it is possible to modify the mixing characteristics in the initial shear layer of the flameholding zone using flow excitation, active control techniques can be used to change the flammability characteristics. Extension of flammability limits is one area which has been demonstrated by other experiments.

Gutmark et al.[118] showed that the jet flames could be stabilized better if the excitation frequency was close to the most amplified frequency given by the linear stability theory. This range of frequencies can be defined by Strouhal number, $f\theta/U$, based on the jet momentum thickness, θ. Their results showed that, in the range of Strouhal number between 0.01 and 0.04, the maximum jet velocity at the blow-off limit could be increased by up to a factor of three, depending on the equivalence ratio and the excitation frequency. A dump combustor experiment by McManus et al.[12] also showed that lean blowout limit could be extended from ϕ (equivalence ratio) of 0.48 to ϕ of 0.45 by directly exciting the shear layer. In liquid-fueled combustor experiments, Yu et al.[119] showed that controlled injection of secondary fuel at the dump extended the blowoff limit substantially by providing effective pilot flames. The lean limit was extended to ϕ of less than 0.2.

7. Outlook for Future Implementation

Active control has an enormous potential as an enabling technology in applications involving chemical reaction. In recent years, as the demand for power and the environmental awareness increased rapidly, there has been a considerable amount of attention given to ACC. The interest in ACC technology also stems from the general trend of future combustors requiring higher pressure and temperature operation for improved efficiency. Future challenges, which include the need for increased portability, reduced emission, and more autonomous operation, could be addressed by implementing ACC technology in practical systems.

Already, there has been a successful example of ACC implementation in an actual system, in Siemens Model V94.3A land-based gas turbine.[103] This ACC system uses a closed-loop actuation of pilot gas injection. While it is uncertain that any performance increase from the first generation ACC system would result in a better profit margin for the users, it is nearly certain that future regulation will soon require some means of obtaining a better performance. One lesson, that the Siemens example has shown, is that ACC approach is certainly a viable option even at full scale. The other lesson is that a thorough understanding of the fundamental physical processes has played the key role in the successful system

implementation. As many other examples in this report have shown, fluid dynamics and combustion play a critical role in ACC processes. Understanding of these processes is an important prerequisite for any successful system implementation.

The progress in actuator and sensor technologies and the increased understanding of the flow and control processes are creating an opportunity to revolutionize the combustion control systems. ACC techniques are based on precise scheduling of temporal events, and do not require unnecessary geometry changes. This switch in emphasis from spatial to temporal precision will allow more flexibility into the combustor development, encouraging modular design approaches in the future. The use of an open-architecture system design, separating the various components such as actuator, sensor, and controller will make the future system upgrade more practical and convenient. To fully realize the potential benefits of ACC, however, it is important to understand various physical processes. Thus, a lot more research and development are still needed especially for the propulsion applications, in which more constraints are placed on the types of hardware and acceptable fuels.

References

1. McManus, K.R., Poinsot, T., and Candel, S., "A Review of Active Control of Combustion Instabilities," *Prog. in Energy & Comb. Sci.*, 19, pp.1-29 (1993)

2. Candel, S.M., "Combustion Instabilities Coupled by Pressure Waves and Their Active Control," *Twenty-Fourth Sympo. (Inter.) on Comb.*, The Combustion Institute, Pittsburgh, PA, pp.1277-1296 (1992)

3. Culick, F.E.C., "Combustion Instabilities in Propulsion Systems," *Combustion Instabilities Driven By Thermo-Chemical Acoustic Sources*, ASME, NCA-Vol. 4, HTD-Vol. 128, pp.33-52 (1989)

4. Billoud, G., Galland, M.A., Huu, C., HuYnh and Candel, S., "Adaptive Active Control of Combustion Instabilities," *Combustion Science and Technology*, Vol. 81, No. 4-6, pp.257-284 (1992)

5. Afanasiev, V. V., Frost, V. A., Kidin, N. I., and Kuzmin, A. K., "Diagnostics and Active Control of Acoustic Instabilities in Combustors by Electrical Discharges and Plasma Jets," *Challenges in Propellants and Combustion: 100 years after Nobel*, ed. Kuo, K.K., Begell House Inc., pp.943-961 (1997)

6. Kidin, N. I, Afanasiev, V. V., and Ilyin, S.V. "Active Control of Combustion Instabilities by Electrical Discharges," *Proc. of Tenth ONR Propulsion Meeting*, pp.118-119 (1997)

7. Joos, F, and Vortmeyer, D., "Self-Excited Oscillations in Combustion Chambers with Premixed Flames and Several Frequencies," *Combustion and Flame*, 65, pp.253-262 (1986)

8. Lang, W., Poinsot, T., and Candel, S., "Active Control of Combustion Instability," *Comb. & Flame*, Vol. 70, pp.281-289 (1987)

9. Gulati, A. and Mani, R., "Active Control of Unsteady Combustion-Induced Oscillations," *J. Propul. & Power*, Vol. 8, No. 5, pp.1109-1115 (1992)

10. Gleis, S., Vortmeyer, D., and Rau, W., "Experimental Investigations on the Transition from Stable to unstable combustion by means of active instability control," *Propulsion and Energetics Panel, 75th Symposium*, AGARD, 22:1-6 (1990)

11. Yu, K., Trouve, A., and Candel, S., "Combustion Enhancement of a Premixed Flame by Acoustic Forcing with Emphasis on Role of Large-Scale Vortical Structures," *AIAA-91-0367*, (1991)

12. McManus, K. R., Vandsburger, U., and Bowman, C. T. Combustor performance enhancement through direct shear layer excitation. *Combust. & Flame*, 82, pp. 75-92 (1990)

13. Choudhury, P.R., Gerstein, M., and Mojaradi, R., "A novel feedback concept for combustion instability in ramjets," *22nd JANNAF Combustion Meeting*, (1985)

14. Poinsot, T., Candel, S., Esposito, E., Lang, W., and Bourienne, F., "Suppression of combustion instabilities by active control," *Journal of Propulsion and Power*, Vol. 5, pp. 14-20 (1989)

15. Gutmark, E., Parr, T. P., Hanson-Parr, D. M., and Schadow, K.C., "On the Role of Large and Small-Scale Structures in Combustion Control," *Combustion Science and Technology*, Vol 66, pp. 107-126 (1989)

16. Gutmark, E., Parr, T. P., Hanson-Parr, D. M., and Schadow, K.C., "Stabilization of combustion by controlling the turbulent shear flow structure," *7th Sympo. Turbulent Shear Flows*, Stanford, CA, (1989)

17. Schadow, K.C., Gutmark, E. and Wilson, K. J., "Active combustion control in a coaxial dump combustor," *Combustion Science and Technology*, Vol.81, No4-6, pp.285-300 (1992)

18. Gutmark,E.; Parr, T. P., Wilson, K. J.; Hanson-Parr, D.M., and Schadow, K.C., "Closed-loop control in a flame and a dump combustor," *IEEE Control Systems*, April, pp. 73-78 (1993)

19. Langhorne, P. J., Dowling, A. P., and Hooper, N., "Practical active control system for combustion oscillations," *Journal of Propulsion and Power*, Vol. 6, No. 3, pp. 324-333 (1990)

20. Yu, K.H., Parr, T.P., Wilson, K.J., Schadow, K.C., and Gutmark, E.J. "Active Control of Liquid-Fueled Combustion Using Periodic Vortex-Droplet Interaction," *Twenty-sixth Symposium (International) on Combustion*, Vol. 2, The Combustion Institute, Pittsburgh, pp. 2843-2850 (1996)

21. Yu, K.H., Wilson, and K.J., Schadow, K.C., "Scale-Up Experiments on Liquid-Fueled Active Combustion Control," *34th AIAA/ASME/SAE/ASEE Joint Propulsion Conference*, Seattle, WA, *AIAA-98-3211* (1998)

22. Yu, K., Wilson, K.J., and Schadow, K.C. "Liquid-Fueled Combustion Control: Scale-Up Experiments and Effect of Fuel Droplet Size," *37th AIAA Aerospace Sciences Meeting*, Reno, NV, *AIAA-99-0328*, (1999).

23. Neumeier, Y., and Zinn, B.T., "Theoretical and Experimental Investigation of the Performance of an Actively controlled Fuel Actuator," *36th Aerospace Science Meeting*, Reno, NV, *AIAA-98-0355* (1998)

24. Parr, T.P., Gutmark, E.J., Wilson, K.J., Hanson-Parr, D.M., Yu, K., Smith, R.A., and Schadow, K.C. "Compact Incinerator Afterburner Concept Based On Vortex Combustion," *Twenty-sixth Symposium (International) on Combustion*, Vol. 2, The Combustion Inst., Pittsburgh, pp. 2471-2477 (1996)

25. Gutmark, E.J., Parr, T.P., Wilson, K.J., Yu, K.H., Smith, R.A., Hanson-Parr, D.M., and Schadow, K.C. "Compact Waste Incinerator Based On Vortex Combustion," *Combustion Science & Technology* 121, pp. 333-349 (1996)

26. Wilson, K.J., Parr, T.P., Smith, R.A., Yu. K.H., and Schadow, K.C. "Mass-flux actuator with high frequency response," *U.S. Patent No.: 6065688*, (2000)

27. Schadow, K. C., Wilson, K. J., Gutmark, E.and Yu, K., "Periodic Chemical Energy Release for Active Combustion Control," *11th International Symposium on Air Breathing Engines*, 11-V1, Tokyo, Japan, (1993)

28. Hermann, J., Orthmann, A.and Hoffmann, S., "Active instability control of combustion oscillations in heavy duty gas turbines," *International Congress on Sound and Vibration*, Vol. 7, (1999)

29. Bloxsidge, G.J., Dowling, A.P., Hooper, N., and Langhorne, P.J., "Active control of Reheat Buzz," *AIAA Journal*, Vol. 26 (7), pp. 783-790 (1988)

30. Bloxsidge, G.J., Dowling, A.P., and Langhorne, P.J., "Reheat buzz: an acoustically coupled combustion instability. Part 2. Theory," *J. Fluid Mech.*, Vol. 193, pp. 445-473 (1988)

31. Trouve, A., Yu, K., and Candel, S. "Excitation d'une flamme turbulente prémélangée par mise en vibration de son stabilisateur," *CNRS/ ONERA Report No. 736706* (1990)

32. Kurtz, A.D., Chivers, J., Ned, A., and Epstein, A.H., "Sensor Requirements for Active Gas Turbine Engine Control," *NATO/RTO Spring 2000 Symposium on Active Control Technology for Enhanced Performance Operation Capabilities of Military Aircraft, Land Vehicles and Sea Vehicles*, Braunschweig, Germany, (2000)

33. Gutmark,E.; Parr, T. P., Wilson, K. J.; Hanson-Parr, D.M., and Schadow, K.C., "Use of Chemiluminescence and Neural Networks in Active Combustion Control," *23rd Symposium (International) on Combustion*, The Combustion Institute, pp.1101-1106 (1990)

34. Yu, K.H., Trouve, A., and Daily, J.W., "Low frequency pressure oscillations in a model ramjet combustor," *J. of Fluid Mechanics*, 232, pp. 47-72 (1991)

35. Parr, T.P., Wilson, K. J., Smith, R. A., Schadow, K. C., Hansell, D.W., and Cole, J.A., "Actively Controlled Afterburner for Compact Waste Incinerator," *1997 International Conference on Incineration and Thermal Treatment Technologies* (1997)

36. Furlong, E.R., Baer, D.S., and Hanson, R.K., "Real-time adaptive combustion control using diode-laser absorption sensors," *27th Symposium (International) on Combustion*, (1998)

37. Furlong, E.R., Mihalcea, R.M., Webber, M.E., Baer, D.S., and Hanson, R.K., "Diode Laser Sensors for Real-Time control of Pulsed Combustion Systems," *AIAA Journal*, Vol. 37 (6) pp. 732-737 (1999).

38. Hanson, R.K., and Baer, D.S., "Diode-Laser Absorption Sensors for Combustion Measurements and Control," *Naval Research Reviews*, Vol 51, No.3-4, pp. 16-23 (1999)

39. Eckbreth, A.C. *Laser Diagnostics For Combustion Temperature And Species*, pp. 281-366, Gordon & Breach Pub., (1986)

40. Mihalcea, R.M., Baer, D.S., and Hanson, R.K., "Advanced diode laser absorption sensor for in-situ combustion measurements of CO_2, H_2O, and temperature," *27th Symposium (International) on Combustion*, (1998)

41. Ho, C-M, and Tai, Y-C, "Review: MEMS and Its Applications for Flow Control," *J. of Fluids Engineering*, Vol. 118, pp. 437-447 (1996)

42. Tsao, T., Liu, C., Tai, Y.C., and Ho, C.M., "Micromachined Magnetic Actuator for Active Fluid Control," *Application of Microfabrication to Fluid Mechanics*, ASME FED Vol. 197, pp. 31-38 (1994)

43. Liu, C., Tsao, T., Tai, Y., Leu, J., Ho, C.M., Tang, W.L., and Miu, D., "Out-of-Plane Permanent Magnetic Actuators for Delta Wing Control," *Proc. IEEE Micro Electro Mechanical Systems*, pp. 7-12 (1995)

44. Liu, C., Tai, YC.., Huang, J., Ho, C.M., "Surface-Micromachined Thermal Shear Stress Sensor," *Application of Microfabrication to Fluid Mechanics*, ASME FED Vol. 197, pp. 9-16 (1994)

45. Lee, J. G., Hong, B.-S., Kim, K. and Yang, V., "Optimization of Active Control Systems for Suppressing Combustion Instability," RTO Meeting Proceedings, *NATO-RTO MP No. 14*, (1999)

46. Fung, Y. T., Yang, V., and Sinha, A., "Active Control of Combustion Instabilities with Distributed Actuators," *Combust. Sci. and Tech.*, Vol. 78, pp. 217-245 (1991)

47. Fung, Y.-T. and Yang, V., "Active Control of Nonlinear Pressure Oscillations in Combustion Chambers," *Journal of Propulsion and Power*, Vol. 8, No. 6, pp. 1282-1289 (1992)

48. Blonbou, R. , Laverdant, A. , Zaleski, S. and Kuentzmann, P., "Active Adaptive Combustion Control Using Neural Networks," *Combustion Science and Technology*, Vol. 156, pp. 25-49, (2000)

49. Liu, G.P.and Daley, S., "Output-model-based predictive control of unstable combustion systems using neural networks," *Control Engineering Practice*, Vol.7, No.5, pp. 591-600 (1999)

50. Vaudrey, M.A., and Saunders, W.R., "Control of Combustor Instabilities Using An Artificial Neural Network," *ASME Turbo Expo 2000*, Munich, Germany (2000)

51. Menon, S. and Sun, Y., "Active Fuzzy Control of Reheat Buzz," *32nd AIAA/ASME/SAE/ASEE Joint Propulsion Meeting*, Orlando, FL, *AIAA-96-2759*, (1996)

52. Annaswamy, A.M., and Ghoniem, A.F., "Active Control in Combustion Systems," *IEEE Control Systems*, pp. 49-63, (1995)

53. Hong, B.S., Yang, V., and Ray, A., "Robust Feedback Control of Combustion Instability with Model Uncertainty," *Combustion & Flame*, 120, pp. 91-106 (2000)

54. Annaswamy, A.M., Fleifil, M., Rumsey, J.W., Hathout, J.P., and Ghoniem, A.F., "An Input-Output Model of Thermoacoustic Instability and Active Control Design," *MIT Report No. 9705* (1997)

55. Kemal, A., and Bowman, C.T., *Twenty-sixth Symposium (International) on Combustion*, Vol. 2, The Combustion Inst., Pittsburgh, pp. 2803-2809 (1996)

56. Koshigoe, S., Komatsuzaki, T., and Yang, V., "Adaptive Control of Combustion Instability with On-Line System Identification," *J. of Propulsion and Power*, 15, pp.383-389 (1999)

57. Vaudrey, M.A., Saunders, W.R., and Baumann, W.T., "An Investigation of Adaptive Signal Processing Approaches to Active Combustion Control," *NATO/RTO Spring 2000 Symposium on Active Control Technology for Enhanced Performance Operation Capabilities of Military Aircraft, Land Vehicles and Sea Vehicles*, Braunschweig, Germany, (2000)

58. Yang, V., A. Sinha, and Y.T. Fung. "State Feedback Control of Pressure Oscillations in Combustion Chambers," *Journal of Propulsion and Power*, pp. 66-73 (1992)

59. Neumeier, Y. and Zinn, B. T., "Experimental Demonstration of Active Control of Combustion Instabilities Using Real Time Modes Observation and Secondary Fuel Injection," *Twenty-sixth Symposium (Inter) on Combustion*, (1996)

60. Culick, F.E.C., "Some Recent Results for Nonlinear Acoustics in Combustion Chambers," *AIAA J.*, 32 (1), pp. 146-169, (1994)

61. Lord Rayleigh, *The theory of sound*, p.227. Dover (1945)

62. Chu, B.-T., and Kovasznay, L.S.G., "Nonlinear Interactions in a Viscous Heat-Conducting Compressible Gas," *J. of Fluid Mechanics*, 3(5), pp.494-512 (1957)

63. Culick, F.E.C., "Nonlinear Growth and Limiting Amplitude of Acoustic Oscillations in Combustion Chambers," *Combustion Science & Technology*, 3 (1), pp.1-16 (1971)

64. Culick, F.E.C., "Nonlinear Behavior of Acoustic Waves in Combustion Chambers, Parts I and II," *Acta Astronautica*, 3, pp.714-757 (1976)

65. Keller, J.O., Vaneveld, L., Korschelt, D., Hubbard, G.L., Ghoniem, A.F., Daily, J.W., and Oppenheim, A.K., "Mechanisms of instabilities in turbulent combustion leading to flashback," *AIAA J.*, 20-2, pp. 254-262, (1982)

66. Smith, D.A. and Zukoski, E.E., "Combustion instability sustained by unsteady vortex combustion," *AIAA*-85-1248, (1985)

67. Sterling, J.D. and Zukoski, E.E., "Longitudinal mode combustion instabilities in a dump combustor," *AIAA*-87-0220, (1987)

68. Poinsot, T., Trouvé, A., Veynante, D., Candel, S.M., and Esposito, E., "Vortex Driven Acoustically Coupled Combustion Instability," *J. Fluid Mech.*, 177, 265-292, (1987)

69. Schadow, K.C., Gutmark, E., Parr, T.P., Parr, D.M., Wilson, K.J., and Crump, J.H., "Large-scale coherent structures as drivers of combustion instability," *Comb. Sci. & Tech..,* 66-1-3, 107-126, (1989)

70. Schadow, K.C., and Gutmark, E.J., "Combustion Instability Related to a Vortex Shedding in Dump Combustors and Their Passive Control," *Prog. Energy Combustion Sci.*, 18, pp. 117-132 (1992)

71. Culick, F.E.C., "Combustion instabilities in liquid-fueled propulsion systems - an overview," *AGARD 72B PEP Meeting,*, Bath, England (1988)

72. K. Kailasanath and E.J. Gutmark, "Combustion Instability," *Propulsion Combustion: Fuels to Emissions*, Roy, G.D., ed., pp. 129-172, Taylor & Francis, (1998)

73. Roy, G.D., "Combustion Enhancement and Control," *Propulsion and Combustion: Fuels to Emissions*, Roy, G.D., ed, pp. 173-212, Taylor & Francis, (1998)

74. Smith, D.A., "An Experimental Study of Acoustically Excited, Vortex Driven, Combustion Instability within a Rearward Facing Step Combustor," *PhD thesis, Calif. Inst. Tech.*, Pasedena, CA, (1985)

75. Langhorne, P.J., Reheat Buzz: an Acoustically Coupled Combustion Instability. Part I. Experiment. *J. Fluid Mech.*, 193, pp. 417-443 (1988)

76. Schadow, K.C., and Gutmark, E.J., Parr, T.P., Parr, D.M., Wilson, K.J., and Crump, J.E., "Large-Scale Coheremt Structures as Drivers of Combustion Instability," *Combustion Sci. Tech.*, 64, pp. 167-186, (1989)

77. Kailasanath, K., Gardner, J.H., Boris, J.P., and Oran, E.S., "Numerical Simulations of Acoustic-Vortex Interactions in a Central-Dump Ramjet Combustor," *J. Prop. Power*, 3, pp.525-533, (1987)

78. Kailasanath, K., Gardner, J.H., Boris, J.P., and Oran, E.S., "Acoustic-Vortex Interactions and Low-Frequency Oscillations in Axisymmetric Combustors," *J. Prop. Power*, 5, pp.165-171, (1989)

79. Menon, S., "Active Combustion Control in a Ramjet Using Large-Eddy Simulations," *Combustion Science and Technology*, Vol. 84, No1-6, pp.51-79 (1992)

80. Menon, S., "Secondary fuel injection control of combustion instability in a ramjet," *Combustion Science and Technology*, Vol. 100, No. 1-6, pp. 385-393 (1995)

81. Yu, K.H., Wilson, K.J., and Schadow. K.C., "Liquid-Fueled Active Instability Suppression," *Twenty-seventh Symposium (International) on Combustion*, Vol. 2, The Combustion Inst., Pittsburgh, pp. 2039-2046 (1998)

82. Chang, E., and Kailasanath, K., "Suppression of Combustion Instabilities Using Timed Injection of High Energy Fuels," *AIAA 98-3765*, (1998)

83. Putnam, A., *Combustion Driven Oscillations in Industry*, Elsevier, New York, (1971)

84. Lazaro, B.J. and Lasheras, J.C., "Paricle dispersion in a turbulent, plane, free shear layer," *Phys. Fluids A* 1: 1035-1044 (1989)

85. Longmire, E.K. and Eaton, J.K., "Structure and control of a partice-laden round jet," *J. Fluid Mechanics*, 236:, pp.217-257 (1992)

86. Glawe, D.D. and Samimy, M., "Dispersion of Solid Particles in Compressible Mixing Layers," *J. Prop. & Power*, 9 (1), pp.83-89 (1993)

87. Chung, J.N. and Troutt, T.R., "Simulation of particle dispersion in an axisymmetric jet," *J. Fluid Mechanics*, 186, pp.199-222 (1988)

88. Chang, E. and Kaliasanath, K., "Numerical Simulations of Particle Dynamics in an Axisymmetric Ramjet Combustor," *AIAA-95-0812* (1995)

89. Chang, E. and Kaliasanath, K., "Simulations of Particle Dynamics in a Confined Shear Flow," *AIAA J.,* 34(6), pp.1160-1166 (1996)

90. Cohen, J. M., Rey, N. M., Jacobson, C. A. and Anderson, T. J., "Active control of combustion instability in a liquid-fueled low-Nox combustor," *Journal of Engineering for Gas Turbines and Power*, Vol. 121, No2, Apr. , pp.281-284 (1999)

91. McManus, K.R., Magill, J.C., and Miller, M.F., "Combustion Instability Suppression in Liquid-Fueled Combustors," *AIAA 98-0642* (1998)

92. Przybylko, S.J., "Active-Control Technologies for Aircraft Engines," *AIAA 97-2769* (1997)

93. Brouwer, J., Ault, B. A., Bobrow, J.E., and Samuelsen, G.S., "Active Control for Gas Turbine Combustors," *Twenty-third Symposium (International) on Combustion*, The Combustion Institute, Pittsburge, PA, pp. 1087-1092 (1990)

94. Jackson, M. D.and Agrawal, A. K., "Active Control of Combustion for Optimal Performance," *Journal of Engineering for Gas Turbines and Power*, Vol. 121(3), pp.437-443 (1999)

95. Richards, G.A., Janus, M.C., Robey, E., Cowell, L., and Rawlins, D., "Control of flame oscillations with equivalence ratio modulation," *J. of Propulsion and Power*, 15, pp. 232-240 (1999)

96. Poppe, C, Sivasegaram, S., and Whitelaw, J.H., "Control of NOx Emissions in Confined Flames by Oscillations," *Combustion and Flame*, 113 (1-2), pp.13-26 (1998)

97. Jones, C. M., Lee, J. G., and Santavicca, D. A., "Closed-loop active control of combustion instabilities using subharmonic secondary fuel injection," *Journal of Propulsion and Power*, Vol. 15, No. 4, July-Aug. 1999, pp. 584-590.

98. Annaswamy, A.M., Fleifil, M., Rumsey, J.W., Prasanth, R., Hathout, J.-P.and Ghoniem, A.F., "Thermoacoustic instability: model-based optimal control designs and experimental validation," *IEEE Transactions on Control Systems Technology*, Vol. 8(6), pp. 905-918, (2000)

99. Sivasegaram, S., and Whitelaw, J.H., "The influence of swirl on oscillations in ducted premixed flames," *Comb. Sci. Technology*, 85, pp. 195 (1991)

100. Paschereit, C.O., Gutmark, E.and Weisenstein, W., "Coherent structures in swirling flows and their role in acoustic combustion control," *Physics of Fluids*, Sept. (1999)

101. Seume, J.R., Vortmeyer, N., Krause, W., Hermann, J., Hantschk, C.-C., Zangl, P., Gleis, S., Vortmeyer, D. and Orthmann, A., "Applications of active combustion instability control to a heavy-duty gas turbine," *Journal of Engineering for Gas Turbines and Power*, Vol. 120 No 4, Oct., pp.721-726 (1998)

102. Sattinger, S. S., Neumeier, Y., Nabi, A., Zinn, B. T., Amos, D. J., and Darling, D. D., "Sub-scale demonstration of the active feedback control of gas-turbine combustion instabilities," *Journal of Engineering for Gas Turbines and Power*, Vol. 122, No. 2, pp. 262-269 (2000)

103. Hermann, J., Orthmann, A., Hoffmann, S., and Berenbrink, P., "Combination of Active Instability Control and Passive Measures to Prevent Combustion Instabilities in a 260 MW Heavy Duty Gas Turbine," *NATO/RTO Spring 2000 Symposium on Active Control Technology for Enhanced Performance Operation Capabilities of Military Aircraft, Land Vehicles and Sea Vehicles*, Braunschweig, Germany, (2000)

104. Sirignano, W.A., and Crocco, L., "A Shock Wave Model of Unstable Rocket Combustors,"*AIAA J.*, 2 (7), pp.1285-1296, (1964)

105. Zinn, B.T., "A Theoretical Study of Nonlinear Combustion Instability in Liquid-Propellant Rocket Engines," *AIAA J.*, 6 (10), pp.1966-1972, (1968)

106. Zinn, B.T., and Powell, E.A., "Application of the Galerkin Method in the Solution of Combustion Instability Problems," *Proc. of the 19th International Astronautical Congress*, 3, pp.59-73, (1970)

107. Mohanraj, R, Neumeier, Y. and Zinn, B. T., "Combustor Model for Simulation of Combustion Instabilities and Their Active Control," *Journal of Propulsion and Power*, Vol. 16, No. 3, pp. 485-492 (2000)

108. Mettenleiter, M., Vuillot, F., and Candel, S., "Numerical Simulation of Adaptive Control Application to Unstable Solid Rocket Motors," *NATO/RTO Spring 2000 Symposium on Active Control Technology for Enhanced Performance Operation Capabilities of Military Aircraft, Land Vehicles and Sea Vehicles*, Braunschweig, Germany, (2000)

109. Crow, S.C., and Champagne, F.H., "Orderly structure in jet turbulence," *J. Fluid Mechanics*, 48(3), 547-591 (1971)

110. Gutmark, E., and Ho, C-M., "Preferred modes and the spreading rates of jets," *Phys. Fluids*, 26(10), pp.2932-2938 (1983)

111. McManus, K.R., and Bowman, C.T., "Effects of Controlling Vortex Dynamics on the Performance of a Dump Combustor,"*Twenty-third Sympo. (Inter.) on Comb.*, The Comb. Institute, Pittsburgh, pp. 1093-1099 (1990)

112. Yu, K., Gutmark, E., Wilson, K. and Schadow, K.C., "Active Control of Organized Oscillations in a Dump Combustor Shear Layer," *1st International Symposium on Pulsating Combustion*, Monterey, CA, Paper No. G-2, (1991)

113. Yu, K., Gutmark, E., Wilson, K. and Schadow, K.C. "Active Combustion Control Using Multiple Vortex Shedding," *AIAA 96-2760* (1996)

114. Correa, S.M., "Power Generation and Aeropropulsion Gas Turbines: From Combustion Science to Combustion Technology," *Twenty-seventh Sympo. (Inter.) on Comb.*, The Comb. Institute, Pittsburgh, pp. 1793-1807 (1998)

115. Haile, E., Delabroy, O., Lacas, F., Veynante, D., and Candel, S., "Structure of Acoustically Forced Spary Flame," *Twenty-sixth Sympo. (Inter.) on Comb.*, The Comb. Institute, Pittsburgh (1996)

116. Lin, K.C., and Faeth, G.M., "Hydrodynamic Suppression of Soot Emissions in Laminar Diffusion Flames," *J. of Propulsion & Power*, 12, pp. 10-17, (1996)

117. Lin, K.C., and Faeth, G.M., "Effects of Hydrodynamics on Soot Formation in Hydrocarbon-Fueled Laminar Opposed Jet Flames," *J. of Propulsion & Power*, 12, pp. 691-698, (1996)

118. Gutmark, E., Parr, T.P., Hanson-Parr, D.M., and Schadow, K.C., "Closed-Loop Amplitude Modulation Control of Reacting Premixed Turbulent Jet," *AIAA J.*, 29 (12), 2155-2162, 1991.

119. Yu, K., Wilson, K.J., Parr, T.P., and Schadow, K.C., "An Experimental Study On Actively Controlled Dump Combustors," *NATO/RTO Spring 2000 Symposium on Active Control Technology for Enhanced Performance Operation Capabilities of Military Aircraft, Land Vehicles and Sea Vehicles*, Braunschweig, Germany, (2000)

Appendix. Rayleigh's criterion

The Rayleigh's criterion is derived in this section. For simplicity, we consider inviscid nonconducting flow in one-dimensional situation. The basic equations governing the flow are

$$\text{continuity} \qquad \frac{D}{Dt}[\rho] = -\rho \frac{\partial u}{\partial x} \qquad (A\ 1)$$

$$\text{momentum} \qquad \frac{D}{Dt}[\rho u] = -\rho u \frac{\partial u}{\partial x} - \frac{\partial p}{\partial x} \qquad (A\ 2)$$

$$\text{energy} \qquad \frac{D}{Dt}\left[\rho e + \frac{1}{2}\rho u^2\right] = -\left(\rho e + \frac{1}{2}\rho u^2\right)\frac{\partial u}{\partial x} + q - \frac{\partial}{\partial x}(pu) \qquad (A\ 3)$$

$$\text{equation of state} \qquad p_o = \rho_o R T_o \qquad (A\ 4)$$

where the Lagrangian derivative operator $D/Dt\ [\ ] \equiv \partial/\partial t\ [\ ] + u\ \partial/\partial x\ [\ ]$ and the usual notations of the variables are used. In the energy equation, q is the rate of volumetric heat release added to the fluid.

If we further assume perfect gas with constant volume process, (A 1) through (A 4) can be reduced to the following:

$$\rho \frac{D}{Dt}[u] = -\frac{\partial p}{\partial x} \qquad (A\ 5)$$

$$\frac{D}{Dt}[p] = (\gamma - 1)q - \gamma p \frac{\partial u}{\partial x} \qquad (A\ 6)$$

(A 5) is often called Euler's equation while (A 6) is the energy equation written in the form of pressure change with the help of the continuity and the equation of state.

Now, we expand each of the variables into the sum of a mean value and a small fluctuating component and put $p = \bar{p} + p'$, $q = \bar{q} + q'$, $\rho = \bar{\rho} + \rho'$ and $u = \bar{u} + u'$ into the equations. Since the mean values must also satisfy (A 5) and (A 6), the resulting equations can be simplified. After neglecting smaller terms, we obtain

$$\bar{\rho}(\frac{\partial u'}{\partial t} + u\frac{\partial u'}{\partial x}) = -\rho'u\frac{\partial \bar{u}}{\partial x} - \frac{\partial p'}{\partial x} \tag{A.7}$$

$$\frac{\partial p'}{\partial t} + u\frac{\partial p'}{\partial x} = (\gamma - 1)q' - \gamma(\bar{p}\frac{\partial u'}{\partial x} - p'\frac{\partial \bar{u}}{\partial x}) \tag{A.8}$$

Multiplying (A 7) by u' and (A 8) by $p'/(\gamma\bar{p})$, and adding the two equations, they can be written in the following form:

$$\frac{\partial}{\partial t}\left[\frac{1}{2}\bar{\rho}u'^2 + \frac{1}{2}\frac{p'^2}{\gamma\bar{p}}\right] + \bar{u}\frac{\partial}{\partial x}\left[\frac{1}{2}\bar{\rho}u'^2 + \frac{1}{2}\frac{p'^2}{\gamma\bar{p}}\right] = \frac{\gamma-1}{\gamma}\frac{p'q'}{\bar{p}} - \frac{\partial\bar{u}}{\partial x}\left[\rho'u'u + \frac{p'^2}{\bar{p}}\right] - \frac{\partial}{\partial x'}(u'p') - \frac{u'p'}{\gamma\bar{p}}\frac{\partial\bar{p}}{\partial x} \tag{A.9}$$

The terms on the left hand side of (A 9) are similar to the Lagrangian derivative of the acoustic energy density ε while those on the right hand side represent the acoustic sources. Since we are considering only those cases in which the heat release becomes the dominating source of acoustic energy generation, (A 9) can be reduced to:

$$\frac{D}{Dt}[\varepsilon] \approx \frac{\gamma-1}{\gamma}\frac{p'q'}{\bar{p}} + \text{higher order terms} \tag{A.10}$$

Then, the acoustic energy of the fluid traveling at the mean flow speed can be approximated by integrating (A 10), and the change in acoustic energy density after one cycle is

$$\Delta\varepsilon \approx \frac{\gamma-1}{\gamma}\int_t^{t+T}\frac{p'q'}{\bar{p}}d\tau \tag{A.11}$$

The equation (A 11) is the mathematical expression of the Rayleigh's criterion.

This page has been deliberately left blank

Page intentionnellement blanche

DYNAMICS OF COMBUSTION SYSTEMS:
FUNDAMENTALS, ACOUSTICS, AND CONTROL

F.E.C. Culick
California Institute of Technology
1200 E. California Blvd., MC 205-45
Pasadena, CA 91125, U.S.A.

ABSTRACT

This pair of lectures is intended to provide the basic ideas for understanding and controlling the dynamics of combustion systems. Any combustion system may be regarded as the combination of two dynamical systems: the combustor itself, including the dynamics of the combustion gases; and the combustion processes. The two dynamical systems are therefore spatially intermingled in a practical system. For purposes of theory, analysis, and understanding, formal distinction of the two systems is an essential aspect of the subject. Internal feedback is provided by the sensitivity of the combustion dynamics to the dynamical motions within the combustor. That view of the global dynamics of a combustion system sets the organization of these two lectures. All matters of controlling a dynamical system rest on its dynamical behavior. A major advantage of the general formulation described here is the ease with which the principles of classical and modern feedback control can be applied. Reduced-order models are easily constructed either as formal results of the theory or as *ad hoc* representations consistent with the general physical model. Such a general framework also provides a convenient basis for assessing various methods of analysis and design and their results. The principles and methods covered in these lectures are intended to form part of the foundation for working out procedures applicable to full-scale combustion systems. The validity of the methods for analyzing combustion dynamics has been established by many years of successful applications to combustion instabilities in solid propellant rockets. The last section of these notes shows how natural is the merging of those methods with the principles of active feedback control.

1. A BRIEF SURVEY OF COMBUSTION INSTABILITIES IN PROPULSION SYSTEMS

We are concerned in these two lectures with the dynamics of combustion systems quite generally. The motivation for addressing the subject arises from particular problems of combustion instabilities observed in all types of propulsion systems. Typically the instabilities are observed as pressure oscillations growing spontaneously out of the noise during a firing. As a practical matter, combustion instabilities are more likely encountered during development of new combustion systems intended to possess considerable increases of performance in some sense. The present state of theory and experiment has not provided a sufficiently strong foundation to provide a credible basis for prediction. Hence there are few guidelines available to help designers avoid combustion instabilities.

Under such conditions, it is extremely important to pay attention to the experience gained in the laboratory as well as in full-scale tests of devices. Moreover, because of the many properties of the behavior common to the various systems, much is to be gained from understanding the characteristics of systems other than the one that may be of immediate concern. It is therefore proper to begin with a survey of some typical examples drawn from many years' experience. Theory is an indispensable aid to making sense of observational results. Conversely, discussion of various experimental observations is a natural place to introduce many of the basic ideas contained in the theory.

During the past few years, considerable effort has been expended on the problem of applying active feedback control to combustion systems. It's an attractive proposition to control or eliminate instabilities with feedback control, particularly because one implication, often made explicit, is that the use of feedback will somehow allow one to get around the difficult problems of understanding the details of the system's behavior. Many laboratory, and several full-scale demonstrations, support that point of view. However, for at least two reasons, serious application of feedback control must be based on understanding the dynamics of the system to be controlled:

(i) all experience in the field of feedback control generally has demonstrated that the better the controlled plant is understood, the more effective is the control;

(ii) without understanding, development of a control system for a full-scale device is an *ad hoc* matter, likely to involve expensive development with neither guarantee of success nor assurance that the best possible system has been designed.

Therefore we begin these lectures with an abbreviated survey of combustion instabilities observed in various systems. The theoretical framework is constructed to accommodate these observations, but later emerges also as a perfect vehicle for investigating the use of active feedback control.

1.1. Introduction and Historical Background. For the kinds of propulsion systems normally used, combustion chambers are intended to operate under conditions that are steady or vary slowly. The central questions addressed in these lectures concern the stability and behavior subsequent to instability of steady states in combustors. If a state is unstable to small disturbances, then an oscillatory motion usually ensues. Such combustion instabilities commonly exhibit well-defined frequencies ranging from 15 hz or less to many kilohertz. Even at the highest amplitudes observed in practice, the instabilities consume only a small fraction of the available chemical energy. Thus, except in extremely severe instances, the oscillations do not normally affect the mean thrust or steady power produced by the systems. Serious problems may nevertheless arise due to structural vibrations generated by oscillatory pressures within the chamber, or by fluctuations of the thrust. In extreme cases, internal surface heat transfer rates may be amplified ten-fold or more, causing excessive erosion of the chamber walls.

An observer perceives an unstable motion in a combustion chamber as "self-excited," a consequence of the internal coupling between combustion processes and unsteady motion. Except in cases of large disturbances (e.g. due to passage of a finite mass of solid material through the nozzle), the amplitude of the motion normally seems to grow out of the noise without the intrusion of an external influence. Two fundamental reasons explain the prevalence of instabilities in combustion systems:

(i) an exceedingly small part of the available energy is sufficient to produce unacceptably large unsteady motions;

(ii) the processes tending to attenuate unsteady motions are weak, chiefly because combustion chambers are nearly closed.

These two characteristics are common to all combustion chambers and imply that the possibility of instabilities occurring during development of a new device must always be recognized and anticipated. Treating combustion instabilities is part of the price to be paid for high-performance chemical propulsion systems. It is a corollary of that condition that the problem will never be totally eliminated. Advances in research will strengthen the methods for solution in practical applications, and will provide guidelines to help in the design process.

The fact that only a small part of the total power produced in a combustor is involved in combustion instabilities suggests that their existence and severity may be sensitive to apparently minor changes in the system. That conclusion is confirmed by experience. Moreover, the complicated chemical and flow processes block construction of a complete theory from first principles. It is therefore essential that theoretical work always be closely allied with experimental results, and vice versa. No single analysis will encompass all possible instabilities in the various practical systems. There are nevertheless many features common to all combustion chambers. Indeed, it is one theme of these lectures that the characteristics shared by propulsion systems in many respects dominate the differences. While it is not possible to predict *accurately* the occurrence or details of instabilities, a framework does exist for understanding their general behavior, and for formulating statements summarizing their chief characteristics. For practical purposes, the theory often serves most successfully when used to analyze, understand, and predict *trends* of behavior, thereby also providing the basis for desirable changes in design. Experimental data are always required to produce quantitative results and their accuracy in turn is limited by uncertainties in the data.

In the U.S., and possibly in other countries, notably Germany and Russia before and during World War II, combustion instabilities were first observed in liquid rocket engines. Subsequent to the war, considerable effort was expanded in Russia and in the U.S. to solve the problem, particularly in large engines. Probably the most

expensive program was carried out during development of the F-1 engine for the Apollo vehicle (Ofelein and Yang, 1993).

Liquid-fueled, air-breathing propulsion systems commonly suffer combustion instabilities. Axial oscillations in ramjet engines are troublesome because their influence on the shock system in the inlet diffuser can reduce the inlet stability margin. Owing to their high power densities and light construction, thrust augmenters or afterburners are particularly susceptible to structural failures.

For any afterburner, conditions can be found under which steady operation is not possible. As a result, the operating envelope is restricted by the requirement that combustion instabilities cannot be tolerated. Due to structural constraints placed on the hardware, combustion instabilities in afterburners are particularly undesirable and are therefore expensive to treat.

In recent years combustion instabilities in the main combustor of gas turbines have become increasingly troublesome. The chief reason is ultimately due to requirements that emission of pollutants, notably oxides of nitrogen, be reduced. A necessary strategy, particularly for applications to flight, is reduction of the average temperature at which combustion takes place. Generation of NO by the thermal or 'Zel'dovich' mechanism is then reduced. Lower combustion temperature may be achieved by operating under lean conditions, when the flame stabilization processes tend to be unstable. Fluctuations of the flame cause fluctuations of energy release, which in turn may produce fluctuations of pressure, exciting acoustical motions in the chamber.

Finally, almost all solid rockets exhibit instabilities, at least during development, and occasionally motors are approved even with low levels of oscillations. Actual failure of a motor itself is rare in operation, but vibrations of the supporting structure and of the payload must always be considered. To accept the presence of weak instabilities in an operational system one must have sufficient understanding and confidence that the amplitudes will not unexpectedly grow to unacceptable levels. One purpose of these lectures is to provide the foundation for gaining the necessary understanding.

In the most general sense, a combustion instability may be regarded as an unsteady motion of a dynamical system capable of sustaining oscillations over a broad range of frequencies. The source of energy associated with the motions is ultimately related to the combustion processes, but the term 'combustion instability,' while descriptive, is misleading. In most instances, and always for the practical problems we discuss here, the combustion processes themselves are stable: uncontrolled explosions and other intrinsic chemical instabilities are not an issue. Observations of the gas pressure or of accelerations of the enclosure establish the presence of an instability in a combustion chamber. Excitation and sustenance of oscillations occur because coupling exists between the combustion processes and the gasdynamical motions, both of which may be stable. What is unstable is the entire system comprising the propellants, the propellant supply system, the combustion products that form the medium supporting the unsteady motions, and the containing structure.

If the amplitude of the motions is small, the vibrations within the chamber are usually related to classical acoustic behavior possible in the absence of combustion and mean flow. The geometry of the chamber is therefore a dominant influence. Corresponding to classical results, traveling and standing waves are found at frequencies approximated quite well by familiar formulas depending only on the speed of sound and the dimensions of the chamber. If we ignore any particular influences of geometry, we may describe the situation generally in the following way, a view valid for any combustion instability irrespective of the geometry or the type of reactants.

Combustion processes are sensitive to fluctuations of pressure, density, and temperature of the environment. A fluctuation of burning produces local changes in the properties of the flow. Those fluctuations propagate in the medium and join with the global unsteady field in the chamber. Under favorable conditions, the field develops to a state observable as a combustion instability. As illustrated schematically in Figure 1.1, we may view the process abstractly in analogy to a feedback amplifier in which addition of feedback to a stable oscillator can produce oscillations. Here the oscillator is the combustion chamber, or, more precisely, the medium within the chamber that supports the unsteady wave motions. Feedback is associated with the influences of the unsteady motions on the combustion processes or on the supply system, which in turn generate fluctuations of the field variables. The dynamical response of the medium converts the local fluctuations to global behavior. In the language of control theory, the field in the chamber is the 'plant,' described by the general equations of motion.
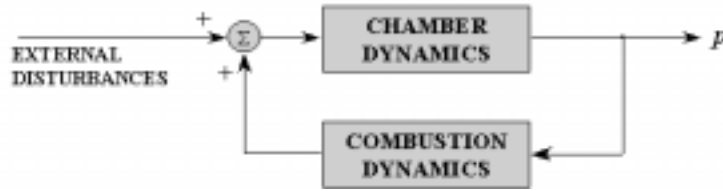
FIGURE 1.1. Schematic Diagram of a Combustion System as a Feedback Amplifier

The diagram in Figure 1.1 illustrates the main emphases of these lectures. Broadly, the subjects covered divide into two categories: those associated with the plant, the fluid mechanics and other physical processes comprising the *combustor dynamics;* and those connected primarily with the feedback path, chiefly combustion processes and their sensitivity to time-dependent changes in the environment, the *combustion dynamics.* The theory we will describe encompasses all types of combustion instabilities in a general framework having the organization suggested by the sketch. External forcing functions are accommodated as shown in the sketch, but the causes associated with the feedback path are far more significant in practice.

Figure 1.1 is motivated by more than a convenient analogy. For practical purposes in combustion systems, we generally wish to eliminate instabilities. Traditionally that has meant designing systems so that small disturbances are stable, or adding some form of energy dissipation to compensate the energy gained from the combustion processes, that is, *passive control.* However, in the past few years interest has grown in the possibility of *active control* of instabilities. If that idea is to be realized successfully, it will be necessary to combine modern control theory with the theory described here in Sections 2–7. It is advantageous to think from the beginning in terms that encourage this merger of traditionally distinct disciplines, the subject of Section 9.

We will later have more to say about control, both active and passive. Any method of control is rendered more effective the more firmly it rests on understanding the problem to be solved. Understanding a problem of combustion instabilities always requires a combination of experiment and theory. For many reasons, including intrinsic complexities and inevitable uncertainties in basic information (e.g., material properties, chemical dynamics, turbulent behavior of the flow field, ...), it is impossible to predict accurately from first principles the stability and nonlinear behavior of combustion systems. Hence the purpose of theory is to provide a framework for interpreting observations, both in the laboratory and full-scale devices; to suggest experiments to produce required ancillary data or to improve the empirical base for understanding; to formulate guidelines for designing full-scale systems; and globally to serve, like any good theory, as the vehicle for understanding the fundamental principles governing the physical behavior, thereby having predictive value as well.

All theoretical work in this field has been carried out in response to observational and experimental results. We therefore spend much of the remainder of this introductory section on a survey of the characteristics of combustion instabilities observed, and occasionally idealized, in the systems to be examined later. The general point of view taken throughout will then be formulated in heuristic fashion, based on experimental results.

Some of the consequences and symptoms of combustion instabilities were first observed in the late 1930s and early 1940s, roughly at the same time for liquid and solid propellant rockets, and apparently somewhat earlier in the Soviet Union than in the U.S. With the later development of turbojet engines, high-frequency instabilities were found in thrust augmenters or afterburners in the late 1940s and early 1950s. Although the problem had been encountered in ramjet engines in the 1950s, it became a matter of greater concern in the late 1970s and 1980s. The introduction of compact dump combustors led to the appearance of longitudinal or axial oscillations that interfered with the inlet shock system, causing loss of pressure margin and 'unstart' in the most severe cases. Owing to availability, almost all of the data cited here as examples will be derived from liquid rockets, solid rockets and laboratory devices. Figure 1.2 is a qualitative representation of the chronology of combustion instabilities. Due to the accessibility of documentation and the experiences of the author, particular cases cited are mainly those reported in the U.S.

The situation was more difficult with solid rockets because of the practical difficulties of installing and cooling pressure transducers. Probably the experience with cooling chamber and nozzle walls helps explain why quantitative results were obtained for instabilities in liquid rockets earlier than for solid rockets (E. W. Price,
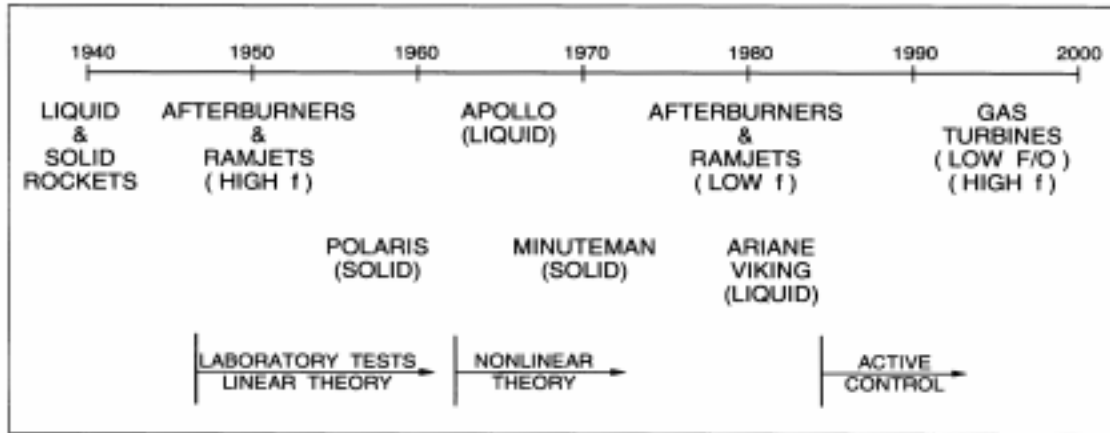
FIGURE 1.2. A Chronology of Combustion Instabilities

private communication). Prior to the appearance of high-frequency instrumentation, the existence of oscillations was inferred from such averaged symptoms as excessive erosion of inert surfaces or propellant grains due to increased heat transfer rates; erratic burning appearing as unexpected shifts in the mean pressure; structural vibrations; visible fluctuations in the exhaust plume; and, on some occasions, audible changes in the noise produced during a firing.

Experimental work progressed for several years before various unexplained anomalies in test firings were unambiguously associated with oscillations. By the late 1940s, there was apparently general agreement among researchers in the U.S. and Europe that combustion instabilities were commonly present in rocket motors and that they were somehow related to waves in the gaseous combustion products. In addition to measurements with accelerometers, strain gauges, and pressure transducers, methods for flow visualization soon demonstrated their value, mainly for studies of liquid propellant rockets (Altseimer 1952; Berman and Logan 1952; and Berman and Scharres 1953). Characteristics of the instabilities as acoustic vibrations, or weak shock waves, were revealed.

High-frequency or 'screech' oscillations were also first encountered in afterburners in the late 1940s; as a result of the experience with rockets and the availability of suitable instrumentation, the vibrations were quickly identified as combustion instabilities. The staff of the Lewis Laboratory (1954) compiled most of the existing data and performed tests to provide a basis for guidelines for design.

Thus by the early 1950s most of the basic characteristics of combustion instabilities had been discovered in both liquid-fueled and solid-fueled systems. Many of the connections with acoustical properties of the systems, including possible generation of shock waves, were recognized qualitatively. Although the frequencies of oscillations found in tests could sometimes be estimated fairly closely with results of classical acoustics, no real theory having useful predictive value existed. During the 1950s and the 1960s the use of sub-scale and laboratory tests grew and became increasingly important as an aid to solving problems of combustion instabilities occurring in the development of new combustion systems.

The situation in respect to instabilities in afterburners seems to have changed little in fundamental respects in more than 20 years. Early work showed that high-frequency oscillations ('screech') could be treated over fairly broad operating conditions by installing passive suppression devices — usually acoustic liners — and by adjusting the distribution and scheduling of the injected fuel. Problems increased as high-bypass engines were developed because the large annular flow passages allowed waves to propagate upstream to the compressor. As a result, instabilities occurred with longer wavelengths and hence lower frequencies (Bonnell *et al.* 1971; Kenworthy *et al.* 1974; Ernst 1976; Underwood *et al.* 1977; Russell *et al.* 1978). Low frequencies are not easily attenuated, so modifications in the supply system and appropriate scheduling of the fuel injection are the main strategy for treating these modes. In any case, it appears that all afterburners are subject to operational constraints set by the need to avoid combustion instabilities. Both because of the operational constraints and because of the high costs

incurred during development to give current operating envelopes, combustion instability in afterburners remains an attractive subject of research.

Instabilities in liquid-fueled ramjet engines are similar in many respects to those in afterburners, an example of the general property that the character of the oscillations is determined largely by the types of propellants used and the geometry of the chamber. In both systems, the steady combustion processes are stabilized behind bluff flameholders. Hence with suitable interpretation, many results of research are applicable to both types of systems. In the late 1970s and 1980s, research programs on combustion instabilities in ramjet engines were initiated by several western countries (see, for example, Hall 1978; Culick 1980; Culick and Rogers 1980; Sivasegaram and Whitelaw 1987; Zetterstrom and Sjöblom 1985; Biron *et al.* 1986). Culick (1988) has given an extensive review of combustion instabilities in all types of liquid-fueled propulsion systems.

Possibly the most interesting and fundamental result of work during the 1980's was demonstration of the importance of coupling between acoustical motions and large coherent vortex structures shed by a rearward facing step or a flameholder, first emphasized by Byrne (1981, 1983). That phenomenon, with or without combustion processes, arises in many situations and will likely long continue to be the subject of research. Problems associated with generation of unsteady vorticity and vortex shedding arise in all types of combustors.

A typical example is that investigated thoroughly in the dump combustor at Caltech (Smith and Zukoski, 1985; Sterling and Zukoski, 1991; Zak, 1993). Figure 1.3 is a sketch of the configuration, in which the flow is subsonic throughout, with premixed gaseous reactants introduced from a plenum chamber and exhausting to the atmosphere. Even for liquid-fueled ramjets, vaporization of the fuel often occurs so rapidly that combustion downstream of the dump plane occurs in a gaseous mixture. The general character of the stability diagram for this geometry has been found in other experimental programs as well: for a given flow rate, the most intense oscillations occur in the vicinity of stoichiometric proportions of the fuel oxidizer.
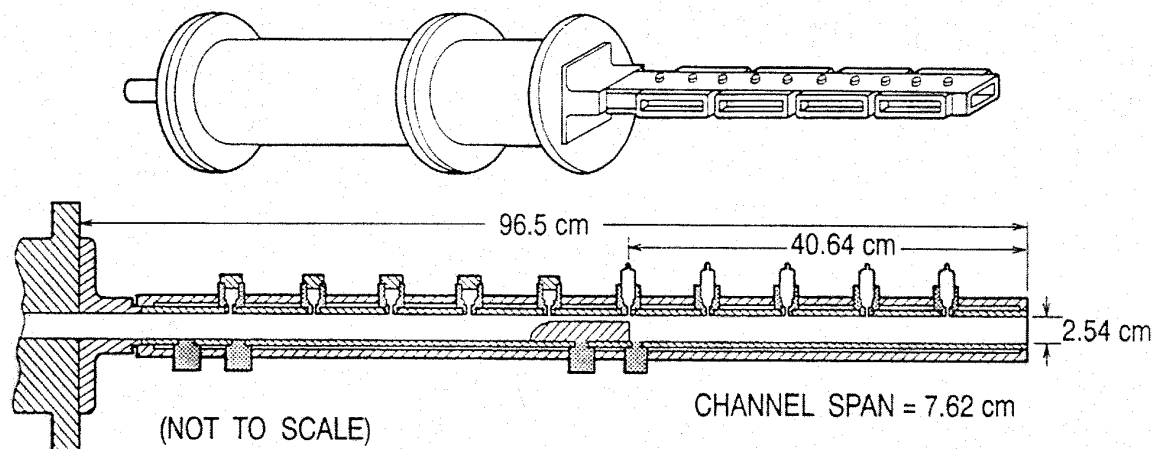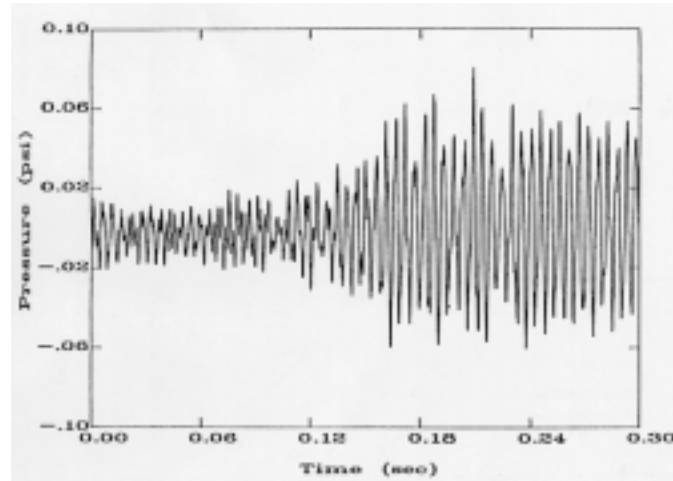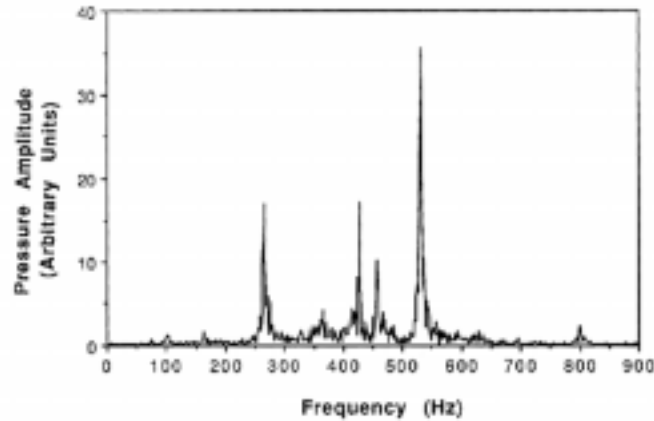

FIGURE 1.3. The Caltech Dump Combustor

The waveform and spectrum for the limiting behavior of an unstable oscillation are shown in Figure 1.4. Evidently the spectrum consists of a small number of peaks imbedded in a background of 'noise' spread over the entire frequency range covered. In this respect the motion seems to be dominated by two oscillations and subharmonics. Estimates based on the assumption of axial acoustic motions have shown (Sterling 1987; Zak 1993) that the two oscillations are normal modes of the system. Explanation of the nonlinear mechanism responsible for the sub-harmonics has not been given.

It is interesting and significant that the 'noise' exhibited in the spectrum seems to appear as a kind of random modulation of the amplitude of the waveform reproduced in Figure 1.4(a). That interpretation is supported by the approximate analysis of nonlinear acoustics and noise covered later. Some recent laboratory results have shown that the level of noise depends on the presence and amplitudes of combustion instabilities, but the cause is unknown, and no such observations exist for full-scale combustors.

Although this example is special, it does illustrate the chief features of combustion instabilities generally: well-defined organized oscillations within an apparently random field, normally called noise. It is quite common that there are more peaks in the spectra than appear in Figure 1.4(b), and that the frequencies tend to be close to those of the normal acoustics modes of the chamber in question. The quantitative aspects vary widely, but the physical behavior suggested by these results broadly defines the general problem to be addressed by the theory.

(a)

(b)

FIGURE 1.4. Waveform and Spectrum for an Instability in the Caltech Dump Combustor

1.2. Mechanisms of Combustion Instabilities. Just as for steady operation, the chief distinctions among combustion instabilities in different combustors must ultimately be traceable to differences in geometry and the states of the reactants. The root causes, or 'mechanisms', of instabilities are imbedded in that context and are often very difficult to identify with certainty. Possibly the most difficult problem in this subject is to quantify the mechanism. Solving that problem requires finding an accurate representation of the relevant dynamics.

The simplest and most convenient characterization of an unstable oscillation is expressed in terms of the mechanical energy of the motion. Linear theory produces the result that the rate of growth of the amplitude is proportional to the fractional rate of change of energy, the sum of kinetic and potential energies. The idea is discussed further in the following section. What matters at this point is that the term 'mechanism' refers to a process that causes transfer of energy to the unsteady motion from some other source. Thus, mechanisms form the substance of the feedback path in Figure 1.1. Generally there are only three sorts of energy sources for unsteady motions in a combustor: the combustion processes; the mean flow, which of course itself is caused by combustion; and a combination of combustion and mean flow simultaneously acting. The distinction is important

because the physical explanations of the energy transfer are very different in the three cases. If the basic physical processes differ, so also must the means of treating instabilities.

Combustion processes are sensitive to the macroscopic flow variables, particularly pressure, temperature and velocity. Even slow changes of those quantities affect the energy released according to rules that can be deduced from the behavior for steady combustion. In general, however, representations of that sort, based on assuming quasi-steady behavior, are inadequate. Combustion instabilities normally occur in frequency ranges such that true dynamical behavior is significant. That is, the transient changes of energy release do not follow precisely in phase with imposed changes of a flow variable such as pressure.

The next simplest assumption is that the combustion processes behave as a first order dynamical system characterized by a single time delay or relaxation time. That idea was apparently first suggested by Karman as a basis for interpreting instabilities discovered in early experiments with liquid propellant rockets at Caltech (Summerfield, 1951). That representation, which came to be called the '$n - \tau$ model' was developed most extensively by Crocco and his students at Princeton during the 1950s and 1960s. Time delays may be due, for example, to processes associated with ignition of reactants. Subsequent to injection as the reactants flow downstream, finite times may be required for vaporization, mixing, and for the kinetics mechanism to reach completion. Those effects may be interpreted in terms of a convective time delay. Under unsteady conditions, the initial state of the reactants, their concentrations, pressure, and velocity, also fluctuate, causing the delay time to be both nonuniform in space and in time. As a result, the rate of energy release downstream in the chamber is also space- and time-dependent, and acts as a source of waves in the combustor.

In the case of liquid-fueled systems, interactions of the injected streams, formation of sheets and break-up into drops are processes sensitive to pressure and particularly velocity fluctuations. Those are purely fluid-mechanical processes impossible to treat analytically and pose extremely difficult problems for numerical simulations. No complete numerical analyses exist and only much simplified models have been used in numerical simulations of combustion instabilities. The true dynamics is not likely to be well-represented by an $n - \tau$ model.

Purely gaseous-fueled systems present a possibility for a different physical model that also leads to first-order behavior. It is an old idea that even in complicated geometries, combustion in a non-premixed system must occur at least partly in elements of diffusion flames. If the gaseous reactants are pre-mixed, then simple configurations such as tubes, or dump combustors, combustion may occur in large stable flame sheets of the flow is laminar, or in fragments of pre-mixed 'flamelets' when the flow is turbulent. In all of these cases it is reasonable to anticipate that at any given time the rate of energy release is roughly proportional to the area of the flame sheets. Then fluctuations of the velocity or processes responsible for ignition and extinction, will cause fluctuations of the energy release rate. Models of this process lead to an equation representing first order behavior (Dowling 1997; Candel 1992; Annaswany *et al.* 2000; Poinsot 1988, for example).

The approximation of first order behavior fails entirely for the dynamics of burning solid propellants (Culick 1968). Although in good first approximation dominated by unsteady heat transfer in the condensed phase, a diffusive process, the combustion dynamics in this case exhibits behavior closer to that of a second order system. The frequency response of that burning rate tends normally to have a large broad peak centered at a frequency falling well within the range of the frequencies characteristic of the chamber dynamics. Hence there is a clear possibility for a resonance and instability suggested by the diagram in Figure 1.1.

Generation of oscillations by the average flow is due to causes roughly like those active in wind musical instruments. In all such cases, flow separation is involved, followed by instability of a shear layer and formation of vortices. Direct coupling between the vortices and a local velocity fluctuation associated with an acoustic field is relatively weak; that is, the rate of energy exchange is in some sense small. However, the interaction between the velocity (or pressure) fluctuation and the initial portion of the shear layer is normally a basic reason that feedback exists between the unsteady field in the volume of the combustor and vortex shedding.

It has long been known experimentally that vortices shed in a chamber more effectively generate acoustic waves if they impinge in an obstacle downstream of their origin (Flandro and Jacobs, 1975; Magiawala and Culick, 1979; Flandro, 1986). The first example of this phenomenon was the solid rocket booster for the Shuttle launch system in the 1970s. It was that problem that motivated the works just cited, but since then vortex shedding has

been recognized as a mechanism for generating acoustic oscillations in other systems as well, notably the booster motors on the Space Shuttle and on the Ariane 5.

Byrne (1981) seems to have been first to suggest that vortex shedding could be responsible for instabilities observed in dump combustors. The idea was developed very actively in the 1980s, both in systems operating at room temperature without combustion (Schadow *et al.*, 1981, 1983, 1984, 1985) and in combustors (Schadow *et al.*, 1985, 1987a, 1987b)

Combustion dynamics and the mean flow created with vortex shedding combine to give a mechanism different from the two kinds just described. Unsteady combustion in vortices was one of the early mechanisms proposed as a cause of combustion instabilities in combustors using bluff body flameholders (Marble and Rogers 1956). It was essentially re-discovered in the 1980's during tests of dump combustors (Smith and Zukoski 1985; Daily and Oppenheim 1986; Stirling and Zukoski 1991; for example). Several attempts have been made to quantify the mechanism with analysis (Norton 1983; Karagozian and Marble 1986) and with numerical simulations (Laverdant and Candel 1989; Samaniego and Mantel 1999). Insufficient progress has been made to construct a model suitable for general analysis of combustion instabilities. Thus there is currently no basis for predictions of combustor dynamics excited by this mechanism. Special cases have been discussed in connection with particular experimental results; see, for example, Stirling 1993.

Combustion instabilities have not historically been a serious problem in gas turbine main combustors. Although instabilities have certainly been observed for many years, they have not been persistently troublesome. Due to proprietary considerations almost no detailed results for full-scale machines have been made public, a situation that is unlikely to change soon. In the past few years combustion instabilities have become a serious problem in gas turbines because of the need to operate close to the lean blowout limit as part of the strategy to reduce generation of pollutants, notably NO_x.

As the operating condition approaches the lean blowout limit, combustion processes ('flame dynamics'), including flame stabilization, are more sensitive to fluctuations than under operation at higher mixture (F/O) ratios. The sensitivity extends to flame fronts and zones as well as the stabilization processes, shear layers and recirculation zones. The latter, associated with injection and stabilization may possess multiple dynamical states, i.e. special bifurcations and hysteresis.

The dynamical behavior of the premixer and injection devices may contribute to instabilities in various ways. Internal resonances, for example, may be excited by oscillations in the chamber, causing perturbations of the energy released in the combustion processes downstream of the injector. There may also be undesirable coupling between elements of an array of premixers and injectors. Such dynamical behavior may also be turned to advantage to extend the operating range of stable operation. That strategy was successfully pursued on several occasions in the Russian liquid rocket community.

It is likely that fluctuations of the mixture ratio (F/O) play an important role in the dynamics of gas turbine combustors. If the F/O ratio of the reactants is at all sensitive to conditions in the combustion chamber, there is an obvious feedback path connecting the combustor and combustion dynamics. The possibility has arisen previously in other combustion systems, but at least anecdotal evidence has suggested that serious attention must be paid to fluctuations of mixture ratio as a fundamental mechanism for instabilities in gas turbines.

1.3. Elementary Interpretation of Combustion Instabilities. Owing to the difficulty of making direct measurements of the flow field within a combustion chamber, virtually all that is known about combustion instabilities rests on close coordination of experiment and theory. The subject is intrinsically semi-empirical, theoretical work being founded on observational data both from full-scale machines and laboratory devices. Conversely, the theoretical and analytical framework occupies a central position as the vehicle for planning experimental work and for interpreting the results. The chief purposes of this section are to summarize briefly the most important basic characteristics of observed instabilities; and to introduce the way in which those observations motivate the formulation of the theoretical framework.

In tests of full-scale propulsion systems, only three types of data are normally available, obtained from pressure transducers, accelerometers, and strain gauges. Measurements of pressure are most direct but are always limited,

and often not possible when the necessary penetration of the enclosure to install instruments is not allowed. Hence the unsteady internal pressure field is often inferred from data taken with accelerometers and strain gauges. In any case, because it is the fundamental variable of the motions, the pressure will serve here as the focus of our discussion.

A combustion chamber contains a non-uniform flow of chemically reacting species, often present in condensed as well as gaseous phases, exhausting through a nozzle that is choked in rockets, ramjets, and afterburners. Moreover, the flow is normally turbulent and may include regions of separation. Yet estimates of the frequencies of oscillations computed with acoustics formulas for the natural modes of a closed chamber containing a uniform gas at rest commonly lie within 10–15 percent or less of the frequencies observed for combustion instabilities, if the speed of sound is correctly chosen.

There are three main reasons that the classical view of acoustics is a good first approximation to wave propagation in combustion chamber: (1) the Mach number of the average flow is commonly small, so convective and refractive effects are small; (2) if the exhaust nozzle is choked, incident waves are efficiently reflected, so for small Mach numbers the exit plane appears to be nearly a rigid surface; and (3) in the limit of small amplitude disturbances, it is a fundamental result for compressible flows that any unsteady motion can be decomposed into three independent modes of propagation, of which one is acoustic (Chu and Kovazsnay 1956). The other two modes of motion are vortical disturbances, the dominant component of turbulence, and entropy (or temperature) waves. Hence even in the highly turbulent non-uniform flow usually present in a combustion chamber, acoustic waves behave in good first approximation according to their own simple classical laws.

Of course, it is precisely the departures from classical acoustics that define the class of problems we call combustion instabilities. In that sense, these lectures are concerned chiefly with perturbations of a very old problem, standing waves in an enclosure. That point of view has significant consequences; perhaps the most important is that many of the physical characteristics of combustion instabilities can be described and understood quite well in a familiar context. The remainder of this section is an elaboration of that conclusion.

The most obvious evidence that combustion instabilities are related to classical acoustic resonances is the common observation that frequencies measured in tests agree fairly well with those computed with classical formulas. Generally, the frequency f of a wave equals its speed of propagation, a, divided by the wavelength, λ:

$$f = \frac{a}{\lambda} \tag{1.1}$$

On dimensional grounds, or by recalling classical results, we know that the wavelength of a resonance or normal mode of a chamber is proportional to a length, the unobstructed distance characterizing the particular mode in question. Thus the wavelengths of the organ-pipe modes are proportional to the length, L, of the pipe, those of modes of motion in transverse planes of a circular cylindrical chamber are proportional to the diameter, D, and so forth. Hence (1.1) implies

$$f \sim \frac{a}{L} \quad \text{longitudinal modes}$$

$$\text{(1.2) a, b}$$

$$f \sim \frac{a}{D} \quad \text{transverse modes}$$

There are two basic implications of the conclusion that the formulas (1.2) a, b, with suitable multiplying constants, seem to predict observed frequencies fairly well: evidently the geometry is a dominant influence on the spatial structure of the instabilities; and we can reasonably define some sort of average speed of sound in the chamber, based on an approximation to the temperature distribution. In practice, estimates use the classical formula $a = \sqrt{\gamma RT}$ with T the adiabatic flame temperature for the chemical system in question, and with the properties γ and R calculated according to the composition of the mixture in the chamber. Usually, mass-averaged values, accounting for condensed species, seem to be close to the truth. If large differences of temperature exist in the chamber, as in a flow containing flame fronts, nonuniformities in the speed of sound must be accounted for to obtain close estimates of the frequencies.

Even for more complicated geometries, notably those often used in solid rockets, when the simple formulas (1.2) a, b are not directly applicable, numerical calculations of the classical acoustic motions normally give good

approximations to the natural frequencies and pressure distributions. Thus quite generally we can adopt the point of view that combustion instabilities are acoustical motions excited and sustained in the first instance by interactions with combustion processes. That the classical theory works so well for estimating frequencies and distributions of the unsteady motions means that computation of those quantities is not a serious test of a more comprehensive theory. What is required first of a theory of combustion instabilities is a basis for understanding how and why combustion instabilities differ from classical acoustics.

In particular, two global aspects of minor importance in most of classical acoustics, are fundamental to understanding combustion instabilities: transient characteristics and nonlinear behavior. Both are associated with the property that with respect to combustion instabilities, a combustion chamber appears to an observer to be a *self-excited system*: the oscillations appear without the action of externally imposed forces. Combustion processes are the sources of energy which ultimately appear as the thermal and mechanical energy of the fluid motions. If the processes tending to dissipate the energy of a fluctuation in the flow are weaker than those adding energy, then the disturbance is unstable.

1.4. Linear Behavior. When the amplitude of a disturbance is small, the rates of energy gains and losses are usually proportional to the energy itself which in turn is proportional to the square of the amplitude of the disturbance; the responsible processes are said to be linear because the governing equations are linear in the flow variables. An unstable disturbance then grows exponentially in time, without limit if all processes remain linear. Exponential growth of the form $A_0 e^{\alpha t}$, where A_0 is the amplitude of the initial small disturbance, is characteristic of the initial stage of an instability in a self-excited system, sketched in Figure 1.5(a). In contrast, the initial transient in a linear system forced by an invariant external agent grows according to the form $1 - e^{-\beta t}$, shown in Figure 1.5(b). The curve $e^{\alpha t}$ is concave upward and evolves into a constant limiting value for a physical system only if nonlinear processes are active. However, the plot of $1 - e^{-\beta t}$ is concave downward and approaches a limiting value for a linear system because the driving agent supplies only finite power.

(a)   (b)
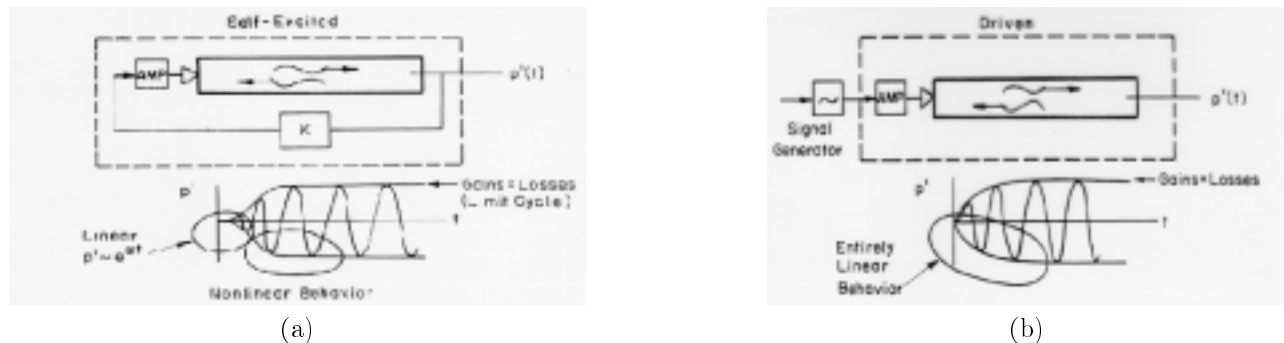
FIGURE 1.5. Transient behavior of (a) Self Excited Linearly Unstable Motions; (b) Forced Motions

Extensive data leave no doubt that the unstable motions in combustion chambers are self-excited, having the characteristics shown in Figure 1.5(a). The physical origin of this behavior is the dependence of the energy gains and losses on the motions themselves. For combustion instabilities, the 'system' is the dynamical system whose behavior is measured by the instrument sensing the pressure oscillations. Thus, in view of earlier remarks, the dynamical system is in some sense the system of acoustical motions in the chamber coupled to the mean flow and combustion processes (recall Figure 1.1).

It is a fundamental and extremely important conclusion that by far most combustion instabilities are motions of self-excited dynamical systems. Probably the most significant implication is that in order to understand fully the observed behavior, and how to affect it and control it, one must understand the behavior of a nonlinear system. When the motion in a combustion chamber is unstable, except in unusual cases of growth to destruction, the amplitude typically settles down to a finite value: the system then executes a limiting motion, usually a periodic limit cycle. For practical applications, it is desirable to know how the amplitude of the limit cycle depends on the parameters characterizing the system. That information may serve as the basis for changing the characteristics to reduce the amplitude, the goal in practice being zero. In any case, good understanding of the properties of the

limit cycle will also provide some appreciation for those variables which dominate the behavior and to which the motions may be most sensitive, a practical matter indeed.

Our global view, then, is that a combustion instability is an oscillatory motion of the gases in the chamber, which can in first approximation be synthesized of one or more modes related to classical acoustic modes. The mode having lowest frequency is a 'bulk' mode in which the pressure is nearly uniform in space but fluctuating in time. Because the pressure gradient is everywhere small, the velocity fluctuations are nearly zero. This mode corresponds to the vibration of a Helmholtz resonator obtained, for example, by blowing over the open end of a bottle. The cause in a combustion chamber may be the burning process itself, or it may be associated with oscillations in the supply of reactants, caused in turn by the variations of pressure in the chamber. In a liquid rocket, structural oscillations of the vehicle or the feed system may also participate, producing the POGO instability.

Whatever the system, most combustion instabilities involve excitation of the acoustic modes, of which there are an infinite number for any chamber. The values of the frequencies are functions primarily of the geometry and of the speed of sound, the simplest examples being the longitudinal and transverse modes of a circular cylinder, with frequencies behaving according to (1.2) a, b. Which modes are unstable depends on the balance of energy supplied by the exciting mechanisms and extracted by the dissipating processes. We consider here only linear behavior to illustrate the point.

In general the losses and gains of energy are strongly dependent on frequency. For example, the attenuation due to viscous effects typically increases with the square root of the frequency. Other sources of energy loss associated with interactions between the oscillations and the mean flow tend to be weaker functions of frequency. That is the case, for example for reflections of waves by a choked exhaust nozzle. The gains of energy usually depend in a more complicated way on frequency.

The sources of energy for combustion instabilities i.e. the mechanisms responsible for their existence, present the most difficult problems in this field. For the present we confine our attention to qualitative features of energy exchange between combustion and unsteady motions. For example, the magnitude of the energy addition due to coupling between acoustic waves and combustion processes for a solid propellant normally rises from some relatively small quasi-steady value at low frequencies, passes through a broad peak, and then decreases to zero at high frequencies. Energy is transferred to a pressure oscillation having a particular frequency at a rate proportional to the part of the coupling that is in phase with the pressure at that frequency.[1] Figure 1.6 is a schematic illustration of this sort of behavior.

In Figure 1.6, the gains exceed the losses in the frequency range $f_1 < f < f_2$. Modes having frequencies in that range will therefore be linearly unstable. An important characteristic, typical of combustion chambers generally, is that in the lower ranges of frequency, from zero to somewhat above the maximum frequency of instability, the net energy transfer is a small difference between relatively larger gains and losses. That implies the difficulty, confirmed by many years' experience, of determining the net energy flow accurately. Unavoidable uncertainties in the gains and losses themselves become much more significant when their difference is formed. That is the main reason for the statement made earlier that analysis of combustion instabilities has been useful in practice chiefly for predicting and understanding *trends* of behavior rather than accurate calculations of the conditions under which a given system is unstable. The ultimate source of all of these difficulties, as cited in Section 1.1, is the property that the motions in question consume and contain only small portions of the total energy available within the system. Hence in both laboratory tests and in operational systems one is confronted with determining the characteristics of essentially small disturbances imbedded in a complicated dynamic environment.

The best and most complete data illustrating the preceding remarks have been obtained with solid propellant rockets. There are several reasons for that circumstance. First, the ignition period—the time to cause all of the exposed propellant surface to begin burning—is relatively short and the average conditions in the chamber quickly reach their intended values. Unless oscillations are severely unstable, and growing rapidly during the ignition transient, there is a good opportunity to observe the exponential growth characteristic of a linear instability.

---

[1]It is possible, due to the behavior of the phase, that in a range of high frequencies the combustion processes may in fact extract energy from the acoustic waves and hence contribute to the losses of energy.
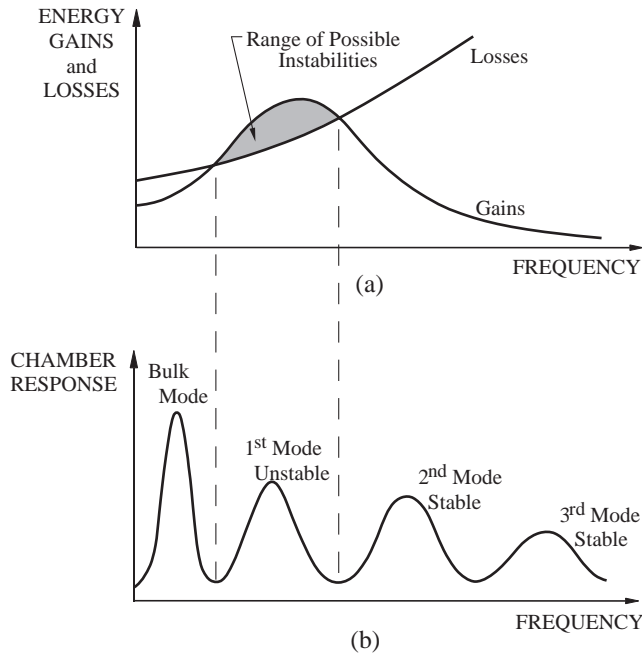
FIGURE 1.6. Qualitative Dependence of (a) Energy Gains and Losses; and (b) the Frequency Response of a Combustor

Secondly, it is probably true that more effort has been spent on refining the measurements and predictions of linear stability for solid rockets than for other systems because of the expense and difficulty of carrying out replicated tests. There is no practical, routine way of interrupting and resuming firings and it is the nature of the system that an individual motor can be fired only once. Particularly for large motors used in space launch vehicles, successive firings involve great expense. Development by empirical trial-and-error is costly; there is considerable motivation to work out methods of analysis and design applicable to individual tests.

In contrast, liquid-fueled systems can be fired repeatedly. Trial-and-error has long been a strategy for development of both liquid rockets and air-breathing systems. It seems that attention in that sort of work has generally been focused on modifications to reduce amplitudes (as in 'bombing' tests) rather than on determining the stability of small-amplitude motions. Very little data exists for values of growth constants, and most of those results have been obtained for model or sub-scale laboratory devices. There are examples of stability boundaries inferred from 'bombing' tests of the sort mentioned earlier and theoretical results exist, but there seem to be no investigations comparable to those carried out for solid rockets. A Standard Stability Prediction (SSP) program has been available for solid rockets for 25 years (Lovine *et al.* 1983, Nickerson *et al.* 1983); no such product exists for liquid rockets and other combustion systems.

We have already noted in Section 1.2 that much progress was achieved in analyzing and understanding combustion instabilities in solid rockets from the late 1960s into the 1980s when there was little work in liquid rockets. During that period, computing resources, microprocessors, and therefore techniques of data acquisition and processing advanced enormously. Hence by comparison with the situation for solid rockets, the subject of combustion instabilities in liquid-fueled systems, especially liquid rockets, did not benefit as greatly from the general progress of supporting technologies. That situation is changing.

Finally, liquid or gaseous fueled systems are intrinsically more difficult to analyze and understand because of the more complicated chemical processes and coupling with the unsteady flow field. It is true that combustion of a heterogeneous solid propellant containing many ingredients, often including a metal, is very complicated indeed and far from completely understood in general. However, from the point of view of treating combustion instabilities, there is the great advantage that under most conditions, virtually all of the significant combustion processes are completed within a thin zone near the solid propellant itself. Coupling to the unsteady flow field may therefore be represented as a boundary condition. Combustion of liquid fuels is necessarily distributed throughout

the volume of the chamber. Making accurate approximations to the spatial dependence is difficult, requiring quite careful treatment of many rate processes, including chemical kinetics and transfer of energy between liquid and gaseous phases. The elementary dynamics of the combustion processes are poorly understood relative to the situation for solid propellants.

2. THE SIMPLEST EXAMPLE OF THERMO-ACOUSTIC INSTABILITIES: THE RIJKE TUBE

Combustion instabilities are the most common forms of motions called more generally thermoacoustic instabilities. The term refers to oscillatory motions excited and sustained by transfer of energy from a source of heating either by passage of electricity, by combustion processes, or by some material store of energy. In the Rijke tube, the simplest source is a sample of heated wire gauge which transfers energy to the surrounding air in a tube. Small flames and electrically heated grids are equally effective, the latter being easier to analyze.

The Rijke tube was invented and first studied by Rijke in the middle of the 19th century. Its behavior inspired Rayleigh's criterion (Lord Rayleigh, 1945). Despite the immense number of related works, a satisfactorily complete analysis and experimental characterization of the device does not exist. Nonetheless it is true that the Rijke tube shares many properties with combustion instabilities; it has therefore been usefully cited in many discussions and has been used in many experimental projects. In this section we examine the Rijke tube as a means of illustrating some ideas and methods to be developed in more general form later.

We consider the simplified form of a Rijke tube open at both ends, supported vertically, and containing a heated wire grid. The grid may be heated electrically, or by a flame subsequently removed. If the grid is in the lower half of the tube, steady oscillations can be sustained, having frequency hardly distinguishable from that of the fundamental frequency of the tube, $\overline{a}/2L$ where a is the speed of sound. The basic questions to be answered
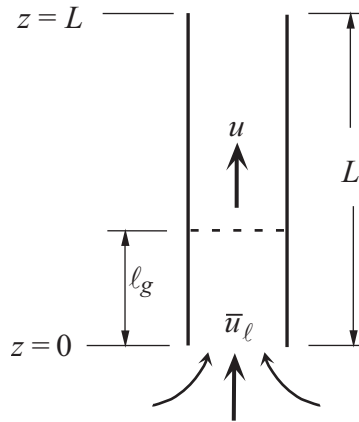
FIGURE 2.1. Sketch of the Simplest Form of Rijke Tube

here is: Why are the oscillations excited and sustained?; and how does the presence of oscillations depend on the location of the grid?

For several reasons, the Rijke tube is a marvelous case to investigate as an example of thermoacoustic oscillations, acoustic waves excited and sustained by heat addition. Perhaps most importantly, this is a situation in which the part of the system that is the source of energy, and provides internal feedback, is clearly distinct from the system that is oscillating, the acoustic field. Thus we can separate analysis of the two parts of the system with minimal approximations. It is that property we take particular advantage of here.

2.1. Mean Flow in a Rijke Tube. Due to the heating by the grid, the temperature of the air is increased, the density is reduced and the air above the grid rises because of its buoyancy. Thus there is a steady flow or draft of air drawn into the lower end, the average velocity being $\overline{u}_\ell$. If the change of temperature across the grid is idealized as a discontinuity, the velocity $\overline{u}_\ell$ is uniform below the grid and above the mean velocity has the higher value $\overline{u}_n$. This follows from continuity of mass flow,

$$\overline{\rho}_\ell \overline{u}_\ell A = \overline{\rho}_u \overline{u}_u A$$

so

$$\overline{u}_u = \frac{\overline{\rho}_\ell}{\overline{\rho}_u} \overline{u}_\ell > \overline{u}_\ell \tag{2.1}$$

where the ratio of average densities is $\overline{\rho}_\ell/\overline{\rho}_u > 1$ because $\rho = p/RT$ and the average pressure is uniform (atmospheric), giving

$$\frac{\overline{\rho}_\ell}{\overline{\rho}_u} = \frac{\overline{T}_u}{\overline{T}_\ell} > 1 \tag{2.2}$$

2.2. Acoustic Field in a Rijke Tube. Superposed on the average flow is the acoustic field, well represented by uniform values transverse to the axis of the tube and varying sinusoidally in the axial direction. The oscillating pressure is closely continuous through the grid and is given approximately by half of a sinusoid, chosen so $p'(0,t) = 0$ at the lower end. We introduce a subscript $(\quad)_1$ to indicate that we are dealing with the lowest, i.e. the first oscillating mode of the tube:

$$p_1'(x,t) = P_1 \sin \omega_1 \sin k_1 x \tag{2.3}$$

With the boundary condition $p_1'(L,t) = 0$, k_1 has the value such that $\sin k_1 L = 0$:

$$k_1 = \frac{\pi}{L} \tag{2.4}$$

The wavenumber k_1 is $2\pi/\lambda_1$ where λ_1 is the wavelength, so

$$\lambda_1 = 2L \tag{2.5}$$

Generally, the frequency of waves is given by $f = \overline{a}/\lambda$, so, as quoted in the introductory remarks,

$$f_1 = \frac{\overline{a}}{2L} \tag{2.6}$$

if we assume $\overline{a}$ is uniform in the tube.

The acoustic velocity fluctuation in general satisfies the equation

$$\overline{\rho}\frac{\partial u'}{\partial t} = -\frac{\partial p'}{\partial x} \tag{2.7}$$

and for $p'(z,t)$ given by (2.3), this equation has the solution

$$u_1'(z,t) = U_1 \cos \omega_1 t \cos k_1 x = \hat{u}_1 \cos k_1 x \tag{2.8}$$

with

$$U_1 = \frac{1}{\overline{\rho}\,\overline{a}} P_1 \tag{2.9}$$

Because of the temperature change through the grid, the speed of sound is greater in the upper part of the tube than in the lower; $\overline{a} = \sqrt{\gamma RT}$ and

$$\frac{\overline{a}_u}{\overline{a}_\ell} = \sqrt{\frac{\overline{T}_u}{\overline{T}_\ell}} \tag{2.10}$$

Moreover, the acoustic velocity suffers a discontinuity at the grid due to the jump in the average density and satisfaction of continuity for the acoustic field:

$$\overline{\rho}_\ell u_\ell' = \overline{\rho}_u u_u'$$

so

$$u_u' = \frac{\overline{\rho}_u}{\overline{\rho}_\ell} u_\ell' < u_\ell' \tag{2.11}$$

For simplification we will ignore the jump in velocity (i.e. we assume a very small temperature jump), which implies weak heating. It's not a realistic approximation but allows the main points to be made here without unnecessary complications.

Hence we take the acoustic pressure and velocity to be approximated by the formulas (2.3) and (2.8), sketched in Figure 2.2. It is particularly important that both the spatial distributions and the phases of the pressure and velocity distributions differ. Those differences explain certain basic characteristics of the Rijke tube discussed below.
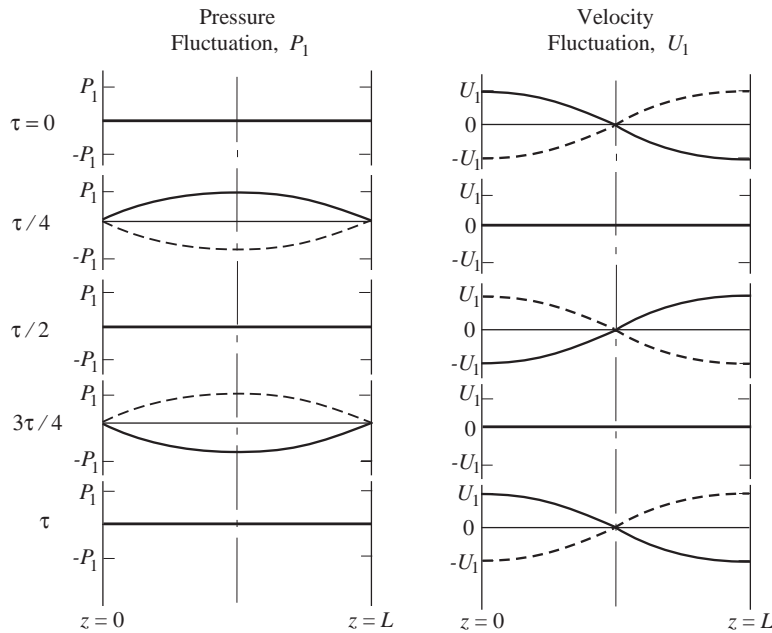
<div align="center">FIGURE 2.2. Pressure and Velocity Distribution in a Tube Open at Both Ends</div>

As a simplified representation, Figure 2.3 is often used, showing the spatial distributions of the envelopes of the fluctuations. It's a convenient form, but the phase relations implied by Figure 2.2 must not be forgotten. The local pressure and velocity oscillate between the values set by their envelopes but with a relative phase of $\pi/4$. This property is best shown graphically with the records in time, Figure 2.4: the pressure fluctuation **lags** the velocity fluctuation by $\pi/4$, a quarter-period.
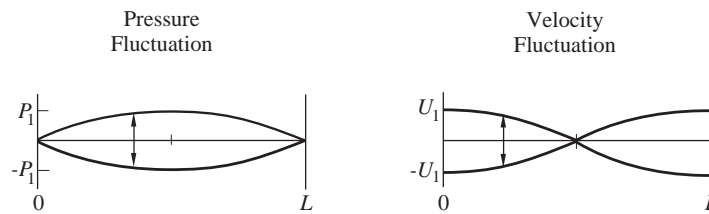
<div align="center">FIGURE 2.3. Mode Shapes of the Pressure and Velocity Fluctuations.</div>
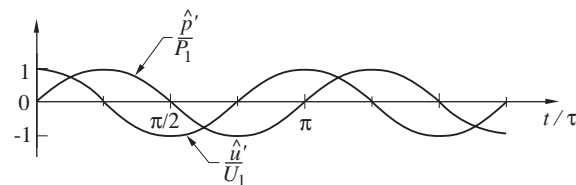
<div align="center">FIGURE 2.4. Spatial Distributions and Temporal Histories of the Pressure and Velocity Oscillations in Figure 2.3.</div>

The results just quoted for the acoustic field are valid strictly for the oscillations in a tube open at both ends without heating and mean flow. In fact, the mode shapes in a Rijke tube must differ from those graphed and given by the formulas (2.3), (2.8) and (2.9). At the very least the non-uniform temperature and hence speed of sound, as well as the discontinuity in velocity at the heater, must cause deviations from the simple acoustic results. It is a basic characteristic of the analytical method worked out in the following sections, that if the deviations are small, we can obtain many useful results for the actual dynamics of the system *without* knowing the actual mode shapes. Consequently, as a practical matter, a great deal of progress in applications can be made in understanding

the dynamical behavior without ever knowing what the true motions are. It is a point often missed. The formal development of the analysis establishes clearly what is meant by 'small'. In this section, we simply carry out the simplest form of the calculations, neglecting also the first order effects of the convective flow and the nonuniform speed of sound on stability. Such contributions cannot be ignored if accurate results are needed.

2.3. Linear Instability and Transient Growth of Oscillations in an Electrically Driven Rijke Tube.

If the heated grid is turned on suddenly, the amplitude of oscillations will soon grow exponentially, finally reaching some limiting amplitude characteristic of a limit cycle. The interval during which the oscillations evolve to their final form involves nonlinear processes and will not be discussed here. However, the initial period of growth is a purely linear phenomenon and can be analyzed approximately without great difficulty. The analysis given in this section is the simplest application of spatial averaging to a problem of thermoacoustic instability. It is intended to show **only** the influence of the process of heat addition, in order to establish several general characteristics, including the well-known dependence of the existence of unsteady oscillations on the position of the grid. A proper and complete analysis of stability must account for the mean flow and acoustics losses discussed in the following section.

In a broad sense, the analysis replaces the representation of a distributed system governed by partial differential equations by that of a discrete system whose motion is described by ordinary differential equations. When heat addition $\dot{Q}$ is accounted for, the classical equations for acoustic momentum and pressure are

$$\overline{\rho}\frac{\partial u'}{\partial t} + \frac{\partial p'}{\partial x} = 0$$
$$\frac{\partial p'}{\partial t} + \gamma \overline{p}\frac{\partial u'}{\partial x} = \frac{R}{C_v}\dot{Q}' \tag{2.12a,b}$$

The wave equation for the pressure fluctuations is found by substituting (2.12)a,b for $\frac{\partial u'}{\partial t}$ in the time derivative of (2.12)a,b:

$$\frac{\partial^2 p'}{\partial t^2} - \overline{a}^2\frac{\partial^2 p'}{\partial x^2} = \frac{R}{C_v}\frac{\partial \dot{Q}'}{\partial t} \tag{2.13}$$

We seek a result measuring in some fashion the influence of $\dot{Q}$ on the stability of waves. The simplest method producing an explicit formula of some generality is based on spatial averaging, constructed on the assumption that the right-hand side of (2.13) is a small disturbance of the classical acoustics problem.

If $\dot{Q} = 0$, then the acoustics field in the Rijke tube is a normal mode for which the pressure fluctuation is given by (2.3) and p_1 satisfies (2.13) with $\dot{Q} = 0$:

$$\frac{\partial^2 p_1'}{\partial t^2} - \overline{a}^2\frac{\partial^2 p_1'}{\partial x^2} = 0 \tag{2.14}$$

We assume that p' and p_1' satisfy the same conditions at the ends of the tube:

$$p_1'(0, t) = p'(0, t) = 0 \qquad (x = 0)$$
$$p_1'(L, t) = p'(L, t) = 0 \qquad (x = L) \tag{2.15 a,b}$$

Rather than try to solve the actual problem described by (2.13), we try to determine a formal characterization of the difference between the actual problem and the unperturbed classical problem. We therefore subtract the two problems, but weighted and then spatially averaged.

Multiply (2.13) by p_1', (2.14) by p', subtract the results and integrate over the volume of the tube to find

$$\int_0^L \left(p_1'\frac{\partial^2 p'}{\partial t^2} - p'\frac{\partial^2 p_1'}{\partial t^2}\right)S dx - \overline{a}^2\int_0^L \left(p_1'\frac{\partial^2 p'}{\partial x^2} - p'\frac{\partial^2 p_1'}{\partial x^2}\right)S dx = \frac{R}{C_v}\int_0^L p_1'\frac{\partial \dot{Q}'}{\partial t}S dx \tag{2.16}$$

Now integrate by parts the second integral on the left-hand side and use the boundary conditions (2.15) a,b:

$$\int_0^L \left(p_1' \frac{\partial^2 p'}{\partial x^2} - p' \frac{\partial^2 p_1'}{\partial x^2} \right) S dx = \int_0^L \frac{\partial}{\partial x} \left(p_1' \frac{\partial p'}{\partial x} - p' \frac{\partial p_1'}{\partial x} \right) S dx - \int_0^L \left(\frac{\partial p_1'}{\partial x} \frac{\partial p'}{\partial x} - \frac{\partial p'}{\partial x} \frac{\partial p_1'}{\partial x} \right) S dx$$

$$= \left[p_1' \frac{\partial p'}{\partial x} - p' \frac{\partial p_1'}{\partial x} \right]_0^L S - 0$$

$$= 0 \tag{2.17}$$

We handle the two terms in the first integral differently. Equation (2.14) is here the equation for steady waves, p_1' being given by (2.3), so

$$\frac{\partial^2 p_1'}{\partial t^2} = -\omega_1^2 P_1 \sin(\omega_1 t) \sin(k_1 x) = -\omega_1^2 p_1' \tag{2.18}$$

Because the heat transfer is assumed to be weak, we assume that its presence doesn't strongly affect the spatial distribution of the pressure fluctuation which we therefore take to be approximately $\sin k_1 x$. However, we seek the transient behavior of the actual pressure so we assume its amplitude $\overline{p}\eta_1(t)$ to vary in time and set

$$p' = \overline{p}\eta_1(t) \sin(k_1 x) \tag{2.19}$$

Substitution of (2.3), (2.18) and (2.19) in the first integral of equation (2.16) gives

$$\int_0^L P_1 \sin(\omega_1 t) \sin^2(k_1 x) \overline{p} \left(\ddot{\eta}_1 + \omega_1^2 \eta_1 \right) S dx \equiv P_1 \overline{p} \sin \omega_1 t \left(\ddot{\eta}_1 + \omega_1^2 \eta_1 \right) S \int_0^L \sin^2(k_1 x) dx \tag{2.20}$$

With (2.17) and (2.20), and (2.3) substituted in the right-hand side, equation (2.16) becomes

$$S \overline{p} P_1 \sin(\omega_1 t) \left(\ddot{\eta}_1 + \omega_1^2 \eta_1 \right) \int_0^L \sin^2(k_1 x) dx = \frac{R}{C_v} S P_1 \sin(\omega_1 t) \int_0^L \sin(k_1 x) \frac{\partial \dot{Q}'}{\partial t} dx$$

Hence the amplitude η_1 is governed by the equation for a forced harmonic oscillator having undamped natural frequency ω_1:

$$\frac{d^2 \eta_1}{dt^2} + \omega_1^2 \eta_1 = \frac{R/C_v}{E_1^2 \overline{p}} \int_0^L \sin(k_1 x) \frac{\partial \dot{Q}'}{\partial t} dx \tag{2.21}$$

where we have defined

$$E_1^2 = \int_0^L \sin^2(k_1 x) dx = \frac{L}{2} \tag{2.22}$$

Note that the dimensions of Q are the same as those of pressure, energy/volume; hence all terms in (2.27) have the dimensions $1/(\text{time})^2$.

Equation (2.21) shows in the clearest possible fashion the obstacle one necessarily must address in solving problems of combustion instabilities: the spatial distribution of the rate of change of power density must be specified. That is the essential problem of modeling the mechanism emphasized in Section 1 of these notes. Rather than construct an explicit model at this point, it is more instructive to deal with general features.

The quantity $\dot{Q}'$ is the fluctuation of the local rate at which energy is added to the flow by the source, here an electric heater. However, it is important to emphasize that, as (2.21) shows, the rate of change $\partial \dot{Q}'/\partial t$ is the source of waves. This property will appear very clearly below. Within the restricted representation we use here, a single mode, we have only two independent variables affecting the rate of heat addition, the local pressure and velocity. If we restrict ourselves to purely linear behavior, then whatever the physical process might be, we will necessarily find $\dot{Q}'$ to be a linear combination of the pressure and velocity fluctuations, possibly with time lags. Hence we assume the form valid only for linear behavior,

$$\dot{Q}' = Ap'(x, \ t - \tau_p) + Bu'(x, \ t - \tau_u) \tag{2.23}$$

where the constants A and B, and the time lags τ_p and τ_u are assumed known. Their values can be determined only by analyzing a detailed model of the process chosen. Because p' and u' are the actual pressure and velocity, not known until the complete problem is solved, assumptions are required to allow proceeding further.

The essential idea at this point is that the right-hand side of (2.21) is supposed to be small. Moreover, local errors in specifying the spatial distribution of $\dot{Q}'$ tend to be smoothed out by the spatial averaging. Hence make the assumption to be justified in the following sections, that p' and u' may be approximated by their classical acoustic forms found when $\dot{Q}' = 0$. Thus p' is given by (2.19) and u' by

$$u_1' = \frac{\dot{\eta}_1}{\gamma k_1} \cos k_1 x \tag{2.24}$$

The motivation for this choice may be seen upon substituting (2.19) and (2.24) in the acoustic momentum equation (2.12)a, giving the equation for η_1:

$$\ddot{\eta}_1 + \omega_1^2 \eta_1 = 0 \tag{2.25}$$

where $\omega_1 = \bar{a} k_1$. Hence simultaneous use of (2.19) and (2.24) implies that $\eta_1(t)$ is approximated by its unperturbed acoustic form, as required in the right-hand side of (2.21). We therefore assume

$$\dot{Q}' = A\bar{p}\eta_1(t - \tau_p) \sin k_1 x + \frac{B}{\gamma k_1^2} \dot{\eta}_1(t - \tau_u) \cos k_1 x \tag{2.26}$$

Finally, for an infinitesimally thin grid, $\dot{Q}'$ is non-zero only at the grid, so we multiply (2.26) by a delta function, giving

$$\dot{Q}' = \left[A\bar{p}\eta_1(t - \tau_p) \sin k_1 x + \frac{B}{\gamma k_1^2} \dot{\eta}_1(t - \tau_p) \cos k_1 x \right] \delta(x - l_g) \tag{2.27}$$

The time derivative of (2.26) is required in (2.21). Again within the approximations used here, we set $\ddot{\eta}_1$ equal to its classical acoustic value, $\omega_1^2 \eta_1$, from (2.28), and

$$\frac{\partial \dot{Q}'}{\partial t} = \left[A\bar{p} \frac{d}{dt}\eta_1(t - \tau_p) \sin k_1 x - \frac{B\omega_1^2}{\gamma k_1^2} \eta_1(t - \tau_u) \cos k_1 x \right] \delta(x - l_g) \tag{2.28}$$

Substitution in (2.21) and rearrangement gives

$$\frac{d^2}{dt^2}\eta_1(t) - \left[2A\frac{R/C_v}{\bar{p}L} \sin^2 k_1 l_g \right] \frac{d}{dt}\eta_1(t - \tau_p) + \omega_1^2 \left[\eta_1(t) + B\frac{R/C_v}{\bar{p}L} \sin 2k_1 l_g \eta_1(t - \tau_u) \right] = 0 \tag{2.29}$$

To investigate stability we assume the usual exponential dependence on time

$$\eta_1 = \text{const} \times e^{\lambda t} \tag{2.30}$$

with

$$\lambda = \alpha + i\omega \tag{2.31}$$

Substitution in (2.29) leads to a complex equation from which the formulas for the real and imaginary parts of λ are

$$\alpha = \frac{1}{2\omega} \left[Ce^{-\alpha\tau_p}(\omega \cos \omega_1 \tau_p - \alpha \sin \omega_1 \tau_p) + \omega_1^2 De^{-\alpha\tau_u} \cos \omega_1 \tau_u \right]$$
$$\omega^2 = \omega_1^2(1 + De^{-\alpha\tau_u} \cos \omega_1 \tau_u) - Ce^{-\alpha\tau_p}(\alpha \cos \omega_1 \tau_p - \omega \sin \omega_1 \tau_p) + \alpha^2 \tag{2.32}a,b$$

where

$$C = 2A\frac{R/C_v}{\bar{p}L} \sin^2 k_1 l_g \quad ; \qquad D = B\frac{R/C_v}{\bar{p}L} \sin 2k_1 l_g \tag{2.33}a,b$$

To gain a clearer idea of the meaning of these formulas, we make the following assumptions:

(i) $\alpha \ll \omega$, a consequence of the smallness of the right-hand side of (2.21), i.e. the heat addition to the waves is a small perturbation;

(ii) $\omega \approx \omega_1$ on the right-hand sides of (2.32)a,b, for the same reason;

(iii) $C = 0$; we assume that the influence of velocity on the heat transfer is more significant than that of the pressure.

Then after insertion of the definitions (2.33)a,b, we find

$$\frac{\alpha}{\omega_1} = B\frac{R/C_v}{2\bar{p}L}e^{-\alpha\tau_u}\cos\omega_1\tau_u\sin 2k_1l_g$$

$$\omega^2 = \omega_1^2\left(1 + B\frac{R/C_v}{2\bar{p}L}e^{-\alpha\tau_u}\sin^2 k_1l_g\right)$$

$$(2.34)\text{a,b}$$

For the heat addition to be *destabilizing*, $\alpha > 0$, which requires

$$0 < \omega_1\tau_u < \frac{\pi}{2}$$

$$0 < 2k_1l_g < \pi$$

$$(2.35)$$

With $k_1 = \pi/L$ and $\omega_1 = \bar{a}k_1 = \pi\bar{a}/L$ these inequalities become

$$0 < \tau_u < \frac{1}{2}\frac{L}{\bar{a}}$$

$$0 < l_g < \frac{L}{2}$$

$$(2.36)\text{a,b}$$

The first of (2.36)a,b shows that if the time lag between a velocity change and the heat transfer is too large, the process is actually stabilizing. More interesting is (2.36)a,b which shows that the heat source is destabilizing for $\tau_u < L/2\bar{a}$ only if the heating grid is located in the lower half of the tube. That is an important result confirmed by experimental observations.

In other words, this analysis has shown that the assumed model (2.27) for the heat addition in the Rijke tube correctly predicts a basic experimental observation. The general implication of this conclusion is that we can use a result obtained from global analysis of the dynamics of the system to infer certain general features of the mechanism of instabilities. This principle has consequences and applications far beyond the Rijke tube.

2.4. Nonlinear Behavior; Consequences of Rectification. No assumptions have been made about the source of energy, $\dot{Q}'$ appearing in (2.21). The analysis need not be restricted to the linear form (2.26). Probably the most obvious sort of nonlinear behavior arises when we suppose that for an electrically heated grid the dominant mechanism for energy addition to the flow is convective heat transfer, dependent chiefly on the velocity of the flow relative to heating element. On intuitive grounds we expect that the heat transfer rate depends on the magnitude and not the direction of the flow; then we may write

$$\dot{Q} = f(|\mathbf{u}|)$$

If we further assume that the bulk flow is essentially parallel to the axis, $\mathbf{u}$ has the single component u which can be considered as the sum of mean and fluctuating values. Hence the total and average heat transfer rates are

$$\dot{Q} = f(|\bar{u} + u'|) ; \qquad \bar{\dot{Q}} = f(|\bar{u}|)$$

and the fluctuation is $\dot{Q}' = \dot{Q} - \bar{\dot{Q}}$

$$\dot{Q}' = f(|\bar{u} + u'|) - f(|\bar{u}|)$$

$$(2.37)$$

The simplest form is $f(|v|) = K|u|$ and (2.37) is

$$\dot{Q}' = K\left[|\bar{u} + u'| - |\bar{u}|\right] = K\bar{u}\left[|1 + \frac{u'}{\bar{u}}| - 1\right] ,$$

$$(2.38)$$

the second equality holding because the mean value is always positive. Figure 2.5 shows the three sorts of behavior accompanying the three possibilities for the relative values of $|u'|$ and $\bar{u}$: $|u'| < \bar{u}$, $|u'| > \bar{u}$ and $\bar{u} = 0$.

The only point to be made here is very simple: for oscillations to occur with this mechanism, there must be a mean flow, a 'draft' through the tube. If $\bar{u} = 0$, $\dot{Q}'$ depends on $|u'|$, which is a rectified sinusoid for simple harmonic oscillations. But the frequency spectrum contains an average (DC) component and oscillations at twice the fundamental frequency, four times the fundamental, ... but nothing at the fundamental frequency.

Hence according to ((2.36)a,b), the fundamental mode cannot be excited—the integral on the right-hand side vanishes. Higher harmonics (the second, fourth, $\cdots$) are driven, but their attenuation is so large that they do not naturally occur in practice. This conclusion can be rendered quantitative by using (2.38) as the model for the energy source $\partial\dot{Q}'/\partial t$ in (2.21).

$$\bar{u}_g(1 + \chi \cos\omega_1 t)$$

$$\bar{u}_g\{|1 + \chi \cos\omega_1 t| - 1\}$$

(a) $\chi < 1$ (b) $\chi > 1$

$$\hat{u}_1 \cos\omega_1 t$$

$$|\hat{u}_1 \cos\omega_1 t|$$

(c) $\bar{u}_g = 0$ $(\chi = \infty)$
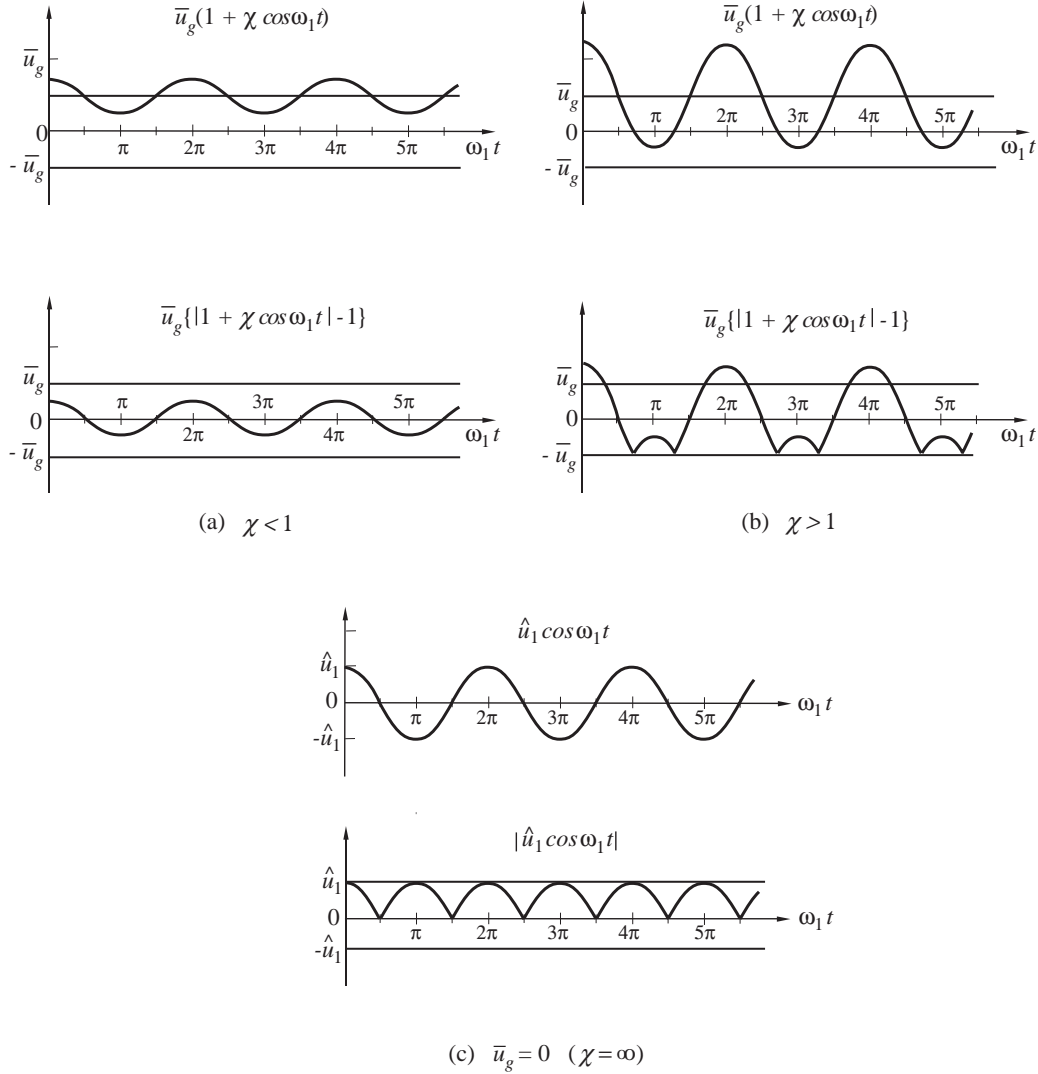
FIGURE 2.5. Graphs of $\dot{Q}'/K$, Equation (2.38).

The implication of this result—that a mean flow is necessary for a Rijke tube to be unstable—is that a horizontal tube will not oscillate. That is a characteristic easily observed. Simply tilt a vertical oscillating tube towards the horizontal. The amplitude of sound decreases as the tube is tipped, and vanishes before the tube is horizontal.

2.5. Active Control and the Source of Energy Addition. The Rijke tube is a particularly good example for illustrating the use of active control. Although the source of the oscillations is within the tube whose dynamics are the 'plant' to be controlled, that is, the combustion dynamics are intermingled with the combustor dynamics, we can distinguish the two dynamical systems and represent the complete system with the block diagram shown in Figure 1.1. We assume that the combustion dynamics depends on the unsteady pressure and velocity (actually the values at the grid) and therefore provides the feedback, thereby coupling the two dynamical systems.

For simplicity we assume here that the combustion dynamics depend only on the pressure fluctuation. It's a good approximation because the temperature and density fluctuation can be related to the pressure with time lag τ. Hence we write

$$\dot{Q}'(p') = Q_o p'(t - \tau) \tag{2.39}$$

It is more conventional in control of linear systems to construct block diagrams in the frequency domain. Begin with the equation (2.21) for the Rijke tube, with an external 'force' added—for example a loudspeaker—and with damping proportional to the rate of change of pressure, $2\alpha\frac{d\eta_1}{dt}$. We also allow the combustion process to be distributed so $\dot{Q}_o$ depends on x and is not restricted to a planar source of heat;

$$\frac{d^2\eta_1}{dt^2} + 2\alpha\frac{d\eta_1}{dt} + \omega_1^2\eta_1 = \frac{2}{\bar{p}L}\frac{R}{C_v}\int_o^L \sin k_1 x Q_o \frac{d\eta_1(t-\tau)}{dt}\sin k_1 x dx = 2\beta\frac{d\eta_1(t-\tau)}{dt} + f_e \qquad (2.40)$$

where

$$2\beta = \frac{R}{C_v}\frac{Q_o}{\bar{p}} \qquad (2.41)$$

Let $N(s)$ be the Laplace transform of $\eta_1(s)$. The Laplace transform of (2.40) then gives

$$N(s)\left[s^2 + 2\alpha s + \omega_1^2\right] = 2\beta s e^{-s\tau}N(s) + F_e(s) \qquad (2.42)$$

where $F_e(s)$ is the transform of $f_e(t)$.

The first term on the right-hand side represents feedback due to the combustion dynamics. Here, (2.40) can be interpreted with a block diagram, Figure 2.6. The block diagram can be solved for $N(s)$ as follows:

$$N(s) = \frac{1}{s^2 + 2\alpha s + \omega_1^2}\left[F_i(s) + F_e(s)\right]$$

$$= \frac{1}{s^2 + 2\alpha s + \omega_1^2}\left[2\beta s e^{-s\tau}N(s) + F_e(s)\right]$$

Hence

$$N(s) = \frac{\frac{1}{s^2+2\alpha s+\omega_1^2}F_e(s)}{1 + \frac{1}{s^2+2\alpha s+\omega_1^2}\left(-2\beta e^{-s\tau}\right)}$$

or

$$N(s) = \left[\frac{1}{s^2 + 2\left(\alpha - \beta e^{-s\tau}\right)s + \omega_1^2}\right]F_e(s) \qquad (2.43)$$

This of course is exactly the same as the solution to (2.42). Using a block diagram in this way, with the Laplace transform, is entirely equivalent to solving the differential equation (2.40) in conventional fashion.
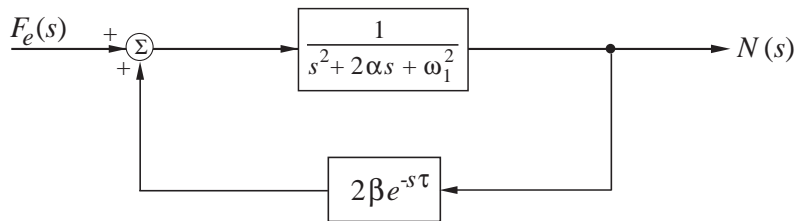
FIGURE 2.6. Block Diagram for an Uncontrolled Rijke Tube

Now define the transfer functions $G(s)$ for the *combustor dynamics* and $Q(s)$ for the *combustion dynamics*. Then (2.43) is

$$N(s) = \frac{G(s)}{1 - G(s)Q(s)}F_e(s) \qquad (2.44)$$

with

$$G(s) = \frac{1}{s^2 + 2\alpha s + \omega_1^2} \; ; \quad Q(s) = 2\beta s e^{-s\tau} \qquad (2.45)$$

According to (2.44), the output of the system, $N(s)$, is non-zero even if the external input F_e is vanishingly small if the numerator in (2.44) vanishes. That condition defines the boundary of linear stability:

$$1 - G(s)Q(s) = 0 \qquad (2.46)$$

The roots of this equation give the frequency and damping of the instability as a function of the parameters defining the system. After substitution of $G(s)$ and $Q(s)$, equation (2.46), gives

$$1 - \frac{2\beta s e^{-s\tau}}{s^2 + 2\alpha s + \omega_1^2} = 0$$

or

$$s^2 + 2\alpha s + \omega_1^2 - 2\beta s e^{-s\tau} = 0 \tag{2.47}$$

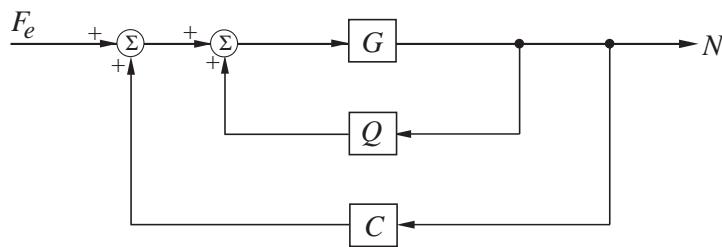If there is no heat addition, $\beta = 0$ [equation (2.41)] and s satisfies the second order equations $s^2 + 2\alpha s + \omega_1^2 = 0$, the usual result for a simple oscillator.

FIGURE 2.7. Block Diagram for a Rijke Tube with Feedback Control

Now suppose that a controller having dynamics $C(s)$ is added to the system in an outer feedback loop, as suggested in Figure 2.7. Instead of (2.44), the output $N(s)$ is related to the input $F_e(s)$ by

$$N(s) = \frac{G}{1 - G(Q + G)} F_e \tag{2.48}$$

Stability is now determined by the roots of the equation

$$1 - G(Q + C) = 0 \tag{2.49}$$

Thus the control can be used to alter the values of the roots. In particular, C can often be chosen so that all roots are stable—i.e. the system is stable—for realistic values of the defining parameters.

These results confirm analytically the intuitive result that the combustion dynamics, represented by $Q(s)$, equation (2.45), with β given by (2.41) are central in the problem of stability. Especially, the last result (2.49) shows that to design an effective control—i.e. assign $C(s)$—then the combustion dynamics $Q(s)$ must be known accurately. Knowing $Q(s)$ is just as important as knowing $G(s)$; the behavior of the combustion system is necessarily dependent on both the *combustion* dynamics and the *combustor* dynamics.

3. EQUATIONS FOR UNSTEADY MOTIONS IN COMBUSTION CHAMBERS

The examples described in Section 1, and many others, establish a firm basis for interpreting unsteady motions in a combustor in terms of acoustic modes of the chamber. That view has been formalized during the past fifty years and has led to the most widely used methods for analyzing combustor dynamics. In this section, we present the foundations of a particularly successful version of methods based on expansion in normal modes and spatial averaging. We assume familiarity with most of the required background in classical fluid dynamics and acoustics. Section 5 covers the principles and chief results of classical acoustics required as part of the foundation for understanding combustion instabilities. The discussions in this and the following sections are quite formal, intended to serve as the basis for a general framework within which unsteady motions, especially combustion instabilities, in all types of combustors may be treated. Analyses using *ad hoc* models will be covered when particular systems are considered, as in Section 2.

3.1. Modes of Wave Motion in a Compressible Medium. In this section, the term 'modes' refers not to natural motions or resonances of a chamber but rather to a *type* or class of motions in compressible flows generally. The brief discussion here is intended to address the question: how is it possible that apparently coherent nearly-classic acoustic waves exist in chambers containing highly turbulent non-uniform flow? It's a fundamentally important observation that such is the case. The explanation has been most thoroughly clarified by Chu and Kovasznay (1957), who elaborated and combined some results known for nearly a century. Their conclusions most significant for present purposes may be summarized as follows:

(1) Any small amplitude (linear) disturbance may be synthesized of three modes of propagation: *entropy waves* or 'spots', small regions having temperatures slightly different from the ambient temperature of the flow; *vortical* or *shear waves* characterized by nonuniform vorticity; and *acoustic waves.*

(2) In the linear approximation, *if the flow is uniform,* the three types of waves propagate independently, but may be coupled at boundaries (e.g. nozzles) or in combustion zones.

Entropy and vortical waves propagate with the mean flow speed ('convected') but acoustic waves propagate with their own speeds of sound. Moreover, in this linear limit, only acoustic waves carry disturbances of pressure. All three types of waves are accompanied by velocity fluctuations. If the flow is non-uniform or at finite amplitudes, the three modes become coupled. As a result, each of the waves then carries pressure, temperature and velocity fluctuations. Extension of the fundamental theory has not been accomplished completely (see Chu and Kovasznay). Some of the consequences of these types of modal coupling arise in the theory developed here, but much remains to be investigated. In particular, interactions between turbulence and an acoustic field is an important process represented by coupling of the basic linear modes of propagation.

3.2. Equations of Motion for a Reacting Flow. Combustion systems commonly contain condensed phases: liquid fuel or oxidizer, and combustion products including soot and condensed metal oxides. Hence the equations of motion must be written for two phases consisting of at least one species each. For investigating the dynamics of combustors, it is entirely adequate to represent each phase as its mass average over all member species. For a medium consisting of a multicomponent mixture of reacting gases and, for simplicity, a single liquid phase, it is a straightforward matter to construct a system of equations representing a single fluid. The procedure is summarized in Appendix A. As a result we can treat combustor dynamics under broad conditions as unsteady motions of a fluid having the mass-averaged properties of the actual medium.[2] The dimensional governing equations are (A.9)–(A.14)

---

[2]We now use $C_v, \gamma, R, \cdots$ to stand for the mass-averaged properties represented by bold-face symbols in Appendix A.

Conservation of Mass

$$\frac{\partial \rho}{\partial t} + \mathbf{u} \cdot \nabla \rho = -\rho \nabla \cdot \mathbf{u} + \mathcal{W} \tag{3.1}$$

Conservation of Momentum

$$\rho \left[\frac{\partial \mathbf{u}}{\partial t} + \mathbf{u} \cdot \nabla \mathbf{u} \right] = -\nabla p + \boldsymbol{\mathcal{F}} \tag{3.2}$$

Conservation of Energy

$$\rho C_v \left[\frac{\partial \mathbf{T}}{\partial t} + \mathbf{u} \cdot \nabla T \right] = -p \nabla \cdot \mathbf{u} + \mathcal{Q} \tag{3.3}$$

Equation for the Pressure

$$\frac{\partial p}{\partial t} + \mathbf{u} \cdot \nabla p = -\gamma p \nabla \cdot \mathbf{u} + \mathcal{P} \tag{3.4}$$

Equation for the Entropy

$$\rho \left[\frac{\partial s}{\partial t} + u \cdot \nabla s \right] = \frac{1}{T} \mathcal{S} \tag{3.5}$$

Equation of State

$$p = R\rho T \tag{3.6}$$

All definitions are given in Appendix A.

It is particularly important to realize that the source functions $\mathcal{W}$, $\boldsymbol{\mathcal{F}}$, $\mathcal{Q}$ and $\mathcal{P}$ contain all relevant processes in the systems to be analyzed here. They include, for example, the modeling and representations of the actions of actuation mechanisms used for active control. Eventually, the most difficult problems arising in this field are associated with modeling the physical processes dominant in the problems addressed.

Both for theoretical and computational purposes it is best to express the equations in dimensionless variables using the reference values:

$$L \ : \text{reference length}$$
$$\rho_r, p_r, T_r, a_r \ : \text{reference density, pressure, temperature and speed of sound}$$
$$C_{vr}, C_{pr}, R_r \ : \text{reference values of } C_v, C_p, R$$

Then define the dimensionless variables represented by $\mathbf{M}$ and the same symbols used for dimensional variables:

$$\mathbf{M} = \frac{\mathbf{u}}{a_r}; \quad \frac{\rho}{\rho_r} \to \rho; \quad \frac{p}{\rho_r a_r^2} \to p; \quad \frac{T}{T_r} \to T; \quad \frac{C_v}{C_{vr}} \to C_v, \text{ etc.}; \quad \frac{s}{C_{vr}} \to s$$

The dimensionless source functions are

$$\frac{L}{\rho_r a_r} \mathcal{W} \to \mathcal{W}; \quad \frac{L}{\rho_r a_r^2} \boldsymbol{\mathcal{F}} \to \boldsymbol{\mathcal{F}}; \quad \frac{L}{\rho_r a_r^3} \mathcal{Q} \to \mathcal{Q}; \quad \frac{L}{\rho_r a_r} \mathcal{P} \to \mathcal{P}; \quad \frac{\mathcal{S}}{\rho_r a_r C_{vr}} \to \mathcal{S}$$

Substitution of these definitions in equations (3.1)–(3.6) leads to the set of dimensionless equations for the single fluid model:

$$Mass: \qquad \frac{D\rho}{Dt} = -\rho \nabla \cdot \mathbf{M} + \mathcal{W} \tag{3.7}$$

$$Momentum: \qquad \rho \frac{D\mathbf{M}}{Dt} = -\nabla p + \boldsymbol{\mathcal{F}} \tag{3.8}$$

$$Energy: \qquad \rho C_v \frac{DT}{Dt} = -p \nabla \cdot \mathbf{M} + \mathcal{Q} \tag{3.9}$$

$$Pressure: \qquad \frac{Dp}{Dt} = -\gamma p \nabla \cdot \mathbf{M} + \mathcal{P} \tag{3.10}$$

$$Entropy: \qquad \rho \frac{Ds}{Dt} = \frac{1}{T} \mathcal{S} \tag{3.11}$$

$$State: \qquad p = \rho R T \tag{3.12}$$

and

$$\frac{D}{Dt} = \frac{\partial}{\partial t} + \mathbf{M} \cdot \nabla \tag{3.13}$$

We emphasize again that the source terms accommodate all relevant physical processes and can be interpreted to include the influences of actuation used in active control.

3.3. Two-Parameter Expansion of the Equations of Motion. The general equations (3.7)–(3.13) are written in the form suggestive of problems that are dominated by fluid mechanical processes, a tactic dictated by the observations described earlier. This point of view is the basis for the approach taken here to construct a general framework within which both practical and theoretical results can be obtained by following systematic procedures.

We are not concerned at this point with simulations or other methods relying essentially on some sort of numerical anaylsis and large scale computations. The nature of the problems we face suggests perturbation methods. If the source terms $\mathcal{W}$, ... were absent from (3.7)–(3.11), the homogeneous equations then represent nonlinear inviscid motions in a compressible fluid: Nonlinear acoustics in a medium without losses. One useful method for investigating such problems is based on expansion of the equations in a small parameter, ε, measuring the amplitude of the motion. Specifically, ε can be taken equal to M_r', a Mach number characteristic of the fluctuating flow, $\varepsilon := M_r'$.

The problems we are concerned with here are defined essentially by the non-zero functions $\mathcal{W}$, ... Because observed behavior seems to be dominated by features recognizable as 'acoustical', those sources which excite and sustain the actual motions must in some sense be small. They should therefore be characterized by at least one additional small parameter. It has become customary to select only one such parameter, $\mu := \bar{M}_r$, a Mach number $\bar{M}_r$ characterizing the mean flow, for the following reasons.[3]

Any operating combustion chamber contains an average steady flow produced by combustion of the fuel and oxidizer to generate products. The intensity of the flow, partly measurable by the Mach number, is therefore related to the intensity of combustion and both processes can in some sense be characterized by the same quantity, namely the Mach number of the average flow. Thus many of the processes represented in the source functions may be characterized by μ, in the sense that their influences become vanishingly small as $\mu \to 0$ and are absent when $\mu = 0$.

---

[3]We use the symbols ε and μ rather than M_r' and $\bar{M}_r$ to simplify writing.

It is important to understand that the two small parameters ε and μ have different physical origins. Consequently, they also participate differently in the formal perturbation procedures. Familiar nonlinear gas dynamical behavior is, in the present context, governed by the parameter ε; steepening of compressive waves is a notable example. In the expansion procedure worked out here, the term 'nonlinear behavior' refers to the consequences of terms higher order in ε.

On the other hand, the parameter μ characterizes perturbations of the gasdynamics due in the first instance to combustion processes and the mean flow. Terms of higher order in μ, but linear in ε, represent linear processes in this scheme. Failure to recognize this basic distinction between ε and μ can lead to incorrect applications of formal procedures such as the method of time-averaging. Instances of this point will arise as the analysis is developed.

3.3.1. *Expansion in Mean and Fluctuating Values.* There is no unique procedure for carrying out a two-parameter expansion. We begin here by writing all dependent variables as sums of mean ($\bar{\ }$) and fluctuating ($)'$ parts without regard to ordering

$$p = \bar{p} + p', \quad \mathbf{M} = \bar{\mathbf{M}} + \mathbf{M}', \dots, \quad \mathcal{W} = \bar{\mathcal{W}} = \mathcal{W}', \quad \boldsymbol{\mathcal{F}} = \bar{\boldsymbol{\mathcal{F}}} + \boldsymbol{\mathcal{F}}', \dots \tag{3.14}$$

We take the fluctuations of the primary flow variables (p', $\mathbf{M}'$, ρ', T', s') to be all of the same order in the amplitude ε of the unsteady motion. Generally, the source terms are complicated functions of the flow variables and therefore their fluctuations will contain terms of many orders in ε. For example, suppose $\mathcal{W} = kp^3$. Then setting $p = \bar{p} + p'$ and expanding, we have

$$\mathcal{W} = k(\bar{p} + p')^3 = k\left[\bar{p}^3 + 3\bar{p}^2 p' + 3\bar{p}p'^2 + p'^3\right]$$

Hence we define orders of the fluctuations of the source $\mathcal{W}$ and write

$$\mathcal{W} = \bar{\mathcal{W}} + \mathcal{W}'_1 + \mathcal{W}'_2 + \mathcal{W}'_3 + \mathcal{W}'_4 + \dots$$

where the subscript denotes the order with respect to the amplitude: Here, for the example $\mathcal{W} = kp^3$, $\mathcal{W}'_2 = (2k\bar{p})p'^2$. All source functions are written symbolically in the general form shown for ω, but modeling is required to give explicit formulas.

Most combustors contain flows of relatively low Mach number, say $\bar{\mathbf{M}} \lesssim 0.3$ or so. Thus we can assume that for a broad range of circumstances, processes depending on the square of $\bar{\mathbf{M}}$, i.e. of order μ^2, probably have small influences on the unsteady motions. We therefore neglect all terms of order μ^2 and higher in the equations. As a practical matter, the equations are greatly simplified with this assumption.

After substituting all variables split into sums of mean and fluctuating values, and collection of terms by orders, we can rewrite (3.7)–(3.13) as[4]

$$\left[\frac{D\bar{\rho}}{Dt} + \bar{\rho}\nabla \cdot \bar{\mathbf{M}} - \bar{\mathcal{W}}\right] + \left[\frac{\partial \rho'}{\partial t} + \bar{\rho}\nabla \cdot \mathbf{M}'\right] + \left[\bar{\mathbf{M}} \cdot \nabla\rho' + \rho'\nabla \cdot \bar{\mathbf{M}} + \mathbf{M}' \cdot \nabla\bar{\rho} + \nabla \cdot (\rho'\mathbf{M}')\right] - \mathcal{W}' = 0 \tag{3.15}$$

$$\left[\bar{\rho}\frac{D\bar{\mathbf{M}}}{Dt} + \nabla\bar{p} - \bar{\boldsymbol{\mathcal{F}}}\right] + \left[\bar{\rho}\frac{\partial\bar{\mathbf{M}}}{\partial t} + \nabla p'\right] + \left[\bar{\rho}\left(\bar{\mathbf{M}} \cdot \nabla\mathbf{M}' + \mathbf{M}' \cdot \nabla\bar{\mathbf{M}}\right) + \bar{\rho}\frac{\bar{D}\bar{\mathbf{M}}}{Dt}\right]$$
$$+ \left[\rho'\frac{\partial\mathbf{M}'}{\partial t} + \bar{\rho}\mathbf{M}' \cdot \nabla\mathbf{M}' + \rho'\left(\bar{\mathbf{M}} \cdot \nabla\mathbf{M}' + \mathbf{M}' \cdot \nabla\bar{\mathbf{M}}\right)\right] + [\rho'\mathbf{M}' \cdot \nabla\mathbf{M}'] - \boldsymbol{\mathcal{F}}' = 0 \tag{3.16}$$

---

[4]We do not include here terms $O(\bar{M}_r M_r'^2)$, i.e. first order in the mean flow and second order in fluctuations.

$$\left[\bar{\rho}C_v\frac{D\bar{T}}{Dt} + \bar{p}\nabla\cdot\bar{\mathbf{M}} - \bar{\Omega}\right] + C_v\left[\bar{\rho}\frac{\partial T'}{\partial t} + \bar{p}\nabla\cdot\mathbf{M}'\right] + \left[\bar{\rho}C_v\left(\bar{\mathbf{M}}\cdot\nabla T' + \mathbf{M}'\cdot\nabla\bar{T}\right) + C_v\rho'\frac{\bar{D}\bar{T}}{Dt} + p'\nabla\cdot\bar{\mathbf{M}}\right]$$
$$+ \left[C_v\bar{\rho}\frac{\partial T'}{\partial t} + C_v\rho'\left(\bar{\mathbf{M}}\cdot\nabla T' + \mathbf{M}'\cdot\nabla\bar{T}\right) + C_v\rho'\mathbf{M}'\cdot\nabla T' + p'\nabla\cdot\mathbf{M}'\right] + [C_v\bar{\rho}\mathbf{M}'\cdot\nabla T'] - \Omega' = 0 \tag{3.17}$$

$$\left[\frac{\partial\bar{p}}{\partial t} + \bar{\mathbf{M}}\cdot\nabla\bar{p} + \gamma\bar{p}\nabla\cdot\bar{\mathbf{M}} - \bar{\mathcal{P}}\right] + \left[\frac{\partial p'}{\partial t} + \gamma\bar{p}\nabla\cdot\mathbf{M}'\right] + \left[\bar{\mathbf{M}}\cdot\nabla p' + \mathbf{M}'\cdot\nabla\bar{p} + \gamma p'\nabla\cdot\bar{M}\right]$$
$$+ \left[\mathbf{M}'\cdot\nabla p' + \gamma p'\nabla\cdot\mathbf{M}'\right] - \mathcal{P}' = 0 \tag{3.18}$$

$$\left[\bar{\rho}\bar{T}\frac{\bar{D}\bar{s}}{Dt} - \bar{\mathcal{S}}\right] + \left[\bar{\rho}\bar{T}\frac{\partial s'}{\partial t}\right] + \left[\bar{\rho}\bar{\mathbf{M}}\cdot\nabla s' + \rho'\bar{T}\frac{\bar{D}\bar{s}}{Dt} + \bar{\rho}\bar{T}\mathbf{M}'\cdot\nabla\bar{s} + \bar{\rho}T'\bar{\mathbf{M}}\cdot\nabla\bar{s}\right]$$
$$+ \left[\rho'\bar{T}\frac{\bar{D}s'}{Dt} + \rho'T'\frac{\bar{D}\bar{s}}{Dt} + \rho'\bar{T}\mathbf{M}'\cdot\nabla\bar{s} + \bar{\rho}T'\mathbf{M}'\cdot\nabla\bar{s} + \bar{\rho}T'\frac{\partial s'}{\partial t}\right]$$
$$+ \left[\left(\bar{\rho}T' + \rho'\bar{T}\right)\mathbf{M}'\cdot\nabla s' + \rho'T'\left(\mathbf{M}'\cdot\nabla\bar{s} + \bar{\mathbf{M}}\cdot\nabla s'\right)\right]$$
$$+ [\rho'T'\mathbf{M}'\cdot\nabla s'] - \mathcal{S}' = 0 \tag{3.19}$$

$$\left[\bar{p} - R\bar{\rho}\bar{T}\right] + \left[p' - R\left(\bar{\rho}T' + \rho'\bar{T}\right)\right] + \left[-R\rho'T'\right] = 0 \tag{3.20}$$

where the convective derivative following the mean flow is

$$\frac{\bar{D}}{Dt} = \frac{\partial}{\partial t} + \bar{\mathbf{M}}\cdot\nabla \tag{3.21}$$

As a convenience in writing, it is useful to introduce some symbols defining groups of ordered terms. The set of equations (3.15)–(3.21) then become:

$$\left[\frac{\bar{D}\bar{\rho}}{Dt} + \bar{\rho}\nabla\cdot\bar{\mathbf{M}} - \bar{\mathcal{W}}\right] + \left(\frac{\partial\rho'}{\partial t} + \bar{\rho}\nabla\cdot M'\right) + \{[\rho]\}_1 + \{\rho\}_2 - \mathcal{W}' = 0 \tag{3.22}$$

$$\left[\bar{\rho}\frac{\bar{D}\bar{\mathbf{M}}}{Dt} + \nabla\bar{p} - \bar{\boldsymbol{\mathcal{F}}}\right] + \left(\bar{\rho}\frac{\partial\mathbf{M}'}{\partial t} + \nabla p'\right) + \{[\mathbf{M}]\}_1 + \{\mathbf{M}\}_2 + \{\mathbf{M}\}_3 - \boldsymbol{\mathcal{F}}' = 0 \tag{3.23}$$

$$\left[\bar{\rho}C_v\frac{\bar{D}\bar{T}}{Dt} + \bar{p}\nabla\cdot\bar{\mathbf{M}} - \bar{\Omega}\right] + \left(\bar{\rho}C_v\frac{\partial T'}{\partial t} + \bar{p}\nabla\cdot M'\right) + \{[T]\}_1 + \{T\}_2 + \{T\}_3 - \Omega' = 0 \tag{3.24}$$

$$\left[\frac{\bar{D}\bar{p}}{Dt} + \gamma\bar{p}\nabla\cdot\bar{\mathbf{M}} - \bar{\mathcal{P}}\right] + \left(\bar{\rho}C_v\frac{\partial P'}{\partial t} + \bar{p}\nabla\cdot M'\right) + \{[p]\}_1 + \{p\}_2 - \mathcal{P}' = 0 \tag{3.25}$$

$$\left[\bar{\rho}\frac{\bar{D}\bar{s}}{Dt} - \bar{\mathcal{S}}\right] + \left(\bar{\rho}\bar{T}\frac{\partial s'}{\partial t}\right) + \{[s]\}_1 + \{s\}_2 + \{s\}_3 + \{s\}_4 = 0 \tag{3.26}$$

$$\left[\bar{p} - R\bar{\rho}\bar{T}\right] + \{p - R\rho T\}_1 + \{R\rho'T'\}_2 = 0 \tag{3.27}$$

The definitions of the bracketted terms $\{\rho\}_1$, $\cdots$ etc. are given in Appendix A, Section A.2; the subscript $\{\ \}_n$ on the brackets identifies the orders of terms with respect to the fluctuations of flow variables, and the square brackets [ ] indicate that the terms are first order in the average Mach number. We have shown here

in each equation terms of the highest order fluctuations generated by the purely fluid mechanical contributions plus sources that must be expanded to orders appropriate to particular applications. Only the entropy equation produces terms of fourth order.

Time derivatives of quantities identified with the mean flow are retained to accommodate variations on a time scale long relative to the scale of the fluctuations. This generality is not normally required for treating combustion instabilities and unless otherwise stated, we will assume that all averaged quantities are independent of time.

3.3.2. *Equations for the Mean Flow.* At this point we have two choices. Commonly the assumption is made that the equations for the mean flow 'satisfy their own equations'. That implies that the square brackets [ ] in (3.22)–(3.27) vanish identically. With the time derivatives absent, the equations for the mean flow are:

$$\bar{\mathbf{M}} \cdot \nabla \bar{\rho} + \bar{\rho} \nabla \cdot \bar{\mathbf{M}} = \bar{\mathcal{W}} \tag{3.28}$$

$$\bar{\rho} \bar{\mathbf{M}} \cdot \nabla \bar{\mathbf{M}} + \nabla \bar{p} = \bar{\boldsymbol{\mathcal{F}}} \tag{3.29}$$

$$\bar{\rho} C_v \bar{\mathbf{M}} \cdot \nabla \bar{T} + \bar{p} \nabla \cdot \bar{\mathbf{M}} = \bar{\mathcal{Q}} \tag{3.30}$$

$$\bar{\mathbf{M}} \cdot \nabla \bar{p} + \gamma \bar{p} \nabla \cdot \bar{\mathbf{M}} = \bar{\mathcal{P}} \tag{3.31}$$

$$\bar{\rho} \bar{T} \bar{\mathbf{M}} \cdot \nabla \bar{s} = \bar{\mathcal{S}} \tag{3.32}$$

$$\bar{p} = R \bar{\rho} \bar{T} \tag{3.33}$$

This set of equations certainly applies when the average flow is strictly independent of time and there are no fluctuations. The time derivatives cannot be ignored when the flow variables change so slowly that the motion may be considered as 'quasi-steady' and fluctuations are still ignorable.

It is possible that when fluctuations are present, interactions among the flow variables cause transfer of mass, momentum and energy between the fluctuating and mean flows, generating time variations of the averaged variables. Then the appropriate equations are obtained by time-averaging (3.22)–(3.27) to give[5]

$$\frac{\bar{D} \bar{\rho}}{Dt} + \bar{\rho} \nabla \cdot \bar{\mathbf{M}} = \bar{\mathcal{W}} - \overline{\{[\rho]\}_1} - \overline{\{\rho\}_2} + \overline{\mathcal{W}'} \tag{3.34}$$

$$\bar{\rho} \frac{\bar{D} \bar{\mathbf{M}}}{Dt} + \nabla \bar{p} = \bar{\boldsymbol{\mathcal{F}}} - \overline{\{[\mathbf{M}]\}_1} - \overline{\{\mathbf{M}\}_2} - \overline{\{\mathbf{M}\}_3} + \overline{\boldsymbol{\mathcal{F}'}} \tag{3.35}$$

$$\bar{\rho} C_v \frac{\bar{D} \bar{T}}{Dt} + \bar{p} \nabla \cdot \bar{\mathbf{M}} = \bar{\mathcal{Q}} - \overline{\{[T]\}_1} - \overline{\{T\}_2} - \overline{\{T\}_3} + \bar{\mathcal{Q}}' \tag{3.36}$$

$$\frac{\bar{D} \bar{p}}{Dt} + \gamma \bar{p} \nabla \cdot \bar{\mathbf{M}} = \bar{\mathcal{P}} - \overline{\{p\}_1} - \overline{\{p\}_2} + \overline{\{p\}_3} \tag{3.37}$$

$$\bar{\rho} \bar{T} \frac{\bar{D} \bar{s}}{Dt} = \bar{\mathcal{S}} - \overline{\{s\}_1} - \overline{\{s\}_2} - \overline{\{s\}_3} - \overline{\{s\}_4} \tag{3.38}$$

$$\bar{p} = \mathbf{R} \bar{\rho} \bar{T} - \overline{\{\rho T\}_1} - \overline{\{\rho T\}_2} \tag{3.39}$$

---

[5] Note that the fluctuations of the source terms, $\mathcal{W}' \cdots$ etc., actually contain squares and higher order products of the dependent variables; hence their time averages will generally be non-zero.

If the mean flow is strictly independent of time, then time averages of all first-order brackets, $\overline{\{\ \ \}}_1$, must vanish. For generality we allow them to be nonzero. There seem to be no analyses in which their variations have been taken into account.

The two sets of equations governing the mean flow in the presence of unsteady motion define two distinct formulations of the general problem. In the first, equations (3.28)–(3.33), computation of the mean flow is uncoupled from that of the unsteady flow. Hence formally we are concerned with the stability and time evolution of disturbances superposed on a given, presumed known, mean flow unaffected by the unsteady motions. That is the setting for all investigations of combustion instabilities founded on the splitting of small flow variables into sums of mean and fluctuating values. This approach excludes, for example, possible influences of oscillations on the mean pressure in the chamber (often called 'DC shift'), not an unusual occurrence in solid propellant rockets. When they occur, DC shifts of this sort are almost always unacceptable in operational motors; they may or may not be significantly and directly affected by the fluctuations.

In contrast, the set (3.34)–(3.39) is strongly coupled to the fluctuating field. The situation is formally that producing the problem of 'closure' in the theory of turbulent flows (see, for example, Tennekes and Lumley, 1972). We will not explore the matter here, but we note only that the process of time averaging terms on the right-hand sides of the equations introduces functions of the fluctuations that are additional unknowns. Formal analysis then requires that those functions be modeled; perhaps the most familiar example in the theory of turbulence is the introduction of a 'mixing length' as part of the representation of stresses associated with turbulent motions.

Numerical simulations of combustion instabilities do not exhibit the problem of closure if the complete equations are used, avoiding the consequences of the assumption (3.14). Thus, for example, the results obtained by Baum and Levine (1982, 1988) do show time-dependence of the average pressure in examples of instabilities in solid rockets. Another possible cause of that behavior, probably more important in many cases, is nonlinear dependence of the burning rate on the pressure or velocity near the surface of a solid propellant rocket. Within the structure given here, that behavior may arise from time-averaged functions of p', $\mathbf{M}'$, ... contained in the boundary conditions, or from some nonlinear dependence such as $|\mathbf{M}'|$.

We use in these lectures the formulation assuming complete knowledge of the mean flow, given either by suitable modeling or by solution to the governing equations (3.28)–(3.33) or (3.34)–(3.39).

3.3.3. *Systems of Equations for the Fluctuations.* The general equations of motion (3.22)–(3.27) and those for the mean flow written in Section 3.3.1 contain a restriction only on the magnitude of the average Mach number. Such generality blocks progress with the analysis and for many applications is unnecessary. The set of equations (3.22)–(3.27) must be simplified to forms that can be solved to give useful results. Many possibilities exist. We follow here a course that previous experience has shown to be particularly fruitful for investigations of combustor dynamics. The choices of approximations and tactics are usually motivated by eventual applications and the type of analysis used.

First we assume that the mean flow is determined by its own system of equations; that is, we avoid the problem of closure and use the first formulation, equations (3.28)–(3.33), discussed in Section 3.3.1. Consequently, the mean flow is taken to be independent of time and the combinations in square brackets [ ], equations (3.22)–(3.27), vanish identically. Using the definitions of the remaining brackets,

$$\frac{\partial \rho'}{\partial t} + \bar{\rho} \nabla \cdot \mathbf{M}' = -\{[\rho]\}_1 - \{\rho\}_2 + \mathcal{W}' \tag{3.40}$$

$$\bar{\rho} \frac{\partial \mathbf{M}'}{\partial t} + \nabla p' = -\{[\mathbf{M}]\}_1 - \{\mathbf{M}\}_2 - \{\mathbf{M}\}_3 + \boldsymbol{\mathcal{F}}' \tag{3.41}$$

$$\bar{\rho} C_v \frac{\partial T'}{\partial t} + \bar{p} \nabla \cdot \mathbf{M}' = -\{[T]\}_1 - \{T\}_2 - \{T\}_3 + \mathcal{Q}' \tag{3.42}$$

$$\frac{\partial p'}{\partial t} + \gamma \bar{p} \nabla \cdot \mathbf{M}' = -\{[p]\}_1 - \{p\}_2 + \mathcal{P}' \tag{3.43}$$

$$\bar{\rho}\bar{T}\frac{\partial s'}{\partial t} = -\{[s]\}_1 - \{s\}_2 - \{s\}_3 - \{s\}_4 + \mathcal{S}' \tag{3.44}$$

The various brackets are defined in Section A.2 of Appendix A. They are formed to contain terms ordered with respect to both the mean Mach number and the amplitude of the fluctuations:

$$
\begin{aligned}
[\;\;] &: 1^{st} \text{ order in } \bar{\mathbf{M}}; \; 1^{st} \text{ order in } \mathbf{M}', \; O(\varepsilon) \\
\{\;\;\}_2 &: 0^{th} \text{ order in } \bar{\mathbf{M}}; \; 2^{nd} \text{ order in } \mathbf{M}', \; O(\varepsilon^2) \\
\{\;\;\}_3 &: 0^{th} \text{ order in } \bar{\mathbf{M}}; \; 3^{rd} \text{ order in } \mathbf{M}', \; O(\varepsilon^3) \\
\{\;\;\}_4 &: 0^{th} \text{ order in } \bar{\mathbf{M}}; \; 4^{th} \text{ order in } \mathbf{M}', \; O(\varepsilon^4)
\end{aligned} \tag{3.45}
$$

No terms have been dropped in passage from the set (3.22–(3.27) to the set (3.40)–(3.44), but fluctuations of the sources $\mathcal{W}', \cdots, \mathcal{S}'$ are not now classified into the various types defined by the brackets (3.45).

We have put the equations in the forms (3.40)–(3.44) to emphasize the point of view that we are considering classes of problems closely related to motions in classical acoustics. If the right-hand sides are ignored, (3.40)–(3.44) become the equations for linear acoustics of a uniform non-reacting medium at rest. The perturbations of that limiting class arise from three types of processes:

(i) interactions of the linear acoustic field with the mean flow, represented by the terms contained in the square brackets, $\{[\;\;]\}$;

(ii) nonlinear interactions between the fluctuations, represented by the curly brackets conveniently referred to as: $\{\;\;\}_2$, second order acoustics; $\{\;\;\}_3$, third order acoustics; and $\{\;\;\}_4$, fourth order acoustics;

(iii) sources associated with combustion processes, represented by the source terms $\mathcal{W}', \boldsymbol{\mathcal{F}}', \mathcal{Q}', \mathcal{P}'$ and $\mathcal{S}'$.

By selectively retaining one or more of these types of perturbations we define a hierarchy of problems of unsteady motions in combustors. We label these classes of problems O, I, II, III, IV according to the orders of terms retained in the right-hand side when the left-hand side comprise only the terms of order $\varepsilon := \mathbf{M}'_r$ defining clssical linear acoustics.

O. **Classical Acoustics**, $(\mu = 0, \varepsilon \to 0)$

Perturbations to first order in ε are retained in (3.40)–(3.44):

$$
\begin{aligned}
\frac{\partial \rho'}{\partial t} + \bar{\rho}\nabla \cdot \mathbf{M}' &= \mathcal{W}' \\
\bar{\rho}\frac{\partial \mathbf{M}'}{\partial t} + \nabla p' &= \boldsymbol{\mathcal{F}}' \\
\bar{\rho}C_v \frac{\partial T'}{\partial t} + \bar{p}\nabla \cdot \mathbf{M}' &= \mathcal{Q}' \\
\frac{\partial p'}{\partial t} + \gamma\bar{p}\nabla \cdot \mathbf{M}' &= \mathcal{P}' \\
\bar{\rho}\bar{T}\frac{\partial s'}{\partial t} &= \mathcal{S}'
\end{aligned} \tag{3.46 a-e}
$$

I. **Linear Stability**, $O(\varepsilon, \mu\varepsilon)$

Retain interactions linear in the average Mach number and in the fluctuations:

$$\frac{\partial \rho'}{\partial t} + \bar{\rho}\nabla \cdot \mathbf{M}' = -\{[\rho]\}_1 + \mathcal{W}'$$

$$\bar{\rho}\frac{\partial \mathbf{M}'}{\partial t} + \nabla p' = -\{[\mathbf{M}]\}_1 + \boldsymbol{\mathcal{F}}'$$

$$\bar{\rho}C_v\frac{\partial T'}{\partial t} + \bar{p}\nabla \cdot \mathbf{M}' = -\{[T]\}_1 + \mathcal{Q}' \qquad (3.47)\text{ a-e}$$

$$\frac{\partial p'}{\partial t} + \gamma\bar{p}\nabla \cdot \mathbf{M}' = -\{[p]\}_1 + \mathcal{P}'$$

$$\bar{\rho}\bar{T}\frac{\partial s'}{\partial t} = -\{[s]\}_1 + \mathcal{S}'$$

II. **Second Order Acoustics**, $O(\varepsilon, \mu\varepsilon, \varepsilon^2)$

Retain the linear interactions and the nonlinear second order acoustics:

$$\frac{\partial \rho'}{\partial t} + \bar{\rho}\nabla \cdot \mathbf{M}' = -[\{[\rho]\}_1 + \{\rho\}_2] + \mathcal{W}'$$

$$\bar{\rho}\frac{\partial \mathbf{M}'}{\partial t} + \nabla p' = -[\{[\mathbf{M}]\}_1 + \{\mathbf{M}\}_2] + \boldsymbol{\mathcal{F}}'$$

$$\bar{\rho}C_v\frac{\partial T'}{\partial t} + \bar{p}\nabla \cdot \mathbf{M}' = -[\{[T]\}_1 + \{T\}_2] + \mathcal{Q}' \qquad (3.48)\text{ a-e}$$

$$\frac{\partial p'}{\partial t} + \gamma\bar{p}\nabla \cdot \mathbf{M}' = -[\{[p]\}_1 + \{p\}_2] + \mathcal{P}'$$

$$\bar{\rho}\bar{T}\frac{\partial s'}{\partial t} = -[\{[s]\}_1 + \{s\}_2] + \mathcal{S}'$$

III. **Third Order Acoustics**, $O(\varepsilon, \mu\varepsilon, \varepsilon^2, \varepsilon^3)$

Retain the linear interactions and the nonlinear acoustics up to third order:

$$\frac{\partial \rho'}{\partial t} + \bar{\rho}\nabla \cdot \mathbf{M}' = -[\{[\rho]\}_1 + \{\rho\}_2] + \mathcal{W}'$$

$$\bar{\rho}\frac{\partial \mathbf{M}'}{\partial t} + \nabla p' = -[\{[\mathbf{M}]\}_1 + \{\mathbf{M}\}_2 + \{\mathbf{M}\}_3] + \boldsymbol{\mathcal{F}}'$$

$$\bar{\rho}C_v\frac{\partial T'}{\partial t} + \bar{p}\nabla \cdot \mathbf{M}' = -[\{[T]\}_1 + \{T\}_2 + \{T\}_3] + \mathcal{Q}' \qquad (3.49)\text{ a-e}$$

$$\frac{\partial p'}{\partial t} + \gamma\bar{p}\nabla \cdot \mathbf{M}' = -[\{[p]\}_1 + \{p\}_2] + \mathcal{P}'$$

$$\bar{\rho}\bar{T}\frac{\partial s'}{\partial t} = -[\{[s]\}_1 + \{s\}_2 + \{s\}_3] + \mathcal{S}'$$

Four other classes of problems possible to define in this context will not be considered here since no results have been reported: second order acoustics with mean flow interactions; fourth order acoustics; and third and fourth order acoustics with nonlinear acoustics/mean flow interactions.

In problems I–III, the source terms $\mathcal{W}', \cdots$ must be expanded to order consistent with the orders of the fluid-mechanical perturbations retained.

3.4. Nonlinear Wave Equations for the Pressure Field. Practically all of the subsequent material in this book will be either directly concerned with pressure waves, or with interpretations of behavior related pressure waves. The presence of unsteady vorticity causes important revisions of such a restricted point of view, as we have already mentioned in Section 3.1, but the basic ideas remain in any event. Hence the wave equation

for pressure fluctuations occupies a meaningful position in all five classes of problems defined in the preceding section. Its formation follows the same procedure used in classical acoustics.

Define $\mathcal{M}$ and $\mathcal{R}$ to contain all possible terms arising in the sets of equations constructed for the problems O–III:

$$\bar{\rho}\frac{\partial \mathbf{M}'}{\partial t} + \nabla p' = -\mathcal{M} + \mathbf{\mathcal{F}}' \tag{3.50}$$

$$\frac{\partial p'}{\partial t} + \gamma \bar{p}\nabla \cdot \mathbf{M}' = -\mathcal{R} + \mathcal{P}' \tag{3.51}$$

where

$$\mathcal{M} = \{[\mathbf{M}]\}_1 + \{\mathbf{M}\}_2 + +\{\mathbf{M}\}_3 \tag{3.52}$$

$$\mathcal{R} = \{[p]\}_1 + \{p\}_2 \tag{3.53}$$

Differentiate 3.50 with respect to time and substitute 3.50 for $\partial \mathbf{M}'/\partial t$:

$$\frac{\partial^2 p'}{\partial t^2} - \gamma \bar{p}\nabla \cdot \left[-\frac{1}{\bar{\rho}}\nabla p' - \frac{1}{\bar{\rho}}\left(\mathcal{M} - \mathbf{\mathcal{F}}'\right) \right] = -\frac{\partial \mathcal{R}}{\partial t} + \frac{\partial \mathcal{P}'}{\partial t}$$

Rearrange the equation to find

$$\nabla^2 p' - \frac{1}{\bar{a}^2}\frac{\partial^2 p'}{\partial t^2} = h \tag{3.54}$$

with

$$h = -\bar{\rho}\nabla \cdot \left[\frac{1}{\bar{\rho}}\left(\mathcal{M} - \mathbf{\mathcal{F}}'\right)\right] + \frac{1}{\bar{a}^2}\frac{\partial}{\partial t}(\mathcal{R} - \mathcal{P}') + \frac{1}{\bar{\rho}}\nabla\bar{\rho}\cdot\nabla p' \tag{3.55}$$

The boundary condition for the pressure field is found by taking the scalar product of the outward normal, at the chamber boundary, with:

$$\hat{\mathbf{n}} \cdot \nabla p' = -f \tag{3.56}$$

$$f = -\bar{\rho}\frac{\partial \mathbf{M}'}{\partial t} \cdot \hat{\mathbf{n}} + (\mathcal{M} - \mathbf{\mathcal{F}}') \cdot \hat{\mathbf{n}} \tag{3.57}$$

Replacing $\mathcal{M}$ and $\mathcal{R}$ by their definitions (3.52), we have the formulation based on the inhomogeneous nonlinear wave equation and its boundary condition:

$$\nabla^2 p' - \frac{1}{\bar{a}^2}\frac{\partial^2 p'}{\partial t^2} = h$$

$$\hat{\mathbf{n}} \cdot \nabla p' = -f \tag{3.57 a,b}$$

with

$$h = -\left[\bar{\rho}\nabla \cdot \frac{1}{\bar{\rho}}\{[\mathbf{M}]\}_1 - \frac{1}{\bar{a}^2}\frac{\partial\{[p]\}_1}{\partial t}\right] - \left\{\bar{\rho}\nabla \cdot \frac{1}{\bar{\rho}}\{\mathbf{M}\}_2 - \frac{1}{\bar{a}^2}\frac{\partial\{p\}_2}{\partial t}\right\} - \bar{\rho}\nabla \cdot \frac{1}{\bar{\rho}}\{\mathbf{M}\}_3$$

$$+ \frac{1}{\bar{\rho}}\nabla\bar{\rho}\cdot\nabla p' + \bar{\rho}\nabla \cdot \frac{1}{\bar{\rho}}\mathbf{\mathcal{F}}' - \frac{1}{\bar{a}^2}\frac{\partial\mathcal{P}'}{\partial t} \tag{3.58}$$

$$f = \bar{\rho}\frac{\partial \mathbf{M}'}{\partial t} \cdot \hat{\mathbf{n}} + \hat{\mathbf{n}} \cdot \left[\{[\mathbf{M}]\}_1 + \{\mathbf{M}\}_2 + \{\mathbf{M}\}_3\right] - \mathbf{\mathcal{F}}' \cdot \hat{\mathbf{n}} \tag{3.59}$$

With this formulation, the wave equations and boundary conditions for the classes of problems defined in Section 3.3 are distinguished by the following functions h and f:

O. **Classical Acoustics**

$$h_O = \bar\rho\nabla\cdot\frac{1}{\bar\rho}\boldsymbol{\mathcal{F}}' - \frac{1}{\bar{a}^2}\frac{\partial\mathcal{P}'}{\partial t}$$

$$f_O = \bar\rho\frac{\partial\mathbf{M}'}{\partial\mathbf{t}}\cdot\hat{\mathbf{n}} - \boldsymbol{\mathcal{F}}'\cdot\hat{\mathbf{n}}$$

(3.60) a,b

I. **Linear Stability**

$$h_I = -\left[\bar\rho\nabla\cdot\frac{1}{\bar\rho}\{[\mathbf{M}]\}_1 - \frac{1}{\bar{a}^2}\frac{\partial\{[p]\}_1}{\partial t}\right] + \frac{1}{\bar\rho}\nabla\bar\rho\cdot\nabla p' + \bar\rho\nabla\cdot\frac{1}{\bar\rho}\boldsymbol{\mathcal{F}}' - \frac{1}{\bar{a}^2}\frac{\partial\mathcal{P}'}{\partial t}$$

$$f_I = \bar\rho\frac{\partial\mathbf{M}'}{\partial t}\cdot\hat{\mathbf{n}} + \hat{\mathbf{n}}\cdot\{[\mathbf{M}]\}_1 - \boldsymbol{\mathcal{F}}'\cdot\hat{\mathbf{n}}$$

(3.61) a,b

Allowing $\boldsymbol{\mathcal{F}}'$ and $\mathcal{P}'$ to be non-zero gives the opportunity for representing sources of mass, momentum, and energy both within the volume and at the boundary. The first term in f_0 accounts for motion of the boundary.

II. **Second Order Acoustics**

$$h_{II} = -\left[\bar\rho\nabla\cdot\frac{1}{\bar\rho}\{[\mathbf{M}]\}_1 - \frac{1}{\bar{a}^2}\frac{\partial\{[p]\}_1}{\partial t}\right] - \left\{\bar\rho\nabla\cdot\frac{1}{\bar\rho}\{\mathbf{M}\}_2 - \frac{1}{\bar{a}^2}\frac{\partial\{p\}}{\partial t}\right\}$$

$$+ \frac{1}{\bar\rho}\nabla\rho'\cdot\nabla p' + \bar\rho\nabla\cdot\frac{1}{\bar\rho}\boldsymbol{\mathcal{F}}' - \frac{1}{\bar{a}^2}\frac{\partial\mathcal{P}'}{\partial t}$$

$$f_{II} = \bar\rho\frac{\partial\mathbf{M}'}{\partial t}\cdot\hat{\mathbf{n}} + \hat{\mathbf{n}}\cdot[\{[\mathbf{M}]\}_1 + \{\mathbf{M}\}_2] - \boldsymbol{\mathcal{F}}'\cdot\hat{\mathbf{n}}$$

(3.62) a,b

III. **Third Order Acoustics**

$$h_{III} = -\left[\bar\rho\nabla\cdot\frac{1}{\bar\rho}\{[\mathbf{M}]\}_1 - \frac{1}{\bar{a}^2}\frac{\partial\{[p]\}_1}{\partial t}\right] - \left\{\bar\rho\nabla\cdot\frac{1}{\bar\rho}\{\mathbf{M}\}_2 - \frac{1}{\bar{a}^2}\frac{\partial\{p\}_2}{\partial t}\right\}$$

$$- \bar\rho\nabla\cdot\frac{1}{\bar\rho}\{\mathbf{M}\}_3 + \frac{1}{\bar\rho}\nabla\bar\rho\cdot\nabla p' + \bar\rho\nabla\cdot\frac{1}{\bar\rho}\boldsymbol{\mathcal{F}}' - \frac{1}{\bar{a}^2}\frac{\partial\mathcal{P}'}{\partial t}$$

$$f_{III} = \bar\rho\frac{\partial\mathbf{M}'}{\partial t}\cdot\hat{\mathbf{n}} + \hat{\mathbf{n}}\cdot[\{[\mathbf{M}]\}_1 + \{\mathbf{M}\}_2 + \{\mathbf{M}\}_3] - \boldsymbol{\mathcal{F}}'\cdot\hat{\mathbf{n}}$$

(3.63) a,b

With these definitions of the functions h and f, the definitions of the four classes of problems considered here are complete, forming the basis for the analysis worked out in the remainder of these lectures. Only problems within classical acoustics can be solved easily. All others require approximations, both in modeling physical processes and in the method of solution. Modeling will be discussed in the contexts of specific applications; a few remarks help clarify the approximate method of solution described in the following section.

Remarks:

    i) The classes of problems I–III defined here are described by inhomogeneous equations that even for linear stability cannot be generally solved in closed form. The chief obstacles to solution arise because the functions h and f contain not only the unknown pressure but also the velocity and temperature. For given functions $\boldsymbol{\mathcal{F}}'$ and $\mathcal{P}'$, numerical solutions could be obtained for a specified combustor and mean flow field. The results would apply only to the special case considered. To obtain some understanding of general behavior it would be necessary to consider many special cases, a tedious and expensive procedure.

ii) Therefore, we choose to work out an approximate method of solution applicable to all classes of problems. Numerical solutions, or 'simulations' then serve the important purpose of assessing the validity and accuracy of the approximate results.

iii) The approximate method of solution is based first on spatial averaging, followed by an iteration procedure involving extension of the expansion in two small parameters defined in this section. This method has been most widely used and confirmed in applications to combustion instabilities in solid propellant rockets, but it can be applied to problems arising in any type of combustor.

iv) Instabilities in solid rockets have been particularly helpful in developing the general theory for at least three reasons: 1) the mean flow field, nonuniform and generated by mass addition at the boundary, requires careful attention to processes associated with interactions between the mean flow and unsteady motions; 2) more experimental results for transient behavior have been obtained for solid rockets than for any other combustion system; and 3) although still far from being satisfactorily understood, the dynamics of burning solid propellants is better known than for any other combustion system.

v) The fluctuations of the source terms, $\mathcal{W}'$, $\mathcal{F}'$, ... $\mathcal{S}'$ will be made explicit as required in particular applications.

4. MODAL EXPANSION AND SPATIAL AVERAGING;
AN ITERATIVE METHOD OF SOLUTION

From the point of view represented in Figure 1.1, we are concerned in this section with representing the combustor dynamics. The procedure, often called 'modeling' is based on the equations of motion constructed in the preceding section and hence in principle will contain all relevant physical processes[6]. For the purposes here, all modeling of combustor dynamics and of combustion dynamics—the mechanisms and feedback in Figure 1.1—must be done in the context developed in Section 1. Thus we always have in mind the idea of wave motions somehow generated and sustained by interactions between the motions themselves and combustion processes, the latter also including certain aspects of the mean flow within the combustor.

The simplest model of the combustion dynamics is a single wave, a classical acoustic resonance as in an organ pipe, but decaying or growing due to the other processes in the chamber. In practice, the combustion processes and nonlinear gasdynamical effects inevitably lead to the presence of more than one acoustic mode. We need a relatively simple yet accurate means of treating those phenomena for problems of the sort arising in the laboratory and in practice. Modeling in this case begins with construction of a suitable method for solving the nonlinear wave equations derived in Section 3.4. In this context we may regard the analysis of the Rijke tube covered in Section 2 as a basic example of the procedure stripped of the formalism covered in this section.

The chief purpose of the analysis constructed here is, to devise methods capable of producing results useful for prediction and interpretation of unsteady motions in full-scale combustion chambers as well as for laboratory devices. That intention places serious demands on the methods used for at least two reasons:

1. processes that must be modeled are usually complicated and their theoretical representations are necessarily approximate to extents which themselves are difficult to assess; and
2. almost all input data required for quantitative evaluation of theoretical results are characterized by large uncertainties.

In this situation it seems that for practical and, as it will turn out, for theoretical purposes as well, the most useful methods will be based on some sort of spatial averaging. Direct solution of the partial differential equations, even for linear problems, is practically a hopeless task except for very special cases for simple geometries. Direct numerical simulations (DNS) or numerical solutions to the partial differential equations are not yet a real alternative for practical purposes at this time, and are usually less attractive for obtaining basic understanding. However, as we will see later, numerical solutions offer the only means for assessing the validity of approximate solutions and always can treat more complicated (realistic?) problems than we can reasonably handle with the analytical methods discussed here. In any event, one should view theory and analysis on the one hand, and numerical simulations on the other, as complementary activities.

The material on analysis and theory of combustion instabilities treated in these two lectures is based on a method of spatial averaging. The essential idea is of course not new, the method being nearly identical with similar methods used in other branches of continuum mechanics. There are a few special characteristics associated with applications to combustor that will appear in the course of the following discussion.

4.1. Application of a Green's Function for Steady Waves. The method used later to analyze nonlinear behavior has its origins in an early analysis of linear combustion instabilities in liquid rocket engines (Culick, 1961, 1963). That work was based on solution to problems of steady waves by introducing a Green's function. It is an effective strategy for this application because departures from a known soluble problem are small, due either to perturbations within the volume or at the boundary, all of order μ in the context developed in Section 3.

---

[6] That seems to be what some people (notably electrical engineers it seems) mean by the term 'physics-based modeling.' What would otherwise be the basis for acceptable modeling of a physical system has not been explained.

The problem to be solved is defined by equation (3.54) and its boundary conditions (3.56) derived in Section 3.4,

$$\nabla^2 p' - \frac{1}{\bar{a}^2}\frac{\partial^2 p'}{\partial t^2} = h$$
$$\hat{\mathbf{n}} \cdot \nabla p' = -f$$
(4.1) a,b

with h and f given by (3.61) a,b for linear stability. Because h and f are linear, various methods are available to build general solutions by applying the principle of superposition to elementary solutions representing steady waves. Hence we assume that the fluctuating pressure field is a steady wave system within the given chamber, having unknown spatial structure and varying harmonically in time:

$$p' = \hat{p}e^{i\bar{a}kt}$$
(4.2)

where k is the complex wavenumber, also initially unknown,

$$k = \frac{1}{\bar{a}}(\omega - i\alpha)$$
(4.3)

As defined here, α positive means that the wave has growing amplitude, $p' \sim e^{\alpha t}$. Of course the wave is not strictly stationary, a condition existing only if $\alpha = 0$, certainly true when $h = f = 0$, as in classical acoustics.

Even when h, f are non-zero, it is still possible that $\alpha = 0$, now defining a state of *neutral stability*. In general one must expect $\alpha \neq 0$; it is a basic assumption in all of the analysis covered in this book that α is small compared with ω, so the waves are slowly growing or decaying—they are 'almost' stationary, and their spatial structure does not change much in time. However, the results obtained are quite robust and seem often to be usable even when α/ω is not small.

The problem here is to determine the spatial distribution $\hat{p}$ and the complex wavenumber k. For steady waves we can write

$$h = \kappa\hat{h}e^{i\bar{a}kt} \; ; \; f = \kappa\hat{f}e^{i\bar{a}kt}$$

where again κ is a small parameter[7] characterizing the smallness of h and f. Substitution in (4.1) a,b and dropping the common exponential time factor gives

$$\nabla^2 \hat{p} + k^2 \hat{p} = \kappa\hat{h}$$
$$\hat{\mathbf{n}} \cdot \nabla \hat{p} = -\kappa\hat{f}$$
(4.4) a,b

This is of course a well-known classical problem thoroughly discussed in many books. Many methods of solution are available for the linear problem. We use here a procedure based on introducing a Green's function discussed, for example, by Morse and Feshbach (1952, Chapter 10). This is an attractive method for several reasons, including:

1. Conversion from a differential equation, and the iterative method of solution this suggests, is an effective means for minimizing the consequences of the uncertainties inherent in problems of combustor dynamics;

2. Explicit results can be obtained for real and imaginary parts of the complex wavenumber in forms that are easily interpreted and remarkably convenient both for theoretical work and for applications;

3. The method has motivated a straightforward extension to nonlinear problems, with considerable success.

Define a Green's function satisfying the homogeneous boundary and the wave equation homogeneous except at the single point where a source is located having zero spatial extent and infinite strength such that is integral over space is finite. Thus the source is represented by a delta function $-\delta(\mathbf{r} - \mathbf{r}_0)$ and G is determined as a solution to the problem

$$\nabla^2 G(\mathbf{r}|\mathbf{r}_0) + k^2 G(\mathbf{r}|\mathbf{r}_0) = \delta(\mathbf{r} - \mathbf{r}_0)$$
$$\hat{\mathbf{n}} \cdot \nabla G(\mathbf{r}|\mathbf{r}_0) = 0$$
(4.5) a,b

---

[7]Later, κ will be identified with μ introduced in Section 3.3 but it is useful in this discussion to maintain a distinction.

The notation $\mathbf{r}|\mathbf{r}_0$ as the argument of $G(\mathbf{r}|\mathbf{r}_0)$ represents the interpretation of the Green's function as the wave observed at point $\mathbf{r}$ due to a steady oscillatory point source at $\mathbf{r}_0$.

Multiply ((4.4) a,b)a by $G(\mathbf{r}|\mathbf{r}_0)$, ((4.5) a,b)a by $\hat{p}(\mathbf{r})$, subtract the results and integrate over volume (in the present case the volume of the chamber) to find

$$\iiint_V \left[G(\mathbf{r}|\mathbf{r}_0)\nabla^2 \hat{p}(\mathbf{r}) - \hat{p}(\mathbf{r})\nabla^2 G(\mathbf{r}|\mathbf{r}_0) \right] dV + k^2 \iiint_V \left[G(\mathbf{r}|\mathbf{r}_0)\hat{p}(\mathbf{r}) - \hat{p}(\mathbf{r})G(\mathbf{r}|\mathbf{r}_0) \right] dV$$
$$= \kappa \iiint_V G(\mathbf{r}|\mathbf{r}_0)\hat{h}(\mathbf{r}) - \iiint \hat{p}(\mathbf{r})\delta(\mathbf{r} - \mathbf{r}_0)dV \tag{4.6}$$

Because $G(\mathbf{r}|\mathbf{r}_0)$ and $\hat{p}(\mathbf{r})$ are scalar functions the second integral on the right-hand side vanishes. The first integral is rewritten using a form of Green's theorem, and the basic property of the delta function is applied to the second integral on the right-hand side:

$$\iiint_V F(\mathbf{r})\delta(\mathbf{r} - \mathbf{r}_0)dV = F(\mathbf{r}) \qquad (\mathbf{r}_1, \mathbf{r}_0 \text{ in } V) \tag{4.7}$$

Hence (4.6) becomes

$$\oiint_S \left[G(\mathbf{r}|\mathbf{r}_0)\nabla \hat{p}(\mathbf{r}) - p(\mathbf{r})\nabla G(\mathbf{r}|\mathbf{r}_0) \right] \cdot \hat{\mathbf{n}}dS = \kappa \iiint_V G(\mathbf{r}|\mathbf{r}_0)\hat{h}(\mathbf{r})dV - \hat{p}(\mathbf{r}_0)$$

where $\hat{\mathbf{n}}$ is the outward normal at the surface of the volume V in question.

Now apply the boundary conditions (4.4) a,b and (4.5) a,b and the last equation can be written in the form

$$\mathbf{p}(\hat{r}_0) = \kappa \left\{ \oiint_V G(\mathbf{r}|\mathbf{r}_0)\hat{h}(\mathbf{r})dV + \iint_S G(\mathbf{r}_\mathbf{s}|\mathbf{r}_0)\hat{f}(\mathbf{r}_s)dS \right\} \tag{4.8}$$

Subscript $(\ )_s$ means the point $\mathbf{r}_s$ lies on the boundary surface (actually on the inside surface of the boundary). Because the operator for scalar waves is *self-adjoint* (see Morse and Feshbach 1952, Chapter 10), the Green's function possesses the property of symmetry

$$G(\mathbf{r}|\mathbf{r}_0) = G(\mathbf{r}_0|\mathbf{r}) \tag{4.9}$$

This property has the appealing physical interpretation that the wave observed at $\mathbf{r}$ due to a point source at $\mathbf{r}_0$ has the same amplitude and relative phase as for the wave observed at $\mathbf{r}_0$ when a point source is located at $\mathbf{r}$. With (4.9) we can interchange $\mathbf{r}$ and $\mathbf{r}_0$ in (4.8) to find for the steady field at position $\mathbf{r}$:

$$\hat{p}(\mathbf{r}) = \kappa \left\{ \iiint_V G(\mathbf{r}|\mathbf{r}_0)\hat{h}(\mathbf{r}_0)d\mathbf{V}_0 + \oiint_S G(\mathbf{r}|\mathbf{r}_{0s})\hat{f}(\mathbf{r}_{0s})dS \right\} \tag{4.10}$$

Equation (4.10) is not an explicit solution for the pressure field due to the source functions $\hat{h}$ and $\hat{f}$, but is rather, an integral equation because $\hat{h}$ and $\hat{f}$ in general depend on the fluctuating pressure and velocity fields themselves. However, because the sources are assumed to be small perturbations of the classical field having no sources, κ is small and $\hat{p}$ will not differ greatly from a solution to the homogeneous problem defined by $h = f = 0$. The result (4.10) represents the solution to the inhomogeneous problem; the complete solution is (4.10) plus a homogeneous solution. Advantage will be taken of the smallness of κ to find an approximate explicit solution for $\hat{p}$ by an iterative procedure discussed in Section 4.1.1.

Whatever tactic one may choose to follow, the result (4.10) is of no practical value without having a representation of $G(\mathbf{r}|\mathbf{r}_0)$. The most convenient form of $G(\mathbf{r}|\mathbf{r}_0)$ for our purpose is expansion in eigenfunctions $\psi_n(\mathbf{r})$, here the normal modes of the classical acoustics problem with no sources in the volume and homogeneous boundary conditions: $G(\mathbf{r}|\mathbf{r}_0)$ is therefore expressed as a *modal expansion*,

$$G(\mathbf{r}|\mathbf{r}_0) = \sum_{n=0}^{\infty} A_n \psi_n(\mathbf{r}) \tag{4.11}$$

where the ψ_n satisfy

$$\nabla^2\psi_n + k_n^2\psi_n = 0$$
$$\hat{\mathbf{n}}\cdot\nabla\psi_n = 0$$

$\qquad$ (4.12) a,b

and the ψ_n are orthogonal functions,

$$\iiint_V \psi_m(\mathbf{r})\psi_n(\mathbf{r})dV = E_n^2\delta_{mn}$$

(4.13)

Substitute (4.11) in ((4.5) a,b)a, multiply by $\psi_m(\mathbf{r})$ and integrate over the volume to find

$$\iiint_V \psi_m\sum_{n=0}^\infty A_n\nabla^2\psi_n dV + k^2\iiint_V \psi_m\sum_{n=0}^\infty A_n\psi_n dV = \int \psi_m(\mathbf{r})\delta(\mathbf{r}-\mathbf{r}_0)dV$$

With (4.7), ((4.12) a,b) and (4.13), this equation produces the formula for A_n:

$$A_n = \frac{\psi_n(\mathbf{r}_0)}{k_n^2 - k^2}$$

(4.14)

Thus the expansion (4.11) for $G(\mathbf{r}|\mathbf{r}_0)$ is

$$G(\mathbf{r}|\mathbf{r}_0) = \sum_{n=0}^\infty \frac{\psi_n(\mathbf{r})\psi_n(\mathbf{r}_0)}{E_n^2(k^2-k_n^2)}$$

(4.15)

the modal expansion of the Green's function. Substitution of (4.15) in (4.10) leads to the formal modal expansion of the pressure field,

$$\hat{p}(\mathbf{r}) = \kappa\sum_{n=0}^\infty \frac{\psi_n(\mathbf{r})}{E_n^2(k^2-k_n^2)}\left\{\iiint_V \psi_n(\mathbf{r}_0)\hat{h}(\mathbf{r}_0)dV_0 + \oiint_S \psi_n(\mathbf{r}_{0s})\hat{f}(\mathbf{r}_{0s})dS_0\right\}$$

(4.16)

Suppose that for κ tending to zero, $\hat{p}(\mathbf{r})$ approaches the unperturbed mode shape ψ_N; let the corresponding function $\hat{p}$ be denoted $\hat{p}_N$, so

$$\hat{p}\underset{\kappa\to 0}{\longrightarrow}\hat{p}_N = \psi_N$$

(4.17)

Now separate the Nth term from the sum in (4.16) and write

$$\hat{p}(\mathbf{r}) = \psi_N(\mathbf{r})\frac{\kappa}{E_N^2(k^2-k_N^2)}\left\{\iiint_V \psi_N(\mathbf{r}_0)\hat{h}(\mathbf{r}_0)dV_0 + \oiint_S \psi_N(\mathbf{r}_{0s})\hat{f}(\mathbf{r}_{0s})dS_0\right\}$$
$$+\kappa\sum_{n=0}^\infty{}' \frac{\psi_n(\mathbf{r})}{E_n^2(k^2-k_n^2)}\left\{\iiint_V \psi_n(\mathbf{r}_0)\hat{h}(\mathbf{r}_0)dV_0 + \oiint_S \psi_n(\mathbf{r}_{0s})\hat{f}(\mathbf{r}_{0s})dS_0\right\}$$

(4.18)

where the prime in the summation sign means that the term $n = N$ is missing. This form is consistent with the requirement (4.17) only if the factor multiplying $\psi_N(\mathbf{r})$ is unity, giving the formula for the perturbed wavenumber

$$k^2 = k_N^2 + \frac{\kappa}{E_N^2}\left\{\iiint_V \psi_N(\mathbf{r}_0)\hat{h}(\mathbf{r}_0)dV_0 + \oiint_S \psi_N(\mathbf{r}_{0s})\hat{f}(\mathbf{r}_{0s})dS_0\right\}$$

(4.19)

and (4.18) becomes

$$\hat{p}(\mathbf{r}) = \psi_N(\mathbf{r}) + \kappa\sum_{n=0}^\infty{}' \frac{\psi_n(\mathbf{r})}{E_n^2(k^2-k_n^2)}\left\{\iiint_V \psi_n(\mathbf{r}_0)\hat{h}(\mathbf{r}_0)dV_0 + \oiint_S \psi_n(\mathbf{r}_{0s})\hat{f}(\mathbf{r}_{0s})dS_0\right\}$$

(4.20)

$\qquad$ Another more direct derivation of (4.19) very useful in later analysis, may be had by first multiplying ((4.4) a,b)a by ψ_N and integrating over the volume:

$$\iiint_V \psi_N\nabla^2\hat{p}dV + k^2\iiint_V \psi_N\hat{p}dV = \kappa\iiint_V \psi_N\hat{h}dV$$

Application of Green's theorem to the first integral gives

$$\iiint\limits_V \hat{p}\nabla^2\psi_N dV + \oiint\limits_S [\psi_n\nabla\hat{p} - \hat{p}\nabla\psi_n]\cdot\hat{\mathbf{n}}dS + k^2\iiint\limits_V \psi_n\hat{p}dV = \oiiint\limits_S \psi_N\hat{h}dV$$

after inserting $\nabla^2\psi_N = -k_N^2\psi_N$ and $\nabla\psi_N\cdot\hat{\mathbf{n}} = 0$, rearrangement gives

$$k^2 = k_N^2 + \frac{\kappa}{\iiint\limits_V \psi_N\hat{p}dV}\left\{\iiint\limits_V \psi_N(\mathbf{r})\hat{h}(\mathbf{r})dV + \oiint\limits_S \psi_N(\mathbf{r}_s)\hat{f}(\mathbf{r}_s)dS\right\} \qquad (4.21)$$

The integral of $\psi_N\hat{p}$ in the denominator of (4.21) can be evaluated by using (4.20) and is exactly E_n^2, providing the series in (4.20) converges. Hence (4.21) is identical to (4.19). This simple calculation has shown that (4.19) and (4.20) are consistent.

The preceding calculation contains several basic ideas behind much of the analysis used in these lectures. In summary, the original problem described by the differential equation ((4.4) a,b)a and its boundary condition ((4.4) a,b)b are converted to an integral equation, in this case (4.10), established by introducing a Green's function. This is not an explicit solution because the functions h and f generally depend on the dependent variable $\hat{p}$. However, formulation as an integral equation forms a convenient basis for approximate solution by iteration.

4.1.1. *Approximate Solution by Iteration.* To apply an iterative procedure, it is necessary first to give the Green's function $G(\mathbf{r}|\mathbf{r}_0)$ explicit form. The natural choice for problems of waves in a chamber is a series expansion in the natural modes of the chamber, a modal expansion, (4.15). For the small parameter κ tending to zero (i.e. all perturbations of the classical acoustics problem are small), a straightforward argument produces the formula (4.19) for the wavenumber and the integral equation (4.20) for $\hat{p}(\mathbf{r})$.

Equation (4.20) must be solved to give $\hat{p}$ before the wavenumber can be computed with (4.19). We should emphasize that for many practical purposes, it is really k that is required, because its imaginary part determines the linear stability of the system ($\alpha = 0$). The great advantage of this approach may be seen clearly with a simple example. Suppose $\hat{f} = 0$ and $\hat{h} = K(1 + \hat{p})$ in (4.4) a,b. Then (4.20) and (4.19) become

$$\hat{p}(\mathbf{r}) = \psi_N(\mathbf{r}) + \kappa K\sum_{n=0}^{\infty}{}' \frac{\psi_n(\mathbf{r})}{E_n^2(k^2 - k_n^2)}\iiint\limits_V \psi_n(\mathbf{r}_0)(1 + \hat{p})dV_0 \qquad (4.22)$$

$$k^2 = k_N^2 + \frac{\kappa K}{E_N^2}\iiint\limits_V \psi_N(1 + \hat{p})dV_0 \qquad (4.23)$$

Because κ is assumed to be small, solution by successive approximation, i.e. an iterative procedure, is a logical way to proceed. The initial (zeroth) approximation to the mode shape $\hat{p}$ is (4.22) for $\kappa = 0$, $\hat{p}^{(0)} = \psi_N$. Substitution in (4.23) gives k^2 correct to first order in κ:

$$\begin{aligned}(k^2)^{(1)} &= k_N^2 + \frac{\kappa K}{E_N^2}\iiint\limits_V \psi_N(1 + \psi_N)dV_0 \\ &= k_N^2 + \kappa\frac{KI_N}{E_N^2}\end{aligned} \qquad (4.24)$$

where I_N stands for the integral.

Calculation of $\hat{p}$ to first order in κ requires setting $\hat{p}$ and k^2 to their *zeroth* order values on the right-hand side of (4.22), $\hat{p}^{(0)} = \psi_N$, $(k^2)^{(0)} = k_N^2$:

$$\begin{aligned}\hat{p}^{(1)}(\mathbf{r}) &= \psi_N(\mathbf{r}) + \kappa K\sum_{n=0}^{\infty}{}' \frac{\psi_n(\mathbf{r})}{E_n^2(k_N^2 - k_n^2)}\iiint\limits_V \psi_n(\mathbf{r}_0)(1 + \psi_N(\mathbf{r}_0))dV_0 \\ &= \psi_N + \kappa\sigma_N\end{aligned}$$

Substitution of this formula for $\hat{p}$ under the integral in (4.23) then gives the second approximation $(k^2)^{(2)}$ to k^2:

$$
\begin{aligned}
(k^2)^{(2)} &= k_N^2 + \frac{\kappa K}{E_N^2} \iiint\limits_V \psi_N (1 + \psi_N + \kappa \sigma_N) dV_0 \\
&= (k^2)^{(1)} + \kappa^2 \frac{K}{E_N^2} \iiint\limits_V \psi_N \sigma_N dV_0
\end{aligned}
\tag{4.25}
$$

A wonderful property of the procedure is already apparent: Calculation of the wavenumber to some order l in the small parameter requires knowing the modal functions only to order $l-1$. That is the basis for the current standard practice of computing linear stability for solid propellant rockets (the Standard Stability Prediction Program, Nickerson *et al.* 1983) using the unperturbed acoustic modes computed for the geometry in question.

The "perturbation-iteration" procedure just described is an old and widely used method to obtain solutions to nonlinear as well as linear problems. Often much attention is paid to achieving more accurate solutions by carrying the iterations to higher order in the small parameter. That is a legitimate process providing the equations themselves are valid to the order sought. In Section 3 we emphasized the importance of the expansion procedure largely for that reason. If the equations are valid, say, only to second order in the amplitude (ε), there is no need—in fact no justification—to try to find a solution to order ε^3 and higher. Similar remarks apply to the expansion in the average Mach number (μ). The procedure is fully explained in Section 4.5 for the equations derived in Section 3.4.

4.2. An Alternative Derivation of the First Order Formula. The results (4.19) and (4.21) for the complex wavenumber and mode shape can be constructively obtained in a different way. Both formulas provide means for computing the differences $k^2 - k_N^2$ and $\hat{p} - \psi_N$ between the actual (perturbed) quantities and the unperturbed quantities. It is reasonable that those results should somehow follow from comparison of the perturbed ($\kappa \neq 0$) and unperturbed ($\kappa = 0$) problems. The idea is to average the difference between the two problems weighted respectively by the other's mode shape. That is, subtract $\hat{p}$ times equation ((4.12) a,b)a from ψ_n times ((4.4) a,b)a and integrate the result over the volume of the chamber:

$$
\iiint\limits_V \left[\psi_N \nabla^2 \hat{p} - \hat{p} \nabla^2 \psi_N \right] dV + \iiint\limits_V (k^2 - k_N^2) \psi_n \hat{p} dV_0 = \kappa \iiint\limits_V \psi_N \hat{h} dV
$$

Now apply Green's theorem to the first integral, substitute the boundary conditions ((4.4) a,b)b and ((4.12) a,b)b and rearrange the result to find (4.21):

$$
k^2 = k_N^2 + \frac{\kappa}{\iiint\limits_V \psi_N \hat{p} dV} \left\{ \iiint\limits_V \psi_N(\mathbf{r}) \hat{h}(\mathbf{r}) dV + \oiint\limits_S \psi_N(\mathbf{r}_s) \hat{f}(\mathbf{r}_s) dS \right\}
\tag{4.26}
$$

If k^2 is to be calculated to first order in κ, then $\hat{p}$ must be replaced by its zero order approximation $\hat{p} = \psi_N$. Because the correction to k_N^2 contains the multiplier κ, any contributions of order κ multiplying κ give terms of order κ^2. Hence to first order, (4.26) of course becomes (4.19).

This approach does not provide a recipe for computing the modal or basis functions to higher order. That does not cause difficulty here because we have the procedure given in the preceding section. We will find later that the simple derivation just given suggests a useful extension to time-dependent nonlinear problems. In that situation there is no result corresponding to (4.20) for computing the mode shapes to higher order. That deficiency is a serious obstacle to further progress, a subject of current research.

4.3. Approximate Solution for Unsteady Nonlinear Motions. The method covered in the preceding two sections, based essentially in the use of Green's functions, was the first application of modal expansions and spatial averaging to combustion instabilities (Culick 1961, 1963). In the early 1970's the procedure was extended

to treat nonlinear problems, necessarily involving time-dependence (Culick 1971, 1975). We summarize that approach here.[8]

We begin with the general problem (4.1) a,b and assume an approximation $\tilde{p}'(\mathbf{r})$ to the pressure field as a truncated expansion in a set of basis functions ψ_m,

$$\tilde{p}'(\mathbf{r}, t) = \bar{p}_r \sum_{m=0}^{M} \eta_m(t)\psi_m(\mathbf{r}) \tag{4.27}$$

In this work we will always take the ψ_m to be acoustic modes defined by the geometry, the distribution of average temperature and suitable boundary conditions.[9] We would like the right-hand side of (4.27) to become more nearly equal to the actual pressure field in the combustor as more terms are included in the series, so that $\tilde{p}' \equiv p'$ in the limit:

$$\lim_{M \to \infty} \tilde{p}(\mathbf{r}; t) = \lim_{M \to \infty} \sum_{m=0}^{M} \eta_m(t)\psi_m(\mathbf{r}) \tag{4.28}$$

Because the ψ_m do not satisfy the correct boundary conditions, this pointwise property certainly cannot be satisfied at the boundary. It is reasonable, however, to expect convergence in integral-squared sense; that is the integral of the square of the difference between the exact solution and (4.27) satisfies

$$\lim_{M \to \infty} \iiint \left[p'(\mathbf{r}, t) - \bar{p}_r \sum_{m=0}^{M} \eta_m(t)\psi_m(\mathbf{r}) \right]^2 dV = 0 \tag{4.29}$$

We will not prove this properly, but assume its truth.

Convergence in the sense asserted by (4.29) is a common idea arising, for example, in formal treatments of Sturm-Liouville problems; see Hildebrand 1952 for a very readable discussion. The matter of convergence of approximate solutions in the present context is more complicated because one must take into account the fact that the governing equations and their solutions are expanded in the two small parameters μ and ε introduced in Section 3. We will also not discuss that problem.

The synthesis of the pressure field expressed by (4.27) does not restrict in any practical fashion the generality of the method. For definitions here we assume that the modal functions satisfy the homogeneous Neumann condition $\hat{\mathbf{n}} \cdot \nabla \psi_n = 0$, but for some applications a different boundary condition, perhaps over only part of the boundary, may serve better. Hence we will assume here that the ψ_n are eigensolutions to the problem (4.12) a,b.

We require that the approximation (4.27) to p' satisfy equation (4.1) a,b. Multiply (4.12) a,b written for ψ_N by $\tilde{p}'(\mathbf{r}, t)$, subtract from (4.1) a,b written for $\tilde{p}'$ multiplied by ψ_N; and integrate the difference over the volume of the chamber to give

$$\iiint_V \left[\psi_N \nabla^2 \tilde{p}' - \tilde{p}' \nabla^2 \psi_N \right] dV - \iiint_V \frac{1}{\bar{a}^2} \frac{\partial^2 \tilde{p}'}{\partial t^2} dV - k_N^2 \iiint_V \tilde{p}' \psi_N dV = \iiint_V \psi_N h dV$$

[8]An alternative form based on an form of Galerkin's method, extended to accommodate the sorts of problems arising in the present context, was introduced first by Zinn and his students. That procedure and the present method give identical equations before the expansion procedure is applied and further approximations are used. The applicability of that method seems to have been blunted in some cases by use of a velocity potential, thereby requiring that the unsteady field be irrotational. It seems also that the ordering procedure (in terms of the small parameters $\bar{M}_r$ and $\bar{M}_r'$) (i.e. μ and ε) has not been followed consistently, causing confusion in some derivations and conclusions. Those matters are discussed elsewhere. It seems likely that the extended form of Galerkin's method could give the same (or nearly so) results as found by the method discussed here, but the early works were not pursued further. There is no basis for comparison.

[9]The selection of boundary conditions is part of the art of applying this method. Examples covered later will clarify the point. For the present, it is helpful to think of the ψ_m as classical acoustic modes for a volume having rigid walls and the same shape as the combustion chamber in question. The ψ_m therefore do not satisfy exactly the boundary conditions actually existing in a combustor. Hence the right-hand side of (4.27) is an approximation in two respects: the series is truncated to a finite number of terms and it does not satisfy the correct boundary conditions. However, the solution carried out to the next order *does* satisfy the boundary conditions to first order. This important point is discussed in Chapter 10 of Morse and Feshbach (1952). The approximate nature of the modal expansion will be clarified as the analysis proceeds.

Apply Green's theorem to the first integral, substitute the boundary conditions (4.1) a,b and (4.12) a,b and rearrange the result to give

$$\iiint\limits_{V} \frac{1}{\bar{a}^2} \frac{\partial^2 \tilde{p}'}{\partial t^2} \psi_N dV + k_N^2 \iiint\limits_{V} \tilde{p}' \psi_N dV = - \left\{ \iiint\limits_{V} h \psi_N dV + \oiint\limits_{S} f \psi_N dS \right\} \tag{4.30}$$

Now substitute the modal expansion (4.27) in the right-hand side:

$$\frac{\bar{p}_r}{\bar{a}_r^2} \sum_{m=0}^{M} \ddot{\eta}_m(t) \iiint\limits_{V} \left(\frac{\bar{a}_r}{\bar{a}}\right)^2 \psi_m \psi_N dV - k_n^2 \bar{p}_r \sum_{m=0}^{M} \eta_m \iiint\limits_{V} \psi_m \psi_N dV = E_N^2 \frac{\bar{p}_r}{\bar{a}_r^2} F_N \tag{4.31}$$

where

$$F_N = -\frac{\bar{a}_r^2}{\bar{p}_r E_N^2} \left\{ \iiint\limits_{V} h \psi_N dV + \oiint\limits_{S} f \psi_N dS \right\} \tag{4.32}$$

and $\bar{a}_r$ is a constant reference speed of sound. The second sum reduces, due to the orthogonality of the ψ_m, to $\eta_n E_n^2$. Under the first integrals, write

$$\Delta_a = 1 - \left(\frac{\bar{a}_r}{\bar{a}}\right)^2 \tag{4.33}$$

Then the first sum in (4.31) is

$$\sum_{m=0}^{M} \ddot{\eta}_m(t) \iiint\limits_{V} (1 - \Delta_a) \psi_m \psi_N dV = E_N^2 \ddot{\eta}_N - \sum_{m=0}^{M} \ddot{\eta}_m(t) \iiint\limits_{V} \Delta_a \psi_m \psi_N dV \tag{4.34}$$

With these changes, equation (4.31) becomes

$$\ddot{\eta}_N + \omega_N^2 \eta_N = F_N + \frac{1}{E_N^2} \sum_{m=0}^{M} \ddot{\eta}_m(t) \iiint\limits_{V} \Delta_a \psi_m \psi_N dV \tag{4.35}$$

The sum on the right-hand side represents part of the effect of a non-uniform speed of sound in the chamber (if $\Delta_a \neq 0$). To simplify writing we will ignore this term until we consider special problems in later chapters. For solid rockets it is a negligible contribution. If the combustor contains flame sheets, the temperature is piecewise uniform and this term also doesn't appear, but the presence of the discontinuities generates corresponding terms arising from F_N. Thus there are useful situations in which we deal with the system of equations:

$$\ddot{\eta}_N + \omega_N^2 \eta_N = F_N \tag{4.36}$$

This result, a set of coupled nonlinear equations with the forcing function F_N given by (4.34), is the basis for practically all of the analysis and theory discussed in the remainder of this book. A corresponding result is given in Appendix B for a purely one-dimensional formulation. In anticipation of later discussions, several general remarks are in order.

(i) The formulation expressed by (4.36) accommodates all relevant physical processes. In the derivation of the conservation equations in Appendix A, only inconsequential approximations were made, notably the neglect of multi-component diffusion and the representation of the reacting multi-phase medium by a single-fluid model. However, only the basic gasdynamics are known explicitly. All other processes must be modeled in suitable forms.

(ii) Despite the apparent generality of (4.36) attention must be paid to an assumption implied in the application of Green's theorem in spatial averaging. That is, the functions involved must possess certain properties of continuity within the volume of averaging. The condition is not satisfied, for example, at a flame sheet, where the velocity is discontinuous, an important exception.

(iii) The selection of functions for the modal expansion (4.27) is not unique; possible alternatives must always be considered. What works best depends on the nature of the boundary conditions. The closer the boundary is to a rigid reflecting surface, the more effective is the choice $\hat{\mathbf{n}} \cdot \nabla \psi_N = 0$, meaning that the acoustic velocity vanishes on the boundary. Because a

combustor must provide for inflow of reactants and exhaust of products, it is simply not possible that the actual enclosure be everywhere rigid and perfectly reflecting. For $\hat{\mathbf{n}} \cdot \nabla \psi_N = 0$ to be a good approximation, as it should be for the modal expansion to serve successfully as a zeroth approximation to the pressure field, the boundary must be 'nearly' reflecting. Choked inlets and outlets satisfy the condition if the Mach number at the chamber side is small (that is, the flow within the volume is consistent with the assumption $\mu \ll 1$). Also, the dynamical response of burning solid propellants is normally such that requiring $\hat{\mathbf{n}} \cdot \nabla \psi_N = 0$ is a good choice. Hence, over a broad useful range of practical conditions, defining the modal expansion functions with (4.12) a,b is a reasonable choice. Exceptions are not rare, however, and care must be exercised. For example, a Rijke tube (Section 2) will contain a heater, or a thin combustion region within the duct. Continuous functions ψ_N may not be good zeroth approximations to the actual behavior discontinuous at the heating zone; moreover, in that case $\hat{\mathbf{n}} \cdot \nabla \psi_N = 0$ at the ends is the proper choice for boundary conditions on the modal functions. More generally, if the temperature field is highly non-uniform, then the zeroth order expansion functions should take that feature into account.

(iv) An enormous advantage of the result (4.36) is its clear interpretation. A general unsteady motion in a combustor is represented by the time-evolution of a system of coupled nonlinear oscillators in one-to-one correspondence with the modes ψ_N. Although the left-hand side of (4.36) describes the motion of a linear oscillator, the forcing function F_N will in general contain terms in η_N representing linear and nonlinear damping, springiness and inertia. Consequently, as we will see, it is easy to find familiar nonlinear differential equations as special cases of (4.36). Such special results aid greatly interpretation of complicated observed behavior in terms of simpler elementary motions. Thus it is important to understand the connections between parameter defining the oscillators, the characteristics of the modes, and the definitions provided in the process of spatial averaging.

(v) Different problems are distinguished chiefly in two respects: Geometry of the combustor; and the form of the forcing function F_N. The forcing function contains the influences of gasdynamics explicitly, but all other processes must be modeled, either with theory or based on experimental results. The geometry and the boundary conditions determine the modal expansion functions ψ_N and the frequencies ω_N. For complicated geometries, as for many large solid propellant rockets and for most gas turbine combustors, computation of the ψ_N and ω_N has been a time-consuming and expensive process. That situation is gradually changing with the development of more capable software.

(vi) The relatively general context in which the oscillator equations have been derived does not exclude simpler problems which can either be treated as special cases or constructed without reference to the procedures worked out here. However, it is then often more difficult to be certain that all important processes are accounted for or properly ignored.

4.4. Application of Time-Averaging. To this point the expansion procedure based on two small parameters has been used only to derive the systems of equations describing successively more difficult classes or problems in Section 3.3.2. There are at least two additional reasons for introducing that procedure. Later we will see how an iterative method based partly on the expansion reduces those systems of equations to more readily soluble forms. In this section we apply time-averaging to convert the second-order equations (4.36) to first order equations. First, two remarks:

(i) Use of time-averaging is motivated by the experimental observation that combustion instabilities commonly show slowly varying amplitudes and phases of the modes contributing to the motions. That behavior is a consequence of the relative weakness of the disturbing processes and is therefore measured by the small parameter μ characteristic of the Mach number of the mean flow. It is essential to understand that it is not the amplitudes themselves (i.e. the parameter ε) that matters. Thus the application of time-averaging in the present context is *not* intended to treat nonlinear behavior, but is based on the weak coupling between the mean flow and the unsteady motions.

(ii) Two-time scaling is an alternative method to time-averaging. The results obtained are identical up to second order acoustics (Section 3.3.3(II) and 3.4), a conclusion not shown here but consistent with similar previous works in other fields.

According to the discussion in Section 3.3.2, we can characterize the functions h and f, and hence the forcing function F_n, as sums of terms each of which is of order μ and of zeroth or first order in ε. Thus for example, the right-hand side of (3.62) a,b has the form

$$-\mu\varepsilon \left\{ \{[\mathbf{M}]\}_1 + \frac{\varepsilon}{\mu} \{\mathbf{M}\}_2 \right\}$$

The divergence of these terms eventually appears in h and F_n. Hence we are justified in taking F_n of order μ; to show this explicitly write (4.36) as

$$\ddot{\eta}_N + \omega_N^2 \eta_N = \mu G_N \tag{4.37}$$

In any event, for μ small, the η_N differ but little from sinusoids so (without approximation) it is reasonable to express $\eta_N(t)$ in the equivalent forms

$$\eta_N(t) = r_N(t) \sin(\omega_N t + \phi_N(t)) = A_N(t) \sin \omega_N t + B_N(t) \cos \omega_N t \tag{4.38}$$

and

$$A_N(t) = r_N \cos \phi_N \; ; \quad B_N = r_N \sin \phi_N$$
$$r_N = \sqrt{A_N^2 + B_N^2} \; ; \quad \phi_N = \tan^{-1}\left(\frac{A_N}{B_N}\right) \tag{4.39}$$

One way to proceed follows a physical argument based on examining the time evolution of the energy of the oscillator having amplitude η_N (Culick 1976). The energy $\mathcal{E}_N$ is the sum of kinetic and potential energies,

$$\mathcal{E}_N(t) = \frac{1}{2}\dot{\eta}_N^2 + \frac{1}{2}\omega_N^2 \eta_N^2 \tag{4.40}$$

The time-averaged values of the energy and power input to the oscillator, due to the action of the force μG_N, are

$$\langle \mathcal{E}_N \rangle = \frac{1}{\tau} \int_t^{t+\tau} \mathcal{E}_N \, dt' \; ; \quad \langle \mu G_N \dot{\eta}_N \rangle = \frac{1}{\tau} \int_t^{t+\tau} \mu G_N \dot{\eta}_N \, dt' \tag{4.41}$$

Conservation of energy requires that the time-averaged rate of change of energy equal the time-averaged rate of work done by μG_N on the oscillator:

$$\frac{d}{dt}\langle \mathcal{E}_N \rangle = \mu \langle G_N \dot{\eta}_N \rangle \tag{4.42}$$

From (4.38), the velocity is

$$\dot{\eta}_N = \omega_N r_N \cos(\omega_N t + \phi_N) + \left[\dot{r}_N \sin(\omega_N t + \phi_N) + \dot{\phi}_N r_N \cos(\omega_N t + \phi_N) \right] \tag{4.43}$$

Following Krylov and Bogoliubov (1947) we apply the 'strong' condition that the velocity is always given by the formula for an oscillator is force-free-motion,

$$\dot{\eta}_N = \omega_N r_N \cos(\omega_N t + \phi_N) \tag{4.44}$$

Hence (4.43) is consistent with this requirement only if

$$\dot{r}_N \sin(\omega_N t + \phi_N) + \dot{\phi}_N r_N \cos(\omega_N t + \phi_N) = 0 \tag{4.45}$$

Now use the definitions (4.36), (4.38), (4.39) and (4.42) to find

$$\mathcal{E}_N = \frac{1}{2}\omega_N^2 r_N^2$$
$$\mu G_N \dot{\eta}_N = \mu G_N \omega_N r_N \cos(\omega_N t + \phi_N) \tag{4.46 a,b}$$

The statement "slowly varying amplitude and phase" means that the fractional changes of amplitude and phase are small in one cycle of the oscillation and during the interval of averaging τ if τ is at least equal to the period of the fundamental mode:

$$\frac{\tau}{r_N}\frac{dr_N}{dt} \ll 1 \; ; \quad \frac{\tau}{2\pi}\frac{d\phi_N}{dt} \ll 1 \tag{4.47}$$

These inequalities imply that r_N and ϕ_N may be treated as constants during the averaging carried out in (4.41). To see this, imagine that r_N for example, is expanded in Taylor series for some time t_1 in the interval τ, $t < t_1 < t+\tau$:

$$r_N(t) = r_N(t_1) + (t - t_1)\left(\frac{dr_N}{dt}\right)_{t_1} + \cdots$$

For r_N slowly varying, $\dot{r}_N$ doesn't vary much during a period and may be assigned some average value. The increment $t - t_1$ has maximum value τ; so the second term is negligible according to the first of (4.41). Therefore $r_N(t) \approx r_N(t_1)$ for any t_1 in the interval of averaging and the assertion is proved.

Substitution of (4.46) a,b in (4.42) then gives

$$\omega_N r_N \frac{dr_N}{dt} = \mu \frac{r_N}{\tau}\int_t^{t+\tau} G_N \cos(\omega_N t' + \phi_N)dt'$$

and

$$\frac{dr_N}{dt} = \mu \frac{1}{\omega_N \tau}\int_t^{t+\tau} G_N \cos(\omega_N t' + \phi_N)dt' \tag{4.48}$$

The corresponding equation for the phase $\phi_N(t)$ is found by substituting (4.38) and (4.39) in (4.45) to give

$$r_N \frac{d\phi_N}{dt} = -\frac{\mu}{\omega_N} G_N \sin(\omega_N t + \phi_N) \tag{4.49}$$

Now time average this equation over the interval τ, the left-hand side is approximately constant for theorem give above, and the equation for $\phi_N(t)$ is

$$r_N \frac{d\phi_N}{dt} = -\mu \frac{1}{\omega_N \tau}\int_t^{t+\tau} G_N \sin(\omega_N t' + \phi_N)dt' \tag{4.50}$$

With the relations (4.39), equations (4.48) and (4.50) can be converted to equations for A_N and B_N:

$$\begin{aligned}\frac{dA_N}{dt} &= \frac{\mu}{\omega_N \tau}\int_t^{t+\tau} G_N \cos\omega_N t' dt' \\ \frac{dB_N}{dt} &= -\frac{\mu}{\omega_N t}\int_t^{t+\tau} G_N \sin\omega_N t' dt'\end{aligned} \tag{4.51 a,b}$$

Whichever pair one chooses to use, (4.48) and (4.50) or (4.51) a,b, the general formal problem of solving a system of coupled second order equations (4.37) for the oscillators, has been converted to the simpler approximate formal problem of solving a system of coupled first order equations. The essential basis for that conversion is the removal of the fast oscillatory behavior with the definition (4.38), a transformation made possible because the changes of amplitudes and phases take place on a much slower (i.e. longer) time scale than do the oscillations. The presence and role of two time scales is more evident in the following alternative derivation:

From the second equality of (4.38), we find the velocity

$$\dot{\eta}_N = \omega_N\left[A_N \cos\omega_N t - B_N \sin\omega_N t\right] + \left[\dot{A}_N \sin\omega_N t + \dot{B}_N \cos\omega_N t\right]$$

Now enforce the condition corresponding to (4.45),

$$\dot{A}_N \sin\omega_N t + \dot{B}_N \cos\omega_N t = 0 \tag{4.52}$$

and the velocity is

$$\dot{\eta}_N = \omega_N\left[A_N \cos\omega_N t - B_N \sin\omega_N t\right] \tag{4.53}$$

Substitution in (4.37) gives

$$\omega_N \left[\dot{A}_N \cos \omega_N t - \dot{B}_N \sin \omega_N t \right] + \omega_N^2 \left[-A_N \sin \omega_N t - B_N \cos \omega_N t \right]$$
$$+ \omega_N^2 \left[A_N \sin \omega_N t + B_N \cos \omega_N t \right] = \mu G_N$$

and

$$\dot{A}_N \cos \omega_N t - \dot{B}_N \sin \omega_N t = \frac{\mu}{\omega_N} G_N$$

Multiply by $\cos \omega_N t$ and substitute (4.52) for $\dot{B}_N \cos \omega_N t$ to give

$$\dot{A}_N \cos^2 \omega_N t - \sin \omega_N t \left[-\dot{A}_N \sin \omega_N t \right] = \frac{\mu}{\omega_N} G_N \cos \omega_N t$$

so

$$\frac{dA_N}{dt} = \frac{\mu}{\omega_N} G_N \cos \omega_N t \tag{4.54}$$

Similarly,

$$\frac{dB_N}{dt} = -\frac{\mu}{\omega_N} G_N \sin \omega_N t \tag{4.55}$$

We now introduce two time-scales, τ_f the first scale, of the order of the period of the fundamental oscillation (in fact, we might as well set $\tau_f = 2\pi/\omega_1$); and τ_s, the slow scale characterizing transient changes of the amplitudes and phases of the oscillations. Two corresponding dimensionless time variables can be defined, $t_f = t/\tau_f$ and $t_s = t/\tau_s$. Thus we consider the amplitudes and phases to be functions of the slow variable t_s while the forcing functions G_N depend on both t_f and to because they depend on the η_N, $(i = 1, 2, \cdots)$

$$\eta_N = A_N(t_s) \sin \left(2\pi \frac{\omega_N}{\omega} t_f \right) + B_N(t_s) \cos \left(2\pi \frac{\omega_N}{\omega_1} t_f \right)$$

In terms of the dimensionless time variables,

$$\frac{1}{\tau_s} \frac{dA_N}{dt_s} = \frac{\mu}{\omega_N} G_N \cos \omega_N t$$

and averaging over the fast variable we have

$$\frac{1}{\tau_s} \int_{t_f}^{t_f + \tau_f} \frac{1}{\tau_s} \frac{dA_N}{dt'_s} dt'_f = \frac{\mu}{\omega_N} \frac{1}{\tau_f} \int_{t_f}^{t + \tau_f} G_N \cos \left(2\pi \frac{\omega_N}{\omega_1} t'_f \right) dt'_f$$

On the left-hand side, dA_N/dt'_s is assume to be sensibly constant in the interval τ_f and we have

$$\frac{1}{\tau_s} \frac{dA_N}{dt'_s} = \frac{\mu}{\omega_N \tau_f} \int_{t_f}^{t + \tau_f} G_N \left(t'_f, t'_s \right) \cos \left(2\pi \frac{\omega_N}{\omega_1} t'_f \right) dt'_f \tag{4.56}$$

Those parts of G_N depending on t'_s are taken also to be constant and if we now rewrite this equation in terms of dimensional variables, we recover (4.51)a with $\tau = \tau_f = 2\pi/\omega$. Similar calculations will produce again (4.51)b. Note that due to the nonlinear coupling, the amplitude and phases of all modes normally change on roughly the same scale as that for the fundamental mode; thus the single interval of averaging works for all modes.

In Section 7.2 we will use a continuation method to assess the ranges of parameters and other conditions for which the first order equations give accurate results when compared with solutions to the complete oscillator equations. In the development of the theoretical matters described in this book, the sets of first order equations have been central. They remain extremely useful both for theoretical work and for applications.

4.5. The Procedure for Iterative Solution. The oscillator equations (4.33) and (4.34) are not yet in a form that can be readily solved because the functions F_N, defined by (4.30) contain not only p' but also the dependent variables ρ', T' and $\mathbf{u}'$ in the functions h and f. With the two-parameter expansion as the basis, the iteration procedure provides a means for expressing F_N in terms of p' only. Thus eventually the oscillator equations become a system soluble for the modal amplitudes $\eta_N(t)$. There are of course approximations required, but magnitudes of their effects can always be estimated in terms of the parameters ε and μ. To appreciate how the procedure is constructed, it is helpful always to keep in mind the correspondence between the smallness of ε and μ, and the distortions they represent of the unperturbed classical acoustic field.

There are two chief types of distortions or perturbations: Those represented by ε, arising as nonlinear effects of finite amplitudes,[10] classified generally as energy transfer between modes; and those measured by μ, consequences of interactions, hence energy transfer, between the steady and unsteady fields. Each of those types of perturbations may be identified within the volume in question and at the boundary. Quite generally, then, we must take into account perturbations of the classical acoustic field, associated with three kinds of energy transfer: linear transfer between the mean and fluctuating motions; nonlinear transfer between modes, or mode coupling, independent of the average flow field; and nonlinear energy transfer between the mean flow and fluctuating fields. The way in which we view and accommodate those perturbations determines our choice of basis functions ψ_N used in the modal expansion (4.27).

4.5.1. *Linear Energy Transfer Between the Mean and Fluctuating Motions.* Any combustor designed for steady, or at most slowly varying conditions on the acoustic time scale, must have provision for supplying reactants and exhausting products. There must therefore be average flow within the volume and through openings in the enclosing boundary. If the reactants are liquid or gaseous, then openings exist for both inflow and outflow. In combustors for solid propellants, flow enters at the boundary but there are not openings for that purpose.

(A) Volumetric Interactions

The general equations of motion in principle contain all interactions between the mean and fluctuating motions within the volume. Many are shown explicitly as the bracketted terms $[\bar{\mathbf{M}}]$, $\{\bar{\mathbf{M}}\}$, $[\rho_1]$, $\{p_1\}$, $\cdots$ defined in Section (3.3). Those terms in the forms given there account for interactions of the mean flow velocity with the acoustic field and have long served that purpose well in investigations of combustion instabilities. Additional consideration are required to treat interactions associated with entropy and vorticity waves, including turbulence and noise, a subject covered in Section (7.4).

Special effects also arise when the average temperature field is nonuniform; the last term in (4.33) represents one consequence of nonuniform average temperature but others are contained in the formula given for h, equation (3.55). Nonuniformities of temperature cause nonuniformities in the speed of sound which may be regarded as nonuniformities in the index of refraction for acoustic waves. Thus in the general context of wave motions, phenomena such as refraction and diffraction must arise. However, the analysis covered here for wave systems slowly varying on the acoustic time scale, obscures wave phenomena of that sort; they have rarely been addressed explicitly in the field of combustion instabilities and then only in connection with very special problems. However, the consequences of refraction and diffraction are contained implicitly in distortions of the structure of the steady waves.

It is extremely important that large differences in the average speed of sound be accounted for as accurately as possible. That is best done by including them in the functions used in the modal expansion. Formally that amounts to including all terms in h representing linear interactions between the acoustic and mean fields, in the equations for the ψ_m. That is, such large perturbations are better not included in the procedure best suited for dealing with small perturbations. In practice, the only example of this tactic have been concerned with flows in ducts containing a compact zone of heating thin relative to the acoustic wavelength. The modal functions are then formed in piecewise fashion, the usual wave equation being solved separately for the two regions characterized by different uniform temperatures upstream and downstream of the zone of heating treated as a surface of discontinuity. Then the functions are joined with suitable matching conditions.

For the most part, therefore, energy transfer between the acoustic field and the mean flow within the volume of a combustor is due to interactions with the mean velocity, characterized by the parameter μ. The analysis is strictly limited to perturbations linear in the Mach number of the mean flow (see the footnote in the preceding page).

(B) Boundary Conditions

The situation in respect to processes at the boundary is considerably more complicated and in fact cannot be placed in a firm basis without detailed examination of ancillary problems. Only two possibilities have so far been

---

[10]Recall that in this work, nonlinear behavior is measured in terms of the amplitude ε of the unsteady motions. It is intrinsic to their derivation (Section 3) that the governing equations are linear in μ, i.e. in the Mach number of the mean flow.

of practical interest: physical openings in the boundary of the combustor; and a burning surface. Conditions to be set on the acoustic field at an opening depend on the flow field through and outside the boundary. In classical acoustics with no flow, an opening into an atmosphere held at constant pressure is almost perfectly reflecting, with the fluctuating pressure nearly zero in the plane of the opening. A perfectly reflecting rigid wall causes the fluctuating velocity to vanish there. Thus in those two limits, the boundary conditions to 0th order on the pressure field are respectively $p' = 0$ and $\hat{\mathbf{n}} \cdot \nabla p' = 0$.

Subsonic flow through an orifice presents a boundary condition to acoustic waves closer to the case of no flow, $p' \approx 0$, than to a rigid wall. On the other hand, if the inlet flow is choked upstream close[11] to the orifice, or the outlet flow exhausts through a choked nozzle, the boundary condition is closer to the for a rigid wall, $\hat{\mathbf{n}} \cdot \nabla p' \approx 0$. That is the case for propulsion systems, with the possible exception of the primary combustion chamber in a gas turbine. The actual boundary conditions are more complicated but for linear behavior can be represented by impedance or admittance functions defined for steady waves. For the more common case of choked flows, that boundary condition is expressed as

$$\hat{\mathbf{n}} \cdot \hat{\mathbf{u}}\left(\mathbf{r}_s, w\right) = A_s\left(\mathbf{r}_s, w\right) \hat{p}\left(\mathbf{r}_s, w\right) = \mu a_s\left(\mathbf{r}_s, w\right) \hat{p}\left(\mathbf{r}_s, w\right) \tag{4.57}$$

where $A_s = \mu a_s$ is the dimensional admittance function shown here to be proportional to the Mach number of the average flow. (Tsien 1952; Crocco and Cheng 1956; Culick 1961, 1963) Generally, A_s is a complex function,

$$A_s = |A_s| e^{i\phi_A} = \mu |a_s| e^{i\phi_A} \tag{4.58}$$

The representation (4.57) is based on the idea that when exposed to an oscillatory fluctuation of pressure, a physical surface responds in first approximation such that its velocity normal to itself is proportional to the impressed pressure, possibly with a phase or time delay. That idea is extended in the present context to describe fluctuations of flow at a fictious surface forming part of the boundary enclosing the combustor volume, or at the downstream edge of the combustion zone at a burning surface. Thus we have a simple and direct way of making explicit the first term in the definition (3.57) of the boundary function f for steady waves:

$$\begin{aligned} \bar{\rho} \frac{\partial \mathbf{M}'}{\partial t} \cdot \hat{\mathbf{n}} = \bar{\rho} \bar{a} \frac{\partial \mathbf{u}'}{\partial t} \cdot \hat{\mathbf{n}} &= \bar{\rho} \bar{a} \frac{\partial}{\partial t} \left[\hat{\mathbf{n}} \cdot \hat{\mathbf{u}}\left(\mathbf{r}_s, w\right) e^{i\bar{a}kt} \right] \\ &= \mu \bar{\rho} \bar{a} a_s\left(\mathbf{r}_s, t\right) i\bar{a}k \hat{p}\left(\mathbf{r}_s, w\right) e^{i\bar{a}kt} \\ &= \mu \bar{\rho} \bar{a}^2 k \left(i |a_s| e^{i\phi_a} \right) \hat{p}\left(\mathbf{r}_s, w\right) e^{i\bar{a}kt} \end{aligned} \tag{4.59}$$

An equivalent form is

$$\bar{\rho} \frac{\partial \mathbf{M}'}{\partial t} \cdot \hat{n} = \mu \bar{\rho} \bar{a}^2 k \left\{ -Im(a_s) + i\, Re(a_s) \right\} \hat{p}\left(\mathbf{r}_s, w\right) e^{i\bar{a}kt} \tag{4.60}$$

Although the admittance function is defined for steady waves initially, (4.49) can be converted to a form approximately applicable to problems having arbitrary dependence on time. The time derivative of some function φ for steady waves, so we can make the correspondence

$$\frac{\partial \varphi}{\partial t} \longleftrightarrow i\bar{a}k \frac{\partial \varphi}{\partial t}$$

Hence we write (4.49) as

$$\bar{\rho} \frac{\partial \mathbf{M}'}{\partial t} \cdot \hat{\mathbf{n}} = \mu \bar{\rho} \bar{a} \left[\bar{a}k\, Im\left\{a_s\right\} p' + Re\left\{a_s\right\} \frac{\partial p'}{\partial t} \right] \tag{4.61}$$

This form of a boundary condition will be useful in later applications.

The chief point here is that for choked inlet and exhaust flows, the function f in the boundary condition $\hat{\mathbf{n}} \cdot \nabla p' = -f$ is of order μ. That is, perturbations from the condition defining a rigid impermeable wall are all proportional to the magnitude of the Mach number of the mean flow. Corresponding reasoning applies to the less important case of subsonic flow exhausting into surroundings held at constant pressure.[12] Now we set the

---

[11]'Close' means within a short distance relative to the wavelength of the dominant oscillation.

[12]Less important for practical applications. However there are many laboratory devices operating at close to atmospheric pressure and exhausting into the atmosphere for which the condition treated here is appropriate.

boundary condition by using (3.51) evaluated at the boundary; for linear steady waves we have

$$p' = \frac{1}{\bar{a}k} \left[\gamma \bar{p} \nabla \cdot \mathbf{M}_1' + \mu\{[p]_1\} - \frac{1}{\varepsilon}\mathcal{P}' \right]_{\mathbf{r}=\mathbf{r}_s} \tag{4.62}$$

Again we may define an admittance function to eliminate $\nabla \cdot \mathbf{M}_1'$ in favor of the local pressure fluctuation. We leave the calculation to special applications.

We conclude that for linear problems, perturbations of the classical acoustics problem due to energy transfer between the mean and unsteady fields are represented to order μ, both within the volume and at the boundary. This result is of course consistent with the order to which the differential equations are valid within the approximation used here (see a remark following equation (3.39). For that reason, we cannot in any event carry terms of higher order in μ unless the governing equations used here are re-derived.

As an example to illustrate some implications of the preceding remarks, consider the case of flow through a uniform duct of length L, supplied through choked valves and exhausting through a choked nozzle. Suppose that by some means, for example by installing a speaker, oscillations can be excited and sustained in the duct. If there were no flow and rigid plates were placed at both ends ($z = 0, L$), classical 'organ pipe' acoustic modes would be found experimentally, having frequencies $\omega_N = n(\bar{a}/L)$. The velocity and pressure distributions for these steady axial modes are proportional to $\sin k_N x$ and $\cos k_N x$ respectively. Suppose we set, for example,

$$p'(z,t) = \hat{p}_0 \cos k_N z \cos \omega_N t \tag{4.63}$$

where $\omega_N = \bar{a}k_N$. The unperturbed acoustic momentum equation,

$$\bar{\rho}\frac{\partial \mathbf{u}'}{\partial t} = -\nabla p'$$

is satisfied with (4.52) if $\mathbf{u}'$ has only the axial component,

$$u'(z,t) = \frac{\hat{p}_0}{\bar{\rho}\bar{a}} \sin k_N z \sin \omega_N t \tag{4.64}$$

The velocity field has nodes ($u' = 0$) at the ends and the pressure field has anti-nodes, reaching maximum amplitude $\hat{p}_0$ when $t = 0, 2\pi/\omega_N, 4\pi/\omega_N, \cdots$. Now suppose that average flow is introduced and that the cross-sectional areas available for the flow upstream and downstream are small fractions of the cross-sectional area of the duct. Then the average Mach numbers at $z = 0, L$ are small ($\mu \ll 1$). Hence the distortions of the classical organ pipe modes are small. In particular, the modes of the velocity field are slightly displaced by the same amounts downstream of their unperturbed positions at $x = 0, L$. Thus the wavelength and frequency of the modes are unchanged and the unperturbed mode shapes are close approximations to the actual shapes with the flow, as sketched in Figure 4.1.
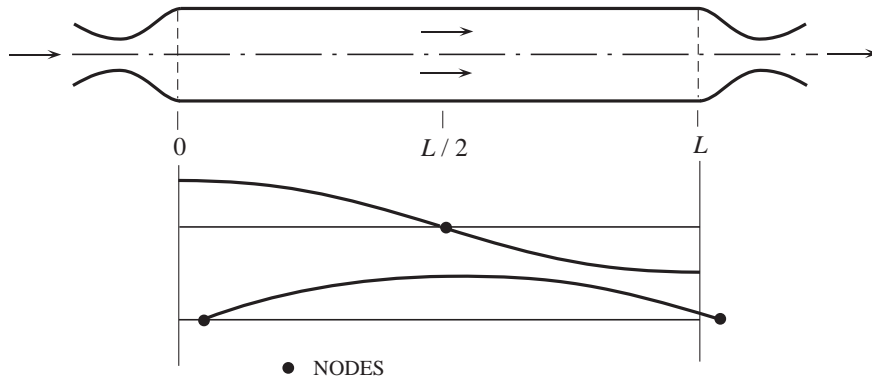
FIGURE 4.1. Fundamental Longitudinal Mode, Velocity Mode Shape: $----$ Classical (no flow); —— Duct with flow choked upstream and downstream

If the Mach numbers at the entrance ($z = 0$) and at the exit ($z = L$) are not small, then the nodes of the velocity wave are displaced by larger amounts, but the wavelength, and hence the frequency, suffer only small changes. This behavior suggests what is true quite generally in practice, that the processes in a combustion

chamber have relatively small effects in the frequencies of the normal modes. Consequently, as we will emphasize repeatedly, comparison of observed frequencies with those predicted is not a useful basis for assessing the correctness of the theory in question.

4.5.2. *Energy Transfer Between Modes; Nonlinear Mode Coupling.* If the functions ψ_N used in the modal expansion are those computed according to classical acoustics, then in general linear coupling between modes will appear in the right-hand sides of the systems (4.33) and (4.34). When the mean flow field is nonuniform, interactions between the mean and fluctuating fields will cause linear mode coupling proportional to the average Mach number. Formally such contributions are included among those discussed in the preceding section, i.e. they are of order μ.

In principle, linear coupling between modes can be formally eliminated by transformation to a new set of modal expansion functions by diagonalizing the matrix of coefficients (Culick 1997). There may be some applications for which the linear coupling should be explicitly treated, but here we assume that either linear coupling is absent on physical grounds or has been eliminated by suitable transformation.

Hence energy transfer between modes is of order ε^2 or higher and is necessarily nonlinear; calculations in the next section show that we can write the system (4.34) schematically in the form

$$\ddot{\eta}_N + \omega_N^2 \eta_N = -\mu\left(D_N \dot{\eta}_N + E_N \eta_N\right) + F_N^{NL} \tag{4.65}$$

The function F_N^{NL} contains all nonlinear processes. According to its development in Section 3 consists of a sum of groups of terms of order ε, ε^2, $\cdots$, $\mu\varepsilon$, $\mu\varepsilon^2$, $\cdots$. In general, F_N cannot be represented by a diagonal matrix: Nonlinear coupling of the modes always exists and, among other consequences, is an important process in the evolution of linear unstable motions into stable limit cycles.

4.5.3. *Zeroth and First Order Solutions to the Oscillator Equation.* We defer to a later section analysis including nonlinear energy transfer of order $\mu\varepsilon$, and we assume that the average temperature is approximately uniform, so the last term of (4.33) is negligible. The problem comes down to solving (4.34) for the $\eta_N(t)$,

$$\ddot{\eta}_N + \omega_N^2 \eta_N = F_N \tag{4.66}$$

with

$$F_N = -\frac{\bar{a}_r^2}{\bar{p}_r E_N^2}\left\{\iiint_v h\psi_N dV + \oiint_S f\psi_N dS\right\} \tag{4.67}$$

and h and f are given by (3.55) and (3.57):

$$
h = -\bar{\rho}\left[\nabla\cdot\left(\bar{\mathbf{M}}\cdot\nabla\mathbf{M}' + \mathbf{M}'\cdot\nabla\bar{\mathbf{M}}\right) - \frac{1}{\bar{a}^2}\frac{\partial}{\partial t}\left(\bar{\mathbf{M}}\cdot\nabla p' + \gamma p'\nabla\cdot\bar{\mathbf{M}}\right)\right]
$$
$$
-\left\{\bar{\rho}\nabla\cdot\left(\mathbf{M}'\cdot\nabla\mathbf{M}' + \frac{\rho'}{\bar{\rho}}\frac{\partial\bar{\mathbf{M}}'}{\partial t}\right) - \frac{1}{\bar{a}^2}\frac{\partial}{\partial t}\left(\mathbf{M}\cdot\nabla p' + \gamma p'\nabla\cdot\mathbf{M}\right)\right\} \tag{4.68}
$$
$$
+\left[\frac{1}{\bar{\rho}}\nabla\cdot\left(\frac{1}{\bar{\rho}}\boldsymbol{\mathcal{F}}'\right) - \frac{1}{\bar{a}^2}\frac{\partial\boldsymbol{\mathcal{P}}'}{\partial t}\right] + \left\{\frac{1}{\bar{\rho}}\nabla\cdot\left(\frac{1}{\bar{\rho}}\boldsymbol{\mathcal{F}}'\right) - \frac{1}{\bar{a}^2}\frac{\partial\boldsymbol{\mathcal{P}}'}{\partial t}\right\}
$$

$$
f = \bar{\rho}\frac{\partial\mathbf{M}'}{\partial t}\cdot\hat{\mathbf{n}} + \hat{\mathbf{n}}\cdot\left[\bar{\rho}\mathbf{M}'\cdot\nabla\bar{\mathbf{M}} + \bar{\mathbf{M}}\cdot\nabla\mathbf{M}'\right] + \hat{\mathbf{n}}\cdot\left\{\bar{\rho}\mathbf{M}'\cdot\nabla\mathbf{M}' + \rho'\frac{\partial\mathbf{M}'}{\partial t}\right\} + [\boldsymbol{\mathcal{F}}']\cdot\hat{\mathbf{n}} + \{\boldsymbol{\mathcal{F}}'\}\cdot\hat{\mathbf{n}} \tag{4.69}
$$

Recall that the left-hand side of (4.55) follows upon inserting in the linear wave operator the modal expansion (4.27) for p';

$$p' = \bar{p}_r \sum_{m=1}^{M} \eta_m(t)\psi_m(\mathbf{r}) \tag{4.70}$$

The iterative procedure is a way of expressing the driving forces F_N in terms of the amplitudes η_m, so (4.55) becomes a system of equations for the amplitudes. As we have explained earlier (Section 3.3) we use ε as a

measure of the size of the pressure disturbance and write always

$$p' = \varepsilon p_1(\mathbf{r}_1, t) \tag{4.71}$$

However, we must allow the other dependent variables vary with ε in a more complicated manner; it is reasonable at this point to assume dependence as a power series in ε:

$$\begin{aligned}
\mathbf{M}' &= \varepsilon \mathbf{M}_1 + \varepsilon^2 \mathbf{M}_2 + \cdots \\
T' &= \varepsilon T_1 + \varepsilon^2 T_2 + \cdots
\end{aligned} \tag{4.72}$$

and so forth. All components of the fluctuations, p_1, $\mathbf{M}_1$, $\mathbf{M}_2$, $\cdots$, T_1, T_2, $\cdots$ become distorted by the mean flow. That possibility is taken into account by writing

$$\begin{aligned}
p' &= \varepsilon p_1 = \varepsilon \left[p_{10} + \mu p_{11} + \mu^2 p_{12} + \cdots \right] \\
\mathbf{M}' &= \varepsilon \mathbf{M}_1 + \varepsilon^2 \mathbf{M}_2 + \cdots = \varepsilon \left[\mathbf{M}'_{10} + \mu \mathbf{M}_{11} + \cdots \right] \\
&\quad + \varepsilon^2 \left[\mathbf{M}'_{20} + \mu \mathbf{M}_{21} + \cdots \right] \\
T &= \varepsilon T_1 + \varepsilon^2 T_2 + \cdots = \varepsilon \left[T_{10} + \mu T_{11} + \cdots \right] \\
&\quad + \varepsilon^2 \left[T_{20} + \mu T_{21} + \cdots \right]
\end{aligned} \tag{4.73}$$

It is apparent that the number of functions to be determined rapidly gets out of hand as more terms are retained in the series expansion. However to the order we choose to investigate here, that difficulty doesn't appear, for the following reason. Examine a typical terms in h say the first in each of the brackets:

$$h = -\bar{\rho} \left[\nabla \cdot \left(\bar{\mathbf{M}}_1 \cdot \nabla \mathbf{M}' \right) + \cdots \right] - \left\{ \bar{\rho} \nabla \cdot \left(\mathbf{M}' \cdot \nabla \mathbf{M}' \right) + \cdots \right\} + \cdots$$
$$= -\mu \bar{\rho} \nabla \cdot \left[\bar{\mathbf{M}}_1 \cdot \nabla \left(\varepsilon \mathbf{M}'_1 + \varepsilon^2 \mathbf{M}'_2 + \cdots \right) + \cdots \right] - \bar{\rho} \left\{ \nabla \cdot \left(\varepsilon \mathbf{M}'_1 + \varepsilon^2 \mathbf{M}'_2 + \cdots \right) \cdot \nabla \left(\varepsilon \mathbf{M}'_1 + \varepsilon^2 \mathbf{M}'_2 + \cdots \right) + \cdots \right\} + \cdots$$

Now substitute (4.62) to give

$$\begin{aligned}
h = &-\mu \bar{\rho} \nabla \cdot \left[\bar{\mathbf{M}}_1 \cdot \nabla \left(\varepsilon \mathbf{M}'_{10} + \varepsilon \mu \mathbf{M}'_{11} + \cdots + \varepsilon^2 \mathbf{M}'_{20} + \varepsilon^2 \mu \mathbf{M}'_{21} + \cdots \right) + \cdots \right] = \\
&-\bar{\rho} \nabla \cdot \left\{ \left(\varepsilon \mathbf{M}_{10} + \varepsilon \mu \mathbf{M}'_{11} + \cdots \right) \cdot \nabla \left(\varepsilon \mathbf{M}'_{10} + \varepsilon \mu \mathbf{M}'_{11} + \cdots \right) + \cdots \right\} + \cdots
\end{aligned}$$

Multiplying the various brackets and showing explicitly only those terms to be retained, we find

$$h = -\mu \varepsilon \bar{\rho} \nabla \cdot \left[\bar{\mathbf{M}}_1 \cdot \nabla \mathbf{M}'_{10} + \cdots \right] - \bar{\rho} \nabla \cdot \left\{ \varepsilon^2 \mathbf{M}_{10} \cdot \nabla \mathbf{M}_{10} + \cdots \right\} + \cdots$$

This procedure leads eventually to the forms for h and f with only terms of order $\mu \varepsilon$ and ε^2:

$$\begin{aligned}
h = &-\mu \varepsilon \left[\bar{\rho} \nabla \cdot \left(\bar{\mathbf{M}}_1 \cdot \nabla \mathbf{M}_{10} + \mathbf{M}_{10} \cdot \nabla \bar{\mathbf{M}}_1 \right) - \frac{1}{\bar{a}^2} \frac{\partial}{\partial t} \left(\bar{\mathbf{M}}_1 \cdot \nabla p_{10} + \gamma p_{10} \nabla \cdot \bar{\mathbf{M}}_1 \right) \right] \\
&- \varepsilon^2 \left\{ \bar{\rho} \nabla \cdot \left(\mathbf{M}_{10} \cdot \nabla \mathbf{M}_{10} + \frac{\rho_{10}}{\bar{\rho}} \frac{\partial \mathbf{M}_{10}}{\partial t} \right) - \frac{1}{\bar{a}^2} \frac{\partial}{\partial t} \left(\mathbf{M}_{10} \cdot \nabla p_{10} + \gamma p_{10} \nabla \cdot \mathbf{M}_{10} \right) \right\} \\
&+ \mu \varepsilon \left[\frac{1}{\bar{\rho}} \nabla \cdot \left(\frac{1}{\bar{\rho}} \boldsymbol{\mathscr{F}}' \right) - \frac{1}{\bar{a}^2} \frac{\partial \boldsymbol{\mathscr{P}}'}{\partial t} \right] + \varepsilon^2 \left\{ \frac{1}{\bar{\rho}} \nabla \cdot \left(\frac{1}{\bar{\rho}} \boldsymbol{\mathscr{F}}' \right) - \frac{1}{\bar{a}^2} \frac{\partial \boldsymbol{\mathscr{P}}'}{\partial t} \right\}_{\varepsilon^2}
\end{aligned} \tag{4.74}$$

$$\begin{aligned}
f = &\bar{\rho} \left[\frac{\partial \mathbf{M}'}{\partial t} \cdot \hat{\mathbf{n}} \right]_{\mu \varepsilon} + \bar{\rho} \left\{ \frac{\partial \mathbf{M}'}{\partial t} \cdot \hat{\mathbf{n}} \right\}_{\varepsilon^2} + \mu \varepsilon \bar{\rho} \hat{\mathbf{n}} \cdot \left[\mathbf{M}_{10} \cdot \nabla \bar{\mathbf{M}}_1 + \bar{\mathbf{M}}_1 \cdot \nabla \mathbf{M}_{10} \right] \\
&+ \varepsilon^2 \bar{\rho} \hat{\mathbf{n}} \cdot \left\{ \mathbf{M}_{10} \cdot \nabla \mathbf{M}_{10} \right\} + \mu \varepsilon \left[\boldsymbol{\mathscr{F}}' \cdot \hat{\mathbf{n}} \right]_{\mu \varepsilon} + \varepsilon^2 \left\{ \boldsymbol{\mathscr{F}}' \cdot \hat{\mathbf{n}} \right\}_{\varepsilon^2}
\end{aligned} \tag{4.75}$$

5. SOME FUNDAMENTALS OF ACOUSTICS

According to the experiences related in Section 1, combustion instabilities may be regarded as unsteady motions closely approximated as classical acoustical motions with perturbations due ultimately to combustion processes. That view, initially an emprical conclusion, motivated the general form of the analytical framework constructed in Section 4. Relatively little knowledge of classical acoustics is required to understand and apply that construction formally.

However, interpretation of the details of observed behavior, and effective use of the theory to develop accurate representations of actual motions in combustors require firm understanding of the fundamentals of acoustics. The purpose of this section is to provide a condensed summary of the basic parts of the subject most relevant to the main subject of this book. We therefore ignore those processes distinguishing combustion chambers from other acoustical systems. Except for brief discussion of nonlinear gas dynamics, we restrict attention to the Problem O defined in Sections 3.3.3 and 3.4.

5.1. The Linearized Equations of Motion; The Velocity Potential. We will be concerned here with unsteady motions in a pure non-reacting gas at rest. The governing equations are 3.40 for Problem O, Classical Acoustics, leading to the corresponding wave equation and its boundary condition, equations 3.52 with h_0 and f_0 given by 3.55 for constant average density $\bar{\rho}$ and written with dimensional variables:

$$\nabla^2 p' - \frac{1}{\bar{a}^2}\frac{\partial^2 p'}{\partial t^2} = \nabla \cdot \boldsymbol{\mathcal{F}}' - \frac{1}{\bar{a}^2}\frac{\partial \mathcal{P}'}{\partial t}$$

$$\hat{\mathbf{n}} \cdot \nabla p' = -\bar{\rho}\frac{\partial \mathbf{u}'}{\partial t} \cdot \hat{\mathbf{n}} - \boldsymbol{\mathcal{F}}' \cdot \hat{\mathbf{n}}$$

(5.1) a,b

In the absence of condensed material, the definitions (A.18) and (A.20) of the unperturbed functions $\boldsymbol{\mathcal{F}}$ and $\mathcal{P}$ are:

$$\boldsymbol{\mathcal{F}} = \nabla \cdot \overleftrightarrow{\boldsymbol{\tau}}_v + \mathbf{m}_e - \mathbf{u}w_e \tag{5.2}$$

$$\mathcal{P} = \frac{R}{C_v}\left[\overleftrightarrow{\boldsymbol{\tau}}_v \cdot \nabla \cdot \mathbf{u} - \nabla \cdot \mathbf{q} - Q_e\right] + RTw_e \tag{5.3}$$

where

$\overleftrightarrow{\boldsymbol{\tau}}_v$: viscous stress tensor (force/area)

$\mathbf{q}$: rate of conductive heat transfer (energy/area-s)

$\mathbf{m}_e$: rate of momentum addition by external sources (mass-velocity/volume-s)

w_e : rate of mass addition by external sources (mass/volume-s)

Q_e : rate of energy addition by external sources (energy/volume-s)

Thus the function $\boldsymbol{\mathcal{F}}$ contains all processes causing changes of momentum of the gas, except for that due to internal pressure differences; and $\mathcal{P}$ represents all sources of energy addition. The linearized forms of the source terms will be constructed as required for specific problems. For most of this section we will treat only problems for which h_0 and f_0 vanish, giving the simplest equations for classical acoustics,

$$\nabla^2 p' - \frac{1}{\bar{a}^2}\frac{\partial^2 p'}{\partial t^2} = 0$$

$$\hat{\mathbf{n}} \cdot \nabla p' = 0$$

(5.4) a,b

With no sources in the volume or on the boundary, motions exist only for initial value problems in which the pressure and its time derivative are specified at some initial time, t_0.

In this case, the wave equation is used to describe freely propagating waves following an initial disturbance or, when the boundary condition (5.13)b is enforced, the normal modes for a volume enclosed by a rigid boundary. The condition $\hat{\mathbf{n}} \cdot \nabla p' = 0$ means that the velocity normal to the boundary is zero, because the acoustic velocity is computed from the acoustic momentum (3.40)b written in dimensional form with $\boldsymbol{\mathcal{F}} = 0$:

$$\bar{\rho}\frac{\partial \mathbf{u}'}{\partial t} = -\nabla p' \tag{5.5}$$

so

$$\hat{\mathbf{n}} \cdot \nabla p' = \bar{\rho} \frac{\partial \mathbf{u}'}{\partial t}$$

from which

$$\frac{\partial}{\partial t} (\hat{\mathbf{n}} \cdot \mathbf{u}') = -\frac{1}{\bar{\rho}} \hat{\mathbf{n}} \cdot \nabla p' = 0 \tag{5.6}$$

Hence $\hat{\mathbf{n}} \cdot \mathbf{u}' = 0$ always

We have just derived the equations for classical acoustics by specializing the general equations of unsteady motion. It is also useful to arrive at the same conclusion in a slightly different way, beginning with the equations for inviscid motion in a homogeneous medium:

$$\text{Conservation of Mass}: \qquad \frac{\partial \rho}{\partial t} + \nabla \cdot (\rho \mathbf{u}) = 0 \tag{5.7}$$

$$\text{Conservation of Momentum}: \qquad \rho \frac{\partial \mathbf{u}}{\partial t} + \rho \mathbf{u} \cdot \nabla \mathbf{u} + \nabla p = 0 \tag{5.8}$$

$$\text{Conservation of Energy}: \qquad \rho \frac{\partial}{\partial t} \left(e + \frac{1}{2} u^2 \right) + \rho \mathbf{u} \cdot \nabla \left(e + \frac{1}{2} u^2 \right) + \nabla \cdot (p\mathbf{u}) = 0 \tag{5.9}$$

$$\text{Equation of State}: \qquad p = \rho R T \tag{5.10}$$

Remove the kinetic energy from the energy equation by subtracting $\mathbf{u} \cdot$ (momentum equation) to give

$$\rho \frac{De}{Dt} + p \nabla \cdot \mathbf{u} = 0 \tag{5.11}$$

where $\frac{D}{Dt} = \frac{\partial (\ )}{\partial t} + \mathbf{u} \cdot \nabla (\ )$. Because all irreversible processes have been ignored the entropy of a fluid element remains constant, $\frac{Ds}{Dt} = 0$, a result that follows directly by substituting the mass and energy equations in the thermodynamic definition of the entropy of an element:

$$\rho \frac{Ds}{Dt} = \rho \frac{De}{Dt} - \frac{p}{\rho} \frac{D\rho}{Dt} = -p \nabla \cdot \mathbf{u} + \frac{p}{\rho} (\rho \nabla \cdot \mathbf{u}) = 0 \tag{5.12}$$

Taking the density to be a function of pressure and entropy, we can write for an isentropic process

$$d\rho = \left(\frac{\partial \rho}{\partial s} \right)_p ds + \left(\frac{\partial \rho}{\partial p} \right)_s dp = \left(\frac{\partial \rho}{\partial p} \right)_s dp = \frac{1}{a^2} dp \tag{5.13}$$

where

$$a^2 = \left(\frac{\partial \rho}{\partial p} \right)_s \tag{5.14}$$

will turn out to be the speed of propagation of small disturbances, the 'speed of sound'. With this definition, we can rewrite the continuity equation (5.7) for the pressure:

$$\frac{\partial p}{\partial t} + \rho a^2 \nabla \cdot \mathbf{u} + \mathbf{u} \cdot \nabla p = 0 \tag{5.15}$$

This result is quite general: in particular, its derivation did not involve using the special characteristics of a perfect gas.

Alternatively, we may derive this equation for the special case of a perfect gas for which $de = C_v(T) dT$ and the equation of state is (5.10). Add T times (5.7) to C_v^{-1} times (5.11) with $de = C_v dT$; then use (5.10) to find

$$\frac{\partial p}{\partial t} + \left(1 + \frac{R}{C_V} \right) p \nabla \cdot \mathbf{u} + \mathbf{u} \cdot \nabla p = 0 \tag{5.16}$$

But $R = C_p - C_v$, so $R/C_v = \gamma - 1$ for a perfect gas. Comparison of (5.14) and (5.15) gives the formula for the speed of sound in a perfect gas:

$$a^2 = \sqrt{\frac{\gamma p}{\rho}} = \sqrt{\gamma R T} \tag{5.17}$$

For an isentropic process of a perfect gas, equation (5.13) can be integrated,

$$d\rho = a^2 dp = \frac{\rho}{\gamma p} dp$$

which gives

$$p = p_0 \left(\frac{\rho}{\rho_0} \right)^{\gamma} \tag{5.18}$$

where ρ_0, p_0 are constant reference values.

We may now eliminate the density from the momentum equation (5.8) to find

$$\frac{\partial \mathbf{u}}{\partial t} + \mathbf{u} \cdot \nabla \mathbf{u} + \frac{1}{\rho_0} \left(\frac{p_0}{p} \right)^{1/2} \nabla p = 0 \tag{5.19}$$

Finally, we obtain the wave equation for the pressure by differentiating (5.16) with respect to time and substituting (5.19) and $a^2 = \gamma p/\rho$:

$$\frac{\partial^2 p}{\partial t^2} - a_0^2 \frac{p}{p_0} \nabla \cdot \left[\frac{\nabla p}{(p/p_0)^{1/\gamma}} \right] = \gamma p \nabla \cdot (\mathbf{u} \cdot \nabla \mathbf{u}) - \gamma \frac{\partial p}{\partial t} \nabla \cdot \mathbf{u} - \frac{\partial}{\partial t} (\mathbf{u} \cdot \nabla p) \tag{5.20}$$

The boundary condition is defined by taking the component of (5.19) normal to the boundary:

$$\hat{\mathbf{n}} \cdot \nabla p = - \left(\frac{p}{p_0} \right)^{1/2} \rho_0 \left[\hat{\mathbf{n}} \cdot \frac{\partial \mathbf{u}}{\partial t} + \hat{\mathbf{n}} \cdot \nabla (\mathbf{u} \cdot \nabla \mathbf{u}) \right] \tag{5.21}$$

Equation (5.20) and its boundary condition are easily linearized by assuming that the gas is at rest and that the fluctuations are all of the same order. To second order in the fluctuations we find

$$\frac{\partial^2 p'}{\partial t^2} - a_0^2 \nabla^2 p' = \left\{ p_0 \nabla \cdot (\mathbf{u}' \cdot \nabla \mathbf{u}') - \gamma \frac{\partial p'}{\partial t} \nabla \cdot \mathbf{u}' - \frac{\partial}{\partial t} (\mathbf{u}' \cdot \nabla p') \right\}$$
$$+ \rho_0 \left\{ (\gamma - 1) \left(\frac{p'}{p_0} \right) \nabla^2 \left(\frac{p'}{p_0} \right) - \left(\nabla \frac{p'}{p_0} \right)^2 \right\} \tag{5.22}$$

$$\hat{\mathbf{n}} \cdot \nabla p' = -\rho_0 \frac{\partial \mathbf{u}'}{\partial t} \cdot \hat{\mathbf{n}} - \rho_0 \left\{ \frac{1}{\gamma} \left(\frac{p'}{p_0} \right) \frac{\partial \mathbf{u}'}{\partial t} \cdot \hat{\mathbf{n}} + \hat{\mathbf{n}} \cdot (\mathbf{u}' \cdot \nabla \mathbf{u}') \right\} \tag{5.23}$$

Equations (5.4) a,b are recovered when the second order terms are neglected.

5.1.1. *The Velocity Potential.* It is often convenient to introduce scalar and vector potentials Φ and $\mathbf{A}$ from which the velocity is found by differentiation:

$$\mathbf{u} = -\nabla \Phi + \nabla \times \mathbf{A} \tag{5.24}$$

With this representation, the dilation and curl (rotation) of the velocity field are separated:

$$\nabla \cdot \mathbf{u}' = -\nabla^2 \Phi \; ; \quad \nabla \times \mathbf{u}' = \nabla \times \nabla \times \mathbf{A} \tag{5.24}$$

In general, both potentials are required if the mean velocity is non-zero or sources are present in the flow. The boundary conditions may also induce non-zero rotational flow. Here only the scalar potential is required for small amplitude motions because in that limit, the classical acoustic momentum is (5.5); taking the curl with uniform average density gives

$$\bar{\rho} \frac{\partial}{\partial t} (\nabla \times \mathbf{u}') = -\nabla \times (\nabla p') = 0$$

Hence if $\nabla \times \mathbf{u}' = 0$ initially, it remains so and we can take $\mathbf{A} = 0$.

The acoustic equations for momentum, 3.40 and 3.40 in dimensional variables are

$$\frac{\partial \mathbf{u}'}{\partial t} + \frac{1}{\bar{\rho}} \nabla p' = 0$$
$$\frac{\partial p'}{\partial t} + \gamma \bar{\rho} \nabla \cdot \mathbf{u}' = 0 \tag{5.25 a,b}$$

Differentiate the first with respect to time and insert the second to give the wave equation for the velocity fluctuation,

$$\frac{\partial^2 \mathbf{u}'}{\partial^2} - \bar{a}^2 \nabla^2 \mathbf{u} = 0 \tag{5.26}$$

Now substitute $\mathbf{u}' = -\nabla\Phi$ to give

$$\nabla \left[\frac{\partial^2 \Phi}{\partial t^2} - \bar{a}^2 \nabla^2 \Phi \right] = 0$$

which is satisfied if the terms in brackets are a function of time only, so

$$\frac{\partial^2 \Phi}{\partial t^2} - \bar{a}^2 \nabla^2 \Phi = f(t) \tag{5.27}$$

The right-hand side represents a source field for the potential, uniform over all space. We may absorb $f(t)$ by defining a new potential $\Phi_1 = \Phi + \int^t dt' \int^{t'} f(t_1) dt_1$ and relabel $\Phi_1 \to \Phi$ to find[13] the wave equation for Φ:

$$\frac{\partial^2 \Phi}{\partial t^2} - \bar{a}^2 \nabla^2 \Phi = 0 \tag{5.28}$$

When the velocity potential is used, the acoustic velocity is calculated with (5.24) and $\mathbf{A} = 0$

$$\mathbf{u}' = -\nabla\Phi \tag{5.29}$$

The acoustic pressure is found by setting $\mathbf{u}' = -\nabla\Phi$ in the momentum equation (5.25) a,b, giving

$$\nabla \left(-\frac{\partial \Phi}{\partial t} + \frac{1}{\bar{\rho}} p' \right) = 0$$

This solution is satisfied if the terms in parentheses are a function of t only, $g(t)$, so

$$p' = \bar{\rho} \left(\frac{\partial \Phi}{\partial t} + g(t) \right) \tag{5.30}$$

As above, we may define a new potential $\Phi(t) + \int^t g(t') dt' = \Phi_1(t)$ and hence absorb $g(t)$ so we may redefine $\Phi_1 \to \Phi$ and

$$p' = \bar{\rho} \frac{\partial \Phi}{\partial t} \tag{5.31}$$

The conditions under which the acoustic field can be completely described by a velocity potential alone are precise and, so far as problems involving combustion are concerned, very restrictive. Any analysis or theory based on the velocity potential alone must also include demonstration that the vector potential can be ignored, i.e. set equal to a constant or zero. In general, the presence of a non-uniform mean flow field and various kinds of sources in the problems we are concerned with in this work, require that the velocity field be derived from both scalar and vector potentials. Use of the unsteady pressure as the primary flow variable provides a simpler approach for many purposes, but, as we will find later, apparently possesses unavoidable fundamental limitations.

5.2. Energy and Intensity Associated with Acoustic Waves. In this section we establish definitions of energy density and the intensity—i.e. the flow of energy—for classical acoustic waves. The definitions are only approximate under the more complicated conditions existing in a combustor but the general ideas remain.

Following Landau and Lifschitz (1959) we return to the basic energy equation (5.9) for inviscid flow. The idea is to establish a connection between the rate of change of something (the energy) within a volume and the flow of something (the intensity) through the closed boundary of that volume. Integrate the energy equation over a volume fixed in space; and apply Gauss' theorem to the terms on the right-hand side:

$$\frac{\partial}{\partial t} \int \rho \left(e + \frac{u^2}{2} \right) dV = - \int \nabla \cdot \left[\rho \mathbf{u} \left(e + \frac{u^2}{2} \right) \right] dV - \int \nabla \cdot (\rho \mathbf{u}) \, dV$$

$$= - \oiint \left(e + \frac{u^2}{2} \right) \rho \mathbf{u} \cdot d\mathbf{S} - \oiint \rho \mathbf{u} \cdot d\mathbf{S}$$

---

[13] Alternatively, one can reason that when the velocity is found by taking the gradient of $\Phi + \iint f$, the term in f contributes nothing and hence can be simply dropped. The desired solution is unaffected by setting $f = 0$.

This relation must be written to second order in the isentropic fluctuations; for example,

$$\rho e = \bar{\rho}\bar{e} + \rho'\left[\frac{\partial}{\partial\rho}(\rho e)\right]_{\bar{\rho}} + \frac{1}{2}\rho'^2\left[\frac{\partial^2(\rho e)}{\partial\rho^2}\right]_{\bar{\rho}\bar{e}} + \dots$$

$$= \bar{\rho}\bar{e} + \rho'\bar{k} + \frac{1}{2}\frac{\rho'^2}{\bar{\rho}\bar{a}^2} + \dots$$

Eventually the result is

$$\frac{\partial}{\partial t}\int \mathcal{E}\,dV = -\oiint \mathcal{E}\mathbf{u}\cdot d\mathbf{S} - \oiint p'\mathbf{u}'\cdot d\mathbf{S} \tag{5.32}$$

where

$$\mathcal{E} = \frac{1}{2}\frac{p'^2}{\bar{\rho}\bar{a}^2} + \frac{1}{2}\bar{\rho}u'^2 \tag{5.33}$$

is the acoustic energy per unit volume and $p'\mathbf{u}'$ is the **intensity**, the flux of acoustic energy through an area normal to the direction of propagation (energy/area-S).

The first term on the right-hand side of (5.32) is third order in the fluctuations and must be dropped. Hence we have the important result interpreted in Figure 5.1.

$$\frac{\partial\mathcal{E}}{\partial t} + \nabla\cdot(p'\mathbf{u}') = 0$$
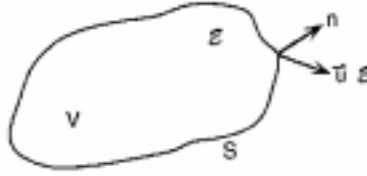
FIGURE 5.1. Acoustic Energy and Intensity

Table 5.1 summarizes the basic properties of plane sinusoidal waves. Brackets $\langle\ \rangle$ denote time averages over some interval τ

$$\langle(\ )\rangle = \frac{1}{\tau}\int_T^{t+\tau}(\ )\,dt' \tag{5.34}$$

5.3. The Growth or Decay Constant. In practice, due to natural dissipative processes, freely propagating waves and oscillations in a chamber will decay in space and time if there is no external source or energy. If there is an internal source of energy, waves may be unstable, having amplitudes increasing in time. The basic measure of the growth or decay of waves is the constant appearing in the exponent describing the sinusoidal spatial and temporal dependence of small amplitude waves, the definitions (5.62). For 'standing' or 'stationary' waves in a chamber, the wavelength, and hence wavenumber, is real and constant, but the frequency is complex:

$$\omega \to \omega + i\alpha \tag{5.35}$$

and the variables of the motion have the behavior in time

$$e^{-i(\omega+i\alpha)t} \equiv e^{-i\omega t}e^{\alpha t} \tag{5.36}$$

For this definition (5.34), $\alpha < 0$ means that the waves decay.

Normally in practice, $\left|\frac{\alpha}{\omega}\right| \ll 1$, implying that the fractional change of amplitude is small in one cycle of the oscillation. Thus when time averaging is carried out over one or a few cycles, $e^{\alpha t}$ may be taken as roughly constant, and the average energy density computed with (5.32) and (5.33), is

$$\langle\mathcal{E}\rangle = e^{2\alpha t}\frac{1}{4}\left[\frac{|\hat{p}|^2}{\bar{\rho}\bar{a}^2} + \bar{\rho}|\hat{u}|^2\right] \tag{5.37}$$

<div align="center">

TABLE 5.1.

Results for Rightward and Leftward Traveling Sinusoidal Waves

</div>

Wave to Right	Wave to Left
$p'_+ = \hat{p}_+ e^{-i(\omega t - kx)}$	$p'_- = \hat{p}_- e^{-i(\omega t + kx)}$
$u'_+ = \hat{p}_+ e^{-i(\omega t - kx)}$	$u'_- = \hat{u}_- e^{-i(\omega t + kx)}$
$\hat{u}_+ = \dfrac{\hat{p}_+}{\rho_0 a_0}$	$\hat{u}_- = -\dfrac{\hat{p}_-}{\rho_0 a_0}$
$\varepsilon_+ = \dfrac{p'^2_+}{\rho_0 a_0}$	$\varepsilon_- = \dfrac{p'^2_-}{\rho_0 a_0}$
$l_+ = p'_+ u'_+ = \dfrac{p'^2_+}{\rho_0 a_0}$	$l_- = p'_- u'_- = -\dfrac{p'^2_-}{\rho_0 a_0^2}$

$$\langle (\quad) \rangle = \frac{1}{\tau} \int_t^{t+\tau} (\quad) dt'$$

$\langle p'^2_+ \rangle = \frac{1}{2}\hat{p}^2_+$	$\langle p'^2_- \rangle = \frac{1}{2}\hat{p}^2_-$
$\langle \varepsilon_+ \rangle = \dfrac{\hat{p}^2_+}{2\rho_0 a_0^2}$	$\langle \varepsilon_- \rangle = \dfrac{\hat{p}^2_-}{2\rho_0 a_0^2}$
$\langle l_+ \rangle = \dfrac{\hat{p}^2_+}{2\rho_0 a_0}$	$\langle l_- \rangle = \dfrac{\hat{p}^2_-}{2\rho_0 a_0}$

More generally: $\quad p' = \hat{p} e^{i(\omega t + \varphi)}$; $\qquad \bar{u}' = \hat{\mathbf{u}} e^{i(\omega t + \varphi)}$

$$\langle \varepsilon \rangle = \frac{1}{4}\left[\frac{|\hat{p}|^2}{\rho_0 a_0^2} + \rho_0 |\hat{u}|^2 \right] = \frac{1}{4}(p'p'^* + \rho_0 \mathbf{u}' \cdot \mathbf{u}'^*)$$

$$\langle l \rangle = \frac{1}{2}|\hat{p}||\hat{\mathbf{u}}|\cos(\varphi - \psi) = \frac{1}{4}(p'^*\mathbf{u}' + p'\mathbf{u}'^*)$$

where ( )* denotes complex conjugate.

Hence we have the important interpretations which serve as the basis for measuring values of α:

$$\alpha = \frac{1}{|\hat{p}|}\frac{d|\hat{p}|}{dt}$$
$$\alpha = \frac{1}{2\langle \mathcal{E} \rangle}\frac{d\langle \mathcal{E} \rangle}{dt}$$

(5.38) a,b

The sign of α is a matter of definition and has no fundamental significance. If the time dependence is taken to be $e^{i(\omega + i\alpha)t}$ then $\alpha < 0$ means that waves are amplified.

The formulas (5.39) define local values of the growth constant. It is often more meaningful to know the value for the entire volume of the system in question, found by using $\int \langle \mathcal{E} \rangle dV$ rather than $\langle \mathcal{E} \rangle$:

$$\alpha = \frac{1}{2\int \langle \mathcal{E} \rangle dV}\frac{d}{dt}\int \langle \mathcal{E} \rangle dV \tag{5.39}$$

5.4. Boundary Conditions: Reflections from a Surface. In the absence of other sources, the linearized boundary condition on the pressure at a surface is the first term of (5.1 b), here in dimensional form:

$$\hat{\mathbf{n}} \cdot \nabla p' = -\bar{\rho}\frac{\partial \mathbf{u}'}{\partial t} \cdot \hat{\mathbf{n}} \tag{5.40}$$

The acoustic surface impedance z_a is defined by

$$\mathbf{u}' \cdot \hat{\mathbf{n}} = \frac{1}{z_a} p' \tag{5.41}$$

and the acoustic surface admittance y_a is the reciprocal of the admittance:

$$y_a = \frac{1}{z_a} \tag{5.42}$$

Then for harmonic motions, $p' = \hat{p} e^{-i\omega t}$, we can rewrite (5.40) as

$$\hat{\mathbf{n}} \cdot \nabla p' = -i \frac{\bar{\rho}\omega}{z_a} p' = -i\bar{\rho}\omega y_a p' \tag{5.43}$$

The units of impedance are (pressure/velocity) $\equiv$ (density $\times$ velocity). Hence for the medium, the product $\bar{\rho}\bar{a}$ is called the characteristic impedance, having value 42 g/cm^2-s. at standard conditions. Dimensionless forms are defined as:

$$\begin{aligned} \text{acoustic impedance ratio:} \quad & \zeta_a = \frac{z_a}{\bar{\rho}\bar{a}} \\ \text{acoustic admittance ratio:} \quad & \eta_a = \frac{1}{\zeta_a} \end{aligned} \tag{5.44}$$

In general, impedance functions are complex; the real and imaginary parts are called:

$$\begin{aligned} Re(z_a): \quad & \text{acoustic resistance} \\ Im(z_a): \quad & \text{acoustic reactance} \end{aligned} \tag{5.45}$$

From (5.41) and (5.42), the surface admittance is

$$y_a = \frac{\mathbf{u} \cdot \hat{\mathbf{n}}}{p'}$$

and the dimensionless surface admittance ratio is

$$\eta_a = \bar{\rho}\bar{a} y_a = \frac{\bar{\rho}\bar{a}^2}{\bar{p}} \frac{\bar{\mathbf{M}}' \cdot \hat{\mathbf{n}}}{p'/\bar{p}} = \gamma \frac{M_n'}{p'/\bar{p}} \tag{5.46}$$

where M_n' is the fluctuation of the Mach number normal to the surface.

If the surface is impermeable, the velocity at the surface is the velocity of the surface itself. However, if the surface is permeable, or, as for a burning propellant, mass departs the surface, then the impedance and admittance functions are defined in terms of the local velocity fluctuations presented[14] to the acoustic field, no matter what their origin.

Quite generally then, the admittance function represents the physical response of processes at the surface. It is of course an assumption that in response to an impressed pressure fluctuation, the fluctuation of velocity normal to the surface is proportional to the pressure change. Alternative definitions of quantities representing the acoustic boundary condition at a surface will arise when we consider special situations.

5.4.1. *Reflections of Plane Waves at a Surface.* Confinement of waves in a chamber to form modes necessarily involves reflections at the boundary surfaces. In solid propellant rockets the processes causing reflection are complicated, being responsible not only for confining the waves but also are the dominant means for transferring energy to the oscillating field in the chamber. Even at inert surfaces, more than the simple process of reflection is involved. Viscous stresses and heat conduction in the region adjacent to a surface cause dissipation of energy, discussed in Section 5.6.

Here we assume that all activity at the surface can be represented by a complex impedance or admittance function. The calculation follows that discussed by Morse and Ingard (1968). We consider reflection of a planar wave, Figure 5.2, allowing for the possibility of unequal angles of incidence and reflection, and for simplicity we

---

[14]For burning propellants, care must be taken with definition of the surface at which the boundary condition is imposed. Usually the velocity at the 'edge' of the combustion zone in the gas phase is the most convenient choice. Thus the admittance presented to the acoustic field is not that at the burning surface itself.

assume that there is no transmitted wave. The incident wave travels in the direction defined by the unit vector $\hat{\mathbf{k}}_i$ and the wavenumber vector is

$$\mathbf{k} = \frac{2\pi}{\lambda}\hat{\mathbf{k}} \tag{5.47}$$

We can represent the acoustic pressure and velocity in this plane wave by
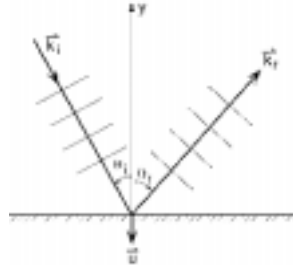
FIGURE 5.2. Reflection of a Plane Wave. Plane waves propagating in direction $\mathbf{k} = \frac{2\pi}{\lambda}\hat{\mathbf{k}}$

$$p'(\mathbf{r};t) = g_i(\mathbf{k}_i \cdot \mathbf{r} - \omega t)$$
$$\mathbf{u}'(\mathbf{r};t) = \frac{\hat{k}_r}{\bar{\rho}\bar{a}}g_i(\mathbf{k}_i \cdot \mathbf{r} - \omega t) \tag{5.48 a,b}$$

Similar formulas hold for the reflected wave with $\mathbf{k}_i$ replaced by $\mathbf{k}_r$ lying in the direction defined by the unit vector $\hat{\mathbf{k}}_r$. The representations are therefore:

Incident Wave		**Reflected Wave**	
p'_i	$= u_i(\xi_i)$	p'_r	$= g_r(\xi_r)$
$\mathbf{u}'_i$	$= \hat{\mathbf{k}}_i \frac{1}{\bar{\rho}\bar{a}}g_i(\xi_i)$	$\mathbf{u}'_r$	$= \hat{\mathbf{k}}_r \frac{1}{\bar{\rho}\bar{a}}g_r(\xi_r)$
ξ_i	$= \mathbf{k}_i \cdot \mathbf{r} - \omega t$	ξ_r	$= \mathbf{k}_r \cdot \mathbf{r} - \omega t$
	$= k(x\sin\theta_i - y\cos\theta_i) - \omega t$		$= k(x\sin\theta_r - y\cos\theta_r) - \omega t$

Because the frequency is the same for the incident and reflected waves, so are the magnitudes of the wavenumbers:

$$|\mathbf{k}_i| = \frac{\omega}{\bar{a}} = |\mathbf{k}_r| \tag{5.49}$$

Reflection is assumed to occur at $y = 0$. By definition of z_a, the surface impedance, with the normal velocity outward from the surface equal to $u_y = \mathbf{u} \cdot \hat{\mathbf{j}} = -\mathbf{u} \cdot \hat{\mathbf{n}}$ where $\hat{\mathbf{n}}$ is the unit outward normal vector:

$$z_a = \left(\frac{p'}{u'_y}\right)_{y=0} = \bar{\rho}\bar{a}\frac{g_i(kx\sin\theta_i - \omega t) + g_r(kx\sin\theta_r - \omega t)}{\cos\theta_i g_i(kx\sin\theta_i - \omega t) - \cos\theta_r g_r(kx\sin\theta_r - \omega t)} \tag{5.50}$$

In general z_a is variable along the surface. Suppose that in fact z_a is constant, independent of x. That can be true if

$$\theta_i = \theta_r = \theta$$
$$g_r(\xi) = \beta g_i(\xi) \tag{5.51}$$

Then (5.50) becomes

$$z_a \cos\theta = \bar{\rho}\bar{a}\frac{1+\beta}{1-\beta} \tag{5.52}$$

and the complex reflection coefficient β is related to the surface impedance by

$$\beta = \frac{z_a \cos\theta - \bar{\rho}\bar{a}}{z_a \cos\theta + \bar{\rho}\bar{a}} \tag{5.53}$$

This result is special because no transmitted wave has been accounted for. For example, if $z_a = \bar{\rho}\bar{a}$—perfect impedance matching exists at the interface—(5.52) gives $\beta = 0$ when $\theta = 0$, so there is no reflected wave. That is true in one sense because in physical terms $z_a = \bar{\rho}\bar{a}$ means that the same gas exists in both sides of the interface. Thus we are simply describing wave propagation in a continuous medium. On the other hand, the physical picture treated here accommodates no transmitted wave, which means that when there is no reflection, processes must exist at the interface providing perfect absorption.

Now suppose $\theta \neq 0$ but $z_a = \bar{\rho}\bar{a}$. Then (5.52) gives β non-zero, i.e. partial absorption and some of the incident wave is reflected.

5.5. Wave Propagation in Tubes; Normal Modes. The simplest form of combustor is a straight tube, having generally non-uniform cross-section and not necessarily axisymmetric. Although the changes of cross-section may be abrupt—even discontinuous—experience has shown that good results may be obtained by assuming that the velocity fluctuations are uniform at every section and parallel to the axis: the flow is treated as one-dimensional. The governing equations are given in Appendix B, equations (B.2)–(B.4) with no sources:

$$Conservation\ of\ Mass: \qquad \frac{\partial\rho'}{\partial t} + \frac{\partial}{\partial x}(\bar{\rho}u'S_c) = 0 \tag{5.54}$$

$$Conservation\ of\ Momentum: \qquad \bar{\rho}\frac{\partial u'}{\partial t} + \frac{\partial p'}{\partial x} = 0 \tag{5.55}$$

$$Conservation\ of\ Energy: \qquad \bar{\rho}C_v\frac{\partial T'}{\partial t} + \bar{p}\frac{1}{S_c}\frac{\partial}{\partial x}(u'S_c) = 0 \tag{5.56}$$

The wave equation for the pressure is:

$$\frac{1}{S_c}\frac{\partial}{\partial x}\left(S_c\frac{\partial p'}{\partial x}\right) - \frac{1}{\bar{a}^2}\frac{\partial^2 p'}{\partial t^2} = 0 \tag{5.57}$$

5.5.1. *Waves in Tubes.*

(a) Normal Modes for a Tube Closed at Both Ends

Results for a tube closed at both ends not only contain many ideas basic to general oscillations in chambers, but also are widely useful for practical applications. For a tube closed by rigid walls, the boundary conditions at the ends are that the velocity must vanish. The momentum equation (5.54) then states that acceleration and therefore the pressure gradient must vanish at the ends for all time:

$$\frac{\partial p'}{\partial x} = 0 \qquad x = 0, L; \quad \text{all } t \tag{5.58}$$

General linear motions within the tube can be constructed as superpositions of *normal modes* defined in general by two properties:

(i) sinusoidal variations in time

(ii) the motion at any point bears always a fixed phase relation with that at any other point in the volume

Those conditions imply here that the pressure can be expressed as

$$p'(x;t) = \hat{p}(x)e^{-i\bar{a}kt} \tag{5.59}$$

where k is the complex wavenumber, related in general to the complex frequency by the formula

$$\bar{a}k = \omega + i\alpha \tag{5.60}$$

Because there are no dissipative processes in this problem, $\alpha = 0$ so the wavenumber is real. Substitution of (5.59) in (5.57) with S independent of x gives

$$\frac{d^2\hat{p}}{dx^2} + k^2\hat{p} = 0 \tag{5.61}$$

A solution to (5.61) satisfying (5.58) at $x = 0$ is $\hat{p} = A\cos kx$. To satisfy the condition at $x = L$, $\cos kL = 0$. Then k can assume only certain values k_l, called *characteristic* or *eigen* values:[15]

$$k_l = l\frac{\pi}{L} \qquad (l = 0, 1, 2, \cdots) \tag{5.62}$$

Corresponding to each k_l is a *characteristic function,* or *eigenfunction,*

$$\frac{\hat{p}_l}{\bar{p}_0} = A_l \cos(k_l x) \tag{5.63}$$

For the problems we treat in this book, the motions represented by the k_l, $\hat{p}_l$, and $\hat{u}_l$ are usually called *normal modes*, $\bar{a}k_l = \omega_l$ being the *normal* or *modal frequency*, and $\hat{p}_l$, $\hat{u}_l$ are the *mode shapes* of pressure and velocity. All of these terms are used for two- and three-dimensional motions as well.

A normal mode is characterized by its frequency and the spatial distributions, or 'shapes' of all dependent variables. The mode shape for the velocity is derived from the mode shape (5.63) by integrating the acoustic momentum equation (5.55) written for $\hat{u}_l$:

$$-i\bar{a}k_l\hat{u}_l = -\frac{1}{\bar{\rho}}\frac{d\hat{p}_l}{dx} = \frac{k_l}{\bar{\rho}}\bar{p}_l A_l \sin k_l x$$

Thus

$$\hat{u}_l = i\frac{\bar{p}_l}{\bar{\rho}\bar{a}}A_l \sin k_l x \tag{5.64}$$

or, written as the Mach number of the mode,

$$\hat{M}_l = i\frac{1}{\gamma}A_l \sin k_l x \tag{5.65}$$

(b) Normal Modes for a Tube Open at Both Ends

In this case, the pressure is assumed fixed at the ends, for example because the tube is immersed in a large reservoir having constant pressure, and $p' = 0$. For isentropic motions, $\frac{\rho'}{\bar{\rho}} = \frac{1}{\gamma}\frac{p'}{\bar{p}}$ so $\rho' = \frac{1}{\bar{a}^2}p'$ and the continuity equation (5.54) is

$$\frac{\partial p'}{\partial t} + \frac{\bar{a}^2}{\bar{\rho}}\frac{\partial u'}{\partial x} = 0 \tag{5.66}$$

Hence if p' is fixed, the velocity gradient must vanish at the ends. Set $p' = Ae^{-i\bar{a}kt}\sin kx$ and substitute in (5.66)

$$i\frac{\bar{a}}{\bar{p}}kAe^{-i\bar{a}kt}\sin kx = -\frac{\bar{a}^2}{\bar{\rho}}\frac{\partial u'}{\partial x}$$

---

[15]Only for $l \geq 1$ do we find wave modes. For $l = 0$, a qualitatively different mode exists for which the pressure is uniform in the volume but pulsates at a frequency well below that for the fundamental wave mode. The velocity is practically zero and the oscillator is sustained by some sort of external action. A prosaic example is the low frequency sound one can create by blowing across the narrow opening at the neck of a bottle. In this case the mode is called the *Helmholtz mode* and the bottle is behaving as a *Helmholtz resonator.*

The left-hand side vanishes (and hence $\partial u'/\partial x = 0$) at $x = 0$ for any k, but at $x = L$, we must have $\sin k_l L = 0$. Hence $k_l = (2l+1)\frac{\pi}{L}$ and the normal mode shape and frequency are

$$\frac{\hat{p}_l}{\bar{p}} = A_l \sin(k_l x) \quad ; \qquad k_l = l\frac{\pi}{L} \quad (l = 1, 2, \cdots) \tag{5.67}$$

and the mode shape for the velocity is

$$\frac{\hat{u}_l}{\bar{a}} = \hat{M}_l = i\frac{1}{\gamma} A_l \cos k_l x \tag{5.68}$$

(c) Normal Modes for a Tube Closed at One End and Open at the Other

Reasoning similar to the above leads in this case to the normal modes when the tube is closed at $x = 0$:

$$\frac{\hat{p}_l}{\bar{p}} = A_l \cos(k_l x) \quad ; \qquad \left(k_l = (2l+1)\frac{\pi}{2L} \right) \quad (l = 1, 2, \cdots)$$
$$\frac{\hat{u}_l}{a} = -i\frac{1}{\gamma} A_l \sin(k_l x)$$

5.5.2. *Normal Modes for Tubes Having Discontinuities of Cross-Sectional Area.* Combustors having discontinuous area distributions are commonly used in solid propellant rockets and in various laboratory devices. Consider the example sketched in Figure 5.3. The boundary conditions at the ends are:

$$\begin{aligned} x = 0: \qquad & \frac{d\hat{p}}{dx} = 0 \\ x = \beta L: \qquad & \hat{p} = 0 \end{aligned} \tag{5.69 a,b}$$
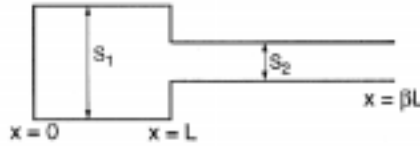
FIGURE 5.3. A Uniform Tube Having a Single Discontinuity.

Possible solutions in the regions to the left and right of the discontinuity are:

$$\begin{aligned} \frac{\hat{p}}{\bar{p}} &= A \cos kx \qquad (0 \le x \le L) \\ \frac{\hat{p}}{\bar{p}} &= B \sin k(\beta L - x) \qquad (L < x \le \beta L) \end{aligned} \tag{5.70 a,b}$$

Note that $k = \omega/\bar{a}$ is the same throughout the tube because the motion occurs everywhere at the same frequency.

Completing the problem comes down to determining the conditions for matching the solutions. Two are required:

(i) continuity of pressure:

$$\lim_{\varepsilon \to 0} [\hat{p}(L - \varepsilon) - \hat{p}(L + \varepsilon)] = 0$$

which gives

$$A \cos kL = B \sin(\beta - 1)kL \tag{5.71}$$

(ii) continuity of acoustic mass flow:

Integrate the wave equation (for harmonic motions) across the discontinuity,

$$\int_{L-\varepsilon}^{L+\varepsilon} \left[\frac{d}{dx}(S_c \frac{d\hat{p}}{dx} + k^2 S_c \hat{p} \right] dx = 0$$

Because $\hat{p}$ is continuous, this relation becomes

$$\lim_{\varepsilon \to 0} \left[\left(S_c \frac{d\hat{p}}{dx} \right)_{L+\varepsilon} - \left(\frac{d\hat{p}}{dx} \right)_{L-\varepsilon} \right] = 0$$

Thus, with $\bar{\rho}$ constant and $\frac{d\hat{p}}{dx} \sim \hat{u}$:

$$(\bar{\rho} S_c \hat{u})_{L+\varepsilon} - (\bar{\rho} S_c \hat{u})_{L-\varepsilon} \tag{5.72}$$

After substituting the waveforms (5.70) a,b, and using (5.71) we find the transcendental equation for the modal wavenumbers:

$$\frac{S_1}{S_2} \tan k_l L = \cot k_l (\beta - 1) L \tag{5.73}$$

This method of solving a problem with discontinuities is only approximate: a practical question is: how large are the errors? To gain some idea of the errors incurred, tests at ambient temperature ('cold flow tests') were carried out by Mathis, Derr and Culick (1973) for the geometry of a T-burner used for measuring the combustion response of burning solid propellants. Results are shown in Figure 5.4. The measured values of both the frequencies and the mode shapes are surprisingly well-predicted by this theory. The principal reason is that the influence of a discontinuity is confined to a relatively small region near the change of area, but the characteristics of the normal modes depend on the motion in the entire volume.
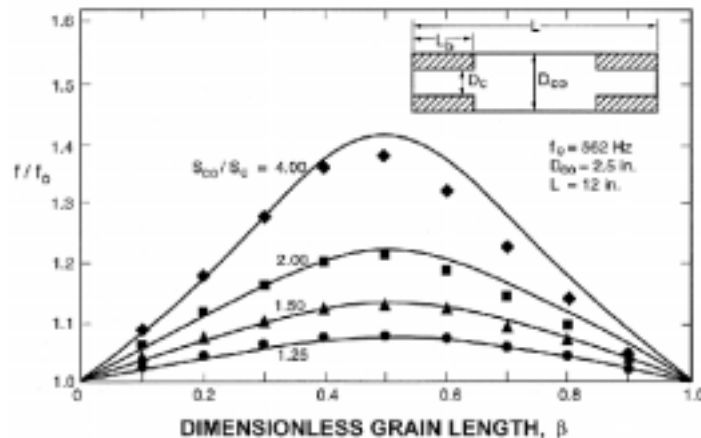
FIGURE 5.4. Comparison of Experimental and Theoretical Results for Normal Frequencies in a T-Burner (Ambient Temperature)

5.6. Normal Acoustic Modes and Frequencies for a Chamber. We now consider a volume of any shape enclosed by a rigid boundary and containing a uniform gas at rest. Unsteady small amplitude motions therefore satisfy the linear wave equation (5.4) a,b and its boundary condition ((5.4) a,b)b requiring that the velocity normal to the boundary vanish at all times. By this definition given in Section 5.5.1, normal modes are solutions to this problem which oscillate sinusoidally in time and have fixed phase relations throughout the volume. We assume the form[16] $p' = \psi e^{-i\bar{a}kt}$. The formal problem is to find ψ satisfying the scalar wave equation, also called the Helmholtz wave equation, with vanishing normal gradient at the surface:

$$\nabla^2 \psi + k^2 \psi = 0$$
$$\hat{n} \cdot \nabla \psi = 0 \tag{5.74 a,b}$$

---

[16]Consistent with the general character of this problem, we replace $\hat{p}$ by ψ, introducing a common notation for normal modes. The velocity potential Φ satisfies the same pair of equations, a result reflected by equation (5.31) which for sinusoidal motions means that p' and Φ are proportional: $p' = i\bar{a}k\bar{\rho}\Phi$.

There are many well-written books covering this problem and its solution, for example Hildebrand (1952), Morse and Feshbach (1952), and Morse and Ingard (1968). The simplest approach is based on the method of separation of variables, applicable for closed form solutions in thirteen coordinate systems; see, e.g., Morse and Feshbach (1952). In practical applications to combustors, only rectangular and circular cylindrical chambers are important.

5.6.1. *Normal Modes for Rectangular Chambers.* The wave equation in Cartesian coordinates is

$$\frac{\partial^2 \psi}{\partial x^2} + \frac{\partial^2 \psi}{\partial y^2} + \frac{\partial^2 \psi}{\partial z^2} + k^2 \psi = 0$$

and $\hat{n} \cdot \nabla \psi$ must vanish on the six flat surfaces each perpendicular to a coordinated axis, Figure 5.5. Applying the method of separation of variables leads to a solution having the form

$$\psi = A \cos(k_x x) \cos(k_y y) \cos(k_z z) \tag{5.75}$$

and

$$k^2 = k_x^2 + k_y^2 + k_z^2 \tag{5.76}$$
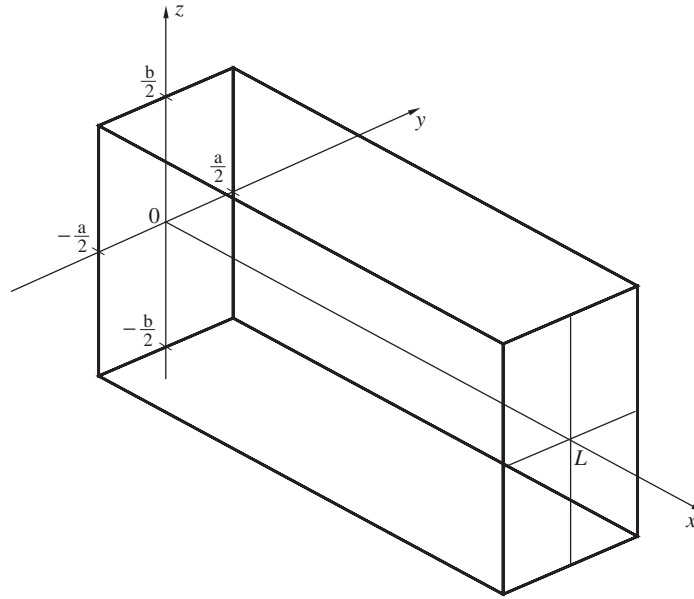
FIGURE 5.5. Rectangular Chamber

The boundary conditions must be satisfied:

$$\frac{\partial \psi}{\partial x} = 0 \qquad x = 0, L$$

$$\frac{\partial \psi}{\partial y} = 0 \qquad y = -\frac{a}{2}, \frac{a}{2} \tag{5.77 a,b,c}$$

$$\frac{\partial \psi}{\partial z} = 0 \qquad z = -\frac{b}{2}, \frac{b}{2}$$

Reasoning similar to that given in Section 5.5.1 leads to the values of the wavenumbers

$$k_x = l\frac{\pi}{L}$$

$$k_y = m\frac{\pi}{b} \tag{5.78 a,b,c}$$

$$k_z = n\frac{\pi}{c}$$

and the mode shapes are

$$\psi_{lmn} = A_{lmn} \cos\left(l\frac{\pi}{L}x\right) \cos m\frac{\pi}{a}\left(y + \frac{a}{2}\right) \cos n\frac{\pi}{b}\left(z + \frac{b}{2}\right) \tag{5.79}$$

The distributions of pressure therefore have the same form in all directions; of course the components (5.78) a,b,c can assume any of the allowed values, and the frequency is given by (5.76), $\omega = \bar{a}k$.

5.6.2. *Normal Modes for a Circular Cylindrical Chamber.* Let x be the polar axis (Figure 5.6) and the wave equation in circular cylindrical coordinates is

$$\frac{1}{r}\frac{\partial}{\partial r}\left(r\frac{\partial \psi}{\partial r}\right) + \frac{1}{r^2}\frac{\partial^2 \psi}{\partial \theta^2} + \frac{\partial^2 \psi}{\partial x^2} + k^2\psi = 0 \tag{5.80}$$
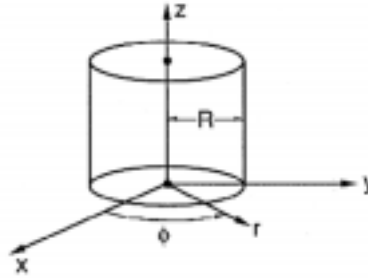
FIGURE 5.6. Circular Cylindrical Coordinates

The boundary condition requires that $\hat{n} \cdot \nabla \psi$ vanish at the ends and on the lateral boundary:

$$\begin{aligned} \frac{\partial \psi}{\partial x} &= 0 & x &= 0, L \\ \frac{\partial \psi}{\partial r} &= 0 & r &= R \end{aligned} \tag{5.81}$$

Application of the method of separation of variables leads to a solution of the form

$$\psi(r, x, \theta; t) = A \begin{Bmatrix} \cos n\theta \\ \sin n\theta \end{Bmatrix} \cos k_l z \, J_m\left(\kappa_{mn}\frac{r}{R}\right) \tag{5.82}$$

To satisfy the boundary conditions, the values of k_l are integral multiples of π/L as above and the κ_{mn} are the roots of the derivative of the Bessel function:

$$\frac{dJ_m(\kappa_{mn})}{dr} = 0 \tag{5.83}$$

Figure 5.7 shows the lowest six modes in the transverse planes, and the identifying values of n and m. More extended results are given in standard texts and collections of special functions.
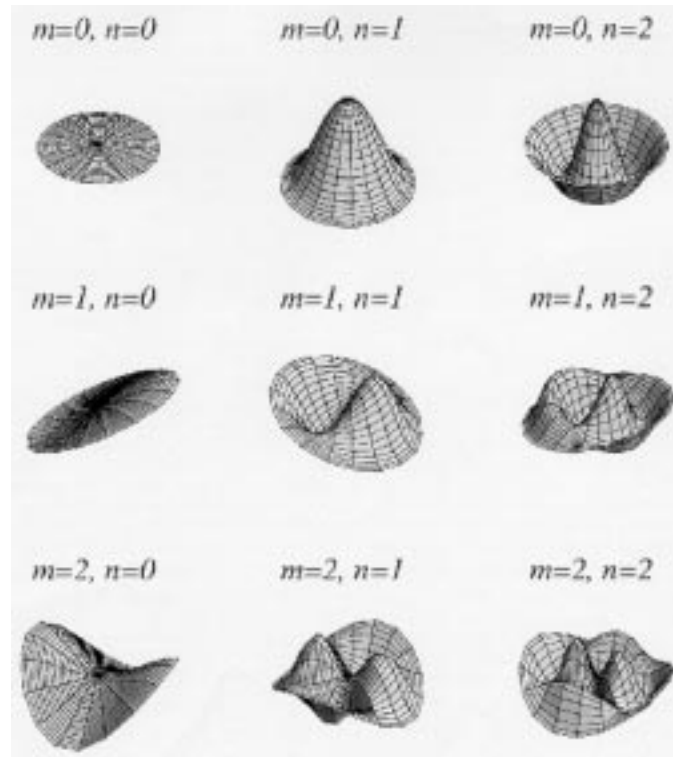
FIGURE 5.7. The First Six Transverse Modes in a Circular Cylinder

6. LINEAR STABILITY OF COMBUSTOR DYNAMICS

All problems of unsteady motion in combustion systems can be divided into the two classes: linearized and nonlinear. From the earliest discoveries of their transient behavior until the late 1950s 'combustion instabilities' implied small amplitude unsteady (and unwanted) motions growing out of a condition of linear instability. Even with the expanding awareness that the nonlinear properties must be understood as well, the linear behavior remains an essential part of understanding all aspects of combustion instabilities, including the consequences of nonlinear processes.

The literature of linear combustion instabilities contains many papers dealing with special problems. There seems often to be a tendency to regard the results as somehow disconnected. However, apparent differences arise chiefly from the differences in the processes accounted for and in the choices of models for those processes. So long as the problems are dominated by oscillating behavior in combustors, probably most, if not practically all of the results can be obtained in equivalent forms by suitable applications of the methods explained here. That statement is not as outrageous as it may seem, following as it does from the generality of the expansion procedures and the method of averaging covered in Section 4.

6.1. Solution for the Problem of Linear Stability.

By 'solution' we mean here formulas for calculating the amplitudes $\eta_n(t)$ of modes retained in the expansion for the pressure field, $p'(\mathbf{r}, t) = \bar{p} \Sigma \eta_n(t) \psi_n(\mathbf{r})$. The amplitudes satisfy the oscillator wave equations (4.36)

$$\frac{d^2\eta_n}{dt^2} + \omega_n^2 \eta_n = F_n + F_n^c \tag{6.1}$$

where F_n^c stands for the generalized 'force' associated with the exercise of control; and F_n is the spatial average of that part (sometimes called the 'projection' on the basis function ψ_n) of the internal processes affecting the motion of the nth oscillator, given by (4.32):

$$F_n = -\frac{\bar{a}^2}{\bar{p}E_n^2} \left\{ \int h\psi_n dV + \oiint f\psi_n dS \right\} \tag{6.2}$$

Here we ignore F_n^c because we are concerned only with the internal behavior of the system. In general, the F_n contain contributions associated with the motions of oscillators other than the nth—i.e. the modes are coupled. For analysis of linear stability we are justified in ignoring that coupling, for reasons given by Culick (1997). Each F_n is therefore a linear function of the amplitude and velocity of the oscillator, having the form

$$F_n = F_n^\eta \eta_n + F_n^{\dot{\eta}} \frac{d\eta_n}{dt} \tag{6.3}$$

where the F_n^η and $F_n^{\dot{\eta}}$ are constants, depending only on the mode.

With these assumptions, the oscillator equations (6.1) are the uncoupled set

$$\frac{d^2\eta_n}{dt^2} - F_n^{\dot{\eta}} \frac{d\eta_n}{dt} + \left(\omega_n^2 - F_n^\eta \right) \eta_n = 0 \tag{6.4}$$

Because the equations are uncoupled, the normal modes ψ_n for the corresponding classical acoustic problem are also the normal modes for the linear problem of combustor dynamics. The general problem of determining linear stability has therefore come down to the problem of determining the stability of the normal modes. In the usual fashion we assume sinusoidal time dependence with complex frequency:

$$\eta_n(t) = \hat{\eta}_n e^{i\Omega t} \tag{6.5}$$

Equation ((5.4) a,b) gives the quadratic equation for Ω_n:

$$\Omega^2 - iF_n^{\dot{\eta}} \Omega + \left(\omega_n^2 - F_n^\eta \right) = 0 \tag{6.6}$$

with solution

$$\Omega = i\frac{1}{2}F_n^{\dot{\eta}} + \omega_n \sqrt{1 - \frac{1}{\omega_n^2}\left[F_n^\eta + \frac{1}{4}\left(F_n^{\dot{\eta}} \right)^2 \right]} \tag{6.7}$$

where we take the $(+)$ sign on the radical to give a positive real frequency. Hence the amplitudes are

$$\eta_n(t) = e^{\frac{1}{2}F_n^{\dot{\eta}}t}e^{-i\omega_n\sqrt{1-\zeta_n^2}\,t} \tag{6.8}$$

and

$$\zeta_n = \frac{1}{\omega_n}\sqrt{F_n^{\eta} + \frac{1}{4}\left(F_n^{\dot{\eta}}\right)^2} \tag{6.9}$$

The nth mode is stable of

$$F_n^{\dot{\eta}} < 0 \tag{6.10}$$

That is, the coefficient of $\dot{\eta}_n$ in the expression for F_n must be positive for the nth mode to be stable.

Now according to the methods of Fourier analysis, an arbitrary disturbance at some initial time (say $t = 0$) in the chamber can be synthesized of the normal modes. The time-evolution of the disturbance is therefore determined by the $\eta_n(t)$. In particular, an arbitrary disturbance in a combustor is stable if (and only if) all of the normal modes are stable and we arrive at the general result for the linear stability of a combustor:

(i) Write the linearized function for the force acting on the nth oscillator (spatially averaged acoustic mode) in the form

$$F_n = F_n^{\eta}\eta_n + F_n^{\dot{\eta}}\frac{d\eta_n}{dt}$$

(ii) Then any initial disturbance in a combustor is stable if and only if all the $F_n^{\dot{\eta}}$ are negative:

$$\text{Linear Stability} \iff F_n^{\dot{\eta}} < 0 \quad (\text{all } n)$$

The preceding calculation and its conclusion, illustrate further a point first made in Section 3. We have found a means of computing the linear stability of a combustor without knowing the linear motions themselves. The complex frequency (6.7) is in fact the frequency for the actual linear modes including the influences of all the processes accounted for. But calculation of the F_n^{η} and $F_n^{\dot{\eta}}$ with the formula (6.2) requires knowledge only of the unperturbed normal modes—their frequencies ω_n and shapes $\psi_n(\mathbf{r})$. The formal statement of this property is that the eigenvalues (Ω_n) to any order in the relevant expansion parameter (here $\bar{M}_r := \mu$) can be computed knowing the eigenfunctions (ψ_n) only to one less order. The eigenvalues Ω_n are here given to first order in the Mach number of the average flow but only the unperturbed classical eigenfunctions ψ_n are required. This is the basic characteristic of the expansion procedures with spatial averaging that makes the method devised here so useful in practice.

6.2. An Alternative Calculation of Linear Stability. An equivalent calculation of the result for linear stability makes direct use of the formula for the wavenumber. Write

$$\eta_n = \hat{\eta}_n e^{-i\bar{a}kt} \quad ; \qquad F_n = \hat{F}_n e^{-i\bar{a}kt}$$

and substitute in (6.1) with F_n^c ignored to find

$$(\bar{a}k)^2 = (\bar{a}k_n)^2 + \frac{1}{\hat{\eta}_n}\left(\hat{F}_n^{(r)} + i\hat{F}_n^{(i)}\right) \tag{6.11}$$

With $\bar{a}k = \omega + i\alpha$, this formula is

$$\omega^2 + i(2\alpha\omega) - \alpha^2 = \omega_n^2 + \frac{1}{\hat{\eta}_n}\left(\hat{F}_n^{(r)} + i\hat{F}_n^{(i)}\right)$$

where $(\quad)^{(r)}$ and $(\quad)^{(i)}$ stand for real and imaginary parts. Because α and $\hat{F}_n$ are of first order in the expansion parameter and terms of higher order must be dropped[17], we ignore α^2 with respect to ω^2. Then the real and imaginary parts of the last equation give

$$\omega^2 = \omega_n^2 + \frac{1}{\hat{\eta}_n}\hat{F}_n^{(r)}$$

$$\alpha = -\frac{1}{2\omega_n}\hat{F}_n^{(i)}$$

---

[17]Recall the remarks in Section 4.

where ω has been set equal to ω_n in the right-hand sides to ensure that higher order terms are not retained. Now take the square root of the first equation and again drop higher order terms to find

$$\omega = \omega_n - \frac{1}{2\omega_n}\frac{\hat{F}_n^{(r)}}{\hat{\eta}_n}$$
$$\alpha = -\frac{1}{2\omega_n}\frac{\hat{F}_n^{(i)}}{\hat{\eta}_n}$$

(6.12) a,b

The system is unstable if $\hat{F}_n^{(i)}$ is negative. This condition is essentially a generalized form of Rayleigh's criteria discussed further in Section 6.4.

After higher order terms are dropped from (6.7), the real and imaginary parts of ω are

$$\omega = \omega_n - \frac{1}{2\omega_n}F_n^{\eta}$$
$$\alpha = \frac{1}{2}F_n^{\dot{\eta}}$$

(6.14) a,b

Comparison of (6.12) a,b and 5.14 gives the connections between the two representations of the forcing function[18]:

$$F_n^{\eta} = \frac{\hat{F}_n^{(r)}}{\hat{\eta}_n}$$
$$F_n^{\dot{\eta}} = -\frac{1}{\omega_n}\frac{\hat{F}_n^{(i)}}{\hat{\eta}_n}$$

(6.15) a,b

Generally F_n will contain several processes, each of which will depend linearly on η_n and $\frac{d\eta_n}{dt}$ and appears additively in F_n. Hence formulas corresponding to (6.15) a,b apply to each of the individual processes. They are often useful, if only for checking correctness, in detailed calculations.

6.3. An Example: Linear Stability with Distributed Sources of Heat and Motion of the Boundary. As a first approximation to problems of combustion instabilities it is useful to ignore all processes involving interactions between the unsteady and steady fields, and focus attention on the two generic causes of instabilities: time-dependent energy addition and motions of the boundary. With suitable interpretation the second may represent the influence of unsteady combustion of a solid propellant. Then in dimensional variables the linearized pressure and momentum equations ((3.46) a-e)d and ((3.46) a-e)b, and the boundary condition (3.57) on the pressure fluctuations are

$$\frac{\partial p'}{\partial t} + \gamma\bar{p}\nabla\cdot\mathbf{u}' = \frac{R}{C_v}\dot{Q}'$$

(6.12)

$$\bar{\rho}\frac{\partial u'}{\partial t} + \nabla p' = 0$$

(6.13)

$$\hat{\mathbf{n}}\cdot\nabla p' = -\bar{\rho}\frac{\partial\mathbf{u}'}{\partial t}\cdot\hat{\mathbf{n}}$$

(6.14)

Now form the wave equation as in Section 3.4, so the problem is governed by the two equations

$$\nabla^2 p' - \frac{1}{\bar{a}^2}\frac{\partial^2 p'}{\partial t^2} = h$$
$$\hat{\mathbf{n}}\cdot\nabla p' = -f$$

(6.19) a,b

where

$$h = -\frac{1}{\bar{a}^2}\frac{R}{C_v}\frac{\partial\dot{Q}'}{\partial t}$$
$$f = -\bar{\rho}\frac{\partial\mathbf{u}'}{\partial t}\cdot\hat{\mathbf{n}}$$

(6.20) a,b

---

[18]The $(-)$ sign in (6.15) a,b arises from the $(-)$ sign in the exponential time dependence.

The expansion procedure and application of spatial averaging leads to the explicit oscillator equations (4.36):

$$\frac{d^2\eta_n}{dt^2} + \omega_n^2 \eta_n = -\frac{\bar{a}^2}{\bar{p}E_n^2}\left\{\int\left[-\frac{1}{\bar{a}^2}\frac{R}{C_v}\frac{\partial\dot{Q}'}{\partial t}\right]\psi_n\,dV + \iint\left[-\bar{\rho}\frac{\partial\mathbf{u}'}{\partial t}\cdot\hat{\mathbf{n}}\right]\psi_n\,dS\right\} \tag{6.21}$$
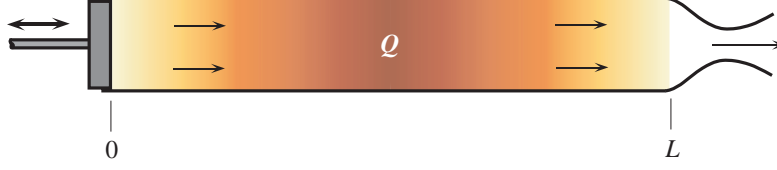
FIGURE 6.1. A Tube with Distributed Heat Addition and an Oscillating Piston to Drive Waves

As a simple example, consider the one-dimensional problem of waves excited in a tube fitted with a piston, Figure 6.1, and with distributed heat addition provided by an electrically heated coil. Only longitudinal modes are accounted for, and

$$\psi_n = \cos(k_n x) \quad , \qquad k_n = n\frac{\pi}{L} \quad , \qquad E_n^2 = \frac{1}{2}S_c L \tag{6.21}$$

where $S_c = \pi R^2$ is the cross-section area of the tube. We ignore any average motion in the tube, and suppose that the average thermodynamic properties are maintained constant and uniform by suitable steady heat losses through the walls of the tube. The heat addition and motion of the piston are sinusoidal, having phases ϕ_Q and ϕ_n with respect to pressure oscillations:

$$\dot{Q}' = \left|\hat{\dot{Q}}(x)\right|e^{-i(\bar{a}kt-\phi_Q)}$$
$$\mathbf{u}'_p\cdot\hat{\mathbf{n}} = |\hat{u}_p|\,e^{-i(\bar{a}kt-\phi_p)} \tag{6.22 a,b}$$

Hence for use in h and f:

$$\frac{\partial\dot{Q}'}{\partial t} = -i\bar{a}k\left|\hat{\dot{Q}}(x)\right|e^{-i(\bar{a}kt-\phi_Q)}$$
$$\frac{\partial}{\partial t}\left(\mathbf{u}'_p\cdot\hat{\mathbf{n}}\right) = -i\bar{a}k\,|\hat{u}_p|\,e^{-i(\bar{a}kt-\phi_u)} \tag{6.23 a,b}$$

With $\eta_n = \hat{\eta}_n e^{i\bar{a}kt}$, substitution in the oscillator equations (6.21) leads to

$$\left[-(\bar{a}k)^2 + \omega_n^2\right]\hat{\eta}_n = -\frac{\bar{a}^2}{\bar{p}E_n^2}\left\{-\frac{1}{\bar{a}^2}\frac{R}{C_v}(-i\bar{a}k)\int\cos(k_n x)\left|\hat{\dot{Q}}(x)\right|e^{i\phi_Q}dV\right.$$
$$\left.+i\bar{\rho}\bar{a}k\oiint\cos(k_n x)|\hat{u}_p|e^{i\phi_u}\right\}$$

After some rearrangement, and setting $\bar{a}k = \omega - i\alpha$, we find

$$(\omega+i\alpha)^2 = \omega_n^2 - i(\omega+i\alpha)\frac{\bar{a}^2}{\bar{p}(\frac{1}{2}S_c L)}\left\{\frac{1}{\bar{a}^2}\frac{R}{C_v}S_c\int_0^L\cos(k_n x)\frac{\left|\hat{\dot{Q}}(x)\right|}{\hat{\eta}_n}e^{i\phi_Q}dx\right.$$
$$\left.-\bar{\rho}S_c\frac{|\hat{u}_p|}{\hat{\eta}_n}e^{i\phi_p}\right\}$$

Because $|\hat{\dot{Q}}|$ and $|\hat{u}_p|$ are small perturbations we can write this equation to first order in small quantities:

$$\omega^2 - i(2\alpha\omega) = \omega_n^2 - i\omega_n\frac{2}{\bar{p}L}\frac{R}{C_v}\int_0^L\left[\cos(k_n x)\frac{\left|\hat{\dot{Q}}(x)\right|}{\hat{\eta}_n}e^{i\phi_p}dx + i\omega_n\frac{2\gamma}{L}\frac{|\hat{u}_p|}{\hat{\eta}_n}e^{i\phi_u}\right]dx$$

Take the real and imaginary parts to find

$$\omega^2 = \omega_n^2 + \frac{2\omega_n}{\bar{p}L}\left(\frac{R}{C_v}\right)\int_0^L\left[\cos(k_n x)\frac{\left|\hat{\dot{Q}}(x)\right|}{\hat{\eta}_n}\sin\phi_Q\,dx - \frac{2\gamma\omega_n}{L}\frac{|\hat{u}_p|}{\hat{\eta}_n}\sin\phi_u\right]dx$$

$$\alpha = \frac{1}{\bar{p}L}\frac{R}{C_v}\int_0^L\left[\cos(k_n x)\frac{\left|\hat{\dot{Q}}(x)\right|}{\hat{\eta}_n}\cos\phi_Q\,dx - \frac{\gamma}{L}\frac{|\hat{u}_p|}{\hat{\eta}_n}\cos\phi_u\right]dx$$

$$(6.24)\ \text{a,b}$$

Internal feedback, and hence a condition for instability, exists of either or both $|\hat{\dot{Q}}|$ and $|\hat{u}_p|$ depend on the fluctuating pressure (or velocity). For example, set

$$|\hat{\dot{Q}}| = q_0\hat{\eta}_n\psi_n = q_0\hat{\eta}_n\cos k_n x$$
$$|\hat{u}_p| = u_0\hat{\eta}_n$$

$$(6.25)\ \text{a,b}$$

and (6.24) a,b becomes

$$\omega^2 = \omega_n^2 + 2\omega_n\left(Aq_0\sin\phi_q - Bu_0\sin\phi_u\right)$$

where

$$A = \frac{1}{2\bar{p}}\frac{R}{C_v} \quad ; \qquad B = \frac{\gamma}{L}$$

$$(6.26)$$

To first order in small quantities we find the results for the frequency and decay or growth constant:

$$\omega = \omega_n + Aq_0\sin\phi_Q - Bu_0\sin\phi_u$$
$$\alpha = Aq_0\cos\phi_Q - Bu_0\cos\phi_u$$

$$(6.27)\ \text{a,b}$$

Remarks:

(i) the nth mode is unstable if $Aq_0\cos\phi_Q > Bu_0\cos\phi_u$

(ii) the first term in α is an example of Rayleigh's criterion discussed in Section 6.3:

  a) if $0 \le \phi_u \le \frac{\pi}{2}$ then a necessary condition for instability is $0 \le \phi_Q \le \frac{\pi}{2}$.

  b) instability of the nth mode is encouraged if $|\hat{\dot{Q}}(x)|\cos k_n x$ is larger,
  i.e. if the heat addition is greater where the mode shape of the pressure.

It is important also to notice that due to the spatial averaging, one cannot distinguish the ultimate effects of volumetric and surface processes. There is an equivalence of the influences of the various processes, their importance in respect to position within the chamber being dominated by their location with respect to the mode shapes. That characteristic has far-reaching consequences.

6.4. Rayleigh's Criterion and Linear Stability. As part of his research on the excitation of acoustic waves by heat addition in chambers, Lord Rayleigh (1878, 1945) formulated the following explanation for the production of tones in a Rijke tube:

> "If heat be periodically communicated to, and abstracted from, a mass of air vibrating (for example) in a cylinder bounded by a piston, the effect produced will depend upon the phase of the vibration at which the transfer of heat takes place. If heat be given to the air at the moment of greatest condensation, or be taken from it at the moment of greatest rarefaction, the vibration is encouraged. On the other hand, if heat be given at the moment of greatest rarefaction, or abstracted at the moment of greatest condensation, the vibration is discouraged."

That paragraph has become probably the most widely cited explanation for the presence of combustion instabilities generally. For easy reference, the explanation has long been referred to as "Rayleigh's Criterion."

It is important to realize that Rayleigh addressed only the conditions under which unsteady heat addition 'encourages' oscillations, i.e. is a destablilizing influence. Other processes, stabilizing or destabilizing are neither

excluded nor included, and there is certainly no implication that satisfaction of the criterion is either a necessary or a sufficient condition for instability to exist. Several published examples exist of quantitative realizations of the criterion (Putnam 1971; Chu 1956; Zinn 1986; Culick 1987, 1992). The purpose of this section is to establish a generalized form of Rayleigh's Criterion by using the analysis based on spatial averaging.

The main idea is that a positive change of the time-averaged energy of a modal oscillator in a cycle of oscillation is exactly equivalent to the principle of linear instability, that the growth constant should be positive for a motion to be unstable. To establish the connection we use the oscillator equations,

$$\frac{d^2\eta_n}{dt^2} + \omega_n^2\eta_n = F_n \tag{6.27}$$

The instantaneous energy[19] of the nth oscillator is

$$\mathcal{E}_n = \frac{1}{2}\left(\dot{\eta}_n^2 + \omega_n^2\eta_n^2\right) \tag{6.28}$$

and the change of energy in one cycle is the integral over one period of the rate at which work is done by the force F_n:

$$\Delta\mathcal{E}_n = \int_t^{t+\tau_n} F_n(t')\dot{\eta}_n(t')dt' \tag{6.29}$$

Under the integral, F_n and $\dot{\eta}_n$ must be real quantities: here we use the real parts of both functions,

$$\eta_n = \hat{\eta}_n e^{-i\bar{a}kt} = |\hat{\eta}_n|e^{-i\bar{a}kt}$$
$$F_n = \hat{F}_n e^{-i\bar{a}kt} = |\hat{F}_n|e^{-i(\bar{a}kt+\phi_F)} = |\hat{F}_n|\left(\cos\phi_F - i\sin\phi_F\right)e^{-i\bar{a}kt} \tag{6.31 a,b}$$

We measure all phases with respect to the pressure, so $\hat{\eta}_n$ is real and, being the maximum amplitude, is positive. Substitution in the oscillator equations gives

$$k^2 = \frac{1}{\bar{a}^2}\left(\omega_n^2 - \frac{\hat{F}_n}{\hat{\eta}_n}\right)$$

of which the real and imaginary parts are to first order in small quantities:

$$\omega^2 = \omega_n^2 - Re\left(\frac{\hat{F}_n}{\hat{\eta}_n}\right) = \omega_n^2 - \left|\frac{\hat{F}_n}{\hat{\eta}_n}\right|\cos\phi_F$$
$$\alpha_n = \frac{1}{2\omega_n}Im\left(\frac{\hat{F}_n}{\hat{\eta}_n}\right) = \frac{-1}{2\omega_n}\left|\frac{\hat{F}_n}{\hat{\eta}_n}\right|\sin\phi_F \tag{6.32a,b}$$

Also for use in (6.29) we have

$$\dot{\eta}_n = i\bar{a}k|\hat{\eta}_n|e^{-i\bar{a}kt} = \bar{a}k|\hat{\eta}_n|e^{-i\left(\bar{a}kt+\frac{\pi}{2}\right)} \approx \omega_n|\hat{\eta}_n|e^{-i\left(\omega_n t+\frac{\pi}{2}\right)}$$

so

$$Re(\dot{\eta}_n) = \omega_n|\hat{\eta}_n|\cos\left(\omega_n t + \frac{\pi}{2}\right) = -\omega_n|\hat{\eta}_n|\sin\omega_n t \tag{6.33}$$

The real part of F_n is

$$Re(F_n) = |\hat{F}_n|\cos\left(\omega_n t + \phi_F\right) = |\hat{F}_n|\{\cos\omega_n t\cos\phi_F - \sin\omega_n t\sin\phi_F\} \tag{6.34}$$

Hence the right-hand side of (6.29) is

$$\Delta\mathcal{E}_n = \int_t^{t+\tau_n} Re(F_n)Re(\eta_n)dt' = \omega|\hat{F}_n|\int_t^{t+\tau_n}\left\{\sin^2\omega_n t'\sin\phi_F - \frac{1}{2}\sin 2\omega_n t'\cos\phi_F\right\}dt'$$
$$= \omega|\hat{F}_n||\hat{\eta}_n|\frac{\tau_n}{2}\sin\phi_F$$

Substitution of (6.32)a,b leads to the formula

$$\Delta\mathcal{E}_n = 2\pi\alpha_n\omega_n|\hat{\eta}_n|^2 \tag{6.35}$$

which establishes the desired connection between Rayleigh's criterion and linear stability:

---

[19] $\mathcal{E}_n$ is not the energy of the nth acoustic mode, which is given by the integral of (5.33) over the volume of the chamber.

Remarks:

(i) Positive α_n (the system is linearly unstable) implies that the average energy of the oscillator increases, and vice-versa.

(ii) Rayleigh's original criterion is equivalent to the principle of linear instability **if** only heat exchange is accounted for and is **neither** a necessary **nor** a sufficient condition for existence of a combustion instability.

(iii) The extended form (6.35) of Rayleigh's criterion is exactly equivalent to the principle of linear instability.

Putnam (1971) has made the widest use of Rayleigh's Criterion in practical situations. His book and papers give many examples of applying the Criterion as an aid to making changes of design to avoid oscillations generated by heat release, particularly in power generating and heating systems.

In the past fifteen years many groups have been making direct observations on laboratory systems to check the validity of the Criterion's implications. The key step is based on the assumption that radiation by certain intermediate species in hydrocarbon reactions (CH and OH are the most common indentifiers) can be interpreted as a measure of the rate of chemical reactions taking place and hence of the rate at which energy is released. Simultaneous measurement we made of the spatial distribution of radiation in a system, and of the pressure oscillations, the results then allow at least a qualitative assessment of the extent to which the oscillations are being driven by the energy released in the combustion field, or whether other mechanisms may be active.

It seems that the first report of that sort of effort appeared in a Ph.D. thesis (Sterling, 1987; Sterling and Zukoski, 1991). Figure 6.2 is a sketch of the dump combustor used as the test device, and Figure 6.3 shows the main result.

FIGURE 6.2. The Caltech Dump Combustor (Sterling 1985)

6.5. Explicit Formulas For Linear Stability. The term 'stability of motions' has several interpretations for flows in combustion chambers, including:

(i) the stability of laminar average flow when viscous and inertial properties of the medium dominate, leading to turbulence, a field of distributed vorticity if the steady flow is unstable;

(ii) the stability of shear layers, commonly producing large scale vortex motions when a shear layer is unstable;

(iii) the stability of laminar flame fronts, responsible for one source of turbulent combustion when fronts are unstable;

(iv) the stability of small disturbances which, when the compressibility and inertia of the medium dominate, can develop into acoustic waves.

In terms of the modes of motion mentioned in Section 3.1 and discussed further in Section 3.3, the phenomena (i)–(iii) are classified as waves of vorticity and the fourth comprises acoustic waves. Here we are concerned only with the stability of acoustic waves. The results are very general, accommodating all relevant processes and applicable, in principle, to any combustion chamber. Eventually the obstacles to successful applications are associated almost entirely with problems of modeling. In the first instance, the formal results given here establish explicitly what modeling is required.

6.5.1. *Linear Stability in Three Dimensions.* The formulas (6.14) a,b are general, restricted only by the approximations used in formulating the analytical framework. Hence the problem of obtaining results specific to any given problem comes down to finding explicit forms for F_n^η and $F_n^{\dot\eta}$, i.e. evaluating the integrals defining F_n,
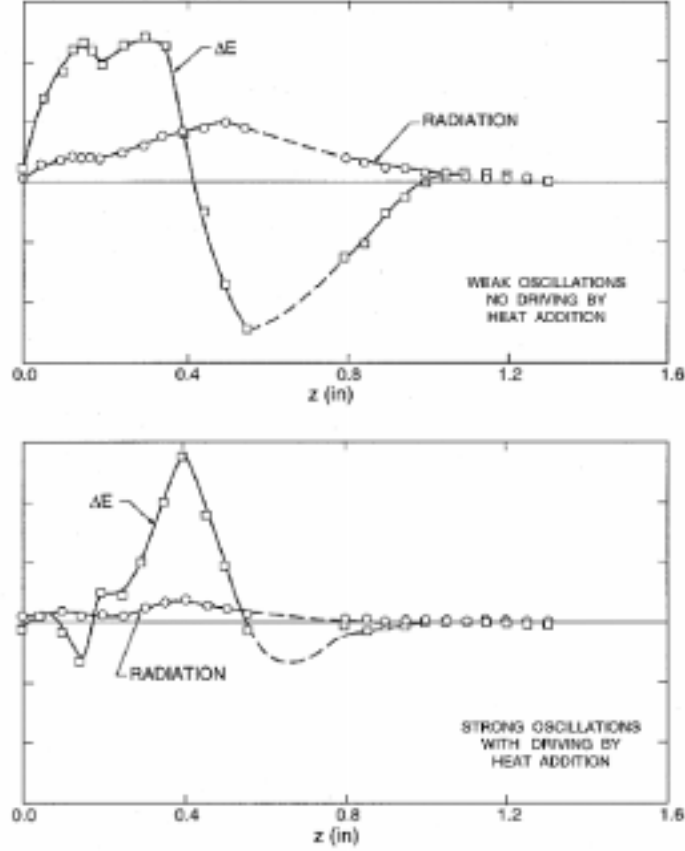
FIGURE 6.3. Experimental Confirmation of Rayleigh's Criteria (Sterling and Zukoski, 1991)

equation (6.2). The functions h and f are given by (4.72) and (4.73) to second order in the fluctuations. Here we need only the linear parts, terms of order $\mu\varepsilon$. With μ and ε absorbed in the definitions of the variables, we have

$$
\begin{aligned}
h = {} & -\bar{\rho}\nabla \cdot \left(\bar{\mathbf{M}} \cdot \nabla\mathbf{M}' + \mathbf{M}' \cdot \nabla\bar{\mathbf{M}}\right) - \frac{1}{\bar{a}^2}\frac{\partial}{\partial t}\left(\bar{\mathbf{M}} \cdot \nabla p' + \gamma p'\nabla \cdot \bar{\mathbf{M}}\right) \\
& + \left[\frac{1}{\bar{\rho}}\nabla \cdot \left(\frac{1}{\bar{\rho}}\mathcal{F}'\right) - \frac{1}{\bar{a}^2}\frac{\partial P'}{\partial t}\right]_{\mu\varepsilon}
\end{aligned} \tag{6.36}
$$

$$
f = \bar{\rho}\left[\frac{\partial\mathbf{M}'}{\partial t} \cdot \hat{n}\right]_{\mu\varepsilon} + \bar{\rho}\hat{n} \cdot \left(\bar{\mathbf{M}} \cdot \nabla\mathbf{M}' + \mathbf{M}' \cdot \nabla\bar{\mathbf{M}}\right) + [\hat{n} \cdot \mathcal{F}']_{\mu\varepsilon} \tag{6.37}
$$

where the subscript $\mu\varepsilon$ means that the quantity in expanded to include only terms of first order in the mean flow and the fluctuations, i.e. terms $O(\bar{M}_r M'_r)$.

Substitution of (6.36) and (6.37) and some rearrangement leads to the result

$$
\begin{aligned}
\int \hat{h}\psi_n dV + \oiint f\psi_n dS = {} & \bar{\rho}k_n^2 \int \left(\bar{\mathbf{M}} \cdot \hat{\mathbf{M}}\right)\psi_n dV \\
& - \bar{\rho}\int \left(\hat{\mathbf{M}} \times \nabla \times \bar{\mathbf{M}}\right) \cdot \nabla\psi_n dV \\
& + i\frac{k_n}{\bar{a}}\int \psi_n\left[\bar{\mathbf{M}} \cdot \nabla\hat{p} + \gamma\hat{p}\nabla \cdot \bar{\mathbf{M}}\right]dV \\
& - i\frac{k_n}{\bar{a}}\int \psi_n\hat{\mathcal{P}}dV - \int \hat{\mathcal{F}} \cdot \nabla\psi_n dV \\
& + \bar{\rho}\bar{a}k_n\oiint\psi_n\hat{\mathbf{M}} \cdot \hat{n}dS
\end{aligned} \tag{6.38}
$$

Note that we have removed the exponential time factor for linear harmonic motions and (6.38) contains the amplitudes of fluctuations, denoted by ($\hat{\;}$). Two remarks are important:

(i) the mean flow field may be rotational ($\nabla \times \bar{\mathbf{M}} \neq 0$) and sources are accommodated ($\nabla \cdot \bar{\mathbf{M}} \neq 0$).

(ii) owing to the ordinary procedure discussed in Section 3, the substitutions of classical acoustic mode shapes are required in the right-hand side:

$$\hat{p} = \bar{p}\hat{\eta}_n \psi_n \; ; \quad \hat{M} = \frac{i}{\gamma k_n^2}\hat{\eta}_n \nabla \psi_n \tag{6.39}$$

where $\hat{\eta}_n = i\bar{a}k_n \eta_n$.

Eventually the complex wavenumber, (6.11), is

$$
\begin{aligned}
k^2 = k_n^2 + \frac{\bar{a}^2}{\bar{p}E_n^2} \Bigg\{ & i\bar{p}\bar{a}k_n \oiint \left(\frac{\hat{\mathbf{M}}}{\hat{\eta}_\mathbf{n}} + \frac{1}{\gamma}\bar{\mathbf{M}}\gamma_n \right) \cdot \hat{n}\gamma_n dS \\
& + i(\gamma - 1)\frac{k_n}{\bar{a}}\bar{p}\int \left(\nabla \cdot \bar{\mathbf{M}} \right) \psi_n^2 dV - i\frac{k_n}{\bar{a}}\int \frac{\hat{\mathcal{P}}}{\hat{\eta}_n}\psi_n dV \\
& - \int \frac{\hat{\mathcal{F}}}{\hat{\eta}_n} \cdot \nabla \psi_n dV \Bigg\}
\end{aligned}
\tag{6.40}
$$

It is important to understand that in the result unsteady gasdynamics (acoustics) and interactions between the acoustics and the mean flow are accounted for 'exactly' to $O(\bar{M}_r)$.

The real and imaginary parts of (6.40), written symbolically as equations (6.12) a,b and (6.14) a,b are sums of contributions from the various processes accounted for. For example, the formula for the growth constant appears in the form

$$\alpha = (\alpha)_{combustion} + (\alpha)_{mean\ flow/acoustics} + (\alpha)_{nozzle} + \cdots$$

Similar results can be derived for the case when the one-dimensional approximation is used. The required basis for the calculations is given by Culick (1998). The results for the frequency and growth constant are:

$$
\begin{aligned}
\omega = \omega_n + \frac{\bar{a}^2}{2\omega_\ell \bar{p}E_\ell^2} \Bigg\{ & -\bar{p}\bar{a}k_\ell \left[\left(\frac{\hat{u}^{(i)}}{\hat{\eta}_\ell}\psi \right) S_c \right]_0^L \\
& + \bar{p}\bar{a}k_\ell \int_0^L \frac{1}{S_c}\int \left(\frac{\hat{u}_b^{(i)}}{\hat{\eta}_\ell} \right) dq\psi_\ell S_c dz \Bigg\} + \text{ volumetric contributions (combustion)}
\end{aligned}
\tag{6.41}
$$

$$
\begin{aligned}
\alpha = -\frac{\bar{a}^2}{2\omega_\ell \bar{p}E_\ell^2} \Bigg\{ & \bar{p}\bar{a}k_\ell \left[\left(\frac{\hat{u}^{(i)}}{\hat{\eta}_\ell}\psi_\ell + \frac{1}{\gamma}\bar{u}\gamma_\ell^2 \right) S_c \right]_0^L \\
& - \bar{p}\bar{a}k_\ell \int_0^L \frac{1}{S_c}\int \left(\frac{\hat{u}_b^{(i)}}{\hat{\eta}_\ell} + \frac{1}{\gamma}\bar{u}_b\psi_\ell \right) dq\psi_\ell S_c dz \\
& + \frac{k_\ell \bar{p}^L}{\bar{a}}\int_0^L \frac{1}{k_\ell^2}\left(\frac{d\psi_\ell}{dz} \right)^2 \frac{1}{S_c}\int \bar{u}_b dq S_c dz \Bigg\} + \text{ volumetric contributions (combustion)}
\end{aligned}
\tag{6.42}
$$

Two remarks on interpretation

(i) the first two terms in the formula for α represent the dynamical response of the enclosing surface and the net effect of linear interactions between the acoustic field and the mean flow.

(ii) the last term represents a dissipative process commonly called 'flow turning' due to inelastic acceleration of the incoming flow, initially normal to the surface, to the local axial velocity parallel to the surface. This process generates unsteady vorticity at the surface; the result shown here does not capture the entire contribution. See Flandro (1995) and Mulhotra (2001).

These results for linear stability have been applied extensively to problems of combustion instabilities in solid propellant rockets. Their validity has long been confirmed. However, their accuracy depends entirely on the accuracy of modeling processes rather than the gasdynamics shown explicitly in (6.40)–(6.42).

Due to the large uncertainties associated with modeling some processes, it is difficult—in fact impossible at this time—to make an entirely satisfactory comparison between theoretical results and measurements. Hence the best way to check theory is to compare results obtained here with results of numerical simulations, all for the same problem. Even this procedure is imperfect because different approximations must be made in the two approaches—it is impossible to solve the 'same' problem numerically and with the analysis given here.

Results of an example for a solid propellant rocket are shown in Figures 6.4–6.6. The calculations were carried out for nonlinear behavior. Figure 6.4 shows the development of the unstable motion into a stable limit cycle and Figure 6.5 is a comparison of the spectra of the waveforms in the limit cycle. The approximate analysis can be carried out only for a finite number of modes. As a consequence, although the frequencies are accurately predicted, the amplitudes have greater errors for the higher modes. Figure 6.6 shows one effect of truncating the modal expansion. For this example the effect is not large—the two-mode approximation seems quite adequate. That is not always true, a matter discussed in the following Section.
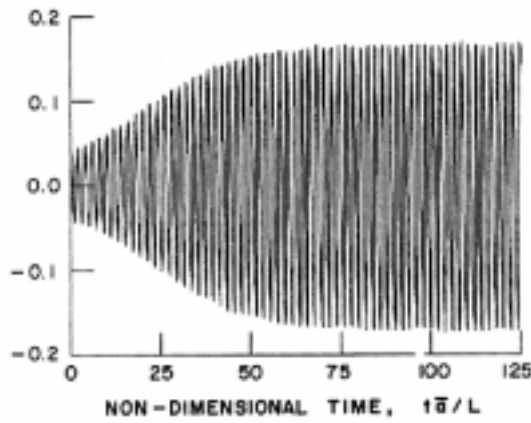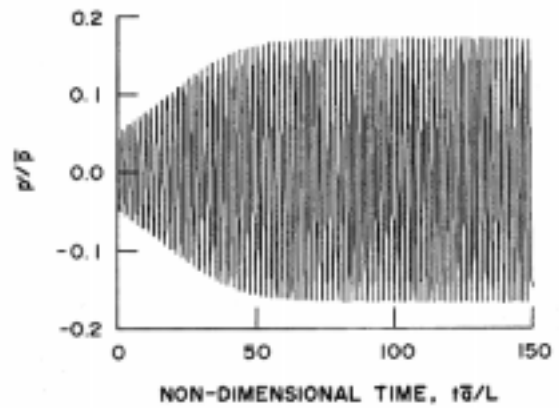
(a) Approximate Analysis   (b) Numerical Simulation

FIGURE 6.4. Growth of Unstable Motions According to (a) the Approximate Analysis; and (b) a Numerical Simulation

	Frequencies and amplitudes of acoustic pressures									
	Frequency, Hz					Amplitude, $|p'/\bar{p}|$				
Mode	1	2	3	4	5	1	2	3	4	5
Numerical	926	1824	2698	3595	4491	0.151	0.042	0.0234	0.0203	——
Approximate	895	1785	2683	3571	4449	0.151	0.0478	0.0280	0.0153	0.0188

(a)
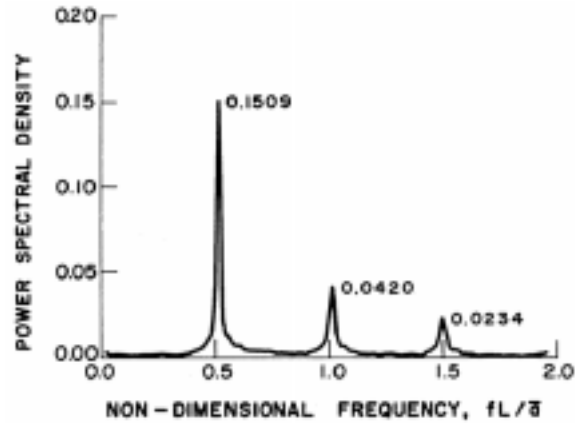
(b)

FIGURE 6.5. Comparison of the Spectra for the Waveforms in Figure 6.4
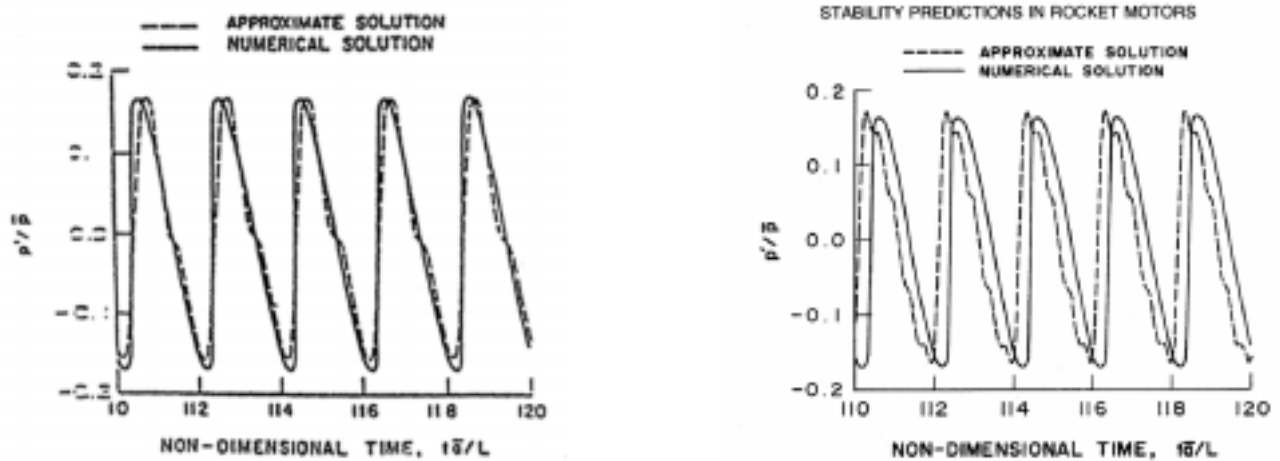
FIGURE 6.6. Effect of Truncation in the Waveforms

7. NONLINEAR BEHAVIOR

It is linear behavior, especially linear stability, that is most easily understood and therefore has dominated discussions of combustion instabilities. Almost no attention has been paid to nonlinear behavior in works on control of combustion instabilities. One justification for that deficiency has been the view that if control of the oscillations works properly, it should stop the growth before the amplitude reaches a large value. There are several reasons why that reasoning is flawed:

- if the growth rates are unusually large the control system may not have a sufficiently large bandwidth to be effective;
- because combustion systems are intrinsically nonlinear design of a control system based only on linear behavior may produce a control system far from optimal;
- linear control demands actuation at the frequency of the oscillation to be controlled, while nonlinear control of particular types are effective at lower frequencies; an example is described in Section 7.
- observed nonlinear behavior contains much information about properties of the system in question and in the interests of understanding should not be ignored.

Existing examples of controlling combustion instabilities have almost totally ignored issues of nonlinear behavior. In no demonstration, either in the laboratory or full-scale, have the amplitudes of the oscillations been predicted or interpreted either before or after control has been exercised. Hence nothing has been learned about why the initially unstable motions reach the amplitudes they did, or, why the control system affected them in the observed way. In fact few attempts exist to determine quantitatively the stability of motions. Hence the subject of controlling the dynamics of combustion systems has largely been a matter of exercising the principles of control with little attention paid to the characteristics of the systems ('plants') being controlled. It seems that following this strategy is likely not the most fruitful way of achieving meaningful progress. Especially, this is not a sound approach to developing the basis for designing control systems. The current state of the art is that feedback control is designed and applied in *ad hoc* fashion for systems already built and exhibiting instabilities.

A central concern of a controls designer is construction of a 'reduced order' model of the system. What that really means in the present context is the need to convert the partial differential equations of conservation developed in Section 3, to a finite system of ordinary differential equations. The analysis developed in Section 3 and 4 accomplishes exactly that purpose. It is not the only approach possible (e.g. proper orthogonal decomposition has been examined briefly) but the method of modal expansion and spatial averaging has many favorable properties and has been proven to work well.

The main purposes of this section are to quote a few results displaying some aspects of the nonlinear behavior arising from gasdynamics; and to illustrate some consequences of truncating the modal expansion, that is, what might be the consequences of reducing the order of the model. Another important issue we will examine briefly is the application of time-averaging. As the calculations in Section 4 showed, the great advantage of time-averaging is that it replaces N second order oscillator equation by $2N$ first order equations. That transformation enormously reduces the cost of obtaining solutions, aids theoretical work, and provides a simplified representation for application of feedback control. But as for truncation, the question arises: How accurate are the results and what are the limits of the validity of time-averaging?

Only the nonlinearities due to gasdynamics are treated in this section. The results must be viewed with that caveat, particularly because the forms of the nonlinearities are very special, if only because the dominant coupling acts to cause energy to flow from low to high frequency waves, the tendency which produces the familiar steepening of compressive disturbances into shock waves.

7.1. The Two-Mode Approximation. This is the simplest class of problems for which nonlinear mode coupling is accommodated. Each mode is characterized by two constants: α (energy gain or loss) and θ (frequency shift). The energy gain or loss may be nonlinear—that is, α could in principle depend on amplitude—but here both α and θ are taken to be constant, characterizing entirely the linear processes. As a result of several works

in the past few years, the two mode approximation is quite well understood (Awad and Culick, 1986; Paparizos and Culick, 1989; Yang and Culick 1990; Jahnke and Culick, 1994; Culick, 1994).
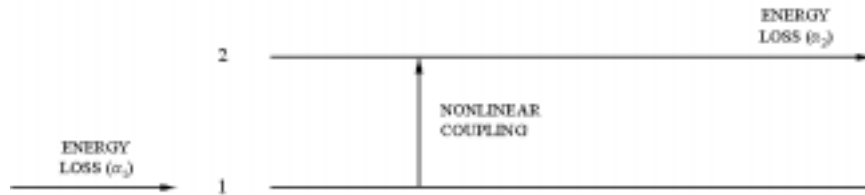
FIGURE 7.1. Energy Flow in the Two Mode Approximation

Only gasdynamic nonlinearities to second order are accounted for here. Their special form allows the convenient closed form solutions to the time-averaged equations, first found by Awad (1983). The results provide much basic understanding which is applicable to more complicated nonlinear problems. For example, contrary to one's expectation based on the behavior of shock waves, nonlinear behavior in the present context need not involve large amplitudes, and the pressure oscillation may appear to be a clean sinusoid, free of significant harmonic content. The basic reason is that here the two-mode system both gains and loses energy; each interaction with the environment is necessary. In the absence of the nonlinear modal coupling, or some other linear process, limit cycles cannot exist. Moreover, both stable and unstable limit cycles exist.

Truncation of the modal expansion to two modes introduces errors because the flow of energy to higher modes is blocked. The amplitude of the highest mode is therefore greater than the correct value in order to provide the higher linear rate of energy loss required to sustain a limit cycle. The example in Section 6.5.1 shows this effect.

It's an interesting feature of the two-mode approximation that nonlinear instability to stable limit cycles seems not to exist. Although no rigorous proof exists, experience with many examples has shown that conclusion to be quite generally true if only the acoustic (gasdynamics) nonlinearities are accounted for. 'Triggering' or pulsing to stable limit cycles does occur for special forms of nonlinear energy gain from the environment (i.e. extinction from the mean flow or supply from combustion processes).

If we ignore linear mode coupling and account for acoustic nonlinearities to second order, the oscillator equations can be put in the form

$$\frac{d^2\eta_n}{dt^2} + \omega_n^2\eta_n = \alpha_n\dot{\eta}_n + \theta_n\eta_n - \sum_{i=1}^{\infty}\sum_{j=1}^{\infty}\{A_{nij}\dot{\eta}_i\dot{\eta}_j + B_{nij}\eta_i\eta_j\} + F_n^{NL} \tag{7.1}$$

where F_n^{NL} represents other nonlinear contributions. The coefficients A_{nij}, B_{nij} are defined as integrals involving the basis functions ψ_{nij}. Hence their values are fixed primarily by the geometry of the chamber in question. See Culick (1976) for additional details of the derivation of (7.1). It is extremely important that the nonlinear gasdynamic terms involve no cross-products $\dot{\eta}_i\eta_j$ and also (not obvious here) no 'self-coupling', terms proportional to $\dot{\eta}_n^2$ or η_n^2. Those properties are the formal reasons that nonlinear instabilities do not exist if only these nonlinearities are included.

Equation (7.1) simplify considerably for longitudinal modes. Due to orthogonality and special properties of the $\cos k_n z$, the double sum becomes a single sum and (7.1) can be put in the form:

$$\frac{d^2\eta_n}{dt^2} + \omega_n^2\eta_n = \alpha_n\dot{\eta}_n + \theta_n\eta_n - \sum_{i=1}^{\infty}\left[C_{ni}^{(1)}\dot{\eta}_i\dot{\eta}_{n-i} + D_{ni}^{(1)}\eta_i\eta_{n-i}\right]$$
$$- \sum_{i=1}^{\infty}\left[C_{ni}^{(2)}\dot{\eta}_i\dot{\eta}_{n+i} + D_{ni}^{(2)}\eta_i\eta_{n+i}\right] + F_n^{NL} \tag{7.2}$$

The time-averaged forms of (7.2) are

$$\frac{dA_n}{dt} = \alpha_n A_n + \theta_n B_n + \frac{n\beta}{2} \sum^i [A_i(A_{n-i} - A_{i-n} - A_{i+n}) - B_i(B_{n-i} - B_{i-n} - B_{i+n})]$$

$$\frac{dB_n}{dt} = -\theta_n A_n + \alpha_n B_n + \frac{n\beta}{2} \sum^i [A_i(B_{n-i} - B_{i-n} - B_{i+n}) - B_i(A_{n-i} - A_{i-n} - A_{i+n})]$$

(7.3) a,b

where as in Section 3, $\eta_n = A_n \cos \omega_n t + B_n \sin \omega_n t$. For longitudinal modes, the frequencies are all integral multiples of the fundamental, a property that is crucial to the forms of (7.3) a,b. For example, for transverse modes in a cylindrical chamber, the nonlinear terms contain factors representing modulation.

For two modes, the four first order equations are

$$\frac{dA_1}{dt} = \alpha_1 A_1 + \theta_1 B_1 - \beta(A_1 A_2 - B_1 B_2)$$

$$\frac{dB_1}{dt} = \alpha_1 B_1 + \theta_1 A_1 - \beta(B_1 A_2 - A_1 B_2)$$

$$\frac{dA_2}{dt} = \alpha_2 A_2 + \theta_2 B_2 - \beta(A_1^2 - B_1^2)$$

$$\frac{dB_2}{dt} = \alpha_2 B_2 + \theta_2 A_2 - 2\beta B_1 A_1$$

(7.4) a,b,c,d

The great advantage of this system of equations is that some useful exact results can be found. One way to find them is to change independent variables to the amplitude and phases (Γ_n, ϕ_n) of the two modes by writing

$$\eta_1(t) = \Gamma_1(t) \sin(\omega_1 t + \phi_1)$$

$$\eta_2(t) = \Gamma_2(t) \sin(2\omega_1 t + \phi_2)$$

where $\Gamma_n = \sqrt{A_n^2 + B_n^2}$. The governing equations for Γ_1, Γ_2 and the effective relative phase $\psi = 2\phi_1 - \phi_2$ are

$$\frac{d\Gamma_1}{dt} = \alpha_1 \Gamma_1 - \beta \Gamma_1 \Gamma_2 \cos \psi$$

$$\frac{d\Gamma_2}{dt} = \alpha_2 \Gamma_2 - \beta \Gamma_1^2 \cos \psi$$

(7.5) a,b,c

$$\frac{d\psi}{dt} = (\theta_1 - 2\theta_1) + \beta(2\Gamma_1 - \frac{\Gamma_1^2}{2}) \sin \psi$$

where

$$\beta = \frac{\theta_2 - 2\theta_1}{2\alpha_1 \alpha_2}$$

(7.6)

The problem of linear stability is solved directly:

$$\alpha_1, \alpha_2 < 0 \iff \text{ small amplitude motions are stable}$$

(7.7)

Nonlinear behavior in general poses two basic questions:

(i) What are the conditions for existence of limit cycles?
(ii) What are the conditions that the limit cycles are stable?

Stability of a limit cycle of course is a matter entirely separate from the linear stability of small amplitude motions. We are concerned here with a system executing a steady limit cycle. If the limit cycle in stable, then if slightly disturbed, the motion will eventually return to its initial form

(a) Existence of Limit Cycles

In this time-averaged formulation, existence of limit cycles corresponds to existence of stationary or equilibrium points of the system (7.5) a,b,c:

$$\frac{d\Gamma}{dt} = \frac{d\Gamma_2}{dt} = \frac{d\psi}{dt} = 0 \iff \text{ transcendental algebraic equations}$$

The solutions are

$$\Gamma_{10} = \frac{1}{K}\sqrt{-\alpha_1\alpha_2(1+\beta^2)}$$

$$\Gamma_{20} = \frac{1}{K}\sqrt{\alpha_1^2(1+\beta^2)} \qquad \text{(7.8) a,b,c}$$

$$\psi_o = \tan^{-1}(-\beta)$$

where

$$K = \frac{\gamma+1}{2\gamma}\omega_1 \qquad (7.9)$$

For Γ_{10} to be real, $-\alpha_1\alpha_2$ must be positive, implying that the constants α_1, α_2 must have opposite signs. The physical interpretation is that if the first mode is unstable, for example, $\alpha > 0$, then the second mode must be stable ($\alpha_2 < 0$): the rate of energy flow into the first mode must equal the rate of loss from the second mode in order that the amplitudes be constant in time. The transfer rate upwards due to coupling must have the same value. Similar reasoning explains the care when the second grade is unstable, requiring that the first mode to be stable.

(b) Stability of Limit Cycles

To determine the stability of the limit cycles, the variables are written as $\Gamma_i = \Gamma_{i0} + \Gamma_i', \quad \psi = \psi_o + \psi'$ and substituted in the governing equations (7.5) a,b,c. The linearized equations for the disturbances are then solved for characteristic value λ in the assumed forms $\Gamma_i' = \Gamma_{i0}'e^{\lambda t}, \cdots$. For stability, an initial disturbance must decay. Applying that requirement produces regions of stability in the plane of the parameters $\beta_o = (\theta_2 - 2\theta_1)^2/(\alpha_2 + 2\alpha_1)^2$ and α_2/α_1, shown in Figure 7.2
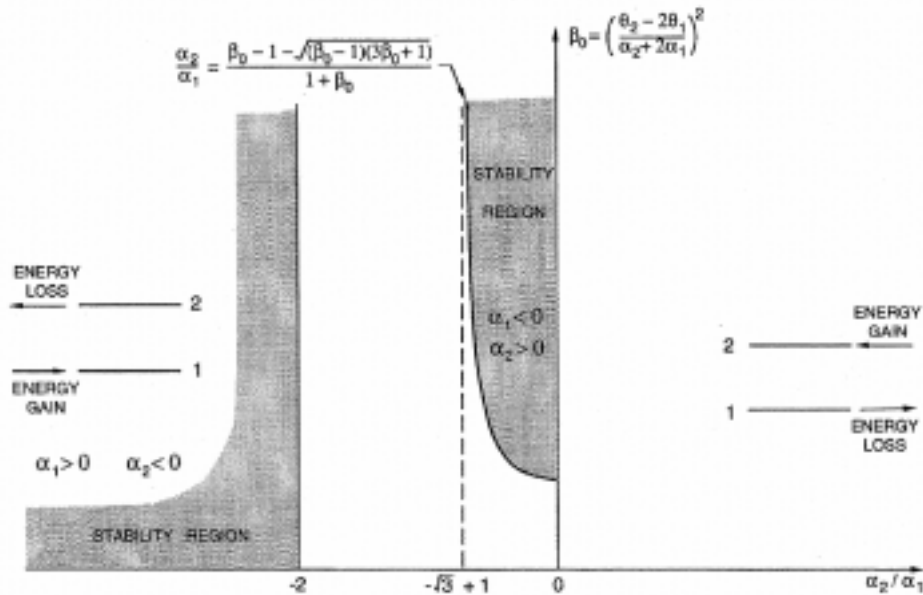
FIGURE 7.2. Regions of Stability for Two Modes, Time-Averaged Equations

There is presently no basis for understanding why stable limit cycles occur only for the special ranges of parameters shown in Figure 7.2. Moreover, it is impossible at this stage to understand the extent to which the shapes of the regions of stability depend on the use of time-averaged equations and on truncation to two modes. It is important for both practical and theoretical reasons to assess and quantify as far as possible the consequences of time-averaging and truncation. Considerable progress has been made in that direction by using a continuation method to solve the systems of oscillator equations. Some results are discussed in the following section.

Here it is useful to examine several special cases. Figure 7.3 shows that if the parameters are chosen so that the operating point lies with the range for stable limit cycles and the first mode is unstable, truncation may have relatively small effects. On the other hand, if the limit cycle is unstable within the two-mode approximation with an unstable first mode, it may become stable (with the same values of $\alpha_1, \alpha_2, \theta_1, \theta_2$) if more stable modes are accounted for.
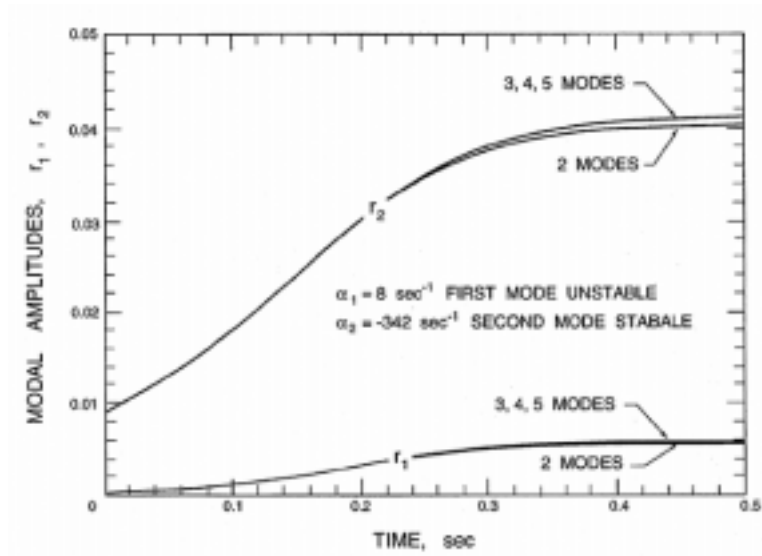
FIGURE 7.3. Effects of Truncation for a Stable Limit Cycle/First Mode Unstable
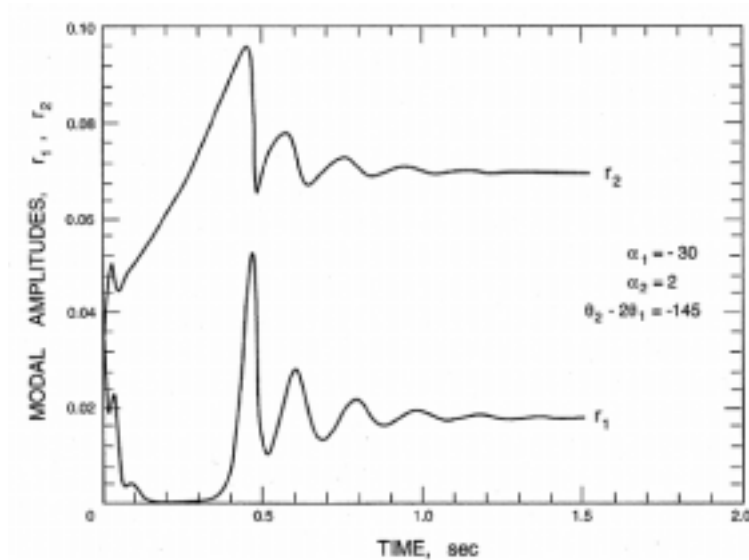
FIGURE 7.4. Development of a Stable Limit Cycle when the Second Mode is Unstable

Figure 7.4 is interesting for a quite different reason. In this case the second mode is unstable, and the motion evolves to a stable limit cycle. However, unlike the example in Figure 7.3, the amplitudes do not grow smoothly and monotonically to their values in the limit cycle. Their erratic behavior is due to the fact that with the second mode unstable, energy must flow from high frequency to low frequency. That is contrary to the direction of flow imposed naturally by the fluid mechanics (of the steepening of a compressive disturbance into a shock wave). The conflict between the natural action of the nonlinear coupling on the one hand and the flow of energy imposed by

energy exchange with the environment causes the amplitudes of the two modes to wander during the transient phase before finally reaching their ultimate values.

7.2. Application of a Continuation Method. Much of the work during the past decade at Caltech on chamber dynamics has been directed to understanding the extent to which nonlinear behavior can be explained on the basis of nonlinear gasdynamics. The reasoning is that first we know the model of gasdynamics—the Navier-Stokes equations for compressible flow—so we can do accurate analysis; and second, those features that cannot be explained must be due to other causes so, by elimination we have some guidelines for what we should seek in other processes. Experience has shown that 'other processes' is this context most probably means combustion.

To carry out this program with numerical simulations—after all, few exact results exist—would be a formidable task because of the number of characteristic parameters. The parameter space comprises those defining the geometry of a chamber and two parameters (α_n, θ_n) characterizing linear behavior of each mode. The effect required to search the parameter space is much reduced by applying a continuation method. The procedure is an efficient system means of locating values of parameters for which the dynamical behavior suffers a qualitative change, i.e. bifurcation points. The simplest—almost trivial—example is the Hopf bifurcation point which arises when for a stable system one of the values α_n changes from a negative to a positive value; the system becomes linearly unstable and under suitable conditions the motion develops into a stable limit cycle. In fact, linear instability is not always such a simple matter. We have found cases with special sorts of nonlinear processes that a Hopf bifurcation may occur when the critical value of the critical α_n is non-zero.

The essential idea of a continuation method applied to limit cycles is illustrated in Figure 7.5 where the variables of the motion are $x(t)$ and μ is the parameter in question, the bifurcation parameter. A continuation method is a computational (numerical) scheme for following, in this case, the changes of a period solution—a limit cycle—as the values of one or more parameters are changed. A picture like Figure 7.5 is impossible to draw for more than three coordinates so the conventional display of information is a bifurcation diagram in which the amplitude of one variable in the limit cycle is plotted versus the parameters varied as the continuation method is applied. Figure 7.5 shows two examples, a Hopf bifurcation, also called a *supercritical bifurcation* and a *subcritical bifurcation* with a turning point. Those are the two types of bifurcation most common in the present context.
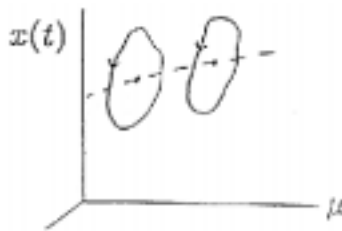
FIGURE 7.5. Schematic Illustration of the Continuation Method Applied to Limit Cycles

Supercritical bifurcation

Subcritical bifurcation with a turning point
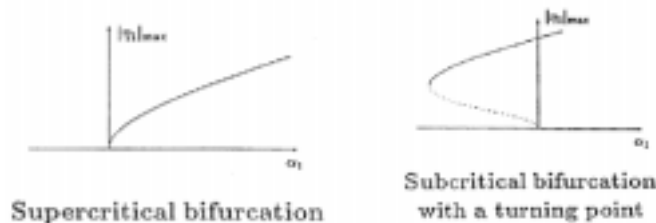
FIGURE 7.6. Two Examples of Bifurcation

Thus a bifurcation diagram is a locus of equilibrium point traced as the bifurcation parameter is changed. As a practical matter, application of a continuation method is more systematic and cheaper to use than use of numerical simulations. We have successfully used a continuation method (Doedel *et al.* 1991a,b; Doedel *et al.* 1997) to investigate four classes of problems:

(i) consequences of time-averaging

(ii) consequences of truncating the modal expansion

(iii) influences of the linear parameters (α_n, θ_n) on nonlinear behavior

(iv) pulsed instabilities: the conditions for existence of stable limit cycles in a linearly stable system.

The problems (i) and (ii) are central to the matter of constructing reduced-order models. Hence it is important to emphasize that in our view, application of the continuation method to investigate the consequences of time-averaging and truncation is part of the procedure for establishing the validity of reduced order models within the framework of analysis based on modal expansion and spatial averaging.

The continuation method is a powerful means for investigating many nonlinear problems in the classic listed above. For more extensive discussions see Jahnke and Culick (1994); Burnley (1996); Burnley and Culick (1996); and Ananthkrishnan and Culick (2002). As an illustration we quote here some results for limit cycles for systems of longitudinal modes when only the gasdynamical nonlinearities are accounted for. We are interested in the consequences of truncation with time-averaging.

In Section 7.1 we cited a few results for the limiting case of two modes described by the four equations found with time-averaging. Figure 7.3 shows the special example of as effect of truncating the series expansion for the time-averaged system: increasing the number of modes apparently widens the region of stability. In fact, use of the continuation method has established the result that the existence for region of stability for limit cycles with two modes is due to truncation. When the first mode is unstable, stable limit cycles exist for all values of α, if more than two modes are taken into account. That is true even if the original oscillator equations are used.

Figure 7.7 shows that if time-averaging is not used, there is a turning point in the bifurcation diagram. If
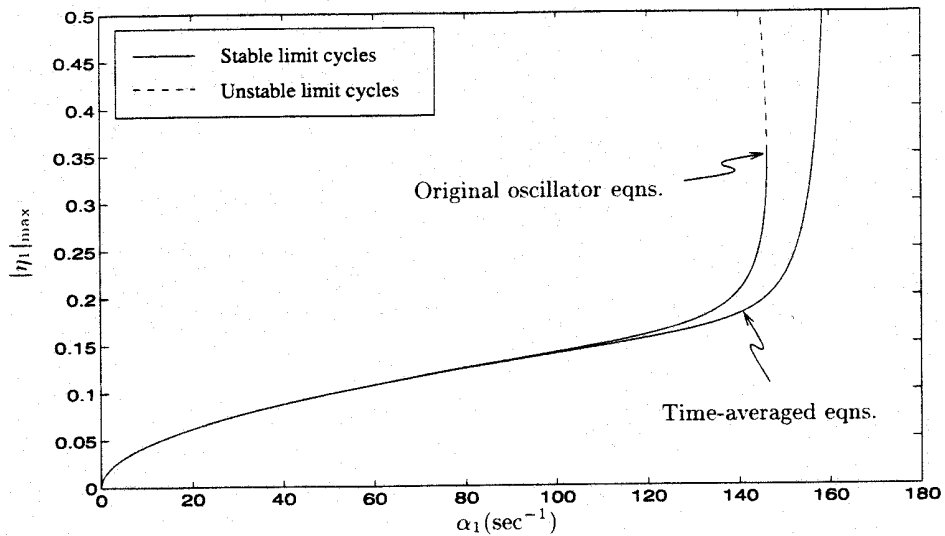
FIGURE 7.7. Effect of Time-Averaging for Two Modes

more than two modes are accounted for, the boundary of stability persists for the time-averaged equations but does not appear if more than two modes are included. Figure 7.8 is the result for the time-averaged equations and Figure 7.9 shows the case of 4 modes computed for the full oscillator equations.

It seems true that if the system is only slightly unstable, then the system of time-averaged equations for two-longitudinal modes is a good approximate model for investigating nonlinear behavior. However, if one is generally interested in producing reduced order models, the effects of truncation and time-averaging should be investigated. Applying a continuation method seems to be the best approach for doing so.
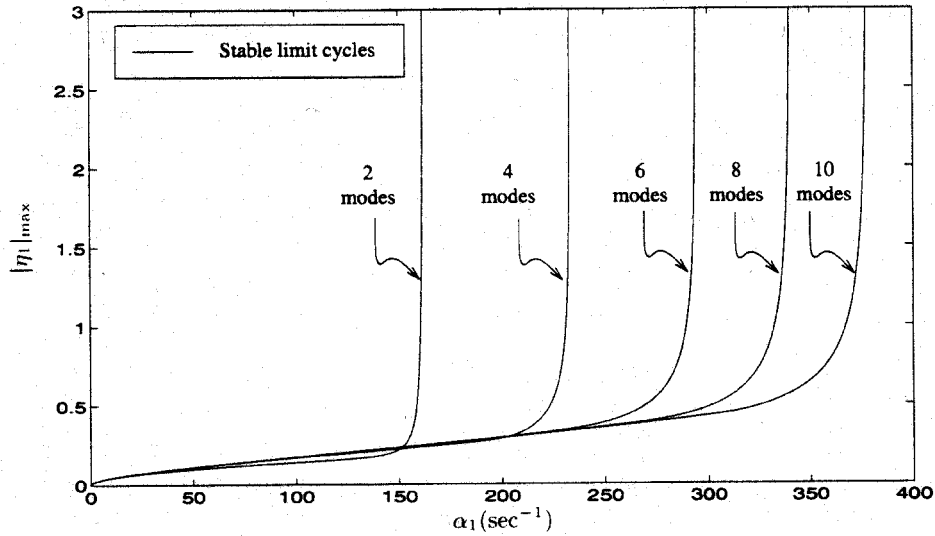
FIGURE 7.8. Stability Boundaries by Truncation of the Time-Averaged Equations
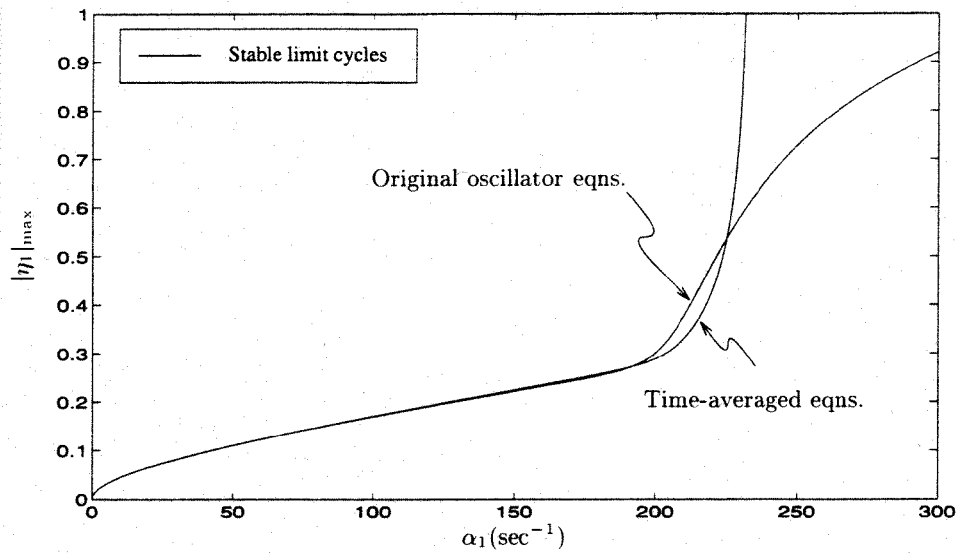
FIGURE 7.9. Maximum Amplitude of η_1 in The Limit Cycle: Four Modes, Comparison of Results for the Full Oscillator and the Time-Averaged Equations

7.3. Hysteresis and Control of Combustion Instabilities. The existence of hysteresis in the dynamical behavior of combustions is both an interesting phenomenon to investigation and a characteristic that has potentially important practical consequences. It seems that the first evidence for hysteresis in combustors was found by Russian researchers concerned with instabilities in liquid rockets (Natanzon *et al* 1993; Natanzon 1999). In that case, Natanzon and his co-workers proposed bifurcation of *steady states* of combustion, and the associated hysteresis, as a possible explanation for the random occurrences of combustion instabilities. The Russian workers were in a special situation affording them the opportunity to make such observations. The large Russian boosters were designed to use many (up to thirty-three) liquid rocket engines in a single stage. Hence large numbers of nominally identical engines were manufactured and tested for operational use. Sufficient data were obtained that statistical analysis of the behavior could be carried out. Hence a basis existed for identifying random behavior. The idea is the following.

In a liquid rocket many zones of recirculation are created at the injector where jets of liquid fuel and/or oxidizer enter the chamber. As an approximation, one may regard a recirculation zone as a chemical reactor whose behavior is known to be well-characterized by the temperature of the incoming gases entrained from the environment, and the average temperature within the zone. A fairly simple calculation based on consideration of energy and mass flows leads to the results sketched in Figure 7.10. The upper and lower branches of the
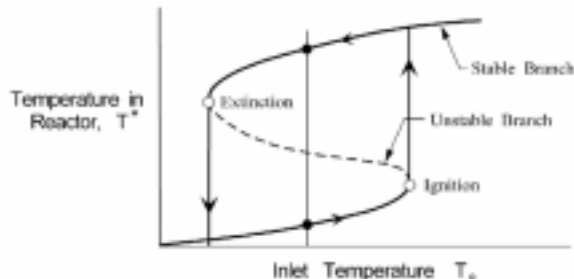
FIGURE 7.10. Hysteresis Loop for a Recirculated Zone Idealized as a Simple Chemical Reactor

hysteresis loop represent different branches of stable combustion. Those states have different influences on the state of combustion in the chamber. It was Natanzon's assertion that the state associated with the lower branch in Figure 7.10 (the cold recirculation zone) is more unstable and prone to lead to combustion instabilities. Which branch is reached depends on the history of the engine, starting from ignition or some other sort of abrupt transient. The final state of a recirculation zone therefore depends on random 'accidents' of history. Therefore random occurences or combustion instabilities may be observed. Figure 7.11 is a sketch of a possible recirculation zone and adjacent flow of a fuel or oxidizer jet, this model has been used as the basis for numerical calculations supporting Natanzon's proposal.
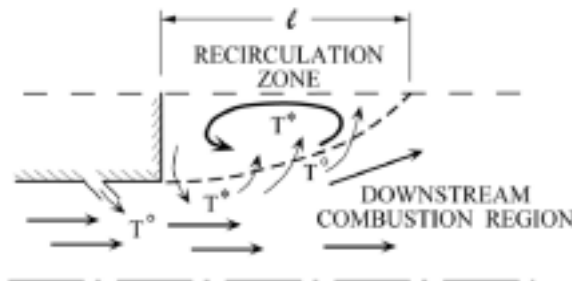
FIGURE 7.11. Sketch of a Recirculation Zone formed by a Jet of Fuel or Oxidizer

In the mid-1980's research with a dump combustor at Caltech revealed the presence of a different kind of hysteresis of dynamical states of combustion (Smith, 1985; Sterling, 1987). The combustor has been described in Section 1, Figure 1.3; Figure 6.2 shows the inlet region and the recirculation zone at the dump plane during steady combustion. The combustor showed combustion instabilities in the neighborhood of the stability boundary defined in the plane of flow rate and equivalence ratio. Figure 7.12(a). Figure 7.12(b) shows the hysteresis loop, observed as dependence of the level if pressure oscillation on equivalent ratio with the total flow rate held constant. This sort of behavior has been observed also in other dump combustors (J. Cohen, UTRC; and G. Richards, METC) as well as as in a flame-driven Rijke tube (Seywert, 2001) and in an electrically driven Rijke tube (Matveev, 2002).

More recent works (Knoop et al. 1996; Isella et al. 1996) have established the physical nature of the hysteresis in this case and have shown how active control can be used to extend the range of steady operation into the hysteretic region. High speed films have confirmed that the upper branch of the loop is associated with shedding of large vortices which, causing periodic combustion of entrained reactants sustain high amplitude pressure oscillations. The lower branch is associated with relatively quiet combustion in a shear layer shed from the lip at the inlet.
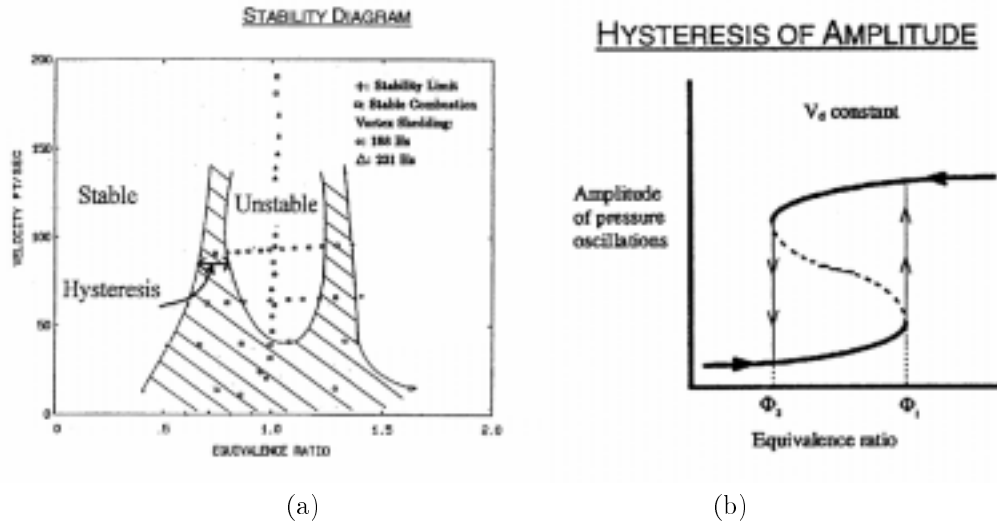
FIGURE 7.12. (a) Stability Boundary and (b) an Idealized Hysteresis Loop for the Caltech Dump Combustor

Familiar considerations of dynamical behavior suggest that it should be possible to achieve pulsed transitions between the two branches of stable dynamical states. Those processes were demonstrated by Knoop *et al* and Isella *et al* by injecting pulses of fuel at the inlet plane. Single pulses of fuel always cause transition from the upper to the lower branch. Thus with suitable sensing and actuation it is possible always to maintain the low level of oscillations (effectively 'noise') within the zone where hysteresis exists.

This is a form of nonlinear control. Although it has been demonstrated only for the range of equivalence ratio covering the zone of hysteresis, it is an important demonstration of active control at a frequency far less than the frequency of the oscillations. That is a significant characteristic because if the reduced bandwidth required of the control system, particularly the actuation.

7.4. Representing Noise in Analysis of Combustor Dynamics. Even a small laboratory combustor radiates considerable noise, generated by turbulent motions (often called 'combustion noise') within the chamber. See, for example, the spectrum reproduced earlier as Figure 1.4. The scaling laws are not known, but it is obvious to any bystander that a full-scale combustor of any sort is noisy indeed. Presently it is not well understood how important noise is to the behavior of combustion instabilities or to the application of feedback control. The purpose of this section is to introduce a means for investigating those matters within the framework developed in Sections 3 and 4.

There are three sorts of problems that will arise:

   (i) formal construction of noise (stochastic) sources in the framework of spatially averaged equa-
       tions for unsteady motions in a combustor;
  (ii) modelling the noise sources;
 (iii) solving the stochastic differential equations.

The first step, as explained in Section 3.1, is to apply the principle of splitting small disturbances into the three basic modes of propagation: acoustic waves, vorticity waves, and entropy waves. All of the discussion so far in these lectures has been devoted to the acoustic field. Noise is associated with the random motions comprising mainly vorticity but also entropy (or temperature) waves in a combustion chamber. Our concern in the present context is directed chiefly to interactions of those motions with the acoustic field. The formal representation will be relatively simple and intuitively persuasive, but modelling the details remains to be accomplished. Numerical results require assumptions that cannot be justified *a priori*.

Following the principle of splitting, we write the flow variables as sums of the three contributions, one each corresponding to the three modes of motion:

$$p' = p'_a + p'_\Omega + p'_s$$
$$\boldsymbol{\Omega}' = \boldsymbol{\Omega}'_a + \boldsymbol{\Omega}'_\Omega + \boldsymbol{\Omega}'_s$$
$$s' = s'_a + s'_\Omega + s'_s \qquad\qquad (7.10)\ \text{a,b,c,d}$$
$$\mathbf{u}' = \mathbf{u}'_a + \mathbf{u}'_\Omega + \mathbf{u}'_s$$

Subscripts $(\ \ )_a$, $(\ \ )_\Omega$, $(\ \ )_s$ denote acoustic, vortical and entropic contributions. Once again, the ordering procedure explained in Sections 3 and 4 allows us to derive meaningful results by considering only the first order components. Hence we assume that only the acoustic waves contain pressure fluctuation; only the waves of vorticity contain vorticity fluctuations; and only the entropy waves have fluctuations of entropy. The velocity field possesses contributions from all three modes.

The idea then is to substitute the assumed general forms of the variables and substitute in the primitive equations of motion expanded to third order in the fluctuations. Then form the nonlinear equation for the pressure and apply spatial averaging. This procedure was first reported by Culick *et al.* (1992) but in revised and corrected form by Burnley (1996) and Burnley and Culick (1999). Eventually one finds the oscillator equations,

$$\ddot{\eta}_n + \omega_n^2 \eta_n = F_n$$

by now F_n contains stochastic sources. The 'general' form of F_n is

$$-\frac{\bar{p}E_n^2}{\bar{a}^2}F_n = \bar{\rho}I_1 + \frac{1}{\bar{a}^2}I_2 + \bar{\rho}I_3 + \frac{1}{\bar{a}^2}I_4 + \bar{\rho}I_5$$
$$+ \oiint \left[\rho\frac{\partial \mathbf{u}'}{\partial t}\cdot\hat{u} + \bar{\rho}\frac{\partial \mathbf{u}'}{\partial t}\right]\cdot\hat{\mathbf{n}}\psi_n dS - \int \boldsymbol{\mathcal{F}}'\cdot\nabla\psi_n dV + \frac{1}{\bar{a}^2}\int\frac{\partial P'}{\partial t}\psi_n dV$$

where

$$I_1 = \int \left[\bar{\mathbf{u}}\cdot\nabla\mathbf{u}' + \mathbf{u}'\cdot\nabla\bar{\mathbf{u}}\right]\cdot\nabla\psi_n dV$$

and similar definitions for the remaining integrals I_1. See the references for details.

Then the unsteady velocity field is split according to (7.10) a,b,c,d. Eventually re-arrangement and application of the assumptions discussed above leads to the result

$$\ddot{\eta}_n + \omega_n^2\eta_n = 2\alpha_n\dot{\eta}_n + 2\omega_n\theta_n\eta_n - \sum_{i=1}^{\infty}\sum_{i=1}^{\infty}\left[A_{nij}\dot{\eta}_i\dot{\eta}_j + B_{nij}\eta_i\eta_j\right]$$
$$+ \sum\left[\xi_{ni}^v\dot{\eta}_i + \xi_{ni}\eta_i\right] + \Xi_n + \left(F_n^{NL}\right)_{other} \qquad (7.11)$$

where the ξ_{ni}^v, ξ_{ni} and Ξ_n are stochastic sources defined as integrals over the vortical and entropic fluctuations of the velocity. See the references cited above for details.

No modeling based on experimental, theoretical or phenomenological grounds has been accomplished. Explicit results have been obtained by approximating the stochastic sources as white noise processes having properties chosen to be realistic, i.e. the results seem to be reasonably consistent with available measurements of actual behavior.

Two types of stochastic influences arise in (7.11):

(i) Ξ_{ni}, Ξ_{ni}^v represent stochastic influences on the 'spring' or natural frequency of the nth mode and on the damping or growth rate. These are formally referred to as 'multiplicative noise sources' because they appear as factors multiplying the dependent variables, the displacement and velocity of the nth oscillator.

(ii) Ξ_n represents a stochastic driving source causing excitation of the nth oscillator even in the absence of driving by combustion processes; the Ξ_n are formally called 'additive noise sources'.

It is evident from the form of (7.11) that the random character of the stochastic sources will appear as random fluctuations imposed on the amplitudes $\eta_n(t)$ of the acoustic modes; exactly the sort of behavior found experimentally. Thus, Fourier synthesis of the pressure field, the modal expansion, continues to serve as a good approximate representation of the deterministic results can be obtained by retaining only a small number of terms.

Results were obtained first for the simplest, case of two modes, with noise sources only in the fundamental mode. Nonlinear gasdynamic coupling transfer stochastic behavior to the second mode. Computations have been carried out with a Monte-Carlo method to give probability density functions, with the equations written in the Stratonovich form of stochastic differential equations (Burnley, 1996). Figure 7.13 shows the pressure trace and spectrum for a simulation in which the first mode is unstable.
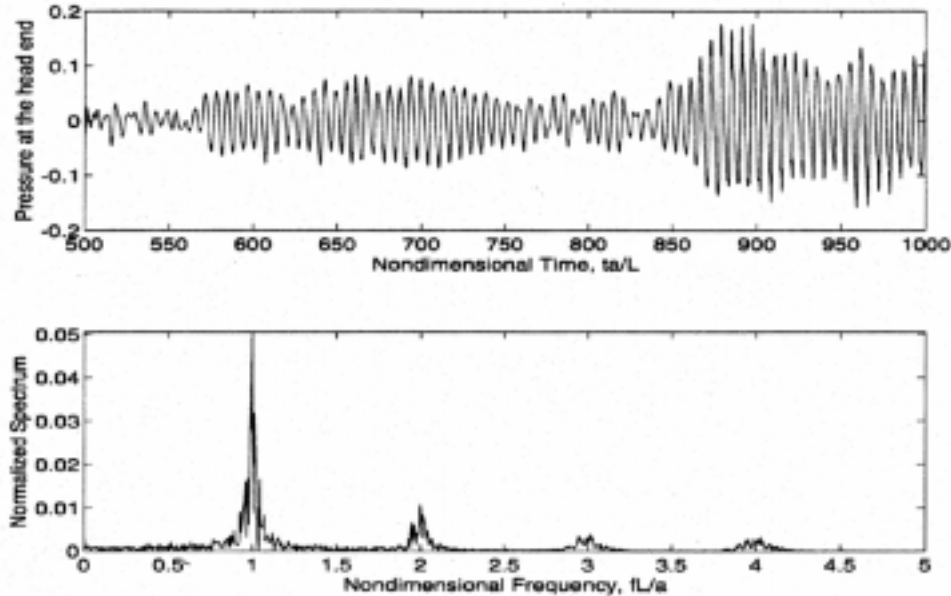
FIGURE 7.13. Pressure Trace and Spectrum for a Simulation with Noise; Four Modes Included, First Mode Unstable

This method of accounted for noise in a combustor seems to be very promising. However modeling the noise sources is in a primitive state, and comparisons of results with experimental observations can only be done qualitatively.

7.5. System Identification for Combustor Dynamics with Noise. Use of system identification in the field of combustor dynamics seems to have been developed first by Russian groups as part of their development of liquid rocket engines, beginning perhaps as early as the 1950's but certainly in the 1960's (Agarkov *et al.* 1993).

In several papers during the 1980's, Hessler (1979, 1980, 1982) and Duer and Hessler (1984), and more recently Hessler and Glick (1998) have asserted that the oscillations observed as combustion instabilities in solid rocket motors are *driven* rather than *self-excited.* The sources of the driving—i.e. the 'mechanisms'—are supposed to be either vortex shedding or noise. Hessler and co-workers conclude that the properties of the noise measured in a stable chamber can be used as the basis for infusing properties of the primary mechanism causing instabilities when they arise or more correctly, such data will provide quantitative information about the static stability margins—how close the dominant acoustic modes are to becoming unstable.

The basic idea is sound. When the mechanisms are interpreted as driving forces independent of the acoustic field, and they are assumed to be broad-band, then the acoustic modes are excited to amplitudes related directly to the amount of damping (α_n). Hence the idea is to process noisy records in such a fashion as to extract the values of the linear parameters (α_n, θ_n). The proposed method can be tested using the oscillator equations with some sources derived in the preceding section.

Seywert and Culick (1999) have reported results of some numerical simulations carried out to check the idea just described. In particular, the main purpose was to determine the accuracy with which the experimental method would give the linear parameters. The procedure is straightforward. To be definite and to keep the computations within practical bounds, we consider a system of four modes, each containing noise sources which, as explained in Section 7.4, are assumed to be white noise. The amplitudes of the noise (rms values) are selected so that random amplitude fluctuations in the pressure spectrum have values in the ranges experimentally observed (Seywert and Culick).

Three types of problems arise, associated with the three types of noise sources: additive noise, Ξ_n; and two kinds of multiplicative noise, ξ_n^v which affects mainly the growth and decay rates, and ξ_n which causes random variations of the frequency. In all cases we are concerned here with discovering the ways in which noise affects the result of system identification. The idea is to select values of the α_n, θ_n and carry out numerical simulations. The data are then processed to give values of the α_n, θ_n which now have mean values and some uncertainties due to the presence of the noise. The questions to be answered are: How close are the mean values to the time values used as inputs? and How large are the uncertainties? These are important practical matters. If the method is effective, then data from hot firings of full-scale combustors could be used to infer the linear parameters characterizing the dynamics represented by several modes. Those parameters identify the poles of the response function of the chamber. Hence a relatively straightforward process would give the information required to proceed with designing a linear control system (see Section 2.5).

Actually there are two ways to get the information: process pressure records naturally occurring; or process the pressure record following an pulse. The method of pulsing has long been used as means of assessing the stability margin of liquid rockets (Harrje and Reardon, 1972). Both methods have been used for a stable system of four longitudinal modes having the parameters given in the table; the fundamental frequency is $900\ s^{-1}$. Figure 7.14 shows a simulated pressure trace and Figure 7.15 shows its power spectrum and construction using Berg's method.[20]

mode	1	2	3	4
$\alpha_n(s^{-1})$	-50	-375	-584	-889
$\theta_n(s^{-1})$	12.9	46.8	-29	-131

TABLE 7.1. Values of the Linear Parameters
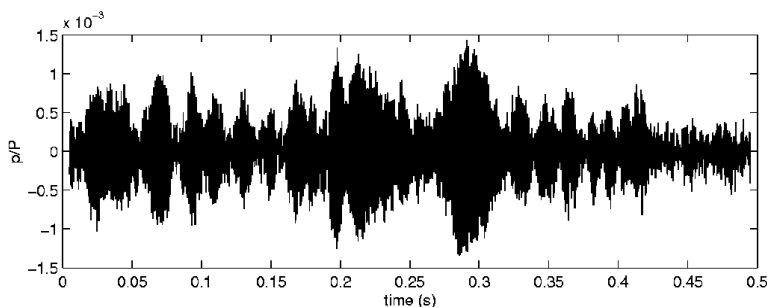
FIGURE 7.14. Simulated Pressure Trace with Noise; All Modes Stable

---

[20]Berg's method is a standard method of signal processing, widely available. We have used the software included in the Signal Processing Toolbox, and extension of MATLAB.

In Figure 7.17, a simulated response to a pulse is fitted by the superposition of four modes:

$$\frac{p'}{\bar{p}} = \sum_{i=1}^{4} A_i e^{\alpha_i t} \cos(\omega_i t + \phi_i)$$

The parameters A_i, α_i, ω_i, ϕ_i are fitted using a least squares method.
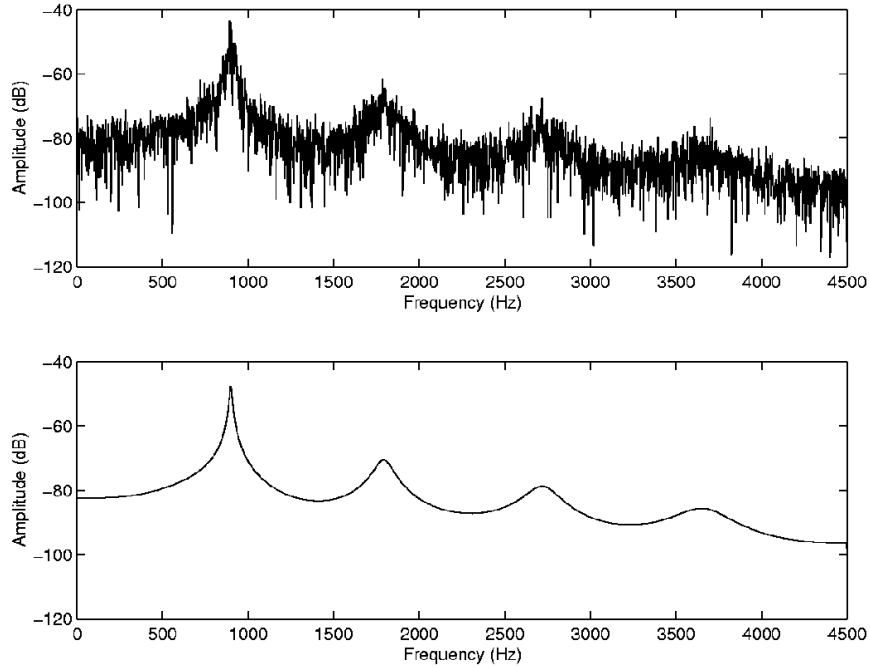
FIGURE 7.15. Application of Berg's Method: Power Spectrum of the Pressure Trace in Figure 7.14 and its Reconstruction
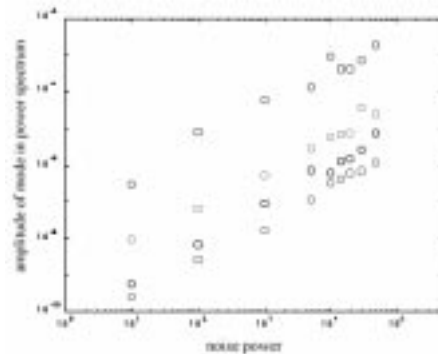
FIGURE 7.16. Dependence of the Peak Amplitudes of the Power Spectra for Four Modes, on Noise Power

Without good data for the noise in an actual combustor and no model, we assume white noise sources. Their amplitudes are chosen so that the average (rms) values of the simulated pressure records are reasonable Table 7.2 shows the relation between the rms value of the system response $(p'/\bar{p})$ and the noise power of Ξ. The 'noisepower' cannot be measured, being the height of the power spectral density of the noise. Figure 7.16 gives a more detailed picture, showing how the amplitudes of the spectra of the four modes increase with noise power.

We use the noise power as a parameter. Figure 7.18 shows an example of the sort of results one finds for multiplicative noise in the modal damping $(\xi_n^v \neq 0;\ \xi_n = 0;\ \Xi_n = 0)$. The corresponding results of using the pulse method are given in Figure 7.19.

Noise Power of Ξ_n	rms Values of $p'/\bar{p}$
10^1	.005%
10^3	.05%
10^5	.5%

TABLE 7.2. Relation Between the Noise Power of Ξ_n and the rms Value of the Simulated Pressure Fluctuation
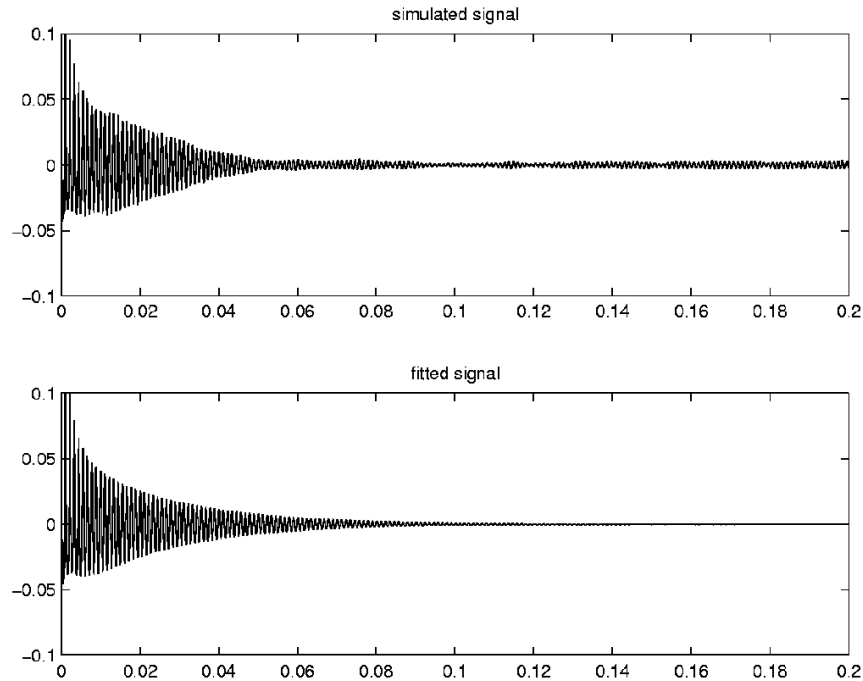
FIGURE 7.17. Reconstructed Pressure Trace for the Transient Response Excited by a 10% Pulse

Noise	α_1	α_2	α_3	α_4
10^1	-57±14	-301±31	-560±84	-886±98
10^2	-51±13	-307±52	-576±75	-903±126
10^3	-47±11	-307±38	-558±78	-901±117
10^4	-56±16	-300±51	-591±88	-883±150
10^5	-59±18	-310±53	-598±95	-914±128
10^6	-53±15	-310±46	-564±84	-905±172
10^7	-59±19	-313±44	-591±83	-887±124
correct	-50	-325	-584	-889
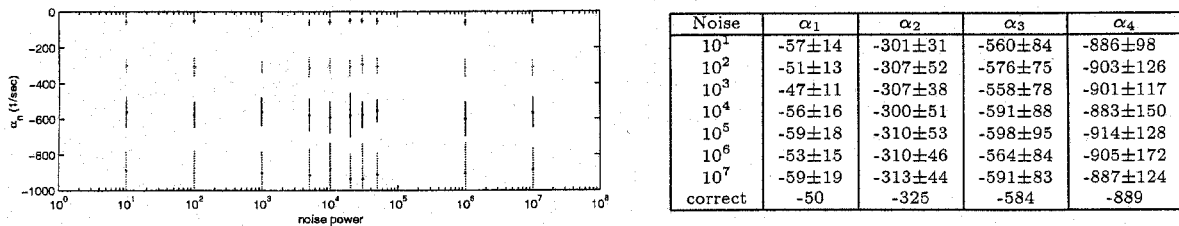
FIGURE 7.18. Values of Decay Rates (Modal Attenuation) Found with Berg's Method with Multiplicative (ξ_n) Noise

We conclude from these results that substantial errors may accompany system identification in the presence of realistic (we believe) noise. How significant the errors are depends the particular application at hand and in how small the stability margins are. For a weakly stable system, values of the margins determined in this way are suspect because of the finite uncertainties. The results would therefore not be useful as a basis for representing the combustor's response function.

Noise	α_1	α_2	α_3	α_4
10^1	-50±2	-323±6	-584±9	-889±35
10^2	-50±2	-325±5	-589±8	-908±36
10^3	-50±2	-322±4	-587±10	-891±44
10^4	-50±3	-326±5	-589±8	-902±37
10^5	-49±3	-326±4	-586±12	-895±35
10^6	-50±2	-324±4	-582±15	-886±43
10^7	-49±3	-327±4	-583±11	-877±51
correct	-50	-325	-584	-889
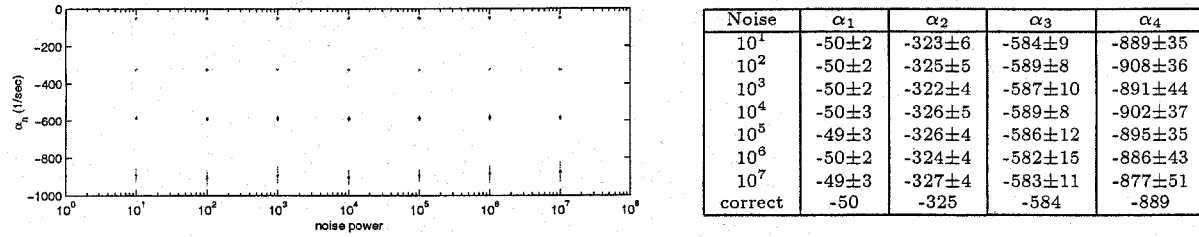
FIGURE 7.19. Values of Decay Rates (Modal Attenuation) Found with the Method of Pulsing

It should be clear from the nature of the methods described here that the system must be stable (i.e. all modes must be stable) for this application. For example, if data (simulated) for a limit cycle are processed in this fashion, the inferred values of α_n, θ_n have no apparent connection with the correct values.

8. PASSIVE CONTROL OF COMBUSTION INSTABILITIES

For several sound reasons, and some not so sound, active control of combustor dynamics has become a subject of lively research, of some development for operational systems, and of much found optimism for successful practical use. However, with one possible exception cited in the following section, there are no installations of active control in operational combustors. Yet, as we have described in Section 1, combustion stabilities have occurred in all types of high performance systems. In almost all cases the amplitudes of the oscillations were reduced to acceptable levels, or eliminated entirely. How? By methods of possible control.

For solid rockets, two sorts of passive control are routinely applied: change the propellant composition; or modify the geometry. It is rarely possible to alter the reactants in liquid fueled systems. Hence methods of passive control have become the usual means of trying to improve the chamber dynamics. There seem to be three classes of methods having histories of success:

  (i) fuel scheduling

  (ii) baffles, acoustic liners and resonators

  (iii) changing the dynamics of the injection system

Fuel scheduling means the history and spatial distribution of fuel injection during a firing. It is a common strategy for extending the envelop of stable operation for afterburners (thrust augmentors). It is a practically effective method for combustors containing an array of many injectors. The way in which the injectors themselves are distributed in the chamber is part of the method. Liquid rockets having many injector elements distributed over the injector face offer a wide range of choices; see, for example, the interesting review of the development of the F-1 engine by Ofelein and Yang (1993). Probably the chief reason for the effectiveness of fuel scheduling is that the distribution of reaction zones and energy release are affected. Rayleigh's criterion (Section 6.4) should be helpful in qualitative interpretation of test results, but no results have been reported. Indeed, because of the strong commercial competition, virtually all details of afterburners are held proprietary.

A standard practice in the development of afterburners is to incorporate acoustic liners as part of the basic design to help avoid instabilities of transverse modes, and use fuel scheduling to treat lower frequencies, those of the longitudinal modes. The latter is an expensive trial and error procedure in practice. Especially costly is the need for many tests under high altitude conditions.

We classify baffles, acoustic liners and resonators together because, although they operate differently, all act directly in the acoustic field. Baffles have at least two important effects (Figure 8.1): extending downstream from the injector face, radial or circumferential baffles effectively shadow responsive regions at the injector face from acoustic velocity fluctuations; and, especially if they extend well into the chamber volume, baffles can cause large modifications of the natural acoustic modes. They impose internal boundary conditions, thereby raising the modal frequencies. This is a useful strategy if the driving mechanism is responsive in a narrow frequency range: the idea is to ensure that the frequencies of the normal modes are not resonant or commensurate with the natural frequencies of the driving.

Acoustic liners are distributed arrays of small resonator mounted usually on the lateral boundary of the combustor in question. Because the resonators are small, liners are normally effective in the frequency range of transverse modes. Most of their influence is due to their dissipation of energy although there is necessarily some effect in the values of the modal frequencies of the chamber. Larger resonators will be effective at lower frequencies but due to volume contraints, installing them is rarely a practical strategy.

The third type of passive control, based on the dynamics of the injection system is considerably more complicated than the first two. There are roughly two courses of action: eliminate harmful dynamics; or design the system to take special advantage of injector dynamics. It has long been known that large pressure drops across injectors provide high impedance and therefore discourages coupling between the dynamics of the chamber and the dynamics of the fuel systems.
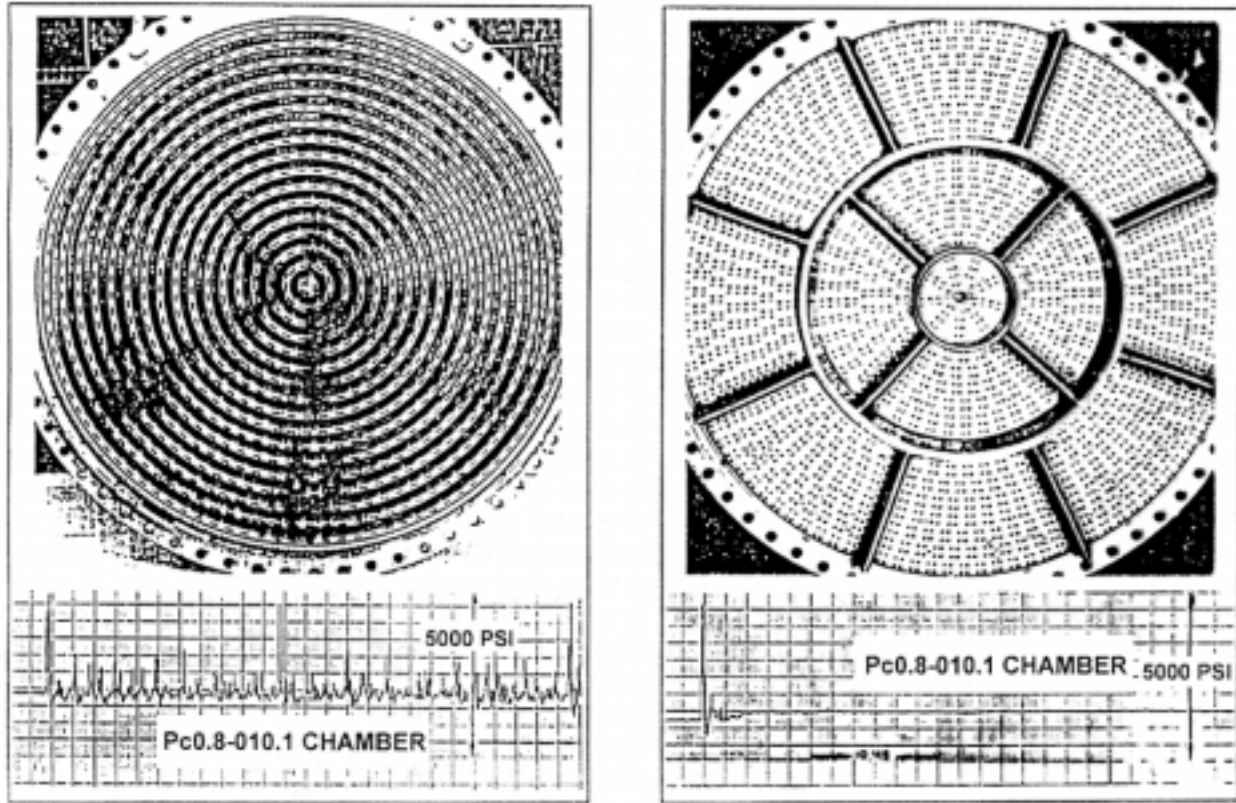
FIGURE 8.1. Examples of Baffles in the F-1 Liquid Rocket Engine

There is much more to the matter because the fluid-mechanical processes immediately downstream of the injector face are very sensitive to details of the design. A particularly good (and expensive) example is the development of the injectors for the F-1 engine reviewed by Ofelein and Yang (1993).

Probably the most extensive work in design of injectors with a view towards passive control of chamber dynamics has been accomplished by Bazarov who accomplished much of his work during the period of most active development of Russian liquid rocket engines (Bazarov 1979, Bazarov and Yang 1998).

Changing the geometry of the chamber itself, other than by introducing baffles has been successfully used to reduce instabilities in solid rockets. Normally that is not an option for treating undesirable dynamics in gas turbines. The main consequence of changing chamber geometry is to change the natural mode shapes and frequencies. One possible result is that the natural frequencies may then lie outside the range where the combustion dynamics tends most strongly to drive instabilities.

In fact that tactic, avoiding close coincidence between the natural frequencies of the chamber and the frequency range where the net driving is greatest, is central to many methods of passive and active control. The point is made with Figure 8.2, an extended form of Figure 1.6. The most important point of Figure 8.2 is that active control offers flexibility equivalent to the possibilities of passive control, but in any case more complete understanding of the plant will allow more effective application of control, whether it be passive or active.

With suitable modeling, all types of passive control can be taken into account within the analytical framework developed in Sections 2 and 3. For example, baffles may affect the mode shapes ψ_n and frequencies ω_n; and acoustic linears can be represented by surface admittance functions.

$G(s)$: Transfer function of chamber without combustion
$Q(s)$: Feedback due to response of combustion processes

PASSIVE CONTROL

(1) Modify G(jw) (Plant)
- Shift resonance frequencies
- Increase attenuation

(2) Modify Q(jw) (Feedback)
- Reduce $|Q|$ in the vicinity of unstable frequency
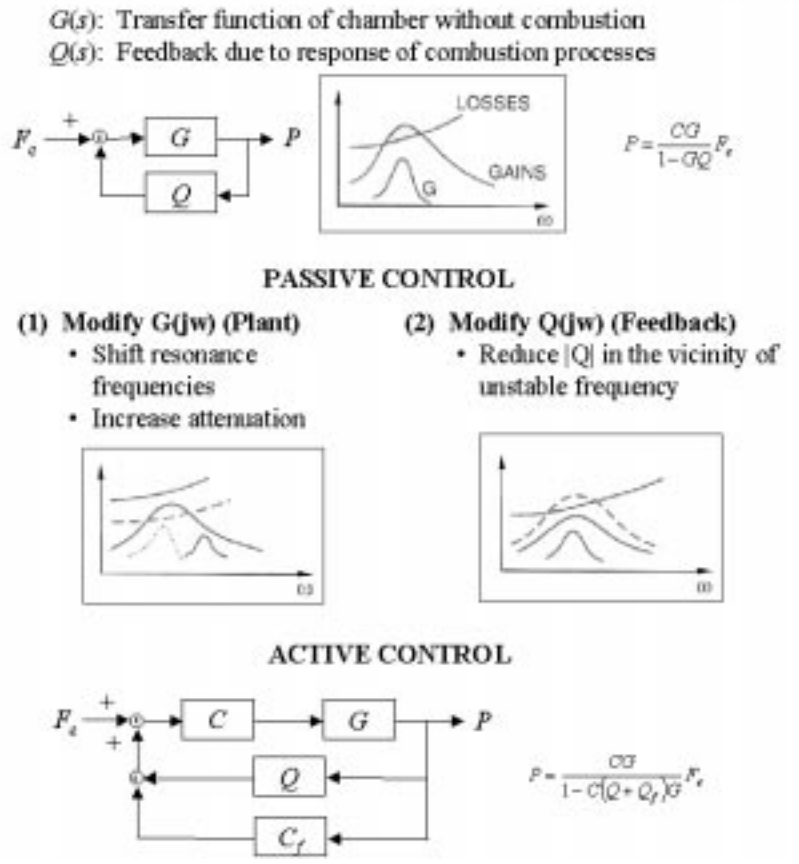
ACTIVE CONTROL

FIGURE 8.2. Qualitative Interpretation of the Action of Linear Passive and Active Control

9. ACTIVE CONTROL OF COMBUSTION INSTABILITIES

Most recent works on active control have been reviewed in other lectures in this course. In this section we restrict the discussion largely to the connection between the framework based on spatial averaging; and the principles of modern control theory.

The chief premise of these two lectures is that for effective control of combustor dynamics—passive or active— it is essential to understand the system as completely as possible. By 'system' we mean the coupled dynamical system labeled in Figure 1.1 'combustor dynamics' and 'combustion dynamics'. Figure 9.3, a form of generic block diagram often appearing in textbooks suggests how the system bring controlled fits into a general control scheme. Actuation and sensing are included as part of the 'plant' being controlled. They are of course crucial items as other lecturers have emphasized, but they are outside our concerns. Their dynamics must be known but are determined by methods outside those discussed in these two lectures.

PLANT : Combustor with Internal Feedback ; Actuation ; Sensing

CONTROLLER : State Estimator ; Regulator

FEEDBACK : Connection between Plant Output and Controller Input (control loop)
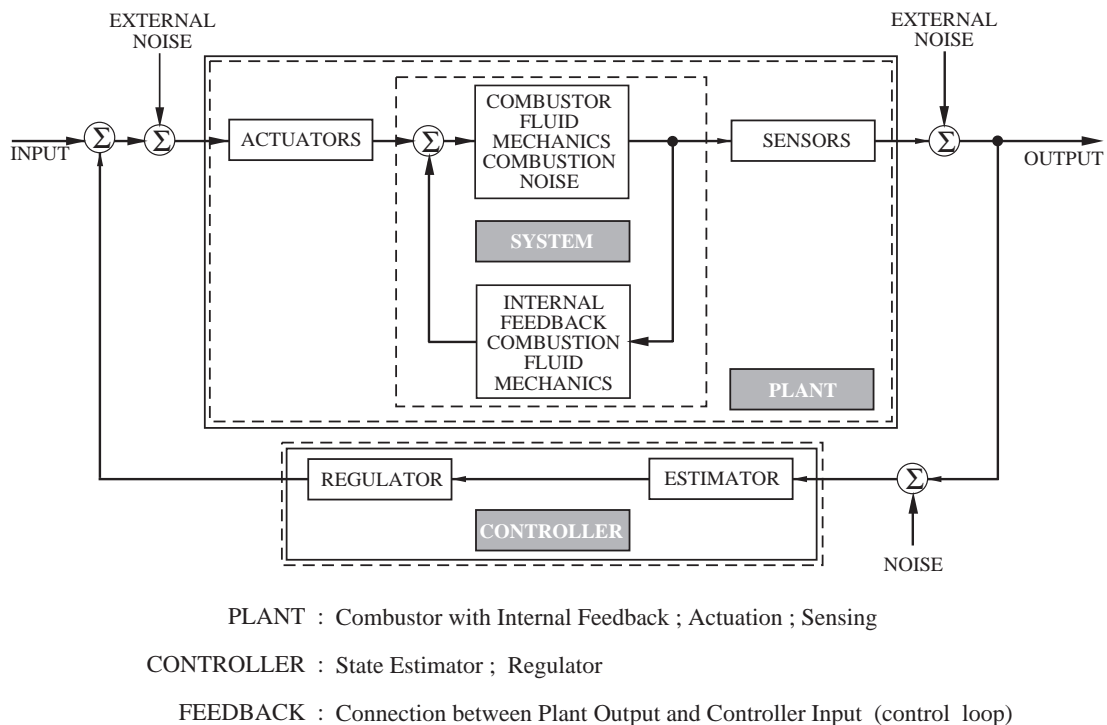
FIGURE 9.3. A Generic Block Diagram for Classical and Modern Control.

Given that at a sufficiently high level practically all control systems fit the picture shown in Figure 9.3, and further that the principles of linear control are well-known and their applications highly developed, it is a reasonable question: what is special about the problem of controlling the dynamics of a combustion system? Probably the best simple answer is that combustion systems bring together at least five defining characteristics each of which individually already may be difficult to treat in a control system:

- internal instabilities
- substantial time lags
- intrinsically nonlinear
- substantial internal noise
- the action of control changes the system

The fact that the system is unstable—the origin, after all, of the problems discussed here—is not unusual, nor is the presence of time lags. Control of nonlinear systems has successfully been treated in special cases and it seems that much is known about controlling some kinds of general nonlinear behavior in other types of physical systems. Presently the significance of the noise in respect to controlling combustion systems is not understood; the matter merits consideration since often the levels of noise are not negligibly small compared with those of the instabilities. When a combustion system is controlled, significant changes in the defining characteristics, such as the distribution of average energy release may occur. In fact those changes may account for elimination of an instability. That sort of behavior is quite different from the usual situation in a mechanical system whose defining properties such as masses, are not affected by the action of control.

All five of the items listed above raise issues of modeling. That situation justifies the principal thrust of these lectures. The general framework based on spatial averaging is attractive for at least two important reasons:

(i) the process of averaging tends to reduce the consequences of errors in details of modeling;

(ii) there is a perfect match between the methods of feedback control in state space on the one hand; and the theory of combustor dynamics based on spatial averaging and expansion in acoustic modes on the other.

In the literature of control theory this merging of control theory and the behavior of a continuous system is often called 'control of a distributed parameter system.' However, that label normally implies representation—i.e. a mathematical model—of the system based on partial differential equations.

The subject of this section is more appropriately called modal control, using a representation of the system based on ordinary differential equations describing the amplitudes and relative phases of the modes. Modal control has been developed mainly in the field of structures, nonflowing systems generally, which can be represented as 'lumped paramter' systems by working with Lagrange's equations: Figure 9.4 summarizes the scheme we have discussed in the preceding seven sections. Matters of control arise in the bottom line of blocks. Our remarks here are limited to linear control, which encompasses both classical and modern control. It is essential to understand the well-established principles of classical control. However, for several reasons it is preferable to treat control of combustion systems within the modern control theory, using the representation in state space.
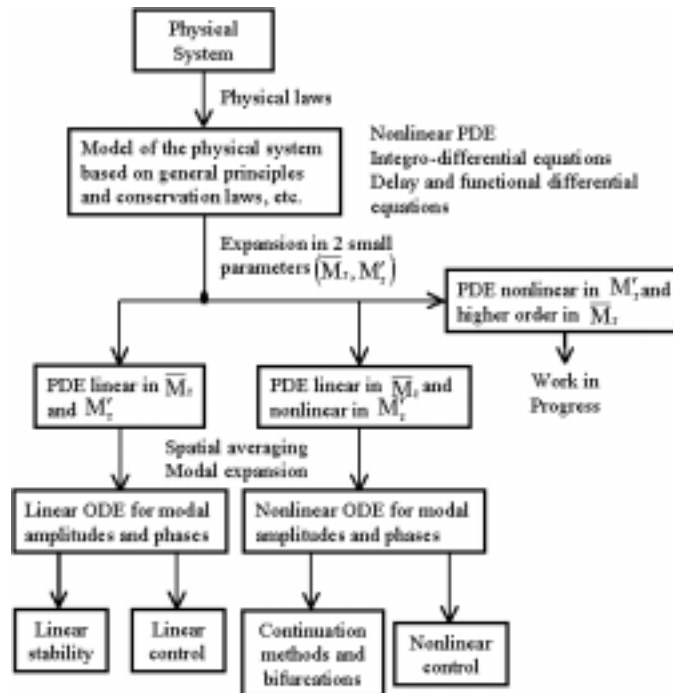
FIGURE 9.4. The General Scheme Connecting the Physical System (a Combustor), Physical Modeling, Mathematical Modeling, Dynamics and Control

First, it happens that the analytical formulation based on spatial averaging becomes a state space representation by simple redefinition of symbols. Hence the entire apparatus of modern control theory becomes immediately applicable. The group at Penn State has taken the most systematic formal advantage of that attractive feature (Fung, Yang and Sinha, 1991; Yang, Sinha and Fung, 1992; Fung and Yang, 1992; Hong, Yang and Ray, 1999; Hong, Yang and Ray, 2000). Other works by groups at MIT, Georgia Tech and at Caltech are closely related in some respects or other.

The basic idea is quite simple and straightforward, following from the form of the equations (3.54) and their boundary conditions (3.56) governing the evolution of arbitrary unsteady motions in a combustor:

$$\nabla^2 p' - \frac{1}{\bar{a}^2} \frac{\partial^2 p'}{\partial t^2} = h + h_c \tag{9.1}$$

$$\hat{\mathbf{n}} \cdot \nabla p' = -f - f_c \tag{9.2}$$

The functions h_c and f_c represent the actions of control. The splitting on the right-hand sides of (9.1) and (9.2) is legitimate for linear problems because any means of control (passive or active) can work only because it affects the mass, momentum and energy of the system; the additivity follows from the assumption of linearity. In principle, h_c and f_c can be computed with the same formulas defining h and f discussed in Section 3. The formalism of spatial averaging can be applied without change to (9.1) and (9.2), giving the extended oscillator equations corresponding to (4.36), written here for the nth mode:

$$\ddot{\eta}_n + \omega_n^2 \eta_n = F_n + F_n^{(c)} \tag{9.3}$$

where $F_n^{(c)}$ is the 'force' of control acting on the nth oscillator, (i.e. the nth mode). The set of equations (9.3) forms the mathematical model used in application of the principles of control. We emphasize once again that the most difficult part of applications consists in modeling the physical processes[21] contained in F_n and $F_n^{(c)}$.

As a simple example of the general procedure, we suppose that the combustor is given and that its internal processes are well-characterized. Thus the mean flow field, and the steady distribution of chemical reactions and energy release are known. Hence we may assume that the basic functions ψ_n and the normal frequencies can be computed and are known. Hidden in F_n are quantities that must be modeled. In particular, the most important is the fluctuation of energy release, $\dot{Q}'$, associated with the chemical reactivity of the flow. Its contribution to F_n has already been introduced in the simple example of the Rijke tube discussed in Section 2:

$$F_N^Q = \frac{\gamma - 1}{\bar{p}} \frac{1}{\int \psi_n^2 dV} \int \psi_n \frac{\partial \dot{Q}'}{\partial t} dV \tag{9.4}$$

In reality $\dot{Q}'$ depends on local fluctuations of pressure, temperature, velocity and species concentrations. It therefore cannot be determined from considerations of chemistry and chemical kinetics only.

A term similar to (9.4) arises in $F_n^{(c)}$ so on the right-hand side of (9.3) we have the combination

$$F_n^Q + F_n^{Q(c)} = \frac{\gamma - 1}{\bar{p}} \frac{1}{\int \psi_n^2 dV} \int \psi_n \left[\frac{\partial \dot{Q}'}{\partial t} + \frac{\partial \dot{Q}'_c}{\partial t} \right] dV \tag{9.5}$$

where $\dot{Q}'_c$ is the local fluctuation of heat release rate ascribed to the controlled actuation. If $\frac{\partial}{\partial t}(\dot{Q}' + \dot{Q}'_c)$ vanishes, then there is no effect of heat in energy release in the excitation and maintenance of unsteady motions. This seems a simple if not almost obvious result. However, it is the formal expression within the analysis developed here, of what is widely accepted as likely the most effective practical means of actively controlling the dynamics of gas turbine combustors, fuel modulation.

The basic idea is that if the fuel supply so modulated, or if a secondary fuel supply is injected in the chamber, and the modulation as effected according to the right control law, then the fluctuation of energy release rate $\dot{Q}'_c$ due to its action may exactly compensate the amount $\dot{Q}'$ due to fluctuations due to other causes. 'Other causes' might include coupling between the mean flow (e.g. vortex shedding) and acoustic modes and destabilization of flame stabilization processes near the lean blowout limit. This kind of control can be interpreted in terms of

---

[21]The formulation here is very general and of course is valid as well for non-reacting flows. Hence, at least in principle, these equations with noise sources included (Sections 7.4 and 8) are applicable as well to active control of sound or noise (Nelson and Elliott, 1992; Peake and Crighton, 2000).

Rayleigh's original criterion, Section 6.4: if $\dot{Q}'_c = -\dot{Q}'$ and only this process is accounted for, then $\nabla \xi_n$, equation (6.28), vanishes. Hence control by modulation of the fuel supply is commonly referred to as a strategy "according to Rayleigh's criterion" or similar words.

9.1. State-Space Representation for Control of Combustor Dynamics. Casting the oscillator equations (9.3) in the state-space representation familiar in control theory is largely a matter of selecting appropriate definitions. We already know from the developments in Section 7, that no matter what processes are accounted for, so long as the behavior is linear, except for the nonlinear gasdynamics required to include noise, F_n will have the form

$$F_n = -\sum_{l=1}^{\infty} [D_{nl}\dot{\eta}_l + E_{nl}\eta_l] + \sum_{i=1}^{\infty} [\xi_{ni}^v(t)\dot{\eta}_i + \xi_{ni}(t)\eta_i] + \Xi_n(t) \tag{9.6}$$

The physical processes associated with actuation must lead to terms linear in the $\dot{\eta}_l$ and η_l; for simplicity we drop stochastic contributions, although they might in fact exist in practice. It is quite conceivable that control can be exercised independently of the state of the system, and the general (noiseless) form of $F_n^{(c)}$ is evidently

$$F_n^{(c)} = -\sum_{l=1}^{\infty} \left[D_{nl}^{(c)}\dot{\eta}_l + E_{nl}^{(c)}\eta_l \right] + u_n(t) \tag{9.7}$$

where the u_n are independent of the η_n and $\dot{\eta}_n$.

We consider only a finite number N of modes and define the state variables

$$x_1 = \eta_1 \ , \ x_1 = \eta_2 \ , \ x_3 = \eta_3 \ , \ \cdots x_N = \eta_N$$
$$x_{N+1} = \dot{\eta}_1 \ , \ x_{N+2} = \dot{\eta}_2 \ , \ x_{N+3} = \dot{\eta}_3 \ , \ \cdots x_{2N} = \dot{\eta}_N$$

More concisely, the state vector is

$$\mathbf{x} = [\eta_1 \ , \ \eta_2 \ , \ \cdots \eta_N \ , \ \dot{\eta}_1 \ , \ \dot{\eta}_2 \ \cdots \dot{\eta}_{2N}]^t \tag{9.8}$$

The first order equations for the state variables are

$$\frac{dx_1}{dt} = x_{N+1}$$
$$\frac{dx_2}{dt} = x_{N+2}$$
$$\vdots$$
$$\frac{dx_N}{dt} = x_{2N}$$
$$\frac{dx_{N+1}}{dt} = \ddot{\eta}_1 = -\omega_1^2 \eta_1 + F_1 + F_1^{(t)} = -\omega_1^2 x_1 + F_1 + F_1^{(c)}$$
$$\vdots$$
$$\frac{dx_{2N}}{dt} = \ddot{\eta}_N = -\omega_N^2 \eta_N + F_N + F_N^{(t)} = -\omega_N^2 x_N + F_N + F_N^{(c)}$$

For example, for the case of two modes ($N = 2$) and with (9.6) and (9.7), this system reduces to:

$$\frac{dx_1}{dt} = x_3$$

$$\frac{dx_2}{dt} = x_4$$

$$\begin{aligned}
\frac{dx_3}{dt} &= -\omega_1^2 x_1 - [D_{11}\dot{\eta}_1 + E_{11}\eta_1 + D_{12}\dot{\eta}_2 + E_{12}\eta_2] \\
&\quad + [\xi_{11}^v \dot{\eta}_1 + \xi_{11}\eta_1 + \xi_{12}^v \dot{\eta}_2 + \xi_{12}\eta_2] + \Xi_1 \\
&\quad - [D_{11}^{(c)}\dot{\eta}_1 + E_{11}^{(c)}\eta_1 + D_{12}^{(c)}\dot{\eta}_2 + E_{12}^{(c)}\eta_2] + u_1 \\
&= -\omega_1^2 x_1 - (E_{11} + E_{11}^{(c)} - \xi_{11})x_1 - (E_{12} + E_{12}^{(c)} - \xi_{12})x_2 \\
&\quad - (D_{11} + D_{11}^{(c)} - \xi_{11}^v)x_3 - (D_{12} + D_{12}^{(c)} - \xi_{12}^v)x_4 + \Xi_1 + u_1
\end{aligned}$$

$$\begin{aligned}
\frac{dx_4}{dt} &= -\omega_2^2 x_2 - (E_{21} + E_{21}^{(c)} - \xi_{21})x_1 - (E_{22} + E_{22}^{(c)} - \xi_{22})x_2 \\
&\quad - (D_{21} + D_{21}^{(c)} - \xi_{21}^v)x_3 - (D_{22} + D_{22}^{(c)} - \xi_{22}^v)x_4 + \Xi_2 + \eta_2
\end{aligned}$$

In matrix form these equations are:

$$\frac{d\mathbf{x}}{dt} = \mathbf{A}\mathbf{x} + \mathbf{B}\mathbf{u} + \mathbf{\Xi} \tag{9.9}$$

where

$$\mathbf{A} = \begin{bmatrix}
0 & 0 & 1 & 0 \\
0 & 0 & 0 & 1 \\
-\omega_1^2 - (E_{11} + E_{11}^{(c)} - \xi_{11}) & -(E_{12} + E_{12}^{(c)} - \xi_{12}) & -(D_{11} + D_{12}^{(c)} - \xi_{12}^v) & -(D_{12} + D_{12}^{(c)} - \xi_{12}^v) \\
-(E_{21} + E_{21}^{(c)} - \xi_{21}) & -\omega_2^2 - (E_{22} + E_{22}^{(c)} - \xi_{22}) & -(D_{21} + D_{21}^{(c)} - \xi_{21}^v) & -(D_{22} + D_{22}^{(c)} - \xi_{21}^v)
\end{bmatrix} \tag{9.10}$$

$$\mathbf{B} = \begin{bmatrix} 0 & 0 & 0 & 0 \\ 0 & 0 & 1 & 0 \\ 0 & 0 & 0 & 1 \end{bmatrix} \qquad \mathbf{\Xi} = \begin{Bmatrix} 0 \\ 0 \\ \Xi_1 \\ \Xi_2 \end{Bmatrix} \tag{9.11}a,b$$

The description is completed with the equation for the observed variables,

$$\mathbf{y} = \mathbf{C}\mathbf{x} ; \quad \mathbf{C} = \begin{pmatrix} 1 & 0 & 0 & 0 \\ 0 & 1 & 0 & 0 \\ 0 & 0 & 1 & 0 \\ 0 & 0 & 0 & 1 \end{pmatrix} \tag{9.12}a,b$$

regarded as the sum of two matrices, one depending on the properties of the uncontrolled chamber, and one, whose elements are identified by the superscript $(\ )^{(c)}$.

$$\mathbf{A}^{(c)} = \begin{bmatrix}
0 & 0 & 0 & 0 \\
0 & 0 & 0 & 0 \\
-E_{11}^{(c)} & -E_{12}^{(c)} & -D_{11}^{(c)} & -D_{12}^{(c)} \\
-E_{21}^{(c)} & -E_{22}^{(c)} & -D_{21}^{(c)} & -D_{22}^{(c)}
\end{bmatrix} \tag{9.13}$$

It is a natural consequence of the way in which we approached the matter here that we have incorporated full-state feedback represented by the matrix $\mathbf{A}^{(c)}$.

Many examples of simulations of feedback control of combustor dynamics have been reported, usually without reference to the general framework described here. With a few exceptions (e.g. Fung et $al.$ 1991; Haddad et $al.$ 1997; Seywert, 2000; Isella, 2000) the intimate connection between the actuation and the physical processes within the combustor are ignored, a tactic that probably detracts from the validity of the simulations. In lieu of modeling the processes that must be taking place for any sort of actuation to work, the control problem is handled in traditional fashion. The properties of the system are assumed to be known and unchanged by the action of control: the state matrix $\mathbf{A}$ is fixed. Moreover, it is obviously convenient if one has complete freedom

to specify the control law without the constraints placed by any requirements to model the internal processes necessary for actuation to affect the system.

Under those circumstances it is virtually pre-ordered that simulations will show that use of active feedback control will be successful. No matter how detailed the behavior of the combustor is described—and whether the calculations are analytic or numerical, any combustor will behave dynamically at least roughly like a system of coupled oscillators—that's intrinsic to the nature of disturbances within the chamber. The control problem then has qualitatively an expected result: unstable disturbances can indeed be controlled.

Without the modeling, however, a wide array of interesting and practically important questions can be answered. The control part of the state matrix, $\mathbf{A}^{(c)}$ can be simply dropped, a common tactic, and the control vector is specified. Alternatively, the rigorous connection between the state feedback represented by $\mathbf{A}^{(c)}$ can be ignored and an arbitrary model used. See the references cited for many examples. In any event, the calculations do not pose serious practical problems: it seems that almost all results desired can obtained with MATLAB and SIMULINK (see Isella, 2000; Seywert, 2000; and Isella, Seywert and Culick, 2000).

A. EQUATIONS OF MOTION

Combustion systems commonly contain condensed phases: liquid fuel or oxidizer and combustion products including soot and condensed metal oxides. Hence the equations of motion must account for two or three phases and at least one species in each. For investigating the dynamics of combustors, it is entirely adequate to represent each phase as its mass average over all member species. It is unnecessary to distinguish liquid and solid material and we assume a single species in the condensed phase, devoted by subscript $(\ )_l$. For some applications it is appropriate to extend the representation slightly to accommodate distributions of particle sizes, not included in this appendix. There is some advantage to treating the gas phase as a multi-component reacting mixture. As the primitive conservation equations we therefore begin with the following set:

A.1. General Equations of Motion. Conservation of Species

$$\frac{\partial \rho_i}{\partial t} + \nabla \cdot (\rho_i \mathbf{u}_i) = w_i + w_i^{(l)} + w_{ei} \tag{A.1}$$

Global Conservation of Mass, Gas Phase

$$\frac{\partial \rho_g}{\partial t} + \nabla \cdot (\rho_g \mathbf{u}_g) = w_g^{(l)} + w_{eg} \tag{A.2}$$

Global Conservation of Mass, Condensed Phase[22]

$$\frac{\partial \rho_l}{\partial t} + \nabla \cdot (\rho_l \mathbf{u}_l) = -w_g^{(l)} + w_{el} \tag{A.3}$$

Global Conservation of Momentum

$$\frac{\partial}{\partial t} \left(\sum^i \rho_i \mathbf{u}_i + \rho_l \mathbf{u}_l \right) + \nabla \cdot \left(\sum \rho_i \mathbf{u}_i \mathbf{u}_i + \rho_l \mathbf{u}_l \right) + \nabla p = \nabla \cdot \overleftrightarrow{\boldsymbol{\tau}}_v + \mathbf{m}_{eg} + \mathbf{m}_{el} \tag{A.4}$$

Global Conservation of Energy

$$\frac{\partial}{\partial t} \left(\sum \rho_i e_{oi} + \rho_l e_{ol} \right) + \nabla \cdot \left(\sum \rho_i \mathbf{u}_i e_{oi} + \rho_l \mathbf{u}_l e_{ol} \right) + \nabla \cdot \left(\sum p_i \mathbf{u}_i \right) = \nabla \cdot \left(\overleftrightarrow{\boldsymbol{\tau}}_v \cdot \mathbf{u}_g \right) - \nabla \cdot \mathbf{q} + Q_e \tag{A.5}$$

Equation of State, Gas Phase

$$p = \rho_g R_g T_g \tag{A.6}$$

For simplification, the above equations already contain some terms involving mass averaging over the species comprising the gas phase, namely the viscous tensor $\overleftrightarrow{\boldsymbol{\tau}}_v$; the vector $\mathbf{q}$ representing heat conduction; and the equation, of state (A.6). For more complete derivations of the equations for multicomponent mixtures, see for example Chapman and Cowling (1958); Hirschfelder, Curtis and Bird (19); Truesdell and Toupin (1960); and Williams (1985). Superscript $(\ )^{(l)}$ means that the liquid phase is the source and subscript $(\ )_e$ denotes an external source. It follows from repeated use of the Gibbs-Dalton law for mixtures of perfect gases that p is the sum of partial pressures, ρ_g is the sum of the densities and R is the mass average of the individual gas species, so for the gas phase we have

$$p = \sum p_i$$
$$\rho_g = \sum \rho_i \tag{A.7 a,b,c}$$
$$R_g = \frac{1}{\rho_g} \sum \rho_i R_i$$

---

[22]Note that ρ_l represents the mass of condensed material per unit volume of chamber, *not* the density of the material itself.

Subscript $(\ )_i$ identifies the ith gaseous species; and in all cases except T_g, $(\ )_g$ means a mass average over all gas species as, for example,

$$\mathbf{u}_g = \frac{1}{\rho_g} \sum \rho_i \mathbf{u}_i = \sum Y_i \mathbf{u}_i \tag{A.8}$$

where $Y_i = \rho_i / \rho_g$ is the mass concentration of the ith species.

Writing equations (A.1)–(A.5) explicitly with sums over species allows proper accounting of the influencesof diffusion, and leads to the formula for energy released by chemical reactions written in the conventional fashion. Thus the basis for subsequently modeling is rigorously set. For analysis of unsteady motins in combustors it is perfectly adequate to reduce the general description for a multicomponent mixture to a model representing a single fluid having the mass-averaged properties of the actual mixture. Details of the procedure may be found elsewhere (Culick 1999). Only the results are germane here. The set of equations forming the basis for the theory and analysis we discuss in these lectures is:

$$\frac{D\rho}{Dt} = -\rho \nabla \cdot \mathbf{u} + \mathcal{W} \tag{A.9}$$

$$\rho \frac{D\mathbf{u}}{Dt} = -\nabla p + \boldsymbol{\mathcal{F}} \tag{A.10}$$

$$\rho \mathbf{C}_v \frac{DT}{Dt} = -p \nabla \cdot \mathbf{u} + \mathcal{Q} \tag{A.11}$$

$$\frac{Dp}{Dt} = -\gamma p \nabla \cdot \mathbf{u} + \mathcal{P} \tag{A.12}$$

$$\frac{Ds}{Dt} = \frac{1}{T} \mathcal{S} \tag{A.13}$$

$$p = \mathbf{R} \rho T \tag{A.14}$$

For completeness we have also included the equation (A.13) for the entropy, obtained in familiar fashion by applying the combined. First and Second Laws of Thermodynamics to an element of fluid. That is, the relation $de = Tds - pdv$ can be written

$$\begin{aligned} \frac{Ds}{Dt} &= \frac{1}{T} \left(\frac{De}{Dt} + p \frac{Dv}{Dt} \right) \\ &= \frac{1}{T} \left(\mathbf{C}_v \frac{DT}{Dt} + p \frac{Dv}{Dt} \right) \end{aligned} \tag{A.15}$$

Substitution of (A.9) and (A.11) gives (A.13) with the source

$$\mathcal{S} = \mathcal{Q} - \frac{p}{\rho^2} \mathcal{W} \tag{A.16}$$

It is important to realize that this formulation contains all relevant physical processes, including those representing the actions of external influences associated, for example, with active control of combustor dynamics.

The source functions in (A.9)–(A.13) are

$$\mathcal{W} = w_e - \nabla \cdot (\rho_l \delta \mathbf{u}) \tag{A.17}$$

$$\boldsymbol{\mathcal{F}} = \nabla \cdot \overset{\leftrightarrow}{\boldsymbol{\tau}}_v + \mathbf{m}_e + \mathbf{m}_D - \boldsymbol{\sigma}_e - \delta \mathbf{u}_l w_g^{(l)} + \mathbf{F}_l + \delta \mathbf{F}_l \tag{A.18}$$

$$\begin{aligned} \mathcal{Q} &= \overset{\leftrightarrow}{\boldsymbol{\tau}}_v \cdot \nabla \cdot \mathbf{u} - \nabla \cdot \mathbf{q} + Q^w + Q_e - (e_{og} w_{og} + e_{ol} w_l) + \chi_D + \sum h_i \nabla \cdot (\rho_g \mathbf{V}_i Y_i) \\ &\quad - \mathbf{u} \cdot (\mathbf{m} - \boldsymbol{\sigma}_e) + (\mathbf{u} \cdot \delta \mathbf{u}) w_g^{(l)} + \delta Q_l + \delta \mathbf{u} \cdot \mathbf{F}_l - \mathbf{u} \cdot (\boldsymbol{\mathcal{F}} - \mathbf{F}_l) \end{aligned} \tag{A.19}$$

$$\mathcal{P} = \frac{\mathbf{R}}{\mathbf{C}_v}\mathcal{Q} + \mathbf{R}T\left[\mathcal{W} - \nabla\cdot(\rho_l\delta\mathbf{u})\right] \tag{A.20}$$

$$\mathcal{S} = \mathcal{Q} - \frac{p}{\rho^2}\mathcal{W} \tag{A.21}$$

The quantities $\delta(\quad)$ represent differences between values for the gas and condensed phases. For example, $\delta T = T_l - T_g$ in the difference in temperature between the temperature T_l of the condensed phase and that, T_g, of the gas phase.

A.2. Expansions in Mean and Fluctuating Variables.
Following the steps suggested in Section 3.3 to produce equations (3.23)–(3.28) will give the expressions for the brackets defined there to simplify the appearance of the equations:

$$\{[\rho]\}_1 = \bar{\mathbf{M}}\cdot\nabla\rho' + \rho'\nabla\cdot\bar{\mathbf{M}} + \mathbf{M}'\cdot\nabla\bar{\rho} \tag{A.22}$$

$$\{\rho\}_2 = \nabla\cdot(\rho'\mathbf{M}') \tag{A.23}$$

$$\{[M]\}_1 = \bar{\rho}(\bar{\mathbf{M}}\cdot\nabla\mathbf{M}' + \mathbf{M}'\cdot\nabla\bar{\mathbf{M}} + \rho'\frac{\bar{D}\bar{\mathbf{M}}}{Dt} \tag{A.24}$$

$$\{M\}_2 = \rho'\frac{\partial\mathbf{M}'}{\partial t} + \bar{\rho}\mathbf{M}'\cdot\nabla\mathbf{M}' + \rho'\left(\bar{\mathbf{M}}\cdot\nabla\mathbf{M}' + \mathbf{M}'\cdot\nabla\bar{\mathbf{M}}\right) \tag{A.25}$$

$$\{M\}_3 = \rho'\mathbf{M}'\cdot\nabla\mathbf{M}' \tag{A.26}$$

$$\{[T]\}_1 = \bar{\rho}C_v\left(\bar{\mathbf{M}}\cdot\nabla T' + \mathbf{M}'\cdot\nabla\bar{T}\right) + C_v\rho'\frac{\bar{D}\bar{T}}{Dt} + p'\cdot\nabla\bar{\mathbf{M}} \tag{A.27}$$

$$\{T\}_2 = C_v\rho'\frac{\partial T'}{\partial t} + C_v\rho'\left(\bar{\mathbf{M}}\cdot\nabla T' + \mathbf{M}'\cdot\nabla\bar{T}\right) + C_v\bar{\rho}\mathbf{M}'\cdot\nabla T' + p'\nabla\cdot\mathbf{M}' \tag{A.28}$$

$$\{T\}_3 = C_v\rho'\mathbf{M}'\cdot\nabla T' \tag{A.29}$$

$$\{[p]\}_1 = \bar{\mathbf{M}}\cdot\nabla p' + \mathbf{M}'\cdot\nabla\bar{p} + \gamma p'\nabla\cdot\bar{\mathbf{M}} \tag{A.30}$$

$$\{p\}_2 = \mathbf{M}'\cdot\nabla p' + \gamma p'\nabla\cdot\mathbf{M}' \tag{A.31}$$

$$\{[s]\}_1 = \bar{\rho}\bar{T}\bar{\mathbf{M}}\cdot\nabla s' + \rho'\bar{T}\frac{\bar{D}\bar{s}}{Dt} + \bar{\rho}\left(\bar{T}\mathbf{M}' + T'\bar{\mathbf{M}}\right)\cdot\nabla\bar{s} \tag{A.32}$$

$$\{s\}_2 = \rho'\bar{T}\frac{\bar{D}s'}{Dt} + \rho'T'\frac{\bar{D}\bar{s}}{Dt} + \left(\rho'\bar{T} + \bar{\rho}T'\right)\mathbf{M}'\cdot\nabla\bar{s} + \bar{\rho}T'\frac{\partial s'}{\partial t} \tag{A.33}$$

$$\{s\}_3 = \left(\bar{\rho}T' + \rho'\bar{T}\right)\mathbf{M}'\cdot\nabla s' + \rho'T'\left(\mathbf{M}'\cdot\nabla\bar{s} + \bar{\mathbf{M}}\cdot\nabla s'\right) \tag{A.34}$$

$$\{s\}_4 = \rho'T'\mathbf{M}'\cdot\nabla s' \tag{A.35}$$

The subscript $\{\quad\}_n$ on the curly brackets means that the contained quantities are written to order n in the fluctuations of flow variables. Similarly, the square brackets indicate that the terms are of first order in the Mach number of the mean flow. Higher order square brackets are not required, as explained in Section 3.3.1.

B. THE EQUATIONS FOR ONE-DIMENSIONAL UNSTEADY MOTIONS

These are many problems for which the flow may be approximated as one-dimensional. Even when the approximation may not seem as accurate as we might like, it is always a good beginning. The desired results are usually obtained without real effect and often are inspiringly close to the truth. An elementary example is computation of the normal modes for a straight tube having discontinuities, Section 5.5.2. Here we are concerned with situations in which influences at the lateral boundary must be accounted for. The formulation of the general problem is then essentially the counterpart of the constitution of the one-dimensional equations for steady flow in ducts thoroughly discussed by Shapiro (1953).

Accounting for changes of area in the one-dimensional approximation is a straightforward matter; following the rules applied to derivations appearing in the three-dimensional equations:

$$\mathbf{u} \cdot \nabla(\quad) \rightarrow u \frac{\partial}{\partial x}(\quad)$$
$$\nabla \cdot (\quad) \rightarrow \frac{1}{S_c} \frac{\partial}{\partial x} S_c(\quad) \tag{B.1}$$
$$\nabla^2(\quad) = \frac{1}{S_c} \frac{\partial}{\partial x} S_c \frac{\partial(\quad)}{\partial x}$$

where the axis of the duct lies along the x-direction and $S_c(x)$ is the distribution of the cross-section area.

More interesting are consequences of processes at the lateral boundary, particularly when there is flow through the surface. The most important applications arise in solid propellant rockets when burning propellant forms all or part of the lateral surface. Inflow of mass momentum and energy must be accounted for (Culick 1971, 1973; Culick and Yang 1992). The equations have the same form as the three-dimensional equations derived in Appendix A, equations (A.9)–(A.13) but the rule (B.1) applied and only the velocity component u along axis of the duct taken to be non-zero:

Conservation of Mass

$$\frac{D\rho}{dt} = -\rho \frac{1}{S_c} \frac{\partial}{\partial x}(S_c u) + \mathcal{W}_1 + \mathcal{W}_{1s} \tag{B.2}$$

Conservation of Momentum

$$\rho \frac{Du}{Dt} = -\frac{\partial p}{\partial x} + \mathcal{F}_1 + \mathcal{F}_{1s} \tag{B.3}$$

Conservation of Energy

$$\rho C_v \frac{DT}{Dt} = -p \frac{1}{S_c} \frac{\partial}{\partial x}(S_c u) + \mathcal{Q}_1 + \mathcal{Q}_{1s} \tag{B.4}$$

Equation for the Pressure

$$\frac{Dp}{Dt} = -\gamma p \frac{1}{S_c} \frac{\partial}{\partial x}(S_c u) + \mathcal{P}_1 + \mathcal{P}_{1s} \tag{B.5}$$

Equation for the Entropy

$$\frac{Ds}{Dt} = \frac{1}{T}(\mathcal{S}_1 + \mathcal{S}_{1s}) \tag{B.6}$$

where

$$\frac{D}{Dt} = \frac{\partial}{\partial t} + u \frac{\partial}{\partial x} \tag{B.7}$$

The source terms $\mathcal{W}_1$, $\mathcal{F}_1$, $\mathcal{Q}_1$, $\mathcal{P}_1$ and $\mathcal{S}_1$ are the one-dimensional forms of (A.17)–(A.21) written for the axial component of velocity only and with the rules (B.1) applied. In addition, sources of mass, momentum and energy associated with flow through the lateral boundary are represented by the symbols with subscript $(\quad)_s$ (Culick 1973, Culick and Yang 1995):

$$\mathcal{W}_{1s} = \frac{1}{S_c} \int m_s dq = \frac{1}{S_c} \int \left[m_s^g + m_s^l \right] dq \tag{B.8}$$

$$\mathcal{F}_{1s} = \frac{1}{S_c} \int \left[(u_s - u) m_s^g + (u_{ls} - u_l) m_s^l \right] dq \tag{B.9}$$

$$\mathcal{Q}_{1s} = \frac{1}{S_c} \int \left[(h_{0s} - e_0) m_s^g + (e_{l0s} - u_{l0}) m_s^l + C_v T m_s^g \right] dq \tag{B.10}$$

$$\mathcal{P}_{1s} = \frac{R}{C_v} Q_{s1} \tag{B.11}$$

$$\mathcal{S}_{1s} = \frac{1}{p} Q_{1s} = \frac{p}{\rho} \mathcal{W}_{1s} \tag{B.12}$$

Superscripts $(\quad)^{(g)}$ and $(\quad)^{(l)}$ refer respectively to the gas and liquid phases and subscript $(\quad)_s$ denotes values at the surface. The mass fluxes at the surface, $m_s^{(g)}$ and $m_s^{(l)}$ are of course computed as values normal to the boundary and are positive for inward flow. Here q stands for the parameter of the local section normal to the axis.

B.1. Equations for Unsteady One-Dimensional Motions. Forming the equations for the fluctuating motions within the one-dimensional approximation is done in exactly the same way as for the general equations, Appendix A. We need only apply the rules (B.1) and add to the inhomogeneous functions h and f the contributions from processes at the boundary. As for the general three-dimensional equations, we defer writing the fluctuations $\mathcal{W}_1'$, $\mathcal{F}_1'$, $\cdots$ until we consider specific problems.

The procedure introduced in Section 3.3.3 for forming the systems of equations for a hierarchy of problems applies equally to one-dimensional motions. As above, the equations are obtained from the three-dimensional equations by applying the rules (B.1): the results can be constructed when needed. However, the contributions from processes at the lateral boundary are special. Written to first order in the fluctuations and the Mach number of the mean flow; the dimensional forms of (B.8)–(B.12) are:

$$\mathcal{W}_{1s}' = \frac{1}{S_c} \int \left(m_s^2 \right)' dq \tag{B.13}$$

$$\mathcal{F}_{1s}' = \frac{1}{S_c} (\bar{u}_s - \bar{u}) \int (m_s^g)' dq + \frac{1}{S_c} (\bar{u}_{ls} - \bar{u}) \int (m_s^l)' dq$$
$$+ \frac{1}{S_c} (u_s' - u') \int \bar{m}_s^g dq + \frac{1}{S_c} (u_{ls}' - u_l') \int \bar{m}_s^l dq \tag{B.14}$$

$$\mathcal{Q}_{1s}' = \frac{1}{S_c} (\bar{h}_{0s} - e_0) \int (m_s^g)' dq + \frac{1}{S_c} + (\bar{e}_{l0s} - \bar{e}_{l0}) \int (m_s^l)' dq + C_v \bar{T} \int (m_s^g)' dq$$
$$+ \frac{1}{S_c} (h_{0s}' - e_0') \int \bar{m}_s^{g'} dq + \frac{1}{S_c} + (e_{l0s}' - e_{l0}') \int \bar{m}_s^l + C_v T \int (m_s^g)' dq \tag{B.15}$$

$$\mathcal{P}_{1s}' = \frac{R}{C_v} Q_{1s}' \tag{B.16}$$

$$\mathcal{S}_{1s}' = \frac{1}{p} Q_{1s}' - \frac{p}{\rho} \mathcal{W}_{1s}' \tag{B.17}$$

REFERENCES

Agarkov, A.F., Denisov, K.P., Dranovsky, M.L., Zavorokinin, I.A., Ivanov, V.N., Pikalov, V.P. and Shibanov, A.A. (1993) "Injector Flame Stabilization Effects on Combustion Instability," 1st International Symposium on Liquid Rocket Combustion Instabilities, Pennsylvania State University, AIAA Progress Series, Vol. 169.

Altseimer, J.H. (1952) "Photographic Techniques Applied to Combustion Studies — Two Dimensional Transparent Thrust Chamber," *Am. Rocket Soc. J.*, March–April, pp. 86–91.

Ananthkrishnan, N. and Culick, F.E.C. (2002) "Modeling and Dynamics of Nonlinear Acoustic Waves in a Combustion Chamber," 40th AIAA Aerospace Sciences Meeting and Exhibit, abstract submitted.

Annaswamy, A.M., Fleifil, M., Rumsey, J.W., Prasanth, R., Hathout, J.-P., and Ghoniem, A.F. (2000) "Thermoacoustic Instability: Model-Based Optimal Control Designs and Experimental Validation," *IEEE Transactions on Control System Technology* Vol. 8, No. 6, pp. 905–918.

Awad, E. and Culick, F.E.C. (1986) "On the Existence and Stability of Limit Cycles for Longitudinal Acoustic Modes in a Combustion Chamber," *Combustion Science and Technology*, Vol. 46, pp. 195–222.

Awad, E. (1983) "Nonlinear Acoustic Instabilities in Combustion Chambers," Ph.D. Thesis, California Institute of Technology.

Baum, J.D. and Levine, J.N. (1982) "Numerical Techniques for Solving Nonlinear Instability Problems in Solid Rocket Motors," *AIAA Journal*, Vol. 20, No. 7, pp. 955–961.

Baum, J.D. and Levine, J.N. (1988) "Pulsed Instability in Rocket Motors: Comparison Between Predictions and Experiments," *Journal of Propulsion and Power*, Vol. 4, No. 4, pp. 308–316.

Bazarov, V.G. and Yang, V. (1998) "Liquid Rocket Engine Injector Dynamics," *J. Propulsion and Power*, Vol. 14, No. 5 pp. 797–806.

Bazarov, V.G. (1979) "Fluid Injector Dynamics," Mashinostroenie Publishing, Moscow, Russia.

Berman, K. and Logan, S.E. (1952) "Combustion Studies with a Rocket Motor Having Full Length Observation Window," *Am. Rocket Soc. J.*

Berman, K. and Scharres, E.H. (1953) "Photographic Techniques in Jet Propulsion Studies," *Am. Rocket Soc. J.*, Vol. 23, No. 3, May–June, pp. 170–173.

Biron, D., Hébrard, P., Pauzin, S., and Laverdant, A. (1986) "Etude du couplage acoustique - instabilities aerodynamiques sur une acoustique, Ecole Centrale de Lyon, Proceedings edited by Springer-Verlag.

Bonnell, J.M., Marshall, R.L., and Rieche, G.T. (1971) "Combustion Instability in Turbojet and Turbofan Augmentors," AIAA/SAE 7th Propulsion Joint Specialist Conference, AIAA Paper No. 71–698.

Burnley, V. (1996) "Nonlinear Combustion Instabilities and Stochastic Sources," Ph.D. Thesis, California Institute of Technology.

Burnley, V.S. and Culick, F.E.C. (1996) "Influence of Random Excitations on Acoustic Instabilities in Combustion Chambers," *AIAA Journal*, 38(8), 1403–1410.

Burnley, V.S. and Culick, F.E.C. (1997) "Comment on 'Triggering of Longitudinal Combustion Instabilities in Rocket Motors: Nonlinear Combustion Response'," *Journal of Propulsion and Power*, 16(1), 164–165.

Byrne, R.W. (1981) "A Note on Longitudinal Pressure Oscillations in Ramjet Combustors," 18th JANNAF Combustion Meeting.

Byrne, R.W. (1983) AIAA/SAE/ASME 19th Joint Propulsion Conference, Seattle, Washington, AIAA Paper 83–2018.

Candel, S.M. (1992) "Combustion Instabilities Coupled by Pressure Waves and Their Active Control," 24th International Symposium on Combustion, pp. 1277–1296.

Chapman, S. and Cowling, T.G. (1958) *The Mathematical Theory of Nonuniform Gases*, Cambridge University Press.

Chu, B.-T. (1956) "Energy Transfer to Small Disturbances in a Viscous Heat Conductive Medium," Department of Aeronautics, Johns Hopkins University (no identifying number).

Chu, B.-T. and Kovasznay, L.S.G. (1957) "Non-linear Interactions in a Viscous Heat Conducting Compressible Gas," *J. Fluid Mech.*, Vol. 3, No. 5, pp. 494–512.

Crocco, L. and Cheng, S.-I. (1956) *Theory of Combustion Instability in Liquid-Propellant Rockets*, AGARDograph No. 8, Butterworths Scientific Publications, London.

Culick F.E.C. (1961) "High Frequency Pressure Oscillations in Liquid Rockets," Sc.D. Thesis, M.I.T. Department of Aeronautics and Astronautics.

Culick F.E.C. (1963) "High Frequency Oscillations in Liquid-Propellant Rockets," *AIAA Journal*, Vol. 1, No. 5, pp. 1097–1104.

Culick, F.E.C. (1968) "A Review of Calculations for Unsteady Burning of a Solid Propellant," *AIAA Journal*, Vol. 6, No. 6, pp. 2241–2255.

Culick, F.E.C. (1971) "Nonlinear Growth and Limiting Amplitude of Acoustic Oscillations in Combustion Chambers," *Combustion Science and Technology*, Vol. 3, pp. 1–16.

Culick, F.E.C. (1976) "Nonlinear Behavior of Acoustic Waves in Combustion Chambers," Parts I and II, *Acta Astronautica*, Vol. 3, pp. 714–757.

Culick, F.E.C. (1980) Report of the JANNAF Workshop on Pressure Oscillations in Ramjets," 17th JANNAF Combustion Meeting.

Culick, F.E.C. and Rogers, T. (1980) "Modeling Pressure Oscillations in Ramjets," AIAA/SAE/ASME 16th Joint Propulsion Conference, Hartford, Connecticut, AIAA Paper 80–1192.

Culick, F.E.C. (1987) "A Note on Rayleigh's Criterion," *Combustion Science and Technology*, Vol. 56, pp. 159–166.

Culick, F.E.C. (1988) "Combustion Instabilities in Liquid-Fueled Propulsion Systems—An Overview," AGARD 72B Specialists' Meeting of the Propulsion and Energetics Panel AGARD CP 450.

Culick, F.E.C., Paparizos, L., Sterling, J. and Burnley, V.S. (1992) "Combustion Noise and Combustion Instabilities in Propulsion Systems," *Proceedings of the AGARD Conference on Combat Aircraft Noise*, AGARD CP512.

Culick, F.E.C. (1992) "Combustion Instabilities and Rayleigh's Criterion," *Modern Research Topics in Aerospace Propulsion*, (In honor of Corrado Casci), pp. 135–151.

Culick, F.E.C. (1994) "Some Recent Results for Nonlinear Acoustics in Combustion Chambers," *AIAA Journal*, Vol. 32, No. 1, pp. 146–169.

Culick, F.E.C. and Yang, V. (1995) "Overview of Combustion Instabilities in Liquid-Propellant Rocket Engines," First International Symposium on Liquid Rocket Engine Combustion Instability, The Pennsylvania State University, AIAA Progress Series, Vol. 169.

Culick, F.E.C. (1997) "A Note on Ordering Perturbations and the Insignificance of Linear Coupling in Combustion Instabilities," *Combustion Science and Technology*, Vol. 126, pp. 359-379.

Culick, F.E.C. (1999) "Combustor Dynamics: Fundamentals, Acoustics and Control," A Short Course of Lectures.

Doedel, E.J., Champneys, A.R., Fairgrieve, T.F., Kuznetsov, Y.A., Sandstede, B., Wang, X. (1997) "AUTO 97: Continuation and Bifurcation Software for Ordinary Differential Equations," Concordia University, Montreal, Canada.

Doedel, E.J., Keller, H.B., Kernevez, J.P. (1991a) "Numerical Analysis and Control of Bifurcation Problems, (I) Bifurcation in Finite Dimensions," *International Journal of Bifurcation and Chaos*, Vol. 1, No. 3, pp. 493–520.

Doedel, E.J., Keller, H.B., Kernevez, J.P. (1991b) "Numerical Analysis and Control of Bifurcation Problems, (II) Bifurcation in Infinite Dimensions," *International Journal of Bifurcation and Chaos*, Vol. 1, No. 4, pp. 745–772.

Dowling, A. (1997) "Nonlinear Self-Excited Oscillations of a Ducted Flame," *J. Fluid Mechanics*, Vol. 346, pp. 271–290.

Duer, J. and Hessler, R. (1984) "Forced Oscillation Theory and Applications," 20th AIAA/ASME/SAE/ASEE Joint Propulsion Conference, AIAA Paper No. 84-1356.

Ernst, R.C. (1976) "A Combustion Model for Low Frequency Instability in Turbofan Augmentors," AIAA/SAE 12th Propulsion Conference, AIAA Paper No. 76–680.

Flandro, G.A. and Jacobs, H.R. (1975) "Vortex Generated Sound in Cavities," in *Aeroacoustics: Jet and Combustion Noise*, Vol. 37 of AIAA Series, *Progress in Astronautics and Aeronautics*.

Flandro, G.A. (1986) "Vortex Driving Mechanism in Oscillatory Rocket Flows," *J. Propulsion and Power*, Vol. 2, No. 3, pp. 206–214.

Fung, Y.-T., Yang, V. and Sinha, A. (1991) "Active Control of Combustion Instabilities with Distributed Actuators," *Combustion Science and Technology*, Vol. 78, pp. 217–245.

Fung, Y.-T. and Yang, V. (1992) "Active Control of Nonlinear Pressure Oscillations in Combustion Chambers," *J. Propulsion and Power*, Vol. 8, No. 6, pp. 1282–1289.

Haddad, W., Leonessa, A., Corrado, J. and Kapila, V. (1997) "Robust Reduced-Order Control of Combustion Instabilities," *Proceedings of the 1997 IEEE International Conference on Control Application*.

Harrje, D.J. and Reardon, F.H. (Ed.) (1972) *Liquid Propellant Rocket Instability*, NASA SP 194.

Hall, P.H. (1978) "Generic Ordnance Ramjet Engine – GORJE Tests of the Inlet Combustor," Naval Weapons Center, China Lake, NWC TP–6068.

Hessler, R. (1979) "Studies of Motor Instability Problems," 16th JANNAF Combustion Sub-Committee Meeting.

Hessler, R. (1980 "Prediction of Finite Pressure Oscillations in Stable Rocket Motors," 17th JANNAF Combustion Sub-Committee Meeting.

Hessler, R. (1982) "Forced Oscillation Prediction," 19th JANNAF Combustion Sub-Committee Meeting.

Hessler, R. and Glick, R. (1998) "Application of Maximum Entropy Method to Passively Extract Motor Stability Information," Workshop 'Measurement of Thermophysical and Ballistic Properties of Energetic Material', Politecnico di Milano, Milan, Italy.

Hildebrand, F.B. (1952) *Methods of Applied Mathematics*, Prentice-Hall, Inc., New York.

Hirschfelder, J.D., Curtiss, C.F. and Bird, R.B. (1964) "Molecular Theory of Gases and Liquids," Wiley, N.Y.

Hong, B.-S., Yang, V. and Ray, A. (2000) "Robust Feedback Control of Combustion Uncertainty with Modeling Uncertainty," *Combustion and Flame*, Vol. 120, pp. 91–106.

Hong, B.-S., Yang, V. and Ray, A. (2000) "Wide-Range Robust Control of Combustion Instability," RTO Symposium "Control of Engine Dynamics."

Isella, G.C. (2001) "Modeling and Simulation of Combustion Chambers and Propellant Dynamics and Issues in Active Control of Combustion Instabilities," Ph.D. Thesis, California Institute of Technology.

Isella, G., Seywert, C., Culick, F.E.C. and Zukoski, E.E. (1996) "A Further Note on Active Control of Combustion Instabilities Based on Hysteresis," *Combustion Science and Technology*, Vol. 126, pp. 381–388.

Jahnke, C. and Culick, F.E.C. (1994) "An Application of Dynamical Systems Theory to Nonlinear Combustion Instabilities," *Journal of Propulsion and Power*, Vol. 10, No. 4, pp. 508–517.

Karagozian, A.R. and Marble, F.E. (1986) "Study of a Diffusion Flame in a Stretched Vortex," *Combustion Science and Technology*, Vol. 45, pp. 65–84.

Kenworthy, M.J., Woltmann, I.E., and Corley, R.C. (1974) "Augmentor Combustion Stability Investigation," Air Force Aero Propulsion Laboratory, Report AFAPL–TR–74–61.

Knoop, P., Culick, F.E.C. and Zukoski, E.E. (1996) "Extension of the Stability of Motions in a Combustion Chamber by Nonlinear Active Control Based on Hysteresis," *Combustion Science and Technology*, Vol. 123, pp. 363–376.

Krylov, N. and Bogoliubov, N. (1947) *Introduction to Nonlinear Mechanics*, Princeton University Press.

Landau, L.D. and Lifschitz, E.M. (1959) *Fluid Mechanics*, Addison-Wesley Publishing Co.

Laverdant, A.M. and Candel, S.M. (1989) "Computation of Diffusion and Premixed Flames Rolled up in Vortex Structures," *J. Propulsion*, Vol. 5, No. 2, pp. 134–143.

Lewis Laboratory Staff (1954) "Summary of Preliminary Investigations into the Characteristics of Combustion Screech in Ducted Burners," NACA TR 1384.

Lord Rayleigh (1878) "The Explanation of Certain Acoustic Phenomena" *Royal Institution Proceedings*, VIII, pp. 536–542.

Lord Rayleigh (1945) *Theory of Sound*, Vol. 2, Dover, New York, Section 322g, pp. 232–234.

Lovine, R. L., Dudley, D. P., and Waugh, R. C. (1983) "Standardized Stability Prediction Method for Solid Rocket Motors," Vol. I, II and III. Aerojet Solid Propulsion Company. Report prepared for the Air Force Rocket Propulsion Laboratory, AFRPL TR–76–32.

McManus, K., Poinsot, T. and Candel, S. (1993) "A Review of Active Control of Combustion Instabilities," *Progress in Energy and Combustion Science*, 19(1): 1–29.

Magiawala, K. and Culick, F. E. C. (1979) "Measurements of Energy Exchange Between Acoustic Fields and Non-Uniform Steady Fields," *Journal of Vibration and Sound*, Vol. 75, pp. 503–512.

Mathis, B., Derr, R.L. and Culick, F.E.C. (1973)

Malhotra, S. (2001) Ph.D. Thesis in preparation, California Institute of Technology

Marble, F.E. and Rogers, D.E. (1956) "A Mechanism of High-Frequency Oscillation in Ramjet Combustors and Afterburners," *Jet Propulsion*.

Matveev, K. (2002) Ph.D. Thesis in preparation, California Institute of Technology.

Morse, P.M. (1936) *Vibration and Sound*, McGraw-Hill Book Co., New York.

Morse, P.M. and Feshbach, H. (1952) *Methods of Theoretical Physics*, McGraw-Hill Book Company.

Morse, P. and Ingard, L. (1968) *Theoretical Acoustics*, McGraw-Hill Book Co., New York.

Natanzon, M.S. and Menshikova, O.M. (1992) "Bifurcation of Steady Combustion Regimes and Their Influence on the Onset of High-Frequency Oscillations in Combustion Chambers," *Physics of Combustion and Explosion*, Vol. 23, No. 4, pp. 10–18.

Natanzon, M. (1999) *Unsteady Combustion in Liquid Rocket Engines*, Electronic translation from the Russian edition (1984) with a revised Chapter 8 on Bifurcations; translation editor F.E.C. Culick.

Nelson, P.A. and Elliott, S.J. (1992) *Active Control of Sound,* Academic Press, New York.

Nickerson, G. R., Culick, F.E.C., and Dang, L.G. (1983) "Standard Stability Prediction Method for Solid Rocket Motors, Axial Mode Computer Program, User's Manual," Software and Engineering Associates, Inc. Report prepared for the Air Force Rocket Propulsion Laboratory, AFRPL TR–83–01.

Norton, P. (1983) "The Effects of Vortex Flames with Finite Reaction Rates," Ph.D. Thesis, California Institute of Technology.

Ofelein, J.C. and Yang, V. (1993) "Comprehensive Review of Liquid-Propellant Combustion Instabilities in F-1 Engines," *Journal of Propulsion and Power,* Vol. 9, pp. 637–677.

Paparizos, L. and Culick, F.E.C. (1989) "The Two-Mode Approximation to Nonlinear Acoustics in Combustion Chambers. I. Exact Solutions for Second Order Acoustics," *Combustion Science and Technology,* Vol. 65(1–3), pp. 39–66.

Peake, N. and Crighton, D.G. (2000) "Active Control of Sound," *Annual Reviews of Fluid Mechanics,* Vol. 32, pp. 137–164.

Poinsot, T. and Candel, S.M. (1988) "A Nonlinear Model for Ducted Flame Combustion Instabilities," *Combustion Science and Technology,* Vol. 61, pp. 121–153.

Putnam, A.A. (1971) *Combustion Driven Oscillations in Industry,* Elsevier, New York.

Russell, P.L., Brant, G., and Ernst, R. (1978) "Low-Frequency Augmentor Instability Study," AIAA/SAE 14th Joint Propulsion Conference, AIAA Paper No. 78–996.

Samaniego, J.-M. and Mantel, T. (1999) "Fundamental Mechanisms in Premixed Turbulent Flame Propagation via Flame-Vortex Interactions Part I Experiment; Part II Numerical Simulation," *Combustion and Flame,* Vol. 118, pp. 537–582.

Schadow, K.C., Crump, J.E., and Blomshield, F.S. (1981) "Combustion Instability in a Research Dump Combustor: Inlet Shock Oscillations," 18th JANNAF Combustion Meeting.

Schadow, K.C., Crump, J.E., and Blomshield, F.S. (1983) "Effect of Dump Plane Design on Pressure Oscillations in a Sudden Expansion Ramjet Combustor," 1983 JANNAF Propulsion Meeting.

Schadow, K.C., Wilson, K.J., Crump, J.E., Foster, J.B., and Gutmark, E. (1984) "Interaction Between Acoustics and Subsonic Ducted Flow with Dump," AIAA 22nd Aerospace Sciences Meeting, Reno, Nevada, AIAA Paper 84–0530.

Schadow, K.C., Wilson, K.J., and Gutmark, E. (1985) "Characterization of Large-Scale Structures in a Forced Ducted Flow with Dump," AIAA 23rd Aerospace Sciences Meeting, Reno, Nevada, AIAA Paper 85–0080.

Schadow, K.C., Crump, J.E., Mahan, V.A., Nabity, J.A., Wilson, K.J., and Gutmark, E. (1985) "Large-Scale, Coherent Structures as Drivers of Ramjet Combustion Instabilities," 1985 JANNAF Propulsion Meeting.

Schadow, K.C., Gutmark, E., Parr, D.M., and Mahan, V.A. (1987a) "Effect of Shear-Flow Dynamics in Combustion Processes," *Proceedings of the Eighth International Symposium on Airbreathing Engines.*

Schadow, K.C., Gutmark, E., Parr, T.P., Parr, D.M., Wilson, K.J., and Crump, J.H. (1987b) "Large Scale Coherent Structures as Drivers of Combustion Instability," AIAA 19th Fluid Dynamics, Plasma Dynamics and Lasers Conference, AIAA Paper No. 87–1326.

Seywert, C. (2001) "Combustion Instabilities: Issues in Modeling and Control," Ph.D. Thesis, California Institute of Technology.

Seywert, C. and Culick, F.E.C. (1999) "Some Influences of Noise on Combustion Instabilities and Combustor Dynamics," 36th JANNAF Combustion Conference.

Shapiro, A. (1953) *The Dynamics and Thermodynamics of Compressible Fluid Flow,* Ronald Press, N.Y.

Sivasegaram, S. and Whitelaw, J.H. (1987) "Suppression of Oscillations in Confined Disk Stabilized Flames", *J. Propulsion,* Vol. 3, No. 4, pp. 291–295.

Smith, D.A. and Zukoski, E.E. (1985) "Combustion Instability Sustained by Unsteady Vortex Combustion," AIAA/SAE/ASME/ASEE 21st Joint Propulsion Conference, AIAA Paper No. 85-1248.

Smith, D.A. (1985) "An Experimental Study of Acoustically Excited, Vortex Driven Combustion Instability Within a Rearward Facing Step Combustor," Ph.D. Thesis, California Institute of Technology.

Sterling, J.D. (1987) "Longitudinal Mode Combustion Instabilities in Air Breathing Engines," Ph.D. Thesis, California Institute of Technology.

Sterling, J.D. (1993) "Nonlinear Analysis and Modelling of Combustion Instabilities in a Laboratory Combustor" *Combustion Science and Technology,* Vol. 89, pp. 167–179.

Sterling, J.D. and Zukoski, E.E. (1991) "Nonlinear Dynamics of Laboratory Combustor Pressure Oscillations," *Combustion Science and Technology,* Vol. 77, pp. 225–238.

Summerfield, M. (1951) "A Theory of Unstable Propulsion in Liquid-Propellant Rocket Systems," *Am. Rocket Soc. J.,* Vol. 21, No. 5, pp. 108–114.

Tennekes, H. and Lumley, J.L. (1972) *A First Course in Turbulence,* M.I.T. Press.

Truesdell, C. and Toupin, R. (1960) "The Classical Field Theories," *Handbuch des Physik,* Vol. III/1, Springer-Verlag, Berlin.

Tsien, H.S. (1952) "The Transfer Functions of Rocket Nozzles," *J. Am. Rocket Soc.,* Vol. 22, pp. 139–143.

Underwood, F.N., Rusnak, J.P., Ernst, P.C., Petrino, E.A., Russell, P.L., and Murphy, P., Jr. (1977) "Low Frequency Combustion Instability in Augmentors," AGARD CP 229, High Temperature Problems in Gas Turbine Engines.

Williams, F.A. (1985) *Combustion Theory,* Benjamin/Cummings, Menlo Park, CA.

Yang, V. and Culick, F.E.C. (1990) "On the Existence and Stability of Limit Cycles for Transverse Acoustic Oscillations in a Cylindrical Combustion Chamber I: Standing Modes," *Combustion Science and Technology,* Vol. 72, pp. 37–65.

Yang, V., Sinha, A. and Fung, Y.-T. (1992) "State-Feedback Control of Longitudinal Combustion Instabilities," *J. Propulsion and Power*, Vol. 8, No. 1, pp. 68–73.

Zak, T. (1993) "An Investigation of the Reacting Vortex Structure Associated with Pulsed Combustion," Ph.D. Thesis, California Institute of Technology.

Zetterstrom, K.-A. and Sjöblom, B. (1985) "An Experimental Study of Side Dump Ramjet Combustors," *International Symposium on Airbreathing Engines*, Paper 85–7024.

Zinn, B.T. (1986) "Pulsating Combustion" in *Advanced Combustion Methods*, A.J. Weinberg (Ed.), Academic Press, London.

Zinn, B.T. and Powell, E.A. (1970a) "Application of the Galerkin Method in the Solution of Combustion Instability Problems," *Proceedings of the 19th International Astronautical Congress*, Vol. 3, pp. 59–73.

Zinn, B.T. and Powell, E.A. (1970b) "Nonlinear Combustion Instability in Liquid-Propellant Rocket Engines," Thirteenth Symposium (International) on Combustion.

Combustion Dynamics: Analysis and Control - Modeling

Sébastien Candel, Sébastien Ducruix, Daniel Durox, Denis Veynante
Laboratoire EM2C, CNRS, Ecole Centrale Paris, 92295 Châtenay-Malabry Cedex, france

This set of lectures describes some of the modeling issues and methods which may be used to analyze combustion instabilities and their active control. Experimental data are first reviewed to exemplify the variety of mechanisms involved in combustion dynamics. The data indicate that the motion of the flame determines to a great extent the response of the flame submitted to acoustic interactions. A proper representation of this motion is essential if one wishes to obtain a suitable description of the nonsteady heat release in the field. It is well known that the distribution of this quantity is the source of acoustic energy and therefore plays a central role in the instabilty phenomenon. Simple and more complex models of nonsteady heat release are examined. In the case of turbulent flames, the large eddy simulation methods provide a suitable framework for combustion dynamics. The combination of an unsteady formulation for the large scale structures with adapted flame models allows a representation of dynamical flame phenomena. This type of approach may be used to analyze the flame response to incoming perturbations. It may be used to study combustion instabilities and may serve as a plateform in the simulation of control.

A review of active control of combustion indicates that development in this area has mainly relied on experiments with some attempts at using low order models to describe the flame dynamics. In simple cases analytical models describe to a certain extent the flame response and this may serve to design the controller. In the general case the reduction to a low order system is not suitable and only gives a crude description of the physical reality. It is therefore logical to see how one may simulate control by coupling an unsteady flow-solver including a dynamical description of the system with a control algorithm. This methodology has not been used extensively up to now but it has great potential for the future. It is shown that among the many problems which arise in this approach, there are three aspects which deserve special care:

- It is first important to devise a numerical description of the actuator. This may be done with a distribution of sources in the field.

- It is then necessary to deal with the very large mismatch between the time stepping needed by the flow simulation module and by the control unit. The two frequencies of operation differ widely (the ratio between the time steps is of the order of 100 or more). This constitutes a source of perturbation and it may introduce unwanted high frequency components in the flow simulation. It is shown that this problem is alleviated by placing a numerical low pass filter at the controller input.

- It is finally necessary to eliminate high frequency perturbations resulting from the sample and hold behavior of the controller output (the fact that the controller output changes by steps). This may be done by placing a low pass filter at the controller output.

These issues are illustrated with a full simulation of active control in the case of vortex shedding instabilities of solid propellant rocket. The dynamics of simplified model of such a motor is simulated with an unsteady flow solver. The instabilities are then adaptively controlled. This example serves to illustrate the simulation methodology and provides insights into the operation of the flow controller. It constitutes a prototype for more difficult combustion instability situations.

This page has been deliberately left blank

Page intentionnellement blanche

Chapter I

Introduction

Combustion instabilities and oscillations constitute a crucial problem in many fields of application: aerospace propulsion systems, gas turbines operating in very lean regimes (LPP). Instabilities are the result of resonant coupling mechanisms between physical processes which may lead to large oscillations of the flow, inducing many undesirable effects: large structural vibrations, increased heat fluxes to the system walls, flashback, flame blow-off and, in extreme cases, total destruction of the system (Fig.I.1).

Complex physical processes are involved in the development of instabilities, depending on the system characteristics, operating conditions, etc. Therefore, a large amount of experimental work has been carried out, in different configurations, to identify the fundamental mechanisms (see early observations of Mallard and Le Chatelier 1883 [1]). Theoretical analysis has also been developed to explain the processes leading to instability. In an early analysis, Rayleigh (1878) [2] established a criterion stating that oscillations are sustained when heat release and pressure fluctuations are in phase. More recently, numerical methods have been devised to test concepts and establish descriptive and predictive models.

Basic classifications of instabilities were proposed by Barrère and Williams (1968) [3] and Putnam *et al.* (1971) [4]. The subject is also examined in detail by Williams (1985) [5]. Reviews of the early work on liquid rocket motor and jet propulsion engine instabilities were established by Crocco (1965) [6], and Harrje and Reardon (1972) [7]. Modern reviews of combustion instabilities are due to Culick (1988) [8] and Candel (1992) [9]. The special topic of active control is reviewed by McManus *et al.* (1993) [10].

I.1 Combustion instabilities

Combustion instabilities result from resonant interactions between coupled mechanisms. A driving process generates perturbations of the flow, a feedback process couples these perturbations to the driving mechanism and produces the resonant interaction which may lead to oscillatory combustion (Fig. I.2).

In general, the feedback process relates the downstream flow to the upstream region where the perturbations are initiated. As a consequence, acoustic wave propagation is most commonly responsible for the feedback path. Practical combustors feature a wide variety of acoustic resonant modes. The propagation of acoustic waves in the system takes place in many ways. These eigenmodes depend on the chamber geometry, boundary conditions and flow field. While other
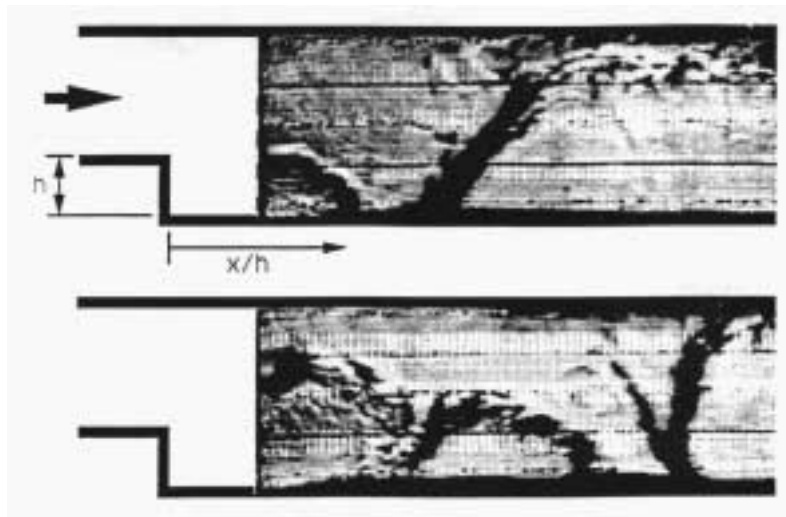
Figure I.1: Sequence of schlieren images presenting flame motion during instability (McManus *et al.* 1993).

processes like structural vibrations or convective modes constitute alternative feedback mechanisms, the following developments concentrate on instabilities coupled by pressure waves.
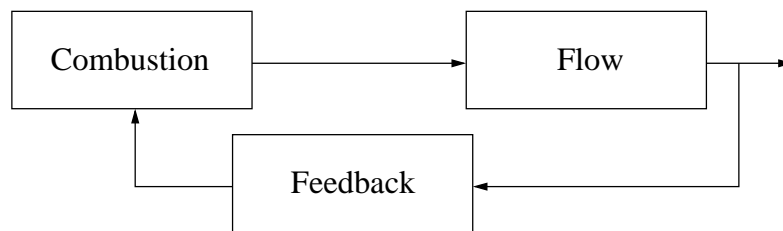
Figure I.2: Typical instability mechanism.

Among the three main classes of instabilities identified by Barrère and Williams 1968 [3] (see also Poinsot 1987 [11]), the first two involve a coupling by pressure waves.

System instabilities involve the entire combustion system, including the supply tanks, fuel lines, combustor and exhaust elements. The typical scales associated with such instabilities and the corresponding wavelengths are large compared to the transverse dimensions, so that the wave propagation is essentially longitudinal and may be described in terms of plane modes. The characteristic frequencies lie in the low range (a few hundred Hz or less). When one component of the system is short with respect to the wavelength, it may be treated as a compact element and described in term of lumped parameter models.

System instabilities appear in all types of situations. For example, they are encountered during the ignition and shut-down sequences of liquid rocket engines, when the pressure drop through the injectors has a reduced value and the supply system is closely coupled to the chamber (see Barrère and Corbeau 1964 [12]). They also arise in certain ranges of the flight envelope of high performance afterburners and ramjets and they may perturb the operation of large scale powerplants.

Chamber instabilities are coupled by the chamber eigenmodes (resonant acoustic modes). The size of the combustor fixes the instability wavelength and consequently the frequency lies in the high range (typically above 1 kHz). In many circumstances, chamber instabilities are coupled by higher order transverse modes of the combustor. The spatial structure of the pressure fluctuation then becomes an important aspect of the problem. When the combustor has an axis of symmetry (as in a cylindrical or annular configuration) the transverse pressure pattern may be stationary or it may be spinning.

Chamber instabilities observed in liquid or solid rocket motor or in ramjets have destructive effects because they enhance the rates of heat transfer to the walls and injection head, leading to hot spots and local melting of the structure. These instabilities require considerable attention in design and extensive testing is used to establish the domain of stable operation (see Rogers and Marble 1956 [13]).

The last class of instabilities described as intrinsic instabilities will be described as being unsteady combustion phenomena resulting from chemical and thermo-diffusive effects, which modify the flame propagation rate. The characteristic length scales associated with these phenomena are of the order of the front thickness. In general, these instabilities depend upon the properties of the reactants. A review of the instability of plane laminar flames due to thermo-diffusive effects is given by Clavin (1990) [14].

I.2   Active control

Control schemes used to damp or eliminate instabilities in combustion systems will be broadly classified as being either passive or active techniques. Passive control techniques include hardware design modifications. The geometry is changed to include baffles, cavities, acoustic liners, etc. The objective is to augment damping. Active control techniques include control systems whose operation depends on a dynamic or time varying, hardware component (actuator). Examples of such components include acoustic driver units fitted to the combustor or to the feed lines to excite acoustic waves, and fast servo-valves used to modulate flow rates to produce a time variation around a given steady state.

The present review will include active control techniques only, and for this discussion it is convenient to categorize the active control system. This classification will be based on three criteria:

- If the control system does not use a time varying input from the combustion system (feedback to determine the control action), the control system will be called "open-loop", and if this information influences the control action the system will be called "closed-loop".

- If the time-scales associated with the controller response and with combustion instability are of the same order, the control system will be called "fast response". If the controller time-scale is much greater than that of the instability, the control system will be called a "trim adjustment" controller.

- Controllers with basic response characteristics, or transfer function, which do not change with time will be called "fixed-parameter" controllers and those which have internal algorithms allowing time-varying transfer functions through parameter optimization will be called "adaptive" controllers.

In the area of fluid mechanics, active feedback control of flow instabilities is now extensively investigated. However, a review of literature indicates that few studies deal with unstable flows coupled by acoustic resonances (see, for example Huang and Weaver 1991 [15] and Billoud *et al.* 1992 [16]).

Moreover a limited number of studies consider adaptive control algorithms in the area of unstable flows (see, for example Billoud *et al.* 1992 [16] or Ziada 1995 [17]). The disadvantage of non-adaptive algorithms in this context is the necessity to change the controller gain and phase with changing flow speed (see, for example Ziada 1995 [17], Huang and Weaver 1991 [15] and Welsh *et al.* 1991 [18] among others).

Early work on active control modeling was developed in studies of low-frequency combustion instabilities in rocket motors. Tsien (1952) [19], Marble and Cox (1953) [20], Crocco and Chen (1956) [21] consider the dynamics of fixed parameter controllers represented schematically in Fig. I.3(a). These models were demonstrated in the prediction of combustion instability suppression through the use of closed-loop controllers; however, the resulting theoretical principles were never verified in practice. Adaptive closed-loop controllers shown in Fig. I.3(b) are considered in more recent studies.
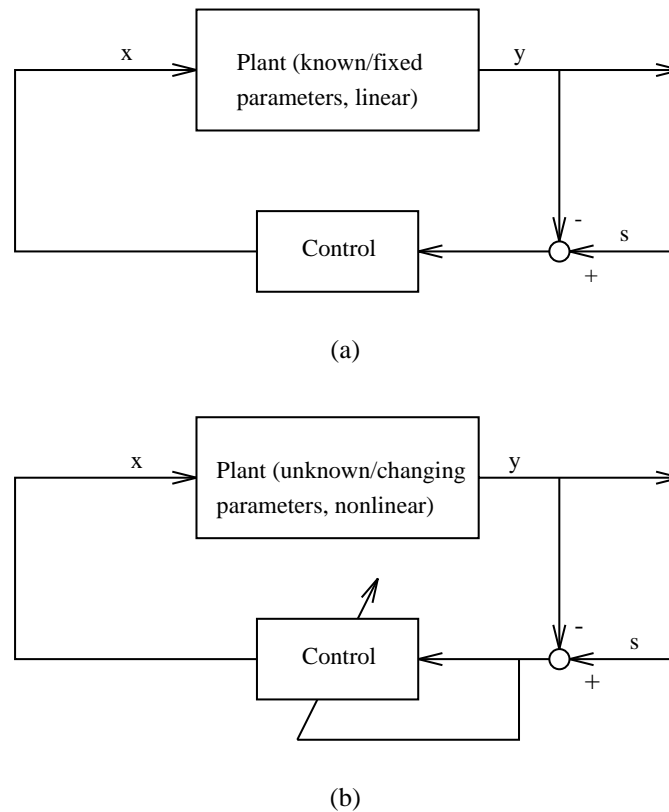
Figure I.3: Block diagrams of (a) fixed-parameter and (b) adaptive closed-loop controllers.

I.3   Contents

In what follows, we will consider system and chamber instabilities and we restrict the analysis to the rather general situation where the instability is coupled by acoustic waves. We will here consider some theoretical modeling methods and focus on numerical simulation strategies.

We begin with a tutorial section on classical theory for combustion instabilities studies (chapter II). An acoustic wave equation is derived for reactive mixtures, the acoustic energy balance in combustor cavities is then established. We use the balance equation to obtain the Rayleigh criterion and show that the nonsteady heat release constitutes the source of acoustic energy.

We then examine some of the physical mechanisms leading to combustion instabilities (chapter III). A model based on the time lag concept is introduced. It describs the linear interaction between heat release source and acoustics. The time lag concept is briefly reviewed in this chapter, and it is used to determine the instabilities in a ducted flame situation. An active control model, to predict the effects of a simple control system applied to the instability model is proposed. The model controller will be adapted to the ducted flame model and the ability of the control system to suppress the acoustically coupled instability may be predicted.

Flame Dynamics is a central element in the description of instabilities and control. This topic is considered in chapter IV. We first propose a complete theoretical determination of the response of a laminar premixed flame to acoustic perturbations. The flame transfer function concept is also presented in this case. An example of Large Eddy Simulation (LES) calculations of combustion instabilities in a turbulent combustor is then analyzed, showing the possibilities in predicting the instabilities.

Chapter V deals with simulation of active control. A review of recent works in the field of adaptive control algorithms is proposed. This chapter considers central issues in the development of software tools for active control. The strategy relies on an unsteady numerical simulation of the system based on the Navier-Stokes equations. A set of calculations are carried out to simulate vortex shedding instabilities of a simplified solid propellant rocket. These instabilities are then adaptively controlled. This example illustrates some of the problems encountered in the numerical simulation of active control.

This page has been deliberately left blank

Page intentionnellement blanche

Chapter II

Acoustics of Reactive Mixtures

S. Candel and T. Poinsot [22]

The objective of this chapter is to relate the pressure field and the heat release in reactive mixtures. The derivation leads to a wave equation which features as source term the rate of change of the heat release. It is also useful to derive a balance equation for the acoustic energy. Both results indicate that combustion dynamics are governed by the non steady heat release and that the phase between this source term and the pressure determines if acoustic energy increases or decreases in the system.

II.1   Introduction

The description of acoustic wave generation and propagation in an inhomogeneous reactive medium may be based on a wave equation (see for example Kotake 1975 [23]). This equation is briefly derived in section II.2 to provide the proper background for studies of combustor cavity modes. The derivation also exhibits the source terms associated with the non-steady heat release.

Equations obtained in this section will be used in section II.3 to derive an acoustic energy balance for general combustor cavities. The examination of the balance of acoustic energy plays a central role in many instability studies. Energy considerations are often put forward in the field of solid rocket instabilities. An early example of this type of reasoning may be found in Cantrell and Hart (1964) [24]. Analyses of the energy balance are also found in studies of gaseous combustor instabilities (as for example in Poinsot *et al.* 1986 [25]). The energy balance for acoustic perturbations is closely related to the Rayleigh criterion which has been quoted and used in many qualitative descriptions of flame instabilities. This is well illustrated in a classical monograph due to Putnam (1971) [4].

We begin section II.3 by deriving an acoustic energy balance equation for a chemically reacting mixture. A global balance is then obtained for acoustic cavities. Results due to Cantrell and Hart [24] for cavities with mean flow are introduced. Expressions for the growth rates of acoustic energy are then derived.

II.2 Acoustic wave equation for a reacting mixture

II.2.1 Derivation of an acoustic wave equation

We start from the general equations describing a chemically reactive mixture of N species. These equations and many alternative expressions may be found in Williams (1985) [5], Kuo 1986 [26]. We use the following forms :

Conservation of mass

$$\frac{\partial \rho}{\partial t} + \boldsymbol{\nabla} \cdot \rho \boldsymbol{v} = 0 \tag{II.1}$$

Conservation of the $k - th$ chemical species

$$\frac{\partial}{\partial t}(\rho Y_k) + \boldsymbol{\nabla} \cdot \rho Y_k (\boldsymbol{v} + \boldsymbol{v}_k^D) = \dot{w}_k \tag{II.2}$$

Conservation of momentum

$$\frac{\partial}{\partial t}(\rho \boldsymbol{v}) + \boldsymbol{\nabla} \cdot \rho \boldsymbol{v} \boldsymbol{v} = -\boldsymbol{\nabla} p + \boldsymbol{\nabla} \cdot \boldsymbol{\tau} + \sum_{k=1}^{N} \rho \boldsymbol{f}_k Y_k \tag{II.3}$$

Conservation of energy (enthalpy form)

$$\frac{\partial}{\partial t}\rho h + \boldsymbol{\nabla} \cdot \rho h \boldsymbol{v} = -\boldsymbol{\nabla} \cdot \boldsymbol{q} + \frac{dp}{dt} + \Phi + \sum_{k=1}^{N} \rho Y_k \boldsymbol{v}_k^D \cdot \boldsymbol{f}_k \tag{II.4}$$

Equation of state

$$p = \rho R T \qquad \text{where} \quad R = R_0 \sum_{k=1}^{N}(Y_k / M_k) \tag{II.5}$$

Enthalpy of the mixture

$$h = \sum_{k=1}^{N} h_k Y_k = \sum_{k=1}^{N}(h_k^\circ + \int_{T_0}^{T} c_{pk} dT) Y_k \tag{II.6}$$

In these equations ρ, p, T, $\boldsymbol{v}$ respectively designate the specific mass, pressure, temperature and velocity of the mixture. Y_k, $\boldsymbol{v}_k^D$, $\boldsymbol{f}_k$, M_k represent the $k - th$ species mass fraction, diffusion velocity, specific body force and molar mass. The mass rate of production of the $k - th$ species per unit volume $\dot{w}_k$ constitutes the source term in the species equation. The global conservation of mass requires that:

$$\sum_{k=1}^{N} \dot{w}_k = 0 \quad \text{and} \quad \sum_{k=1}^{N} \rho Y_k \boldsymbol{v}_k^D = 0 \tag{II.7}$$

The equation describing the balance of enthalpy also involves the viscous dissipation function $\Phi = \boldsymbol{\tau} : \boldsymbol{\nabla}\boldsymbol{v}$ where $\boldsymbol{\tau}$ is the viscous stress tensor and a heat flux $\boldsymbol{q}$. Neglecting coupled effects and radiative heat transfer this flux may be written in the form:

$$\boldsymbol{q} = -\lambda\boldsymbol{\nabla}T + \sum_{k=1}^{N}\rho Y_k \boldsymbol{v}_k^D h_k \tag{II.8}$$

In the general case the diffusion velocities are obtained by solving a system of multicomponent diffusion equations (see Williams 1985, [5]).

Now the system of equations (II.1)-(II.6) may be simplified by neglecting the specific body forces $\boldsymbol{f}_k$. It is also convenient to introduce the material derivative $d/dt = \partial/\partial t + \boldsymbol{v}\cdot\boldsymbol{\nabla}$ and derive an equation for the temperature by combining the species and energy equations. The following system is obtained :

$$\frac{d\rho}{dt} = -\rho\boldsymbol{\nabla}\cdot\boldsymbol{v} \tag{II.9}$$

$$\rho\frac{d\boldsymbol{v}}{dt} = -\boldsymbol{\nabla}p + \boldsymbol{\nabla}\cdot\boldsymbol{\tau} \tag{II.10}$$

$$\rho c_p \frac{dT}{dt} = -\boldsymbol{\nabla}\cdot\boldsymbol{q} + \frac{dp}{dt} + \Phi - \sum_{k=1}^{N} h_k \dot{w}_k + \sum_{k=1}^{N}(h_k\boldsymbol{\nabla}\cdot\rho Y_k\boldsymbol{v}_k^D) \tag{II.11}$$

where $c_p = \sum_{k=1}^{N} c_{pk}$ designates the specific heat of the mixture. The last equation may be simplified by introducing expression (II.8) for $\boldsymbol{q}$:

$$\rho c_p \frac{dT}{dt} = \boldsymbol{\nabla}\cdot\lambda\boldsymbol{\nabla}T + \frac{dp}{dt} + \Phi - \sum_{k=1}^{N} h_k \dot{w}_k - \sum_{k=1}^{N}(\rho Y_k\boldsymbol{v}_k^D c_{pk})\cdot\boldsymbol{\nabla}T \tag{II.12}$$

If it is assumed that all the specific heats of the species are equal $c_{pk} = c_p$ the last term of this equation disappears. We now divide the energy equation (II.12) by $\rho c_p T$ and use the equation of state (II.5) to get:

$$\frac{1}{\gamma_p}\frac{dp}{dt} - \frac{1}{\rho}\frac{d\rho}{dt} = \quad \frac{1}{\rho c_p T}\{\boldsymbol{\nabla}\cdot\lambda\boldsymbol{\nabla}T + \Phi \tag{II.13}$$

$$-\sum_{k=1}^{N} h_k\dot{w}_k \quad -\sum_{k=1}^{N}(\rho Y_k\boldsymbol{v}_k^D \cdot c_{pk}\boldsymbol{\nabla}T)\} \quad +\frac{1}{R}\frac{dR}{dt}$$

This last expression combined with the mass conservation equation yields:

$$\frac{1}{\gamma_p}\frac{d}{dt}\ln p + \boldsymbol{\nabla}\cdot\boldsymbol{v} = \quad \frac{1}{\rho c_p T}\{\boldsymbol{\nabla}\cdot\lambda\boldsymbol{\nabla}T + \Phi \tag{II.14}$$

$$-\sum_{k=1}^{N} h_k\dot{w}_k \quad -\sum_{k=1}^{N}(\rho Y_k c_{pk}\boldsymbol{v}_k^D \cdot \boldsymbol{\nabla}T)\} \quad +\frac{1}{R}\frac{dR}{dt}$$

We now write equation (II.10) in the form:

$$\frac{d\boldsymbol{v}}{dt} + \frac{c^2}{\gamma}\boldsymbol{\nabla}\ln p = \frac{1}{\rho}\boldsymbol{\nabla}\cdot\boldsymbol{\tau} \tag{II.15}$$

where $c^2 = \gamma p/\rho$ designates the local speed of sound. The last two equations may now be combined by taking the divergence of the second and subtracting the material derivative of the first :

$$\boldsymbol{\nabla} \cdot \frac{c^2}{\gamma} \ln p - \frac{d}{dt}\left(\frac{1}{\gamma}\frac{d}{dt} \ln p\right) = \boldsymbol{\nabla} \cdot (\rho^{-1}\boldsymbol{\nabla} \cdot \boldsymbol{\tau})$$

$$- \frac{d}{dt}\left\{\frac{1}{\rho c_p T}\left[\boldsymbol{\nabla} \cdot \lambda\boldsymbol{\nabla} T + \Phi - \sum_{k=1}^{N} h_k \dot{w}_k - \sum_{k=1}^{N}(\rho Y_k c_{pk}\boldsymbol{v}_k^D \cdot \boldsymbol{\nabla} T)\right]\right\}$$

$$- \frac{d^2}{dt^2}(\ln R) - \boldsymbol{\nabla}\boldsymbol{v} : \boldsymbol{\nabla}\boldsymbol{v} \tag{II.16}$$

This is a wave equation for the logarithm of the pressure. A similar expression was established by Phillips (1960) in a classical analysis of the aerodynamic generation of sound in non reactive turbulent gas flows. It has been pointed out by Doak (1973) [27] that such an equation has an essential flaw because terms appearing in the right hand side describe features of the propagation of sound in the medium and should be included in the left hand side. This point is also discussed by Kotake (1975) in a study of combustion noise [23].

Despite these objections we will regard the terms appearing in the right hand side of equation (II.16) as the source terms generating the pressure waves in the reactive mixture. The main source terms arise from entropy fluctuations associated with perturbations in the heat flux, viscous dissipation, chemical heat release and from turbulent velocity fluctuations. An order of magnitude analysis (see Kotake 1975) indicates that the dominant source terms are associated with the chemical heat release fluctuations and velocity perturbations. Neglecting all other terms one obtains:

$$\boldsymbol{\nabla} \cdot \frac{c^2}{\gamma}\boldsymbol{\nabla} \ln p - \frac{d}{dt}\left(\frac{1}{\gamma}\frac{d}{dt} \ln p\right) = \frac{d}{dt}\left(\frac{1}{\rho c_p T}\sum_{k=1}^{N} h_k \dot{w}_k\right) - \boldsymbol{\nabla}\boldsymbol{v} : \boldsymbol{\nabla}\boldsymbol{v} \tag{II.17}$$

If one considers low speed reactive flows, the convective term in the material derivative may be neglected $d/dt \sim \partial/\partial t$. Assuming in addition that the specific heat ratio is constant, equation (II.17) becomes:

$$\boldsymbol{\nabla} \cdot c^2\boldsymbol{\nabla} \ln p - \frac{\partial^2}{\partial t^2} \ln p = \frac{\partial}{\partial t}\left(\frac{1}{\rho c_v T}\sum_{k=1}^{N} h_k \dot{w}_k\right) - \gamma\boldsymbol{\nabla}\boldsymbol{v} : \boldsymbol{\nabla}\boldsymbol{v} \tag{II.18}$$

This equation is not linearized and it may be used to describe finite amplitude waves. However, in many circumstances, the pressure waves are relatively weak and linearization is appropriate. The pressure is then expressed as a sum of a mean and a fluctuating component: $p = p_0 + p_1$ with $p_1/p_0 \ll 1$. Then $\ln p \simeq p_1/p_0$ and equation (II.18) becomes:

$$\boldsymbol{\nabla} \cdot c^2\boldsymbol{\nabla}\left(\frac{p_1}{p_0}\right) - \frac{\partial^2}{\partial t^2}\left(\frac{p_1}{p_0}\right) = \frac{\partial}{\partial t}\left(\frac{1}{\rho c_v T}\sum_{k=1}^{N} h_k \dot{w}_k\right) - \gamma\boldsymbol{\nabla}\boldsymbol{v} : \boldsymbol{\nabla}\boldsymbol{v} \tag{II.19}$$

In practical continuous combustion devices the mean pressure does not change by more than a few percent, the spatial derivatives of p_0 may be neglected and hence equation (II.19) may be written as:

$$\boldsymbol{\nabla} \cdot c^2\boldsymbol{\nabla} p_1 - \frac{\partial^2}{\partial t^2} p_1 = \frac{\partial}{\partial t}\left[(\gamma - 1)\sum_{k=1}^{N} h_k \dot{w}_k\right] - \gamma p_0\boldsymbol{\nabla}\boldsymbol{v} : \boldsymbol{\nabla}\boldsymbol{v} \tag{II.20}$$

In addition to this equation we also need an expression for the acoustic velocity. This may be obtained by linearizing the momentum equation (II.15) and neglecting the viscous stresses. This yields:

$$\frac{\partial \boldsymbol{v}_1}{\partial t} = -\frac{1}{\rho_0}\boldsymbol{\nabla} p_1 \tag{II.21}$$

Equations (II.20) and (II.21) describe the propagation and generation of small perturbations in the reactive mixture. To perform a modal analysis, one first assumes that all waves are harmonic and contain the common factor $\exp(-i\omega t)$. The modes are the eigensolutions of the Helmholtz equation:

$$\boldsymbol{\nabla} \cdot c^2 \boldsymbol{\nabla} p_1 + \omega^2 p_1 = 0 \tag{II.22}$$

and the corresponding velocity field is obtained from

$$\boldsymbol{v}_1 = (1/\rho_0 i\omega)\boldsymbol{\nabla} p_1 \tag{II.23}$$

This equations must be solved under the usual boundary conditions:

$$\begin{cases} \boldsymbol{v}_1 \cdot \boldsymbol{n} = 0 & \text{on a rigid wall} \\ p_1 = 0 & \text{open plane exit} \end{cases} \tag{II.24}$$

Equation (II.22) and the related boundary conditions may be used to determine the combustor modes of oscillation. The effects of temperature non-uniformity is taken into account because the spatial variations of the sound speed are correctly represented in equation (II.22). Such a modal analysis is performed by Laverdant *et al.* (1985) [28] in the case of a gaseous dump combustor or more recently by Le Helley (1994) [29] and the reader may find further details in these references.

II.2.2   The non-steady heat release source term

Let us consider again the source term corresponding to the non-steady heat release:

$$\frac{\partial}{\partial t}[(\gamma - 1)\sum_{k=1}^{N} h_k \dot{w}_k]$$

Now assume that the chemical change occurs by a single reaction step. Then if Δh_f° designates the change of formation enthalpy per unit mass of the mixture and if $\dot{w}$ represents the rate of reaction, the chemical source term becomes:

$$\frac{\partial}{\partial t}(\gamma - 1)(-\Delta h_f^{\circ})\dot{w}$$

In most cases the only time dependence in this expression is due to the non-steady rate of reaction term and as a consequence the acoustic source term associated with the chemical reaction may be written in the form:

$$(\gamma - 1)(-\Delta h_f^{\circ})\frac{\partial \dot{w}}{\partial t}$$

II.3   Derivation of a energy balance equation

II.3.1   Energy balance for acoustics in a reacting medium

The derivation of an energy balance equation for acoustic perturbations in a reacting medium may be based on the conservation relations given in section II.2. These relations are repeated below for convenience:

$$\boldsymbol{\nabla} \cdot c^2 \boldsymbol{\nabla} p_1 - \frac{\partial^2 p_1}{\partial t^2} = \frac{\partial}{\partial t}[(\gamma - 1) \sum_{k=1}^{N} h_k \dot{w}_k] - \gamma p_0 \boldsymbol{\nabla} \boldsymbol{v} : \boldsymbol{\nabla} \boldsymbol{v} \tag{II.25}$$

$$\rho_0 \frac{\partial \boldsymbol{v}_1}{\partial t} + \boldsymbol{\nabla} p_1 = 0 \tag{II.26}$$

Now let us only retain the heat release source term in equation (II.25) and replace $\boldsymbol{\nabla} p_1$ in that equation by its expression in terms of $\boldsymbol{v}_1$ as given by (II.26).

This yields:

$$\boldsymbol{\nabla} \cdot \rho_0 c^2 \frac{\partial \boldsymbol{v}_1}{\partial t} + \frac{\partial^2 p_1}{\partial t^2} = -\frac{\partial}{\partial t}[(\gamma - 1) \sum_{k=1}^{N} h_k \dot{w}_k] \tag{II.27}$$

Only the non-steady heat release source terms contribute to this equation and $\dot{w}_k$ may be replaced by $\dot{w}_k^{(1)}$ which represents the unsteady rate of production of the $k - th$ chemical species.

Now the time derivative appearing in all three terms may be discarded and the following relation is obtained:

$$\boldsymbol{\nabla} \cdot \rho_0 c^2 \boldsymbol{v}_1 + \frac{\partial p_1}{\partial t} = -(\gamma - 1) \sum_{k=1}^{N} h_k \dot{w}_k^{(1)} \tag{II.28}$$

Consider the quantity $\rho_0 c^2 = \gamma p_0$. In many situations the pressure is nearly a constant in the flow and equation (II.28) may be cast in the form:

$$\boldsymbol{\nabla} \cdot \boldsymbol{v}_1 + \frac{1}{\rho_0 c^2} \frac{\partial p_1}{\partial t} = -\frac{\gamma - 1}{\rho_0 c^2} \sum_{k=1}^{N} h_k \dot{w}_k^{(1)} \tag{II.29}$$

Multiplying this equation by p_1, taking the scalar product of equation (II.26) by $\boldsymbol{v}_1$ and adding the resulting expressions yields:

$$\frac{\partial}{\partial t} \mathcal{E} + \boldsymbol{\nabla} \cdot \boldsymbol{\mathcal{F}} = -\frac{\gamma - 1}{\rho_0 c^2} p_1 \sum_{k=1}^{N} h_k \dot{w}_k^{(1)} \tag{II.30}$$

where $\mathcal{E} = \frac{1}{2} \frac{p_1^2}{\rho_0 c^2} + \frac{1}{2} \rho_0 v_1^2$ is the instantaneous acoustic energy and $\boldsymbol{\mathcal{F}} = p_1 \boldsymbol{v}_1$ stands for the acoustic energy flux.

The source term appearing on the right hand side corresponds to the non-steady heat release in the reactive mixture. This term may be written in the form:

$$\mathcal{S} = -\frac{\gamma - 1}{\gamma}\frac{p_1}{p_0}\sum_{k=1}^{N} h_k \dot{w}_k^{(1)} \tag{II.31}$$

The meaning of this term is best understood under the following assumptions. The set of reactions taking place in the mixture is replaced by a single global equation $F + O \rightarrow P$. The rate of this reaction is $\dot{w}$ and the change of formation enthalpy per unit mass of mixture is Δh_f°. If the specific heat of the mixture does not depend on the composition it is possible to write:

$$-\sum_{k=1}^{N} h_k \dot{w}_k^{(1)} = (-\Delta h_f^\circ)\dot{w}^{(1)} \tag{II.32}$$

and the source term in equation (II.30) becomes:

$$\mathcal{S} = \frac{\gamma - 1}{\gamma}(-\Delta h_f^\circ)\frac{p_1}{p_0}\dot{w}^{(1)} \tag{II.33}$$

When this term is positive energy is fed into the acoustic oscillation, when it is negative energy is extracted from that oscillation.

A global energy balance is easily derived from expression (II.30) by integrating over the volume of the combustor :

$$\frac{\partial}{\partial t}\int_V \mathcal{E}dV + \int_A \boldsymbol{\mathcal{F}}\cdot\boldsymbol{n}dA = \int_V \mathcal{S}dV \tag{II.34}$$

Let us now examine a situation where all the acoustic perturbations are quasi-periodic oscillations and contain the common factor $\exp(-i\omega t)$. The complex amplitudes $p_1(t)$, $\boldsymbol{v}_1(t)$, $w(t)$ are now slowly varying with time. An average energy balance may be obtained by integrating (II.34) over a period of oscillation $T = 2\pi/\omega$ and dividing the resulting expression by the period. This procedure yields:

$$\frac{\partial}{\partial t}\int_V EdV + \int_A \boldsymbol{F}\cdot\boldsymbol{n}dA = \int_V SdV \tag{II.35}$$

where E, $\boldsymbol{F}$ and S are period averages of the instantaneous quantities $\mathcal{E}, \boldsymbol{\mathcal{F}}, \mathcal{S}$:

$$E = \frac{1}{4\rho_0 c^2}p_1 p_1^* + \frac{1}{4}\rho_0 \boldsymbol{v}_1 \cdot \boldsymbol{v}_1^* \tag{II.36}$$

$$\boldsymbol{F} = \frac{1}{2}Re(p_1 \boldsymbol{v}_1^*) \tag{II.37}$$

$$S = \frac{\gamma - 1}{\rho_0 c^2}(-\Delta h_f^\circ)\frac{1}{2}Re[p_1 \dot{w}^{(1)*}] \tag{II.38}$$

Expression (II.35) together with the period averages E, $\boldsymbol{F}$ and S provide a global acoustic energy balance for the cavity of volume V surrounded by the surface A. According to this expression the energy contained in the acoustic perturbations existing in the volume may be changed in two ways. One contribution is due to the volume integral of $Re[p_1 \dot{w}^{(1)*}]$ while

the other comes from the surface integral of the normal flux. The energy is increased if the surface integral of the flux is positive. The growth rate of the acoustic perturbations may be deduced from the global energy balance. For this let us assume that the slow variation of the perturbations is of the form:

$$p_1 = p_1 e^{\alpha t}, \ \boldsymbol{v}_1 = \boldsymbol{v}_1 e^{\alpha t}, \ \dot{w}^{(1)} = \dot{w}^{(1)} e^{\alpha t} \tag{II.39}$$

where $\alpha T \ll 1$ (i.e. the growth of the perturbation over a single period is small). The global energy balance then yields:

$$2\alpha = \left[-\int_A \boldsymbol{F} \cdot \boldsymbol{n} dA + \int_V S dV \right] / \int_V E dV \tag{II.40}$$

where factors of the form $e^{\alpha t}$ may be discarded from all the terms appearing in this expression. To obtain a practical result let us use the surface admittance Y on the cavity surface and introduce the complex ratio of the non-steady volume rate of reaction to the pressure perturbation:

$$Y = \boldsymbol{v}_1 \cdot \boldsymbol{n}/p_1 \tag{II.41}$$
$$D = \dot{w}^{(1)}/p_1 \tag{II.42}$$

Both Y and D are complex numbers. With these definitions the growth rate is given by:

$$2\alpha = \left[-\frac{1}{2}\int_A p_1 p_1^* Re(Y^*)dA + \frac{1}{2}\int_V p_1 p_1^* Re(D^*)dV \right] / \int E dV \tag{II.43}$$

II.3.2 Acoustic energy balance in cavities with mean flow

Extension of the previous results to cavities with mean flow is due to Cantrell and Hart (1964) [24]. Their results will be presented without the derivation which may be found in the original paper. The basic assumptions are that the mean flow is irrotational and isentropic. These assumptions are rather restrictive but the results are nevertheless useful. For simplicity one assumes that the volume rate of reaction is also absent but this term may be included with little effort.

Now let $\boldsymbol{v}_0$ designate the mean flow velocity in the cavity, the global energy balance averaged over a period takes the form:

$$\frac{\partial}{\partial t}\int_V E dV + \int_A \boldsymbol{F} \cdot \boldsymbol{n} dA = 0 \tag{II.44}$$

where now:

$$E = \frac{1}{4}\frac{p_1 p_1^*}{\rho_0 c^2} + \frac{1}{4}\rho_0 v_1 \cdot \boldsymbol{v}_1^* + \frac{1}{2}Re(\frac{p_1}{c^2}\boldsymbol{v}_0 \cdot \boldsymbol{v}_1^*) \tag{II.45}$$

$$\boldsymbol{F} = \frac{1}{2}Re\{p_1 v_1^* + \frac{p_1 p_1^*}{\rho_0 c^2}\boldsymbol{v}_0 + \rho_0 \boldsymbol{v}_1(\boldsymbol{v}_0 \cdot \boldsymbol{v}_1^*) + \frac{p_1}{c^2}\boldsymbol{v}_0(\boldsymbol{v}_0 \cdot v_1^*)\} \tag{II.46}$$

The previous expressions may be interpreted as the time averages of the acoustic energy and flux in the moving medium.

Growth rates of the acoustic perturbations may be estimated from the previous energy balance. Assuming that p_1, $\boldsymbol{v}_1$ are of the form $e^{\alpha t}$ one obtains

$$2\alpha = \left[-\int_A \frac{1}{2} Re\{p_1 v_1^* + \frac{p_1 p_1^*}{\rho_0 c^2}\boldsymbol{v}_0 + \rho_0 \boldsymbol{v}_1(\boldsymbol{v}_0 \cdot \boldsymbol{v}_1^*) + \frac{p_1}{c^2}\boldsymbol{v}_0(\boldsymbol{v}_0 \cdot \boldsymbol{v}_1^*)\} \cdot \boldsymbol{n} dA \right] /$$
$$\int_V \left[\frac{1}{4}\frac{p_1 p_1^*}{\rho_0 c^2} + \frac{1}{4}\rho_0 \boldsymbol{v}_1 \cdot \boldsymbol{v}_1^* + \frac{1}{2} Re \frac{p_1}{c^2}(\boldsymbol{v}_0 \cdot \boldsymbol{v}_1^*) \right] dV \tag{II.47}$$

II.3.3 The Rayleigh criterion

A result which is often used in the analysis of combustion instabilities is a criterion due to Rayleigh. The result dates back to 1878 [2] and is presented in Rayleigh's classical book on the theory of sound (Rayleigh 1945 [30]). This criterion states that the pressure perturbation and the non-steady heat addition must be in phase for amplification.

There are many possible derivations of this result, one of which relies on the acoustic energy balance relations presented in this section (see Culick 1987 for an alternative presentation [8]). Consider once more the local energy balance:

$$\frac{\partial \mathcal{E}}{\partial t} + \boldsymbol{\nabla} \cdot \boldsymbol{\mathcal{F}} = \frac{\gamma - 1}{\rho_0 c^2}(-\Delta h_f^\circ) p_1 \dot{w}^{(1)} \tag{II.48}$$

The source term on the right hand side will enhance the acoustic energy if p_1 and $\dot{w}^{(1)}$ have the same sign. If the previous equation is averaged over a period of oscillation it becomes:

$$\frac{\partial E}{\partial t} + \boldsymbol{\nabla} \cdot \boldsymbol{F} = S \quad \text{where} \quad S = \frac{\gamma - 1}{\rho_0 c^2}(-\Delta h_f^\circ)\frac{1}{2} Re(p_1 \dot{w}^{(1)*}) \tag{II.49}$$

Now let φ designate the phase between the pressure and the rate of reaction perturbations. The source term S becomes:

$$S = \frac{\gamma - 1}{\rho_0 c^2}(-\Delta h_f^\circ)\frac{1}{2} P_1 \dot{W}^{(1)*} \cos \varphi \tag{II.50}$$

The source term will be positive and the amplitude of oscillation will increase if $-\pi/2 \le \varphi \le \pi/2$ (i.e. if the pressure and unsteady heat release are in phase). The source term will be negative and the amplitude of oscillation will decrease if $\pi/2 \le \varphi \le 3\pi/2$ (i.e. if the pressure and heat release are out of phase).

In other words, this criterion states that if the local unsteady heat release $Q_1(x,t)$ is in phase with the local pressure fluctuation $p_1(x,t)$, the pressure wave associated with the fluctuation will be locally amplified. Rayleigh's criterion has often been used in combustion instability studies to quantify the coupling between unsteady heat release and acoustic pressure fields (see for example Poinsot *et al.* 1987 [31], or Bloxsidge *et al.* 1988, [32]). A Rayleigh index, $G(\mathbf{x})$ can be defined (Putnam 1971, [4]):

$$G(\mathbf{x}) = \frac{1}{T}\int_T Q_1(\mathbf{x}, t)p_1(\mathbf{x}, t)dt \tag{II.51}$$

where T represents the time of one oscillation cycle. Rayleigh's criterion states that if $G(\mathbf{x}) > 0$, local amplification of flame-acoustic interaction takes place and if $G(\mathbf{x}) < 0$ damping occurs. Equation (II.51) may be expressed in the frequency domain as follows:

$$G(\mathbf{x}) = 2 \int_0^\infty |S_{pq}(\mathbf{x}, f)| \cos \phi_{pq}(\mathbf{x}, f) df \qquad (\text{II.52})$$

where $S_{pq}(f)$ are the Fourier coefficients of the cross-spectrum of $p_1(\mathbf{x}, t)$ and $Q_1(\mathbf{x}, t)$ and $\phi_{pq}(f)$ are the relative phase angle. Rayleigh's criterion predicts flame driving for phase angles between $-\pi/2$ and $\pi/2$ (modulus 2π).

The direct measurement of these quantities is often attempted in experiments. A typical setup for such measurements is shown in Fig. II.1. Pressure is obtained from probes mounted on the combustor walls. Heat release is deduced from free radical radiation imaging. It is then possible to estimate the local Rayleigh index $G(\mathbf{x})$ which determines regions of driving and regions of damping (Fig. II.2, Samaniego 1993 [33]).
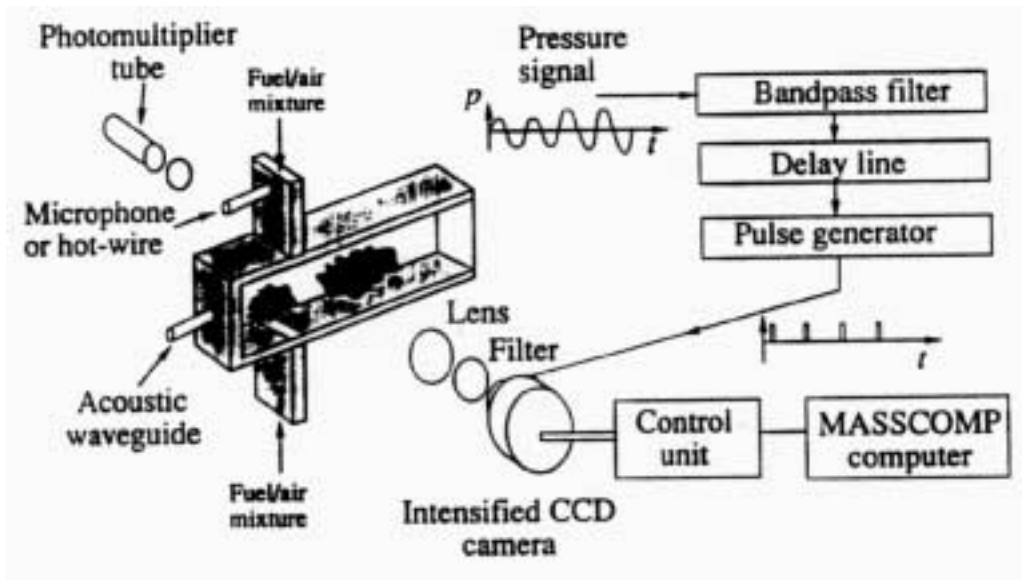
Figure II.1: Typical setup for simultaneous emission imaging and pressure detection (Samaniego *et al.* 1993).
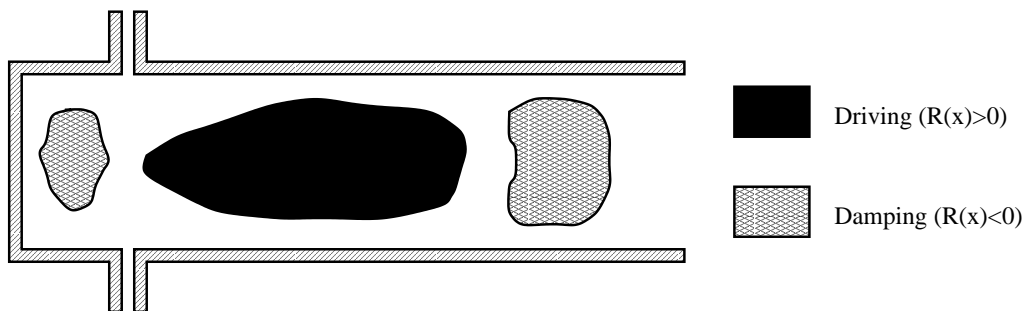
Figure II.2: Determination of the regions of driving and damping in a side dump combustor using Rayleigh's criterion (Samaniego *et al.* 1993).

This page has been deliberately left blank

Page intentionnellement blanche

Chapter III

A Simple Model for Instability and Control

K. McManus, T. Poinsot, S. Candel [10]

III.1   Introduction

As a general introduction to combustion instability and control mechanisms, it is useful to consider a simple model describing the linear interaction between an unsteady heat release source and an acoustic resonator (Crocco, 1952) [34]. The model described in section III.2 has been successfully applied in the study of combustion instability associated with a ducted premixed flame by Lang *et al.* (1987) [35] and by Le Helley (1994) [29]. In the following, the basic equations describing such a system are developed (section III.2), along the lines of McManus *et al.* (1993) [10].

It appears that the response of the flame to acoustic waves is a crucial parameter. Determining this relation is by no means a trivial exercise due to the complex relationship between the time varying flow variables and the dynamic response of the flame. This issue will be analyzed in depth in chapter IV. In the present chapter, the global response of flames to acoustic waves is represented in a simple way The model allows an analytical investigation and it is useful in this respect.

The sensitive time lag, or $n - \tau$, formulation is extensively used in the early literature dealing with combustion in rocket motors. This concept is still of interest because it allows construction of simple instability models and because it provides a basic understanding of one important instability mechanism. Numerous applications may be found in the literature dealing with liquid rocket instabilities (Crocco and Cheng 1956 [21]). The time lag concept is briefly explained in section III.2, and it is used to determine the instabilities in the duct in section III.3.

The control model which will be developed in this section is simpler than those described in earlier studies and is more appropriate for the present discussion in that it is easily adapted to the ducted flame model.

III.2   Linear model

Combustion instability mechanisms in practical combustion systems are quite complex because of many coupled interactions and inherent non-linearities. In general, combustion involves tur-

bulent fluctuations, exothermic chemical reactions, acoustic pressure perturbations, etc. As a result, most instability mechanisms cannot be modeled or described using standard analytical techniques until many simplifications have been made to render the problem tractable. The validity of certain simplifying assumptions will depend on the combustion system under consideration. In many cases the analytical description may result in an oversimplified view of the reality.

For example, if a natural hydrodynamic instability existing in the initial region of the combustor is a key element in the instability mechanism, a model which ignores this phenomenon may not be useful in predicting instabilities for that system. Due to this, a universal model for predicting combustion instabilities does not exist and combustion instability modeling has generally been carried out on a case by case basis.

III.2.1   Basic equations

We consider the mean flow of a combustible mixture through a long duct (an acoustic resonator), opened at one end and closed at the other one, with a flame stabilized at the axial location $x = a$ (Fig III.1, McManus *et al.* 1993 [10]). In this development, the following assumptions will be made:

- The frequencies of the acoustic waves considered are low compared to the duct cut-off frequency and these waves correspond to plane waves propagating along the longitudinal duct axis.

- The dissipation of acoustic waves throughout the duct is negligible.

- The open end of the duct corresponds to a pressure node and the closed end to a pressure anti-node.

- The mean flow Mach number is small, thus the flow velocity is negligible when compared to the sound speed.

- The flame is compact compared to the acoustic wavelength so that the region of heat release may be approximated as a thin sheet located at $x = a$.

We denote the portion of the duct upstream of the flame-holder as region 1, with a non-reacted gas density ρ_1 and with sound speed c_1. Region 2 corresponds to the post-combustion zone downstream of the flame-holder, with a reacted gas density ρ_2 and with sound speed c_2.

For longitudinal plane waves traveling along the duct, the pressure p and the acoustic velocity u may be expressed in the following form:

Region 1

$$p_1(x,t) = A \exp(ik_1(x-a) - i\omega t) + B \exp(-ik_1(x-a) - i\omega t) \tag{III.1}$$

$$u_1(x,t) = \frac{1}{\rho_1 c_1} \left[A \exp(ik_1(x-a) - i\omega t) - B \exp(-ik_1(x-a) - i\omega t) \right] \tag{III.2}$$
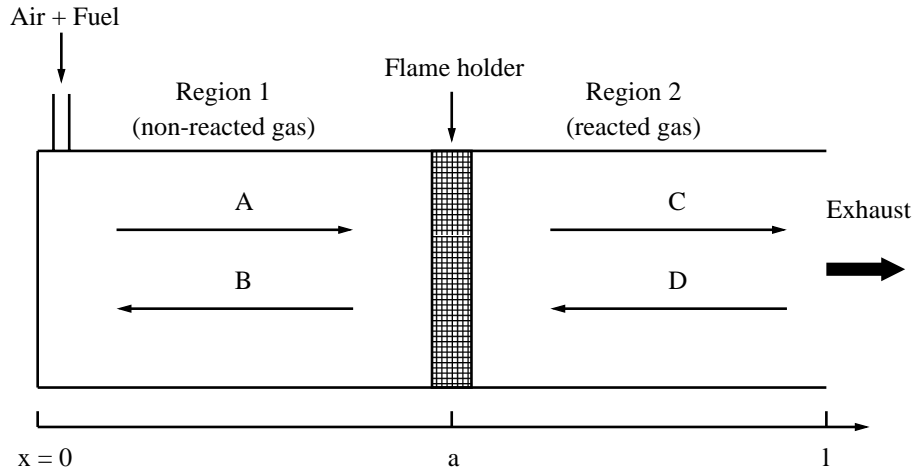
Figure III.1: Sketch of the model geometry (McManus *et al.* 1993).

Region 2

$$p_2(x, t) = C \exp(ik_2(x - a) - i\omega t) + D \exp(-ik_2(x - a) - i\omega t) \tag{III.3}$$

$$u_2(x, t) = \frac{1}{\rho_2 c_2} \left[C \exp(ik_2(x - a) - i\omega t) - D \exp(-ik_2(x - a) - i\omega t) \right] \tag{III.4}$$

where $k = \omega/c$ is the wave number and A, B, C and D represent the amplitudes of acoustic traveling waves in the duct.

By assuming that the outlet of the duct ($x = l$) acts as a pressure node and that the upstream end ($x = 0$) is a rigid wall, one may write:

$$p_2(l, t) = 0 \tag{III.5}$$
$$u_1(0, t) = 0 \tag{III.6}$$

Furthermore, we will use a matching condition to prohibit a pressure jump across the flame ($x = a$), this may be expressed as follows:

$$p_1(a_-, t) = p_2(a_+, t) \tag{III.7}$$

By applying these boundary conditions to Eqs (III.1)-(III.4), we are left with the following relations:

$$A \exp(-ik_1 a) - B \exp(ik_1 a) = 0 \tag{III.8}$$
$$C \exp(ik_2(l - a)) + D \exp(-ik_2(l - a)) = 0 \tag{III.9}$$
$$A + B = C + D \tag{III.10}$$

Up to this point, we did not consider the effects of heat release from the flame and its physical significance in the problem formulation. Combustion acts as a velocity source term

due to strong dilatation associated with the heat release. This effect may be quantified using the linearized acoustic equations for a reacting flow (see chapter II) and leads to:

$$u_2(a_+, t) - u_1(a_-, t) = (\gamma - 1)\frac{Q_1}{\rho_1 c_1^2} \tag{III.11}$$

where Q_1 represents the instantaneous heat release rate and γ is the ratio of specific heats. If we suppose that Q_1 oscillates sinusoidally, we may write:

$$Q_1 = Q \exp(-i\omega t) \tag{III.12}$$

where Q may be considered constant and represents the maximum level of heat release obtained during combustion. Substituting these expressions into Eqs (III.1)-(III.4), we obtain:

$$\zeta(C - D) - (A - B) = (\gamma - 1)\frac{Q}{c_1} \tag{III.13}$$

where $\zeta = \rho_1 c_1 / \rho_2 c_2$ is the specific acoustic impedance. Equations (III.8), (III.9), (III.10) and (III.13) constitute a linear system which may be solved to yield the wave amplitude coefficients, A through D, provided that we can express the heat release rate Q_1 as a function of A through D.

Determining the functional form of $Q_1(A, B, C, D)$ is by no mean a trivial exercise due to the complex relationship between the time varying flow variables and the dynamic response of the flame.

Furthermore, it is not clear that the heat release term, or the flame dynamics, may be appropriately modeled as a function of the acoustic wave amplitudes alone. this term may well depend on other phenomena, which are not implicitly described by the wave amplitudes (turbulence characteristics, wall heat transfer properties, non-linear chemical effects). Chapter IV will be dedicated to this problem.

For the present example, the modeling of the heat release term will be simplified and an approach using a "sensitive time lag" hypothesis will be employed [34]. The formulation for this approach will be outlined in the next section.

III.2.2   The sensitive time lag formulation

In the present formulation, a heuristic argument will be used to derive a simplified form of the $n - \tau$ model. As before, we assume that the combustion process in the duct may be treated as being one-dimensional and that the heat release occurs in an infinitesimally thin region at $x = a$.

If we then suppose that the perturbations in the heat release rate are created uniquely by velocity perturbations existing at the flame holder ($u_1(x = a, t)$), but after a time lag τ, we may write the following relation:

$$(\gamma - 1)\frac{Q_1}{\rho_1 c_1^2} = n u_1(a, t - \tau) \tag{III.14}$$

where the non-dimensional constant n is called the interaction index and describes the intensity of coupling between the velocity and heat release oscillations. For the case considered here, we take τ as being constant.

We also know that for our problem, u_1 oscillates sinusoidally with time, thus we have:

$$(\gamma - 1)\frac{Q_1}{\rho_1 c_1^2} = n \exp(i\omega\tau)u_1(a) \tag{III.15}$$

This expression may also be written in terms of the maximum heat release rate, Q:

$$(\gamma - 1)\frac{Q}{\rho_1 c_1^2} = \frac{n}{\rho_1 c_1}(A - B)\exp(i\omega\tau) \tag{III.16}$$

After substituting this expression into Eq. (III.13), we are left with a linear system of equations which allows the determination of the wave amplitude coefficients:

$$\zeta(C - D) - (A - B)(1 + n\exp(i\omega\tau)) = 0 \tag{III.17}$$
$$A\exp(-ik_1 a) - B\exp(ik_1 a) = 0 \tag{III.18}$$
$$C\exp(ik_2 b) + D\exp(-ik_2 b) = 0 \tag{III.19}$$
$$A + B = C + D \tag{III.20}$$

where $b = l - a$. This system has a non-trivial solution only if its determinant is zero and this condition yields:

$$\zeta\cos(k_1 a)\cos(k_2 b) - \sin(k_1 a)\sin(k_2 b)\left[1 + n\exp(i\omega\tau)\right] = 0 \tag{III.21}$$

where $k_1 = \omega/c_1$ and $k_2 = \omega/c_2$. For any given set of values for n and τ, the roots of Eq. (III.21) will provide complex value of ω. Since the necessary condition for instability for the linear problem is simply to have a growth in the magnitude of the oscillations, instability is predicted when the imaginary part of ω is positive. The frequency of the instability is given by the real part of ω.

III.3   Solution in a simplified case

For the general case, Eq. (III.21) requires a numerical solution. However, it is quite useful to consider simpler cases where we can derive the exact solution. One method is derived in Lang *et al.* (1987) [35], where small perturbations around the acoustic mode frequency without combustion are considered. We will consider here another case where one can determine the complete solution by choosing certain values for the parameters. Let us assume:

$$a = b \quad c_1 = c_2 = c \quad \rho_1 = \rho_2 \quad (\zeta = 1) \tag{III.22}$$

This is the case of a flame located in the center of a duct of length $2a$ and creating a negligible temperature jump. Neglecting the temperature jump is unrealistic; however, the resulting solution retains the same qualitative properties as that for the more complex case with a temperature jump.

In this case, Eq. (III.21) may be written (without approximation) as:

$$\cos(2ka) - \sin^2(ka)n\exp(i\omega\tau) = 0 \tag{III.23}$$

or

$$\cos(2ka) = 0.5 \frac{n \exp(i\omega\tau) + 0.5n^2}{1 + n \cos(\omega\tau) + 0.25n^2} \qquad \text{(III.24)}$$

or, if we assume that $n < 1$:

$$\cos(2ka) = 0.5n \exp(i\omega\tau) \qquad \text{(III.25)}$$

The solution of the problem will be considered in two steps: first, we will study the case without combustion ($n = 0$) and find the corresponding resonant frequency $\omega_0 = k_0 c$; then we will consider perturbations around this value of ω_0 with combustion ($0 < n < 1$).

We will describe this analysis for the first longitudinal mode of the cavity (quarter wave) at a frequency $\omega_0 = k_0 c$ where $k_0 = \pi/4a$ is the spatial wave number.

III.3.1   The quarter wave mode

Without combustion ($n = 0$), the first resonant frequency $\omega_0 = k_0 c$ is real ($\text{Im}(\omega_0) = 0$) and is given by:

$$\cos(2ka) = 0 \quad \text{or} \quad k_0 a = \pi/4 \qquad \text{(III.26)}$$

This mode has a wavelength given by:

$$\lambda = \frac{2\pi}{\omega_0} c = 8a \qquad \text{(III.27)}$$

which is four times the duct length. It is the first resonant longitudinal mode of the duct (often referred to as the quarter wave-mode) and has a pressure antinode at $x = 0$ and a pressure node at $x = l$. Note that this mode is not amplified ($\text{Im}(\omega_0) = 0$): if energy is not supplied to the system, the oscillations will not grow with time.

In the presence of combustion ($n > 0$), we can expand the solution about the wavenumber, k_0, corresponding to the frequency of oscillations, ω_0, by defining $k = k_0 + k'$. Assuming that $k' \ll k_0$, we obtain, from a Taylor series expansion of equation (III.25):

$$\text{Re}(k') = -\frac{n}{4a} \cos(\omega_0\tau) \qquad \text{(III.28)}$$

$$\text{Im}(k') = -\frac{n}{4a} \sin(\omega_0\tau) \qquad \text{(III.29)}$$

A more general expression of these equations may be found in Lang *et al.* (1987).

We see that the system will be unstable (i.e $\text{Im}(k') > 0$) when $\sin(\omega_0\tau)$ is negative. In this case, an acoustic oscillation near the spatial wave number k_0 (which corresponds to the first eigenmode found in the absence of combustion) will be amplified due to the oscillatory combustion and will lead to an acoustically coupled instability.

The criterion for this instability is therefore:

$$\sin(\omega_0\tau) < 0 \quad \text{or} \quad -\pi + 2j\pi < \omega_0\tau < 2j\pi \qquad \text{(III.30)}$$

where j is an integer. Rewriting this result as:

$$-\frac{T_0}{2} + jT_0 < \tau < jT_0 \quad \text{with} \quad T_0 = \frac{2\pi}{\omega_0} \qquad \text{(III.31)}$$

reveals that the growth of a given mode will occur if the time delay introduced by combustion is greater than half the acoustic mode period T_0 (modulus T_0).

III.3.2   Application of the Rayleigh criterion

As seen in chapter II, this criterion states that if the local unsteady heat release $q'(x,t)$ is in phase with the local pressure fluctuation $p'(x,t)$, the pressure wave associated with the fluctuation will be locally amplified. This can be used to check the instability condition given by the model (Eq. (III.30)) by calculating the phase ϕ between the pressure and heat release using the model equations. Because the flame is concentrated near the flame-holder, we only need to consider the pressure at $x = a$ and the total unsteady reaction rate Q_1. The pressure is given by:

$$p_2(a,t) = (A + B)\exp(-i\omega_0 t) \tag{III.32}$$

and the expression for total unsteady heat release becomes:

$$Q_1 = n(A - B)\exp(-i\omega_0(t - \tau)) \tag{III.33}$$

Substituting Eq. (III.26) into Eq. (III.18) yields $A = iB$, so that:

$$p_2(a,t) = (1 + i)B\exp(-i\omega_0 t) \tag{III.34}$$

and the expression for total unsteady heat release becomes:

$$\begin{aligned}
Q_1 &= n(i - 1)B\exp(-i\omega_0(t - \tau)) \\
&= n(1 + i)B\exp(-i\omega_0(t - \tau) + i/pi/2)
\end{aligned} \tag{III.35}$$

The phase between $p_2(a,t)$ and Q_1 is then given by:

$$\phi = \omega_0 \tau + \pi/2 \tag{III.36}$$

Substituting this expression into the condition deduced from Rayleigh's criterion for flame driving leads to:

$$-\pi + 2j\pi < \omega_0 \tau < 2j\pi \quad \text{with} \quad j = 1, 2, ... \tag{III.37}$$

which is identical to the criterion obtained with the instability model (see relation (III.30)).

III.4   A Model for Active Control

The principle behind this controller is to create a time-varying acoustic boundary condition in the duct which will inhibit the amplification of longitudinal acoustic waves and minimize the combustion oscillations. This is a fast-response closed-loop system with fixed parameters. The control system consists of four elements including a microphone (sensor), an acoustic driver (actuator), a time delay generator (controller element) and an audio-amplifier (controller element). The controller will be adapted to the model combustor by replacing the closed end of the duct with the acoustic driver to allow the imposition of a non-zero velocity boundary condition at $x = 0$. The acoustic pressure near the flame location ($x = a$) will be monitored by the microphone and will be used as the feedback signal. A mathematical model describing the controller will be given in the next paragraph.

III.4.1   Basic equations

To describe the input/output relation of the controller, a control transfer function can be written which is simply the ratio of the time-varying velocity created by the acoustic driver to the time-varying pressure at the microphone location and in dimensionless form may be written as (Fig. III.2):

$$\delta = \frac{u_1(0,t)\rho_1 c_1}{p_1(a,t)} \tag{III.38}$$
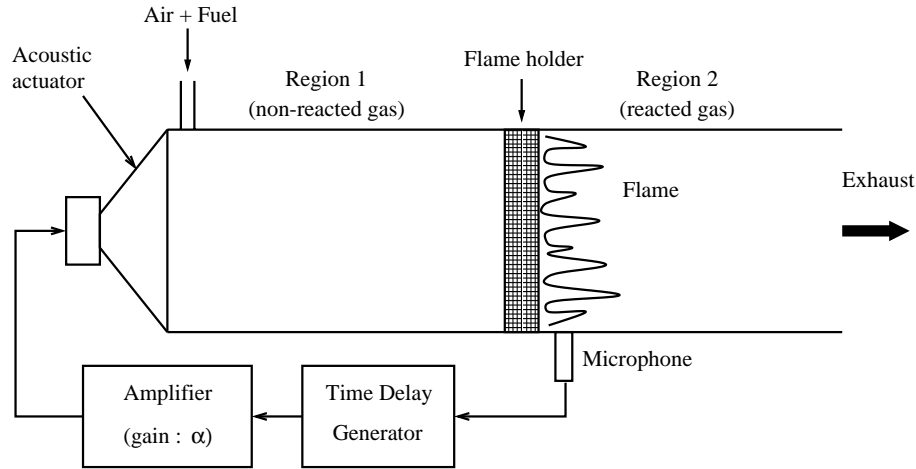
Figure III.2: Integration of the active control system to the model geometry (McManus *et al.* 1993).

The transfer function can be express in terms of a time delay ϕ, and gain α and can be written as follows:

$$\delta = \alpha \exp(i\phi) \tag{III.39}$$

with $\delta_r = \alpha \cos\phi$ and $\delta_i = \alpha \sin\phi$.

With the control system adapted to the model geometry, the analysis performed in chapter III may be repeated with a change in the boundary condition at $x = 0$. Eq. (III.8) becomes:

$$A\exp(-ik_1 a) - B\exp(ik_1 a) = \delta(A + B) \tag{III.40}$$

The determinant of the system of equations is now given by:

$$\zeta \cos(k_1 a)\cos(k_2 b) - \sin(k_1 a)\sin(k_2 b)\left[1 + n\exp(i\omega\tau)\right]$$
$$+i\sin(k_2 b)\delta(1 + n\exp(i\omega\tau)) = 0 \tag{III.41}$$

As before, we will make the simplification that the flame is located at one half of the duct length and produces a negligible temperature rise. With these assumptions, Eq. (III.41) becomes:

$$\cos(2ka) - \sin^2(ka)n\exp(i\omega t) + i\sin(ka)\delta(1 + n\exp(i\omega\tau)) = 0 \tag{III.42}$$

III.4.2   The quarter wave mode

Without combustion ($n = 0$), the first resonant frequency of the duct is given by $\omega_0 = k_0 c$. With combustion and active control, there is a slight frequency shift of the eigenmode, due to the presence of the control system and can be expressed as a shift in the wavenumber k_0. Thus we will define $k = k_0 + k'$. A Taylor series expansion of Eq. (III.42) about k_0, taking δ and n as small parameters, yields the following values of k':

$$\mathrm{Re}(k') = -\frac{n}{4a}\cos(\omega_0\tau) - \frac{\delta_i}{2a\sqrt{2}} \tag{III.43}$$

$$\mathrm{Im}(k') = -\frac{n}{4a}\sin(\omega_0\tau) + \frac{\delta_r}{2a\sqrt{2}} \tag{III.44}$$

Without active control ($\delta = 0$), it has been shown that the quarter wave mode is unstable when $\sin(\omega_0\tau) < 0$. With active control on, the instability condition becomes:

$$-\frac{n}{4a}\sin(\omega_0\tau) + \frac{\delta_r}{2a\sqrt{2}} > 0 \tag{III.45}$$

or

$$\delta_r > \delta_c^0 \tag{III.46}$$

with $\delta_c^0 = 0.5n\sqrt{2}\sin(\omega_0\tau)$. This last quantity ($\delta_c^0$) is called a critical parameter and if the controller operation is such that:

$$\delta_r = \delta_c^0 \tag{III.47}$$

the instability will be suppressed.

This model might be improved for example by including viscous losses and other damping effects in the model equations. However, this simple linear model serves well in reproducing certain general operating characteristics of real controllers of this type.

This page has been deliberately left blank
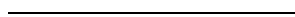
Page intentionnellement blanche

Chapter IV

Modeling, Simulation and Identification

S. Ducruix, D. Durox and S. Candel [36,37]
S. Candel, D. Durox, S. Ducruix and D. Thibaut [38]
C. Nottin, R. Knikker, M. Boger, D. Veynante [39]

IV.1 Introduction

Because combustion instabilities have so many facets, they have been examined with a wide variety of theoretical models. New experimental evidence and some earlier observations indicate that the instabilities involve large oscillations of the flame front, pulsations of the injected reactant streams, hydrodynamic instabilities, vortex roll-up, burning and interactions (see for example Keller *et al.* 1981 [40], Candel 1992 [9], McManus *et al.* 1993 [10]).

The fundamental problem is to represent the flow dynamics coupled with the flame motion. This is well discussed in a number of earlier studies and in review articles. Marble and Candel (1978) [41] first indicated that the non-steady response of the flame could be a possible source of low frequency oscillations in afterburners or large utility powerplants. Their model describes the dynamics of fresh and burnt gases submitted to axial pressure waves as well as the motion of the flame sheet. The flame is presented as a sheet which is thin compared to the characteristic wavelength of the problem. Poinsot and Candel (1988) [42] used an integral technique coupled with a description of the flame position to represent the response of a premixed turbulent flame stabilized in a duct. In their model the flame was treated as a thin discontinuity separating fresh and burnt streams. Mean velocities on the two sides of the flame, pressure as well as the flame position were the main dynamical variable. This led to a time-dependent one-dimensional problem. One limitation of this analysis is that the flame cannot feature large wrinkles which typically occur during high amplitude instabilities.

More recently, Fleifil *et al* (1996) [43], Dowling (1999) [44] and Ducruix *et al* (2000) [37] proposed descriptions of flame front dynamics in the simple case of a laminar conical flame. Section IV.2 reviews the model derived by Ducruix *et al* (2000). The aim of this section is to characterize the flame front behavior in a simplified case and to determine a relation between heat release fluctuations and velocity variations at the burner outlet.

Section IV.3 is dedicated to Large Eddy Simulation (LES). In an interesting article Najm and Ghoniem (1993) [45] combined a random vortex method of solution for the flow with a volume of fluid technique to track the flame treated as an interface. The front was assumed to propagate at a laminar speed including curvature effects. Another important study was carried out by Menon and Jou (1991) [46]. Combining a large eddy simulation of the flow with a

description of the front motion (the G-equation of Kerstein *et al.* 1988 [47]), these authors were able to represent the flame response to instabilities as observed in model scale ramjet experiments.

The flame motion is an essential aspect of the problem. It is in particular important to describe the interaction between the unsteady flow field, the reaction front and the associated heat release. In previous investigations the flame was considered as a thin interface. This provided a convenient simplification because the internal structure of the flame was not resolved. However tracking techniques are not easy to extend in three dimensions while methods based on the level-set G-equation pose problems when one wishes to include gas expansion processes (i.e. to describe the large change in mass density occurring at the flame, a problem explored by Piana *et al.* (1996) [48]).

An alternative representation of the flame on a coarse mesh consists in artificially thickening the flame front while keeping a realistic propagation speed. To do this we use a method initially devised by Butler and O'Rourke (1976) [49] to deal with laminar flames propagating in large cavities. This technique has been used recently by Thibaut and Candel (1998) [50], Angelberger *et al.* (1998) [51] and Nottin *et al.* (2000) [39]. It will be exploited in what follows to describe the flame response to large turbulent structures and organized perturbations. It has the advantage of keeping an internal flame structure and of naturally accounting for gas expansion. This formulation also avoids problems of cusp formation which are encountered in front tracking algorithms.

Our objective will be to demonstrate that the method is well suited to combustion dynamics analysis. We adopt the LES framework to describe the fine grained turbulence but the calculations are carried out in two dimensions with a basic subgrid model. The generalization to three-dimensional situations including more sophisticated dynamic subgrid models will pose no conceptual difficulties but will require augmented computational resources.

In section IV.3, the formulation of the LES model and its numerical implementation are presented. The geometrical configuration investigated are described. We then discuss reactive computations carried out for several operating conditions, demonstrating the ability to simulate unsteady flame propagation.

IV.2   Description of flame front dynamics

The transfer function of premixed flames has been studied by several authors. In 1956, Merk [52] proposed a first-order model, predicting general trends of flame behavior. With laminar axisymmetrical flames, Blackshear (1953) [53] and De Sœte (1964) [54] and more recently Baillot *et al.* (1992) [55] and Le Helley [29] (1994) have shown that flames behave like low-pass filters.

Becker and Günther (1971) [56] have studied turbulent flat flames, using a pressure sensor placed in the mixing chamber. They obtained the transfer function of their specific configuration. For turbulent stoichiometric premixed flames, anchored above burners of 8 to 10 mm exit diameters, Lenz and Günther [57] observed no decrease of the transfer function amplitude, for low frequencies ($f \leq 100$ Hz). Goldschmidt *et al.* [58] have obtained a monotonic relation between cut-off frequency and flame height. The configuration analyzed by Matsui (1981) consisted in a flat burner with different types of slots [59]. The transfer function, determined

using microphones, confirmed the general trend observed in [56–58]. Matsui reviewed formers models, and proposed a new description, close to that of Merk [52].

Fleifil *et al.* (1996) [43] and Annaswamy *et al.* (1997) [60] have analyzed the flame transfer function, in the case of axisymmetrical configurations, using a set of simplifications. While their model leads to a compact description in the linear small perturbation regime, it deserves further analysis and a comparison with experiments.

Developments in laser techniques have been made, and velocimetry measurements are now extremely precise. Experimental data, concerning axisymmetrical burners and correlating heat release fluctuations to velocity variations, are not widely available. However, they are necessary for direct comparisons with the models.

In this section, the response of laminar conical premixed flames to acoustic modulations is determined experimentally, and compared to the theoretical model. This configuration is simpler than found in practical burners, but it makes it possible to analyze which parameters are relevant. Experimental results may easily be used to validate simulation codes, and general trends of the behavior of real configurations can be deduced from the present results. First, the analytical model is derived. The experimental setup is then described. Finally, results and their interpretations are presented.

IV.2.1 Flame response model

The model described in this section relies on that devised by Fleifil *et al.* [43]. Their analysis is extended to a more general situation. The flame front is placed in a flow characterized by its mean and perturbation components. The flow and flame parameters are sketched in Fig. IV.1.
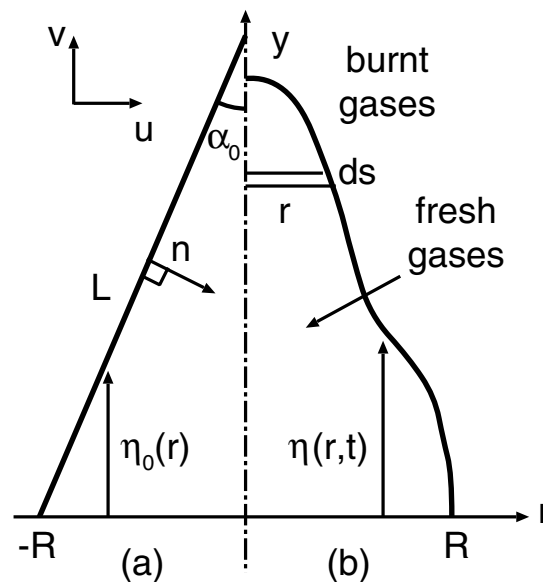
Figure IV.1: Sketch of the flame and flow parameters, (a) in the steady situation and (b) in the perturbed situation.

Description of the flame front

A G variable, increasing from burnt gases to fresh gases, is used to describe the flame position:

$$\frac{\partial G}{\partial t} + \mathbf{v} \cdot \boldsymbol{\nabla} G = -S_D |\boldsymbol{\nabla} G| \tag{IV.1}$$

where $\mathbf{v} = (u, v)$ is the velocity vector, and S_D is the flame displacement speed. In the following, S_D is assumed to be a constant, equal to the laminar burning velocity, S_L. Then, it does not depend on the flow stretch.

The radial velocity u is supposed to be negligible, compared to v. The fresh mixture flow is essentially axial. Fig. IV.1 shows that G may be replaced by $\eta - y$, where η indicates the flame position. The following relations are easily derived:

$$\boldsymbol{\nabla} G = \begin{bmatrix} \dfrac{\partial \eta}{\partial r} \\ -1 \end{bmatrix} \quad \text{and} \quad \frac{\partial G}{\partial t} = \frac{\partial \eta}{\partial t} \tag{IV.2}$$

It is then possible to write Eq. (IV.1) for any flame shape, as long as η is well-defined:

$$\frac{\partial \eta}{\partial t} + u \frac{\partial \eta}{\partial r} - v = -S_L \left[1 + \left(\frac{\partial \eta}{\partial r} \right)^2 \right]^{1/2} \tag{IV.3}$$

In the following, subscript 0 indicates steady state variables, and subscript 1 the first order perturbation variables. Relation (IV.3) may be derived for steady state flames (η_0, Fig. IV.1(a)):

$$u_0 \frac{\partial \eta_0}{\partial r} - v_0 = -S_L \left[1 + \left(\frac{\partial \eta_0}{\partial r} \right)^2 \right]^{1/2} \tag{IV.4}$$

To understand this expression, one may divide it by $|\boldsymbol{\nabla} G_0|$. Components from the flame front normal vector then appear:

$$n_r^0 = \frac{\partial \eta_0 / \partial r}{\left[1 + \left(\frac{\partial \eta_0}{\partial r} \right)^2 \right]^{1/2}} \quad \text{et} \quad n_y^0 = \frac{-1}{\left[1 + \left(\frac{\partial \eta_0}{\partial r} \right)^2 \right]^{1/2}} \tag{IV.5}$$

Considering the conical flame, α_0 is the angle between the flame front and the vertical axis (cf figure IV.1). Relation (IV.4) becomes :

$$u_0 \cos \alpha_0 + v_0 \sin \alpha_0 = S_L \tag{IV.6}$$

When u_0 is supposed negligible, one finally obtains the well-known relation:

$$S_L = v_0 \sin \alpha_0 \tag{IV.7}$$

Deriving Eq. (IV.3) for the perturbed situation, with $\eta = \eta_0 + \eta_1$, where η_0 characterizes the steady flame shape, and $\eta_1 \ll \eta_0$ (Fig. IV.1(b)), one may develop the resulting equation at the first order. Eq. (IV.3) may then be written:

$$\frac{\partial \eta_1}{\partial t} - (v_0 + v_1) = -S_L \underbrace{\left[1 + \left(\frac{\partial \eta_0}{\partial r} \right)^2 + 2 \frac{\partial \eta_0}{\partial r} \frac{\partial \eta_1}{\partial r} + \left(\frac{\partial \eta_1}{\partial r} \right)^2 \right]^{1/2}}_{f(\eta)} \tag{IV.8}$$

Moreover, considering only first-order terms:

$$f(\eta) \simeq \left[1 + \left(\frac{\partial \eta_0}{\partial r}\right)^2\right]^{1/2} + \frac{\partial \eta_0 / \partial r}{\left[1 + \left(\frac{\partial \eta_0}{\partial r}\right)^2\right]^{1/2}} \frac{\partial \eta_1}{\partial r} \tag{IV.9}$$

For the perturbed flame, one finally derives:

$$\frac{\partial \eta_1}{\partial t} = S_L \cos \alpha_0 \frac{\partial \eta_1}{\partial r} + v_1 \tag{IV.10}$$

Solutions of this equation may be obtained by using Laplace Transform:

$$\frac{d\tilde{\eta}_1}{dr} = \frac{s}{S_L \cos \alpha_0} \tilde{\eta}_1 - \frac{\tilde{v}_1}{S_L \cos \alpha_0} \tag{IV.11}$$

In the following, we use the method of constant variations to solve the problem:

$$\tilde{\eta}_1 = C \exp\left(\frac{s}{S_L \cos \alpha_0} r\right) \tag{IV.12}$$

where C is a function of r. Integrating the transform equation (IV.11), one can write:

$$C = \int_R^r -\frac{\tilde{v}_1}{S_L \cos \alpha_0} \exp\left(-\frac{s}{S_L \cos \alpha_0} r'\right) dr' + D \tag{IV.13}$$

C can be replaced in expression (IV.12), using the boundary condition $\tilde{\eta}_1(R, s) = 0$, we can deduce that $D = 0$. Writing $x = r - r'$, one obtains:

$$\tilde{\eta}_1 = \int_r^0 \frac{\tilde{v}_1}{S_L \cos \alpha_0} \exp\left(\frac{s}{S_L \cos \alpha_0} x\right) dx = \frac{\tilde{v}_1(s)}{s} - \frac{\tilde{v}_1(s)}{s} \exp(-\tau s) \tag{IV.14}$$

with $\tau = (R - r)/(S_L \cos \alpha_0)$

To deal with the right-hand side of the equation, one notes that the inverse transform of the first term is:

$$\mathcal{L}^{-1}\left[\frac{\tilde{v}_1(s)}{s}\right] = \int_0^t v_1(t') dt' \tag{IV.15}$$

The second term is:

$$\mathcal{L}^{-1}\left[\frac{\tilde{v}_1(s)}{s} \exp(-\tau s)\right] = \left[\int_0^t v_1(t') dt'\right] H(t' - \tau) dt' \tag{IV.16}$$

where H is the Heavyside function. Then, when $t > \tau$ (which will be considered in the following):

$$\eta_1(r, t) = \int_{t-\tau}^t v_1(t') dt' \quad \text{with} \quad \tau = \frac{R - r}{S_L \cos \alpha_0} \tag{IV.17}$$

IV.2.2 Heat release fluctuations

To determine the heat release fluctuations, it is necessary to evaluate the flame surface variations. The area of the flame surface is defined by the relation (Fig. IV.1):

$$A = \int_0^R 2\pi r \frac{ds}{dr} dr \tag{IV.18}$$

The arc length ds can be expressed with dr and $d\eta$.

$$ds = (dr^2 + d\eta^2)^{1/2} = dr \left[1 + \left(\frac{\partial \eta}{\partial r} \right)^2 \right]^{1/2} \tag{IV.19}$$

Introducing A_0 the area of the steady flame surface, one can write:

$$A_0 = \int_0^R 2\pi r \left[1 + \left(\frac{\partial \eta_0}{\partial r} \right)^2 \right]^{1/2} dr \tag{IV.20}$$

and writing $A_1 = A - A_0$ the area fluctuations:

$$A_1 = - \cos \alpha_0 \int_0^R 2\pi r \frac{\partial \eta_1}{\partial r} dr \tag{IV.21}$$

Assuming that $\eta_1(R, t) = 0$, one derives:

$$A_1 = 2\pi \cos \alpha_0 \int_0^R \eta_1 dr \tag{IV.22}$$

The heat release fluctuations Q_1 are given as a function of the area fluctuations of flame surface:

$$Q_1 = \rho_u S_L \Delta q A_1 \tag{IV.23}$$

where ρ_u is the unburnt gas density, and Δq the heat release per unit mass of mixture. Consider time derivation of expression (IV.23):

$$\dot{Q}_1 = K \int_0^R \frac{\partial \eta_1}{\partial t} dr \tag{IV.24}$$

where $K = \rho_u S_L \Delta q 2\pi \cos \alpha_0$. Using Eq. (IV.17), one can deduce:

$$\dot{Q}_1 = K \int_0^R \left(S_L \cos \alpha_0 \frac{\partial \eta_1}{\partial r} + v_1 \right) dr \tag{IV.25}$$

Moreover:

$$\int_0^R \frac{\partial \eta_1}{\partial r} dr = -\eta_1(0, t) \tag{IV.26}$$

Assuming that v_1 does not depend on r, one obtains for dQ_1/dt:

$$dQ_1/dt = K \left[-S_L \cos \alpha_0 \eta_1(0, t) + R v_1 \right] \tag{IV.27}$$

where $K = \rho_u S_L \Delta q 2\pi \cos \alpha_0$.

IV.2.3 Determination of the transfer function

To determine Q_1, one considers sinusoidal velocity modulations in the following paragraph:

$$v_1 = a \cos \omega t \tag{IV.28}$$

It is then possible to complete the derivation of η_1.

$$\eta_1(r,t) = \frac{a}{\omega} \left\{ \sin(\omega t) - \sin\left[\omega t - \frac{\omega}{U_C}(R-r)\right] \right\} \tag{IV.29}$$

with:

$$U_C = S_L \cos \alpha_0 \tag{IV.30}$$

It is also possible to derive relation (IV.17). One finally writes for Q_1:

$$Q_1 = \frac{aKU_C}{\omega^2} \left[\frac{\omega R}{U_C} \sin(\omega t) + \cos(\omega t) \right.$$
$$\left. - \cos(\omega t) \cos\left(\frac{\omega R}{U_C}\right) - \sin(\omega t) \sin\left(\frac{\omega R}{U_C}\right) \right] \tag{IV.31}$$

Introducing the reduced frequency as:

$$\omega_* = \omega R / S_L \cos \alpha_0 \tag{IV.32}$$

One can write for Q_1:

$$Q_1 = \frac{aKR^2}{2U_C} \frac{2}{\omega_*^2} \left[(1 - \cos \omega_*) \cos(\omega t) + (\omega_* - \sin \omega_*) \sin(\omega t) \right] \tag{IV.33}$$

The constant term appearing in this equation may be written as:

$$\frac{KR^2}{2U_C} = \rho_u \Delta q \pi R^2 \tag{IV.34}$$

Multiplying this quantity with v_0 gives the mean heat release per mass unit, Q_0.
Then:

$$\frac{Q_1}{Q_0} = \frac{a}{v_0} \frac{2}{\omega_*^2} \left[(1 - \cos \omega_*) \cos(\omega t) + (\omega_* - \sin \omega_*) \sin(\omega t) \right] \tag{IV.35}$$

Relation (IV.35) describes the flame response to acoustic modulation as a transfer function F between the reduced heat release fluctuations and the reduced velocity variations.

The amplitude and phase are easily obtained from expression (IV.35):

$$\begin{aligned}
|F(\omega_*)| &= 2 \left[(1 - \cos \omega_*)^2 + (\omega_* - \sin \omega_*)^2 \right]^{1/2} / \omega_*^2 \\
\phi(\omega_*) &= \tan^{-1} \left[(\omega_* - \sin \omega_*)/(1 - \cos \omega_*) \right]
\end{aligned} \tag{IV.36}$$

As proposed by Merk [52] and Fleifil *et al.* [43], it may also be interesting to approximate the transfer function as a first order system:

$$H(\omega_*) = \frac{\beta}{\beta + i\omega_*} \tag{IV.37}$$

where β is a fitting parameter. Values for β will be estimated later on. The amplitude and phase of the first order transfer function (IV.37) are respectively :

$$\begin{aligned}
|H(w_*)| &= \beta / \left(\beta^2 + \omega_*^2\right)^{1/2} \\
\psi(\omega_*) &= \tan^{-1}\left(\omega_*/\beta\right)
\end{aligned} \tag{IV.38}$$

IV.2.4 Experimental Setup

Experiments were carried out with flames stabilized above a Bunsen type burner (Fig. IV.2). Its end piece is a cylindrical tube 30 mm long, of 22 mm exit diameter. The burner consists in a converging nozzle which is water cooled, and a cylindrical tube 120 mm long, placed upstream from the nozzle, and containing various grids and honeycombs to produce a laminar flow. A driver unit, fed by a synthesizer and an amplifier occupies the base of the burner.
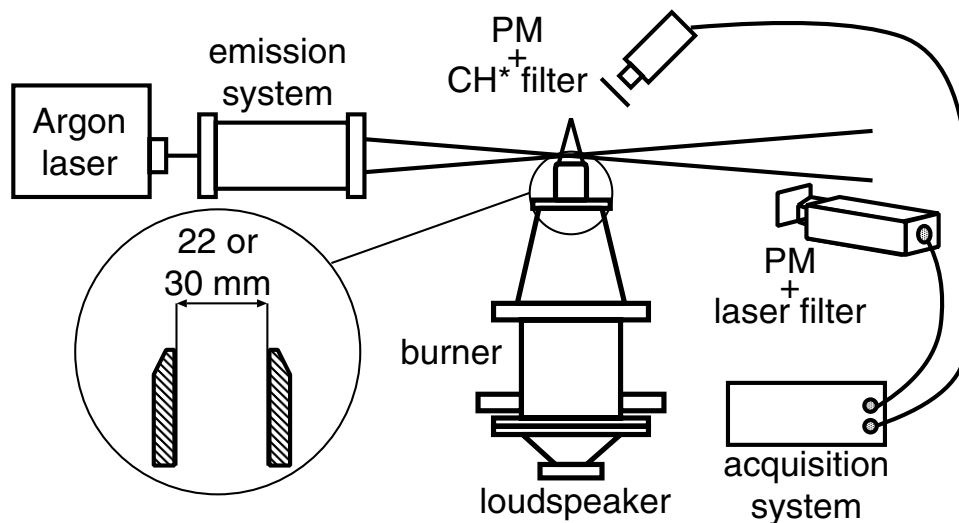
Figure IV.2: Experimental Setup.

In this study, results have been obtained for methane-air premixed flames, with an equivalence ratio $\Phi = 0.95$. Flames are anchored naturally at the burner exit. Fig. IV.3 shows an instantaneous schlieren image obtained using the 22 mm diameter burner, for a modulation frequency of 75 Hz. Perturbations wrinkle the flame front, and the shape of the perturbed flame depends on the frequency and the amplitude of the modulation. Other images of this process are provided in [53] and [61].

To determine the transfer function, one has to measure the flame heat release and the velocity at the burner exit. Tests on steady flames have shown that, in a first approximation, the
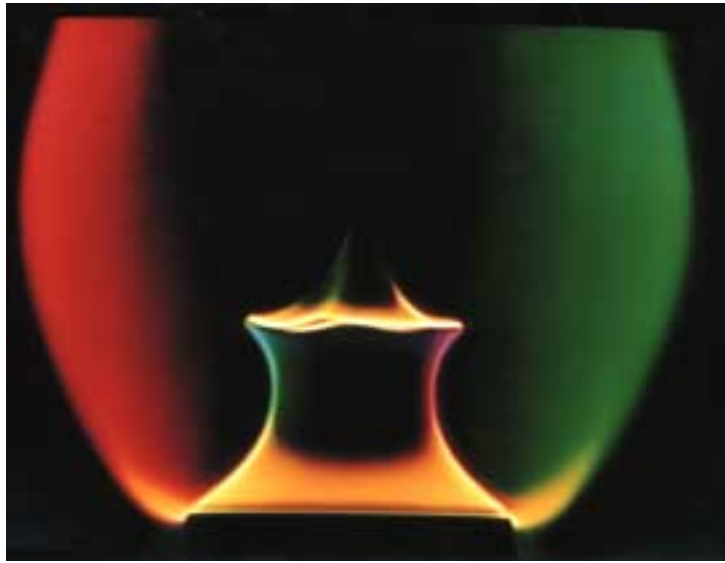
Figure IV.3: Schlieren image. The equivalence ratio Φ is 0.95, and the mean flow velocity is $v_0 = 0.96$ m.s^{-1}. Modulation frequency: 75 Hz (Ducruix 2000 [37]).

global heat release is proportional to the global spontaneous emission of CH* radicals [62,63]. The CH* emission was measured using a photomultiplier (PM) coupled with a 431 nm CH*-filter. The whole flame emission was recorded by the PM placed at a distance of 30 cm from the flame.

The velocity modulation at the burner exit was obtained using laser Doppler velocimetry (LDV). The axial component of the velocity was measured on the symmetry axis, at a z-coordinate equal to 1.5 mm. A large amount of oil droplets, with a mean diameter of about 2.5 μm, were used to seed the flow. The heat release and the velocity at the burner exit were then simultaneously recorded.

As can be seen in Fig. IV.4, the axial velocity was almost sinusoidal, for all modulation conditions that have been tested. According to the modulation frequency, the shape of the heat release signal is not exactly sinusoidal, but a spectral analysis shows that the main peak is associated with the modulation frequency, and that all other harmonics are small, compared to the fundamental level. For higher modulation amplitudes, nonlinear effects become non-negligible [64]. The transfer function amplitude is given by the ratio between the reduced root-mean-square (rms) PM intensity, I_1/I_0 and the reduced rms velocity v_1/v_0, where v_1 is measured on the axis, at $z = 1.5$ mm. I_0 is the mean PM intensity value, measured on the steady conical flame. The mean flow velocity v_0 is integrated on the surface of the burner exit plane. The phase difference between the heat release signal and the velocity signal is determined using cross-correlation.

The transfer function is determined for frequencies between 5 and 300 Hz. Beyond 300 Hz, no heat release fluctuations could be observed. All the measurements were done with a modulation amplitude v_1 equal to 0.192 m.s^{-1}. These values were small enough to maintain sinusoidal signal shapes, and large enough to allow measurements. Reduced with the mean axial velocity at the burner exit, the modulation rate varies between 8 and 20%. The velocity modulation was checked to be nearly uniform in the burner exit plan.
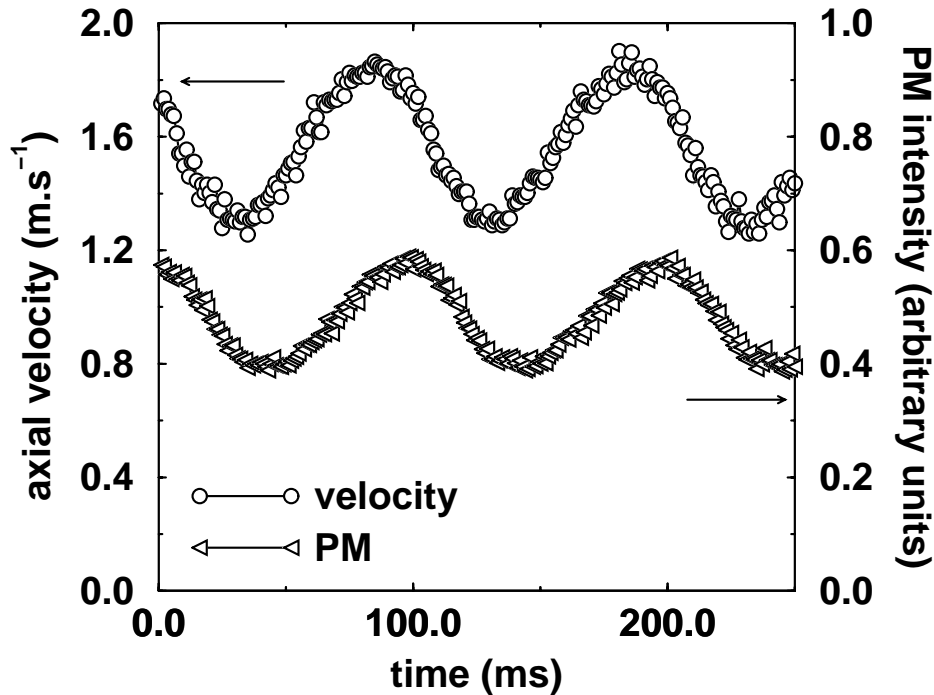
Figure IV.4: Simultaneous measurements of the axial component of the velocity, measured at $z = 1.5$ mm above the burner exit, and of the global spontaneous emission of CH* radical in the whole flame ($\Phi = 0.95$, $f_{mod} = 10$ Hz and mean flow velocity $v_0 = 1.2$ m.s^{-1}, integrated on the exit plane). Ducruix (2000) [37]).

IV.2.5   Analytical predictions and experimental results

Figure IV.5 displays flame transfer functions. To compare theoretical predictions and experimental results, the ratio $(I_1/I_0) \cdot (v_0/v_1)$ is represented as a function of the reduced frequency ω_*. The conversion factor K_c between the modulation frequency (Hz) and the reduced frequency is close 0.2. The phase difference between the PM signal and the velocity measurements is also plotted as a function of ω_*. Analytical predictions are given in Fig. IV.5, in dashed lines for the exact model and in dotted lines for the first order approximation with $\beta = 3$ (Eq. (IV.38)). This value differs from that of the first order model derived by Annaswamy *et al.* [60] (with our notations their value would be $\beta = 2$). This will be discussed below.

Amplitude of the transfer function

Experimental results show that for ω_* between 1 and 2, the ratio $(I_1/I_0) \cdot (v_0/v_1)$ is almost constant, close to one, for all mean velocities (top of Fig. IV.5). This indicates that, in the low frequency range, the heat release fluctuations follow linearly the velocity modulations. Beyond $\omega_* = 2$, the transfer function amplitude decreases sharply and is equal to 0.2 for ω_* close to 8. The low-pass filter behavior of the flame can clearly be seen. When ω_* varies between 8 and 20, $(I_1/I_0) \cdot (v_0/v_1)$ increases, up to 0.3 for some conditions. Eventually, for $\omega_* \geq 40$, heat release fluctuations essentially vanish, as assumed by Blackshear [53]. The flame surface area does not
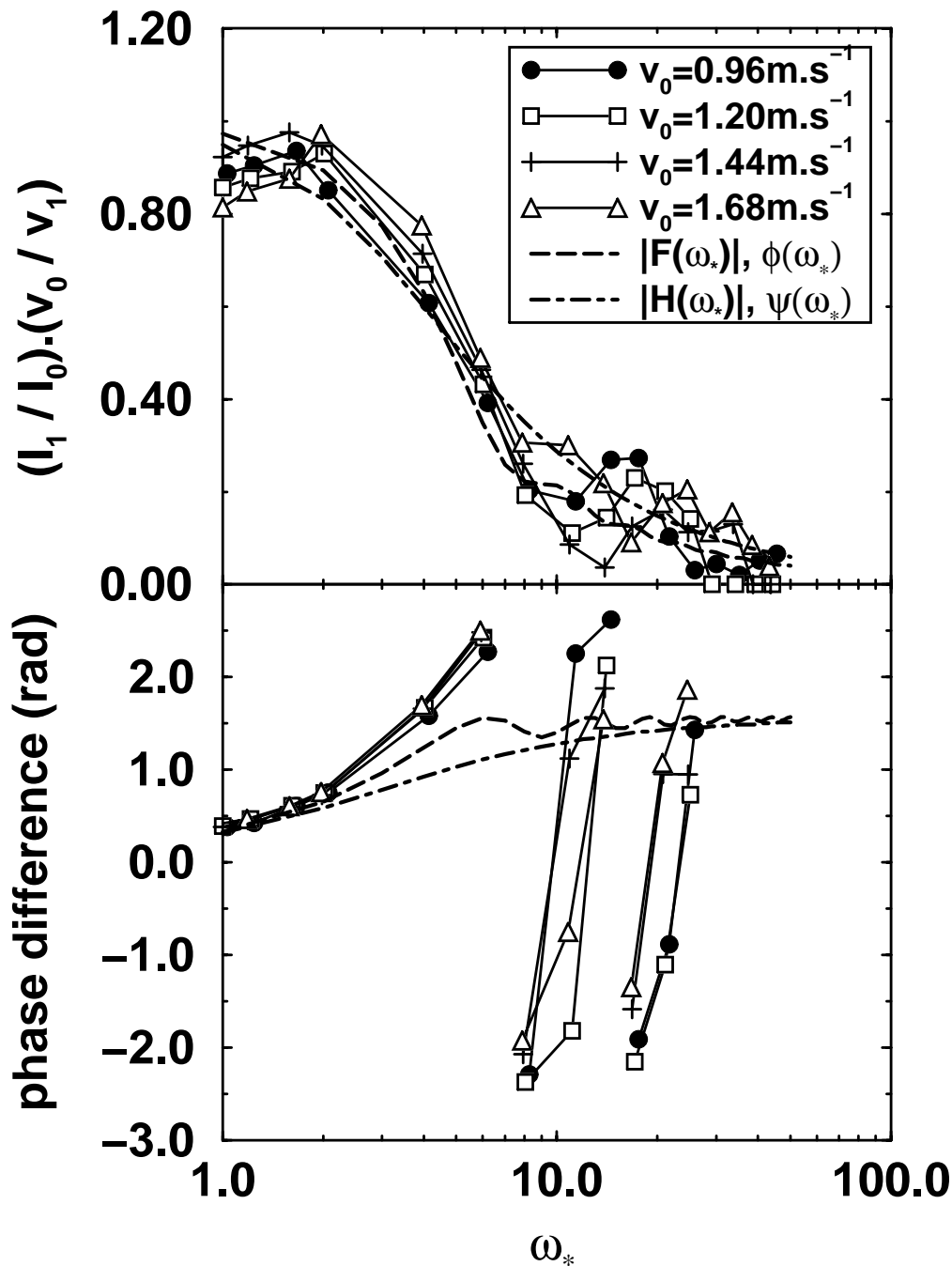
Figure IV.5: Comparisons between analytical predictions and experimental results for the flame transfer function. Velocity fluctuation: $v_1 = 0.192$ m.s^{-1}. Symbols indicates measurements, for different mean flow velocity v_0. The conversion factor between ω_* and the modulation frequency (Hz) is respectively, for increasing values of v_0: 0.207, 0.201, 0.198, and 0.197. (F, ϕ) is the exact model, and (H, ψ) is the first order approximation (Ducruix 2000 [37]).

vary during a period (Fig. IV.3), because of a compensation between bulges and contractions.

Figures IV.5 show that the models proposed in Eq. (IV.36) and (IV.38) gives good predictions for $(I_1/I_0) \cdot (v_0/v_1)$ up to $\omega_* = 8$. They do not predict the non-monotonic behavior observed for ω_* between 8 and 20. However, the reduced frequency corresponding to the change of slope in the model is in good agreement with the reduced frequency associated with the experimental change of slope. The first order approximate model suitably fits the amplitude data. The amplitude is slightly underestimated in the low frequency range, but, in the intermediate range ($8 \leq \omega_* \leq 10$), the approximate model gives better results than the exact model.

Defining the cut-off frequency as the reduced frequency for which the reduced amplitude of the transfer function is half the maximum reduced amplitude, ω_{cut}^* is around 5. The theoretical cut-off frequency is 4.8, and that of the first order model is 5.2, indicating that both models predict well the transfer function amplitude in the low frequency range. Assuming that perturbations are convected on the flame front with the velocity $v_c = v_0 \cos \alpha_0$ [29], and noting that $v_0 \sin \alpha_0 = S_L$, one derives the time needed by the perturbation to propagate from the bottom to the top of the flame $\tau_p = L/v_c = R/(S_L \cos \alpha_0)$ (see Fig. IV.1). The reduced frequency ω_p^* associated with the propagation time τ_p is then equal to 2π, a value close to the cut-off frequency ω_{cut}^* determined experimentally. This indicates that the cut-off frequency corresponds to the modulation for which the wavelength is close to the cone length.

Phase of the transfer function

The phase difference between the PM and LDV signals, named ζ in the following, is plotted, in the range $[-\pi, \pi]$, in Fig. IV.5. Experimental results show that, whatever the mean velocity v_0, ζ increases with ω_* up to $\omega_* = 25$, for which $I_1 = 0$.

Phase differences greater than 2π are observed. Snellink and Kiers [65] have also measured phase differences larger than $\pi/2$ for turbulent propane-air flames, using a small burner of 5 mm in diameter. With very turbulent flames, Lenz and Günther (1981) [57], Matsui (1981) [59], and Antnam *et al.* (1974) [66] have obtained values larger than 2π. ζ increases continuously and regularly, up to $\omega_* = 25$ (see Fig. IV.5, representation in the range $[-\pi, \pi]$). With the larger burner, ζ increases slower, and exhibits a plateau for ω_* between 6 and 9, whatever the mean velocity v_0 is. The value 2π is reached for $\omega_* = 20$.

The analytical predictions match the experimental values for ω_* lower than 2. Between 2 and 6, ϕ and ψ underestimate ζ, giving a maximum value equal to $\pi/2$ for $\omega_* = 2\pi$. For ω_* greater than 6, ϕ features an oscillation, remaining close to $\pi/2$. For this range of values, model predictions do not fit the experimental results, whatever the burner. The first order approximation correctly predicts the experimental behavior for ω_* lower than 2. Beyond this value, predictions underestimate the experimental data. Both models show their limits in the high frequency range. They can not be used to determine the phase differences between heat release fluctuations and velocity modulations.

Since ζ increases regularly with ω_*, it is possible to describe ζ as a time lag $\tau_L = \zeta/\omega$, with ω the angular frequency. The time lag τ_L is a constant, around 12 ms. It may be compared to the mean time necessary for the perturbation to be convected from the exit plane to the flame front. When there is less than one perturbation on the flame front at the same time ($\omega_* \leq 2\pi$), a simple calculation shows that $\tau_L = R(1 - 1/2^{1/2})/S_L \simeq 0.3R/S_L$, where R is the burner radius, or $\tau_L = 9$ ms. The general trend is good, even though the boundary layer effects, which modify the velocity profile at the flame base, are not taken into account. Merk [52] had proposed a similar calculation, giving a time lag equal to $R/3S_L$, which is remarkably close to the relation

found in this study. It is now possible to relate the fitting parameter β and the time lag τ_L, writing the first order Eq. (IV.37) as:

$$H(\omega) = \frac{1}{1 + i\omega\tau_L} \qquad\qquad\qquad (IV.39)$$

Then, $\omega\tau_L = \omega_*/\beta$, and one obtains, using Merk's relation: $\beta = 3/\cos\alpha_0 \simeq 3$, in agreement with the fitting parameter chosen in Fig. IV.5.

Conclusion

The model indicates that the amplitude and phase of the transfer function may be represented as a function of the reduced frequency $\omega_* = R\omega/S_L\cos\alpha_0$. The transfer function has also been determined for other equivalence ratio and other burner diameters [36]. For a given equivalence ratio, graphs are well superimposed. Using ω_*, it is easy to predict the flame response, for burners of different geometry, mean velocity and laminar burning velocity. The model assumptions concerning the velocity field and the flame displacement speed may probably be acceptable for slightly wrinkled flames, with a small radial component of the velocity field. These flames remain almost conical and correspond to low frequency modulations. In contrast, these assumptions are too strong for larger reduced frequencies. The heat release fluctuations are not negligible in these cases, and can produce strong acoustic-combustion interactions. Further data (see [36]) with PIV indicate that the velocity in the fresh gases is not uniform and that a radial flow exists near the exhaust. An improved model should take these features into account.

IV.3 Large eddy simulations of reacting flows

C. Nottin[*], R. Knikker, M. Boger, D. Veynante [39]

Centre de Recherche sur la Combustion Turbulente
Laboratoire E.M2.C.
E.C.P. and C.N.R.S., Chatenay-Malabry, France
[*] Aerospatiale-Matra Missiles, Chatillon, France

IV.3.1 Abstract

Large eddy simulation (LES) is a promising tool for numerical simulations of reacting flows, especially when combustion instabilities are encountered. In a first step towards prediction of such instabilities, LES of acoustically excited turbulent premixed flames is performed using a thickened flame approach, coupled to a subgrid scale model. Numerical results are carefully compared to experimental data obtained using planar laser induced fluorescence on the OH radical. Flame surface densities, wrinkling factors and reaction rates are extracted from images under a flamelet assumption. The large coherent motions observed in experiments are also found in simulations but the subgrid scale model is not able to recover the right locations of

maximum values of reaction rates. In fact, the subgrid scale model, implicitly based on the vorticity field, increases reaction rates in highly stretched regions whereas, according to experimental data, larger values of unresolved flame surfaces correspond to highly curved flame front regions. Therefore, a dynamic approach, where unresolved flame surfaces could be estimated from resolved flame front curvatures, appears as a promising next step.

IV.3.2 Introduction

Large eddy simulation (LES), where largest motions are explicitely computed, appears as a promising tool for numerical simulations of turbulent reacting flows [67] because they generally exhibit large scale coherent structures [68], especially when combustion instabilities occur [69]. Such instabilities, due to a coupling between heat release, hydrodynamic flow field and acoustic waves have to be avoided because they induce noise, variations of the system characteristics, large heat transfers and may lead to the system destruction. Then, LES could be a powerful tool to predict their occurences and to numerically test passive or active control techniques. Large eddy simulations also allow a better description of turbulence / combustion interactions than classical closures of the Reynolds averaged Navier-Stokes equations (RANS) because, in LES, large structures are explicitly determined and instantaneous fresh and burnt gases zones, where turbulence characteristics are quite different, are clearly identified.

In large eddy simulations, any quantity Q is filtered in the spectral space (components greater than a given spatial cut-off frequency are suppressed) or in the physical space (weighted averages over a given volume). The filtered quantity $\overline{Q}$ is defined as:

$$\overline{Q}(\mathbf{x}) = \int Q(\mathbf{x}') \, \mathcal{G}(\mathbf{x} - \mathbf{x}') \, d\mathbf{x}' \tag{IV.40}$$

where $\mathcal{G}$ is the LES filter. For non constant density flows, a Favre (mass-weighted) filter $\widetilde{Q}$ is introduced as $\overline{\rho}\widetilde{Q} = \overline{\rho Q}$. Applying this filter to the instantaneous fuel mass fraction balance equation:

$$\frac{\partial \rho Y_F}{\partial t} + \nabla \cdot (\rho \, \mathbf{u} \, Y_F) = \nabla \cdot (\rho \, D \, \nabla Y_F) + \dot{\omega}_F = \rho w_F |\nabla Y_F| \tag{IV.41}$$

leads to:

$$\frac{\partial \overline{\rho} \widetilde{Y}_F}{\partial t} + \nabla \cdot \left(\overline{\rho} \, \widetilde{\mathbf{u}} \, \widetilde{Y}_F \right) + \nabla \cdot \left[\overline{\rho} \left(\widetilde{\mathbf{u} Y}_F - \widetilde{\mathbf{u}} \widetilde{Y}_F \right) \right] = \nabla \cdot \left(\overline{\rho \, D \, \nabla Y_F} \right) + \overline{\omega}_F = \overline{\rho w_F |\nabla Y_F|} \tag{IV.42}$$

where D is the molecular diffusivity, using the Fick law, $\dot{\omega}_F$ the instantaneous reaction rate of fuel and w_F the displacement speed of Y_F-isosurfaces. Three unknown terms require modeling: the unresolved transport $\widetilde{\mathbf{u} Y}_F - \widetilde{\mathbf{u}} \widetilde{Y}_F$, the filtered molecular diffusion flux, $\overline{\rho \, D \, \nabla Y_F}$, and the filtered reaction rate, $\overline{\omega}_F$. These two last terms may be modeled together as a filtered flame front displacement term, $\overline{\rho w_F |\nabla Y_F|}$ [70].

A difficult problem is encountered for large eddy simulations of premixed flames: the flame thickness δ_l^0, about 0.1 to 1 mm, is generally smaller than the LES mesh size $\bar{\Delta}$ [67]. Therefore, species mass fractions and temperature are very stiff variables and cannot be resolved on the computational grid. Three main approaches have been proposed to overcome

this difficulty: simulation of an artificially thickened flame [71,72,51,73], flame front tracking technique [74,47,75] (G-equation) or using a filter larger than the computational mesh size [70].

The objective of this paper is to investigate the ability of the thickened flame model to describe combustion instabilities. A first preliminary step is to predict the response of a turbulent flame to acoustic excitations. In fact, actual instabilities involve an additive feature, not investigated here: the feedback action of the unsteady heat release to drive the acoustic excitation. Nevertheless, numerical simulations of flame responses to acoustic excitations are of interest to predict flame transfer functions, an important ingredient in simplified models, such as the so-called $n - \tau$ approach, for combustion instabilities [76]. In the following, large eddy simulations of a premixed turbulent flame submitted to acoustic excitations are performed and compared to experimental data.

IV.3.3   Theoretical analysis

Thickened flame model

The basic idea of the thickened flame model (TFM) is to artificially increase the flame thickness, keeping constant the laminar flame speed s_l^0 [71]. Following simple theories for 1D laminar premixed flames [5,26], the flame speed s_l^0 and the flame thickness δ_l^0 may be estimated as:

$$s_l^0 \propto \sqrt{D\overline{W}} \qquad ; \qquad \delta_l^0 \propto \frac{D}{s_l^0} \tag{IV.43}$$

where $\overline{W}$ is the mean reaction rate. Then, an increase of the flame thickness δ_l^0 by a factor F with a constant flame speed s_l^0 is easily achieved by multiplying thermal and molecular diffusivities by F and replacing the reaction rate $\overline{W}$ by $\overline{W}/F$. For sufficiently large values of F, the thickened flame front is resolved on the LES computational mesh. The reaction rate remains expressed using an Arrhenius law, as in direct numerical simulations.

Unfortunately, when the flame is thickened from δ_l^0 to $\delta_l^1 = F\delta_l^0$, the turbulence / chemistry interaction is modified because the Damköhler number, Da, comparing turbulent (τ_t) and chemical (τ_c) time scales:

$$Da = \frac{\tau_t}{\tau_c} = \frac{l_t}{u'}\frac{s_l^0}{\delta_l^0} \tag{IV.44}$$

decreases by a factor F and becomes Da/F. As shown in [77], the flame becomes more and more insensitive to turbulence motions when the length scale ratio between the turbulence integral length scale and the laminar flame thickness, l_t/δ_l^0, is decreased. This ratio is decreased by a factor F when the flame is thickened. On the other hand, the thickened flame is more sensitive to strain than the actual flame [51]. These points have been investigated using direct numerical simulations (DNS) [51,73] and an efficiency function, acting as a subgrid scale model, has been proposed to incorporate the effects of the unresolved wrinkled flame area on the resolved consumption speed. This efficiency function E is estimated as the ratio of the wrinkling factor (i.e. the ratio of the subgrid scale surface to its projection in the propagating direction) for the

actual flame, $\Xi\left(\delta_l^0\right)$, to the wrinkling factor of the thickened flame, $\Xi\left(F\delta_l^0\right)$:

$$
E = \frac{\Xi\left(\delta_l^0\right)}{\Xi\left(\delta_l^1\right)} = \frac{1 + \alpha\Gamma\left(\frac{\Delta_e}{\delta_l^0}, \frac{u'_{\Delta_e}}{s_l^0}\right)\frac{u'_{\Delta_e}}{s_l^0}}{1 + \alpha\Gamma\left(\frac{\Delta_e}{\delta_l^1}, \frac{u'_{\Delta_e}}{s_l^0}\right)\frac{u'_{\Delta_e}}{s_l^0}}
\tag{IV.45}
$$

where Δ_e is the LES filter size. The Γ function is fitted from DNS:

$$
\Gamma\left(\frac{\Delta_e}{\delta_l^1}, \frac{u'_{\Delta_e}}{s_l^0}\right) = 0.75 \exp\left[-\frac{1.2}{\left(u'_{\Delta_e}/s_l^0\right)^{0.3}}\right]\left(\frac{\Delta_e}{\delta_l^1}\right)^{\frac{2}{3}}
\tag{IV.46}
$$

where u'_{Δ_e} denotes the subgrid scale velocity fluctuations. α is derived from dimensional arguments as [73]:

$$
\alpha = \beta\frac{2\ln(2)}{3c_{ms}\left[Re^{1/2} - 1\right]}
\tag{IV.47}
$$

In our simulations, $\beta = 1$ and $c_{ms} = 0.28$ [73]. The turbulent Reynolds number, Re, depends on spatial location and is roughly estimated from the subgrid scale velocity, u'_{Δ_e} and the filter size Δ_e.

Then, the thickened flame model is implemented as:

$$
\frac{\partial\overline{\rho}\widetilde{Y}_F}{\partial t} + \nabla\cdot\left(\overline{\rho}\,\widetilde{\mathbf{u}}\,\widetilde{Y}_F\right) = \nabla\cdot\left(\overline{\rho}\,D\,F\,E\,\nabla\widetilde{Y}_F\right) + \frac{E}{F}\dot{\omega}_F
\tag{IV.48}
$$

where $\dot{\omega}_F$ is determined from an Arrhenius law using filtered quantities, such as density, $\overline{\rho}$, species mass fractions, $\widetilde{Y}_i$, and temperature, $\widetilde{T}$. In the above equation, the diffusivity $E\,D$, before multiplication by F to thicken the flame front, may be decomposed as $E\,D = D + (E - 1)\,D$ and corresponds to the sum of the molecular diffusivity, D, and a turbulent subgrid scale diffusivity, $(E - 1)\,D$, depending on turbulence and flame characteristics. In fact, $(E - 1)\,D$ could be viewed as a turbulent diffusivity used to close the unresolved scalar transport in Eq. (IV.42). Eq. (IV.48) achieves the same goal as a G-equation and propagates a flame front at a subgrid turbulent flame speed Es_l^0, keeping the flame brush thickness under control and about $F\delta_l^0$. As the chemistry is still described using an Arrhenius law, the thickened flame model directly handles flame stabilization mechanisms (but the correct prediction remains to be checked).

Estimate of the subgrid scale turbulence

The subgrid scale efficiency function E used in the thickened flame model requires the estimate of the flame front wrinkling factor based on the subgrid scale turbulent velocity, u'_{Δ_e} (Eq. IV.45). This point is discussed in detail in [73] and is briefly summarized here. u'_{Δ_e} could be estimated from the subgrid scale viscosity, ν_t, provided, for example, by the Smagorinsky model:

$$
u'_{\Delta_e} = \frac{\nu_t}{C_s\Delta_e} = C_s\Delta_e\sqrt{2\bar{S}_{ij}\bar{S}_{ij}}
\tag{IV.49}
$$

where $\bar{S}_{ij}$ is the resolved stress tensor and C_s a model constant. This approach has two main drawbacks. First, subgrid scale viscosity models have been designed to predict the right level of

turbulent kinetic dissipation rates and not to estimate velocity fluctuations at any scale. Without turbulence, expression (IV.49) does not provide $u'_{\Delta_e} = 0$ because $\bar{S}_{ij}$ is influenced by the thermal expansion due to heat release.

Assuming scale similarities (i.e. that subgrid scale phenomena are mainly controled by the largest unresolved motions, close to the smallest resolved ones [78]), Colin *et al.*[73] propose to estimate the subgrid scale velocity fluctuation as:

$$\mathbf{u}'_{\Delta_e} = c_2 \, \bar{\Delta}_e^{\,3} \, \nabla^2 (\nabla \times \bar{\mathbf{u}}) \tag{IV.50}$$

where, in our simulations, $c_2 = 2$. This expression, based on the vorticity field, is not sensitive to thermal expansion.

IV.3.4   Experimental set-up and diagnostics

The experimental set-up is displayed in Fig. IV.6. A premixed propane/air flow is injected into a rectangular combustor. The height, depth and length of the combustion chamber are respectively 50, 80 and 300 mm. The lateral walls are transparent artificial quartz windows allowing visualization of the whole chamber. The upper and lower walls are made of thick ceramic material including two narrow windows used to introduce laser sheets. A triangular flame-holder, corresponding to a 50 % blockage ratio, is embedded in the lateral windows. A V-shape flame is investigated at a fixed air flow rate of 40 g/s, corresponding to an upstream mean velocity of about 10 m/s (turbulence level about 5 %) and an equivalence ratio $\phi = 1.0$. The flow field is acoustically excited using two loudspeakers plugged in the inlet duct. The excitation frequency and amplitude are respectively 870 Hz and 150 Pa. A microphone located 0.1 m upstream the flame-holder records a phase reference signal to compare numerical simulations and experimental data.

Qualitative OH concentration images are obtained using planar laser induced fluorescence. A Nd:YAG laser, operating at 10 pulses per second with a typical pulse duration of 7 ns, is frequency doubled to pump a dye-laser operating on Rhodamine 590. The dye-laser beam then passes through a frequency doubling crystal and is transformed into a laser sheet (typical pulse energy 12 mJ at wavelength 283 nm). Radical OH concentrations are measured by absorption on the $Q_1(5)$ line in the $A^2\Sigma^+(v' = 0) <= X^2\Pi(v'' = 0)$ band, collecting the broadband radiation around 310 nm with an intensified CCD camera. The images cover up to 12 cm downstream from the flame-holder with a spatial resolution of 0.25 mm/pixel. A typical PLIF image is displayed on Fig. IV.7. The combusting flow exhibits strong symmetrical periodic coherent structures due to the acoustic excitation. The instantaneous flow field is dominated by these large motions and may be, in a first step, assumed to be two-dimensional, at least up to 10 cm downstream from the flame holder as evidenced in cross-section OH images (Fig IV.8). All postprocessing procedures assume two-dimensional flow fields.

The flame front is located using the OH concentration gradients. Assuming a thin flame, PLIF images are binarized to separate fresh gases (progress variable $c = 0$) from burnt gases ($c = 1$). Then, the subgrid scale flame surface density, Σ, and the subgrid scale wrinkling factor, Ξ, are extracted using a gaussian spatial filter. The filter size, $\Delta_e = 3\,mm$, is chosen to recover a resolved flame front having a thickness corresponding to the simulated thickened flame obtained using $F = 10$. According to [70], flame surface quantities are related to the

filtered progress variable $\bar{c}$ as:

$$\Sigma = \Xi|\nabla\bar{c}| = \underbrace{|\nabla\bar{c}|}_{\text{resolved part}} + \underbrace{(\Xi-1)|\nabla\bar{c}|}_{\text{unresolved part}} \tag{IV.51}$$

Under a flamelet assumption, the filtered fuel reaction rate in Eq. (IV.42) is estimated as $\bar{\bar{\omega}}_F = \rho_0 s_l^0 Y_F^0 \Sigma$ where ρ_0 and $Y_F^0 = 0.059$ denote respectively the density and the fuel mass fraction in the fresh gases. $s_l^0 = 0.45\,m/s$ is the laminar flame speed. Experimental results are phase averaged over 20 instantaneous images to ensure statistical stability of subgrid scale quantities.

IV.3.5 Numerical simulations

The thickened flame model, combined with the efficiency function (Eq. IV.45), has been implemented in AVBP, a LES solver, developed at CERFACS on top of a parallel library COUPL produced jointly by CERFACS and Oxford University [79,80], able to handle complex geometries. Subgrid scale turbulent viscosity is modeled using a filtered Smagorinsky model derived from the filtered structure function [81]. As the flow field appears mainly controlled by two dimensional large scale motions, 2D numerical simulations are performed. The computational domain contains 50 000 points (maximum grid size downstream from the flame-holder $\Delta_x = 0.6$ mm), starts 60 cm upstream the flame holder and continues up to 30 cm downstream. Acoustic waves are generated adding a pulsating term in the energy balance equation close to the flow inlet. The oscillation amplitude has been adjusted to recover the experimental pressure signal at the microphone location. The propane / air chemistry is described using a two-species (fuel and oxidizer), single step ICC scheme [82]:

$$\dot{\omega}_F = A\rho^{\alpha_F + \alpha_O} Y_F^{\alpha_F} Y_O^{\alpha_O} \exp\left(-\frac{T_a}{T}\right) \tag{IV.52}$$

where $\alpha_F = 1.0$, $\alpha_O = 0.5$, $A = 1.09\,10^8\,kg^{-0.5}m^{1.5}s^{-1}$ and $T_a = 10064\,K$. The thickening flame factor is $F = 10$.

IV.3.6 Results and discussions

Numerical fields of fuel reaction rate, $E\dot{\omega}_F/F$ (Eq. IV.48), together with the modeled subgrid scale contribution $(E-1)\dot{\omega}_F/F$ are displayed on Fig. IV.9 and IV.10 for phases $2\pi/3$ and $4\pi/3$ relative to the microphone signal. Corresponding experimental results are also shown. Both numerical simulations and experimental data exhibit strong symmetrical resolved coherent structures. For example, the large motion located at about 4 cm downstream observed on experimental visualizations (phase $2\pi/3$; Fig. IV.9c) is clearly apparent at the same location on numerical simulations (Fig. IV.9a). However, some discrepancies between numerical simulations and experimental results are observed. In fact, global statistical comparisons, not displayed here, are very good but LES is designed to describe unsteady phenomena and must be validated using accurate instantaneous fields.

The spatial location of the subgrid scale contribution to the reaction rate in LES (i.e. $(E-1)\dot{\omega}_F/F$) does not exactly correspond to the experimental data ($\rho_u s_l^0 Y_F^0(\Xi-1)|\nabla\bar{c}|$, where Y_F^0 is the fresh gases fuel mass fraction). This point may be analyzed, for example, looking at

the coherent structures located between 3 to 5 cm downstream from the flame holder for phase $2\pi/3$. On experimental data (Fig. IV.9d), the maximum value of the unresolved reaction rate is observed about 4 cm at the head of the vortex where the highly curved instantaneous flame front is not resolved by the filtered flame. In numerical simulations (Fig. IV.9b), the largest values of the unresolved reaction rate is located about 4 cm downstream from the flame-holder but correspond now to stretched regions of the vortices. A rough scheme of this mechanism is displayed on Fig. IV.11. Accordingly, despite the coherent structures are well predicted by LES, large values of the reaction rate are not found at the same locations as in experimental data. This discrepancy would be missed comparing time averaged fields but is of importance for combustion instabilities predictions and explains the phase difference observed between experimental and numerical integrated reaction rates, displayed on Fig. IV.12b. On Fig. IV.12, experimental and numerical reaction rates are integrated over three boxes defined on Fig. IV.6 and plotted as a function of phase to analyze the flame response to the acoustic perturbation. First, reaction rate amplitudes are slightly larger in experiment, but this finding may be due, at least in part, to the flamelet assumption where the actual reaction rate per unit of flame area is estimated as $\rho_u s_l^0$. Without the subgrid scale model (Fig. IV.12a), reaction rate amplitudes remain very low. A larger modulation is observed when using the efficiency function E (Fig. IV.12b), but a phase lag of about 70°, due to the subgrid model (Fig. IV.11), is found with experimental data. Moreover, the modulation amplitude slightly decreases in LES when moving downstream, because of decreasing turbulence fluctuations u'_{Δ_e}, but remains roughly constant in experiment.

The comparison between unresolved reaction rate contributions predicted by our model and estimated from experimental data shows that the subgrid scale sensor used in the efficiency function E (Eq. IV.45), the subgrid scale velocity fluctuation u'_{Δ_e}, is not well suited to our situation. As previously described, u'_{Δ_e} and, therefore, the efficiency function and the unresolved reaction rate are estimated from flow vorticity and detect highly stretched vortex regions. Unfortunately, maximum values of the reaction rates are experimentaly observed where instantaneous flame fronts are highly wrinkled, leading to large unresolved flame surface densities. As these regions correspond also to large values of the resolved flame front curvatures, a dynamic formulation, where high subgrid scale wrinkling factors could be estimated from high resolved flame front curvatures, appears as an attractive approach to be developed in the future.

IV.3.7 Conclusions

Large eddy simulations of an acoustically excited turbulent premixed flames are performed using the thickened flame model combined with a subgrid scale efficiency function. Numerical results are compared to experimental data using OH planar laser induced fluorescence. Flame surface densities, wrinkling factors and reaction rates are extracted from images under a flamelet assumption. The large coherent motions observed in our experiment are well predicted by simulations but careful comparisons show that maximum values of reaction rates, experimentally located in high flame front curvature regions, are numerically predicted in the vortex-stretched regions. This discrepancy is due to the unresolved contribution to the reaction rate, computed here from estimates of the subgrid scale velocity fluctuations, and induces a time lag between experimental and numerical evolution of the reaction rate. A dynamic subgrid scale model, based on resolved flame front curvatures, then appears as a promising next step.

Numerical simulations have been performed on Cray T3E provided by IDRIS (Institut
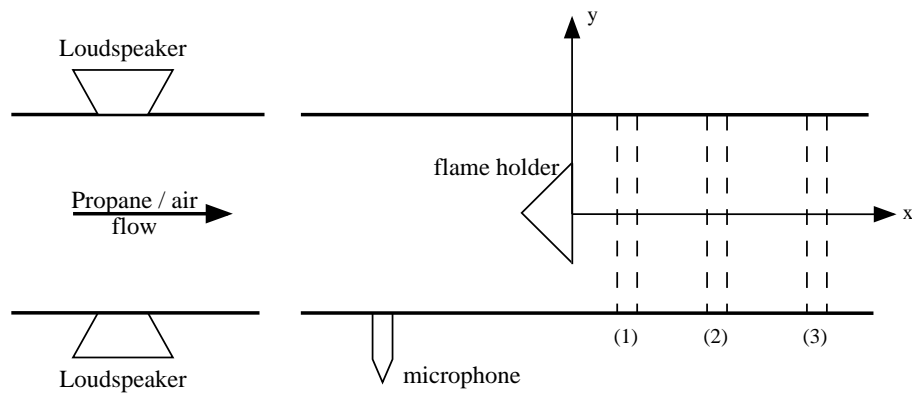
Figure IV.6: Experimental configuration. A premixed propane / air flow (mean velocity 10 m/s; turbulence fluctuations 5 %, equivalence ratio $\phi = 1$) is injected in a rectangular combustor. A turbulent flame is stabilized behind a triangular flame holder (blockage ratio 50 %). The turbulent flame may be submitted to acoustic waves generated by two loudspeakers. A microphone records a reference signal. Signal phases are analyzed integrating the reaction rate over three regions (dashed lines) of 1 cm width, labeled 1, 2, and 3 and located respectively 1, 5 and 9 cm downstream from the flame-holder.
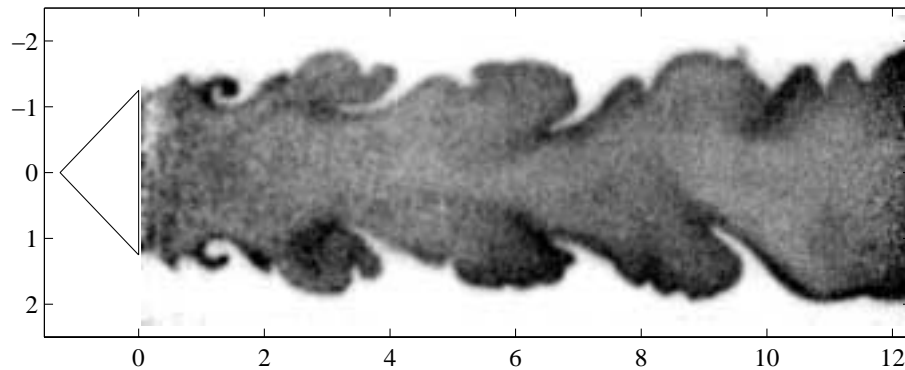
Figure IV.7: Instantaneous PLIF image of the OH radical. The flow field is dominated by strong two dimensional motions controlled by the acoustic excitation at a frequency $f_e = 870$ Hz. The flame front location is determined from OH concentration gradients.

(a)   (b)
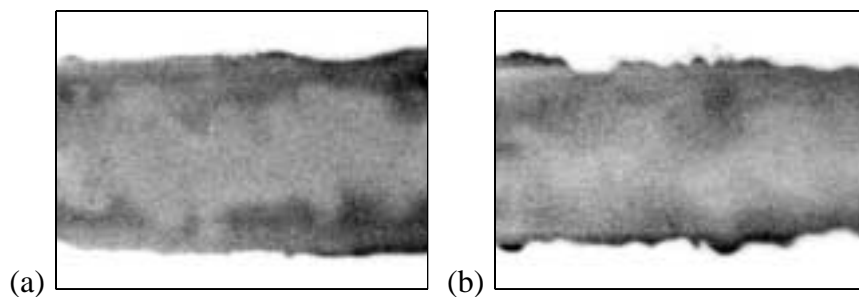
Figure IV.8: Instantaneous cross-section PLIF images of the OH radical. The laser sheet is perpendicular to downstream direction. (a) 4 cm and (b) 8 cm downstream from the flame holder. The flow field may be assumed two-dimensional at least up to 8 cm downstream from the flame-holder.
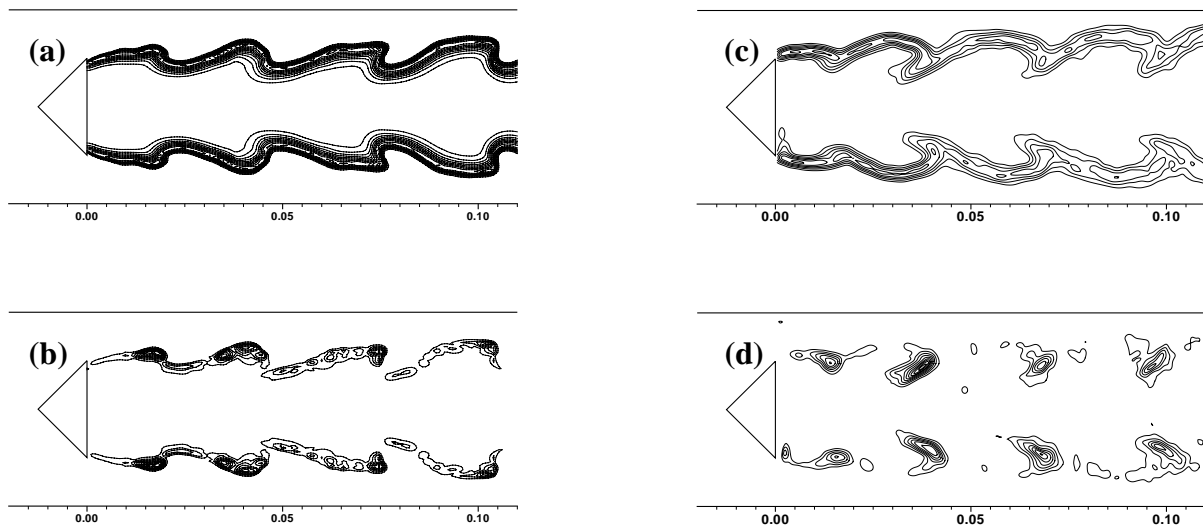
Figure IV.9: Acoustically excited ($f_e = 870 \, Hz$) turbulent premixed flame at phase $2\pi/3$, relatively to the microphone pressure signal. Large eddy simulations fields of the instantaneous reaction rate. (a) total fuel reaction rate, $E\dot{\omega}_F/F$, in Eq. (IV.48). (b) modeled subgrid scale contribution, $(E-1)\dot{\omega}_F/F$. Corresponding experimental data (20 images, corresponding to the same phase, have been averaged to ensure statistical stability of the unresolved contributions): (c) total fuel reaction rate, $\rho_u s_l^0 Y_F^0 \Sigma = \rho_u s_l^0 Y_F^0 \Xi |\nabla \overline{c}|$; (d) unresolved subgrid scale contribution $\rho_u s_l^0 Y_F^0 (\Xi - 1)|\nabla \overline{c}|$.
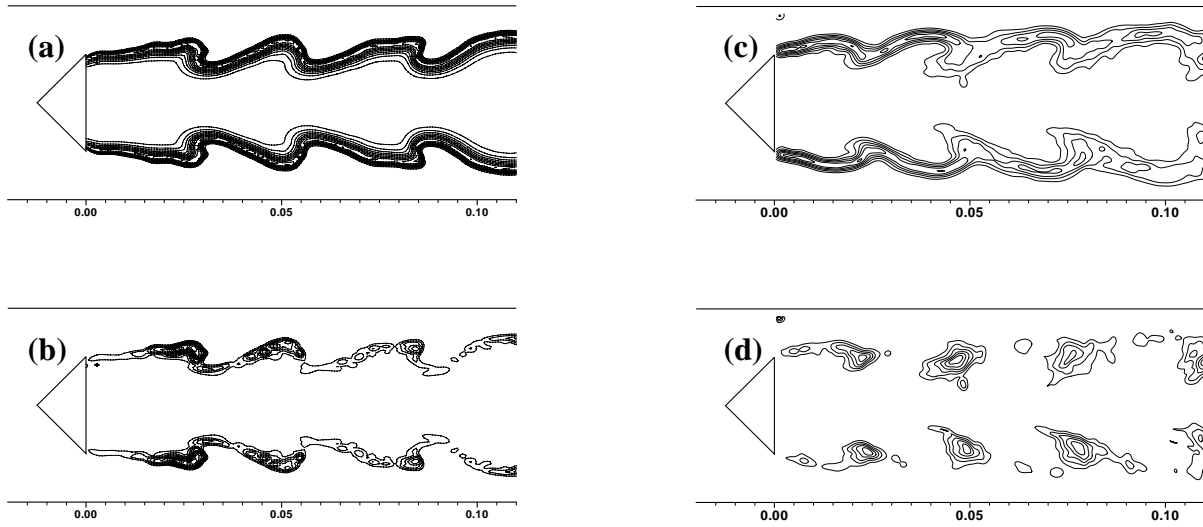
Figure IV.10: Acoustically excited ($f_e = 870\,Hz$) turbulent premixed flame at phase $4\pi/3$, relatively to the microphone pressure signal. Large eddy simulations fields of the instantaneous reaction rate. (a) total fuel reaction rate, $E\dot{\omega}_F/F$, in Eq. (IV.48). (b) modeled subgrid scale contribution, $(E-1)\dot{\omega}_F/F$. Corresponding experimental data (20 images, corresponding to the same phase, have been averaged to ensure statistical stability of the unresolved contributions): (c) total fuel reaction rate, $\rho_u s_l^0 Y_F^0 \Sigma = \rho_u s_l^0 Y_F^0 \Xi |\nabla \overline{c}|$; (d) unresolved subgrid scale contribution $\rho_u s_l^0 Y_F^0 (\Xi - 1)|\nabla \overline{c}|$.
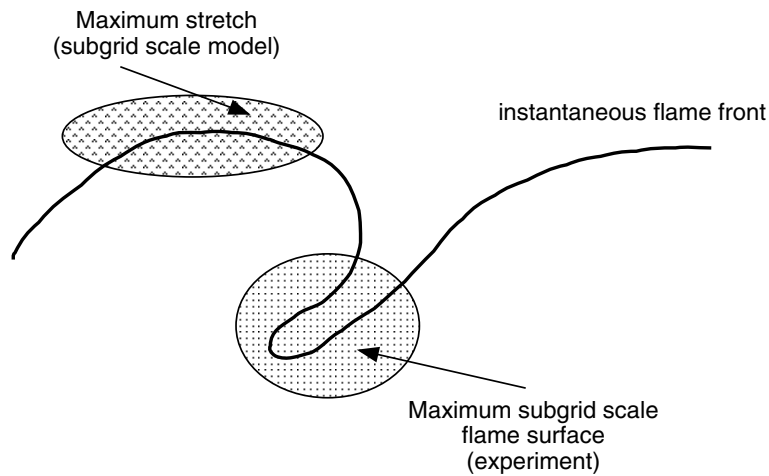
Figure IV.11: A rough scheme comparing regions of maximum values of the unresolved reaction rate in numerical prediction and in experimental data. Maximum contributions of the subgrid scale model are observed in the stretched regions because of the subgrid scale velocity fluctuation detection (Eq. IV.50). Experimental results display maximum values of the wrinkling factor Ξ at the vortice head where highly curved intantaneous flame fronts are not resolved on the filtered flame front.
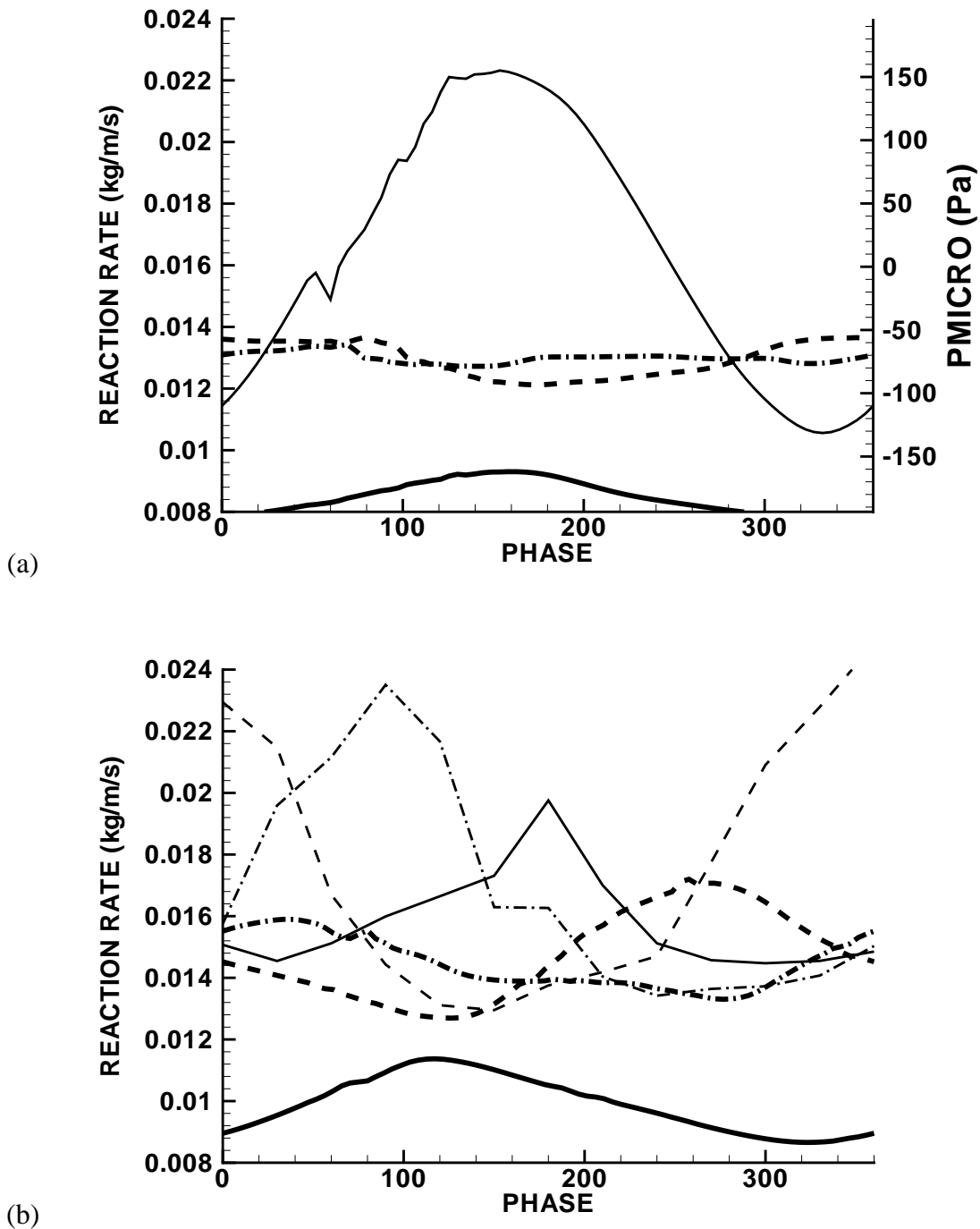
Figure IV.12: Time evolution of experimental and numerical reaction rates integrated over 3 boxes of 1 cm length (see Fig. IV.6), plotted as a function of phase. (a) Without subgrid scale model ($E = 1$): —— reference pressure signal; bold lines correspond to LES respectively for boxes 1 (——), 2 (----) and 3 (—·—). (b) With subgrid scale model. Thin lines correspond to experimental data and bold lines to LES respectively for boxes 1 (——), 2 (----) and 3 (—·—). A constant phase lag, of about 70°, is found between experimental and numerical data and is due to different locations of largest values of the unresolved reaction rate, as explained on Fig. IV.11.

This page has been deliberately left blank

Page intentionnellement blanche

Chapter V

Numerical Simulations of Active Control

M. Mettenleiter[†], F. Vuillot[‡] and S. Candel[†] [103]

[†] Laboratoire E.M2.C.
E.C.P. and C.N.R.S., Chatenay-Malabry, France
[‡] ONERA Châtillon, Châtillon, France

V.1 Abstract

This section describes current developments in the numerical simulation of active control. The objective is to devise software tools for the development of active control. The present approach uses a numerical simulation of the system based on the Navier-Stokes equations. It differs from the more standard simulations relying on lower order dynamical models. The main difficulties associated with the present strategy are related to the representation of the actuator in the flow simulation module and with the interfacing of this module with the adaptive control routine. These issues require careful treatment to obtain a suitable numerical model of flow control. It is first shown that the actuator may be described by a distribution of sources in the field. The time stepping needed by the flow simulation module and by the control unit differ widely (the ratio between the time steps is of the order of 100 or more). This constitutes a source of perturbation and it may introduce unwanted high frequency components in the flow simulation. It is shown that this problem is alleviated by placing numerical filters at the controller input and output. A set of calculations are carried out to simulate vortex shedding instabilities of a simplified solid propellant rocket. These instabilities are then adaptively controlled. This example serves to illustrate the simulation methodology and provides insights into the operation of the flow controller.

V.2 Introduction

Active control strategies have been mainly developed from experiments. Some recent efforts have been directed at simulating control on the computer with the objective of testing and improving control algorithms. Simulation complements experimentation and it has considerable potential in the development of flow control methods. The aim of this section is to adress problems arising when one wishes to couple a flow simulation module and an adaptive control

algorithm. This development is based on research directed at the control of vortex driven insta-
bilities found in solid segmented rocket motors. The control principle is shown schematically in
Figure V.1. The motor develops low amplitude pressure and thrust oscillations at frequencies of
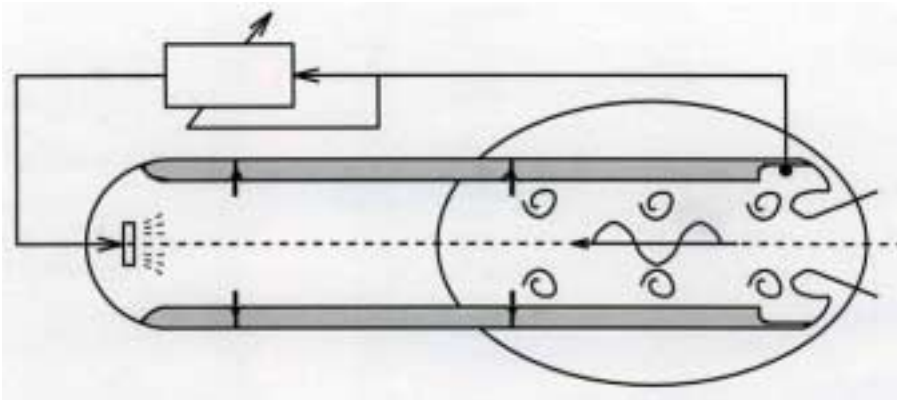
Figure V.1: Active control applied to segmented solid rocket motor.

the first longitudinal acoustic modes (see for example Blomshield and Mathes [83], Vuillot [84],
Dotson, *et al.* [85]). The oscillation is at low frequency and it may couple with the launcher
structural modes. The driving mechanisms have been identified to be linked with internal flow
instability. The strong coupling with acoustics generates large scale coherent vortices. To con-
trol this process, a sensor is placed close to the region where vortices are shed and its signal is
input to a controller which drives an actuator.

This scheme is typical of many active control applications. It is simulated in the present
work by solving the Navier-Stokes equations using the Sierra software. The flow simulation
module has been used extensively to analyze vortex instabilities in configurations of interest
in solid propellant propulsion. It is here used as a platform for active control. Numerical
simulation is now increasingly used to predict the behaviour of unstable subscale solid rocket
motors. A recent example is given by Le Breton, *et al.* [86], which shows industrial applications
of this kind of simulation.

After a short review of the literature dealing with simulation of flow control, the flow
solver is briefly described. One important aspect of the problem is to devise a suitable repre-
sentation of an actuator or of a set of actuators. It is shown that this is best accomplished by
distributing sources in the field. This representation is also closer to the possible use of a con-
trolled injection of an evaporating and/or reacting substance in an actual motor. Such a physical
device would provide a distributed source of mass and a source or sink of energy. Momentum
exchange might also take place depending on the type of injection geometry but is usually less
effective than mass injection.

Modifications of the Sierra code are described. A series of open loop tests not shown
here indicate that the sources operate as expected. Problems related to the coupling of the flow
simulation module with the control algorithm are considered. Specific issues arise because flow
simulation and control require very different time sampling rates. The time step of the flow
solver is much smaller than the sampling period of the controller. It is then necessary to take
some precautions when dealing with the input and output of the control routine. The last part
of this section provides numerical simulations of vortex instabilities in a small rocket motor

and control of these instabilities using an adaptive algorithm. In the situation considered here the controller input is a pressure signal provided by a sensor located near the nozzle while the actuator is located near the motor head. This example serves to show that the active control simulator is flexible and may be used to study the control strategy and examine the modification of the flow under control.

V.3 Active control simulation studies

Active control simulation studies may be divided in two main groups. In the first group physical systems are described by dynamical models coupled to simple or more complex control schemes. A typical example from the field of sound and vibration control is due to Koshigoe, *et al.* [87]. This article considers adaptive algorithms to reduce the noise from a confined cavity. Vibrations originating from outside the cavity walls may induce large pressure fluctuations in the cavity. The problem arises during space launchers take-off, the noise induced under the fairings may harm the payload and have detrimental effects on the future operation of the spacecraft. A dynamical model of the system is formulated and used to test the filtered X-LMS algorithm with off-line identification of the secondary path [88]. On line identification is explored with the same model in a more recent study [89] and the LMS algorithm is compared to other control schemes [90] with regard to the convergence rate.

In the field of combustion instability Hathout, *et al.* [91] developed a dynamical first order model of thermoacoustic interactions in a small laminar burner. This model is then used to design a controller and simulate its operation. The control algorithm is then used in the experiment. To account for changes in the system dynamics an adaptive controller is devised and compared with simulations carried out with an LMS algorithm (Annaswamy, *et al.* [92]). Culick, *et al.* [93] take into account linear and nonlinear coupling in their comprehensive dynamical model of instability. It is thus possible to describe some of the effects which lead to limit cycle oscillations found in practical systems. Yang and Fung [94] use this general formalism to design a PI controller of pressure oscillations in a combustion chamber. Annaswamy, *et al.* [60] study the influence of mode coupling on controller design using the same general formulation. Koshigoe, *et al.* [95] propose an adaptive algorithm with on-line identification to control a dynamical model of combustion instability.

In the second group of studies dealing with simulation of active control , the flow is calculated by solving the Navier-Stokes equations. This provides a more realistic description of the flow dynamics and of the complex couplings taking place in practical devices. This approach uses the recent advances made in computational fluid dynamics. Menon [74] is perhaps the first to investigate active control in an unsteady simulation of a dump combustor typifying the geometry of a 2D ramjet. His controller uses a simple gain and phase applied to a pressure sensor signal and reinjected through a loudspeaker located at the backward facing step. Neumeier and Zinn [96] devise a special observer which identifies the unstable modes of the system. The modes are then amplified and phase delayed by a controller and reinjected into the computational domain. The balance equations are solved in one dimension. Kestens [97] considers the adaptive (LMS) multiple channel control of aeroacoustic instabilities of cavities driven by an adjacent flow. The Navier-Stokes equations are solved in two dimensions. An actuator of the loudspeaker type or a pulsed jet is used to reduce the pressure level observed by different sensors.

Analysis of work belonging to this second group shows that some success has been reached but that the methodology needs further consolidation. Some of the key issues are considered in this section. We specifically consider the coupling of a non-steady Navier-Stokes solver with an adaptive controller. The analysis is carried-out using an adaptive scheme for the following reasons : (i) The system to be controlled is nonlinear and may change with time, (ii) Control using adaptive methods has been successfully demonstrated in related experiments, (iii) The controller has a self adjusting capability which is quite attractive. No attempt was made to test a simpler linear (non adaptive) controller.

Aspects to be considered in the next sections are as follows:

- Numerical representation of the actuator.

- Actuator effect in open loop simulation tests.

- Problems of controller interfacing.

V.4   The flow simulation in the C1-geometry

The Sierra code is used to simulate the large scales of flow in order to analyze aeroacoustic instabilities generated in internal geometries found in solid rocket motors. The code operates in the planar or axisymmetric modes. It was designed by Lupoglazoff and Vuillot [98] (see these references for details on this platform). The Navier-Stokes equations are solved with a second order finite volume centered scheme. Time marching is explicit and uses the MacCormack predictor/corrector method. Artificial viscosity is calculated with the Jameson method (see Jameson and Schmidt [99]). Sierra is used in what follows to simulate the flow in a specific geometry designated as C1 (this is the first test case of a systematic research program on the aerodynamics of segmented solid rocket motors). This computational case was defined by Onera to study the strong aeroacoustic oscillations resulting from vortex shedding from the propellant edge coupled with one of the modes of the system (see Lupoglazoff and Vuillot [100]). This generic case is well documented and requires a limited amount of grid nodes (less than 10000) allowing long computational sequences. Grid independence of the solution was checked by replacing the standard mesh of 318×31 nodes by a finer grid of 454×43 points. The C1 geometry features a marked acoustic resonance which organizes the large scales of the flow. Vortices are shed in the present case from the edge of the propellant grain. The flow in that region is essentially governed by a balance between inertial and pressure forces, this being typical of such solid propellant flows. Under such circumstances, turbulence is of lesser importance and it is not necessary to use a subgrid model. It was also shown by Comte, *et al.* [101]that a full 3D large eddy simulation including a subgrid scale model did not change the overall structure of the unsteady flow. In practice, numerical viscosity acts as a subgrid model and dissipates the smaller scales of turbulence.

In the present simulations the flow is nonreactive but this allows a suitable description of the vortex-acoustic resonance in such a flow geometry. Parameters adopted in the simulations are gathered in Table V.1. Indices i and j specify locations of actuators and sensors with respect to the mesh. Figure V.2 shows their positions in the computational domain. Pressure sensors are placed at the head-end (p_H) and at the nozzle entrance (p_A). An additional sensor is placed just upstream of p_A to measure the local pressure difference ($\Delta p = p_A - p_B$). In detecting Δp,

Parameters	Case 1	Case 2
Number of grid points	318×31	318×31
Pressure sensor p_B (i, j)	(210,1)	(210,1)
Pressure sensor (error signal) p_A (i, j)	(245,1)	
Forward plane pressure sensor p_H (i, j)	(1,30)	(1,30)
x-velocity sensor u_E (i, j)	(245,24)	(245,24)
Vorticity sensor (error signal) ω_E (i, j)		(245,24)
Actuator position (i_d, i_f, h)	(1,2,30)	(64,74,5)
Reference length	0.47 m	0.47 m
Reference velocity	1075.3 m s^{-1}	1075.3 ms^{-1}
Integration time step Δt	0.244 μs	0.244 μs
Resonance frequency (close to 2L)	2540 Hz	2540 Hz

Table V.1: Parameters of the C1 computations.

the aim is to filter out the acoustic pressure signal. The pressure difference is then proportional to the hydrodynamic pressure gradient. The filtering is based on the difference in characteristic length scales between acoustic and hydrodynamic perturbations. Two additional sensors placed at the nozzle entrance detect axial velocity and vorticity fluctuations u_E and ω_E.

The actuators will be defined as a distribution of sources on the computational mesh. As explained previously these sources correspond to mass addition. The actuator location is specified by the first and last values (i_d and i_f) of index i corresponding to the source and by the transverse size of the source specified in terms of elementary cells by index h (see Table 1). The actuator source locations are shown in Figure V.2.

The computational domain is represented in Figure V.2. The lower boundary 1 delivers a uniform stream of gases and represents the solid propellant surface. The mass flow rate per unit surface is imposed at this boundary, the gas temperature is prescribed and the tangential velocity component is zero at this limit. The boundary 2 represents the motor front head, the velocity vanishes on this boundary and the temperature is imposed. The line 3 is a symmetry plane. The outflow in section 4 is supersonic so that numerical boundary conditions in this section are treated by simple extrapolation from the computational domain. At the wall 5 the flow velocity vanishes and the temperature is imposed.

In a first attempt at controlling the instabilities observed in the C1 case the actuator was simulated by a modified front end boundary condition. Perturbations were imposed on the incoming characteristic lines while outgoing waves were allowed to propagate out of the domain without reflection. Systematic tests carried-out in this situation indicated that the simulated flowfield did not respond adequately to the imposed fluctuations. For a given modulation frequency differing from that of the instability and for a small level of perturbation, one expects to find a superposition of acoustic waves in the system and a beating between these two waves if the frequencies are close. If that were the case it would have been possible to act on the signal delivered by the pressure sensor to control the vortex shedding. Calculations however indicated that beating was only produced at the beginning of the simulation and that vortices were very rapidly synchronized by the excitation signal introduced by the actuator. Closed loop control could not be achieved under these circumstances. This behavior was due to the modified bound-
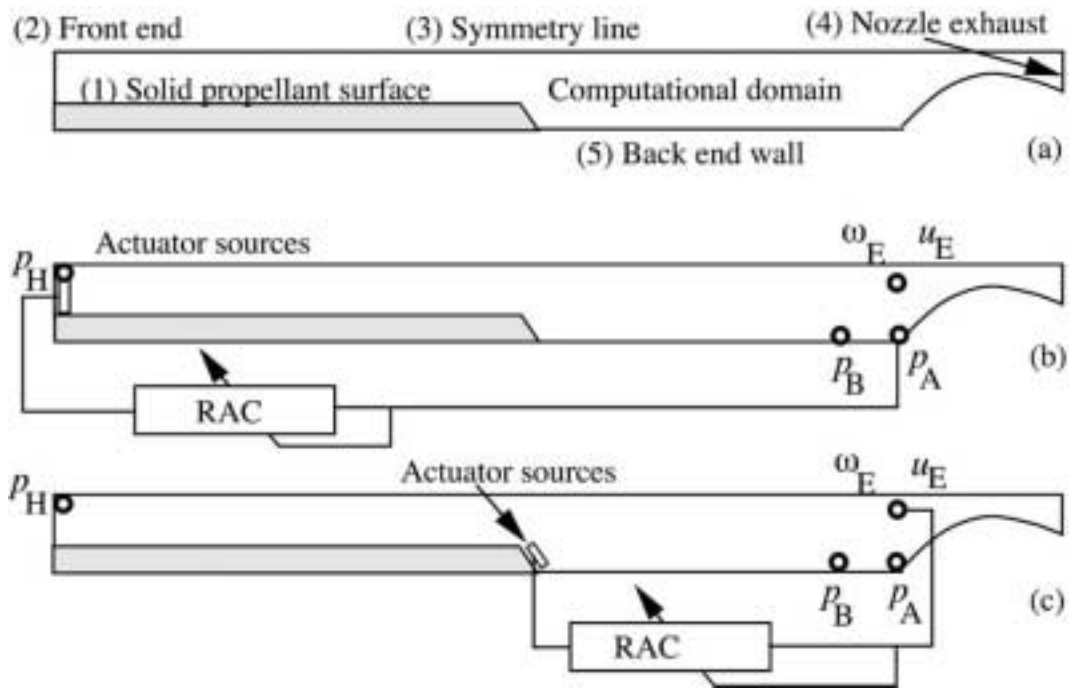
Figure V.2: The C1 geometry. (a) Definition of computational domain, (b) Locations of actuator sources and sensors for case 1, (c) Locations of actuator sources and sensors for case 2.

ary condition used to represent the actuator. Because the boundary did not reflect the incident waves the resonant properties of the system were changed and the vortex shedding phenomenon was altered.

It was then decided to use an alternative method to model the actuator. The boundary conditions were left untouched but source terms were distributed in the field. A somewhat similar approach was devised independently by Mohanraj, *et al.* [102] who use sources in a one dimensional version of Euler's equations. Without describing the details of the Sierra code, we only summarize the steps required to incorporate source terms in the balance equations.

- In the first step one has to specify the number, location and type of source. This is done in a "driver" module which is read at the simulation beginning. This driver also contains information on the sensors used in the control scheme.

- During the calculation and at each time step the sources and sensors are updated.

- After each step the sources are added to the right hand side of the discretized balance equations.

If $\dot{\omega}_s$ designates the volumetric rate of mass addition, the discretized balance of mass, momen-

tum and energy are modified as follows :

$$\rho_c^{n+1} = \rho^{n+1} + \delta t \dot{\omega}_s^n \tag{V.1}$$

$$(\rho u)_c^{n+1} = (\rho u)^{n+1} + (\delta t \dot{\omega}_s^n) u_s^n \tag{V.2}$$

$$(\rho v)_c^{n+1} = (\rho v)^{n+1} + (\delta t \dot{\omega}_s^n) v_s^n \tag{V.3}$$

$$(\rho E)_c^{n+1} = (\rho E)^{n+1} + (\delta t \dot{\omega}_s^n)(e_s + k_s)^n \tag{V.4}$$

The superscript n corresponds to time discretization while subscript c designates the controlled variables. Velocity components u_s, v_s and the internal energy of the injected stream e_s may be freely specified. The kinetic energy k_s is a function of u_s and v_s. In the present calculations the value adopted for the internal energy e_s is that of the surrounding fluid. In order to focus on mass addition effects, the velocities u_s, v_s and the corresponding kinetic energy k_s are set equal to zero. The rate of mass addition $\dot{\omega}_s$ may be defined in various ways. In open loop tests this term is explicitly defined by one of the following expressions :

$$\dot{\omega}_s = a \tag{V.5}$$

$$\dot{\omega}_s = b \sin[2\pi f(t - t_0) + \phi] \tag{V.6}$$

$$\dot{\omega}_s = c\,S(t, t_1, t_2; f_1, f_2) \tag{V.7}$$

where a, b, c are constants, f is a given frequency, t_0 is a time origin, and the function S defines a sinewave with a frequency sweep from f_1 to f_2 begining at time t_1 and ending at t_2. It is thus possible to simulate a constant injection of mass ($a \neq 0$), a sinusoidal modulation ($b \neq 0$) or a linear frequency modulated sinusoide ($c \neq 0$). The mass injection term $\dot{\omega}_s$ may also follow the controller output designated in what follows as "RAC" : $\dot{\omega}_s = \mathrm{rac}(t)$.

In this application the adaptive controller RAC is fed by one of the sensors defined in Figure V.2. Tests of the source terms were carried out systematically to verify the proper operation of the concept [103,105].In the first test series the sources are placed in a constant section duct with closed/open left and right sections filled with fluid. The sources are shown to excite the expected duct mode distributions.

A second test series [105] was aimed at analyzing the response of the vortex driven flow in the C1 configuration under an external excitation. Parameters were those of case 1 in Table V.1. The calculation begins with an established oscillation in the flow. Effects of different levels of source excitation were considered. When the excitation amplitude is augmented two frequencies are detected, a further increase in amplitude leads to a decrease of the instability frequency level. Analysis of other sensor signals confirm this behaviour (for more detailed information, see [103,105]).

These test series indicates that the C1 configuration responds to the new source terms placed in the field. The following points are noticeable:

- The instability phenomenon coexists with the frequency delivered by the actuator when the level of excitation is low.

- The frequency shifts towards the excitation frequency when the level of modulation is larger.

- The vortex shedding process is reorganized when the excitation frequency is very large.

Before describing closed loop calculations we now consider the control algorithm and examine issues related to interfacing.

V.5 Interfacing control algorithm and flow simulation module

The interface between the flow simulation module Sierra and the subroutine RAC which corresponds to the adaptive controller is designed to come as close as possible to a typical experimental configuration. The Sierra code is then used as a black box providing signals detected by different sensors and receiving the signal driving the actuator. The integration step in the simulations is of $\Delta t = 2.44 \ 10^{-7}$ s, which corresponds to a sampling frequency $f_{\text{sierra}} = 4.096 \ 10^6$ Hz. Results are recorded periodically every $d_w = 25\Delta t$. The writing frequency is $f_{\text{write}} = 1.64 \ 10^5$ Hz. It is not necessary and not recommendable to use the adaptive filter at these very high rates. Such frequencies would require very long filters (with more than a few hundred coefficients) in order to represent the system with sufficient precision. The filter renewal should be effected at a much lower rate, typically at a frequency $f_{\text{rac}} = 20.48$ Hz. This value corresponds to the Sierra frequency divided by a factor $d_s = 200$.

To link a typical flow experiment featuring an analog sensor to the discrete control algorithm one uses an anti-aliasing filter (AAF). The same precaution seems necessary in connecting the flow simulation module Sierra to the control routine RAC. The sampling rate reduction by a large factor $d_s = 200$ induces a loss of information and may lead to problems of spectral overlap as those found when analog signals are sampled into discrete sequences. This justifies filtering of the controller input with an AAF as shown in Figure V.3. The flow simulation module Sierra yields an input to the controller RAC at each integration step. One may then choose to keep each d_s value provided by Sierra or one may first low pass filter the values generated by Sierra and then keep the result every d_s sample.
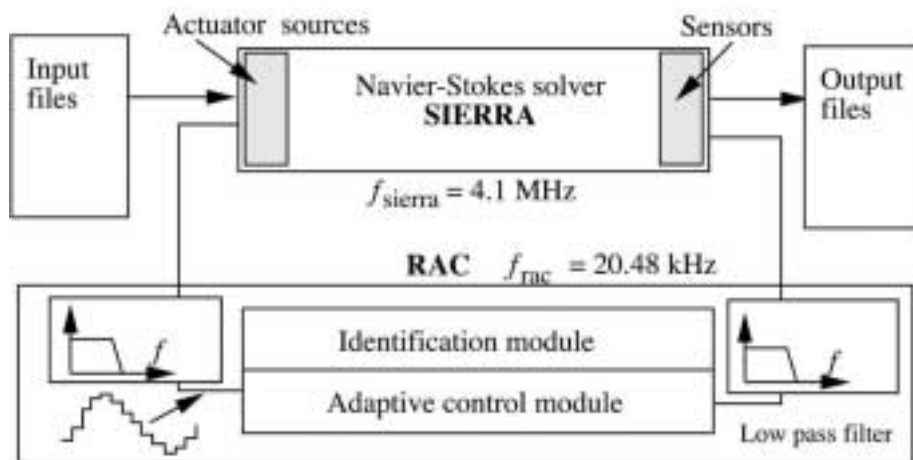
Figure V.3: Block diagram of the Sierra interface with the adaptive controller RAC.

A similar situation prevails at the controller output. One possibility is to use a "sample and hold" which keeps a constant value of the RAC output during the following d_s integration

steps of Sierra. Or one may low pass filter the output in order to eliminate the high frequencies introduced by the successive jumps in the sampled and blocked values returned by the controller (see Figure V.3).

The effects of filtering may be examined with the following tests. In a first trivial case (which is not shown here) $d_w = d_s = 25$. This means that the sensor values are written at the same frequency by Sierra as they are updated and written by RAC. Hence, the sensor and actuator signals measured by RAC and Sierra are identical. In the second test case the sampling rates differ : $d_w = 25$ and $d_s = 200$. These values are adopted later on in the simulations with control. The corresponding results are now displayed in Figure V.4 (upper figure: actuator signal generated by RAC; second figure: pressure sensor measured by RAC; third figure: actuator signal measured by Sierra; bottom figure: pressure sensor measured by Sierra). The actuator signal measured by Sierra clearly shows the discretisation effect. In this case, Sierra receives a discretized sinusoid (third curve from the top). It is worth underlining that this is not a quantization error but is the consequence of the sample and hold operation of the controller output. Although this would have no effect on the controller performance it generates high frequency components as seen in the signal detected by the pressure sensor which features high frequency oscillations (lower left plot in Figure V.4). These oscillations were not observed in the previous test. The high frequencies introduced by the sampled signal feeding the actuator interfere with the calculation. When the controller input is formed by the samples without filtering (second plot from the top), high frequency components are present. This perturbs the controller and the initial frequency is less visible.

Using the same downsampling as in the previous test ($d_w = 25$ and $d_s = 200$) but including a low pass filter at the controller input and output one obtains the results shown in Figure V.5. The actuator signal seen by the Sierra sensor is smooth. The high frequency components in the pressure sensor signal are essentially suppressed. The controller input is noise free but a phase is introduced by the filter.

V.6 Active control simulation results

An instability control algorithm (NSC) described in Mettenleiter, *et al.* [104] is used in the simulations presented in this section. It is based on a Least Mean Square (LMS) method. To control the C1 flow it is first necessary to identify the system seen by the controller. This is designated as the "secondary path" which combines the chamber dynamics and the AAF and LPF transfer functions. With this information the controller filter may be brought to convergence to a steady solution.

V.6.1 Secondary path identification

Off-line identification is used in the context of this simulation to describe the secondary path. As in experiments it is possible to get this information in two regimes of operation :

- Identification may be carried out in the presence of the vortex instability phenomenon.

- Identification may be carried out in the absence of vortex shedding. This is achieved by multiplying the viscosity by a factor which is typically of the order of 20
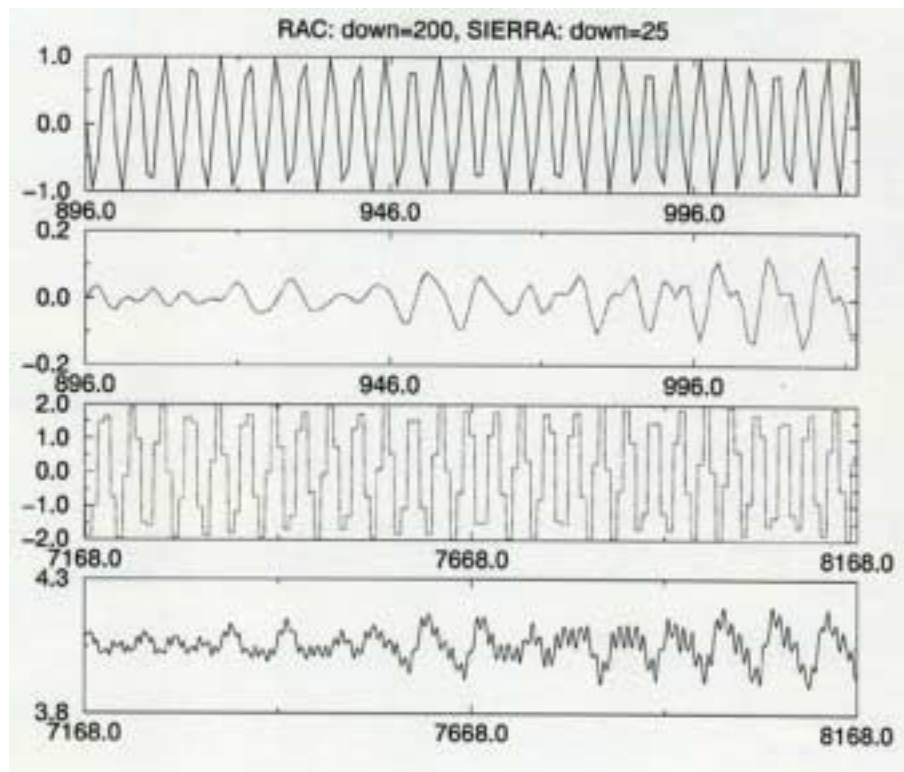
Figure V.4: Actuator and sensor signal records. No filtering of RAC input and output signals. From top to bottom : actuator signal output generated by RAC, pressure signal input to RAC, actuator signal input to Sierra, pressure signal output from Sierra. $d_w = 25$, $d_s = 200$.

During identification, the controller RAC delivers a frequency which varies linearly in time (a siren signal). The signal detected by the pressure sensor (p_A) is recorded by RAC and Matlab is used to calculate an Infinite Impulse Response (IIR) filter comprising 21 coefficients in its numerator and denominator.

The results obtained in the two cases are shown in Ref.[105]. It is found that both filters reproduce the real behavior well. On physical grounds it seems more appropriate to use the identification result obtained in the presence of the vortex shedding process. The corresponding transfer function is used in what follows.

V.6.2   Adaptive control

The control loop is closed when the flow simulation has reached a limit cycle with a well established vortex shedding instability. Figure V.6 shows signal records after the controller is switched on. This event is represented by a vertical line. The error signal (pressure sensor p_A) is shown on the top. A considerable reduction is observed in the beginning but the algorithm does not converge to a steady state. A stationary solution is reached after a transient phase featuring short modulations. The actuator signal shown at the bottom left also features pulsations before converging to a steady state. One also notices that a large amplitude is initially generated to act on the process. This amplitude diminishes later and converges to a lower level when the signal
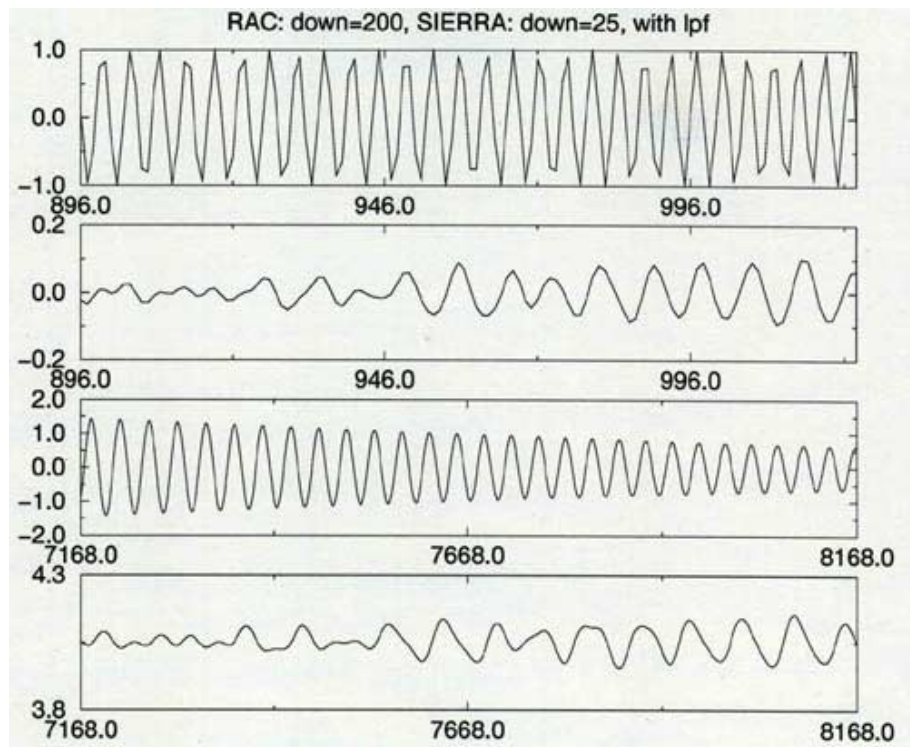
Figure V.5: Actuator and sensor signal records. Low pass filtering, applied to RAC input and output signals. From top to bottom : actuator signal output generated by RAC, pressure signal input to RAC, actuator signal input to Sierra, pressure signal output from Sierra. $d_w = 25$, $d_s = 200$.

becomes stationnary. To check the stability of the controlled state, many cycles were calculated after the stabilized amplitude was reached. Except for a slight increase in controller output, a stable behavior is observed. This behaviour is also noticed in experiments (see Mettenleiter, *et al.* [105]) suggesting that the controller acts on the vortex shedding process which drives the oscillation in the system.

This interpretation is confirmed by the velocity signal u_E not shown here. After an initial phase with modulations the amplitude is stabilized at a lower level. The frequency also changes and the shift during the transition may be at the source of modulations detected by all the sensors. Finally, the pressure sensor p_H placed on the motor front end (not shown) features a notable reduction of amplitude when the controller is on but it is worth recalling that this signal is not used in the control process.

The power spectral densities calculated during steady state operation confirm the controller influence on the instability phenomenon. In the pressure signal p_A without, the component at the instability frequency vanishes completely (> 40 dB) but a new peak appears at a different frequency at a much reduced level (factor of 10). The spectral density of the velocity signal u_E also clearly shows that the oscillation is shifted to a higher frequency. The initial peak has disappeared. The new component reaches a significantly reduced level (by a factor of 3). This peak at 3900 Hz is close to the 3L mode of the C1 configuration which corresponds to the next available mode for acoustic resonance. A similar behaviour can be observed for the
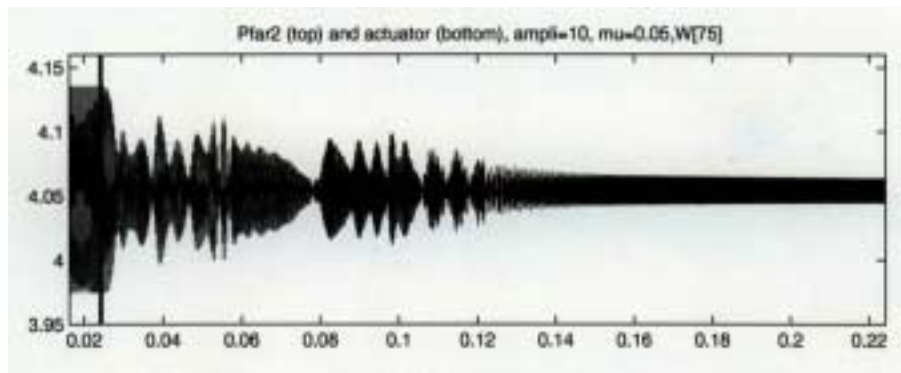
Figure V.6: Control results in case 1. Pressure signal record $p_A(t)$ before and after the controller is switched on (the vertical line indicates control switch on).
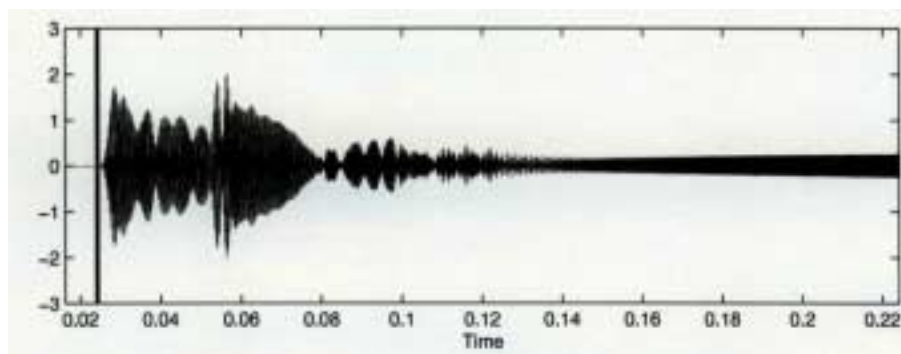
Figure V.7: Control results in case 1. Actuator signal record before and after the controller is switched on (the vertical line indicates control switch on).

pressure signal p_H. The peak at the initial frequency vanishes and the phenomenon is shifted to the higher mode. The overall level is reduced by a factor of 3. These results are not shown here.

The controller does not suppress the vortex shedding but it shifts the phenomenon to another eigenmode. The intensities at this new frequency are nevertheless significantly reduced. The vorticity field before and after control are displayed in FiguresV.8 and V.9 respectively. The no-slip condition imposed on the head end produces a vorticity layer in the first columns of computational cells but this has no consequence for the calculation. The lower image corresponding to the controlled operation shows that coherent vortices are still present but their size and shedding frequency are modified in agreement with observations of the velocity spectral density.

It appears that in the numerical simulation the vortex shedding is more persistent than in the experimental case. This could be explained by the difference in the broad band content of the signals detected in the two situations. Without coupling the acoustic signal is submerged in the broad band noise existing in the experimental facility and it cannot trigger the vortices in a coherent fashion. The shedding takes place more randomly (this is demonstrated in experiments described in Mettenleiter [103]) or it may even be completely suppressed as described by Huang and Weaver [15]. In the numerical simulation, the flow conditions are much "cleaner". There

is no broad band noise which could prevent the synchronization between acoustics and vortex dynamics. The vortices find in all circumstances a phase reference even when the acoustic signal level is strongly reduced. No attempt was made to introduce broad-band noise to simulate more realistic conditions.
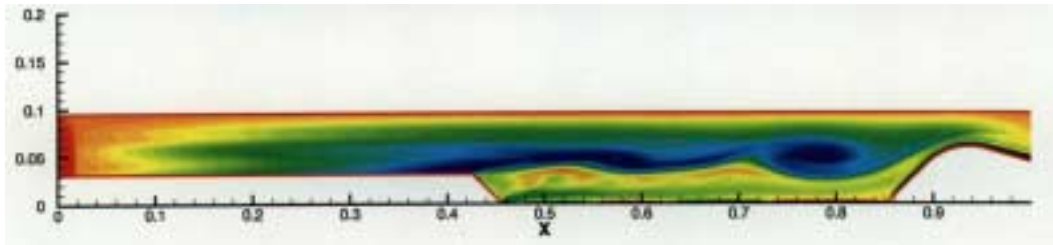
Figure V.8: Vorticity field before control. The controller input is the pressure signal p_A (case 1).
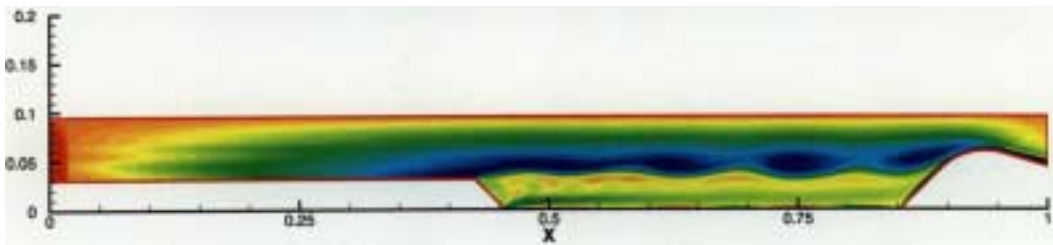
Figure V.9: Vorticity field after control. The controller input is the pressure signal p_A (case 1).

In the case examined, the controller acts on the acoustics and then indirectly through coupling on the vortex shedding. A more efficient reduction of velocity fluctuations could be obtained by acting directly on the shear layer. It is interesting to see if an additional decrease in the signal amplitude could be obtained with a another arrangement in which the actuator is set at the edge of the propellant surface and the sensor provides a vorticity signal (case 2 in Table V.1). This case is treated in Ref.[105]. In general, the same frequency shift can be observed as in case 1. The initial peaks disappear and the oscillation is shifted to the 3L mode, where it reappears with largely reduced levels. It is worth noting that convergence in this second case is smoother perhaps because the controller acts more directly on the instability process.

V.7 Conclusions

The simulation of active control is investigated in this section. A Navier-Stokes solver is coupled to an adaptive control algorithm. It is shown that the actuator may be defined by distributing sources in the computational domain. This method is first used in open loop tests. The coupling of the flow simulation module with the control algorithm is then considered. Because the rates of operation of the flow solver and active control are widely different the signals at the controller input and output must be filtered. It is shown that this eliminates high frequency

components which would otherwise perturb the calculation. The simulation of active control is then developed in a solid rocket motor geometry in which vortex shedding takes place which leads to acoustic resonance of the system. Results obtained demonstrate that control is feasible and that the method may be used to examine the changes in the flow field induced by the controller. However convergence and stability issues related to adaptive control algorithms would need further investigation.

Chapter VI

Conclusion

This set of lectures has focused on modeling and simulation of combustion instability and control studies. After a presentation of some basic results, the paper deals with different facets of the problem. simple time lag models, flame front dynamics, LES simulations of turbulent flames interacting with acoustic waves, simulations of active control.

Dynamical combustion problems are exemplified in laminar and turbulent configurations. The laminar case may be used to understand the mechanism and to validate numerical tools. The modeling of acoustic interactions with external perturbations and turbulent flames is carried out in an LES framework in which the large scale motions are computed while the smaller ones are modeled.

The combination of an unsteady formulation for the large structures with an adapted flame model allows the representation of complex combustion phenomena. Such an approach might be used to study combustion instability mechanisms in combustors. The new approaches together with recent experimental data have enhanced the current understanding of combustion instability. The prediction of instability of turbulent combustors is however not yet achieved and remains a problem for current research.

Under application of the active control system, the stability and extinction domains of a combustor are dramatically altered. The instabilities can be completely suppressed and the instability-related flame extinctions are eliminated. The simulation of active control is investigated in the last section. A Navier-Stokes solver is coupled to an adaptive control algorithm. It is shown that the actuator may be defined by distributing sources in the computational domain. The coupling of the flow solver with the controller algorithm pose problems which must be considered with care. It is in particular important to deal with the mismatch between the timestepping required by the flow solver and that needed by the control algorithm. A full simulation of active control is then developed in the case of a solid rocket motor geometry in which vortex shedding takes place leading to acoustic resonance of the system. Results obtained demonstrate that control is feasible and that the simulation method may be used to examine the changes in the flow field induced by the controller. However convergence and stability issues related to adaptive control algorithms would need further investigation.

This page has been deliberately left blank

Page intentionnellement blanche

Bibliography

[1] E. Mallard and H. Le Châtelier. Recherches experimentales et théoriques sur la combustion de mélanges gazeux explosifs. *Ann. Mines, Paris Series*, 8:274–377, 1883.

[2] L. J. W. S. Rayleigh. The explanation of certain acoustic phenomena. *Nature*, 18:319–321, 1878.

[3] M. Barrère and F.A. Williams. Comparison of combustion instabilities found in various types of combustion chambers. In *Twelfth Symposium (International) on Combustion*, pages 169–181. The Combustion Institute, 1968.

[4] A. A. Putnam. *Combustion Driven Oscillations in Industry*. Elsevier, New York, 1971.

[5] F. A. Williams. *Combustion Theory*. Benjamin Cummings, Menlo, CA ; Reading, MA, 1985.

[6] L. Crocco. Theoretical studies on liquid-propellant rocket instability. In *Tenth Symposium (International) on Combustion*, pages 1101–1128. The Combustion Institute, 1965.

[7] D. J. Harrje and F. H. Reardon. *Liquid Propellant Rocket Instability*, volume SP-194. NASA, 1972.

[8] F. E. C. Culick. Combustion instabilities in liquid-fueled propulsion systems: an overview. In *AGARD Conference on Combustion Instabilities in Liquid-Fueled Propulsion Systems*, 1988.

[9] S. Candel. Combustion instabilities coupled by pressure waves and their active control. In *Twenty-Fourth Symposium (International) on Combustion*, pages 1277–1296. Combustion Institute, 1992.

[10] K. McManus, T. Poinsot, and S. Candel. A review of active control of combustion instabilities. *Prog. Energ. Combust. Sci.*, 19:1–29, 1993.

[11] T. Poinsot. *Analyse des Instabilités de Combustion de Foyers Turbulents Prémélangés*. PhD thesis, Université de Paris-Sud, 1987.

[12] Barrère M. and J. Corbeau. Les instabilités de combustion dans les fusées à propergol liquide. In *Fifth Agard Colloquium, Braunschweig*, 1964.

[13] D. E. Rogers and Marble F. E. A mechanism for high frequency oscillations in ramjet combustors and afterburners. *Jet Propulsion*, 26:456–462, 1956.

[14] P. Clavin, P. Pelcé, and L. He. One-dimensional vibratory instability of planar flames propagating in tubes. *J. Fluid Mech.*, 216:299–322, 1990.

[15] X. Y. Huang and D. S. Weaver. On the active control of shear layer oscillations across a cavity in the presence of pipeline acoustic resonance. *J. Fluids Struct.*, 5:207–219, 1991.

[16] G. Billoud, C. Huynh, M. Galland, and S. Candel. Adaptive active control of combustion instabilities. *Combust. Sci. Tech.*, 81:257, 1992.

[17] S. Ziada. *Flow-Induced Vibration*, chapter Feedback Control of Globally Unstable Flows: Impinping Flows, pages 579–591. A. A. Balkema, Rotterdam, P. W. Bearman edition, 1995.

[18] M. C. Welsh, K. Hourigan, R. J. Alfredson, and P. D. Lin. Active control of flow excited acoustic resonance: Higher order acoustic modes. In *IMech E*, 1991.

[19] H. S. Tsien. Servo-stabilization of combustion in rocket motors. *Rocket society Journal*, 22:256–263, 1952.

[20] F. E. Marble and D. W. Cox. Servo-stabilization of low frequency oscillations in a liquid bipropellant rocket motor. *Journal of the American Rocket Society*, 23:63–74, 1953.

[21] L. Crocco and S. L. Cheng. Theory of combustion instability in liquid propellant rocket motors. *Agardograph, Butterworths Science Publication*, 8, 1956.

[22] S. Candel and T. Poinsot. A tutorial on acoustics. Cours de l'Ecole Centrale Paris, 1988.

[23] S. Kotake. On combustion noise related to chemical reactions. *J. Sound Vib.*, 42:399–410, 1975.

[24] R. H. Cantrell and R. W. Hart. Interaction between sound and flow in acoustic cavities: Mass, momentum and energy considerations. *Jounal of the Acoustical Society of America*, 36:697–706, 1964.

[25] T. Poinsot, C. Le Chatelier, S. Candel, and E. Esposito. Experimental determination of the reflection coefficient of a premixed flame in a duct. *J. Sound Vib.*, 107(2):265–278, 1986.

[26] K.K. Kuo. *Principles of Combustion*. J. Wiley & Sons, 1986.

[27] P.E. Doak. Fundamentals of aerodynamic sound theory and flow duct acoustics. *J. Sound Vib.*, 28(3):527–561, 1973.

[28] A. M. Laverdant, T. Poinsot, and S. Candel. Influence of the mean temperature field on the acoustic mode structure in a dump combustor. *AIAA J.*, 85:1249, 1985.

[29] P. Le Helley. *Etude Théorique et Expérimentale des Instabilités de Combustion et de leur Contrôle dans un Brûleur Laminaire Prémélangé*. PhD thesis, Ecole Centrale Paris, 1994.

[30] L. J. W. S. Rayleigh. *Theory of Sound*. 1945.

[31] T. Poinsot, A. Trouvé, D. Veynante, S. Candel, and E. Esposito. Vortex-driven acoustically coupled combustion instabilities. *J. Fluid Mech.*, 177:265–292, 1987.

[32] G. J. Bloxsidge, A. P. Dowling, N. Hooper, and P. J. Langhorme. Active control of reheat buzz. *AIAA J.*, 26:783, 1988.

[33] J. M. Samaniego, B. Yip, T. Poinsot, and S. Candel. Low frequency combustion instability in a side dump combustor. *Combust. Flame*, 94:363–380, 1993.

[34] L. Crocco. *J. Aeronaut. Res. Soc.*, 21 and 22, 1952.

[35] W. Lang, T. Poinsot, and S. Candel. Active control of combustion instability. *Combust. Flame*, 70:281–289, 1987.

[36] S. Ducruix. *Dynamique des Interactions Acoustique-Combustion*. PhD thesis, Ecole Centrale Paris, 1999.

[37] S. Ducruix, D. Durox, and S. Candel. Theoretical and experimental determinations of the transfer function of a laminar premixed flame. In *Twenty-Eighth Symposium (International) on Combustion*, 2000.

[38] S. Candel, D. Durox, S. Ducruix, and D. Thibaut. Dynamics of flames interacting with pressure waves. In *Paper 98 S-1. Plenary Lecture of the Western States Section of the Combustion Institute*. University of California, Berkeley, 1998.

[39] C. Nottin, R. Knikker, M. Boger, and D. Veynante. Large eddy simulations of an acoustically excited turbulent premixed flame. In *28th Symposium (International) on Combustion*. The Combustion Institute, 2000.

[40] J. O. Keller, L. Vaneveld, D. Korschelt, G. L. Hubbard, A. F. Ghoniem, Daily J. W., and A. K. Oppenheim. Mechanisms of instabilities in turbulent combustion leading to flashback. *AIAA J.*, 20:254–262, 1981.

[41] F. E. Marble and S. Candel. An analytical study of the non-steady behavior of large combustors. In *Seventeenth Symposium (International) on Combustion*, pages 761–769. The Combustion Institute, 1978.

[42] T. Poinsot and S. Candel. A nonlinear model for ducted flame combustion instabilities. *Combust. Sci. Tech.*, 61:121–153, 1988.

[43] M. Fleifil, A.M. Annaswamy, Z.A. Ghoneim, and A.F. Ghoniem. Response of a laminar premixed flame to flow oscillations: a kinematic model and thermoacoustic instability results. *Combust. Flame*, 106:487–510, 1996.

[44] A.P. Dowling. A kinematic model of a ducted flame. *J. Fluid Mech.*, 394:51–72, 1999.

[45] H. N. Najm and A. F. Ghoniem. Modeling pulsating combustion due to flow-flame interactions in vortex stabilized premixed flames. *Combust. Sci. Tech.*, 94:259–278, 1993.

[46] S. Menon and W. Jou. Large-eddy simulations of combustion instability in an axisymmetric ramjet combustor. *Combust. Sci. Tech.*, 75:53–72, 1991.

[47] A.R. Kerstein, W. Ashurst, and F.A. Williams. Field equation for interface propagation in an unsteady homogeneous flow field. *Phys. Rev. A*, 37(7):2728–2731, 1988.

[48] J. Piana, D. Veynante, and S. Candel. Direct numerical simulation analysis of the G-equation in premixed combustion. In *Ercoftac Colloquium on Direct and Large Eddy Simulation*, Grenoble, France, 1996.

[49] T. Butler and P. O'Rourke. A numerical method for two dimensional unsteady reacting flows. In *Sixteenth Symposium (International) on Combustion*, pages 1503–1515. Combustion Institute, 1976.

[50] D. Thibaut and S. Candel. Numerical study of unsteady turbulent premixed combustion: Application to flashback simulation. *Combust. Flame*, 113:53–65, 1998.

[51] C. Angelberger, D. Veynante, F. Egolfopoulos, and T. Poinsot. Large eddy simulation of combustion instabilities in premixed flames. Annual research briefs, Center for Turbulence Research, 1998.

[52] H. J. Merk. An analysis of unstable combustion of premixed gases. In *Sixth Symposium (International) on Combustion*, pages 500–512. The Combustion Institute, 1956.

[53] P.L. Blackshear. Driving standing waves by heat addition. In *Fourth Symposium (International) on Combustion*, pages 553–566. The Combustion Institute, 1953.

[54] G. De Sœte. Etude des flammes vibrantes. Application à la combustion turbulente. *Revue de l'Institut Français du Pétrole et Annales des Combustibles Liquides*, 19:766–785, 1964.

[55] F. Baillot, D. Durox, and R. Prud'Homme. Experimental and theoretical study of a premixed vibrating flame. *Combust. Flame*, 88:149–168, 1992.

[56] R. Becker and R. Günther. The transfer function of premixed turbulent jet flames. In *Thirteenth Symposium (International) on Combustion*, pages 517–526. The Combustion Institute, 1971.

[57] W. Lenz and R. Günther. Influence des flammes sur la production d'auto-oscillations dans les chambres de combustion. *Report VDI, Karlsruhe*, 423:111–118, 1981.

[58] V. W. Goldschmidt, R. G. Leonard, J. F. Riley, G. Wolfbrandt, and P. K. Baade. *ASHRAE Transactions*, 2:466–476, 1978.

[59] Y. Matsui. An experimental study on pyro-acoustic amplification of premixed laminar flames. *Combust. Flame*, 43:199–209, 1981.

[60] A.M. Annaswamy, M. Fleifil, J.P. Hathout, and A.F. Ghoniem. Impact of linear coupling on the design of active controllers for the thermoacoustic instability. *Combust. Sci. Tech.*, 128:131–180, 1997.

[61] G. R. A. Groot, R. Rook, K. R. A. M. Schreel, L. P. H. De Goey, J.H.M. ten Thije Boonkkamp, and M. H. J. Anthonissen. Evaluation of two models for the acoustic response of 2D laminar premixed flames. In *Seventeenth ICDERS*, 1999.

[62] R.B. Price, I.R. Hurle, and T.M. Sugden. Optical studies of the generation of noise in turbulent flames. In *Twelfth Symposium (International) on Combustion*, pages 1093–1102. The Combustion Institute, 1968.

[63] J. O. Keller and K. Saito. Measurements of the combusting flow in a pulse combustor. *Combust. Sci. and Tech.*, 53:137–163, 1987.

[64] A. Bourehla and F. Baillot. Appearance and stability of a laminar conical premixed flame subjected to an acoustic perturbation. *Combust. Flame*, 114:303–318, 1998.

[65] G. Snellink and A. Kiers. In *Proceedings of the Second European Symposium on Combustion*, 1975.

[66] J. D. Antnam, R. G. Leonard, and V. W. Goldschmidt. In *ASME Symposium on Fluid Mechanics of Combustion*. Montreal, 1974.

[67] D. Veynante and T. Poinsot. *New Tools in Turbulence Modeling*, chapter Reynolds-Averaged and Large Eddy Simulation Modeling for Turbulent Combustion. O. Métais and J. Ferziger, Les Editions de Physique, 1997.

[68] C.M. Coats. Coherent structures in combustion. *Progress in Energy and Combustion Science*, 22:427 – 509, 1996.

[69] T. Poinsot. Large eddy simulation of combustion instabilities. In *First Symposium on Turbulent Shear Flow Phenomena*, Santa Barbara, CA (U.S.A.), 1999.

[70] M. Boger, D. Veynante, H. Boughanem, and A. Trouvé. Direct numerical simulation analysis of flame surface density concept for large eddy simulation of turbulent premixed combustion. In *Twenty-seventh Symposium (International) on Combustion*, pages 917 – 925. The Combustion Institute, 1998.

[71] T.D. Butler and P.J. O'Rourke. A numerical method for two-dimensional unsteady reacting flows. In *Sixteenth Symposium (International) on Combustion*, pages 1503 – 1515. The Combustion Institute, 1977.

[72] P. O'Rourke and F. Bracco. Two scaling transformations for the numerical computation of multidimensional unsteady laminar flames. *J. Comput. Phys.*, 33(2):185–203, 1979.

[73] O. Colin, F. Ducros, D. Veynante, and T. Poinsot. A thickened flame model for large eddy simulations of turbulent premixed combustion. *Phys. Fluids*, 12(7):1843–1863, 2000.

[74] S. Menon. Active combustion control in a ramjet using large-eddy simulations. *Combustion Science and Technology*, Vol.84 , 1992, pp. 51-79.

[75] V. Smiljanovski, V. Moser, and R. Klein. A capturing-tracking hybrid scheme for deflagration discontinuities. *Combustion Theory and Modelling*, 1(2):183 – 215, 1997.

[76] L. Crocco. Research on combustion instability in liquid propellant rockedts. In *12th Symposium (International) on Combustion*, pages 85–99, 1969.

[77] T. Poinsot, D. Veynante, and S. Candel. Quenching processes and premixed turbulent combustion diagrams. *J. Fluid Mech.*, 228:561–606, 1991.

[78] J. Bardina, J.H. Ferziger, and W.C. Reynolds. Impoved subgrid scales models for large eddy simulations. In *AIAA 13th Fluid & Plasma Dyn. Conf.*, Snowmass, Colorado, 1980. AIAA Paper 80-1357.

[79] F. Nicoud, F. Ducros, and T. Schönfeld. Towards direct and large eddy simulations of compressible flows in complex geometries. In *5th French-German Workshop*. Munich, 1996.

[80] F. Ducros, F. Nicoud, and T. Schnfeld. Large eddy simulations of compressible flows on hybrid meshes. In *Eleventh Symposium on Turbulent Shear Flows*, Grenoble, France, 1997.

[81] M. Lesieur and O. Métais. New trends in large-eddy simulation of turbulence. *Annu. Rev. Fluid Mech.*, 28:45–82, 1996.

[82] B. Bedat, F. Egolfopoulos, and T. Poinsot. Integrated combustion chemistry (ICC) for direct numerical simulation: Applications to premixed and non-premixed combustion. In *Western States Section Meeting of the Combustion Institute*, WSS/CI 97F-122, Los Angeles, USA, 1997.

[83] F. Blomshield and H. B. Mathes., Pressure oscillations in post-Challenger Space Shuttle redesigned solid rocket motors. *Journal of Propulsion and Power*, Vol.9 , No.2, 1993, pp. 217-221.

[84] F. Vuillot. Vortex shedding in solid rocket motors. *Journal of Propulsion and Power*, No.4, 1995, pp. 626-639.

[85] K.W. Dotson, S. Koshigoe and K.K. Pace. Vortex shedding in a large solid rocket motor without inhibitors at the segment interfaces. *Journal of Propulsion and Power*, Vol.13 , No.2, 1997, pp. 197-206.

[86] P. Le Breton, J.-F. Guéry, F. Vuillot and M. Prevost. Recent advances in the prediction of srm thrust oscillations *Proceedings of the 1st European Colloquium on Launcher Technology* (Toulouse), CNES, 1999.

[87] S. Koshigoe, J.T. Gillis, and E.T. Falangas. A new approach for active control of sound transmission through an elastic plate backed by a rectangular cavity. *Journal of the Acoustical Society of America*, Vol.97 , No.2, 1993, pp. 900-907.

[88] S. Koshigoe, A. Teagle and A. Gordon. A time domain study of active control of sound transmission due to acoustic pulse excitation. *Journal of the Acoustical Society of America*, Vol.97 , No.1, 1995, pp. 313-323.

[89] S. Koshigoe, A. Teagle, C.-H. Tsay, S. Morishita and S. Une. Numerical simulation of active control with on-line system identification of sound transmission through an elastic plate. *Journal of the Acoustical Society of America*, Vol.99 , No. 5, 1996, pp. 2947-2954.

[90] S. Koshigoe, A. Teagle, C.-H. Tsay. A rapidly convergent adaptive controller applied to suppression of random noise transmission. *Journal of Vibration and Acoustics*, Vol.120 , No 1998, pp. 449-454.

[91] J.P. Hathout, A.M. Annaswamy, M. Fleifil and A.F. Ghoniem. A model-based active control design for thermoacoustic instability *Combustion Science and Technology*, Vol.132 ,1998, pp. 99-138.

[92] A.M. Annaswamy, O.M. El Rifai, M. Fleifil, J.P. Hathout and A.F. Ghoniem. A model-based self-tuning controller for thermoacoustic instability. *Combustion Science and Technology*, Vol. 135 , 1998, pp. 213-240.

[93] F.E.C. Culick, W.H. Lin, C.C. Jahnke and J.D. Sterling. Modeling for active control of combustion and thermâlly driven oscillations. *Proceedings of the American control conference* (Boston), 1991.

[94] V. Yang and Y.T. Fung. Active control of nonlinear pressure oscillations in combustion chambers. *Journal of Propulsion and Power*, Vol.8 , No.6, 1992, pp. 1282-1289.

[95] S. Koshigoe, T. Komatsuzaki and V. Yang. Adaptive control of combustion instability with on line system identification. *Journal of Propulsion and Power*, Vol.15 , No.3, 1999, pp. 383-389.

[96] Y. Neumeier and B. Zinn. Active control of combustion instabilities using real time identification of unstable combustor modes. *Proceedings of the IEEE Conference on Control Applications* , 1995. pp. 691-698.

[97] T. Kestens. Etude numérique du contrôle adaptatif multivoies des instabilités aéroacoustiques des cavités. Doctoral thesis, Institut National Polytechnique de Toulouse, 1999.

[98] N. Lupoglazoff and F. Vuillot. Two-dimensional numerical simulation of the stability of solid prropellant solid rocket motor. AIAA Paper 91-0205, Jan. 1991.

[99] A. Jameson and W. Schmidt. Some recent developments in numerical methods for transonic flows. *Computer Methods in Applied Mechanics and Engineering*, Vol.51 , No 1985, pp. 467-493.

[100] N. Lupoglazoff and F. Vuillot. Numerical simulations of vortex shedding phenomenon in 2D test case solid rocket motors. AIAA Paper 92-0776, Jan. 1992.

[101] P. Comte, J.H. Silvestrini and P. Begou. Streamwise vortices in large-eddy simulations of mixing layers. *European Journal of Mechanics B*, Vol.17 , 1998, pp. 615-637.

[102] R. Mohanraj, Y. Neumeier and B.T. Zinn. Characteristic-based treatment of source terms in Euler equations for Roe scheme. *AIAA Journal*, Vol.37 , No.4, 1999, pp. 417-424.

[103] M. Mettenleiter. Contrôle adaptatif des instabilités aéroacoustiques. Doctoral thesis, Ecole Centrale Paris, 2000.

[104] M. Mettenleiter, E. Haile and S. Candel. Adaptive control of aeroacoustic instabilities. *Journal of Sound and Vibration*, Vol.230 , No. 4, 2000, pp. 761-789.

[105] M. Mettenleiter, F. Vuillot and S. Candel. Numerical simulation of active control in unstable rocket motors. *Proceedings of the RTO (AGARD) Symposium on Active Control*, May 2000, Braunschweig, Germany.

This page has been deliberately left blank

Page intentionnellement blanche

Combustion Dynamics: Application of Active Instability Control to Heavy Duty Gas Turbines

J. Hermann, A. Orthmann

IfTA Ingenieurbüro für Thermoakustik GmbH
Industriestr. 33
D-82194 Gröbenzell/Munich, Germany
E-mail: jakob.hermann@ifta.com, armin.orthmann@ifta.com

Summary

Self-excited combustion oscillations constitute an important problem for the development of modern combustion systems. Methods to avoid these oscillations by active instability control (AIC) to provide safe operations for the corresponding combustion system are the subject matter of this paper. In addition to applications of this technology for a land-based gas turbine, basic actuation possibilities, methods of measuring oscillation quantities and requirements to be met by control strategies are described. Following this general section, the installation of AIC systems for gas turbines of the Siemens Vx4.3A family will be explained. This type of turbine features an annular combustion chamber with a total of 24 burners. In order to be able to damp combustion oscillations arising within this type of combustion chamber - appearing as azimuthal modes spreading along the circumference of the combustion chamber - every burner was fitted with a direct drive valve. This type of valve creates mass flow modulations within the pilot gas supply of the burner which are anti-cyclical to the oscillations characterising the heat release rate within the flame, thus extinguishing them. Input signals for the feedback control system are obtained by measuring sound pressures within the combustion chamber indirectly at the burner flanges. Finally, this type of gas turbine was fitted with a 12-channel controller and 12 sensors in order to allow a damping of the azimuthal modes excited around the circumference of its annular combustion chamber. Exploiting the symmetry characterising azimuthal modes, two actuators are driven by every feedback loop. In tests run on various type V94.3A gas turbines delivering up to 267 MW of electric power according to ISO, AIC systems were used to damp successfully a great variety of combustion oscillations for several burner variants and operating points. Thus, it was possible to obtain stable gas turbine operations over their full power ranges. In addition to the high AIC flexibility in damping various oscillation problems at different gas turbine operating points, this technology has proved to provide a high degree of fault tolerance and good long-term characteristics.

Introduction

Primary development aims for all modern combustion systems are minimising pollutant emission values, enhancing efficiency and increasing power density in order to achieve design dimensions as compact as possible. This imposes strict operating limits for efficiency and power density; moreover, in order to achieve low NOx emissions, lean premixed combustion is favoured in most cases. One unwanted side-effect is the appearance of a special form of combustion instability, so-called self-excited combustion oscillations. For low thermal power combustion systems, these instabilities primarily lead to increased noise levels. For combustion systems delivering high heat release rates, such as process gas heaters, or for combustion systems working under pressure, such as gas turbines, the sound pressure generated will reach very high levels. Owing to the large surfaces of such systems, high mechanical loads on the

combustion chamber as well as on upstream and downstream components will arise. Also the thermal load on the chamber walls will rise considerably. Depending on sound pressure amplitudes, components will fail sooner or later; thus, this kind of oscillation must be avoided by all means if those combustion systems are to be operated safely. In view of the high requirements to be met by up-to-date, highly optimised combustion systems and their low degree of flexibility as regards operating parameters, the scope available for avoiding oscillations by modifying burner operation is decreasing all the time. New methods to prevent oscillations will have to be found.

Basically, the possibilities available to prevent self-excited combustion oscillations can be subdivided into passive and active measures. For instance, increasing acoustical attenuation, acoustically detuning systems by design modifications, and operational modifications are considered passive measures.[1-4] By contrast, active measures imply creating an external feedback loop using an actuator to influence combustion oscillations so as to damp them down. With this type of "Active Instability Control" (AIC), the combustion system, properly speaking, does not have to be redesigned, and operations can continue as usual.

The basic idea to suppress combustion oscillations by an active feedback loop was published in a theoretical paper on rocket engines by Tsien as early as 1952.[5] However, it took until the eighties to convert this idea into a practical device. Various authors described successful tests based on laboratory-scaled burners with a thermal power of between 1 kW and 250 kW.[6-8] For all these publications, attenuation of combustion oscillations is achieved by anti-sound signals generated via loudspeakers. In addition to this method, other types of intervention and control strategies were researched for various combustion systems; however, all tests were performed at lab scales.[9-16] The first industrial-size application was realised by Seume et al.[17] in 1996 based on a land-based gas turbine delivering 160 MW of electrical power. For this gas turbine, active control was achieved by means of anti-cyclical fuel injection, with direct drive valves serving as actuators. This technique was then also extended to the largest type of this family of gas turbines, the V94.3A with an electric power output of 267 MW.[18, 19] Full scale tests on afterburners have been published by Moren et al.[20], and on a 67.5° sector of a liquid-fuelled lean premixed combustor by Hibsman et al.[21]

The way this technology was implemented and the problems encountered in doing so constitute the subject matter of chapter 3. To begin with, however, chapter 2 explains the necessary fundamentals, the main possibilities for actuation, as well as the components available to do so, such as sensors and actuators. Moreover, practical requirements to be met by this technology will be illustrated. Results achieved with AIC are discussed in chapter 4. Chapter 5 and 6 deal with long-term experience and a short evaluation of the advantages offered by AIC as compared to passive measures.

Fundamentals

Origin of self-excited combustion oscillations

In numerous cases, self-excited combustion oscillations are due to the feedback mechanism shown in a simplified diagram in Fig. 1. The injection of a turbulent air and fuel spray will generate broadband sound. Excitation of acoustic resonant frequencies within the combustion chamber may thus particularly amplify specific discrete frequencies. These sound pressure perturbations will create periodical flow modulations, i.e. periodically change the inflows into the combustion chamber, if appropriate preconditions at the combustion chamber inlet are given. Within the flame, these periodical flow fluctuations will cause the heat release rate to fluctuate with the same period. If its oscillations are in phase with sound pressure oscillations within the combustion chamber, further excitation will result according to Rayleigh's criterion,[22] so that oscillations will keep building up. Within this feedback cycle, the decisive link between combustion and flow is constituted by the acoustics.

$\dot{m}_0$ $const.\,mass\,flow$

$\tilde{\dot{m}}$ $mass\,flow\,fluctuation$

$\dot{m}$ $total\,mass\,flow$

$\dot{Q}_0$ $const.\,heat\,release\,rate\,of\,the\,flame$

$\tilde{\dot{Q}}$ $fluctuation\,of\,the\,heat\,release\,rate\,of\,the\,flame$

$\dot{Q}$ $total\,heat\,release\,rate\,of\,the\,flame$

$\tilde{p}$ $sound\,pressure$
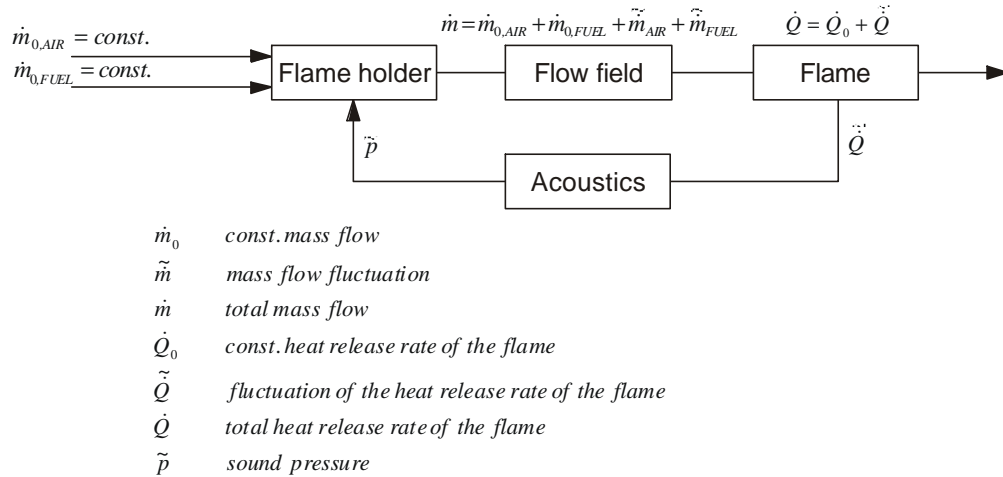
Fig. 1:   *Simplified model of a self-excited combustion oscillation. The feedback loop is determined by combustor acoustics.*

Active control of combustion oscillations

When actively suppressing self-excited combustion oscillations, some physical quantity such as the sound pressure characterising the oscillation is measured; the signal thus obtained is then fed into a controller. Using an appropriate control strategy, the controller generates an output signal designed to counteract the oscillation via an actuator. Thus, the sound pressure signal is attenuated. For this purpose, the actuator superimposes some separately generated oscillation on some quantity contributing to combustion oscillations so that self-excited oscillations will be extinguished. Fig. 2 shows this principle schematically. In this instance, sound pressure is used as controller input signal driving the actuator to modulate the fuel mass flow $\dot{m}_{0,Fuel}$ injected.
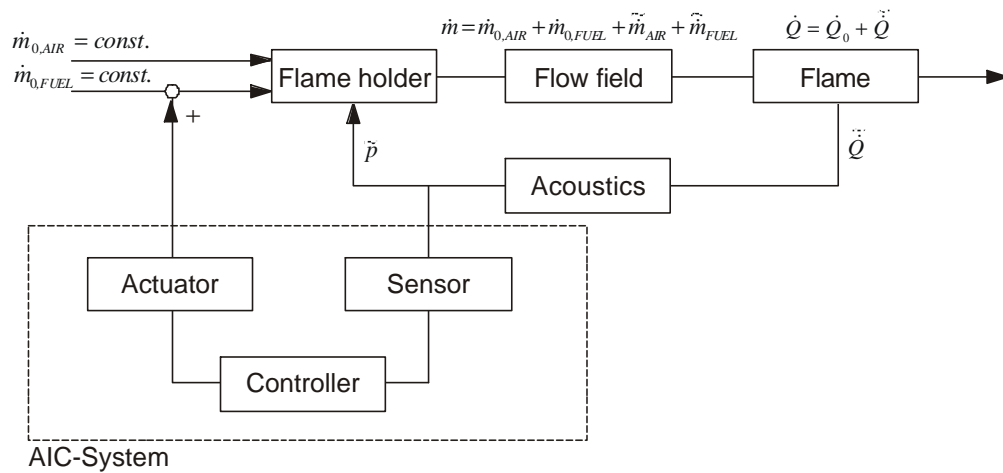
Fig. 2:   *Schematic of the AIC system. Combustion instabilities are neutralised by modulation of the fuel flow rate anti-cyclically to the heat release rate of the flame.*

POINTS OF ACTUATION AND ACTUATORS AVAILABLE

According to the mechanism generating self-excited combustion oscillations, schematically shown in Fig. 1, there are two basic possibilities for active control of combustion instabilities via actuators: by influencing the combustion system acoustics or by controlling the flame itself. For actively intervening via acoustical means, sound pressure fluctuations within the combustion chamber are damped by means

of an anti-sound signal. Owing to the direct coupling between sound pressure fluctuation and related oscillations of the heat release rate within the flame, the combustion zone itself will likewise be smoothed out. By contrast, when actively controlling via the flame, fluctuations of the heat release rate are attenuated by anti-cyclically injecting air and/or fuel mass flows. Seeing that the unsteady flame with its unsteady heat release rate constitutes the source of sound, the sound field within the combustion system will likewise be damped.

When implementing various possible means of controlling combustion instabilities, different problems will occur depending upon the type of intervention or the physical quantities influenced. More particularly, acting upon acoustics by superimposing an anti-sound signal, say, by means of a loudspeaker, soon runs up against practical limits. For combustion systems operating under pressure or characterised by high volume flow rates, the acoustic power that can be generated by loudspeakers is insufficient to appropriately damp any self-excited sound field. Moreover, there will be problems with installing this type of actuator. For instance, loudspeakers have to be built in as flush as possible with the chamber walls in order to guarantee good sound emission. In view of the high wall temperatures characterising combustion systems, doing so is normally impractical. Installing acoustic actuators within the air/fuel supply system likewise creates practical problems if mass flows are pre-heated or flammable.

Compared to acoustics, influencing the flows introduced into combustion systems offers a better control potential. Fuel supplies are normally particularly suitable because, in industrial combustion systems, volume flow rates of fuel are often substantially lower than those of air. This is particularly true for gaseous fuels supplied under high pressure, for highly caloric gaseous fuels, or when burning liquid fuels. Fig. 2 shows this type of control schematically. Given sufficiently reduced volume flow rates, correspondingly small valves can be used as actuators for high-frequency opening and closing. Various authors have presented and/or tested this type of valve. Most of these valves are actuated by means of electromagnetic linear motors or by piezo or magneto-restrictive drives.[16, 15, 23] In addition to such valves, other devices were successfully used in the past to modulate fuel flows, such as an actuator featuring a piezo driven piston designed to superimpose a sound field upon a liquid fuel flow that generates mass flow fluctuations at the injection nozzle.[15]

In addition to actuation through modulation of the mean fuel supply, there is the possibility of damping the oscillations prevailing within the flame by injecting additional fuel directly into it. Certain papers have shown that, depending on the actuator type used, the fuel injection point, or the spray characteristics, no more than 3-4% of additional fuel will be required to control combustion oscillations.[10, 14]

No matter which type of actuator is employed, its correct installation is highly important. This includes actuator positioning, taking due account of functional principles and the sound field prevailing in any specific case. For instance with loudspeakers, care has to be taken to install them in the sound pressure anti-node area of the eigenmode for active control to be effective. In addition to this requirement, actuators for industrial AIC systems need high reliability; in some cases, it must be possible to use them even at high ambient and media temperatures.

AIC INPUT SIGNALS

Basically, every parameter that is part of the oscillation at issue can be used as input signal for an active feedback control. In practice, however, only those will be used that can be measured easily by suitable sensors, i.e. mainly sound pressure and heat release rate of the flame. Sound pressure can be measured very easily, e.g. by microphones or piezo pressure transducers, while photomultipliers or photodiodes are particularly useful to measure the unsteady heat release rate of the flame. In order to obtain a resolution sufficient for the time scales of the oscillations, the emissions of short-lived intermediate reaction products are measured, such as the formation of free OH radicals. In order to be able to capture only the radiation emitted by them at 306.5 nm, appropriate optical bandpass filters will be used.

AIC sensors have to be positioned in spots where the parameter to be measured correlates sufficiently with combustion oscillations and is reasonably proportional. Optical sensors to measure heat release rates for the AIC must cover no less than that area of the combustion zone where fluctuations of the reaction

rate occur, the entire combustion zone being preferable. If only a small portion of the combustion zone is covered, any displacement of this zone may blind the sensor to prevailing oscillations. A further problem with optical sensors is fouling, e.g. by soot.

REQUIREMENTS TO BE MET BY A CONTROLLER

The least complicated controller for an AIC system is an amplifier/phase shifter combination appropriately amplifying input signals and shifting their phases so as to ensure the required anti-cyclical operation of the actuator. However, this type of controller will only work satisfactorily if the oscillation frequency excited is constant and if there is only one oscillation frequency. Further requirements imposing more complex control strategies are entailed by combustion systems having several burners distributed over the modes excited. Under certain circumstances, they may require multi-channel control signal processing. Moreover, in industrial applications, a self-adapting control strategy and/or control parameter compensation depending on operating points are indispensable. Thus, in the past, a great variety of control strategies such as model-based controllers, self-adapting controllers based on LMS algorithms or self-tuning controllers were researched. A summary of the work published on this topic is to be found in a recent publication of Dowling.[24]

Installing AIC on Siemens type Vx4.3A land-based gas turbines

The following section describes the installation of an AIC system on type Vx4.3A land-based Siemens gas turbines. Fig. 3 shows a longitudinal section through the upper half of this gas turbine. In contrast to former types of Siemens gas turbines that were fitted with silo combustion chambers, this family of gas turbines features ring combustion chambers (see left-hand illustration in Fig. 4). In total, this gas turbine comprises 24 Siemens hybrid burners spread uniformly over the circumference of its annular combustion chamber.
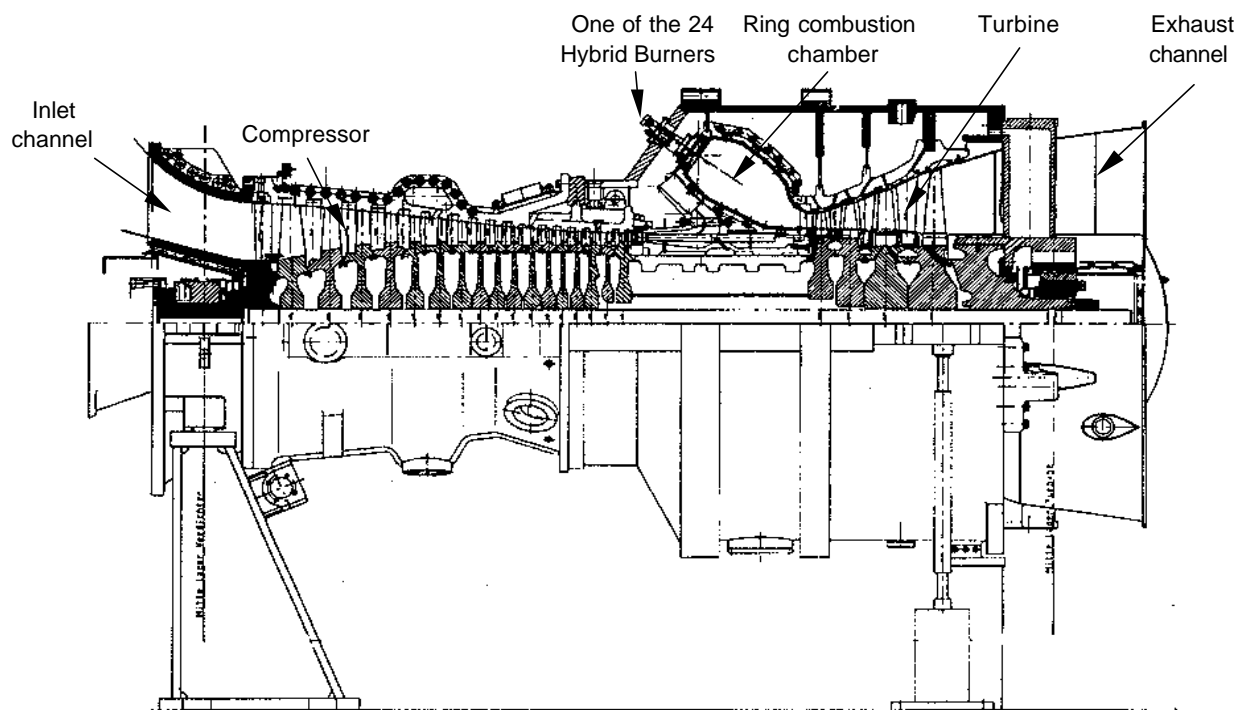
Fig. 3:   Half-section drawing of a Vx4.3A series gas turbine.

2nd harmonic with a frequency of 170 Hz

Premix flame

On of the 24 burners

Combustion chamber

Sound Pressure

$t = 0.75 \cdot T$

Circumferential coordinate

Burner

$t = 0 \cdot T, 0.5 \cdot T$ and T

Ring Combustion Chamber

$t = 0.25 \cdot T$

Period of oscillation: $T = 1 / f$
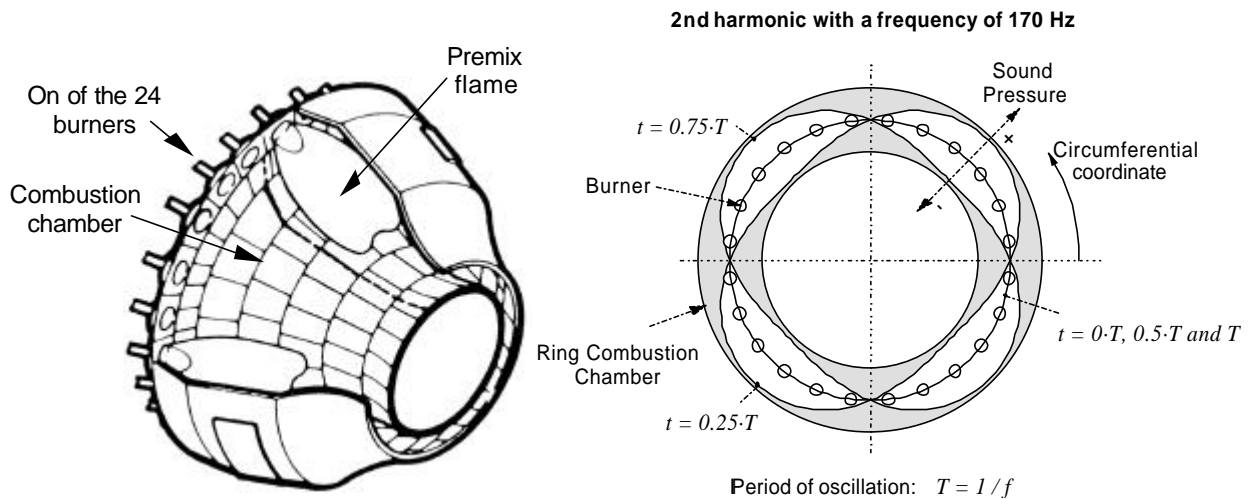
Fig. 4:   Left: Three-dimensional drawing of the annular combustion chamber of the Vx4.3A with a total of 24 burners. Right: Excited azimuthal modes for the second harmonic in the V94.3A.

Any Siemens hybrid burner may be operated both on liquid and gaseous fuels. At start-up and with gaseous fuel, the burner is operated in diffusion mode. When a specific turbine power is reached, there will be a switch-over from pure diffusion to so-called mixed operation. For this purpose, a combination of diffusion and premix flames is used. When the temperature within the combustion chamber is sufficiently high to stabilise a pure premix flame, operation is switched from this mixed mode to purely premixed operation. To stabilise the premix flame, every Siemens hybrid burner features an additional pilot burner. This is a diffusion burner delivering approx. 10% of the thermal power provided by the complete burner unit.

Instability problem

During the test phase of the prototype and the commissioning of the type of gas turbine described above, there were problems with self-excited combustion oscillations in various power ranges depending on the modifications performed on the hybrid burner used. Due to the low frequency of these instabilities, this effect is sometimes called "humming".

Research on this oscillatory phenomenon described by Seume et al.[17] showed that standing sound waves are generated within the annular combustion chamber by self-excited combustion oscillations. According to the direction of propagation of these waves along the circumference of the annular combustor they are designated "azimuthal modes". They are characterised by regions where sound pressure amplitudes are high, called "sound pressure anti-nodes", and regions where these amplitudes are very low, called "sound pressure nodes". The number of nodes and antinodes varies according to the prevailing frequencies. The right-hand side of Fig. 4 shows the azimuthal modes of the second harmonic, characterised by a total of 4 nodes and 4 anti-nodes. For the largest version of this gas turbine type, V94.3A, this eigenmode is excited at a frequency of approx. 170 Hz.

The equation $f = n \times c/(p \times d)$ provides a theoretical estimate for the characteristic acoustical frequencies of any annular combustion chamber. At an average combustion chamber diameter of d=3 m and a speed of sound of c=844 m/s (assuming an average combustion chamber temperature of 1,500°C), the resulting frequency for a V94.3A is 179 Hz for the second harmonic, a value agreeing well with experimentally determined characteristic frequencies. For smaller versions of this turbine family, the above equation returns higher frequencies for the occurrence of combustion oscillations, due to the reduced diameter of their combustion chambers (see Seume et al.[17]).

AIC installation

In order to avoid the oscillation problem described, an AIC system for this type of gas turbine was developed in addition to passive measures such as burner design modifications.[4] Fig. 5 provides a simplified schematic diagram of the basic design of this AIC.
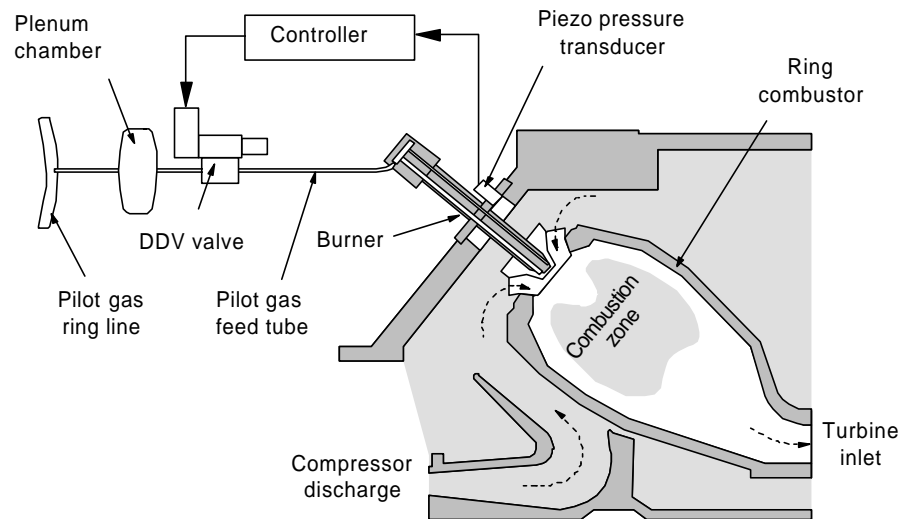
Fig. 5:   Schematic AIC diagram of the Siemens model Vx4.3A heavy duty gas turbine

SENSOR

By way of input quantity, this AIC system uses the sound pressure measured at the burner flanges. There, wall temperatures are substantially lower than within the combustion chamber so that high-temperature piezo pressure transducers can be used without requiring any additional cooling . It was verified in a number of tests that the sound pressure signals measured at the burner flanges coincide sufficiently well in amplitude and phase with the pressure signals within the combustion chamber.

During some initial tests, potential uses of optical probes for measuring AIC input signals were researched in addition to sound pressure measurements at the burner flanges. However, owing to the limited field of view and due to thermal problems with probe installation, this method was soon given up.

ACTUATOR

The crucial problem for implementing any AIC system of the type described here is actively influencing the combustion. Owing to the elevated air and fuel volume flows through Vx4.3A gas turbines, these flows cannot be sufficiently modulated in full, neither by means of acoustical actuators nor by valves. Detailed research showed that the main premix flame of the Siemens hybrid burner – controlled by much smaller pilot diffusion flames – will respond very precisely to fluctuations in the conversion rates of those pilot flames. Accordingly, it is possible, by modulating the pilot gas mass flow, which comprises no more than approx. 10% of the entire mass flow, to control not only the pilot flames themselves but also the premixed main flame to a significant extent. Pilot flames are supplied via their own fuel line. The actuator, a direct drive valve (DDV) – shown in Fig. 6 - developed specifically for this application by Moog Germany, is integrated in this fuel line. In order to obtain maximum control levels for main flames and, accordingly, for the combustion oscillations arising within the gas turbine, every burner of the turbine was fitted with its own valve. Thus, a total of 24 valves was installed around the annular combustor of the gas turbine.

In the absence of any AIC signal, DDV valves will be 50% open, so that the pilot gas mass flows required for normal premixed operation will reach the burners. In order to modulate individual pilot gas mass flows and thus the pilot flames themselves, valve spools will be moved around their static opening value of 50%, i.e. opened further or closed down at the frequency of the combustion oscillation to be damped. The level of fuel flow modulation achieved can be determined by valve spool stroke. According

to the frequency response of the used valve type – shown in Fig. 7 – the valves allow the control of combustion oscillations with frequencies of up to 400 Hz.
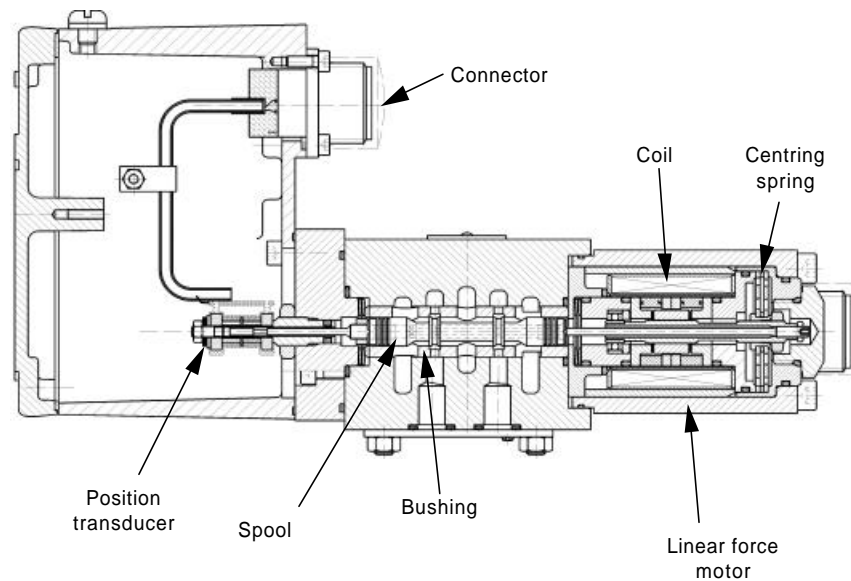
Fig. 6: Schematic diagram of the DDV valve used
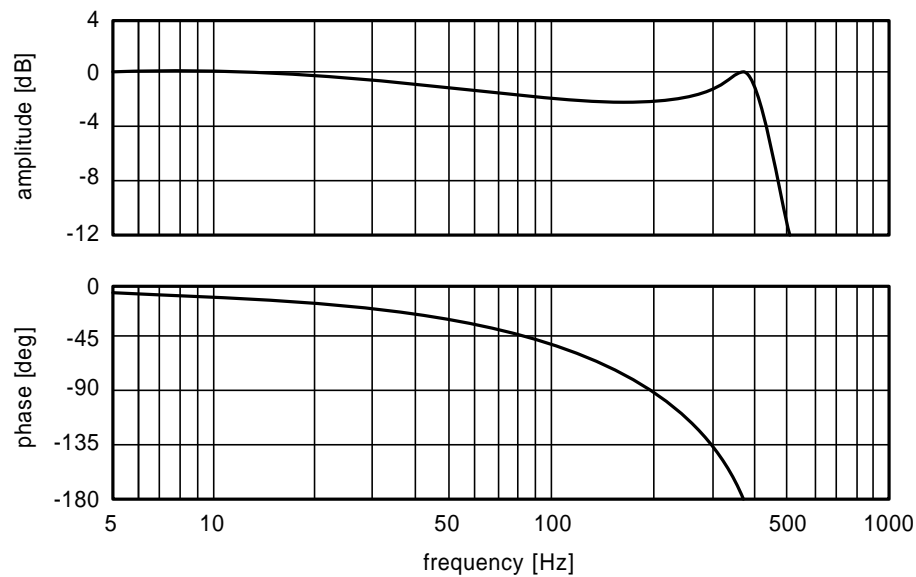
Fig. 7: Frequency response of the DDV valve used

By moving the valve spools at frequencies within this range, sound waves will be generated within the pilot gas systems. The resulting effects on the modulation of the pilot gas mass flow must be taken into account and the pilot gas system must be tuned as described in Hermann et al.[15] and Hantschk et al.[16]

CONTROLLER

As described in Seume et al.[17], azimuthal modes are excited within ring combustion chambers by combustion oscillations. This means that the pressure fluctuations excited along the combustion chamber circumference are characterised by both different amplitudes and different phases, and that the burners placed evenly along the circumference of the annular combustion chamber are accordingly located at positions characterised by differing amplitude and phase values. Seeing that fluctuations of the heat release rate are coupled characteristically with pressure oscillations (self-excitation), any heat released at

the various burners will fluctuate at differing amplitudes and phases. Since AIC requires both anti-phase and in-amplitude influencing of the unsteady flame, this means that it must be possible to control every burner individually. The least complicated case would require a sensor and a feedback loop for every burner, so that a 24-channel AIC system would have to be installed.
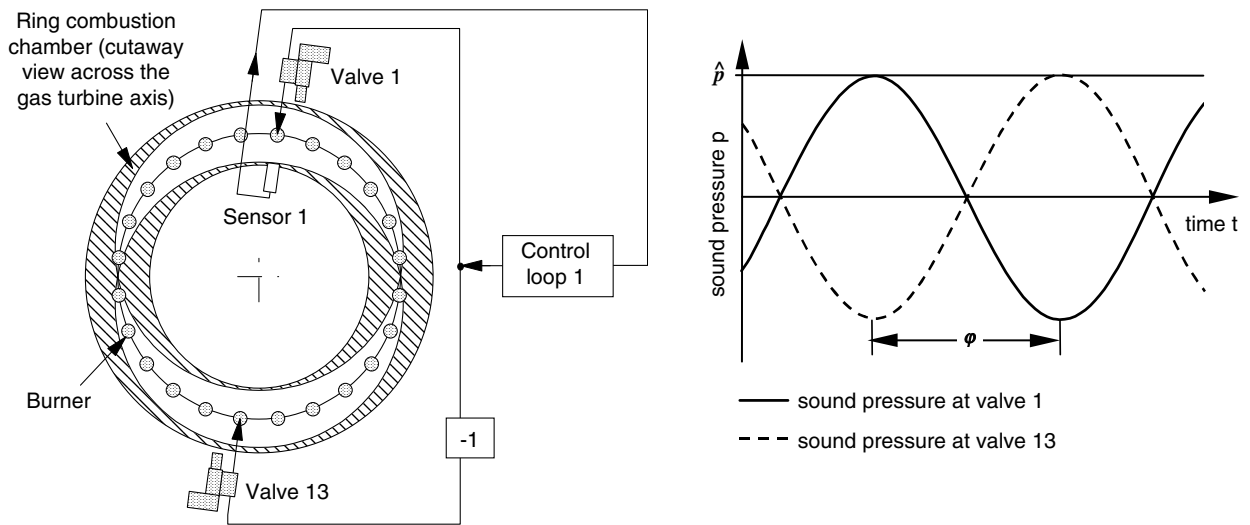
Fig. 8:   *Left: Exploiting the symmetry of azimuthal modes, e.g. for the first harmonic. One sensor and one controller provide the input signals for two DDVs. Right: Sound pressure at the two valve positions.*

For minimising this high number of feedback loops, the symmetry of azimuthal modes arising within the combustion chamber was exploited. As shown by the azimuthal mode corresponding with the first harmonic in Fig. 8, the sound pressure fluctuations for two precisely opposite burners are characterised by identical amplitudes $\hat{p}$ and a phase shift j amounting to *180°* with respect to each other. As indicated in Fig. 8, for an AIC system this means that a signal measured at a specific position by one sensor can be used to control not only the actuator for this position but also the one located at the precisely opposite point of the combustion chamber by merely inverting the controller output signal for the second actuator.

In the event of second or even higher harmonics, the number of feedback loops can be reduced even further, as shown in Fig. 9. Here, a total of 4 actuators are controlled via one input signal and one feedback loop. For the control system of V94.3A burners, an installation as in Fig. 8 was chosen since, for this type of gas turbine, the first harmonic will likewise appear due to self-excited oscillations. In total, this type of gas turbine was fitted with 12 sensors and 12 feedback loops.
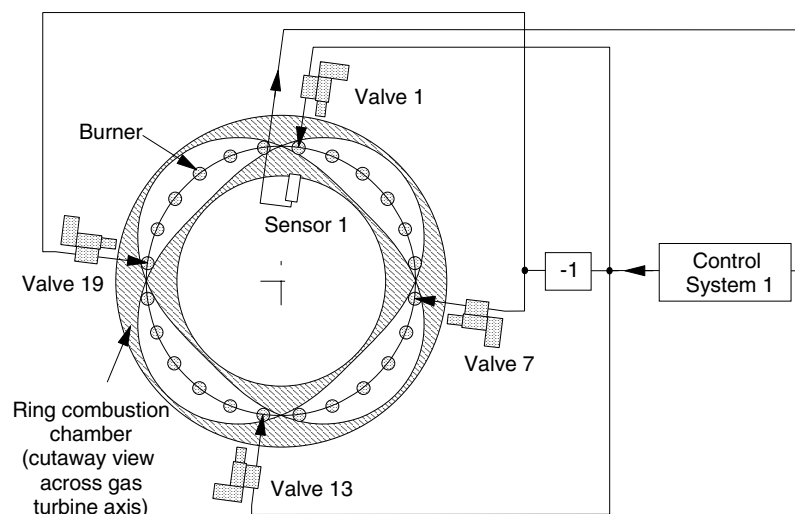
Fig. 9:   *Exploiting the symmetry of azimuthal modes, e.g. for the second harmonic. One sensor and one controller provide the input signals for four DDVs.*

Those 12 loops were realised by means of 6 signal processors, every processor handling two input signals and generating four output signals. The algorithm used works within the frequency range; it is suitable for controlling two frequencies, a restriction entailed by the limited computing capacity of the type of signal processor used. The necessary control parameters depend on the operation parameters of the gas turbine and are set automatically during continuous operation. Hermann et al.[19] provides a detailed description of this control system.

Results

The AIC system described above was implemented in two differently sized gas turbines within the Vx4.3A family. The first tests were run using a type V84.3A machine delivering 170 MW of electric power at Siemens test facilities in Berlin. Detailed specifications of the AIC structure used and the tests performed are to be found in Seume et al.[17] Owing to these successful tests , AIC systems were subsequently built into type V94.3A machines for field testing purposes. Depending on the version used, these machines deliver between 233 MW and 267 MW of electrical power under ISO conditions. For this purpose, the electronic system and the control strategy used for V84.3A were completely redesigned and further developed into an industrial-grade system.

During field tests, AIC systems were used on V94.3A machines together with various burner configurations showing oscillation problems at various operating points of the corresponding gas turbine. Below, tests on three different burner configurations are presented.

Burner configuration A: active control at switch-over

Burner configuration A mainly presented problems due to combustion oscillation during switch-over from mixed to premixed operation, i.e. when transitioning from a combination of diffusion and premixed flame to a purely premixed flame. To stabilise the premixed flame, the pilot burner is switched on while switch-over is in progress. Fig. 10 shows this process without (left) and with activated AIC system (right). From top to bottom, the following quantities are plotted:

- maximum sound pressure spectrum calculated on the basis of the signals delivered by the 12 AIC sensors at three different moments in time;
- maximum RMS value of the sound pressure versus time, calculated on the basis of the signals delivered by the 12 AIC sensors;
- opening cross-section versus time for the gas valves actuated during switch-over, as a percentage of the maximum opening cross-section for the corresponding valve.

As shown in Fig. 10 in the diagrams on the left, strong combustion oscillations occur approx. 3.5 seconds after opening the pilot gas main valve (= start of switch-over, marked in the bottom diagram by a vertical arrow) as the pilot gas flows into the combustion chamber. After another 2 seconds, the diffusion gas valve is closed and the premix gas valve opens, with the thermal power within the combustion chamber being kept constant during that process. About 10.5 seconds after initiating the switch-over (t=15s), i.e. as the diffusion gas valve closes, the combustion oscillation amplitude slightly weakens before it returns, after another 5 seconds, to the value characterising constant operation. At the t=20s moment in time, the gas turbine is running in its fully stabilised premix mode. Considering the frequency spectrum of the sound pressure measured at various times during switch-over, it becomes obvious that, in the beginning, the first harmonic dominates at around 90 Hz (t=9.7s). At t=13.7s, this frequency will have dropped to approx. 80 Hz. By way of non-linear effect, high amplitudes of the first harmonic will additionally produce its higher-order harmonics.

The diagrams on the right-hand side of Fig. 10 show the same switch-over process, but subject to an activated AIC system. As the sound pressure history for the RMS value indicates, this leads to an almost complete attenuation of combustion oscillations. Only a specific position of the diffusion gas valve (t=15.2s) produces a short peak lasting approx. 0.5 s, its RMS value already substantially reduced. Considering this moment in time on the frequency spectrum, it becomes apparent that the harmonic excited is no longer the first but the third one, at approx. 250 Hz. To achieve even further damping for

this oscillation by means of an AIC system, the system was pre-set for both frequencies (first and third harmonics). As shown by the spectrum of another switch-over recorded some 10 minutes later, the amplitude of this oscillation was further attenuated, without influencing, yet damping of the first harmonic. It has to be stated that the damping achieved by AIC was more than sufficient for safe gas turbine operation.
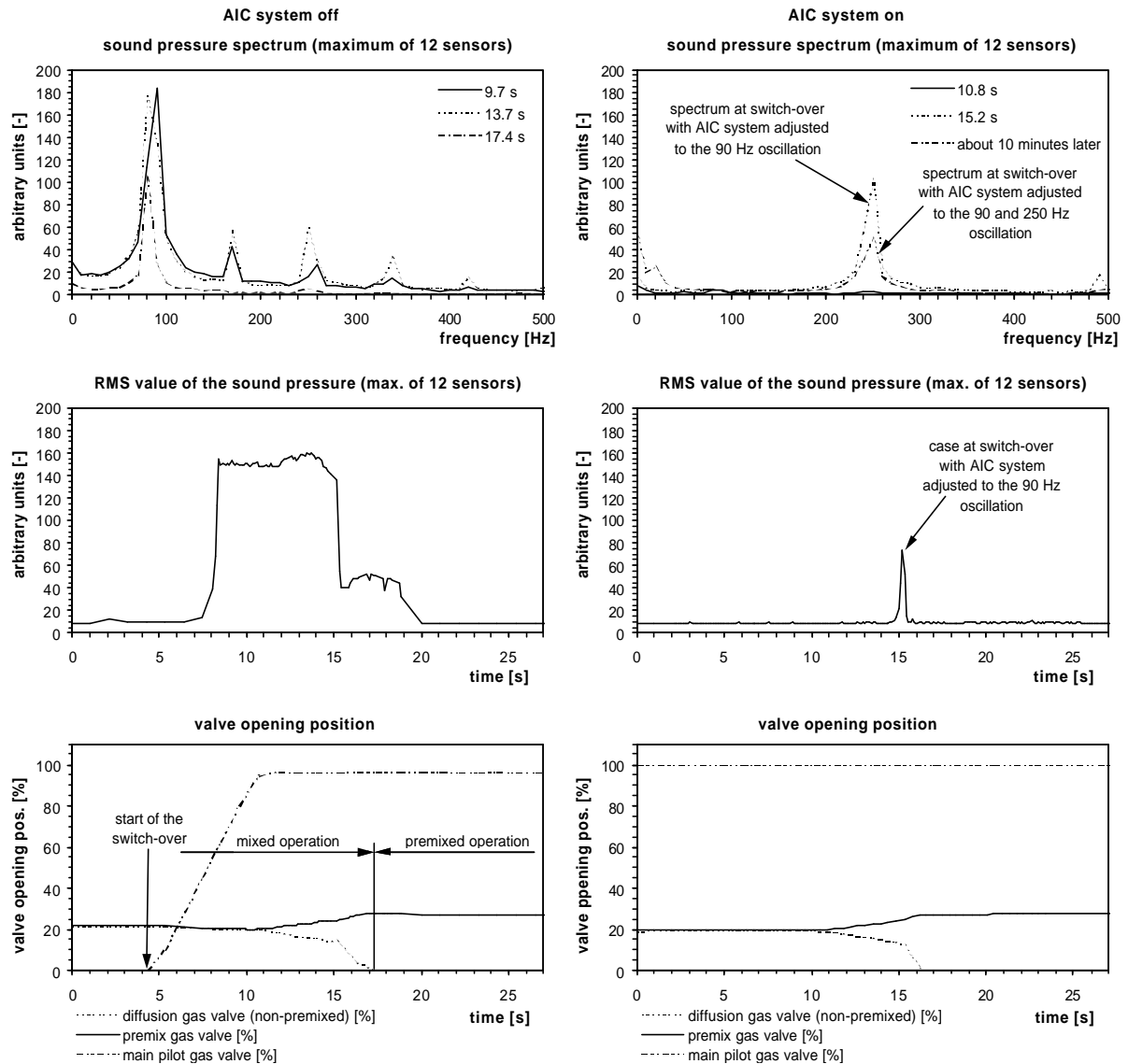
Fig. 10: Switch-over from mixed to premixed operation without (left) and with AIC (right). The inlet guide vane remained permanently closed.

Burner configuration B: active control at load change during premixed operation

During premixed operation over a power range of 60% to 100% of base load, burner configuration B was characterised by self-excited combustion oscillations. If this gas turbine is operated without AIC, increased amplitudes for the third harmonic at a frequency of 270 Hz may appear as early as at 60% of base load. At approx. 80% of base load, this frequency shifted to 170 Hz, corresponding to the second harmonic of the combustion chamber.

By activating the AIC system, the oscillations were attenuated enough to allow safe turbine operations up to 100% of base load power. Fig. 11 demonstrates the AIC operation for a load increase (left) and a load

decrease (right). From top to bottom, the following oscillation and operating parameters of the turbine are shown, all of them plotted versus time:

- maximum RMS sound pressure value calculated on the basis of the signals of 12 AIC sensors;
- maximum sound pressure amplitude of the two characteristic frequencies for which the AIC is tuned;
- electrical power output of the gas turbine.
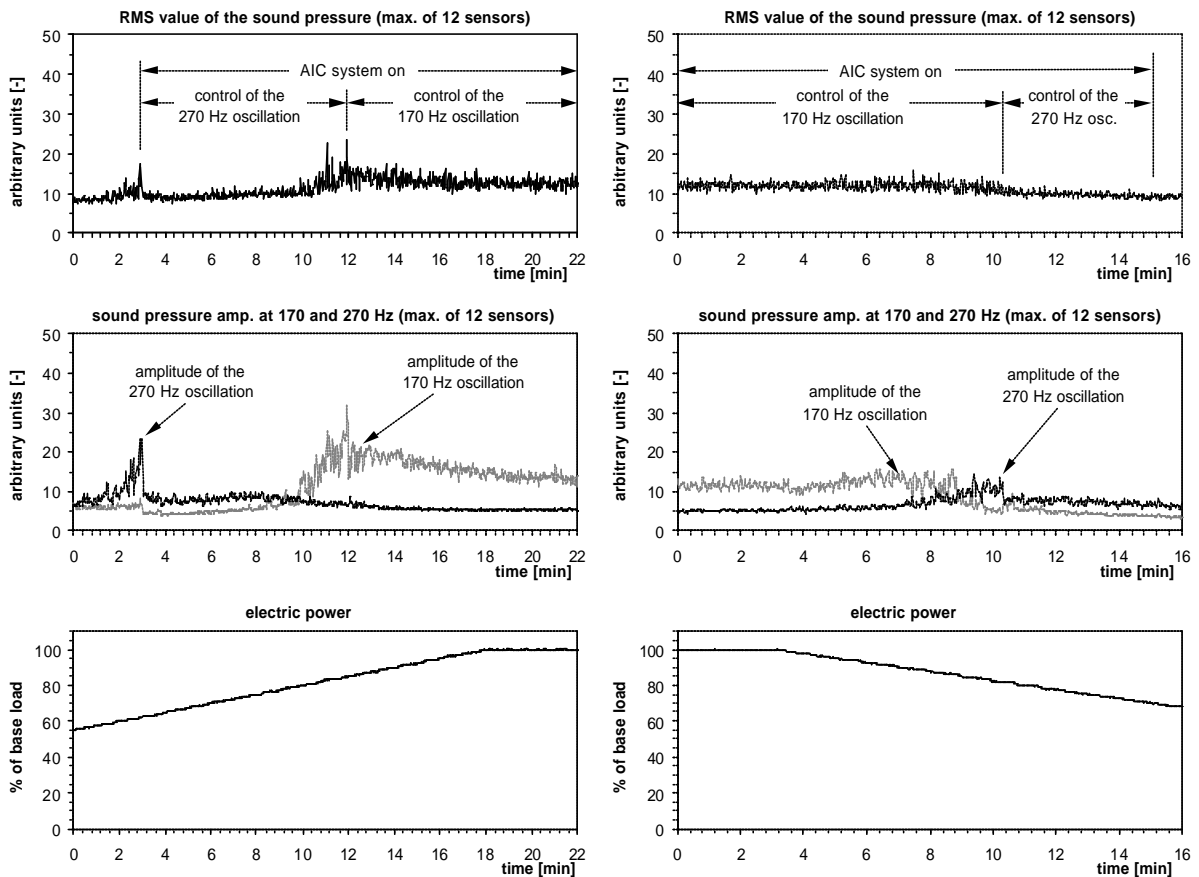
Fig. 11: Load increase to base load (left) and decrease to part load (right) in premixed operation with activated AIC system. While running up the gas turbine, the system must be activated earlier than when the gas turbine is being run down. The AIC system was also always activated at base load to suppress combustion instabilities.

First the AIC is tuned to the third harmonic at approx. 270 Hz, and automatically activated at 60% of base load power. Immediately after AIC activation, the amplitudes characterising the oscillations already present are damped by approx. 65% and remain at more or less this level, as the load is further increased up to 80% of base load power. At about that level, the second harmonic is excited at around 170 Hz, while the amplitude of the third harmonic continues to decrease further. By converting the AIC target frequency to the one characterising the second harmonic, its amplitude is reduced immediately by around 30%. Switching over AIC from the third to the second harmonic, as described, was required since, at that point of the test runs, simultaneously damping even and odd-numbered modes had not yet been implemented for the AIC system.

The same damping efficiency as shown above for the case of a load increase was likewise achieved when the load level was decreased even though, in this case, switching from the second to the third harmonic did not produce any significant amplitudes. The right-hand trend diagrams in Fig. 11 demonstrate this AIC operation.

Burner configuration C: active control at start-up and at lower part load operation of the gas turbine

This type of gas turbine is started - and subsequently operated, at its lower part load range – exclusively in diffusion mode where flames are easier to stabilise despite the low level of combustion chamber temperatures still prevailing. Once a certain temperature limit has been reached, there will be switch-over to mixed operation. In this lower part load range – from start to switch-over into mixed operation – burner configuration C will be subject to problems caused by self-excited combustion oscillations, with the second and the fourth harmonics being excited simultaneously within the ring combustion chamber.

Even though the AIC application presented relies on modulating pilot gas mass flow and pilot flames which are, in principle, provided only for premixed operations, it proved possible to use the AIC system successfully even during part load operations. For this purpose, the pilot burners were used together with diffusion flames, and the AIC system was activated. The system was tuned for the two frequencies excited.

As shown in Fig. 12, which displays the maximum frequency spectrum of the 12 AIC sensors with and without AIC for this point within the operational range, it was possible to damp both excited frequencies almost completely. For the second and fourth harmonics, damping levels amounted to 20 dB and 14 dB respectively.
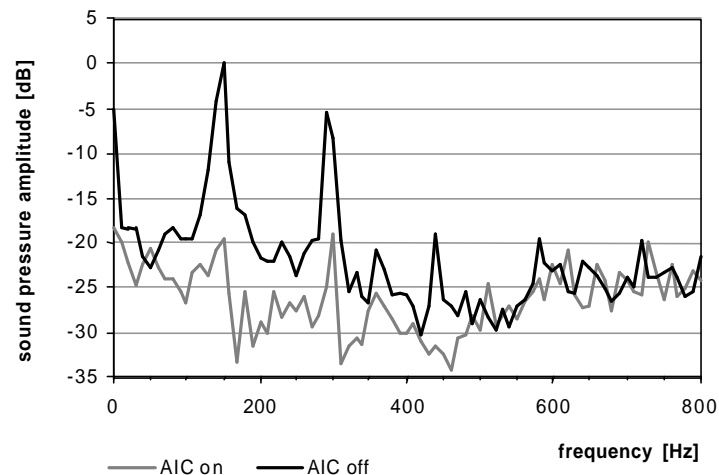
Fig. 12: Suppression of two frequency peaks by AIC during part load operation.
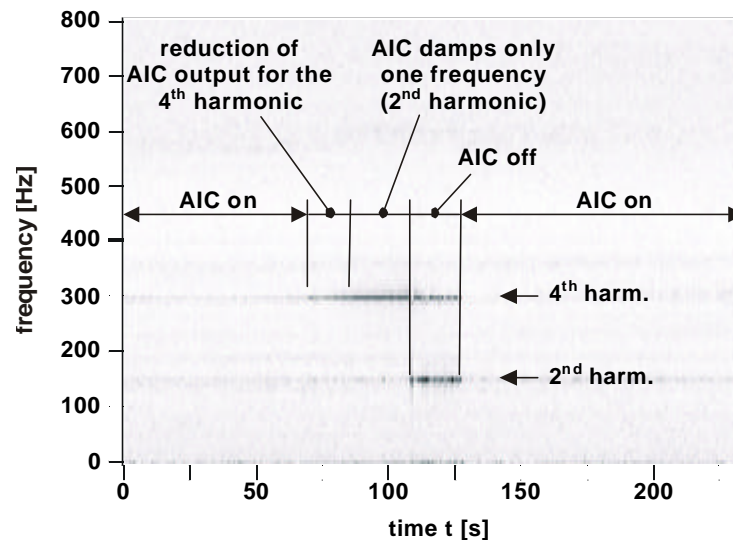
Fig. 13: Separate damping of two dominant eigenmodes of a combustion instability by AIC.

The separate damping of two eigenmodes by AIC, as described above, is exemplified again in Fig. 13. The diagram plots sound pressure as a spectrogram (maximum values for the 12 sensors) versus time. Dark areas indicate high amplitudes, lighter areas the general noise level. The two horizontal bars at completely deactivated AIC mark the two eigenmodes excited, in this case, at 145 Hz and 290 Hz. Starting at t = 70 s, by slowly reducing the AIC output signal to suppress the fourth harmonic at 290 Hz within the 70 s < t < 85 s range, the amplitudes of this harmonic increase. During the next 23 seconds, AIC only damps oscillations at 145 Hz. By completely switching off the AIC system at t=108 s, the second harmonic is likewise excited at 145 Hz. By reactivating the AIC for both frequencies at t=127 s, the two oscillations are damped out completely once again. This example demonstrates that both oscillations can be self-excited independently of each other and that in general - if combustion oscillations are to be avoided completely - both will have to be damped by using AIC.

AIC fault tolerance and long-term experiences

In order to research the influence of a failure of any feedback loop on AIC damping characteristics, for instance, due to defective pressure transducers or valves, specific loops were switched off on purpose during test runs. It was shown that reducing the number of feedback loops to ten – corresponding to no more than 20 active valves – had no significant influence on damping characteristics.

In test runs to determine the long-term suitability of the AIC system, it was kept operating for more than 8,000 hours in some gas turbines. No valve failure and no decrease in the damping efficiency occurred and abrasion of the moving parts of actuators was negligible. During these long-term tests, AIC systems were operated automatically in conjunction with the corresponding gas turbine control units and had to control automatically a wide range of operating conditions and situations so as to damp any arising combustion oscillations safely.

Conclusions

As compared to passive measures, AIC systems have a number of advantages. While the damping effect of passive measures frequently remains restricted to narrow frequency or operating ranges of the combustion system concerned, the AIC is distinguished by its high degree of flexibility and its wide range of operation. The examples described – different types of oscillation problems occurring for a variety of operational situations being solved successfully – make this obvious. For damping low frequency oscillations numerous passive measures such as Helmholtz resonators or sound absorbers require a great deal of space and thus cause much unwanted design complications, while the AIC system needs little space and can be installed in a comparatively simple manner.

Another AIC advantage is that – thanks to its degree of development reached by now – it takes significantly less time to install and requires fewer tests. Accordingly, novel combustion systems can be commissioned faster and take less time to market. By comparison, developing suitable passive measures is still mostly a trial-and-error process and takes much experimenting, i.e. time and money. Thus, higher expenses frequently required for AIC systems soon pay off in most cases.

In addition to the already mentioned benefits of AIC, this system may render it possible to operate certain combustion systems at lower emission levels. In the tests run in premixed mode presented above, it was possible with an activated AIC to operate the gas turbine at lower levels of pilot gas mass flows than without the system. Since pilot flames are important for influencing NOx emissions of gas turbines, the AIC system allowed to reduce them by more than 60% in certain cases.

References

1 Culick, F. E. C., "Combustion Instabilities in Liquid-Fuelled Propulsion Systems - An Overview", AGARD Conference on Combustion Instabilities in Liquid-Fuelled Propulsion Systems, Bath, AGARD-CP-450, pp. 1-1 - 1-73, (1988).

2   Konrad, W., Brehm, B., Kameier, F., Freeman, C., Day, I. J., "Combustion Instability Investigations On The BR710 Jet Engine", ASME-Paper No. 96-TA-36, presented November 5-7, 1996 at the ASME Turbo Asia Conference, Jakarta, Indonesia, (1996).

3   Scalzo, A.J., Sharkey, W.T., Emmerling, W. C., "Solution of Combustor Noise in a Coal Gasification Cogeneration Application of 100-MW-Class Combustion Turbines", Transactions of the ASME Journal of Engineering for Gas Turbines and Power, Vol. 112/39, (1996).

4   Berenbrink, P., Hoffmann, S.: Suppression of Dynamic Combustion Instabilities by Passive and Active Means. 2000-GT-0079, Proceedings of: ASME TURBOEXPO 2000, May 8-11, Munich, Germany, (2000).

5   Tsien, H. S.: Servo-stabilisation of combustion in rocket motors. Am. Rocket Soc. J., Vol. 22, pp. 256-263, (1952).

6   Lang, W., Poinsot, T., and Candel, S., "Active Control of Combustion Instability", Combustion and Flame, Vol. 70, pp. 281-289, (1987).

7   Gulati, A., Mani, R., "Active Control of Unsteady Combustion-Induced Oscillations," J. Propulsion and Power, Vol. 8, No. 5, pp. 1109-1115, (1992).

8   Poinsot, T., Veynante, Bourienne, F., Candel, S., and Esposito, E., "Initiation and Suppression of Combustion Instabilities by Active Control", 22nd Symposium (International) on Combustion, Seattle, pp. 1363-1370, (1988).

9   Bloxsidge, G., Dowling, A., Hooper, N., Langhorne, P.: Active control of reheat buzz. AIAA Journal, Vol. 26 (7), pp. 783-790, (1988).

10 Langhorn, P.J.: "Reheat Buzz an acoustically coupled combustion instability," J. Fluid Mech. vol. 193, pp. 417-443, (1988).

11 Poinsot, T., Candel, S., Esposito, E., Lang, W., Bourienne, F., "Suppression of combustion instabilities by active control," Journal of Propulsion and Power, Vol. 5, pp. 14-20, (1989).

12 Wilson, K. J.; Gutmark, E.; Schadwo, K. C.: Flame-Kernel Pulse Actuator for Active Combustion Control. ASME 1992, Active Control of Noise and Vibration, DSC-Vol. 38, pp. 75-81, (1992).

13 Yu, K.H., Parr, T.P., Wilson, K.J. Schadow, K.C., Gutmark, E.J., "Active Control of Liquid-Fueled Combustion Using Periodic Vortex-Droplet Interaction, "Twenty-sixth Symposium (International) on Combustion, Vol. 2, pp. 2843-2850, (1996).

14 Yu, K., Wilson, K.J., Schadow, K.C.: "Scale-Up Experiments on Liquid-Fueled Active Combustion Control," AIAA 98-3211, (1998).

15 Hermann, J., Gleis, S., and Vortmeyer, D., "Active Instability Control (AIC) of Spray Combustors by Modulation of the Liquid Fuel Flow Rate,", Combust. Sci. and Tech., Vol. 118, pp. 1-25, (1996).

16 Hantschk, C., Hermann, J., and Vortmeyer, D., "Active Instability Control with Direct Drive Servo Valves in Liquid-Fuelled Combustion Systems," 26. Int. Symp. on Combustion, Naples, (1996).

17 Seume, J. R., Vortmeyer, N., Krause, W., Hermann, J., Hantschk, C.-C., Zangl, P., Gleis, S., Vortmeyer, D., Orthmann, A., "Application of Active Combustion Instability Control to a Heavy Duty Gas Turbine", ASME Paper No. 97-AA-119, presented September 30 – October 2, 1997 at the ASME ASIA ´97 Congress & Exhibition, Singapore, (1997).

18 Hoffmann, S., Weber, G., Judith, H., Hermann, J. and Orthmann, A., "Application of Active Combustion Control to Siemens Heavy Duty Gas Turbines," Presented at the Symposium of the AVT Panel on Gas Turbine Engine Combustion, Emissions and Alternative Fuels, Lisbon 12-16, October, RTO Meeting Proceedings 14, pp. 40-1 – 40-13, (1998).

19 Hermann, J., Orthmann, A., Hoffmann, S., „Application of Active instability control to a heavy duty gas turbine," XIV ISABE, 5-10 Sept., Florence, Italy, A99-34186, (1999).

20 Moran, A.J., Steele, D., Dowling, A.P., "Active Control and its Application," NATO/RTO Active Control Symposium, May 8-12, Braunschweig, Germany, (2000).

21 Hibshman, JR, Cohen, JM, Banaszuk, A, Anderson, TJ, Alholm, HA, " Active Control of Combustion Instability in a Liquid-Fueled Sector Combustor," ASME, 99-GT-215, (1999).

22 Rayleigh, Lord J. W. S., "The Explanation of Certain Acoustical Phenomena", Nature, July 18, pp. 319-321, (1878).

23 Neumeier, Y., Zinn, B. T., "Theoretical and Experimental Investigation of the Performance of an Actively controlled Fuel Actuator," 36th Aerospace Science Meeting, Reno, NV, AIAA-98-0355, (1998).

24 Dowling, P. A., "Active Control of Instabilities in Gas Turbines," NATO/RTO Active Control Symposium, May 8-12, Braunschweig, Germany, (2000).

Combustion Dynamics: Passive Combustion Control

K.C. Schadow
Strategic Analysis, Inc.
2896 Calle Heraldo
San Clemente, CA 92673, USA
E-mail: schadowkc@home.com

Summary. This lecture summarizes research to explore the driving mechanism of dump combustor instabilities with emphasis on the role of vortex dynamics. It is shown that the development of coherent flow structures and their breakdown into fine-scale turbulence can lead to periodic heat release, which, when in phase with the pressure oscillation, can drive the oscillations. The physical processes associated with vortex development and breakdown are described using results from non-reacting, flame, and combustor experiments. This understanding is used to passively control and reduce the pressure oscillations using geometric changes at the dump, such as multi-step and triangular geometries, to prevent development of coherent structures. The physical understanding of the flow/combustion interactions was used to extend lean blow-out limits of a premixed flame by acoustic forcing at the initial shear-layer instability frequency.

Introduction. This lecture discusses passive control of flow/acoustics interactions in dump combustors and its effect on combustion processes, in particular on the amplitude of low-frequency pressure oscillations. The approach is based on the physical understanding of dump combustor flow characteristics, which are addressed in a broader context of shear-flow instabilities associated with jets. These instabilities may develop large-scale structures through interaction with chamber acoustics as the source for periodic heat release and consequently combustion instabilities.

The role of these flow dynamics as likely mechanism for dump combustor instabilities cannot be separated completely from other phenomena, such as spray combustion. In fact, it has been long known qualitatively from experience gained in engine development that the fuel distribution has a substantial effect on instabilities. However, it can be argued that even with spray combustion the dynamics of the vortex structures remain the dominant feature. In fact, the laboratory tests discussed in this lecture have used gaseous fuels.

The general idea of periodic combustion, associated with unstable shear layers, was first independently reported by Kaskan and Noreen[1] and Rogers and Marble[2] in the mid-fifties. In particular, the latter work, discussing premixed gaseous fuel and air flowing past a flameholder, proposed that delayed periodic combustion in shed vortices can drive an acoustic field, associated with transverse oscillations at high frequency. In the present lecture, pressure oscillations at low frequencies are addressed, which became a growing concern during the development of compact ramjet combustors in the early-eighties. These longitudinal oscillations interfered with the inlet shock system causing loss of performance due to inlet unstart.[3,4] Byrne[5,6] suggested vortex shedding as a likely cause of the oscillations, also pointing out a relationship between flow dynamics observed in acoustically excited jets and ramjet pressure oscillations. An Office of Naval Research (ONR) program in the late eighties has addressed the role of flow instabilities in various types of combustor[7] (Figure 1). The present lecture will concentrate on tests with a simple, axisymmetric dump combustors, which have been performed at the Naval Air Warfare Center Weapons Division.

In dump combustors vortices are formed in the shear layer between the high and low speed streams at the rearward-facing step (dump) (Figure 2). The vortex formation is stabilized in the presence of acoustic pressure oscillations. In general, the high-speed stream consists of an unburnt mixture of air and fuel, while the low speed stream is composed largely of hot combustion products forming the flameholding recirculation zone behind the dump plane. The vortex structure has a significant influence on the combustion process. In the early phase of the vortex development, with the unburnt mixture on one side of an interface and the hot combustion products on the other side, intense (fine-scale) mixing and burning are limited due to high strain rates (velocity gradients) between the high and low speed streams. It can be conjectured that the fine-scale turbulent production is abruptly enhanced during the roll-up of the vortices. During the vortex roll-up process a large interface between the air/fuel mixture and the hot products develops, leading to fine-scale

turbulence enhancement and sudden heat release. This process is repeated during each cycle of the pressure oscillations resulting in periodic heat release. When a proper phase relationship between the periodic heat release and pressure oscillations exists (Rayleigh criterion)[8] high amplitude pressure oscillations may be excited.
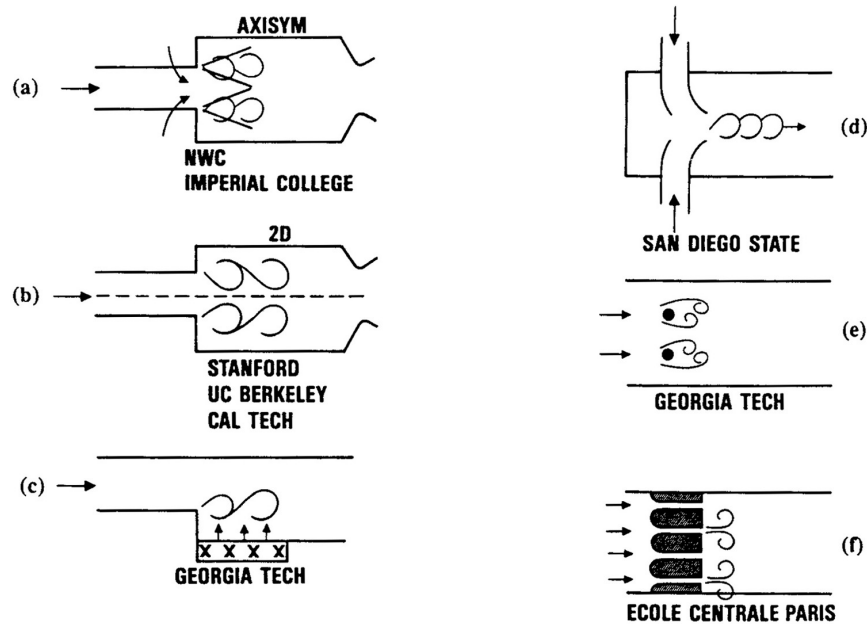
Figure 1. Investigations of Flow Instabilities as Driving Mechanism of Combustion Instabilities.
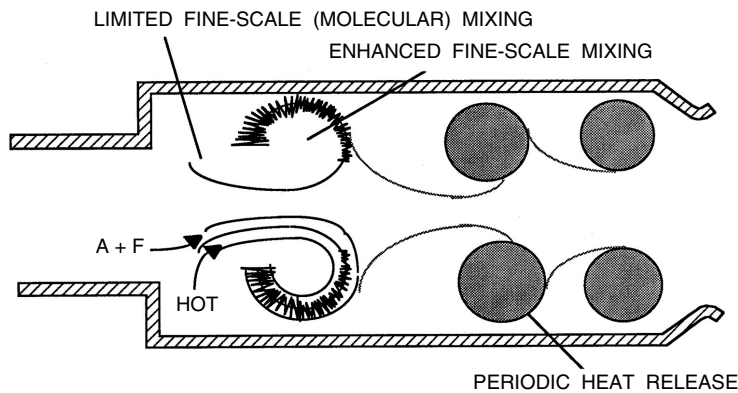
Figure 2. Effect of Coherent Vortices on Combustion.

The evolution of the vortices is discussed in the general context of the interactions between shear-layer instabilities and acoustic instabilities in the combustor. The commonly known vortex shedding from rearward facing steps is a special case of these flow instabilities and the vortices will be referred to as large-scale coherent structures. From the discussions of the non-reacting and reacting dump combustor tests, a detailed understanding of the combustion instability driving mechanism is derived, which can be used to passively control the pressure amplitude by modifying the shear-flow development by distinct geometric changes at the dump.

The research results do not provide combustor design criteria to reduce pressure oscillations. More important, the research provides insight into a dominant driving mechanism, which can guide the designer in the development of passive shear-flow control methods for reduced pressure oscillation. Examples of passive control are presented for the dump combustor configuration only, but may be applied to other configurations. The physical understanding of flow/combustion interactions can be also used for active combustion control, as demonstrated for extension of flammability limits as an example.

Large-Scale Structures in Isothermal Shear Layers. In order to explore the role of vortex dynamics in driving of dump combustor instabilities, it is necessary to consider the role of organized vortices in shear-layer dynamics. This approach was initiated by the discovery of large-scale structures by Brown and Roshko[9] and has been reviewed by Ho and Huerre.[10] Based on laboratory low-Reynolds number studies of various turbulent flows, it was shown that the shear layer develops instability waves in its initial region. When the amplified waves reach a certain energy level, they roll up into vortices (Figure 3). The initial vortex shedding frequency, f_i, which is also called the most amplified frequency, is determined by various characteristics of the exit velocity profile, such as shape, turbulence structure, initial shear-layer momentum thickness, θ_o, and the jet exit velocity U_o. The initial most amplified frequency, when scaled with θ_o, and U_o yields a nondimensional frequency or Strouhal number, $St_i = f_i \theta_o / U_o$ that is predicted to be close to $St_i = 0.017$ by linear instability theory[11] The initial vortices of the shear layer grow and merge as they are convected downstream. Due to merging and entrainment, the shear layer spreads, and the frequency associated with the dominant large vortices decreases. In the shear layer of a jet, several vortex interactions can occur between the initial separation of the shear layer and the end of the jet's potential core. Therefore, the shear layer is characterized by several instability frequencies associated with different sizes of vortices.
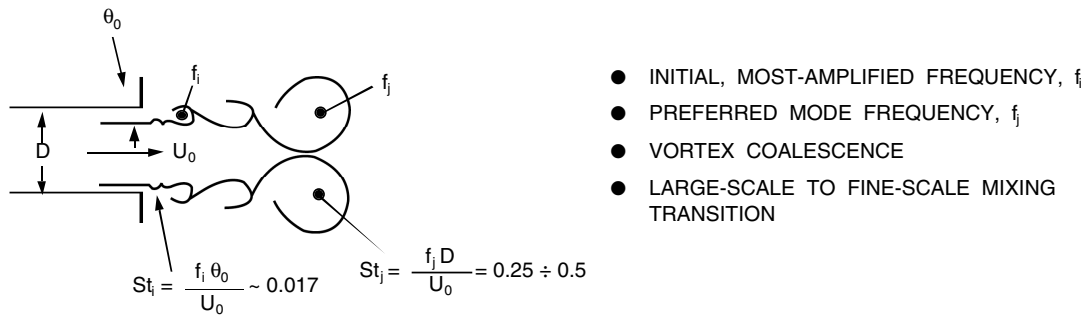
Figure 3. Development of Large-Scale Structures in Jet Shear Layers.

The region at the end of the potential core is governed by the jet-column instability.[12] The velocity fluctuations in this region were observed to have a characteristic frequency, called the preferred-mode frequency, f_j, which is typically in the second or third sub-harmonic range of the initial shear-layer instability frequency. Because the coherence of the large-scale structures has decreased, the preferred-mode frequency is indicated by a characteristic energy hump in the velocity fluctuation spectra as compared to a distinct peak in the initial shear layer and the $-5/3$ slope in the inertial sub-range (Figure 4). The jet preferred frequency scales with the jet exit diameter, D, and exit velocity, U_o, to yield the preferred-mode Strouhal number of $St_j = f_j \cdot D/U_o$. The range of St_j was found in previous investigations to be between 0.25 and 0.5.[13]

When acoustic waves interact with the shear layer, the vortex size can be stabilized depending on the matching between the acoustic frequency and the shear-layer instability frequencies. The size of the vortices will be smallest when the acoustic frequency equals the initial vortex shedding frequency; it will be largest when the acoustic frequency is near the preferred-mode frequency. Significant large-scale mixing enhancement can be obtained at the preferred-mode forcing frequency. If the acoustic frequency is much lower than that of the initial shear-layer instability, collective interaction occurs as the initially shed vortices roll-up into a single large vortex.[14]

To generate coherent structures at the end of the potential core of an axisymmetric jet, the acoustic frequency has to match the preferred-mode frequency. This is illustrated in Figure 5, describing experiments in which turbulent fluctuations were measured with hot-wire anemometry near the end of the potential core of a free jet.[15] The preferred-mode frequency was identified from the maxima in the turbulent velocity fluctuations spectra as shown for the unforced (UNF) case with $U_o = 71$ m/sec yielding $f_j = 340$ Hz with a corresponding nondimensional frequency of $St_j = 0.30$. In a second test with low-amplitude forcing at $f_F = 190$ Hz and $U_o = 50$ m/sec, the turbulence spectra from the potential core showed, in addition to the f_j-maxima at 270 Hz, a distinct second peak at the forcing frequency (dotted line). For this test condition, a mismatch between f_F and f_j existed. When U_o was further reduced to 35 m/s, f_j was reduced to 190 Hz, and a match between f_F and f_j was obtained, resulting in one high-energy peak at $f_F = f_j$. The high Ev peak indicates that as a result of matching between the natural flow instability frequency near the end of the potential core, f_j, and the acoustic forcing frequency, f_F, highly coherent, large-scale structures were

generated. The flow structures were shown to have high azimuthal coherence and high spatial and temporal periodicity near the dump using hot-wire anemometry; however their coherence was reduced while convected downstream, which was also visualized in water tunnel experiments (Figure 6).[16] Forcing at the preferred-mode frequency generates the most energetic coherent structure and therefore changes the shear-flow characteristics most effectively. Forcing at higher frequencies produces smaller coherent vortices, which are less amplified by the flow instability and consequently less effective in modifying the shear layer spreading rate.
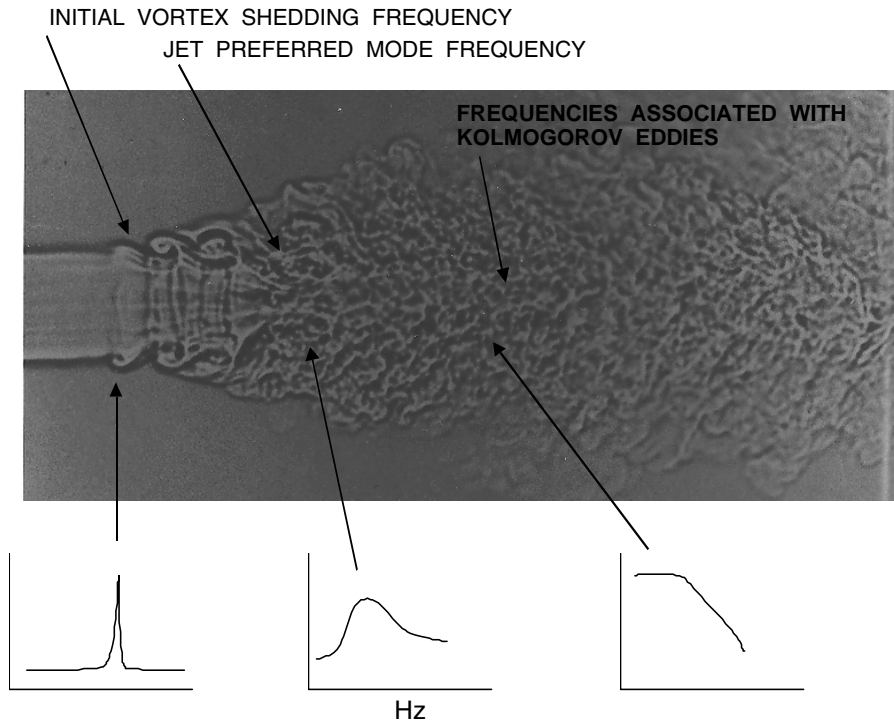
Figure 4. Jet Flow Instability Frequencies.
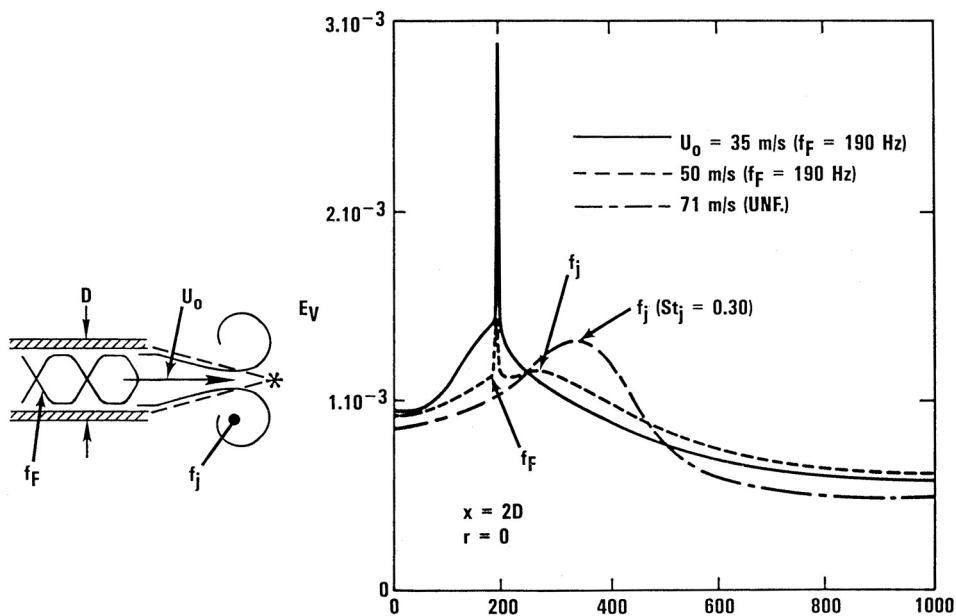
Figure 5. Development of Coherent Structures by Matching Jet Preferred Mode Frequency and Acoustic Forcing Frequency.
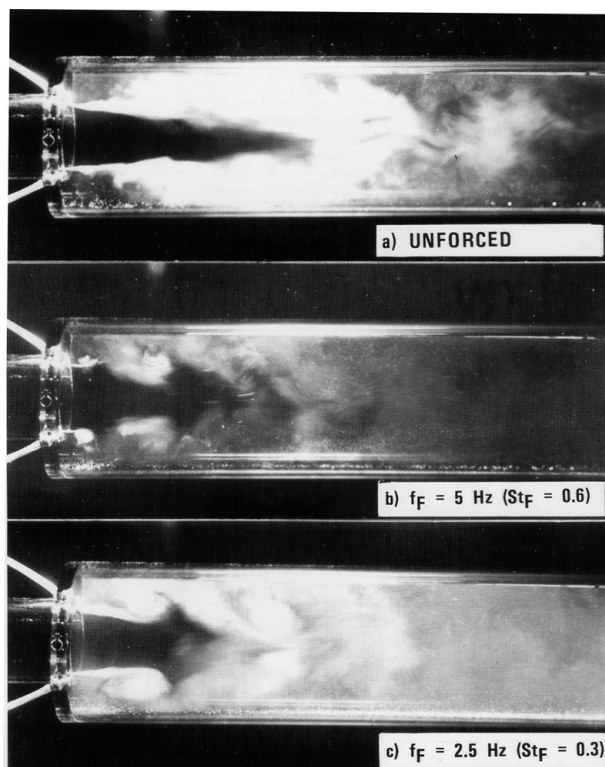
Figure 6. Water Flow Visualization of Unforced and Forced Ducted Jets.

The critical role of large-scale, coherent structures in combustion processes and in driving pressure oscillations will be discussed in the following.

Large-Scale Structures in Reacting Shear Layer. Experiments in annular diffusion flames provided insight into the effect of the vortex dynamics on combustion using an XeCl eximer laser and a diode array camera for Planar Laser Induced Fluorescence (PLIF) imaging of OH.[17,18] To stabilize vortices in the flame, the air flow was excited using a loudspeaker located in the plenum chamber. An instantaneous picture (7 nsec) of the flame acoustically excited at the preferred mode of the air jet (St = 0.44) is shown in Figure 7. The difference in black/white tones indicate different intensities of OH-fluorescence, which in this flame indicate the location of the reaction zone. It may be seen that the flame consisted of large-scale structures, similar to those observed in non-reacting shear flows. The combustion was initiated (highest OH levels) at the circumference of large-scale structures, where secondary streamwise small-scale eddies are growing, initiating the process of transition to fully turbulent flow. The braids connecting adjacent vortices had low OH levels as a result of local quenching due to high straining rates in these regions. The vortices were convected downstream, and the combustion reached the vortex core (Figure 8). From these experiments it is clear that the combustion is related to the flow structures generated by acoustic forcing in the shear layer. Due to the fluid dynamic/combustion interaction, the heat release was periodic and pockets of high-temperature flow were convected downstream from the burner exit.

The PLIF visualization tests were also done in the coaxial dump combustor.[18] These tests, at conditions which led to high amplitude pressure oscillations, confirmed that, even at realistic combustor conditions, the combustion oscillations were associated with periodic flow structures generated through interaction between flow instabilities and chamber acoustics (Figure 9).

Measurements with ionization probes in the same combustor also showed that heat was released periodically due to the convecting vortices.[17] In addition, these tests showed the role of the non-reacting preferred mode (flow) instability in determining which of the combustor acoustic mode was excited.
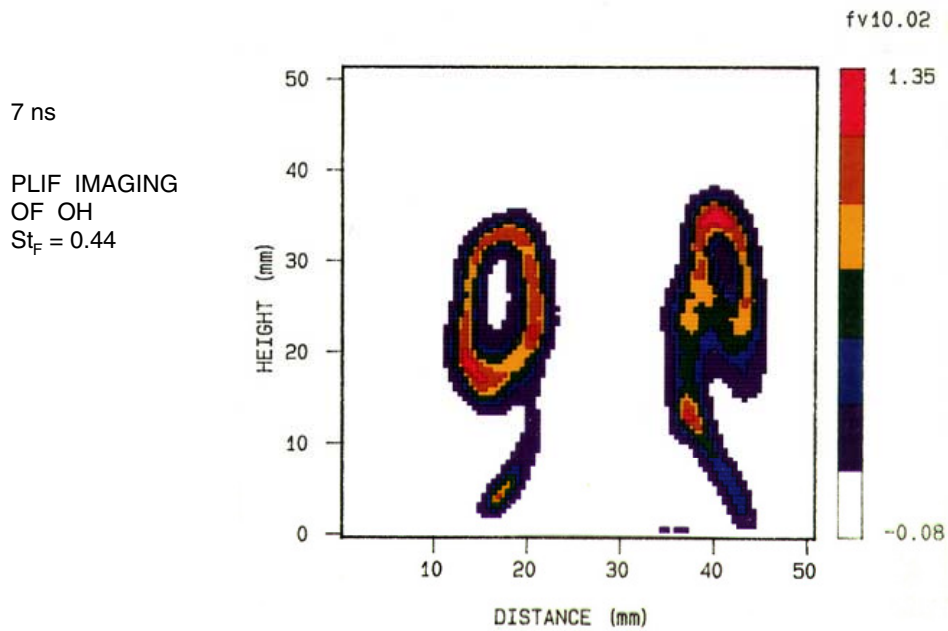
Figure 7. PLIF Imaging of Forced Diffusion Flame.
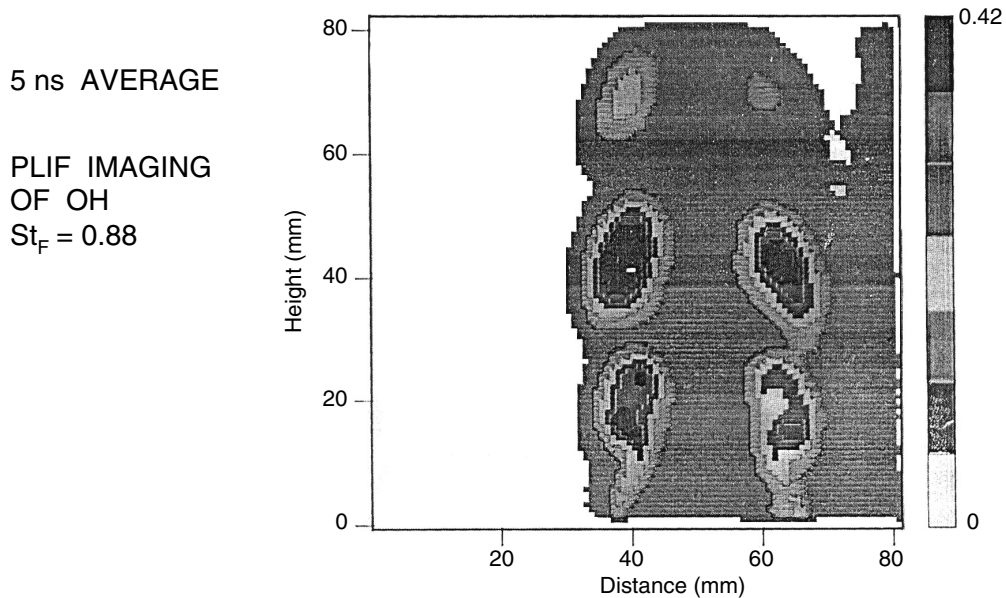
Figure 8. Vortex Dynamics in Forced Diffusion Flame.

Combustor tests were made to determine the acoustic frequency and mode for varying preferred-mode frequencies. For example, for U_o = 38 m/s a preferred-mode frequency of fj = 148 Hz was determined in non-reacting tests (Figure 10). The Strouhal number corresponding to this frequency is 0.25. This value is within the range of preferred-mode Strouhal numbers in jets. In the combustion test with the same U_o, the acoustic bulk mode near the flow instability was excited[17] (Figure 10).

Figure 11 identifies the strongest pressure frequency peaks in the power spectra for a wide range of flow conditions.[19] A Strouhal number of 0.3 appears to provide a good correlation between the observed pressure instability frequencies and the frequency of the flow instability calculated on the basis of a constant Strouhal number. The amplitude of pressure is substantially amplified when the fluid dynamic frequency (or jet preferred-mode frequency) is equal or near the bulk-mode or acoustic frequency of the combustor.

LIMITED FINE-SCALE MIXING (QUENCHING)
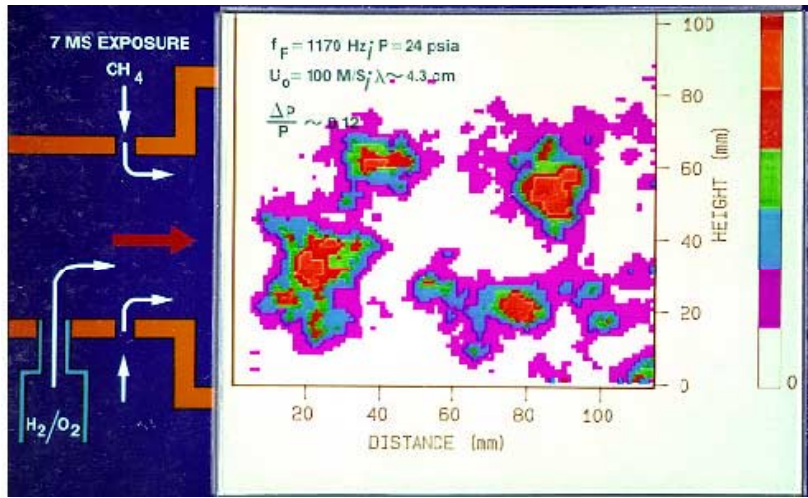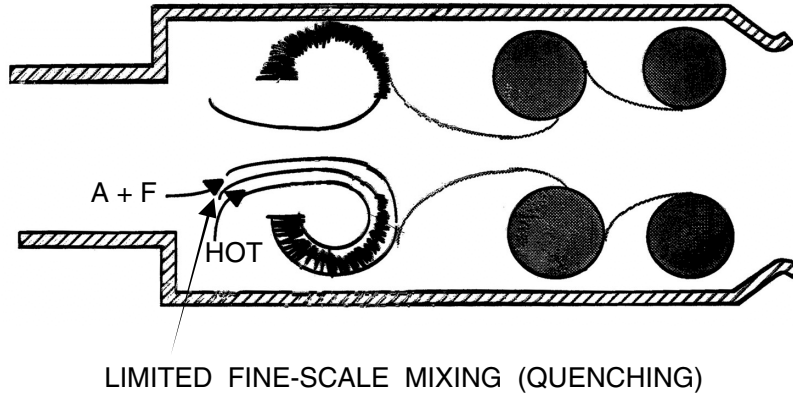
Figure 9. Vortex Combustion in the Presence of Combustion Instability in Dump Combustor.
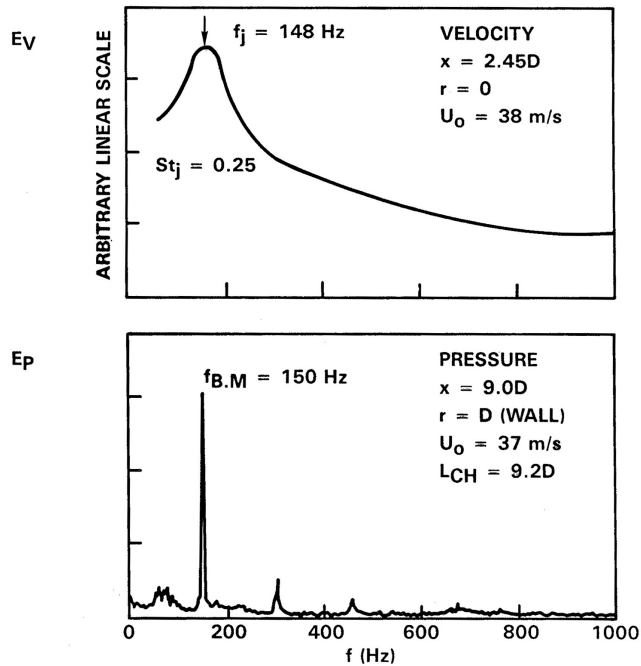
Figure 10. Excitation of Acoustic Combustion Instability by Jet Preferred Mode Instability.
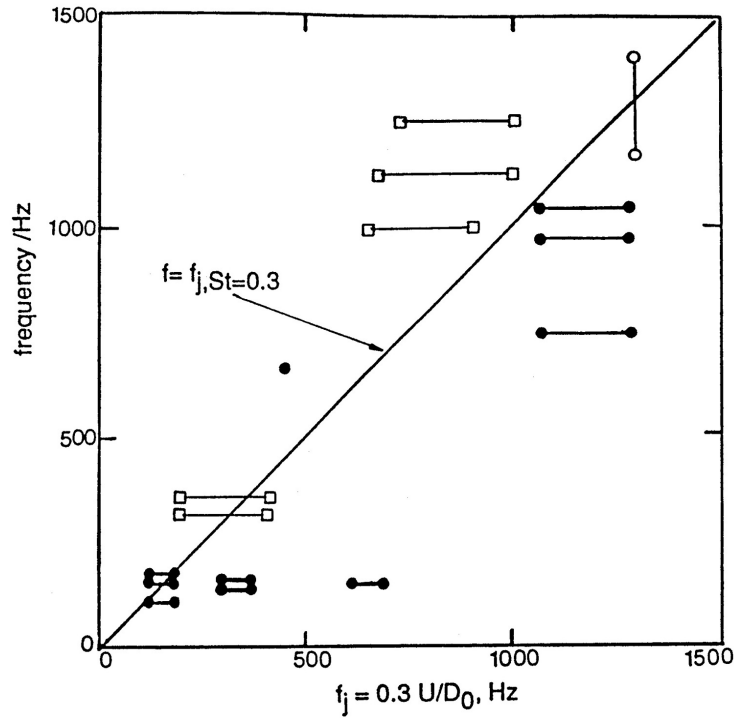
Figure 11. Relationship between Jet Preferred Mode Frequency and Combustion Instability Frequency.

Ionization probes were used to determine the effect of the pressure oscillation on the temperature fluctuations in the shear layer of the jet issuing from the dump. The temperature spectrum measured by the ionization probe at the tip of the jet's potential core was similar to the pressure spectrum (Figure 12). Cross-correlations of two ionization-probe signals showed that the temperature fluctuations were convected at the convection speed of burning vortices past the ionization probes (Figure 13). These experiments confirm that vortices generated at the acoustic frequency during the combustion process were releasing heat periodically while being convected in the downstream direction.
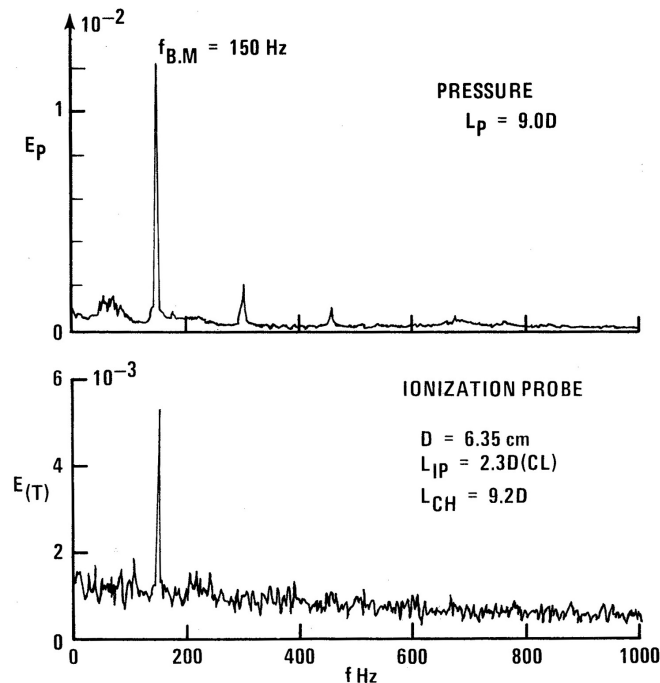
Figure 12. Pressure and Temperature (Ionization Probe) Spectra during Combustion Instability.
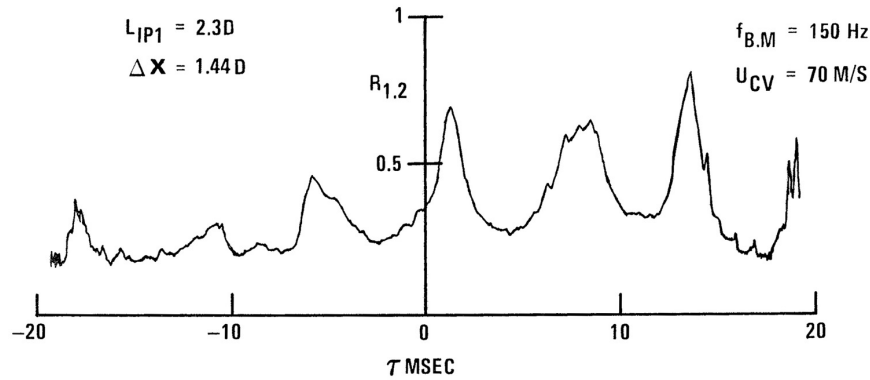
Figure 13. Cross-Correlation of Temperature Signals Indicating Convection of Vortices.

Driving Mechanism. The preceding results suggest that a combustor flow, which is dominated by vortex flow in the flameholding region, is associated with periodic heat release. If the heat release is in phase with the pressure oscillations, driving occurs as stated by the Rayleigh criterion. To determine if the periodic heat release is a driving force, it is necessary to have a complete knowledge of the spatial and temporal distributions of heat release and acoustic pressure. These measurements were performed in the Caltech dump combustor using pressure transducer and radiation intensity measurements.[20.21] By taking the cross spectrum and phase of the pressure and radiation intensity at a given location in the combustion chamber, the relative magnitude of the driving at that location can be determined. For the example in Figure 14, the driving occurs primarily at the front of the combustor.[20] Damping occurs further downstream. The net value of the integral of the curve determines if driving (positive net value) or damping (negative net value) occurs. The net value will change if combustor parameters which determine the heat release and pressure distributions are varied. The heat release depends on fluid dynamic mixing and chemical reaction and is therefore affected by dump geometry, initial condition of the shear layer, fuel type, and local equivalence ratio, while the pressure distribution depends on the dominant acoustic mode, which is excited during the combustion instability.
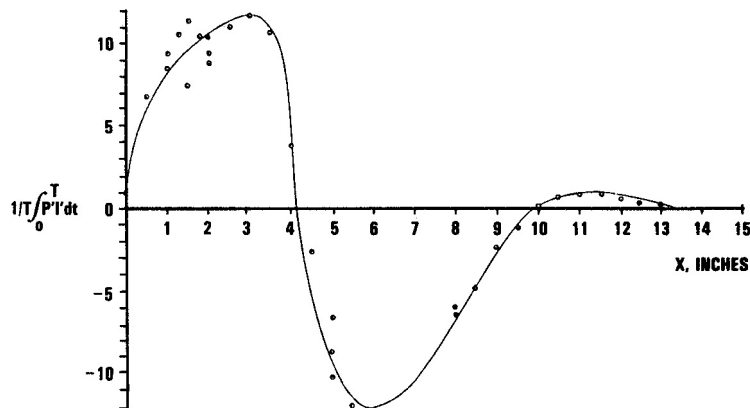
Figure 14. Rayleigh's Criterion for Dump Combustor Instabilities.

Passive Control. The physical understanding of the driving process suggests possible methods for controlling the oscillations in unstable combustion. Several passive methods are available, including driving the periodic heat release and the acoustic pressure oscillations out of phase with each other using Rayleigh criterion or designs, which provide a mismatch between acoustics resonant frequencies of different sections of the combustor and a mismatch of these acoustic frequencies with the jet preferred mode frequency. In this lecture the discussions of passive control will focus on geometric changes at the dump to manipulate the shear-flow development and minimize vortex coherence. Non-reacting and reacting shear-flow dynamics of nozzles with corners (triangular nozzle) and downstream-facing steps (multi-step nozzle) were investigated.[22,23]

The experimental methods included (1) hot-wire anemometry to compare fluctuating velocities for circular, triangular and multi-step nozzles, the latter having three downstream facing steps with varying length-to-step height ratios from L/H = 3.5 to 7.0 and 10, (2) visualization in a water tunnel to compare the flow characteristics, (3) annular diffusion flame experiments with propane injection from the lip of the nozzles into the developing shear flows using PLIF imaging of in situ OH-radicals, and (4) experiments with a laboratory coaxial dump combustor to compare the amplitude of combustion-induced pressure oscillations for a standard sudden dump configuration with a combustor with a multi-step dump (Figure 15) and a triangular air inlet (Figure 16).
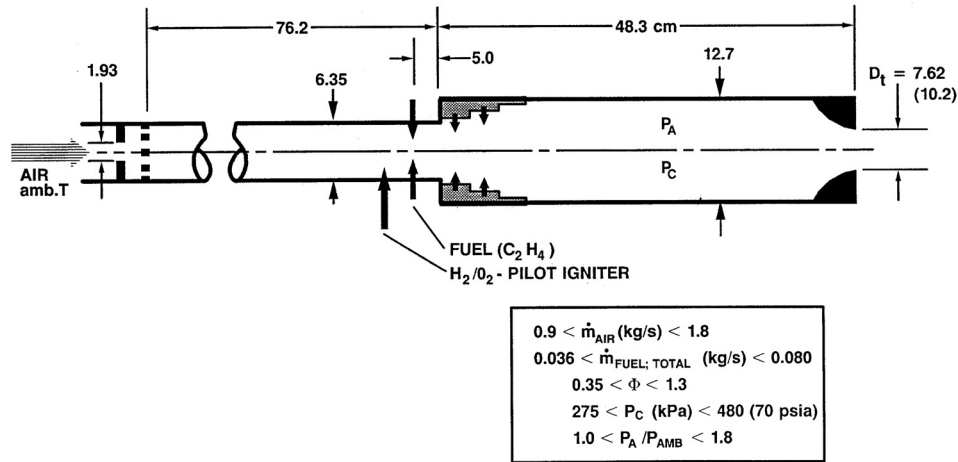
Figure 15. Combustor with Fuel Injection from Multi-Step Dump.
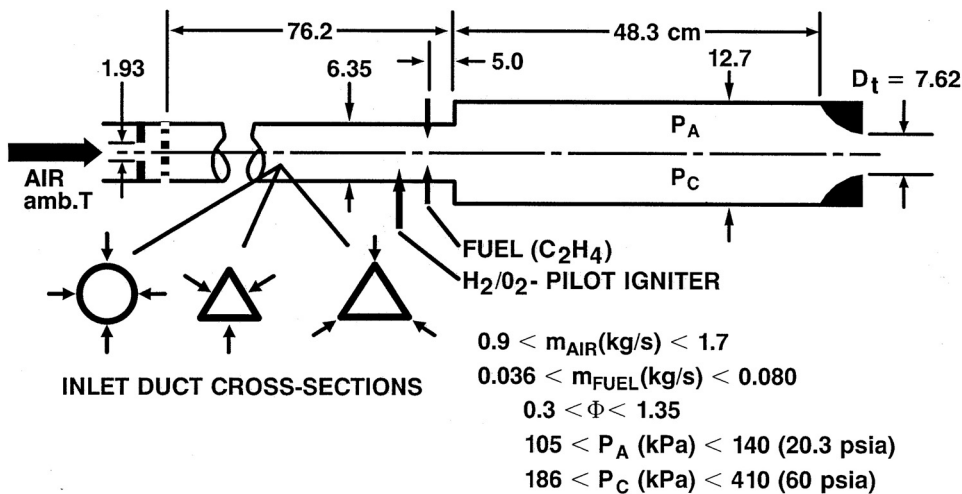
Figure 16. Combustor with Fuel Injection from Circular and Triangular Inlet Ducts.

With the multi-step nozzle, the turbulent intensity was significantly enhanced compared to the circular nozzle as visualized in water tunnel tests. The turbulence enhancement was maximized at (L/H) = 7 at which reattachment of the separated boundary layers occurred near the downstream end of the steps. The flow did not develop large-scale flow structures, even when it was forced with a butterfly valve at a velocity fluctuation amplitude of 3% of the mean velocity, which was $U_o = 0.5$ m/s. The excitation frequency was $f_F = 2.5$ Hz. At (L/H) = 3, the flow separated without reattachment at the first step and the turbulence intensity in the jet core at the nozzle exit became similar to the pipe flow without steps. At (L/H) = 10, the flow was restabilized after flow reattachment, and the turbulence intensity was again lower than at (L/H) = 7.

The observations in the water tunnel tests were quantified in the air-flow experiments (Figure 17). At the nozzle exit the turbulence intensity of the multi-step nozzle with (L/H) = 7 was increased by a factor of 5 compared to the circular jet. Because of the high turbulence the multi-step exit flow did not develop shear layers as in the circular nozzle, thus preventing the growth of large-scale coherent structures. The turbulence intensity was significantly lower for (L/H) = 3.5 and (L/H) = 10.

- ● ENHANCEMENT OF SMALL-SCALE TURBULENCE
  (OR ELIMINATION OF LARGE-SCALE VORTICES) BY
  MULTIPLE SEPARATING/REATTACHING FLOW REGIONS
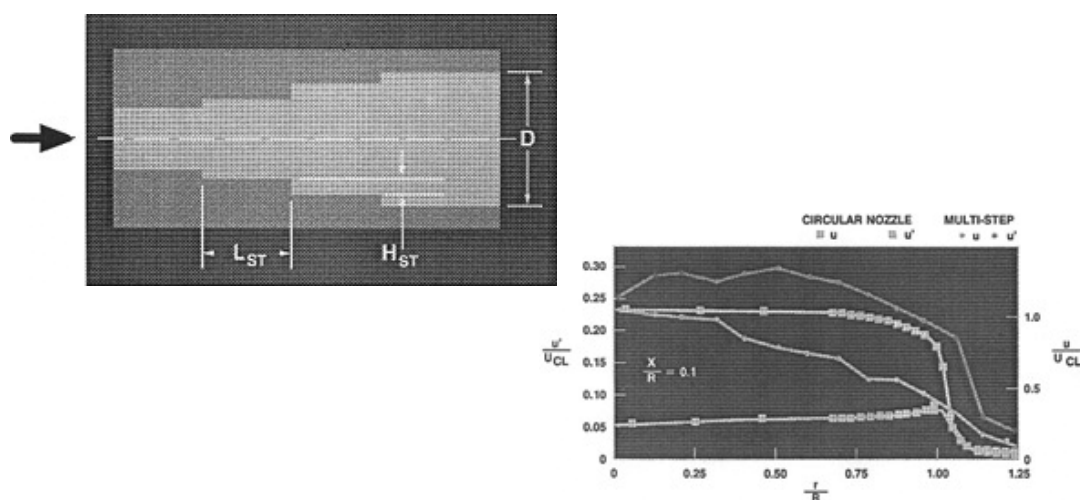
Figure 17. Fine-Scale Turbulence Enhancement in Multi-Step Nozzle.

The fine-scale turbulence augmentation or prevention of large-scale structure development with multiple steps had a strong effect on the flame stability and intensity of the diffusion-flame burner (Figure 18). In the circular burner combustion was limited to the shear layer and traces of large-scale structures were observed. In the multi-step burner, the flame spread into the jet core, and development of large-scale structures was avoided.

With the multi-step dump, pressure oscillations were reduced below $\Delta P_{RMS}/P_C = 0.10$ (Fig. 19) with $\Delta P_{RMS}/P_C$ the root-mean-square pressure amplitude normalized by the combustor pressure. The lean flame blow-out limit was slightly extended to lower equivalence ratios v's with the multi-step dump relative to the sudden dump; however, rich flame blow-out occurred at a lower equivalence ratio for the multi-step dump $(0.8 < \phi < 0.9)$ than for the sudden dump $(\phi > 1.3)$. The combustion efficiency with the multi-step dump was higher than with the sudden dump (Figure 20).

To obtain suppression over a wide range of equivalence ratio, the distribution of fuel injection into the flow over the steps is critical. It has to be distributed along the steps so that it is mixed into the fine-scale turbulence downstream of each step.

With the triangular jet, different shear-flow behaviors were observed on the corner and flat-side as evident in the mean and fluctuating velocity measurements. Iso-kinetic contours for the equilateral triangular jet are shown in Figure 21 for the four axial locations at x/D_e = 0.1, 0.4, 1.0, and 2.0 with D_e the equivalent diameter of the triangle (same area as circular nozzle). The initial momentum thickness at the corner (vertex) side was significantly larger than at the flat side as indicated by the contour for 0.5 U_{CL} (velocity at 50% of the centerline velocity) at the nozzle exit at x/D_e = 0.1 (shape switching). The momentum thickness difference produced a substantial difference in spreading rates on both sides resulting in a quasi-axisymmetric jet shape at about 5 D_e. The initial turbulence level at the corner was nearly 20% of the mean velocity and about four times higher than at the flat side (Figure 22). The turbulence grew by a factor of four between $0.1 < x/D_e < 7$ at the flat side, however remained almost constant at the corner side. The turbulence growth at the flat side is typical to disturbance amplification pattern of a regular shear layer, through the process of vortex shedding and vortex interaction, which makes this side more receptive to forcing. On the

other hand, the high initial turbulence level at the corner side indicates the highly three-dimensional, incoherent structure of the corner flow, which changes the amplification characteristics of the shear layer and makes it less receptive to forcing.

UNFORCED
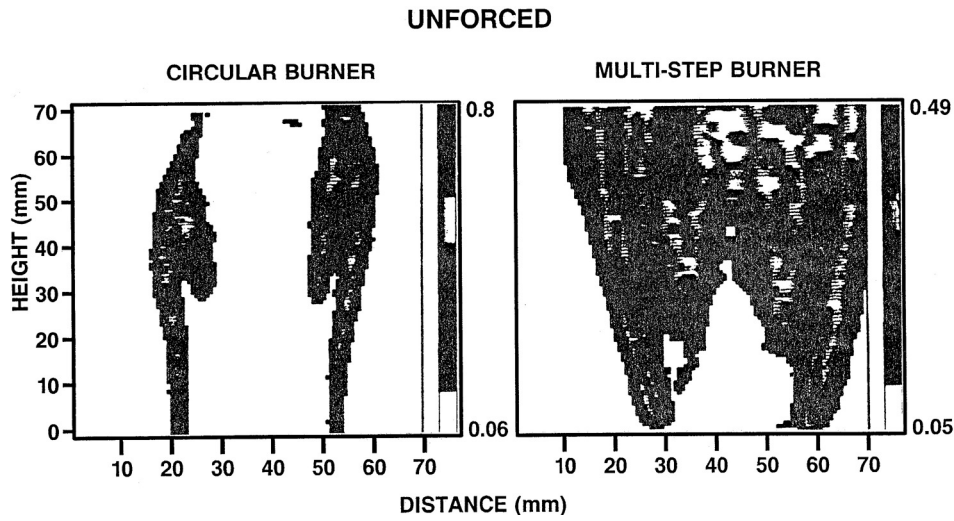
Figure 18. Combustion Enhancement in Multi-Step Burner.
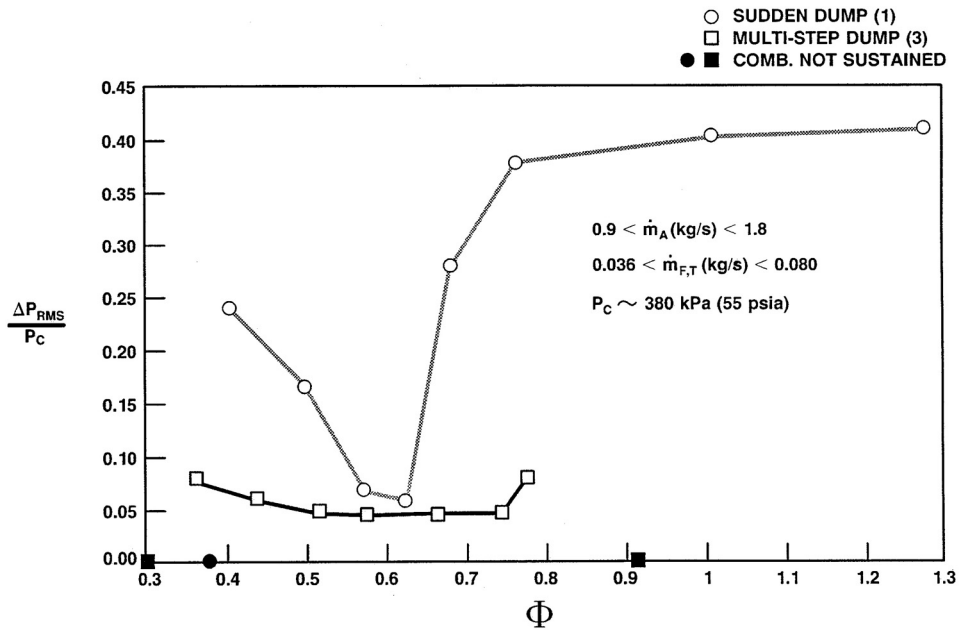
Figure 19. Reduction of Combustion Instability Amplitude with Multi-Step Dump.

The shape switching in the initial region of the triangular jet and the resulting turbulence amplification characteristics yield a special combination of mixing pattern. At the flat side the large spreading rate results in an intense bulk mixing while the intense turbulence at the vertices contribute to the fine-scale mixing process. This coexistence of large and fine scale in the same flow is a unique property of the triangular jet.
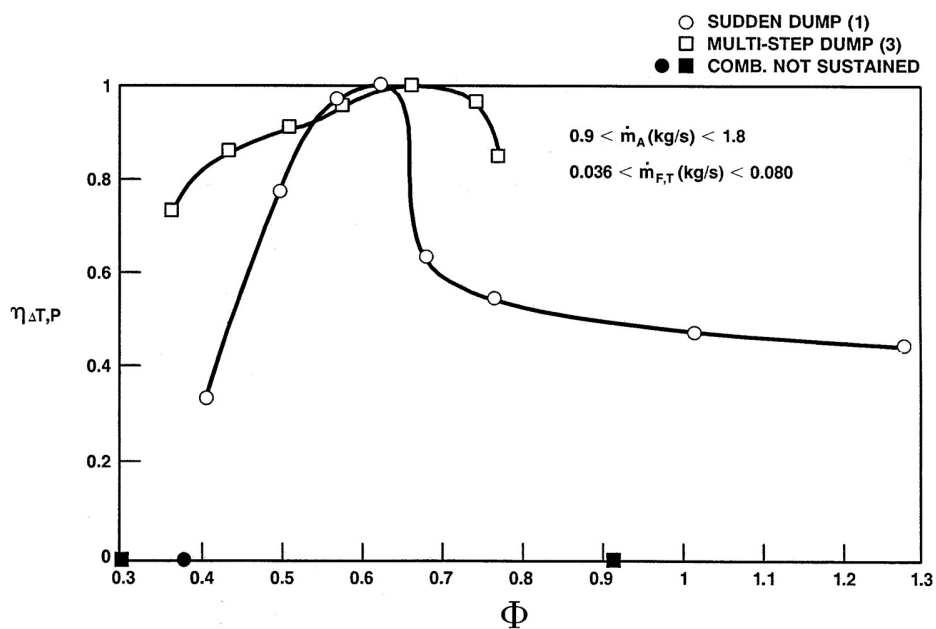
Figure 20. Combustion Efficiency Enhancement with Multi-Step Dump.
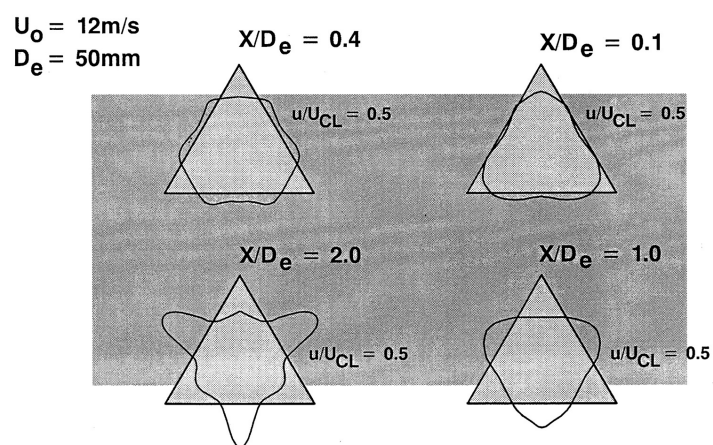
Figure 21. Mean Velocity Contours for Triangular Jet.
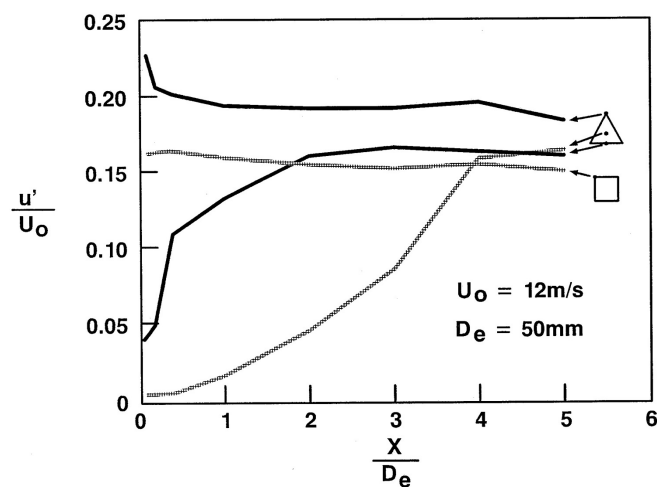
Figure 22. Comparison of Turbulence Intensity in Corner Flow and on Flat Side Shear Layer of Triangular Jet.

The effect of forcing on the corner and flat side of the triangular jet was studied in the water flow tunnel (Figure 23). When the jet was forced near the preferred mode frequency, the asymmetric development along the two sides was visualized. The shear layer shed from the flat side was much thinner than the shear layer emanating from the jet corner. The flat-side shear layer rolled up into organized structures, while the flow coming out at the triangle's corner was highly turbulent and had no sign of coherent motion even under forcing. The tests suggest that corner fuel injection is beneficial to initiate combustion because it will be efficient (high degree of fine-scale or molecular mixing) and periodic heat release can be avoided (absence of coherent flow structures).

The combustion characteristics of the triangular jet during preferred-mode forcing showed that the combustion at the flat side (left flame side) was dominated by reacting vortical structures and that combustion at the corner (right flame side) was initiated at the nozzle exit and was incoherent making the corner the preferred fuel injection location for efficient, periodicity-free combustion (Figure 24).
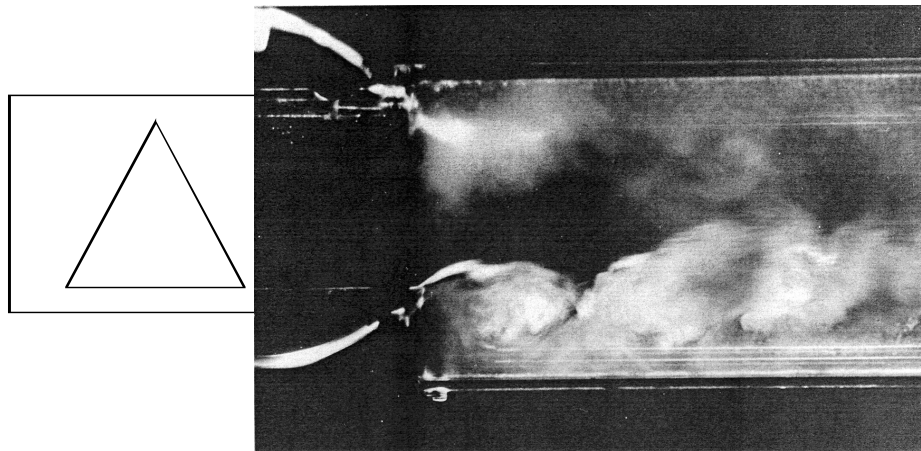
Figure 23. Water Flow Visualization of Forced Triangular Jet.

7 ns EXPOSURE

PLIF IMAGING
OF OH
$f_F = 100$ Hz
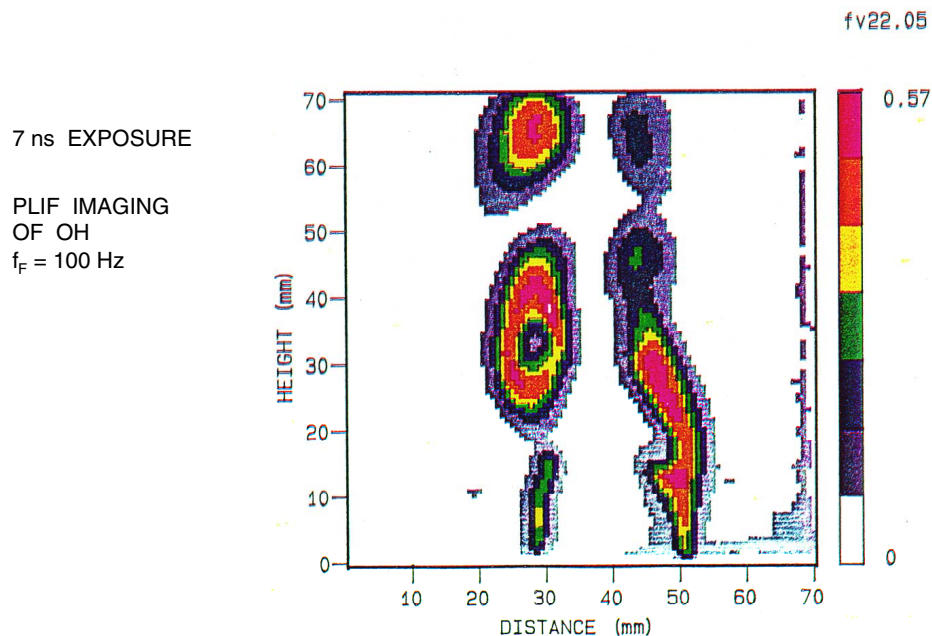
Figure 24. Flame Characteristics in Corner Flow and Flat Side Shear Layer of Forced Triangular Diffusion Flame.

Combustion-induced pressure oscillations were compared for the triangular and circular inlet ducts. Figure 25 shows a comparison of the triangular inlet duct with the circular inlet duct. For the circular inlet, the pressure amplitude increased from $\Delta P_{RMS}/P_c = 0.12$ at $\phi = 0.65$ to $\Delta P_{RMS}/P_c = 0.30$ near the lean

blow-out limit of $\phi = 0.45$ and to $\Delta P_{RMS}/P_C = 0.37$ with ϕ approaching one. The circular-duct pressure amplitude was significantly higher than with corner injection. In these tests the pressure amplitude is dependent on fuel injector orientation relative to the airstream and injector-depth position. The best results were achieved with fuel injection in-line with the airstream to achieve good mixing with the fuel and the turbulent corner flow.

The suppression of the pressure oscillations with the triangular inlet duct was obtained in the majority of the tests with an increase in combustion efficiency (Figure 26).
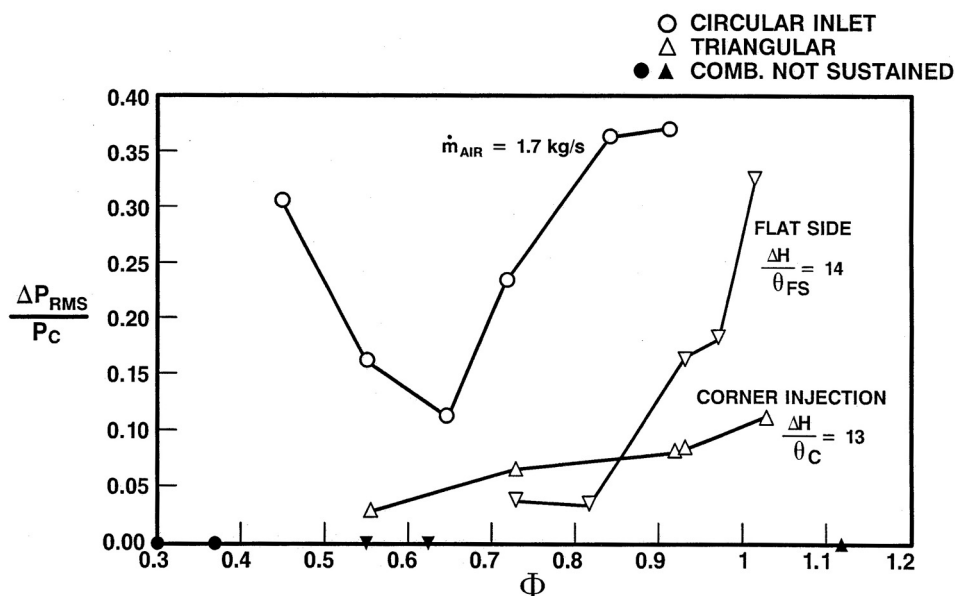
Figure 25. Combustion Efficiency Amplitude Reduction with Fuel Injection into Corner Flow of Triangular Inlet Duct.
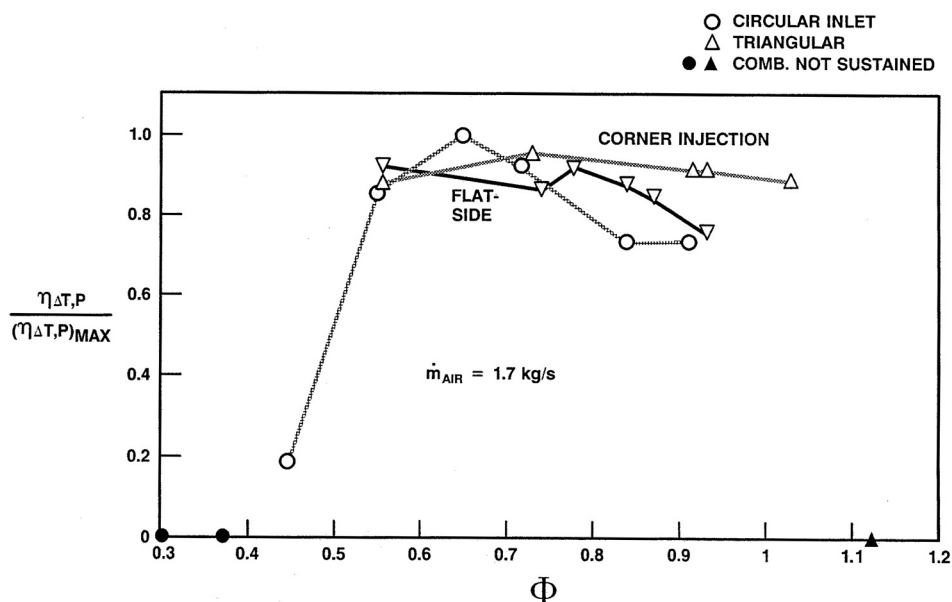
Figure 26. Combustion Efficiency Enhancement with Corner Fuel Injection from Triangular Inlet.

In the previous discussions it was shown that the detailed understanding of shear-flow dynamics can be used to passively control combustion dynamics. The same physical understanding can also be used to obtain the combustion improvements through active control, for example to enhance combustion stability and

extend lean blow-out limits. For passive control multi-step nozzles were used to enhance fine-scale mixing. For active control, discussed in the following, shear-layer excitation at the right frequencies, will be explored.

Related Active Control Experiments. A propane/air premixed circular flame was actively controlled in order to extend the lean blow-out limit.[24] The flame could be excited by a set of four speakers mounted in an acoustic resonant chamber (Figure 27). The speakers were driven at controlled frequencies and amplitudes using a dual phase locked loop and audio power amplifier. The PLIF laser system was phase locked to acoustic excitation of the flame jet so that the flame structure at a specific phase relative to the forcing could be determined. The forcing frequencies, amplitudes, and relative phase angles were monitored (in cold flow) by using a calibrated hot-wire anemometer which was also used to measure the mean and turbulent velocities of the air.
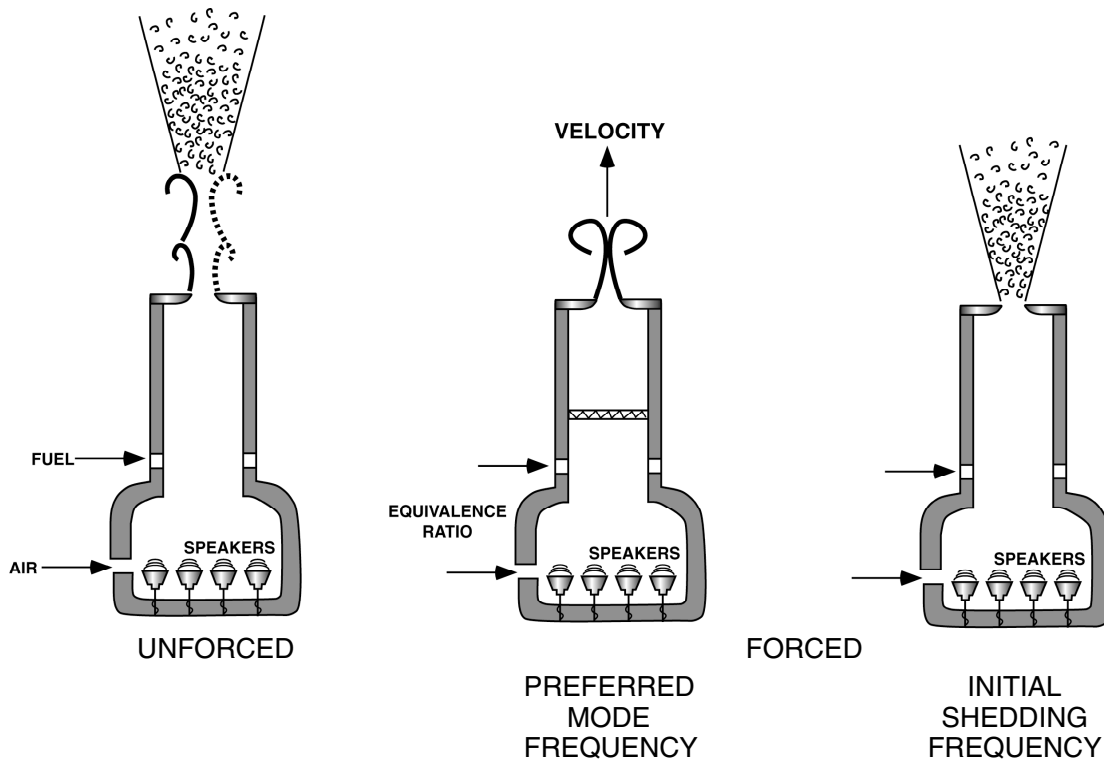
Figure 27. Forced Premixed Flame for Extension of Flammability Limits.

The lean stability limit of the flame was studied in a range of equivalence ratio from 0.6 to 1.6. The fuel flow rate was kept constant, at different values in this range, and the air flow rate was increased gradually to obtain a stable lift-off, followed by blow-out.

When the jet was forced near the preferred jet frequency of $St = 0.48$ and at a forcing level of 13% of the mean velocity, coherent structures dominated the flow. The flameholding location jumped from one vortex to the other according to the evolution phase of the vortices. As a result of this unstable behavior, the lean flammability limit remained almost unaffected by the preferred mode forcing. Subsequently the forcing frequency was increased, thus generating smaller vortices. In the higher frequency range the most effective forcing was within the amplification range of the initial jet shear layer. At this forcing frequency, the flame structure was changing with the increased forcing level as shown in the phase-average OH-images in Figure 28. A small forcing amount of 0.7% was sufficient to cause the lifted-off flame to reattach to the flameholder (Figure 28b). The combustion in the vortices became more apparent in the high forcing level of 11% and 19% as shown in the instantaneous images in Figures 28c and 28d.
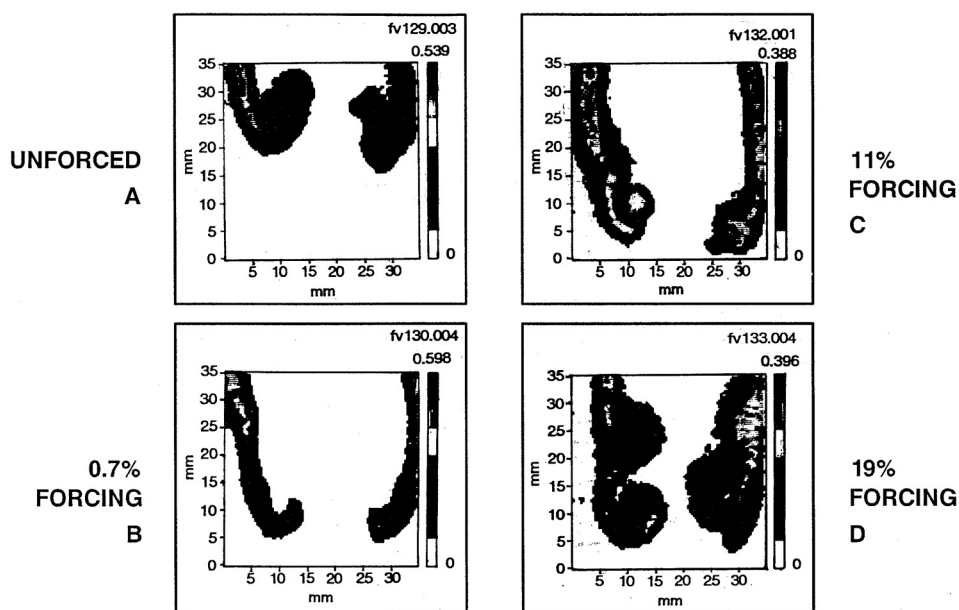
Figure 28. Instantaneous (18 nsec) PLIF Images of Forced Premixed Flame.

Figure 29 shows the effect of forcing at the initial jet shear layer instability on lean blow-out extension in comparison to preferred-mode forcing. Different frequencies in this initially unstable range were tested and all forcing frequencies in that range extended the flammability limit to lower equivalence ratios. The most effective forcing, however, was at a Strouhal number of $St_\theta \approx 0.02$ (Figure 30) which is close to the most amplified instability frequency.
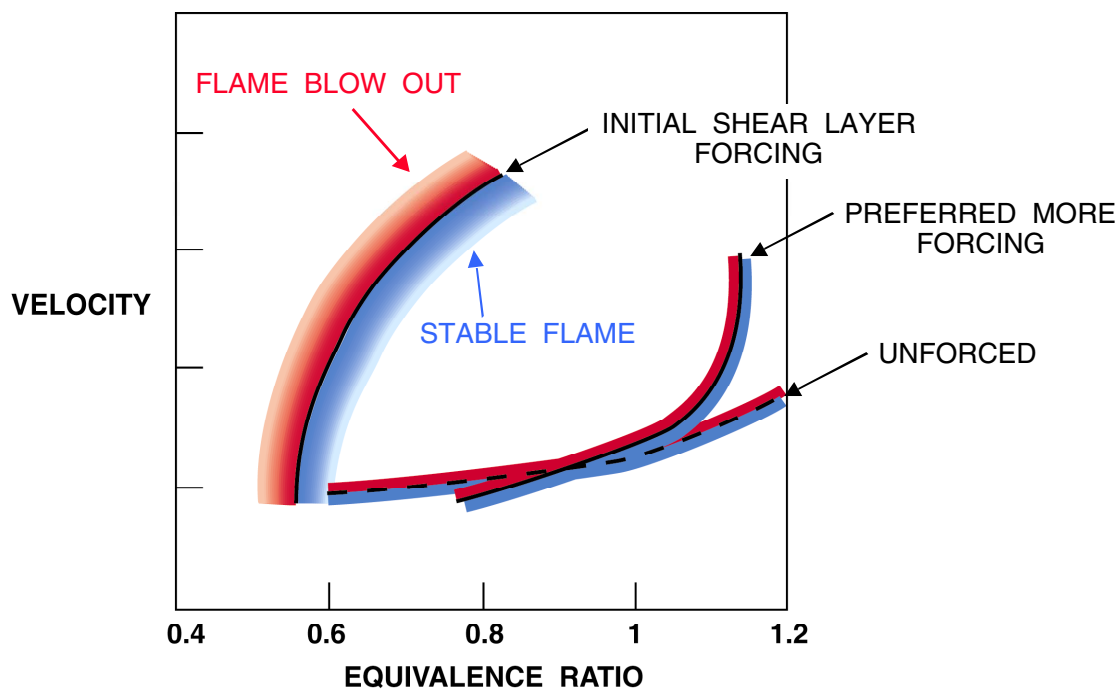
Figure 29. Flammability Extension in Forced Premixed Flame.
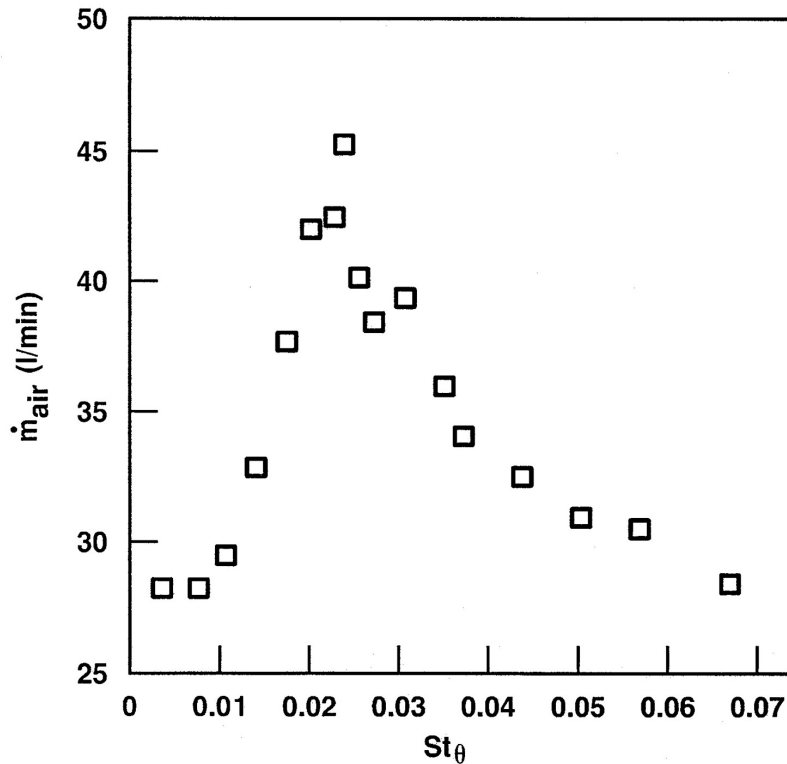
Figure 30. Optimal Flammability Extension with Forcing at Initial Most
Amplified Shear Layer Instability Frequency.

Conclusions. Combustion instabilities related to an axisymmetric dump combustor were studied. The experiments showed that the instability was associated with the formation of large-scale vortices in the mixing layer, which coupled with the acoustic pressure to excite strong oscillations.

Cold flow tests showed that the roll-up of vortices is related to initial instabilities in the separating shear layer behind the dump. The frequency of this instability scales with a typical length scale, which can be either the initial thickness of the shear layer or the jet inlet diameter, and the flow velocity.

When the flow is forced by either the upstream or downstream duct resonant acoustic modes or by an external source, vortices can be generated at a much larger scale relative to the initial instability. Since the acoustic emission of the non-reacting vortices is low, there was no detectable feedback between the flow and the acoustic pressure in the chamber in the non-reacting tests.

In reacting mixing layers the large periodic energy release associated with the burning inside the vortices provides the link for the necessary feedback loop to drive oscillations. The mixing layer rolls up into vortices with enhanced reaction. The energy release, which is periodic in nature, reaches a maximum when the vortices break down to small-scale turbulence. The fluctuating heat release can feed energy into the acoustic pressure oscillations provided that the two are in phase with each other, as stated by the Rayleigh criterion. As the pressure oscillations are amplified, they drive velocity oscillation at the mixing layer, which further enhance the generation of coherent vortices in the shear layer.

There can be other mechanisms that may lead to periodic heat release such as vortex interaction, vortex impingement or collision with each other or on a solid surface, and vortex merging.

The understanding of this process suggests possible passive methods for controlling the oscillations in unstable combustion. The methods described are based on geometrical changes in the design of the combustor to hamper the evolution of large-scale structures and promote production of small-scale turbulence, thus maintaining a uniform rather than pulsating combustion process. The multi-step and triangular nozzles showed a certain success in suppressing combustion instabilities but they require careful design of the fuel injection system to take full advantage of these methods.

The physical understanding of the flow/combustion interactions was also used to extend lean blow-out limit of a premixed flame by acoustic forcing at the initial shear-layer instability frequency.

References

1. W. E. Kaskan, W. E., and Noreen, A. E., *ASME Transactions* **77**, 885-895 (1955).

2. Rogers, D. E., and Marble, F. E., *Jet Propulsion* **26**, 456-462 (1956).

3. Hall, P. H., *AIAA Paper 80-1118* (1980).

4. Schadow, K. C., Crump, J. E., and Blomshield, F. S., *Proceedings of the 18th JANNAF Combustion Meeting*, CPIA Publication No. 347, Vol. III (1981).

5. Byrne, R. W., *Proceedings of the 18th JANNAF Combustion Meeting*, CPIA Publication No. 347 (1981).

6. Byrne, R. W., *AIAA Paper 83-2017* (1983).

7. Schadow, K.C. and Gutmark, E., *Prog. Energy Combustion Sciences*, **18**, 117-132 (1992)

8. Rayleigh, J. W. S., *The Theory of Sound*, Dover Publications, New York, 1945

9. Brown, G. L., and Roshko, A. *Journal of Fluid Mechanics* **64**, 775-816 (1974).

10. Ho, C. M., and Huerre, P., *Annual Review of Fluid Mechanics* **16**, pp. 365-424 (1984).

11. Michalke, A., *Journal of Fluid Mechanics* **23**, 521-544 (1965).

12. Crow, S. C., and Champagne, F. H., *Journal of Fluid Mechanics* **48**, 547-591 (1971).

13. Gutmark, E., and Ho, C. M., *The Physics of Fluids* **26**, 2932-2938 (1983).

14. Ho, C. M., and Nosseir, N. S., *Journal of Fluid Mechanics* **105**, 119-142 (1981).

15. Schadow, K. C., Gutmark, E., Parr, D. M., Mahan, V. A., and Ferrell, G. B., *Journal of Combustion Science and Technology* **54**, 103-116 (1987).

16. Schadow, K. C., Wilson, K. J., and Gutmark, E., *AIAA Journal* **25**, 1164-1170 (1987)

17. Schadow, K. C., Gutmark, E., Parr, T. P., Parr, D. M., and Wilson, K. J., *Combustion Science and Technology* **64**, 167-186 (1989).

18. Gutmark, E., Parr, T. P., Parr, D. M., and Schadow, K. C., *Journal of Heat Transfer* **111**, 148-155 (1989).

19. Gutmark, E., Schadow, K. C., Sivasegaram, S., and Whitelaw, J. H., *Combustion Science and Technology*, **79**, 161-166 (1991)

20. Sterling, J. D., and Zukoski, E. E., *AIAA Paper 87-0220* (1987).

21. Smith, D. A., and Zukoski, E. E., *AIAA Paper 85-1248* (1985).

22. Schadow, K. C., Gutmark, E., Wilson, K. J., and Smith, R. A., *Journal of Propulsion and Power* **6**, 407-411 (1990).

23. Schadow, K. C., Gutmark, E., Wilson, K. J., and Smith, R. A., *Combustion Science and 2Technology*, **73**, 537-553 (1990)

24. Gutmark, E., Parr, T. P., Hanson-Parr, D. M., and Schadow, K. C., *Combustion Science and Technology*, **73**, 521-535 (1990)

This page has been deliberately left blank

_____

Page intentionnellement blanche

Analysis of Compression System Dynamics

James D. Paduano
Gas Turbine Laboratory, 31-213
Massachusetts Institute of Technology
Cambridge, MA 02139, USA

Summary

Modelling of rotating stall and surge dynamics in compression systems is discussed. The primary aim here is to provide a comprehensive set of models for active control applications, as well as a thorough tutorial on advanced modelling methods. The Moore-Greitzer family of models has proven to be the environment best suited to control applications, and so it is the focus of this document. The basic model is derived, and a description of its linear and non-linear behaviour is given. Extensions and variants to the basic model are also provided. These include the Galerkin formulation, which provides the lowest order non-linear description that captures both rotating stall and surge. The state-space formulation provides a more detailed, multi-dimensional framework for both linear and nonlinear control studies. This framework allows extensions to the basic model to be incorporated, including distortion, unsteady loss dynamics, sensor models, and actuator models. These extensions and their impact on the stability behaviour are described.

Nomenclature

A	area of compressor duct, also stall cell amplitude (in Galerkin form)	U	speed of the rotor at mean radius
a	speed of sound	V	plenum volume
b	blade chord length	x	axial position in compressor annulus
B	surge stability parameter (dimensionless ratio of compliance to inertia)	γ	throttle area coefficient, also IGV deflection (function of θ)
D	diagonal transformation matrices	λ	rotor inertia parameter
E	transformation matrix for impedances	μ	rotor + stator inertia parameter
F	Fourier transform matrix	λ	flow coefficient, (*axial velocity*)/U
K_T	throttle loss coefficient	Φ_T	flow coefficient map for throttle
K_B	$= 1/4B^2$	θ	circumferential position in annulus
ℓ	(duct length)/(compressor mean radius), also loss states in unsteady loss model	Θ	non-dimensional velocity potential
		ρ	density
L	loss characteristic (function of ϕ), also dimensional inlet duct length	σ, ω	growth and rotation rate of modal wave
m_C	slope of the compressor characteristic	τ	lag time for unsteady loss development
m_T	slope of throttle characteristic	υ	(*circumferential velocity*)/U
S, T	bookkeeping matrices, state space model	Ψ	non-dimensional pressure rise or drop
t	dimensionless time	ψ	(*pressure*)/($\frac{1}{2}\rho U^2$), static unless specified

Subscripts

a	actuator	t	total (pressure)
b	bleed	T	throttle
c	overall duct (ℓ_c)	u	upstream
C	compressor	n, N	harmonic number in Fourier decomp.
d	downstream	θ	denotes matrix transformation that
j	jet		approximates $\partial/\partial\theta$
p	plenum	$(\bar{\cdot})$	circumferential average
pb	plenum bleed		
r, s	rotor and stator	$(\dot{\cdot})$	time derivative w/respect to t
s, c	sine and cosine parts (in Galerkin)	$(\tilde{\cdot})$	spatial Fourier coefficient (SFC)
ss	steady state		

1 Introduction

This document is organised as follows. In this section, background on compressor phenomenology and past research is provided. This is followed by a derivation of the basic Moore-Greitzer PDEs in Section 2. Section 3 gives a tutorial on the linear and non-linear stability properties implied by the model. Section 4 is devoted to advanced modelling methods, including the Galerkin and state-space formulations. Finally, extensions to the model to incorporate unsteady losses, distortion, sensing, and actuation are discussed.

1.1 Phenomenology of Compressor Behaviour

The operating condition of a compressor is determined by its mass flow as characterized by its 'constant-speed characteristic' or 'map', which shows how the pressure rise of the device changes with mass flow. Figure 1 shows two schematic compressor characteristics: as the mass flow through the compressor is decreased the pressure rise increases. This trend continues until the system goes into either surge or rotating stall. Both of these conditions are disruptions of the steady, symmetric flow of air through the device. Surge is a symmetric, unsteady operating condition involving limit-cycle type oscillation of both pressure rise and mass flow through the entire compression system. Reverse flow and flame-out are often the consequences of surge. Rotating stall, on the other hand, is a severely asymmetric distribution of axial velocity around the annulus of the compressor, taking the form of a wave or 'stall cell', that propagates in the circumferential direction at a fraction of the rotor speed. At rotating stall inception, the mean pressure rise of the compressor drops dramatically, after which it remains relatively fixed. This is sometimes termed 'deep stall', because recovery from the rotating stall condition can be very difficult, sometimes requiring engine restart. Obviously both rotating stall and surge are unacceptable operating conditions in gas turbine compressors. Figure 1 also shows the time history of a compressor experiencing surge (from Weigl, [1]) – note that each surge cycle contains a short period of rotating stall. This time history illustrates the relative time scales of the two events. Rotating stall waves rotate at about half the rotor frequency, while surge cycles are much slower, typically requiring many rotor revolutions to go through one cycle.

The time history in Figure 1 also serves to illustrate our terminology for different time periods in a typical transient into rotating stall or surge. Fully developed rotating stall refers to the large amplitude (50-100% mass flow fluctuations) rotating stall, during which amplitude variations of the perturbations are insignificant. Stall inception is the transient from asymmetric, small perturbation flow conditions to rotating stall, and thus includes large disturbances whose amplitudes change with time.
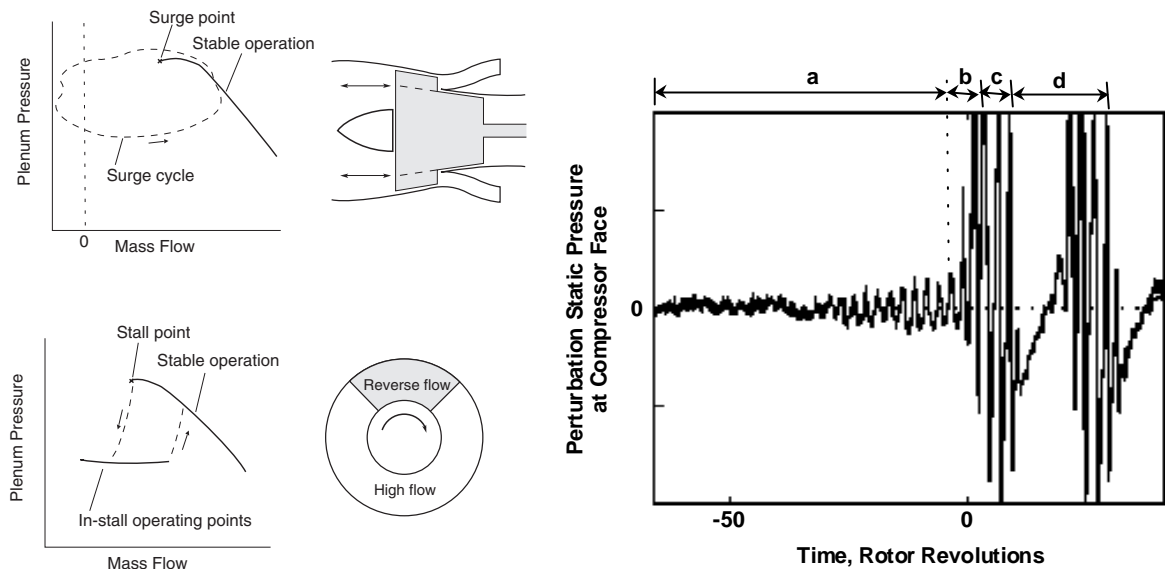
Figure 1 – Phenomenology of rotating stall and surge. In mass flow vs. pressure rise plots, solid lines are steady-state operation of the compressor, dashed lines are transient operation. On time history, regions are as follows: (a) pre-stall, (b)stall inception, (c) fully developed stall, and (d) one full cycle of surge.

Pre-stall refers to the period of time immediately prior to stall inception, during which compressor operation is steady but may exhibit small amplitude (on the order of 1%) dynamics. Perturbations associated with these dynamics are small compared both to stall inception and to fully developed stall perturbations. These three regions – pre-stall, stall inception, and fully developed stall – are difficult to separate precisely; rather the terminology is introduced to facilitate discussion.

The fourth region, simply called surge, is actually one of the most complex and varied conditions of operation. In the example shown (and in many real engines) each surge cycle begins with rotating stall, which causes the pressure rise through the machine to drop dramatically. This catastrophic loss of pumping capability allows the flow through the machine to decelerate rapidly, sometimes reversing. When the pressure behind the compressor has sufficiently relaxed from this 'blow down' event, rotating stall clears and the compressor begins to pump the downstream collector (combustion chamber or 'plenum') up to full pressure again. The process then repeats itself. This relaxation oscillation involves non-linear coupling between stall inception, itself an asymmetric non-linear phenomenon, and the nonlinear dynamics of the mean flow. Because it involves complex coupling phenomena between various physical components and length scales, surge can take several forms, which are described in detail in Section 3.3.

It is important not only to understand the dynamics of stall and surge, but also the effect of operating conditions on these dynamics. Several operational issues must be addressed. Foremost among these is inlet distortion, or non-uniformity of the flow entering the compressor [2]. Distortion can be introduced by bends and turns in the ducts leading to the compressor (as in a buried engine installation), by inlet lip separation, by hot gas ingestion, or by boundary layer separation. The most important forms of distortion are total pressure and temperature distortion. Deviation from clean flow can be either circumferential or radial; typically stall instabilities are exacerbated more severely by the former.

Another operational consideration is engine wear. Tight clearances combined with structural and thermal loads on an engine can cause deformation of the casing, temporary rubbing of the rotor blade tips on the casing, and increased vibration levels. These combined effects cause the tip gap to increase during the engine's lifetime, which can have a significant impact on stability [3], particularly if tip gap becomes non-uniform [4]. Coupling between rotor-dynamics and tip clearance effects can also play a role in stability behaviour, although the extent of this coupling in real applications is not well understood.

Finally, acceleration from idle to full power causes flow transients in the compressor that can induce stall. Combinations of the above effects must also be accommodated. The net result is that during engine design a significant portion (on the order of 20%) of the pressure rise capability of the

compressor is given over to 'surge margin', which is defined as the distance between the surge operating condition and the nominal operating line. Table 1 gives the an example of a typical surge margin budget for a military fan (taken from ARP 1420, "Aerospace recommended practice: Gas turbine engine inlet flow distortion guidelines" [5]). In this chart stall margin is expressed in percent pressure ratio, with the operating line pressure ratio taken as the baseline.

Table I – Typical Stall Margin Budget (from [5])

Destabilizing Effects	Fan Stall Margin Budget	
	Random	Non-Random
• OPERATING LINE		
➢ Inlet Distortion	0.5	--
➢ PLA Transients	4.0	--
➢ Variable Geom. Control Tolerances	--	±1.1
➢ Engine to Engine Variation	--	±1.2
• SURGE LINE		
➢ Reynolds Number	1.87	--
➢ Inlet Distortion	**6.25**	--
➢ Engine to Engine Variation	--	±1.3
• TOTAL	**12.62**	±2.083
• BASE SURGE MARGIN	25.0	
• NET SURGE MARGIN	10.30	

1.2 Overview of Compressor Stability Research

All of the phenomenology described in the previous section can be understood from the perspective of the fluid mechanical models described in this document. As such, the models we will describe represent a powerful set of first-principals tools for developing practical solutions, and for research into advanced techniques such as active control. Before describing these tools, however, it is instructive to place them in the context of past and present research in compressor dynamics, and to catalogue the modeling techniques currently available. This discussion will hopefully help the reader make an informed decision about the modeling effort that is consistent with the problem at hand.

Compressor dynamics research falls into four major categories: detailed flow observations, stall detection methods, stall control, and modeling and model validation. We give a brief review here; for a more thorough review see [32,33]. Modelling is given somewhat more attention here, for obvious reasons.

Much early work concentrated on experimental studies of phenomenology and detailed flow observations [6]. This research continues [7], as the 'root cause' of rotating stall is sought, and as deeper understanding of the flow details motivates more careful measurements.

Stall detection research attempts to develop methods that can issue a warning during the pre-stall phase when stall is imminent [8]. Typically one is looking for a 'signature' or other indication that the flow through the compressor has become less stable. Often such detection schemes are able to see indications of impending stall 100 to 1000 revolutions prior to stall; however a complete study of the false alarm to success rate of such detection filters is difficult to obtain, because a statistically significant number of stall experiments are rarely performed. One of the primary conclusions of this

body of research is that the stall inception process varies greatly from compressor to compressor, so that although many general concepts apply to a wide variety of compressor, stall detection algorithms must invariably be tuned to the compressor being tested [8, 9].

Stall control research might be considered the 'next step' after stall detection, but this is not necessarily true. In some cases the control strategy that has been employed is in fact to detect impending stall and then actuate by some means to improve the health of the compressor. Other methods, however, are aimed at continually measuring and feeding back flow perturbations in such a way to fundamentally alter the compressor as a dynamic system [1]. Rather than relying on quick detection, these methods rely heavily on modeling of the dynamics and understanding how they might be altered by continuous feedback control.

Modelling of compressor dynamics obviously plays a role in all of the previously mentioned endeavors. It motivates the measurements one might take experimentally, and provides a means to interpret the results. Modeling also motivates detection and control schemes. Finally, predictive modeling has been considered, as a means to assess stability in the design phase. Because of the diversity of the applications, a wide variety of models exist for simulating compressor dynamics, each with its own strengths and limitations. Table II summarizes the types of models that have been developed. The list proceeds from 1D to 3D characterizations, and within each level from low to high order. In this paper, we concentrate primarily on Moore-Greitzer [10] based models, which have the following advantages: They are very low order, they capture most nonlinear and operational effects at least to first order, and they are physical ('first principals') rather than computational models, so that they lend insight into phenomena. The primary disadvantages of Moore-Greitzer approaches are that they do not describe short length-scale events, and multistage effects and compressibility are not modeled. These shortcomings become important as the level of required fidelity increases, but in control studies (the primary application we address here) have not been debilitating.

Table II – Compression System Modeling Techniques

	Dimension	Compressible/ Multistage	Nonlinear/ Distortion,Pips	Suitable for Control (Model Order)
Multistage Surge/1D [11]	1	✓	1D effects	Linearized O(100)
Moore-Greitzer Based [10, 2]	2		✓, no pips	Nonlinear, O(10)
2D Hydrodynamic Stability [12,13]	2	✓, centrifs		Linear, O(100)
2D, Nonlinear Blade Rows [14,15]	2	✓	✓	O(10,000)
3D Hydrodynamics Stability [16]	3			O(1,000)
2D/3D Body Force Models [17]	2/3	✓	✓	O(100,000)

2 Derivation of the Moore-Greitzer PDEs

In this section, the Moore-Greitzer PDEs in their original form [10] are presented. The discussion starts with a description of the equilibrium behaviour of compressors, and continues with a derivation of the unsteady perturbation behaviour of each of the components in Figure 2. Finally, the equations are assembled into the fundamental equations for the compression system.
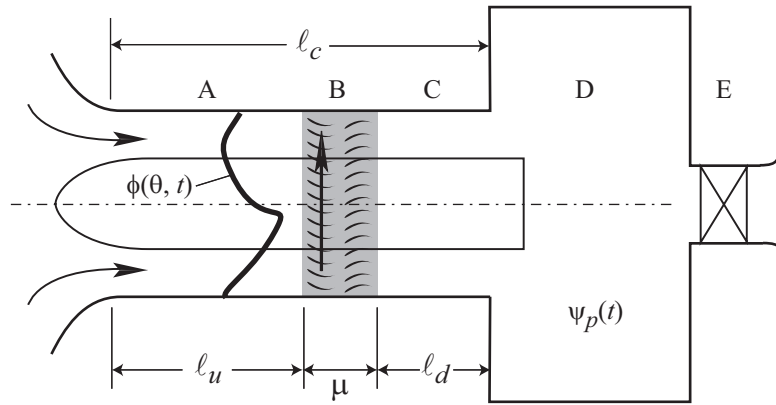
Figure 2 – Schematic compression system.
A – inlet duct, B – compressor, C – exit duct, D – plenum, E – throttle.
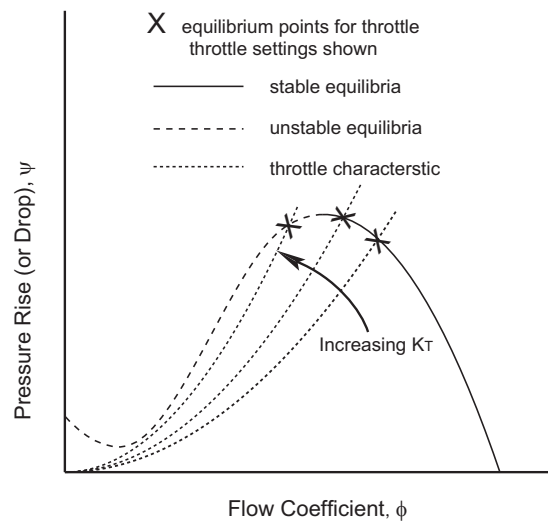
Figure 3 – Equilibrium operation of compressor-throttle combination.

2.1 Equilibrium Behaviour and Nomenclature

Consider the schematic diagram of an axial compressor in Figure 2. It consists of an upstream annular duct, a compressor modelled as an actuator disk, a downstream annular duct, and a throttle. During stable operation, flow through the compressor can be assumed to be circumferentially uniform (axi-symmetric), and a single non-dimensional measure of flow through the compressor determines the system state. This measure is the 'flow coefficient', which is simply the nondimensionalized value of the axial velocity:

$$\phi = \frac{(axial\ velocity)}{(rotor\ speed)}.$$

During quasi-steady operation, the total-to-static pressure rise delivered by the compressor is simply determined by its 'total-to-static pressure rise characteristic,' denoted $\Psi_C(\phi)$:

$$\Psi_C = \frac{(downstream\ static\ pressure) - (upstream\ total\ pressure)}{\frac{1}{2}\rho U^2},$$

where ρ is the ambient air density and U is the rotor velocity at the mean radius. The pressure rise is balanced by a pressure loss across a throttling device, which can be either a simple flow restriction (used for testing compressors as components) or the combustor and turbine in a gas turbine engine. The balance between pressure rise across the compressor and pressure drop across the throttle is depicted as

an intersection between the characteristics of the two devices, $\Psi_C(\phi)$ and $\Psi_T(\phi)$, where, for low pressure ratios, $\Psi_T(\phi)$ is usually taken to be a quadratic function of ϕ:

$$\psi_T = \frac{1}{2} K_T \phi^2 , \tag{1}$$

where Ψ_T is non-dimensionalized in the same way as Ψ_T, and K_T depends on the degree of throttle closure. In a typical experiment, the throttle is slowly closed, the throttle characteristic becomes steeper (modelled by adjusting K_T in (1)), the intersection point between $\Psi_C(\phi)$ and $\Psi_T(\phi)$ changes, and the equilibrium operating point of the compressor moves from high flow to low flow (see Figure 3).

The stability of the equilibrium point represented by the intersection between $\Psi_C(\phi)$ and $\Psi_T(\phi)$ has been the topic of numerous studies, due to its importance in the safe, high performance operation of gas turbine engines. In our model, the system state under unsteady, possibly asymmetric (i.e. circumferentially varying) conditions is characterized by two terms: the annulus averaged pressure rise delivered by the compressor, $\overline{\psi}$, and the spatially distributed flow coefficient, denoted ϕ:

$$\phi : \quad \phi(x, \theta, t),$$

where x is the axial position in the compressor, non-dimensionalized by the mean rotor radius (the origin is chosen to be at the compressor face), θ is the circumferential position, and t is non-dimensional time (in rotor revolutions).

Note that evaluation of $\Psi_C(\phi)$ and $\Psi_T(\phi)$ must now be conducted more carefully due to the unsteady and asymmetric character of the flow: $\Psi_C(\phi)$ is evaluated at $x = 0$ (the compressor face), and varies with both t and θ. Thus the compressor is viewed as a distributed memoryless nonlinearity operating on the local (in θ) flow coefficient. For the throttle, we realise that the plenum pressure ψ_p is unsteady and thus cannot be completely specified by $\Psi_T(\overline{\phi})$. It is, however, consistent with the unsteady situation to say that flow through the throttle depends on pressure drop across it, i.e. to invert $\Psi_T(\overline{\phi})$:

$$\Phi_T(\psi_p) = \sqrt{\frac{2\psi_p}{K_T}} . \tag{2}$$

ψ_p is non-dimensionalized by $\frac{1}{2}\rho U^2$, as are all pressures throughout this document; similarly Φ_T and all subsequent velocities are non-dimensionalized by the mean wheel speed U.

One additional variable must be introduced in order to set up the system of equations. The upstream flow field, being two dimensional, admits both axial velocity perturbations (ϕ) and circumferential velocity perturbations. On the assumption that the upstream flow field is inviscid and irrotational, we introduce the non-dimensional velocity potential Θ, such that

$$\frac{\partial \Theta}{\partial x} = \phi \qquad \text{and} \qquad \frac{\partial \Theta}{\partial \theta} = \upsilon = \frac{(circumferential\ velocity)}{U} . \tag{3}$$

We will see that Θ and υ can ultimately be eliminated from the equations, along with all of the partial derivatives with respect to space, leaving an ordinary-differential relationship.

In the remaining subsections we present the relationships for the upstream and downstream duct flows. We then present the modified actuator disk representation of the compressor. Finally, the plenum and throttle relationships are given. The modelling components are subsequently assembled into the nonlinear PDEs.

2.2 Upstream Duct

Linearity of the duct flow fields is the key assumption that must be made in order to derive a tractable set of equations for control law design. This assumption has been used by many researchers (see Longley [18] for a review), and has been validated against experimental data by Lavrich [19], and more recently for the upstream flow field by Van Schalkwyk [20]. In both the upstream and downstream duct, this assumption must be carefully applied to accurately account for the relevant flow field effects.

In the upstream flow field, the clean inlet flow situation is easily understood. The upstream boundary condition is irrotational, the flow is incompressible for low Mach number flows, and high Reynolds numbers insure that the flow behaves in an inviscid manner. With these assumptions, the flow is potential, and a very simple impedance relation can be derived upstream. Lavrich tested the validity of the upstream potential flow assumption during fully developed stall, and in that study it was quite adequate.

Under the above assumptions, the upstream flow can be assumed linear (even when the flow perturbations at the compressor face are large), which leads to a potential flow representation of the flow:

$$\frac{\partial^2 \Theta}{\partial x^2} + \frac{\partial^2 \Theta}{\partial \theta^2} = 0 \,. \tag{4}$$

The solution for the upstream flow is found by considering the following general form for Θ, which satisfies the Laplacian:

$$\Theta = \sum_{n \neq 0} A_n(t) e^{in\theta} e^{|n|x} + A_0(t)x + B_0(t) \,. \tag{5}$$

Note that perturbations that grow in the upstream direction ($e^{-|n|x}$ terms) are not considered here – this simplification requires that the distance between the compressor and the inlet is sufficiently long (say 2 to 3 rotor radii) and the inlet flow is uniform. The final two terms represent the 0th harmonic (spatial mean part of the flow perturbations). Based on the potential flow relations (3), ϕ has a similar form:

$$\phi = \sum_{n \neq 0} \tilde{\phi}_n(t) e^{in\theta} e^{|n|x} + \bar{\phi} \qquad x \leq 0 \,, \tag{6}$$

where:

$$\bar{\phi} = A_0 \text{ and } \tilde{\phi}_n = |n| A_n \,.$$

To find the value of B_0 in (5), substitute into the unsteady Bernoulli equation:

$$\frac{\partial \Theta}{\partial t} + \delta \psi_t = \text{Constant} = 0 \,, \tag{7}$$

where the constant is evaluated far upstream of the compressor to obtain zero. Since total pressure perturbations $\delta \psi_t$ are approximately zero at $x = -\ell_u$, we have $B_0 = \ell_u \bar{\phi}$, which results in the following representation of Θ at the compressor face (evaluating (5) at $x=0$):

$$\Theta\big|_{x=0^-} = \sum_{n \neq 0} \frac{1}{|n|} \tilde{\phi}_n(t) e^{in\theta} + \ell_u \bar{\phi} \tag{8}$$

The total pressure at the compressor face is found by applying unsteady Bernoulli (7) at $x=0$, yielding

$$\psi_t\big|_{x=0} = -\sum_{n \neq 0} \frac{1}{|n|} \dot{\tilde{\phi}} e^{in\theta} - \ell_u \dot{\bar{\phi}} \,. \tag{9}$$

where total pressure has been non-dimensionalized by $\frac{1}{2}\rho U^2$, as are all pressures in this analysis.

2.3 Downstream Duct

The downstream flow field is also assumed to behave linearly to simplify the analysis. The flow in this region is assumed 2D, incompressible, and inviscid, but it is vortical due to the upstream introduction of vorticity by the compressor. The linearized Euler equation (appropriately non-dimensionalized) provides a starting point for analysis of this flow field:

$$\frac{\partial \phi}{\partial t} - \phi \frac{\partial \upsilon}{\partial \theta} + \upsilon \frac{\partial \phi}{\partial \theta} = -\frac{\partial \psi}{\partial x} \qquad x \geq 0 \tag{10}$$

Two assumptions, which are not necessary to complete the analysis, simplify further derivation considerably. If the last row of stators directs the flow axially, then υ, the mean swirl downstream of the compressor, is zero. In addition, if the last stator row executes turning perfectly (i.e. the solidity is very high so that deviations are small), $\frac{\partial \upsilon}{\partial \theta}$ is also zero. In [19], Longley removes these assumptions; doing so complicates the results but does not change the basic behaviour of the system. Therefore, we will use the simplified equation

$$\frac{\partial \psi}{\partial x} = -\frac{\partial \phi}{\partial t} , \tag{11}$$

and, recognizing that the downstream flow is incompressible and thus static pressure perturbations must satisfy a Laplacian (see Moore and Greitzer [10]):

$$\frac{\partial^2 \psi}{\partial x} + \frac{\partial^2 \psi}{\partial \theta^2} = 0 , \tag{12}$$

we have the following representation of the downstream static pressure:

$$\psi = \sum_{n \neq 0} C_n(t) e^{in\theta} e^{-|n|x} + C_0(t)x + D_0(t) , \tag{13}$$

where we have assumed here that perturbations that grow in the *downstream* direction ($e^{|n|x}$ terms) are not present. To satisfy (11), downstream velocity perturbations must take a similar form:

$$\phi = \sum_{n \neq 0} \tilde{\phi}_n(t) e^{in\theta} e^{-|n|x} + \overline{\phi} \qquad x \geq 0 . \tag{14}$$

This representation allows us to relate ϕ and ψ, and to solve for C_0 and D_0 by integrating (13) and introducing the plenum pressure ψ_p as a variable. Performing the integration from any position x to ℓ_d we have

$$C_n = \frac{1}{|n|}\dot{\tilde{\phi}}_n, \ \ C_0 = -\dot{\overline{\phi}}, \text{ and } D_0 = \psi_p + \dot{\overline{\phi}}\ell_d . \tag{15}$$

This results in the following equation for the static pressure immediately downstream of the compressor:

$$\psi\big|_{x=0^+} = \sum_{n \neq 0} \frac{1}{|n|}\dot{\tilde{\phi}}_n e^{in\theta} + \left(\psi_p + \ell_d \dot{\overline{\phi}}\right). \tag{16}$$

2.4 Compressor Matching

The duct impedance relationships derived above allow us to determine the total to static pressure difference across the compressor as a function of the axial velocity at the compressor face. It remains to 'match' this with the pressure rise delivered by the compressor. This matching determines how much of the unsteady pressure difference is supported by the pressure rise of (or work done by) the compressor, and how much is causing local acceleration of fluid in the blade passages. The detailed derivation of this matching condition is given in other documents [2, 10, 18, 21]. Here we simply give the equation that results:

$$\psi\big|_{x=0,\,downst.} - \psi_t\big|_{x=0,\,upst.} = \Psi_C(\phi) - \lambda\frac{\partial\phi}{\partial\theta} - \mu\frac{\partial\phi}{\partial t} \, , \qquad (17)$$

where Ψ_C is the steady-state total-to-static pressure rise of the compressor, and the remaining two terms capture the pressure-driven acceleration of flow in the compressor blade passages. λ is the non-dimensional inertia parameter for the fluid in the rotating blade passages; μ represents the overall inertia of the rotor+stator blade passages.

2.5 Plenum and Throttle

The equations in this section link the flow in the duct to the evolution of pressure in the downstream plenum, which is a 'mass storage' device: mass flow enters through the compressor duct and exits through the throttle (see Figure 2). When the flow is unsteady, these mass flows may not balance. Build up of mass in the plenum creates an increase in pressure, with the volume acting as a fluid 'spring'. When this spring is coupled to the inertia of the annulus-averaged portion of the upstream flow, a spring-mass system is generated which can be underdamped or unstable, resulting in surge.

The following relationship for the mass balance and compressibility in the plenum can be derived through application of continuity and the ideal gas law (isentropic compression):

$$\dot{\psi}_p = \frac{1}{4B^2\ell_c}\left\{\bar{\phi} - \Phi_T(\psi_p)\right\} \qquad (18)$$

where we rely on continuity of the mean flow to allow the use of $\bar{\phi}$ (the mean flow at $x=0$) to represent the duct flow, and Φ_T is the throttle characteristic, as discussed previously:

$$\Phi_T(\psi_p) = \sqrt{\frac{2\psi_p}{K_T}} \, . \qquad (19)$$

The parameter B in (18) is Greitzer's stability parameter, $B = \left(\frac{U}{2a}\right)\sqrt{\frac{V}{AL}}$, which gives the ratio of compliance to inertia for a system with ambient speed of sound a, plenum volume V, and duct area and length A and L. Greitzer [22, 23] gives an account of the importance of this parameter to compressor stability and to the coupling between rotating stall and surge.

2.6 Summary and Discussion

In the discussion so far, we have presented partial and ordinary differential equations for the flows through the various components in Figure 2. Where possible, we have also presented the solutions to these equations, which are expressed in terms of the Spatial Fourier Coefficients (SFCs) of the flow variables. Time derivatives have purposely been left unsolved in these solutions. We have done this because it is our desire to represent the system in a form amenable to control. In this context we wish to derive ordinary differential equations. We seek homogeneous ODEs for the present, but in Section 4 we introduce effects of forcing from both actuators and disturbance sources.

Table III summarizes the equations derived thus far, and their Fourier coefficient form. Since we are assuming that the flow fields upstream and downstream can be treated as linear, even when the flow in the compressor itself exhibits large perturbations, these equations remain the same throughout this document. The non-linearities associated with the compressor and the throttle, however, cannot be ignored during stall inception and fully developed stall. Therefore we choose here to maintain the nonlinear representation of these equations, adopting a somewhat unwieldy notation in the Fourier space. In discussing the solutions, we will look at both linear and non-linear forms of the solutions resulting from the equations in Table III.

Table III – Equations For Moore-Greitzer Model ($\mathcal{F} \equiv$ Fourier Transform)

Part	Spatial Domain	Fourier Domain $(n \neq 0)$	Fourier Domain $(n = 0)$
Upstr. Duct	$\dfrac{\partial \Theta}{\partial t} + \psi_t = 0$, Θ satisfies Laplacian	$\tilde{\psi}_{t\,n0^-} = -\dfrac{1}{\lvert n \rvert}\dot{\tilde{\phi}}_n$	$\overline{\psi}_{t0^-} = -\ell_u \dot{\overline{\phi}}$
Comp.	$\psi\big|_{x=0^+} - \psi_t\big|_{x=0^-} = \Psi_c(\phi) - \lambda\dfrac{\partial \phi}{\partial \theta} - \mu\dfrac{\partial \phi}{\partial t}$	$\tilde{\psi}_{n0^+} - \tilde{\psi}_{t\,n0^-} = \mathcal{F}\{\Psi_c(\phi)\}_n - in\lambda\tilde{\phi}_n -$	$\overline{\psi}_{0^+} - \overline{\psi}_{t0^-} = \overline{\Psi_c(\phi)} - \mu\dot{\overline{\phi}}$
Downst. Duct	$\dfrac{\partial \psi}{\partial x} = -\dfrac{\partial \phi}{\partial t}$, ψ satisfies Laplacian	$\tilde{\psi}_{n0^+} = \dfrac{1}{\lvert n \rvert}\dot{\tilde{\phi}}_n$	$\overline{\psi}_{0^+} = \psi_p + \ell_d \dot{\overline{\phi}}$
Plenum	$\dot{\psi}_p = \dfrac{1}{4B^2\ell_c}\left\{\overline{\phi} - \Phi_T(\psi_p)\right\}$	0	$\dot{\psi}_p = \dfrac{1}{4B^2\ell_c}\left\{\overline{\phi} - \Phi_T(\psi_p)\right\}$
Throttle	$\Phi_T(\psi_p) = \sqrt{\dfrac{2\psi_p}{K_T}}$	0	$\Phi_T(\psi_p) = \sqrt{\dfrac{2\psi_p}{K_T}}$

3 Homogeneous Behavior of Compressor Dynamics

This section concentrates on describing the implications of the equations presented in the previous section. We will consider linearized and nonlinear behavior, for both surge and rotating stall. In the linear case surge and rotating stall are decoupled and can be considered separately, using standard analysis methods. In the nonlinear case, surge and rotating stall are coupled, a wide range of detailed behaviors and interactions can occur, and one must resort to nonlinear simulations. Therefore a less general treatment is given for the nonlinear behaviour.

3.1 Linearized Behavior – Surge

Linearized surge dynamics are the most basic form of compressor instability. We first introduce notation for the compressor and throttle slope at a given equilibrium point (one of the X's in Figure 3):

$$m_C = \frac{d\Psi_C}{d\phi}\bigg|_{eq.\,\phi} \;;\quad m_T^{-1} = \frac{d\Phi_T}{d\psi_p}\bigg|_{eq.\,\psi_p} \tag{20}$$

Using these definitions, and eliminating variables in the $n=0$ column of Table III, we obtain the following system of ODEs (note: $\ell_c = \ell_u + \mu + \ell_d$):

$$\dot{\overline{\phi}} = \frac{1}{\ell_c}\left(m_C\overline{\phi} - \psi_p\right)$$

$$\dot{\psi}_p = \frac{1}{4B^2\ell_c}\left(\overline{\phi} - \frac{1}{m_T}\psi_p\right) \tag{21}$$

In so-called 'state space' form, these equations are written:

$$\begin{bmatrix} \dot{\overline{\phi}} \\ \dot{\psi}_p \end{bmatrix} = \frac{1}{\ell_c}\begin{bmatrix} m_C & -1 \\ K_B & -K_B m_T^{-1} \end{bmatrix}\begin{bmatrix} \overline{\phi} \\ \psi_p \end{bmatrix}, \quad K_B = \frac{1}{4B^2}. \tag{22}$$

The characteristic equation for the systems is

$$s^2 + \frac{1}{\ell_c}\left(\frac{K_B}{m_T} - m_C\right)s + \frac{K_B}{\ell_c}\left(1 - \frac{m_C}{m_T}\right) = 0. \tag{23}$$

For realistic values of m_C and m_T near stall, the third term is approximately equal to $1/4B^2\ell_c$; the natural frequency of the system depends on the Greitzer's 'B' parameter. Stability is determined by the following criterion (based on the necessity for all coefficients in (23) to be positive for stability):

$$m_C < \frac{1}{4B^2 m_T} \tag{24}$$

Since both m_T and B are always positive, the negatively sloped portion of the compressor characteristic is always stable. For typical compression systems, the surge mode becomes unstable very near the value where $m_c = 0$.
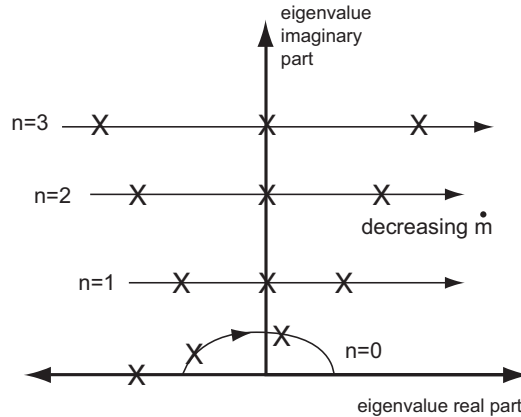
Figure 4 – Migration of eigenvalues for both surge and rotating stall. X's indicate eigenvalue locations at three separate mass flows (same three values along each line). Complex conjugate eigenvalues not shown.

Figure 4 shows the migration of the eigenvalues (labeled "n=0") as m_C goes from negative to positive. At instability, an oscillatory pair of eigenvalues exists, indicating a resonant, or dynamic, instability. This instability involves coupled oscillation of the mass flow in the ductwork and the pressure in the plenum. One can draw an analogy between these oscillations and the oscillation of a mass-spring-damper system. In this analogy, the fluid in the upstream duct acts as the mass, the compression of the fluid in the plenum acts as the spring, and the throttle acts as a damper (see [22-24]). The compressor in this analogy behaves like a damper that can either dissipate or add energy to the system, depending on the sign of m_C.

Just as in a mass-spring-damper system, where the ratio of mass to spring constant determines whether the system experiences large displacements or large compressive forces in the spring during transients, the linearized transient behavior of the compressor near surge depends on the B parameter, which is the ratio of compliance to inertia in the system. For large B parameters (soft spring), mass flow fluctuations (displacements) are large while plenum pressure (compressive force) is small. For small B parameter (analogous to a mechanical system with a stiff spring), the pressure in the plenum varies strongly for relatively small changes in mass flow in the ducts. These two types of behavior are shown in Figure 5. Note that the large mass flow variations associated with large B parameter make it more likely that the compressor will exhibit destabilizing nonlinearities, since mass flow determines compressor pressure rise and slope (see Figures 2 and 3).
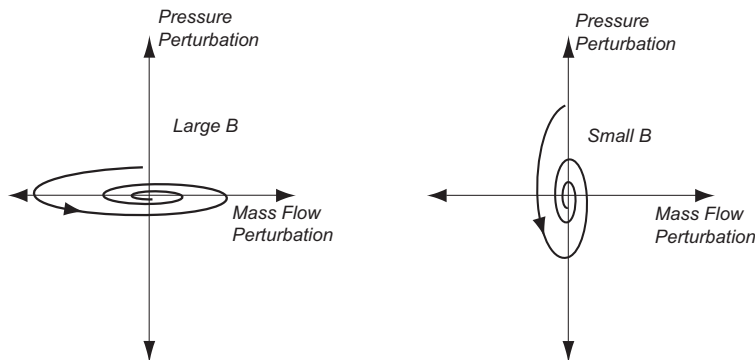
Figure 5 – Transient response of surge system to a perturbation pressure, for large and small values of Greitzer's B parameter.

3.2 Linearized Behavior – Rotating Stall

Linear rotating stall modes behave in a very simple way that is directly linked to the physical parameters originally defined by Moore and Greitzer. Unfortunately, the spatial nature of the problem, and the use of complex Fourier coefficients to represent this spatial nature, makes understanding the link between the mathematics and the physics somewhat difficult. Eliminating variables in the linearized equations for $n \neq 0$ in Table III, we obtain the following ODE for the nth Spatial Fourier Coefficient (SFC):

$$\dot{\tilde{\phi}}_n = \left(\frac{m_c - in\lambda}{2/|n| + \mu} \right) \tilde{\phi}_n.$$

(25)

Thus each SFC obeys a first-order ODE, whose solution we can immediately write as:

$$\tilde{\phi}_n = A e^{(\sigma_n - i\omega_n)t},$$

(26)

where A is a constant determined by the initial conditions,

$$\sigma_n = \frac{m_c}{2/|n| + \mu}, \text{ and } \omega_n = \frac{n\lambda}{2/|n| + \mu}.$$

(27)

It is easier to understand the implications of this solution if we first rewrite it in the spatial domain. Taking the real part of the nth harmonic of ϕ (or, equivalently, combining the nth and $-n^{th}$ SFC's) in equation (6), and rewriting in terms of a sinusoid,

$$\phi(x = 0, \theta, t) = M e^{\sigma_n t} \cos\left(n\left(\theta - \frac{\omega_n}{n} t \right) + \beta \right).$$

(28)

M and β depend only on A, the initial condition, and therefore are not of interest. We see that σ_n is the growth rate of the rotating wave, and ω_n / n is the wave's rotation rate. Figure 6 illustrates the behavior of the sinusoidal mode as it travels around the compressor annulus. Studying equation (27), we see that the sign of m_c governs stability; the system is stable for negatively sloped regions of the compressor characteristic, and unstable for positively sloped regions (similar to surge). Rotation rate is governed by the ratio of rotor blade passage inertia, λ, and overall compressor blade passage inertia, μ, with a weak dependence on n. The n in the numerator of the ω_n does not indicate that higher harmonic waves rotate proportionally faster; rather it indicates that all waves maintain roughly the same group velocity (i.e. wave peaks travel at approximately the same rate ω_n / n).
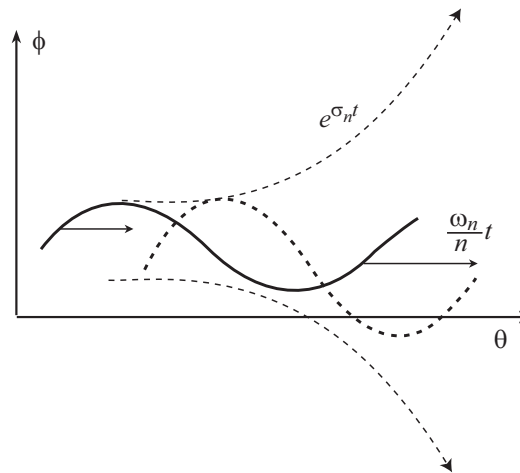
Figure 6 – Relationship between differential equation solution and physical behaviour of rotating stall waves.

Migration of eigenvalues is depicted in Figure 4. Note that all harmonics go unstable at the same flow coefficient, and that this is typically a higher flow coefficient than surge. Also note that prior to the instability point, higher harmonics are more stable, but beyond the stability boundary, higher harmonics are more unstable (i.e. grow faster). Eigenvalue frequency is relatively invariant with mass flow. These features give clues to the nonlinear behavior to be discussed in the next section.

Another way to represent the rotating stall dynamics is in real-valued state space form [26]. This form is useful for the application of control theory, which usually requires that the ODEs describing any given system are real-valued. It is also useful for developing nonlinear simulations. The idea is to write the flow coefficient ϕ in terms of sine and cosine coefficients instead of complex Fourier coefficients. Consider the following representation of ϕ :

$$\phi\big|_{x=0} = \sum_{n\neq 0}\left(\tilde{\phi}_{c_n}(t)\cos(n\theta)+\tilde{\phi}_{s_n}(t)\sin(n\theta)\right)+\bar{\phi} \ . \tag{29}$$

The coefficients $\tilde{\phi}_{c_n}$ and $\tilde{\phi}_{s_n}$ are the real and imaginary parts of $\tilde{\phi}_n$, respectively. By taking the real and imaginary parts of (25), we can derive the following real-valued, state-space equations:

$$\begin{bmatrix}\dot{\tilde{\phi}}_c \\ \dot{\tilde{\phi}}_s\end{bmatrix}_n = \begin{bmatrix}\sigma_n & -\omega_n \\ \omega_n & \sigma_n\end{bmatrix}\begin{bmatrix}\tilde{\phi}_c \\ \tilde{\phi}_s\end{bmatrix}_n \ . \tag{30}$$

In this representation we see that the states of the system form a second-order oscillatory system; the sine and cosine coefficients oscillate in quadrature to create a rotating wave. This form of the equations is the most amenable to a nonlinear formulation, discussed in the next section.

3.3 Nonlinear Behaviour – Coupling Between Rotating Stall and Surge

As indicated by the linearized modelling discussion, compressors typically exhibit rotating stall instability first. The experimental data in Figure 1 shows that as rotating stall perturbations get large, they can trigger surge oscillations. The Moore-Greitzer model captures this nonlinear coupling between rotating stall and surge, and helps to explain the parametric situations associated with different types of stall/surge behavior.
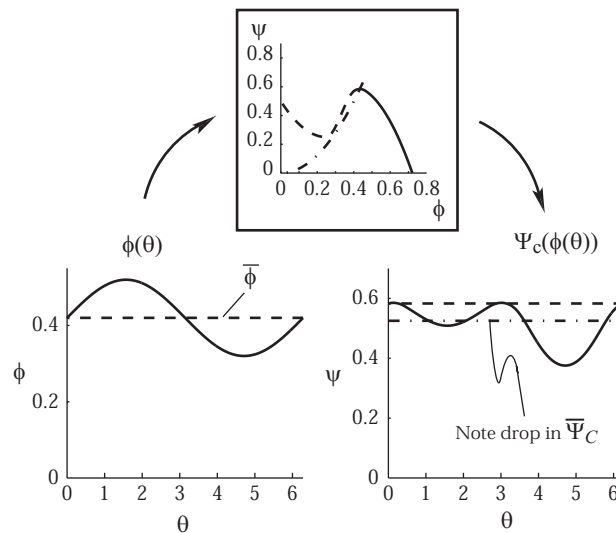
Figure 7 – Effect of nonlinear map on pressure forces that act to accelerate a velocity perturbation. Pressure forces (on right) below the mean value act to decelerate the flow. Note the significant cross-feed between the 1st harmonic and the 0th and 2nd harmonics. From Mansoux, [25].

The key nonlinearity in the model is $\Psi_C(\phi)$, the compressor map. The model assumes that at each circumferential location, the instantaneous, local value of flow coefficient determines the instantaneous, local pressure rise. Thus there is a distributed nonlinear map between the flow and the accelerating pressure force introduced by the compressor. To understand the influence of the nonlinearity in $\Psi_C(\phi)$

on stall inception, consider a sinusoidal velocity perturbation being mapped through the compressor characteristic, shown in Figure 7. From the figure it is clear that at the peak of the characteristic, a linear representation of $\Psi_C(\phi)$ is insufficient; the slope of the characteristic is near zero, so higher order derivatives become important. Both velocities higher than the equilibrium value and lower than the equilibrium value result in pressure forces that are less than the equilibrium pressure rise (i.e. decelerating with respect to equilibrium). This has two effects. First, it couples first harmonic perturbations into the second and higher harmonics, causing the wave shape to deform as rotating stall inception proceeds. Second, the nonlinearity causes a drop in the mean pressure delivered by the compressor, coupling the first harmonic to the 0th harmonic, that is the surge dynamics. We will show both of these effects in nonlinear simulations, after a brief description of the computational approach to nonlinear simulation. A more detailed description of nonlinear modeling appears in Section 4.

In order to compute the effects of nonlinear coupling, a simulation that accounts for both rotating stall and surge must be set up. The most direct way to do this (and the one originally applied by Chue et al. [21]) is using a Fourier collocation method. Again referring to Table III, we can set up an iterative algorithm that computes, over one cycle, the acceleration of the flow at the compressor face:

0. Initialize $\phi(x = 0, \theta, t = 0)$ and ψ_p.
1. Compute SFCs of ϕ, that is $\tilde{\phi}_n, n = -N, \cdots, N$
2. Compute $\Psi_C(\phi)$ and its SFCs $\tilde{\Psi}_{C_n}$.
3. Compute acceleration of $\tilde{\phi}_n$:

$$\left(\frac{2}{|n|} + \mu\right)\dot{\tilde{\phi}}_n = \tilde{\Psi}_{C_n} - in\lambda\tilde{\phi}_n \quad n = -N, \cdots N, n \neq 0$$

$$\dot{\bar{\phi}} = \frac{1}{\ell_c}\left(\tilde{\Psi}_{C_{n=0}} - \psi_p\right) \quad (Note: \bar{\phi} = \tilde{\phi}_{n=0})$$

4. Compute acceleration of ψ_p:

$$\dot{\psi}_p = \frac{1}{4B^2\ell_c}\left(\bar{\phi} - \Phi_T(\psi_p)\right)$$

5. Integrate in time to update $\tilde{\phi}_n$ and ψ_p.
6. Perform inverse Fourier transform of $\tilde{\phi}_n$ to obtain spatial distribution of flow, $\phi(x = 0, \theta, t_k)$
7. Continue at Step 2.

Each iteration in the above algorithm contains one Fourier transform and one inverse Fourier transform, because the nonlinearity $\Psi_C(\phi)$ must be applied in the spatial domain, but the flow calculations are more efficiently computed in the Fourier domain. Note that the third step indicates that the quantity $(2/|n| + \mu)\dot{\tilde{\phi}}_n$ should be computed rather than $\dot{\tilde{\phi}}_n$; we have found this approach to have better numerical properties. In this case the integration step updates this quantity directly. Another numerical consideration is Fourier truncation; some method to insure that the highest modes do not diverge must be employed. Careful numerical treatment is especially important when simulating the interaction between rotating stall and surge; the disparate time scales involved make capturing this interaction challenging.

Using a simulation such as this we can study how the coupling between rotating stall and surge manifests itself for various types of compression systems. The most important parameter in this respect is the B parameter; Figure 8 shows how the one dimensional states of the system evolve for three different values of *B*, which span the range of possible behaviours in the model. These cases show how

the drop in pressure delivered by the compressor as it enters rotating stall couple into surge oscillations. This is the coupling between higher modes and the zeroth mode discussed previously.
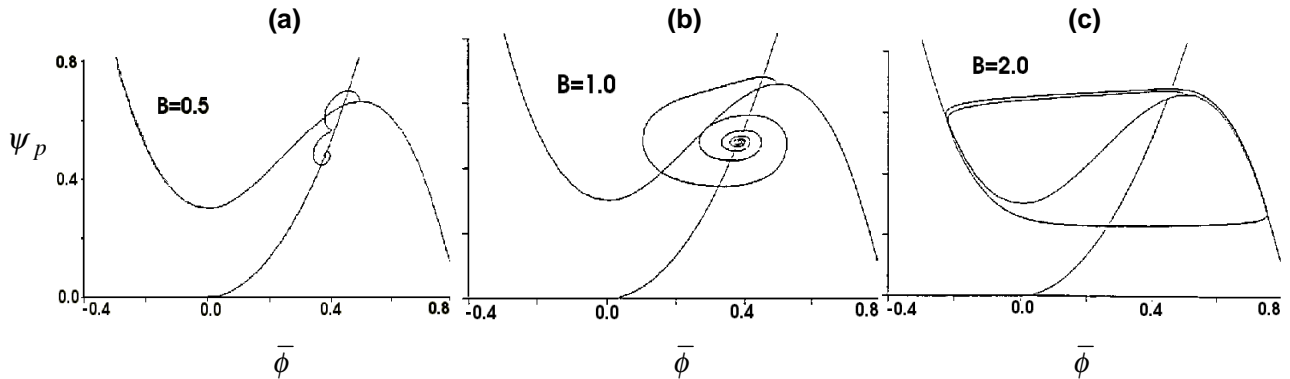
Figure 8 – Time evolution of numerical simulations of coupled rotating stall and surge (from Greitzer [23]). y axis is plenum pressure, compressor total-to-static pressure rise, and throttle pressure drop. x axis flow coefficient

All the simulations shown in Figure 8 are conducted with the same throttle and compressor characteristics, so that the (unstable) equilibrium point is the same in every case. All parameters except *B* are the same for all theses cases. For low values of *B*, the system behaves in a manner similar to the case with no plenum chamber – the result of rotating stall inception is that the system finds a new equilibrium in the mean flow quantities $\bar{\phi}$ and ψ_p. At this equilibrium rotating stall has constant, large amplitude, and is highly nonlinear. Although the mean flow no longer resides on the compressor map, each circumferential location has a pressure rise consistent with the map; the mean result is that shown in Figure 8a.

For values of the B parameter near 1, oscillations of the plenum pressure and mean flow interact with rotating stall oscillations, so that there are large excursions in these quantities. In some cases, like that shown in Figure 8b, the system eventually converges to rotating stall. In other cases, known as 'classic' surge, the surge oscillations do not die away, although they are small relative to 'deep' surge, which is shown in Figure 8c.

For large values of *B*, the compliance of the plenum is such that very large mass flow perturbations exist. These perturbations actually cause rotating stall to be squelched during part of the surge limit cycle. The process of plenum blowdown, refilling, and subsequent re-initiation of surge through the action of rotating stall is that described in Section 1.1.

To illustrate the effect of coupling between lower modes and higher modes, shown in Figure 7, we must look at the asymmetric flow patterns in the compressor. This is done by placing fictitious 'sensors' at various places around the sensor annulus, and displaying the resulting time traces of local flow coefficient as offset traces. Figure 9 shows the results of simulations using this technique, where three local velocities are displayed.

This plot also shows the concurrence of the results with experimental data. This concurrence is based on tuned parameters, so it does not depict the predictive capability of the model. Rather it illustrates that the model captures the main features of the experimental results. The focus here is on two features of the transient into stall. First, at low amplitude, one can see a wave whose peak amplitude rotates around the annulus (this can be seen by drawing a line between the peaks of the sinusoidal oscillations in the plots). Second, it is clear that at approximately 25 rotor revolutions, the sinusoidal wave becomes much sharper and more localized. The minimum-flow portion of the wave is
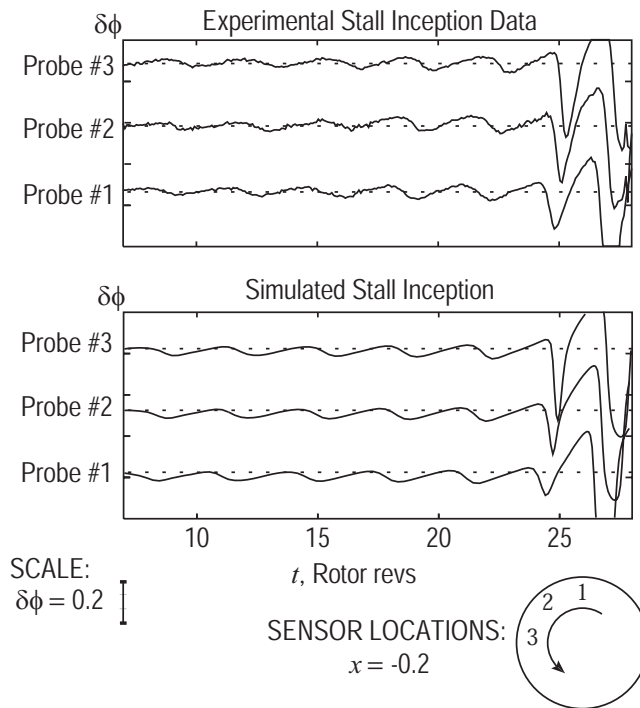
Figure 9 – Stall inception nonlinear simulation, with comparison to data (arbitrary time axis). From Mansoux et. al, [25].

experiencing severe deceleration, because the compressor characteristic drops off sharply at low flow coefficients. This causes the local flow to drop in this region, coupling in harmonics higher than the first, as illustrated in Figure 7. Figure 10 shows the evolution of the first 5 Fourier harmonics during a similar simulation. During stall inception, what began as a 1st harmonic perturbation becomes a multi-harmonic perturbation, eventually transitioning again to a 1st-harmonic-dominated fully develop stall cell.
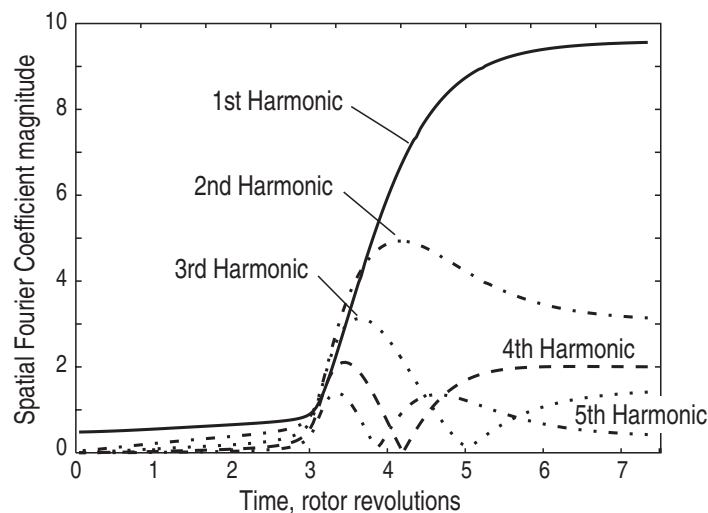
Figure 10 – Participation of the 1st 5 Fourier harmonics in stall inception. Note that harmonics 2 and 3 temporarily become larger than the 1st harmonic during stall inception. From Mansoux, [25].

4 Advanced Modeling Methods

The previous sections were focused on providing an understanding of the basic approach to Moore-Greitzer modeling, and on the behavior that these models describe. The primary strength of the Moore-Greitzer model is that it captures the salient physics of rotating stall and surge in a very low-order model. This strength can be, and has been, capitalized upon in many ways. We have shown how it can be used to understand the basic stability properties of compressors, the coupling between rotating stall

and surge, and the influence of physical parameters on the system behavior. Much more has been done in this regime of study, using among other techniques the Galerkin approximation method. Beyond this, the model has been augmented in various ways to increase its accuracy, to understand the role of forcing functions such as inlet distortion and asymmetric tip clearance, and to model the effects of actuators for active control.

In this section we discuss these additional uses and extensions of the Moore-Greitzer model. We begin by giving a brief account of the 3-state Galerkin approximation, which has had a major impact on the study of compressor stability and control. We then adopt a very general framework for representing the equations, and in this framework develop models for unsteady losses, inlet distortion, and some of the actuator types that have been used in experimental control work. The framework presented represents a comprehensive description of the state of the art in Moore-Greitzer based modeling, and should be considered a starting point for additional research in the area of rotating stall modeling for control.

4.1 Galerkin Projection

We begin from a slightly more general framework for Galerkin approximation than that originally presented by Moore and Greitzer, and then present the 3-state approximation as a special case. Although the 3-state model has been by far the most valuable to research work, higher order models represent the highest accuracy approach to simulation, so may be of interest for this reason alone.

The approach is to optimally project the equations in Table III onto the same set of basis functions used for linearization, that is spatial sinusoids. For control applications the real-valued Fourier decomposition is often useful:

$$\phi = \bar{\phi} + \sum_{n=1}^{N} \left[\tilde{\phi}_{cn} \cos(n\theta) + \tilde{\phi}_{sn} \sin(n\theta) \right] \tag{30}$$

To apply the Galerkin procedure, we simply substitute in this assumed form for the solutions, and then form an inner product with each of the basis functions. The substitution step leads to the following equations:

$$\left(\frac{2}{n} + \mu \right) \dot{\phi} = \lambda \sum_{n=1}^{N} \left[\tilde{\phi}_{cn} n \sin(n\theta) - \tilde{\phi}_{sn} n \cos(n\theta) \right] + \Psi_c(\phi) - \psi_p \tag{31}$$

$$4B^2 \ell_c \dot{\psi}_p = \bar{\phi} - \Phi_T(\psi_p) \tag{32}$$

Taking the inner product with the basis functions $\bar{\phi}$, $\tilde{\phi}_{cn}$, and $\tilde{\phi}_{sn}$ on both sides of these equation is the same as taking the Fourier transforms. The results are equations for the surge dynamics and rotating stall dynamics, coupled through the spatial Fourier coefficients of the compressor nonlinearity, as follows:

$$\ell_c \dot{\bar{\phi}} = \overline{\Psi_c(\phi)} - \psi_p \tag{33}$$

$$4B^2 \ell_c \dot{\psi}_p = \bar{\phi} - \Phi_T(\psi_p) \tag{34}$$

$$\left(\frac{2}{|n|} + \mu \right) \dot{\tilde{\phi}}_{cn} = -n\lambda \tilde{\phi}_{sn} + \frac{1}{2\pi} \int_0^{2\pi} \Psi_c(\phi) \cos n\theta \, d\theta \tag{35}$$

$$\left(\frac{2}{|n|} + \mu \right) \dot{\tilde{\phi}}_{sn} = -n\lambda \tilde{\phi}_{cn} + \frac{1}{2\pi} \int_0^{2\pi} \Psi_c(\phi) \sin n\theta \, d\theta \tag{36}$$

This is the general form for a Galerkin model for rotating stall and surge. The overbar in equation (33) denotes spatial mean (0th Fourier coefficient). Evaluating the integrals in (35) and (36) is simplified if the compressor characteristic is represented by a linear regression, such as a polynomial in ϕ. In this case, we can write Ψ_C as follows:

$$\Psi_C(\phi) = \begin{bmatrix} 1 & \phi(\theta) & \phi^2(\theta) & \dots & \phi^q(\theta) \end{bmatrix} \begin{bmatrix} a_o \\ a_1 \\ \vdots \\ a_q \end{bmatrix} = [\Psi_C(\phi)]\mathbf{a} \tag{37}$$

The integrals (35-36) can be carried out on each of the regressors separately. This leads to a regression matrix in the chosen state space, which provides the nonlinear coupling terms in the Galerkin projection. For instance, if we perform the integral for a cubic representation of the compressor characteristic (q=3 in (37)), the two-mode Galerkin expansion is

$$\begin{bmatrix} \ell_c\dot{\phi} \\ \mu_1\dot{c}_1 \\ \mu_1\dot{s}_1 \\ \mu_2\dot{c}_2 \\ \mu_2\dot{s}_2 \end{bmatrix} = \begin{bmatrix} -\psi_p \\ -\lambda s_1 \\ \lambda c_1 \\ -\lambda s_2 \\ \lambda c_2 \end{bmatrix} + [\tilde{\Psi}]\mathbf{a} \tag{38}$$

$$4B^2\ell_c\dot{\psi}_p = \bar{\phi} - \Phi_T(\psi_p)$$

where $\mu_n = 2/|n| + \mu$, and the cross-coupling between Fourier harmonics is encapsulated in the integral of the regressor matrix:

$$[\tilde{\Psi}] = \begin{bmatrix} 1 & \bar{\phi} & \left[\bar{\phi}^2 + \frac{1}{2}(R_1+R_2)\right] & \left\{\frac{3}{2}\bar{\phi}\left(\frac{2}{3}\bar{\phi}^2 + R_1 + R_2\right) + \frac{3}{4}\left[c_2\left(c_1^2 - s_1^2\right) + (2c_1s_1)s_2\right]\right\} \\ 0 & c_1 & \left[2\bar{\phi}c_1 + c_1c_2 + s_1s_2\right] & \left[\frac{3}{4}c_1\left(4\bar{\phi}^2 + R_1 + 2R_2\right) + 3\bar{\phi}(s_1s_2 + c_1c_2)\right] \\ 0 & s_1 & \left[2\bar{\phi}s_1 + c_1s_2 + s_1c_2\right] & \left[\frac{3}{4}s_1\left(4\bar{\phi}^2 + R_1 + 2R_2\right) + 3\bar{\phi}(c_1s_2 - s_1c_2)\right] \\ 0 & c_2 & \left[2\bar{\phi}c_2 + \frac{1}{2}\left(c_1^2 - s_1^2\right)\right] & \left[\frac{3}{4}c_2\left(4\bar{\phi}^2 + 2R_1 + R_2\right) + \frac{3}{2}\bar{\phi}\left(c_1^2 + s_1^2\right)\right] \\ 0 & s_2 & \left[2\bar{\phi}s_2 + c_1s_1\right] & \left[\frac{3}{4}s_2\left(4\bar{\phi}^2 + 2R_1 + R_2\right) + 3\bar{\phi}c_1s_1\right] \end{bmatrix}.$$

The following abbreviations have been employed to make the expressions more succinct:

$$\begin{aligned} c_1 &= \tilde{\phi}_{c1} \\ s_1 &= \tilde{\phi}_{s1} & R_1 &= c_1^2 + s_1^2 \\ c_2 &= \tilde{\phi}_{c2} & R_2 &= c_2^2 + s_2^2 \\ s_2 &= \tilde{\phi}_{s2} \end{aligned} \tag{39}$$

Of course these equations become even more complex as the number of modes incorporated is increased; symbolic manipulation software such as Mathematica or Maple is necessary. But for understanding some of the fundamental properties of the system, a 0th and 1st-mode only Galerkin expansion has been the most often used. In the general formulation presented above, this would yield four equations. But one can obtain a 3-state representation by considering the amplitude and phase of the rotating wave, rather than the sine and cosine coefficients. Setting $s_2 = c_2 = R_2 = 0$ in the above equations, and converting into amplitude-phase form by approximating the rotating stall amplitude A and phase β as follows:

$$\begin{aligned} A^2 &= c_1^2 + s_1^2 \\ \beta &= \tan^{-1}\left(\frac{c_1}{s_1}\right), \end{aligned} \tag{40}$$

we arrive at the following equations, originally derived by Moore and Greitzer [10] (albeit for specific values of the parameters, **a**):

$$\ell_c \dot{\bar{\phi}} = \Psi_c\left(\bar{\phi}\right) - \psi_p + \left(\frac{1}{2}a_2 + \frac{3}{2}a_3\bar{\phi}\right)A^2 ;$$

$$4B^2\ell_c\dot{\psi}_p = \bar{\phi} - \sqrt{\gamma\psi_p} ; \tag{41}$$

$$(2+\mu)\dot{A} = \left(a_1 + 2a_2\bar{\phi} + 3a_3\bar{\phi}^2\right)A + \frac{3}{4}a_3A^3 .$$

Although they appear to be complex, once the physical parameters **a**, B, ℓ_c, μ, and γ are specified, (41) is a simple system of three nonlinear ODEs. The 4th ODE, for β, simply indicates that the rotating stall wave rotates at constant speed, and therefore is not of interest. So the three states of the Galerkin Moore-Greitzer model are velocity in the compressor duct ($\bar{\phi}$), pressure in the plenum (ψ_p), and the amplitude of the 1st Fourier harmonic of velocity at the compressor face (*A*). The amplitude *A* is the Galerkin representation of the rotating stall cell amplitude. Note that in this model, full developed rotating stall is not an unsteady situation; in fact it is a *set of equilibria* along which *A* is non-zero. Figure 11 shows the equilibria of MG3 and the open-loop stability properties. Note that there are four separate branches of equilibria, two that are stable, and thus achievable/measureable in an open loop environment, and two that are unstable. The equilibrium to which the system settles is set by the intersection of the equilibrium branches with the throttle surface, $\Phi_T\left(\psi_p\right) = \sqrt{\gamma\psi_p}$ (see equation (1); γ is an input parameter that sets the throttle area). The throttle surface is independent of *A* and intersects either one or two of the stable solutions. The inset in Figure 11 shows the migration of equilibria with γ, which is the most commonly used 'bifurcation parameter' for describing how the equilibria evolve.

The two stable equilibrium branches are the points along the speed line, for which *A*=0, and the rotating stall characteristic, along which *A* is large. As shown in Figure 11b, as γ goes down in an uncontrolled compressor the system jumps from the no-stall branch to the in-stall branch in an abrupt way, which is undesirable. The hysteresis associated with recovery is also undesirable, as is the existence of two equilibria, one of which is rotating stall, at a given value of the throttle area parameter γ.

The first unstable equilibrium branch is the one along which *A*=0. This is the axisymmetric-flow extension of the compressor characteristic; stabilizing this set of equilibria is the goal of most modal control techniques. The second unstable equilibrium branch connects the peak of the compressor map and the rotating stall map; this is the focus of 'operability enhancement', or bifurcation-based, control schemes. If a control scheme can stabilize these equilibria, its existence may prevent the compressor from jumping directly between stable operation and fully developed rotating stall.

Figure 11c can also be interpreted as a bifurcation diagram with respect to a *disturbance* throttle area. The throttle characteristic is the same as described above, but here it represents effects which tend to undermine operability – changes in fuel flow, acceleration transients, etc. The fact that at a certain value of throttle area, the system jumps to a large amplitude rotating stall equilibrium, and that the throttle area must be increase significantly before the system returns to normal operation, indicates that points near γ_{peak}, even if they are stable in the small-amplitude (linear) sense, tend to easily transition into rotating stall. Proof that these points do in fact have poor operability requires one to analyse the nonlinear stability properties of the equilibria; this can be done either through simulation or in a more general theoretical context.
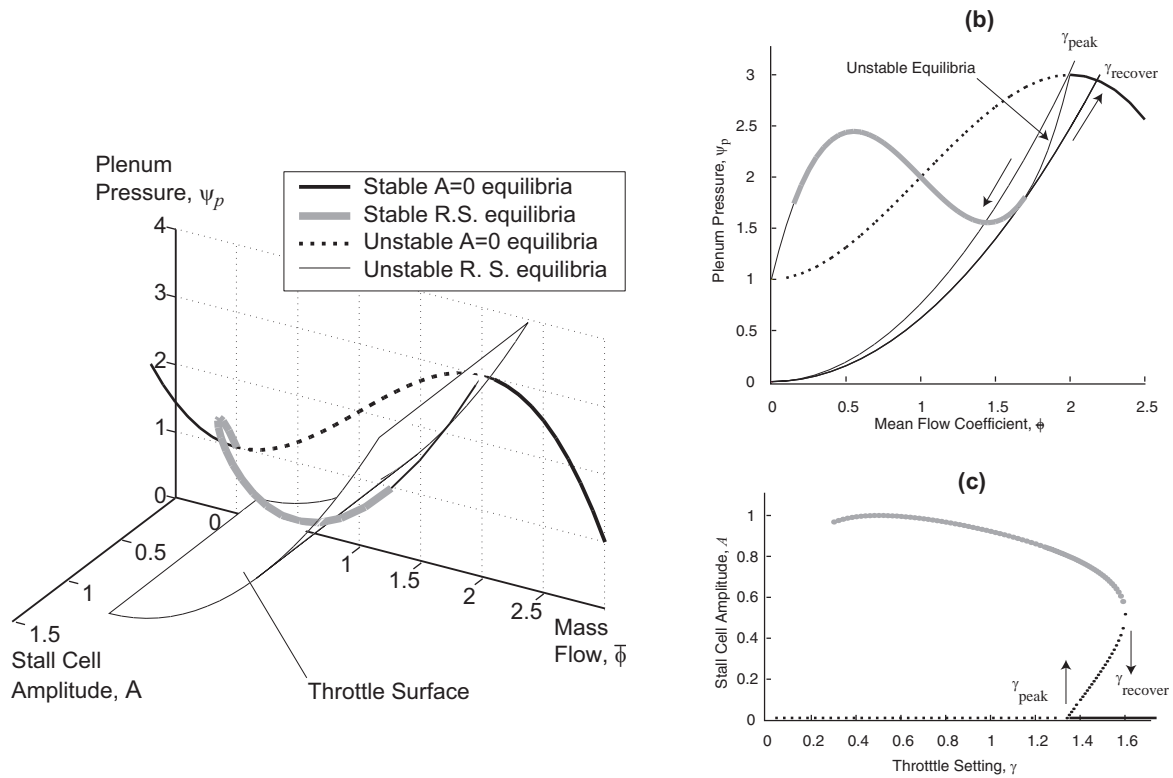
Figure 11 – Equilibria of the 3-State Galerkin approximation of the Moore-Greitzer model.
(a) three dimensional view of equilibria; (b) two dimensional view in the
$\overline{\phi} - \psi_p$ **plane; (c) equilibria viewed as bifurcations of the parameter γ.**

4.2 State-Space Representation

Although the Galerkin projection method is an efficient approach when the number of spatial harmonics to be incorporated is very low, it is unwieldy for larger dimensions. The source of complexity is representation of the nonlinearity $\Psi_C(\phi)$ using spatial Fourier coefficients. In this section, we instead represent the ODEs in the spatial domain, so that the nonlinearities are easily evaluated. The resulting equations are in 'state space' form, a form useful for application of control theory. The state-space Moore-Greitzer model is also a straightforward formulation for incorporation of unsteady loss dynamics, distortion, and actuators.

The reason that we have used the spatial Fourier domain so far is that the linearized flow field relationships are in this domain. If we begin with a circumferential flow coefficient distribution, $\phi(x = 0, \theta, t_0)$, we must first convert to SFCs, then apply the equations in Table II to determine the time derivative of ϕ and update, and then convert back to the spatial domain to determine the effects of the nonlinearities (refer to the algorithm in Section 3.3).

But the fact that all of the operations to represent the flow field are linear means that they can be applied directly to the differential equations, yielding linear operators that can be represented as matrix multiplications (if the Fourier coefficient representation of ϕ is truncated). Consider step 3 in the algorithm in Section 3.3:

$$\left(\frac{2}{|n|} + \mu \right) \dot{\tilde{\phi}}_n = \tilde{\Psi}_{C_n} - in\lambda\tilde{\phi}_n \quad n = -N, \cdots N, \ n \neq 0$$

$$\dot{\overline{\phi}} = \frac{1}{\ell_c} \left(\tilde{\Psi}_{C_{n=0}} - \psi_p \right) \quad (Note: \ \overline{\phi} = \tilde{\phi}_{n=0})$$

(42)

We first represent this in vector-matrix form:

$$\begin{bmatrix} \frac{2}{|-N|} + \mu & & & \\ & \ddots & & \\ & & \ell_c & \\ & & & \ddots & \\ & & & & \frac{2}{|N|} + \mu \end{bmatrix} \begin{bmatrix} \dot{\tilde{\phi}}_{-N} \\ \vdots \\ \dot{\bar{\phi}} \\ \vdots \\ \dot{\tilde{\phi}}_{-N} \end{bmatrix} = \begin{bmatrix} iN\lambda & & & \\ & \ddots & & \\ & & 1 & \\ & & & \ddots & \\ & & & & -iN\lambda \end{bmatrix} \begin{bmatrix} \tilde{\phi}_{-N} \\ \vdots \\ \vdots \\ \tilde{\phi}_N \end{bmatrix} + \begin{bmatrix} \tilde{\Psi}_{C-N} \\ \vdots \\ \tilde{\Psi}_{C0} \\ \vdots \\ \tilde{\Psi}_{CN} \end{bmatrix} - \begin{bmatrix} 0 \\ \vdots \\ \psi_p \\ \vdots \\ 0 \end{bmatrix} .\tag{43}$$

We wish to apply a matrix implementation of the inverse Fourier transform to this equation. Because we have truncated the SFC representation of the flow, and because the domain is periodic in θ, the *discrete* Fourier transform (DFT) is appropriate here. This transform has two important properties: (1) it yields a discrete representation of the flow field in the spatial domain, and (2) it can be represented as a matrix multiplication. Periodicity in θ insures that no information is lost in going between the truncated SFC domain and the discrete spatial domain (the truncated approximation is retained exactly). The transform pair for the discrete Fourier transform is:

$$\tilde{\phi}_n = \sum_{k=0}^{2N+1} \phi(\theta_k) e^{-j\theta_k n}$$
$$\phi(\theta_k) = \frac{1}{2N+1} \sum_{n=-N}^{N} \tilde{\phi}_n e^{j\theta_k n} \qquad \theta_k = \frac{2\pi k}{2N+1} . \tag{44}$$

We can represent both transforms as matrix multiplications:

$$\begin{bmatrix} \tilde{\phi}_{-N} \\ \tilde{\phi}_{-N+1} \\ \vdots \\ \tilde{\phi}_N \end{bmatrix} = \begin{bmatrix} e^{-2\pi(0)(-N)/N} & e^{-2\pi k(1)(-N)/N} & \cdots & e^{-2\pi k(2N+1)(-N)/N} \\ e^{-2\pi k(0)(-N+1)/N} & e^{-2\pi k(1)(-N+1)/N} & & \\ \vdots & & \ddots & \\ e^{-2\pi k(0)(N)/N} & & & e^{-2\pi k(2N+1)(N)/N} \end{bmatrix} \begin{bmatrix} \phi(\theta_0) \\ \phi(\theta_1) \\ \vdots \\ \phi(\theta_{2N+1}) \end{bmatrix} = F\underline{\phi} ; \tag{45}$$

$$\begin{bmatrix} \phi(\theta_0) \\ \phi(\theta_1) \\ \vdots \\ \phi(\theta_{2N+1}) \end{bmatrix} = \frac{1}{2N+1} \begin{bmatrix} e^{2\pi(0)(-N)/N} & e^{2\pi k(0)(-N+1)/N} & \cdots & e^{2\pi k(0)(N)/N} \\ e^{2\pi k(1)(-N)/N} & e^{2\pi k(1)(-N+1)/N} & & \\ \vdots & & \ddots & \\ e^{2\pi k(2N+1)(-N)/N} & & & e^{2\pi k(2N+1)(N)/N} \end{bmatrix} \begin{bmatrix} \tilde{\phi}_{-N} \\ \tilde{\phi}_{-N+1} \\ \vdots \\ \tilde{\phi}_N \end{bmatrix} = F^{-1}\underline{\tilde{\phi}} , \tag{46}$$

where we introduce the notation F and F^{-1} for the matrix DFT and its inverse, as well as as $\underline{\phi}$ and $\underline{\tilde{\phi}}$ for the vector representations of the flow at $x=0$ and its DFT (the elements of the latter matrix are the SFCs we have been using throughout this document).

Using these definitions, we can rewrite Equation (42) into a vector-matrix ODE:

$$D_E F\underline{\phi} = D_A F\underline{\phi} + F\left[\Psi_C(\underline{\phi})\right] - \underline{e_0}\psi_p . \tag{46}$$

D_E and D_A are matrices, defined based on Equation (43):

$$D_E = \begin{bmatrix} \frac{2}{|-N|} + \mu & & & \\ & \ddots & & \\ & & \ell_c & \\ & & & \ddots & \\ & & & & \frac{2}{|N|} + \mu \end{bmatrix} \qquad D_A = \begin{bmatrix} iN\lambda & & & \\ & \ddots & & \\ & & 1 & \\ & & & \ddots & \\ & & & & -iN\lambda \end{bmatrix} . \tag{47}$$

The notation $\left[\Psi_C(\underline{\phi})\right]$ indicates a vector whose elements are $\Psi_C(\phi(\theta_k))$. The vector $\underline{e_0}$ simply applies the scalar ψ_p to the zeroth-mode equation in the centre of the matrix:

$$\underline{e_0} = \begin{bmatrix} 0 & 0 & \cdots & 0 & 1 & 0 & \cdots & 0 & 0 \end{bmatrix}^T \tag{48}$$

The final step to create a standard state-space representation is to take the inverse Fourier transform of both sides of equation (46), so that the nonlinearity $\Psi_C(\phi)$ can be directly evaluated. The result is:

$$F^{-1}D_E\,F\,\dot{\underline{\phi}} = F^{-1}D_A\,F\,\underline{\phi} + F^{-1}F\big[\Psi_C\big(\underline{\phi}\big)\big] - F^{-1}\underline{e_0}\psi_p\,, \tag{49}$$

or, by recognizing that $F^{-1}F$ is the identity and introducing notation for the three other matrix operators (which, after all, can be computed once off-line to a simulation or control study):

$$E\dot{\underline{\phi}} = A\underline{\phi} + \big[\Psi_C\big(\underline{\phi}\big)\big] - T\psi_p\,. \tag{49}$$

The ODEs are completed by converted the plenum equation into vector matrix form:

$$\dot{\psi}_p = \frac{1}{4B^2\ell_c}\big(S\underline{\phi} - \Phi_T\big(\psi_p\big)\big). \tag{50}$$

The following definitions for the transformation matrices are readily verified:

$$\begin{aligned}
E &= F^{-1}D_E F\\
A &= F^{-1}D_A F\\
T &= \begin{bmatrix}1 & 1 & \cdots & 1 & 1\end{bmatrix}^T\\
S &= \frac{1}{2N+1}\begin{bmatrix}1 & 1 & \cdots & 1 & 1\end{bmatrix}
\end{aligned} \tag{51}$$

Equations (49) and (50) encapsulate the entire algorithm described in Section 3, where all of the Fourier transform and inverse transform steps have been folded into the matrix multiplications. The only approximation introduced is the truncation of the Fourier series. This state space formulation is indispensable for conceptualization and design of control laws, as well as for compact representation of the model extensions to be presented in the next sections.

4.3 Unsteady Loss Modeling

The compressor representation $\Psi_C(\phi)$ models how much of the unsteady pressure difference across the actuator disk is supported by the pressure rise of (or work done by) the compressor (see Equation (17)). So far we have assumed that Ψ_C is a nonlinear, memoryless operator on ϕ. Here we introduce a more detailed representation that accounts for the time required for pressure rise to develop across the compressor. This is done by allowing losses in the rotor and stator passages to develop over time according to first-order lags. To do this, we must first break the compressor map into components that separately account for ideal turning, viscous losses in the rotor, and viscous losses in the stator:

$$\Psi_c^{ss}(\phi) = \Psi_c^{id}(\phi) - L_s^{ss}(\phi) - L_r^{ss}(\phi). \tag{52}$$

$\Psi_c^{id}(\phi)$ is the ideal compressor characteristic, which never becomes negatively sloped (the blade passages continue to turn the flow efficiently as the flow coefficient is reduced). L_s^{ss} and L_r^{ss} account for the viscous loss effects, which grow as incidence increases, that is as the flow coefficient is reduced.

Next we must model what occurs in unsteady situations. Nagano et. al [27] performed one of the few measurements of the unsteady characteristics of a blade row, concluding that a first-order lag in the development of unsteady losses is a reasonable approximation (see Mazzawy, [31]). This leads to the following unsteady model for the compressor pressure rise, Ψ_c:

$$\begin{aligned}
\Psi_c &= \Psi_c^{id}(\phi) - \ell_s - \ell_r\\
\tau_s(\phi_3)\dot{\ell}_s &= L_s^{ss}(\phi) - \ell_s\\
\tau_r(\phi)\left\{\dot{\ell}_r + \frac{\partial}{\partial\theta}\ell_r\right\} &= L_r^{ss}(\phi) - \ell_r
\end{aligned} \tag{53}$$

The term in brackets is the time derivative of flow in the rotor passages, which depends on the shape of the perturbation through which the rotor is passing (similar to a convective derivative). ℓ_r and ℓ_s are the unsteady stator and rotor loss values respectively; note that the equations are constructed so that these values approach the nonlinear functions L_s^{ss} and L_r^{ss} exponentially, so that (52) and (53) are identical in steady state, uniform flow.

The time constants τ_r and τ_s are approximated, after Nagano et. al, as the flow-through times in the blade passages, which in turn depend on the blade chord and the flow coefficient:

$$\tau_{r,s}(\phi) = k_\tau \frac{\bar{b}_{r,s}}{\phi(\theta,t)}, \tag{54}$$

where $\bar{b}_r$ and $\bar{b}_s$ are the mean stator and rotor chord lengths and k_τ is an experimentally identified coefficient, typically near one.

We can introduce this new model of the compressor into the state-space formulation by first representing the $\frac{\partial}{\partial\theta}$ operator with a matrix operator on the approximate vector $\underline{\phi}$:

$$\left[\frac{\partial}{\partial\theta}\phi(\theta_k)\right] \cong F^{-1}\left[\partial\!\!\!/_{\partial\theta}\right]\underline{\tilde{\phi}}, \tag{55}$$

where

$$\left[\partial\!\!\!/_{\partial\theta}\right] = diag\left\{[i(-N+1) \quad i(-N) \quad \cdots \quad in \quad \cdots \quad iN]\right\}$$

is a diagonal matrix that performs the derivative on the Fourier coefficients. A matrix operator that performs the partial derivative is thus derived, as:

$$D_\theta = F^{-1}\left[\partial\!\!\!/_{\partial\theta}\right]F .$$

Using this relation to convert equations (53) into state space form, and combining with equations (49-50) yields an expanded model of rotating stall and surge that takes into account lags in the development of viscous losses:

$$\begin{bmatrix} E\dot{\underline{\phi}} \\ \tau_s \dot{\underline{\ell}}_s \\ \tau_r \dot{\underline{\ell}}_r \\ \dot{\psi}_p \end{bmatrix} = \begin{bmatrix} A & -I & -I & -T \\ 0 & -I & 0 & 0 \\ 0 & 0 & -I - \tau_r D_\theta & 0 \\ \frac{K_B}{\ell_c}S & 0 & 0 & 0 \end{bmatrix} \begin{bmatrix} \underline{\phi} \\ \underline{\ell}_s \\ \underline{\ell}_r \\ \psi_p \end{bmatrix} + \begin{bmatrix} \Psi_C^{id}(\phi) \\ L_s^{ss}(\phi) \\ L_r^{ss}(\phi) \\ -\frac{K_B}{\ell_c}\Phi_T(\psi_p) \end{bmatrix} \tag{56}$$

Note that since rotor and stator loss are distributed parameters, ℓ_r and ℓ_s have been made into vectors of the same dimension as $\underline{\phi}$. This triples the dimension of the non-linear simulation; in a linearized setting it alters the eigenvalue problem for each circumferential mode to a third order problem. This additional complexity appears to be necessary, however, to accurately capture the stability properties of higher circumferential harmonics. Figures 12 and 13, taken from the study of Haynes et. al [28], demonstrate this fact. They show the real and imaginary parts (growth rate and rotation rate) of the first three harmonics in a low speed research compressor, obtained using system identification methods. Without the unsteady loss model presented here, the Moore-Greitzer model does not accurately capture the eigenvalue behaviour as a function of mass flow. However, with the unsteady loss dynamics included, the model's ability to capture the eigenvalues is markedly improved. Not that this is not a demonstration of the predictive capability of the model, which is generally imperfect; model parameters must typically be tuned based on experimental data. Instead, it is a demonstration of the model's ability to capture the observed behaviour, such as the relative stability of the eigenmodes, the trends with mass flow, etc. This ability to capture the dynamics, rather than predict them, is the sufficient for most control applications.
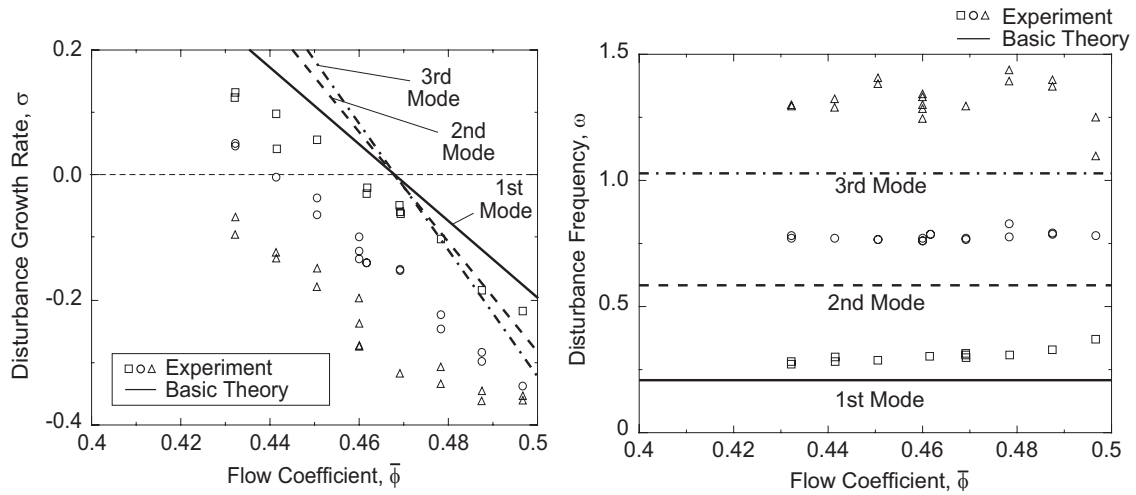
Figure 12 – Modeling results vs. measurement for Moore-Greitzer model *without* inclusion of lag in the development of losses. From Haynes et al., [28].
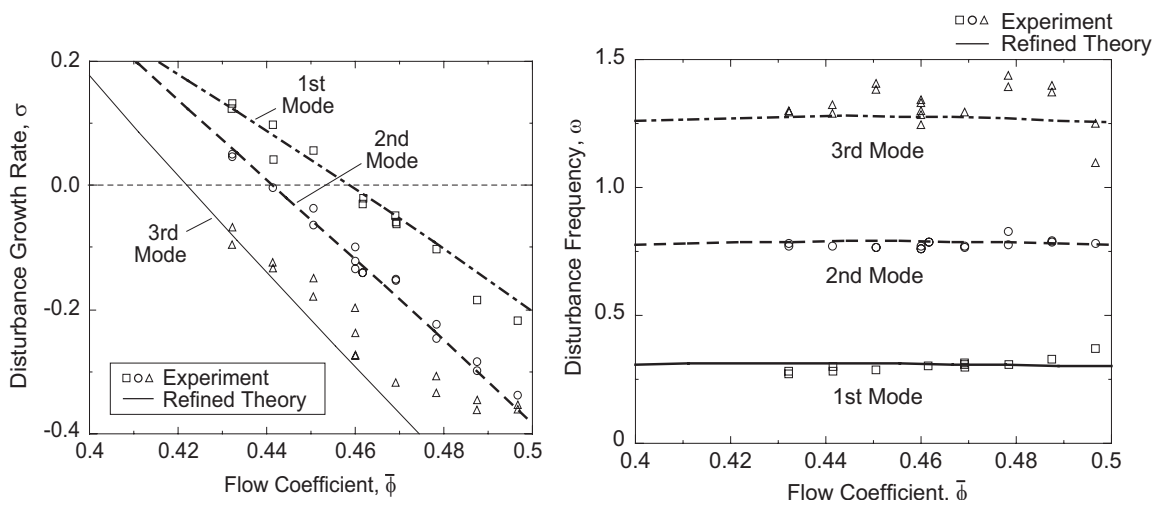
Figure 13 – Modeling results vs. measurement for Moore-Greitzer model *including* lag model for the development of losses. From Haynes et al., [28].

4.4 Inlet Distortion Modeling

Inlet distortion, resulting from separation of the lip or inlet, side gusts, hot gas ingestion, etc. is known to have a significant impact on compressor stability. In the state-space, control theoretic framework being presented here, inlet distortion can be represented as external forcing. The character of this forcing can be either steady or unsteady. It is a non-uniformity in either the circumferential or radial flow, or both. The primary forms of inlet flow non-uniformity are total pressure and temperature. We will consider steady, circumferential, total pressure distortions here; our formulation is also suitable for the study of *unsteady* circumferential total pressure distortion. Temperature distortion and radial distortion can be represented in the Moore-Greitzer framework, but these models involve approximations and additional calculations.

When inlet distortion is added at the inlet, the upstream flow field assumptions must be rethought. This is done in detail by Hynes and Greitzer [2] and by Chue et al [21]. To develop a model, an experimental distortion scenario (rather than an operational environment) is modelled. When distortion is studied experimentally, a semi-porous screen is placed in the upstream annular duct, creating a loss or blocking over some fraction of the circumference (typically 90 to 180 degrees). The total pressure loss across this screen convects downstream, causing some parts of the compressor to experience lower total pressure than others. Thus the compressor operates in two different regimes, and the flow velocities accelerate until a fluid mechanical balance is reached. Inertia in the blade passages, as well as the upstream and downstream flow relations, determine the resulting axial velocity pattern, which is non-uniform but steady (i.e. a new, distorted equilibrium). As the compressor is throttled into stall, lightly damped eigenmodes of this new equilibrium appear and eventually go unstable. The character

of these eigenmodes is completely different from the uniform flow eigenmodes, which are sinusoidal waves rotating at constant speed. However, the physics that govern distorted-flow eigenmodes are the same. Straight-forward modifications to the model already developed can capture the behaviour of the dynamics quite accurately.

The approach to modelling this experimental scenario is to assume that the streamlines downstream of the distortion screen remain straight and parallel throughout the upstream flow. Thus no nonlinear redistribution of the flow field is allowed. Although this will clearly not be the case behind a significant pressure loss screen, the error for typical screens is acceptable – the important feature to capture is the total pressure non-uniformity. The velocity field is assumed to continue to satisfy the linearized relations already presented – that is, it is a potential flow. Longley [29] validated this model in an indirect way by showing that the complete model described distorted flow phenomena well. More recently, van Schalkwyk [20] directly compared the upstream flow field predicted by this model, the predictions of a fully nonlinear 2D Euler simulation, and measurements in a heavily instrumented low speed research compressor. He found that while there was some flow redistribution behind the screen (i.e. curvature of streamlines), it was small and had negligible impact the accuracy of stability predictions.

Based on these assumptions the model of the distortion screen is that it introduces a total pressure profile at the compressor face that is determined by a screen loss function $S_C(\theta)$. This screen loss function can be viewed as a 2D generalization of a throttle:

$$\psi_{t\,screen} = -\frac{1}{2}S(\theta)\bar{\phi}^2. \tag{57}$$

Superimposed on this effect is the impedance relation of the potential flow perturbations. The resulting equations for the upstream flow can be written as follows:

$$\psi_{t\,x=0} = -\frac{\partial \Theta}{\partial t} - \frac{1}{2}S(\theta)\bar{\phi}^2. \tag{58}$$

Comparing this equation to the one in the first column of Table III, we see that the only change is an additional term, which can be considered as an external forcing term if the mean flow is not allowed to vary. This will be the case if the system is still stable and the throttle is used to set the compressor mass flow. The view of distortion as an external force is not strictly correct during large oscillations of the mean flow in our experimental scenario, since mean flow variations will cause the distortion to change. In an operational environment, large flow oscillations induced by the compressor may also alter the nature of the distortion-producing element (such as the inlet lip). However, to understand distortion and to characterise many practical issues, it is relevant to treat distortion as external forcing (i.e. not coupled to the system dynamics).

If distortion is simply an external forcing function, one might ask how it can change the homogeneous behaviour of the system. In linear systems, external forcing has no effect on the eigenvalues; details of its introduction only effect the system's forced or 'input-output' properties. However, in non-linear systems, steady external forcing can change the *equilibrium* of the system, and the homogeneous properties at this new equilibrium may be different. To study this effect, Hynes and Greitzer first solved for the equilibrium flow properties, and then linearized the dynamics about this new equilibrium. We can perform the same analysis in our new framework by introducing (57) into our state-space model (49-50), and computing the steady solution:

$$\begin{aligned} 0 &= A\underline{\phi} + \left[\Psi_C\left(\underline{\phi}\right)\right] - T\psi_p - \underline{s_c} \\ S\underline{\phi} &= -\Phi_T\left(\psi_p\right) \end{aligned}. \tag{59}$$

The second equation simply allows the mean flow to be set using the throttle. The first equation is the steady version of equation (49), with the addition of an external forcing vector defined to be equal at each circumferential location (that is, for each vector element) to $\psi_{t\,screen}(\theta)$ in equation (57). The solution to this non-linear equation must be found iteratively. The result is $\phi(\theta_k)$, the circumferential distribution of flow coefficient, contained in the vector $\underline{\phi}$. One also obtains ψ_p at the equilibrium point. Figure 14 shows a typical profile, for a low-speed experimental compressor. Clearly the

equilibrium has changed dramatically – and one can expect that the unsteady character will change accordingly.
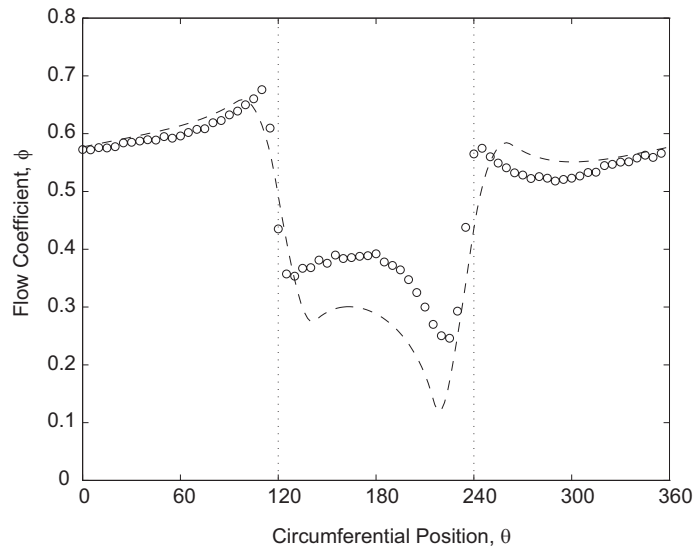
Figure 14 – Steady state effect of inlet distortion. Flow coefficient variation with circumference. Dashed lines are the boundaries of the 'spoiled sector', that is the region behind the distortion screen. From van Schalkwyk, [20].

Our state space formulation is also well suited to computing the linearized unsteady character of the flow resulting from distortion. To linearize about the new equilibrium, we simply create a diagonal matrix of local linearizations of the compressor map (the only non-linear term in equation (49)). Each circumferential location of the annulus will have a different local linearization because the flow coefficient is different at each location. Denote this diagonal matrix P_d:

$$P_d = diag\left\{ \frac{d\Psi_c}{d\phi}\bigg|_{\phi(\theta_1)}, \frac{d\Psi_c}{d\phi}\bigg|_{\phi(\theta_2)}, \cdots, \frac{d\Psi_c}{d\phi}\bigg|_{\phi(\theta_N)} \right\} \tag{60}$$

The throttle slope, since it operates only on the mean flow, is linearized as in equation (20), $m_T^{-1} = \dfrac{d\Phi_T}{d\psi_p}$.

Introducing these linearizations into equations (49-50) results in the following linearized, state-space representation:

$$\begin{bmatrix} \dot{\underline{\phi}} \\ \dot{\psi}_P \end{bmatrix} = \begin{bmatrix} E^{-1}(A+P_d) & -T \\ \dfrac{1}{4B^2\ell_c}S & \dfrac{1}{m_T 4B^2\ell_c} \end{bmatrix} \begin{bmatrix} \underline{\phi} \\ \psi_p \end{bmatrix}. \tag{61}$$

Note that we have neglected to linearize equation (57) in this formulation – this will introduce extra damping on the mean flow, because the screen behaves in a manner similar to the throttle from the perspective of the mean-flow. This is a simple addition to the above analysis that we omit for brevity.

To understand the effect of distortion on the stability and character of perturbation waves, one simply computes the eigenvalues and eigenvectors of the matrix on the right-hand side of (61). Since the states include the flow coefficient distribution, the real parts of the eigenvectors directly represent the spatial distribution of the flow coefficient. Modulating these eigenvectors by a unity phasor and then computing the real part gives the spatial distribution as the wave rotates around the annulus (neglecting the effect of growth or decay rate). This allows the character of the rotating wave to be compared to the uniform flow case, where the flow coefficient distribution is always sinusoidal. Figure 15 shows the result of such a calculation, including a plot of the steady flow coefficient (i.e. the values that determine the diagonal elements of the matrix P_d). Each line in the top plot in Figure 15 represents the distribution for a different circumferential position of the wave, as it travels around the

annulus. The interweaving pattern is the result of a growing and shrinking process the wave undergoes as it rotates around. This can be understood by considering the slope of the compressor characteristic in various regions of the annulus. In regions where the slope is negative (due to high local flow coefficient), perturbations decay. Regions of lower flow experience positive local compressor slopes, so waves in that region tend to grow. The stability of the is determined by the interplay of these regions of growth and decay.
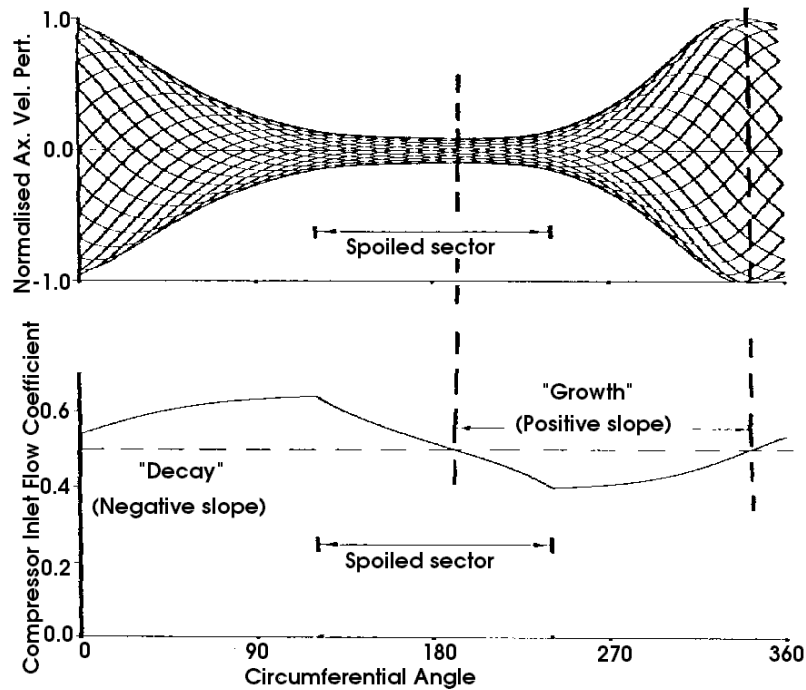
Figure 15 – Superimposed snapshots of a rotating stall precursor wave at various points around the annulus. From Hynes and Greitzer, [2].

4.5   Sensor and Actuator Models

Our discussion of modelling for control of rotating stall would not be complete without a discussion of sensors and actuators. Various sensors and actuators have been proposed and/or implemented for control of rotating stall. For each, the equations must be reconsidered and modified appropriately. We begin with a description of sensor choices and associated modelling considerations. We then present the modifications introduced by four different types of actuators, as a catalogue of possible actuators and a record of their behaviour. Considered are one-dimensional bleed from the duct downstream of the compressor, bleed from the plenum, inlet guide vane actuation, and injection of high-momentum air upstream of the compressor.

To represent the additional elements that we will add to the fluid system, we need to introduce several additional stations in the compressor schematic. Figure 16 shows these additional stations, as well as the locations of the sensors and actuators that we will discuss.
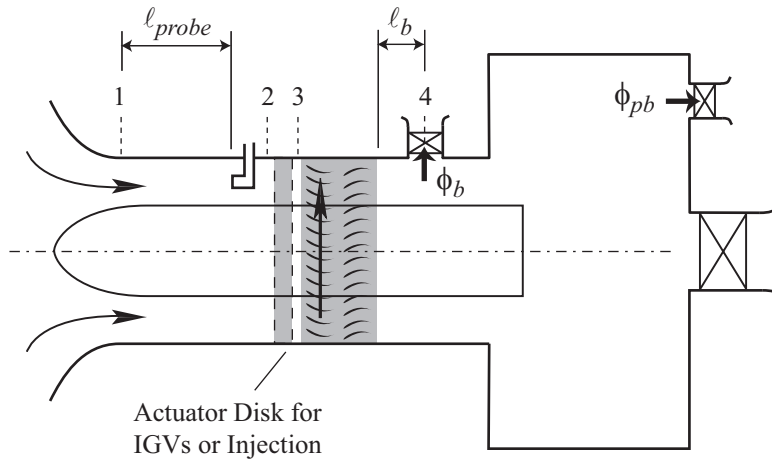
Figure 16 – Compression system schematic with additional notation for actuator modelling.

INTRODUCING SENSORS

Sensors fall into two broad categories: sensors that measure one-dimensional, mean flow properties, and sensors that measure local flow properties, and are often arranged in arrays to allow one to approximately determine the circumferential distribution of the two-dimensional flow variables. One-dimensional flow measurements can be approximated by averaging a distributed array of sensors in an annulus; in this case we model them as ideal mean-flow measurements.

One-dimensional measurements for control of surge are discussed in detail by Simon [24]. The choices are mean total pressure, static pressure, and velocity (or mass flow) measured in the duct upstream or downstream of the compressor, and static pressure measured in the plenum. Eveker et al. [34] also approximated the derivative of velocity for their control laws; this can be accomplished simply by measuring the static pressure difference across a section of duct as will be described presently.

Obviously mean duct velocity and plenum pressure measurements are directly represented in the compressor model already described – no additional modelling is necessary to represent these. To model mean total pressure at any station, we can write a modified version of the unsteady Bernoulli relation in equation (9), which assumes that the total pressure at the inlet to the upstream duct is zero. Our modifications to (9) are to eliminate the higher harmonics, and to take into account the duct length between the inlet and the probe, ℓ_{probe}:

$$\overline{\psi_{t\ probe}} = -\ell_{probe}\dot{\overline{\phi}} \ . \tag{62}$$

Substituting in the equation for $\dot{\overline{\phi}}$ (for instance (33)), we have:

$$\overline{\psi_{t\ probe}}\bigg|_{upstream} = \frac{-\ell_{probe}}{\ell_c}\left(\overline{\Psi_c(\phi)}-\psi_p\right) \tag{63}$$

This is the non-dimensional, perturbation value of total pressure at an arbitrary station in the upstream duct. It can be linearized or converted to state-space form as appropriate for the analysis at hand.

In the downstream duct, we can determine static pressure in a similar manner, using the static pressure in the plenum as a reference. In this case we modify equation (16), arriving at the following relation:

$$\overline{\Psi_{probe}}\bigg|_{downstream} = \psi_p + \frac{(\ell_c - \ell_{probe})}{\ell_c}\left(\overline{\Psi_c(\phi)}-\psi_p\right). \tag{64}$$

The term in numerator is the distance from the probe to the plenum. Note that since $\dot{\overline{\phi}}$ is utilised to derive this equation as well, one could deduce $\dot{\overline{\phi}}$ by placing one static pressure transducer in the

plenum and another set (sufficient to determine mean static pressure) some distance upstream of the plenum. Finally, we note that the formulation of Moore-Greitzer is based on static pressure upstream and total pressure downstream of the compressor, but one can relate the two at any station to complete the modelling:

$$\overline{\psi}_{probe} = \overline{\psi_t}_{probe} - \overline{\phi}^2 \text{ (any station)} \tag{65}$$

The two-dimensional or local-flow probe types that have been used to date in most experiments are arrays of hot wires and arrays of high-response, static pressure transducers (mounted in the casing). Several measurements are typically taken at the same axial station and combined using the discrete Fourier transform relations in equation (44)-(46) to estimate Spatial Fourier Coefficients (SFCs). To model these arrays, we again rely on the Moore-Greitzer derivation. Velocity at the compressor face is directly available from the model; however hot wires may be placed some distance upstream. In this case we apply a transformation based on equation (6), which states that higher harmonic components of the velocity distribution at the compressor face are attenuated:

$$\tilde{\phi}_n\big|_{probe} = e^{-|n|\chi}\tilde{\phi}_n \tag{66}$$

where $\chi = \ell_u - \ell_{probe}$ is the distance from the probe to the compressor face. This relation can be translated into state space form in a manner similar to the other relations derived so far; the result being:

$$\underline{\phi}_{probe} = F^{-1}D_{probe}F\overline{\phi} \tag{67}$$

where $D_{probe} = diag\left\{e^{-N\chi},\ e^{-(N-1)\chi},\ \cdots\ e^{-2\chi},\ e^{-\chi},\ 1,\ e^{-\chi},\ e^{-2\chi}\ \cdots,\ e^{-(N-1)\chi},\ e^{-N\chi}\right\}$.

Note that the zeroth-harmonic contribution is included in this formulation, and is not attenuated. Equation (67) is valid in the upstream duct. Although one could derive a similar relation downstream, hot wires in this region are uncommon because of the increased noise introduced by blade wakes.

Finally, we consider distributed static pressure sensors. It is sufficient at this point to give the relationship between static pressure and velocity in SFC form, and allow the reader to deduce the state space equivalent. Upstream of the compressor, as with hot wires, is a much more common location for these sensors than downstream (unsteady static pressure sensors are also often placed within the compressor itself; modelling these would require one to introduce additional details about inter-blade pressure rise characteristics). In the upstream case we can apply the unsteady Euler equation, $\partial\psi_t/\partial x = -\partial\phi/\partial t$. Combining this equation with the upstream solution and the definition of total pressure, and linearizing yields:

$$\tilde{\psi}_n\big|_{probe} = -\dot{\tilde{\phi}}_n\big|_{probe} + \overline{\phi}\,\tilde{\phi}_n\big|_{probe}. \tag{68}$$

In this equation, the time derivative of the flow coefficient at the compressor face must be computed using for instance (25) or (49), and then projected to the probe location using (66).

The remaining sections describe various models for actuators that have been used for rotating stall control in the past. Although this list is not all-inclusive, it does give a sampling of the type of actuators that have been used, and the assumptions and approximations that have been found to be appropriate.

1D BLEED FROM DOWNSTREAM DUCT AND PLENUM BLEED

Many researchers have investigated the use of purely one-dimensional actuation, either for control of surge in compressors not prone to rotating stall (centrifugal compressors, primarily), or for application of bifurcation-based methods to control rotating stall. One-dimensional actuation is the simplest to model, so it is described first. Two types of actuation will be introduced in this context. The first is one-dimensional bleed from the duct downstream of the compressor (see Figure16). Continuity and 1D momentum arguments in the downstream duct lead to the following modification to equation (16):

$$\psi\big|_{x=0^+} = \sum_{n\neq 0}\frac{1}{|n|}\dot{\tilde{\phi}}_n e^{in\theta} + \left(\psi_p + \ell_d\dot{\bar{\phi}}\right) - \left(\ell_d - \ell_b\right)\dot{\phi}_b \qquad (69)$$

where ϕ_b is the normalised mass flow exiting through the bleed. Equation (18) must also be modified to reflect the fact that less mass flow will go into the plenum if it is bled off upstream. We can combine this change with the change introduced by a *plenum* bleed, which only modifies the plenum mass balance:

$$\dot{\psi}_p = \frac{1}{4B^2\ell_c}\left\{\bar{\phi} - \Phi_T\left(\psi_p\right) - \phi_b - \phi_{pb}\right\} \qquad (70)$$

both ϕ_b and ϕ_{pb} can be related through throttle characteristics to the area of the throttle opening and the pressure drop across it; these relationships are similar to the main throttle relation. One can imagine implementing a control law that commands ϕ_{pb} and subsequently determines the throttle opening required to achieve this based on the pressure in the plenum and a previously identified set of throttle maps.

INLET GUIDE VANES

Inlet guide vane (IGV) actuation is of interest primarily in an experimental setting. Consider a set of inlet guide vanes that are independently actuated in incidence (or, alternatively, incorporate flaps or circulation control to change their degree of flow turning). These IGVs would be able to change the incidence of the flow introduced to the rotor in a non-uniform manner. In this way, IGV actuators provide a direct method to change the local pressure rise delivered by the compressor. For modelling purposes, this effect is represented by simply replacing $\Psi_c^{id}(\phi)$ in equation (53) (or, alternatively, $\Psi_c(\phi)$, if unsteady losses will not be considered) with $\Psi_c^{id}(\phi,\gamma)$, where γ is the circumferentially distributed IGV incidence (perturbation from mean turning). Thus a two-parameter, non-linear, steady state function must be identified experimentally to capture both the compressor map and its sensitivity to IGV incidence. Because IGVs have a direct impact on the source of rotating stall instability (compressor pressure rise), one can quite readily use them for rotating stall control, provided they have sufficient circumferential resolution. Twelve circumferentially distributed and actuated guide vanes, for instance, are capable of actuating modes zero through six (the Nyquist frequency), although in practice only modes up to the third or fourth are accessible.

Modulation of incidence is not the only effect of modulating the IGVs. If two adjacent IGVs are deflected in opposite directions, they form a converging passage. Such a passage causes the flow to increase in velocity to satisfy continuity. In addition, total pressure variations will occur due to acceleration of flow within the passage. The details of this process are described by Paduano [26], and result in the following relationships upstream of the compressor:

$$\phi_2 = \left(1 + \mu_a\frac{\partial\gamma}{\partial\theta}\right)\phi_3$$
$$\psi_{t3} = \psi_{t2} - \mu_a\frac{\partial}{\partial t}\left(\phi_3 + \frac{1}{2}\mu_a\frac{\partial\gamma}{\partial\theta}\phi_3\right) \qquad (71)$$

The additional terms and axial stations in these equations are defined in Figure 16. These additional equations, together with the new representation of the compressor characteristic, form the actuation model for IGVs.

INJECTION OF HIGH-MOMENTUM FLOW

Another type of actuation that is currently being investigated is injection of high-momentum air into the upstream annulus. Injectors are assumed here to be uniformly distributed circumferentially; this restriction can be removed if care is taken to take into account the more localized injection effects that would be introduced by an array of discrete injectors.

A two dimensional, evenly distributed set of injectors has three effects. First, it can be directed in such a way that it changes the incidence angle of the first stage rotor (if no IGVs are present). This, like IGV deflection, changes the pressure rise delivered by the compressor. Second, it adds momentum to the flow, which translates into additional pressure rise from the compressor/actuator combination. Third, the mass flow through the system is altered; thus the mass flow through each of the various elements of the system will be modified.

To include incidence effects, we first (as in the case of IGVs) replace $\Psi_c^{id}(\phi)$ with $\Psi_c^{id}(\phi, q)$, where q is the area of the injector opening nondimensionalized by the annulus area. To include momentum effects, a momentum balance is done across the actuator disk containing the injectors – this is described by Vo [29]. A simplified relationship approximates the primary effects (see [30]):

$$\psi_{t_3} = \psi_{t_2} + (\phi_j - \phi_2)\phi_j q \,. \tag{72}$$

where the stations are defined in Figure 16 and ϕ_j is the normalised injection velocity. Finally, continuity considerations yield the third relationship:

$$\phi_2 = \phi_3 - \phi_j q \tag{73}$$

5 Conclusions

These notes attempt to give a comprehensive account of modeling techniques used for control of rotating stall and surge. Because such modeling has been primarily based on the Moore-Greitzer model, that has been the focus of the technical discussion. This is not to say that more computationally intensive methods have not yielded information useful to the endeavor of active control. On the contrary, for the design of actuators, for understanding where those actuators would have the most influence, and for understanding the detailed nature of flow instabilities, such computational approaches have been invaluable. However, for control law design and developing a basic understanding of the forces at work in a compressor, especially when the compressor is influenced by large scale forcing functions such as circumferential distortion and non-uniform tip clearance, the models presented here are "as simple as they can be while not being too simple", and yield insight into the main effects that are important.

6 References

1. Weigl, H. J., Paduano, J. D., Frechette, L. G., Epstein, A. H., Greitzer, E. M., Bright, M. M., and Strazisar, A. J., 1998, "Active Stabilization of Rotating Stall in a Transonic Single Stage Axial Compressor," 97-GT-411, *ASME J. of Turbomachinery*, October, Vol. 120, No. 4, pp. 625-636.
2. Hynes, T. P. and Greitzer, E. M. 1987, "A Method of Assessing Effects of Circumferential Flow Distortion on Compressor Stability," *ASME J. of Turbomachinery*, Vol. 109, pp. 371-379.
3. Spakovszky, Z. S., Gertz, J. B., Sharma, O. P., Paduano, J. D., Epstein, A. H., and Greitzer, E. M., 2000, "Influence of Compressor Deterioration on Engine Dynamic Behavior and Transient Stall Margin," 97-GT-439, *ASME J. of Turbomachinery*, July, Vol. 122, No. 3, pp. 477-484.
4. Graf, M. B., Wong, T. S., Greitzer, E. M., Marble, F. E., and Tan, C. S., 1998, "Effects of Non-axisymmetric Tip Clearance on Axial Compressor Performance and Stability," *ASME J. of Turbomachinery*, July, Vol. 120, No. 4, pp. 648-661.
5. ARP 1420, "Aerospace recommended practice: Gas turbine engine inlet flow distortion guidelines"
6. Emmons, H. W., Pearson, C. F., and Grant, H. P., 1955, "Compressor Surge and Stall Propagation," Trans. of the ASME, Vol. 79.
7. Camp, T. R., and Day, I. J., 1997, "A Study of Spike and Modal Stall Phenomena in a Low-Speed Axial Compressor," 97-GT-526, *ASME J. of Turbomachinery*, Vol. 120, No. 3, pp. 393-401.
8. Tryfonidis, M., Etchevers, O., Paduano, J. D., Epstein, A. H., and Hendricks, G. J., 1995, "Pre-Stall Behavior of Several High-Speed Compressors," *ASME J. of Turbomachinery*, Vol. 117, No. 1, pp. 62-80.
9. Day, I. J., Breuer, T., Escuret, J., Cherrett, M., Wilson, A., 1997, "Stall Inception and the Prospects for Active Control in Four High Speed Compressors," 97-GT-281, ASME Turbo Expo '97, June 2-5, Orlando.

10. Moore, F. K. and Greitzer, E. M., 1986, "A Theory of Post-Stall Transients in Axial Compression Systems, Part I - Development of Equations, and Part II - Application, " ASME J. of Engineering for Gas Turbines and Power, Vol. 108, pp. 68-97.

11. O'Brien, W. F., "Dynamic Simulation of Compressor and Gas Turbine Performance," in *Steady and Transient Performance of Gas Turbine Engines,* AGARD Lecture Series 183, June 1992.

12. Hendricks, G. J., Bonnaure, L. P., Longley, J. P., Greitzer E. M., Epstein A. H., 1993, "Analysis of Rotating Stall Onset In High-Speed Axial Flow Compressors," AIAA paper 93-2233, 29th Joint Propulsion Conference, June 28-30, Monterey.

13. Feulner, M. R., Hendricks, G. J., and Paduano, J. D., 1994, "Modeling for Control of Rotating Stall in High Speed Multi-Stage Axial Compressors," 94-GT-200, ASME Turbo Expo '94, June 13-16, The Hague, Netherlands.

14. Hendricks, G. J., Sabnis, J. S., and Feulner, M. R., 1997, "Analysis of Instability Inception in High-Speed Multistage Axial-Flow Compressors," *Trans. ASME* October, Vol. 119.

15. Longley, J. P., "Calculating the Flowfield Behaviour of High-Speed Multi-Stage Compressors," 97-GT-468, Proc. ASME Turbo Expo '97, Orlando, FL.

16. Sun, X. F., 1996, "Three-Dimensional Compressible Flow Stability Theory of Rotating Stall," BUAA Technical Report BH-B4765, May.

17. Gong, Y., Tan, C. S., Gordon, K. A., and Greitzer, E.M., 1999, "A Computational Model for Short Wave-Length Stall Inception and Development in Multistage Compressors," *ASME J. of Turbomachinery*, October, Vol. 121, No. 4, pp. 726-734.

18. Longley, J. P., 1993, "A Review of Non-Steady Flow Models for Compressor Stability," ASME Paper 93-GT-17, 1993 ASME Turbo Expo, Cincinnati, May 24-27.

19. Lavrich, P. L., 1988, "Time Resolved Measurements of Rotating Stall in Axial Flow Compressors," GTL Report #194, Ph.D. Thesis, MIT Dept. of Aeronautics and Astronautics, August.

20. van Schalkwyk, C. M., Paduano, J. D., Greitzer, E. M., and Epstein, A. H., 1997, "Active Stabilization of Axial Compressors with Circumferential Inlet Distortion," 97-GT-279, ," *ASME J. of Turbomachinery*, July, Vol. 120, No. 3, pp. 431-439.

21. Chue, R., Hynes, T. P., Greitzer, E. M., Tan, C. S., and Longley, J. P., 1989, "Calculations of Inlet Distortion Induced Compressor Flow Field Instability," *International J. of Heat & Fluid Flow,* September, Vol. 10, No. 3, pp. 211-223.

22. Greitzer, E. M., 1981 "The Stability of Pumping Systems – The 1980 Freeman Scholar Lecture," *ASME J. of Turbomachinery*, June, Vol. 103, pp. 193-242.

23. Greitzer, E. M., 1975, "Surge and Rotating Stall in Aaxial Flow Compressors*," ASME Journal of Eng. for Power*, April, Vol. 98, pp. 190-217.

24. Simon, J. S., Valavani, L., Epstein, A. H., and Greitzer, E. M., 1993, "Evaluation of Approaches to Active Compressor Surge Stabilization," *ASME J. of Turbomachinery*, Vol. 115, January, pp. 57-67.

25. Mansoux, C. A., Gysling, D. L., Setiawan, J. D., and Paduano, J. D., 1994, "Distributed Nonlinear Modeling and Stability Analysis of Axial Compressor Stall and Surge," American Control Conference, July, Baltimore.

26. Paduano, J. D., Valavani, L., Epstein, A. H., Greitzer, E. M. and Guenette, G. R., "Modeling for Control of Rotating Stall," Automatica, Vol. 30, No. 9, September 1994, pp. 1357-1373.

27. Nagano, S., Machida, Y., and Takata, H., 1971, "Dynamic Performance of Stalled Blade Rows," Japan Soc/ of Mech. Eng. Paper #JSME-11, Presented at the Tokyo Joint Int. Gas Turbine Conf., Tokyo, Japan, Oct.

28. Haynes, J. M., Hendricks, G. J., and Epstein, A. H., 1994, "Active Stabilization of Rotating Stall in a Three-Stage Axial Compressor," *ASME J. of Turbomachinery*, Vol. 116, pp. 226-239.

29. Longley, J. P., 1980, "Measured and Predicted Effects of Inlet Distortion on Axial Compressors", ASME Paper 90-GT-214, Proc. 1990 ASME Turbo Expo, June 11-14, Brussels, Belgium.

30. Hendricks, G. J., and Gysling, D. L., "A Theoretical Study of Sensor-Actuator Schemes for Rotating Stall Control," 28th Joint Propulsion Conference, Nashville, TN, 1992.

31. Mazzawy, R. S., 1977, "Multiple Segment Parallel Compressor Model for Circumferential Flow Distortion,", *ASME J. of Eng. For Power*, Vol. 100, April.

32. Paduano, J. D., Greitzer, E. M., Epstein, A. H., Guenette, G. R., and Gysling, D. L., 1993, "Smart Engines: Concept and Application," *Integrated Computer-Aided Engineering*, Vol. 1, No. 1, pp. 3-29

33. Paduano, J. D., Greitzer, E. M., and Epstein, A. H., 2001, "Compression System Stability and Active Control," Annual Review of Fluid Mechanics, Vol. 33, pp. 491-517.

34. Eveker, K. M., Gysling, D. L., Nett, C. N., and Sharma, O. P., 1998, "Integrated Control of Rotating Stall and Surge in High-Speed Multi-Stage Compression Systems," ASME J. of Turbomachinery, Vol. 120, No. 3, pp. 440-445.

Compression System Dynamics: Control and Applications

Richard M. Murray

Robert L. Behnken   Simon Yeung   Yong Wang

Control and Dynamical Systems 107-81
California Institute of Technology
Pasadena, CA 91125 USA

1 Overview

These notes provide an introduction to active control techniques applied to compression system instabilities, chiefly rotating stall and surge. The material is derived from a number of sources, including material from the thesis work of Robert Behnken [4], Simon Yeung [41] and Yong Wang [37] and a variety of papers and books by the author [6, 29, 38, 42]. We also rely on a recent survey paper by Paduano et al. [31]. More detailed references are given in the individual sections.

1.1 Background

The design process for gas turbine engines has become quite mature over the past several decades and substantial performance increases have become harder to achieve. While most avenues in the design process have been deeply explored, one area of performance enhancement that has not be fully exploited is that of control. One reason for this is that the amount of complexity added by a control system has been, until recently, a major concern. Currently, the presence of full authority digital engine controllers (FADECS) on most modern aircraft has decreased the amount of additional hardware required to take advantage of more sophisticated control techniques. In addition to computation power, engine hardware is also being added to aid engine operability and to help eliminate startup transients. This additional equipment could also be exploited for control purposes.

It was recently shown that passive control techniques can be used to increase both engine efficiency and power output on actual full scale engines. The simulation study by Smith et al. [34] reported a 15% increase in thrust and 3% decrease in fuel consumption with the use of a controller that scheduled engine parameters, and experimental validation of these results was presented by Gilyard and Orme [12]. The experiments involved subsonic flight tests of an F-15 airplane at the NASA Dryden Flight Research Center, and showed up to 15% increase in thrust and a 1–2% decrease in fuel consumption. These increases in performance and efficiency for one of the highest performance aircraft in the world suggest that other aircraft would also see benefits from similar controls.
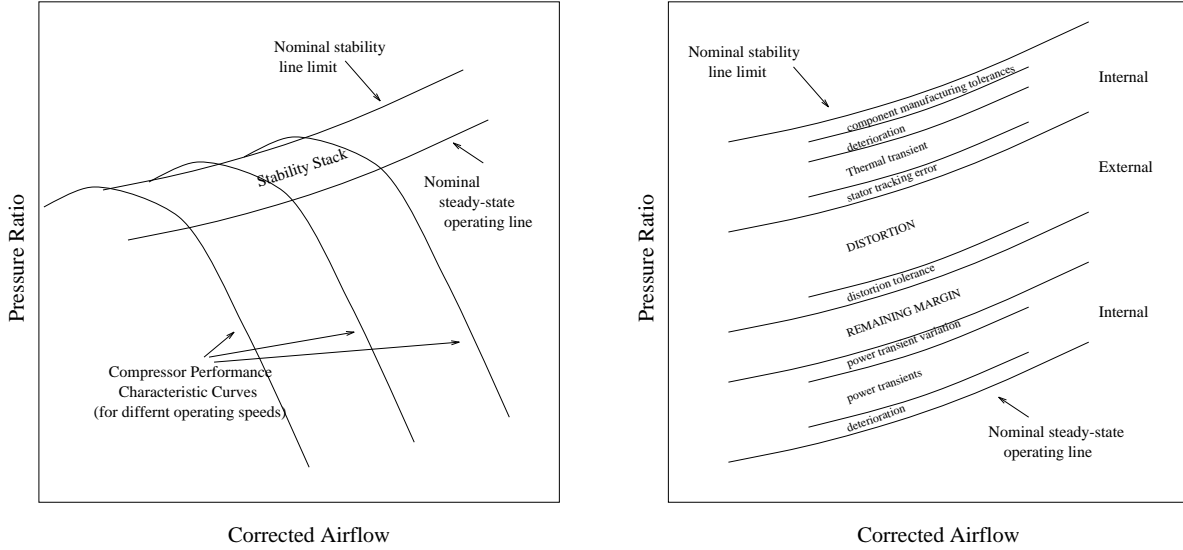
Figure 1: Typical components of the stability stack for a jet engine.

These results for passive control suggest that active techniques could also be beneficial for increasing performance and efficiency, by allowing the operation of the engine in previously unusable regions. These unusable regions are typically due to the presence of instabilities in the compression system under low flow/high pressure rise conditions. Unfortunately, the peak performance of the compressor is also achieved near the operating conditions at which these instabilities occur.

Two of the performance limiting factors for which active control holds promise are rotating stall and surge. Rotating stall is a non-axisymmetric instability that is localized to the compressor, and involves periodic stalling and unstalling in the blade passages. Surge is a violent system level axisymmetric oscillation that is due to the overall dynamics of the pumping system.

Figure 1 shows a *stability stack* for a typical jet engine, which is a graph of the amount of margin required to avoid performance limiting instabilities due to different factors. On the left side of the figure, several compressor performance characteristics are shown along with the stability stack. These characteristics show the pressure that is delivered by the compressor at a given flow rate. The *nominal stability line* is where a compressor system would start to exhibit some sort of instability (typically rotating stall or surge) under ideal operating conditions. Since the operating conditions are never ideal, the compressor must be operated some distance away from this curve in order to avoid instability. The stability margin for a given effect is the distance away from the nominal stability line that the compressor must be operated in order to avoid instability. Examples of effects for which stability margins are included are distortion and power transients; others are listed in the figure. The *nominal steady state operating line* is the curve where compressor system would start to exhibit instability under worst case operating conditions. This worst case is obtained by adding up all of the individual margins, and this sum of all of the individual margins is called the stability stack. The stability stack therefore tells how much margin must be included in order to avoid instability. An open area of research is in determining how to sum the individual margins into the stability stack; it is not clear that a linear combination is the correct way to combine the margins. Each of the components in the stack could possibly be decreased if the performance limiting instabilities (rotating stall and surge) could be damped by active control. In order to better describe the possibilities for active control, further description of the performance limiting instabilities is now in order.

2
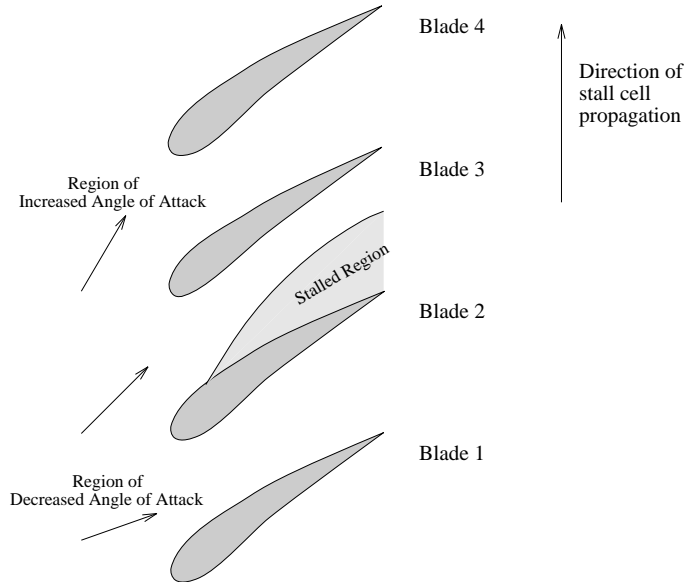
Figure 2: Emmons model for stall cell propagation.

The Emmons [9] model for rotating stall is shown in Figure 2, and provides a simple explanation for stall cell formation and propagation. As the throttle on the compressor is slowly closed, the angle of attack on the blades increases to a point where the flow separates on one of the blades; this creates a blockage that the flow is redirected around. This flow redirection causes the angle attack for the passage below the stalled region to be decreased; this makes this lower passage less likely to stall. On the blade passage above the stalled passage the angle of attack is increased; this makes this above passage more likely to stall. This effect causes the stall cell to rotate around the compressor annulus.

Surge is caused by the alternating storage and release of compressed air in the downstream ducting of the compressor. The compressibility of the air acts as a spring system, and the nonlinear compressor performance characteristic provides negative damping to this spring system under some operating conditions, and this effect leads to surge.

While these two instabilities are often modeled as separate phenomena, there is coupling between them, and rotating stall is a precursor to the onset of surge in many engines. In fact, work by Day [8] suggests that rotating stall causes the onset of surge. In addition to the coupling with surge, rotating stall has a large hysteresis loop associated with it. This hysteresis results in the requirement of large swings in operating conditions in order to recover from a stalled condition (in practice, recovery is often accomplished by shutting the engine down and restarting it). A more detailed description of these and other instabilities that limit the performance of compression systems can be found in the survey paper by Greitzer [14].

While these two instabilities limit performance, there are other reasons that they must be avoided. On high speed engines (high speed refers to the Mach number being high, and therefore that compressibility effects are important), rotating stall leads to drastic increases in compressor stage temperature and can lead to titanium fires [8]. During deep surge, reverse flow through the engine can lead to combustion gases exiting the engine inlet and can create large pressure spikes in the combustor. Rotating stall and surge must therefore be avoided not only because of the performance limitations that they are associated with, but also because they can cause severe damage to, or even failure of, the engine. Active control research for axial flow compressors therefore

3

focuses on developing techniques for both decreasing the performance limitations associated with these instabilities and on developing active disturbance rejection techniques for avoiding them.

1.2 Brief review of the literature

There has been substantial work in the area of active control of rotating stall and search in the past ten years. We provide a brief overview here, somewhat skewed toward those most relevant for our own research results. Additional information on some of the history of active control can be found in the recent survey article by Paduano et al. [31].

Modeling and analysis

The centerpiece of nearly all theoretical work in the area of control of rotating stall and surge for axial flow compressors is the model developed by Greitzer beginning with [13] and Moore in [27]. Their work culminated in what is now referred to as the MG-3 model, for Moore and Greitzer three state model, and was first presented in [28]. This work is significant because it provides a low order nonlinear model which captures many of the qualitative features seen in these types of compression systems. Initial work at showing how the MG-3 model captures the behavior previously seen in experiments was performed by the same authors [15]. The Moore and Greitzer model consists of a partial differential equation (PDE) which describes the dynamics of an axial flow compressor. By assuming a potential flow solution for the flow perturbations in the inlet duct in the form of a Fourier series, the MG-3 model can be developed from this PDE by truncating the series at a single mode.

The first dynamical systems analysis performed on this model was presented by McCaughan in [25] and [26], where it was shown that the transition to rotating stall is captured as a transcritical bifurcation and that the transition to surge is captured as a Hopf bifurcation in the MG-3 model. Greitzer originally developed the B parameter [13] in order to calculate whether a given compressor would surge or transition to rotating stall, and McCaughan showed that the value of this parameter in the MG-3 model did help decide which of the instabilities would be dominant. She went on to show that the phenomena of classical and deep surge and the hysteresis associated with the jump to rotating stall were all present in the model, and could be explained from a dynamical systems standpoint. A similar analysis was performed by Abed et al. [1].

While the MG-3 model does capture much of the qualitative behavior of axial flow compressors, it does a poor job of quantitatively matching experimental data. In order to better match experimental measurements of rotating stall dynamics other researchers have included more terms in the Fourier series of the original Moore and Greitzer PDE description, and have extended the model to include additional effects. These additional modes and effects increase the order of the model substantially, but result in better correlation with experimental data. One of the most successful modeling examples was presented by Mansoux et al. [24], where time traces from flow measurements directly upstream of the compressor rotor face matched simulation results extremely well. The model used by Mansoux et al. has been labeled as the distributed model and includes higher Fourier modes for the flow perturbations at the rotor face as well as dynamics for the pressure rise delivered by the compressor as the flow rate through the system is changed. These dynamics (also referred to as unsteady loss dynamics) for the response of the compressor pressure delivery to changes in the flow conditions were suggested by Haynes et al. [18], and are essential for matching simulation and experimental data.

Initial work in active control for axial flow compressors focused on designing throttle controllers for the low order MG-3 model. Throttle control techniques are one dimensional in nature since

they act only on the circumferential averaged flow through the compressor. Liaw and Abed [23] developed the first model based controller for rotating stall. The most interesting aspect of their results is that the control law can eliminate the hysteresis loop associated with rotating stall. This is accomplished by stabilizing an unstable solution to the MG-3 equations which corresponds to small amplitude rotating stall (small is relative to the fully developed rotating stall that is open loop stable in the MG-3 model). Additional throttle controller design on the MG-3 model was performed by Krstić et al. [22] using backstepping techniques. The resulting controllers had similar effects of stabilizing the unstable equilibria associated with small amplitude rotating stall and, in addition, stabilized the surge dynamics.

The first extensive studies on 2-D actuation schemes for preventing rotating stall were performed by Hendricks and Gysling [19]. This work compared the linear stability of different actuator and sensing strategies to determine which was the most successful at extending the operating region of a compressor system. The result for actuation techniques was that the injection of air upstream of the rotor was the most promising method of controlling the transition to rotating stall. Further work on modeling air injection was presented by Gysling [16], where aeromechanical feedback was used to open a set of air injection ports upstream of the compressor face in response to static pressure perturbations at the outer wall of the compressor annulus.

Over the last five years, additional work in modeling and analysis has been used to better understand some of the limits of performance of actively controlled compression systems. Krstic et al. [21] have explored the use of nonlinear techniques such as backstepping to provide global controllers for stall, building on the nonlinear modeling work described above. Analysis of the limits of performance due to actuator magnitude and rate limits has been explored by Wang et al. [38].

Experimental results

There are several active control techniques that have been experimentally shown to decrease the detrimental effects of rotating stall in axial flow compressors, including active inlet guide vanes, high speed bleed valves, and air injection.

Control using inlet guide vane actuators works by damping out the small amplitude circumferential flow perturbations which grow into rotating stall. Paduano et al. [30, 32] and Haynes et al. [18] have both succeeded in controlling rotating stall using this type of actuation. By damping out the first several circumferential Fourier modes of the inlet flow perturbations, inlet guide vanes have been successfully used to extended the operating region of full size axial flow compressors. These methods provided as high as 18% decrease in the stalling mass flow [32].

High speed bleed valves work to control rotating stall by using the coupling between the surge and the rotating stall dynamics as described by the MG-3 model. Experimental results for controlling rotating stall using this method were presented by Badmus et al. [2], and a combined surge and rotating stall bleed valve controller was presented by Eveker et al. [10]. These actuators have been successful at eliminating the hysteresis associated with rotating stall and stabilizing the surge dynamics. One area which is problematic is the requirement of relatively high bandwidth actuators in order to control rotating stall using this actuation method.

Air injection has also proven successful at controlling rotating stall in experiments. Gysling's work [16] was based on using aeromechanical feedback for controlling a circumferential array of air injectors upstream of the rotor face. The aeromechanical feedback was based on the increased static pressure that is present in regions of the compressor annulus where rotating stall occurs. By clever valve design, this effect was used to inject air which damped out small amplitude flow perturbations

at the compressor inlet which would have grown into rotating stall cells. This actuation scheme provided for a 10% decrease in the stalling mass flow rate through the compressor for the closed loop case, compared with the steady air injection case. Twenty-four valves where used to accomplish this control technique, and the mass flow addition was approximately 4% of the stalling mass flow rate.

Further work using air injection to control rotating stall was performed by Day [7]. His work focused on using several different techniques for damping out the flow perturbations which grow into rotating stall cells. Two methods were investigated, one which attempted to measure the rotating stall modes (using hot-wires) and cancel them, and a second which measured local flow perturbations and attempted to reject them individually. Both of these methods were successful at extending the operating region of the compressor system. Day also showed that this sort of rotating stall control has a beneficial effect of damping out surge oscillations.

D'Andrea et al. [5] showed that the effect of continuous air injection was to shift the steady state compressor performance characteristic and then explored the use of this for closed loop control. The result was a controller which eliminated the hysteresis region associated with rotating stall. Further work by the same authors [6] showed results for air injection control of rotating stall and surge that are similar to those of Day [7], even though the injected air flow was not axial in nature.

These early studies have been extended to more realistic operating conditions in a number of recent papers. Weigl et al. [39] implemented a controller for rotating stall using air injection on a transonic, single state axial compressor at NASA and Rolls-Royce has reported results of control of surge and stall on a full scale engine [11]. Additional experimental results are reported in [31].

1.3 Outline

These notes provide an introduction to the basic concepts of active control of compression systems, focusing on rotating stall. Our emphasis is on *nonlinear* techniques for analysis and control of instabilities since these are the most relevant for compression system instabilities. A brief introduction to the definitions and tools of nonlinear control theory are given in Section 2. We then introduce the notion of active control of compression system instabilities in Section 3, focusing first on linear control techniques. Section 4 describes the use of nonlinear control methods, including bifurcation control, as applied to compression systems.

2 Introduction to Nonlinear Dynamics and Control

Rotating stall and surge represent system level instabilities in which nonlinear effects play an important role. In this section we give a brief introduction to some of the specific tools that have been used to analyze and control compression system dynamics. We assume familiarity with linear control techniques (covered elsewhere in the course).

2.1 Lyapunov Stability

In this section we review the tools of Lyapunov stability theory. These tools will be used to analyze stability of actively controlled compression systems. We present a survey of the results that we shall need in the sequel, with no proofs. The interested reader should consult a standard text, such as Vidyasagar [36] or Khalil [20], for details.

Basic definitions

Consider a dynamical system modeled by a smooth set of ordinary differential equations

$$\dot{x} = f(x) \qquad x(t_0) = x_0 \qquad x \in \mathbb{R}^n, \tag{1}$$

where x denotes the state of the system and x_0 is the initial condition for the system at time $t = t_0$. We will assume that $f(x)$ satisfies the standard conditions for the existence and uniqueness of solutions. A point $x^* \in \mathbb{R}^n$ is an *equilibrium point* of (1) if $f(x^*) \equiv 0$. We say an equilibrium point is *locally stable* if all solutions which start near x^* (meaning that the initial conditions are in a neighborhood of x^*) remain near x^* for all time. The equilibrium point x^* is said to be *locally asymptotically stable* if x^* is locally stable and, furthermore, all solutions starting near x^* tend toward x^* as $t \to \infty$.

By shifting the origin of the system, we may assume that the equilibrium point of interest occurs at $x^* = 0$. If multiple equilibrium points exist, we will need to study the stability of each by appropriately shifting the origin.

Definition 1. Stability in the sense of Lyapunov
The equilibrium point $x^* = 0$ of (1) is *stable (in the sense of Lyapunov)* at $t = t_0$ if for any $\epsilon > 0$ there exists a $\delta(\epsilon) > 0$ such that

$$\|x(t_0)\| < \delta \quad \implies \quad \|x(t)\| < \epsilon, \quad \forall t \geq t_0. \tag{2}$$

Lyapunov stability is a very mild requirement on equilibrium points. In particular, it does not require that trajectories starting close to the origin tend to the origin asymptotically. Asymptotic stability is made precise in the following definition:

Definition 2. Asymptotic stability
An equilibrium point $x^* = 0$ of (1) is *asymptotically stable* at $t = t_0$ if

1. $x^* = 0$ is stable, and

2. $x^* = 0$ is locally attractive; i.e., there exists δ such that

$$\|x(t_0)\| < \delta \quad \implies \quad \lim_{t \to \infty} x(t) = 0. \tag{3}$$
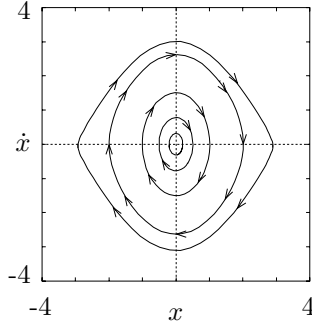
(a) Stable in the sense of Lyapunov
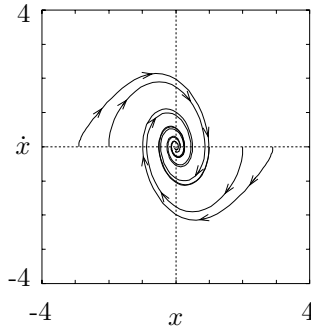
(b) Asymptotically stable
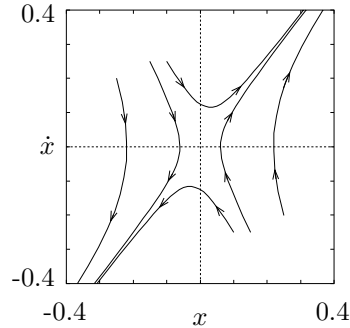
(c) Unstable (saddle)

Figure 3: Phase portraits for stable and unstable equilibrium points.

Finally, we say that an equilibrium point is *unstable* if it is not stable. Figure 3 illustrates the difference between stability in the sense of Lyapunov, asymptotic stability, and instability.

Definitions 1 and 2 are *local* definitions; they describe the behavior of a system near an equilibrium point. We say an equilibrium point x^* is *globally* stable if it is stable for all initial conditions $x_0 \in \mathbb{R}^n$. Global stability is very desirable, but in many applications it can be difficult to achieve. We will concentrate on local stability theorems and indicate where it is possible to extend the results to the global case.

It is important to note that the definitions of asymptotic stability do not quantify the rate of convergence. There is a strong form of stability which demands an exponential rate of convergence:

Definition 3. Exponential stability, rate of convergence
The equilibrium point $x^* = 0$ is an *exponentially stable* equilibrium point of (1) if there exist constants $m, \alpha > 0$ and $\epsilon > 0$ such that

$$\|x(t)\| \leq m e^{-\alpha(t-t_0)} \|x(t_0)\| \tag{4}$$

for all $\|x(t_0)\| \leq \epsilon$ and $t \geq t_0$. The largest constant α which may be utilized in (4) is called the *rate of convergence.*

Exponential stability is a strong form of stability; in particular, it implies asymptotic stability. Exponential convergence is important in applications because it can be shown to be robust to perturbations and is essential for the consideration of more advanced control algorithms, such as adaptive ones. A system is *globally exponentially stable* if the bound in equation (4) holds for all $x_0 \in \mathbb{R}^n$. Whenever possible, we shall strive to prove global, exponential stability.

8

The direct method of Lyapunov

Lyapunov's direct method (also called the second method of Lyapunov) allows us to determine the stability of a system without explicitly integrating the differential equation (1). The method is a generalization of the idea that if there is some "measure of energy" in a system, then we can study the rate of change of the energy of the system to ascertain stability. To make this precise, we need to define exactly what one means by a "measure of energy." Let B_ϵ be a ball of size ϵ around the origin, $B_\epsilon = \{x \in \mathbb{R}^n : \|x\| < \epsilon\}$.

Definition 4. Locally positive definite functions (lpdf)
A continuous function $V : \mathbb{R}^n \times \mathbb{R}_+ \to \mathbb{R}$ is a *locally positive definite function* if for some $\epsilon > 0$ and some continuous, strictly increasing function $\alpha : \mathbb{R}_+ \to \mathbb{R}$,

$$V(0) = 0 \quad \text{and} \quad V(x) \geq \alpha(\|x\|) \qquad \forall x \in B_\epsilon, \, \forall t \geq 0. \tag{5}$$

A locally positive definite function is locally like an energy function. Functions which are globally like energy functions are called positive definite functions:

Definition 5. Positive definite functions (pdf)
A continuous function $V : \mathbb{R}^n \times \mathbb{R}_+ \to \mathbb{R}$ is a *positive definite function* if it satisfies the conditions of Definition 4 and, additionally, $\alpha(p) \to \infty$ as $p \to \infty$.

Using these definitions, the following theorem allows us to determine stability for a system by studying an appropriate energy function. Roughly, this theorem states that when $V(x)$ is a locally positive definite function and $\dot{V}(x) \leq 0$ then we can conclude stability of the equilibrium point. The time derivative of V is taken along the trajectories of the system:

$$\dot{V}\Big|_{\dot{x}=f(x)} = \frac{\partial V}{\partial x} f.$$

In what follows, by $\dot{V}$ we will mean $\dot{V}|_{\dot{x}=f(x)}$.

Theorem 1. Basic theorem of Lyapunov
Let $V(x)$ be a non-negative function with derivative $\dot{V}$ along the trajectories of the system.

1. *If $V(x)$ is locally positive definite and $\dot{V}(x) \leq 0$ locally in x, then the origin of the system is locally stable (in the sense of Lyapunov).*

2. *If $V(x)$ is locally positive definite and $-\dot{V}(x)$ is locally positive definite, then the origin of the system is locally asymptotically stable.*

3. *If $V(x)$ is positive definite and $-\dot{V}(x)$ is positive definite, then the origin of the system is globally asymptotically stable.*

The conditions in the theorem are summarized in Table 1.

Theorem 1 gives sufficient conditions for the stability of the origin of a system. It does not, however, give a prescription for determining the Lyapunov function $V(x)$. Since the theorem only gives sufficient conditions, the search for a Lyapunov function establishing stability of an equilibrium point could be arduous. However, it is a remarkable fact that the converse of Theorem 1 also exists: if an equilibrium point is stable, then there exists a function $V(x)$ satisfying the conditions of the theorem. However, the utility of this and other converse theorems is limited by the lack of a computable technique for generating Lyapunov functions.

Theorem 1 also stops short of giving explicit rates of convergence of solutions to the equilibrium. It may be modified to do so in the case of exponentially stable equilibria.

9

Table 1: Summary of the basic theorem of Lyapunov.

	Conditions on $V(x)$	Conditions on $-\dot{V}(x)$	Conclusions
1	lpdf	≥ 0 locally	Stable
2	lpdf	lpdf	Asymptotically stable
3	pdf	pdf	Globally asymptotically stable

Theorem 2. Exponential stability theorem

$x^* = 0$ *is an exponentially stable equilibrium point of* $\dot{x} = f(x)$ *if and only if there exists an* $\epsilon > 0$ *and a function* $V(x)$ *which satisfies*

$$\alpha_1 \|x\|^2 \leq V(x) \leq \alpha_2 \|x\|^2$$
$$\dot{V}|_{\dot{x}=f(x)} \leq -\alpha_3 \|x\|^2$$
$$\|\frac{\partial V}{\partial x}(x)\| \leq \alpha_4 \|x\|$$

for some positive constants $\alpha_1, \alpha_2, \alpha_3, \alpha_4$, *and* $\|x\| \leq \epsilon$.

The rate of convergence for a system satisfying the conditions of Theorem 2 can be determined from the proof of the theorem [33]. It can be shown that

$$m \leq \left(\frac{\alpha_2}{\alpha_1}\right)^{1/2} \qquad \alpha \geq \frac{\alpha_3}{2\alpha_2}$$

are bounds in equation (4). The equilibrium point $x^* = 0$ is globally exponentially stable if the bounds in Theorem 2 hold for all x.

The indirect method of Lyapunov

The indirect method of Lyapunov uses the linearization of a system to determine the local stability of the original system. Consider the system

$$\dot{x} = f(x) \tag{6}$$

with $f(0) = 0$. Define

$$A = \left.\frac{\partial f(x)}{\partial x}\right|_{x=0} \tag{7}$$

to be the Jacobian matrix of $f(x)$ with respect to x, evaluated at the origin. It follows that the remainder

$$f_1(x) = f(x) - Ax$$

approaches zero as x approaches zero and, more specifically,

$$\lim_{\|x\| \to 0} \frac{\|f_1(x)\|}{\|x\|} = 0. \tag{8}$$

If equation (8) holds, then the system

$$\dot{z} = Az \tag{9}$$

is referred to as the *linearization* of equation (1) about the origin. When the linearization exists, its stability determines the local stability of the original nonlinear equation.
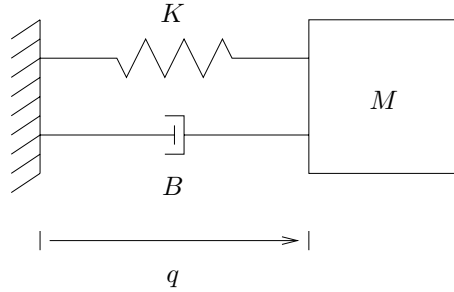
Figure 4: Damped harmonic oscillator.

Theorem 3. Stability by linearization
Consider the system (6) *and assume equation* (8) *holds. If 0 is a asymptotically stable equilibrium point of* (9) *then it is a* locally *asymptotically stable equilibrium point of* (6).

The indirect method says that if the eigenvalues of

$$A = \left. \frac{\partial f(x)}{\partial x} \right|_{x=0}$$

are in the open left half complex plane, then the origin is asymptotically stable.

This theorem proves that *global* asymptotic stability of the linearization implies *local* asymptotic stability of the original nonlinear system. The estimates provided by the proof of the theorem can be used to give a (conservative) bound on the domain of attraction of the origin. Systematic techniques for estimating the bounds on the regions of attraction of equilibrium points of nonlinear systems is an important area of research and involves searching for the "best" Lyapunov functions.

Examples

We now illustrate the use of the stability theorems given above on a few examples.

Example 1. Linear harmonic oscillator
Consider a damped harmonic oscillator, as shown in Figure 4. The dynamics of the system are given by the equation

$$M\ddot{q} + B\dot{q} + Kq = 0, \tag{10}$$

where M, B, and K are all positive quantities. As a state space equation we rewrite equation (10) as

$$\frac{d}{dt} \begin{bmatrix} q \\ \dot{q} \end{bmatrix} = \begin{bmatrix} \dot{q} \\ -(K/M)q - (B/M)\dot{q} \end{bmatrix}. \tag{11}$$

Define $x = (q, \dot{q})$ as the state of the system.

Since this system is a linear system, we can determine stability by examining the poles of the system. The Jacobian matrix for the system is

$$A = \begin{bmatrix} 0 & 1 \\ -K/M & -B/M \end{bmatrix},$$

which has a characteristic equation

$$\lambda^2 + (B/M)\lambda + (K/M) = 0.$$

11
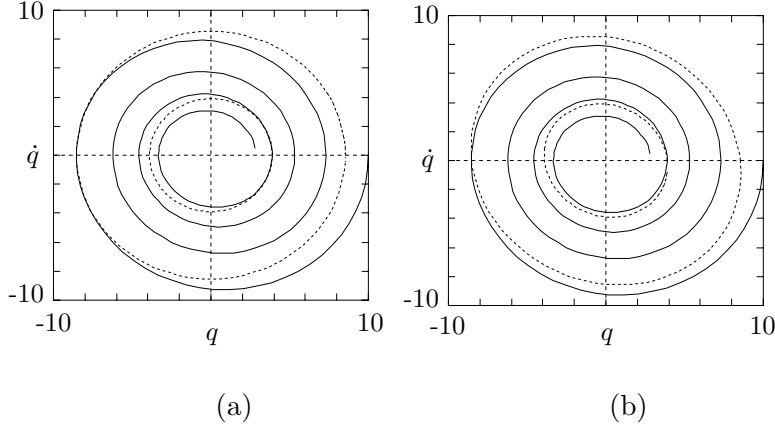
Figure 5: Flow of damped harmonic oscillator. The dashed lines are the level sets of the Lyapunov function defined by (a) the total energy and (b) a skewed modification of the energy.

The solutions of the characteristic equation are

$$\lambda = \frac{-B \pm \sqrt{B^2 - 4KM}}{2M},$$

which always have negative real parts, and hence the system is (globally) exponentially stable.

We now try to apply Lyapunov's direct method to determine exponential stability. The "obvious" Lyapunov function to use in this context is the energy of the system,

$$V(x) = \tfrac{1}{2} M \dot{q}^2 + \tfrac{1}{2} K q^2. \tag{12}$$

Taking the derivative of V along trajectories of the system (10) gives

$$\dot{V} = M \dot{q} \ddot{q} + K q \dot{q} = -B \dot{q}^2. \tag{13}$$

The function $-\dot{V}$ is quadratic but not locally positive definite, since it does not depend on q, and hence we cannot conclude exponential stability. It is still possible to conclude *asymptotic* stability using Lasalle's invariance principle (see [40]), but this is obviously conservative since we already know that the system is exponentially stable.

The reason that Lyapunov's direct method fails is illustrated in Figure 5a, which shows the flow of the system superimposed with the level sets of the Lyapunov function. The level sets of the Lyapunov function become tangent to the flow when $\dot{q} = 0$, and hence it is not a valid Lyapunov function for determining exponential stability.

To fix this problem, we skew the level sets slightly, so that the flow of the system crosses the level surfaces transversely. Define

$$V(x) = \frac{1}{2} \begin{bmatrix} q \\ \dot{q} \end{bmatrix}^T \begin{bmatrix} K & \epsilon M \\ \epsilon M & M \end{bmatrix} \begin{bmatrix} q \\ \dot{q} \end{bmatrix} = \tfrac{1}{2} \dot{q} M \dot{q} + \tfrac{1}{2} q K q + \epsilon \dot{q} M q,$$

where ϵ is a small positive constant such that V is still positive definite. The derivative of the Lyapunov function becomes

$$\dot{V} = \dot{q} M \ddot{q} + q K \dot{q} + \epsilon M \dot{q}^2 + \epsilon q M \ddot{q}$$

$$= (-B + \epsilon M) \dot{q}^2 + \epsilon(-K q^2 - B q \dot{q}) = - \begin{bmatrix} q \\ \dot{q} \end{bmatrix}^T \begin{bmatrix} \epsilon K & \tfrac{1}{2} \epsilon B \\ \tfrac{1}{2} \epsilon B & B - \epsilon M \end{bmatrix} \begin{bmatrix} q \\ \dot{q} \end{bmatrix}.$$

12

The function $\dot{V}$ can be made negative definite for ϵ chosen sufficiently small and hence we can conclude *exponential* stability. The level sets of this Lyapunov function are shown in Figure 5b.

Example 2. Stability of the MG-3 equations
Consider the three state Moore-Greitzer equations, which provide a simple model of the dynamics of a compression system:

$$\dot{\Phi} = \frac{1}{l_c}\Big(\Psi_c(\Phi) - \Psi + \frac{J}{4}\frac{\partial^2\Psi_c(\Phi)}{\partial\Phi^2}\Big)$$

$$\dot{\Psi} = \frac{1}{4l_cB^2}\big(\Phi - \Phi_T(\Psi,\gamma)\big) \qquad (14)$$

$$\dot{J} = \frac{2}{m+\mu}J\Big(\frac{\partial\Psi_c(\Phi)}{\partial\Phi} + \frac{J}{8}\frac{\partial^3\Psi_c(\Phi)}{\partial\Phi^3}\Big).$$

Here, Φ represents the (annulus-averaged) flow through the system, Ψ is the pressure rise between the inlet and outlet, and J is the square of the amplitude of the first mode of rotating stall. The parameters l_c, B, m and μ depend on the compressor configuration and are described in Paduano's course notes as well as [28].

The two functions $\Psi_c(\Phi)$ and $\Phi_T(\Psi,\gamma)$ represent the compressor and throttle characteristics. The throttle characteristic models the pressure loss at the outlet of the compressor and can be written as

$$\Phi_T(\Psi,\gamma) = \gamma\sqrt{\Psi},$$

where γ is the *throttle parameter*. The compressor characteristic curve gives the pressure rise across the compressor as a function of the mass flow through the compressor (see Figure 6). Together, these two characteristic curves determine the nominal operating point of the system since when $J = 0$, the equilibrium solution for the system is given by the solution of the algebraic equations

$$\Psi^* - \Psi_c(\Phi^*) = 0 \qquad \text{and} \qquad \Phi^* - \Phi_T(\Psi^*,\gamma) = 0. \qquad (15)$$

A representative set of curves is show in Figure 6. The operating point when $J^* = 0$ is at the intersection of the two curves.

We now consider the stability of this system at an equilibrium point $x^* = (\Phi^*, \Psi^*, 0)$. We assume that γ is chosen such that

$$m_C = \frac{\partial\Psi_c}{\partial\Psi}(\Phi^*) < 0 \qquad \text{and} \qquad m_T = \frac{\partial\Phi_T}{\partial\Phi}(\Psi^*) > 0$$

and we let

$$\phi = \Phi - \Phi^* \qquad \psi = \Psi - \Psi^*.$$

We use the indirect method of Lyapunov and compute the linearization around the equilibrium point:

$$\dot{\phi} = \frac{1}{l_c}(m_C\phi - \psi)$$

$$\dot{\psi} = k_B(\frac{1}{l_c}\phi - m_T\psi)$$

$$\dot{J} = \frac{2}{m+\mu}m_C J$$

where $k_B = 1/(4B^2)$. The characteristic equation for this system is given by

$$(s - m_C)\left(s^2 + \frac{1}{l_c}(\frac{k_B}{m_T} - m_C)s + \frac{k_B}{l_c}(1 - \frac{m_C}{m_T})\right) = 0.$$

13
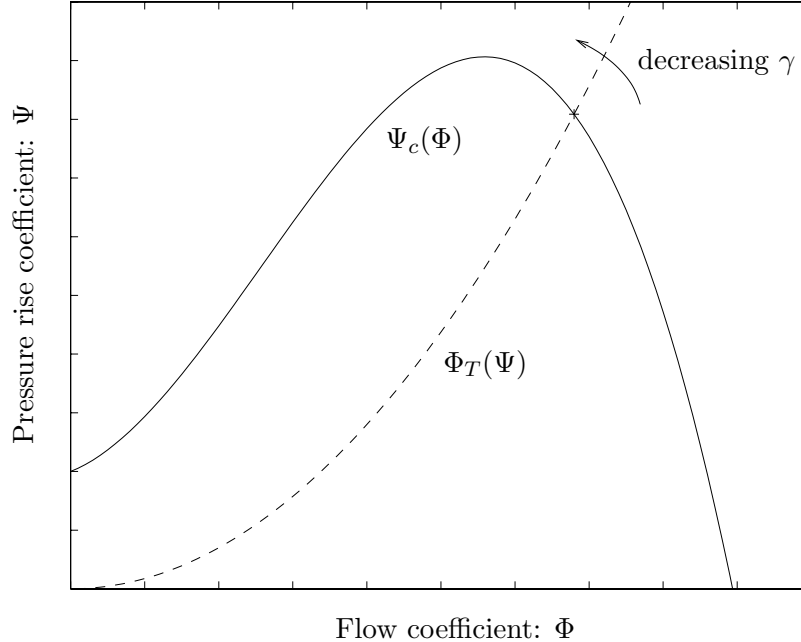
Figure 6: Compressor and throttle characteristic curves.

Assuming that $m_C/m_T \ll 1$, we can simplify the last term in the equation and stability is given by the conditions

$$m_C < \frac{1}{4B^2 m_T} \qquad \text{and} \qquad m_C < 0.$$

We thus see that if the slope of the compressor characteristic is negative, then the linearized system is stable (since B and m_T are positive).

Stability of the linearized equation allows us to conclude *local* stability of the full equations when $m_C < 0$. If $m_C > 0$, it is easy to show that the equations are unstable and J grows if perturbed away from zero. If, on the other hand, $m_C \equiv 0$, then a linear analysis is not sufficient and we must resort to a fully nonlinear analysis. This case can be found in the paper by McCaughan [25] and is discussed in more detail below.

2.2   Nonlinear Control Using Lyapunov Functions

The use of Lyapunov functions to characterize stability leads to a variety of techniques for design of control laws based on the properties of Lyapunov functions. In this section we consider a system of the form

$$\dot{x} = f(x, u) \qquad x(t_0) = x_0 \qquad x \in \mathbb{R}^n, \quad u \in \mathbb{R}^m, \tag{16}$$

where u denotes the *inputs* to the system. We wish to design a feedback control law $u = \alpha(x)$ such that the resulting closed loop system

$$\dot{x} = f(x, \alpha(x))$$

is stable.

We consider two such techniques in this section: control Lyapunov functions and backstepping. More information on Lyapunov-based control design can be found in the the textbook by Krstic et al. [22].

14

Control Lyapunov Functions

Control Lyapunov functions are an extension of standard Lyapunov functions and were originally introduced by Sontag [35]. They allow constructive design of nonlinear controllers and the Lyapunov function that proves their stability. We give a brief introduction here, driven by relevant examples. A more complete treatment is given in [22].

Definition 6. Control Lyapunov Function
A locally positive function $V : \mathbb{R}^n \to \mathbb{R}_+$ is called a *control Lyapunov function (CLF)* for a control system (16) if

$$\inf_{u \in \mathbb{R}} \left(\frac{\partial V}{\partial x} f(x, u) \right) < 0 \qquad \text{for all } x \neq 0.$$

For systems that are affine in the control

$$\dot{x} = f(x) + g(x)u, \qquad f(x) = 0$$

the CLF condition simplifies to

$$\frac{\partial V}{\partial x} f(x) + \frac{\partial V}{\partial x} g(x)u \leq -W(x)$$

for some locally positive definite function $W(x)$. If such a V exists, then a particular control law that stabilizes the system is given by *Sontag's formula*:

$$u = \begin{cases} -\dfrac{\frac{\partial V}{\partial x} f + \sqrt{\left(\frac{\partial V}{\partial x} f\right)^2 + \left(\frac{\partial V}{\partial x} g\right)^4}}{\frac{\partial V}{\partial x} g} & \frac{\partial V}{\partial x} g \neq 0 \\ 0 & \frac{\partial V}{\partial x} g = 0. \end{cases}$$

Example 3. CLF example
Consider the scalar system given by the component of the Moore-Greitzer equations that describe the evolution of rotating stall, with an additional term to represent a control input:

$$\dot{J} = \frac{2}{m + \mu} \left(\frac{\partial \Psi_c}{\partial \Phi} + \frac{J}{8} \frac{\partial^3 \Psi_c}{\partial \Phi^3} \right) J + u$$

We assume here that Φ and Ψ are constants.

Consider the control Lyapunov function candidate

$$V(J) = \tfrac{1}{2} J^2$$

This function is positive definite and hence we need to check the condition on $\dot{V}$ to see if it is a control Lyapunov function:

$$\dot{V} = J \left(\frac{2}{m + \mu} \left(\frac{\partial \Psi_c}{\partial \Phi} + \frac{J}{8} \frac{\partial^3 \Psi_c}{\partial \Phi^3} \right) J + u \right)$$

It is easy to verify that we can always find a u such that $\dot{V} < 0$ for $J \neq 0$. Once such control is given by $u = -kJ$, in which case we have

$$\dot{V} = \frac{2}{m + \mu} \left(\frac{\partial \Psi_c}{\partial \Phi} - k \right) J^2 - \frac{J^3}{8(m + \mu)} \frac{\partial^3 \Psi_c}{\partial \Phi^3}$$

and if k is chosen sufficiently large, then $\dot{V} < 0$ for J small. Thus we can conclude that we have *local* asymptotic stability.

Backstepping

In general, it is difficult to find a control Lyapunov function for a complex, nonlinear system. For example, if we consider the entire Moore-Greitzer equations, it would be much less obvious how to choose an appropriate V.

Backstepping is a constructive approach to build controllers and Lyapunov functions for certain classes of systems. The essence of the technique is contained in the following lemma:

Lemma 4. *Consider an affine nonlinear system augmented by an integrator:*

$$\dot{x} = f(x) + g(x)u \tag{17}$$
$$\dot{u} = v \tag{18}$$

and supposed that $V(x)$ is a control Lyapunov function for the system (17) and $u = \alpha(x)$ is a control law that stabilizes the system. Then

$$V_a(x, u) = V(x) + \frac{1}{2}\left(u - \alpha(x)\right)^2$$

is a CLF for the full system.

This lemma allows us to iteratively design a CLF for a system as well as constructively build a control law for the complete system. The basic idea is that we can "backstep" a controller through an integrator and obtain a controller for the larger system. The following example illustrates this approach.

Example 4. Stabilization of the MG-3 model via backstepping

Consider the *controlled* MG-3 equations

$$\dot{\Phi} = \frac{1}{l_c}\left(\Psi_c(\Phi) - \Psi + \frac{J}{4}\frac{\partial^2 \Psi_c(\Phi)}{\partial \Phi^2}\right)$$
$$\dot{\Psi} = \frac{1}{4l_c B^2}\left(\Phi - \Phi_T(\Psi, \gamma) + u\right) \tag{19}$$
$$\dot{J} = \frac{2}{m + \mu}J\left(\frac{\partial \Psi_c(\Phi)}{\partial \Phi} + \frac{J}{8}\frac{\partial^3 \Psi_c(\Phi)}{\partial \Phi^3}\right).$$

The input here corresponds (roughly) to the effect of a bleed valve downstream from the compressor, and hence is somewhat realistic. We wish to stabilize the system around the equilibrium point $x^* = (\Phi^*, \Psi^*, 0)$ corresponding to the peak of the compressor characteristic curve, where $\frac{\partial \Psi_c}{\partial \Psi} = 0$.

To simplify the derivation, we assume a cubic compressor characteristic of the form

$$\Psi_C(\Phi) = a_0 + a_1\Phi - a_3\Phi^3 \tag{20}$$

where each $a_i > 0$ and $\Phi^* = \sqrt{a_1/(3a_3)}$ at the peak of the compressor characteristic. We then rewrite the Moore-Greitzer equations in a different order:

$$\dot{J} = \frac{2}{m + \mu}J\left(\frac{\partial \Psi_c(\Phi)}{\partial \Phi} + \frac{J}{8}\frac{\partial^3 \Psi_c(\Phi)}{\partial \Phi^3}\right)$$
$$\dot{\Phi} = \frac{1}{l_c}\left(\Psi_c(\Phi) - \Psi + \frac{J}{4}\frac{\partial^2 \Psi_c(\Phi)}{\partial \Phi^2}\right)$$
$$\dot{\Psi} = \frac{1}{4l_c B^2}\left(\Phi - \Phi_T(\Psi, \gamma) + u\right).$$

We begin by trying to stabilize J using Φ as a "virtual" control, which we assume for the moment that we can control directly (as if it were an input). Setting Φ to the desired value of $\Phi_d(J) = \Phi^* + kJ$, we see that the $\dot{J}$ equation becomes

$$\dot{J} = \frac{2}{m+\mu}\left(-6a_3\Phi^*kJ^2 - \frac{3}{4}a_3J^2 - 3a_3k^2J^3\right)$$

(where we have made use of the particular compressor characteristic in equation (20)).

This equation is *nonlinearly* stable under the assumption that $J \geq 0$ and given the signs of the various coefficients. It is important to note that if we had instead applied this control at an operating point with $m_C = \frac{\partial \Psi_c}{\partial \Phi} \neq 0$ then there would be a linear term that would determine stability. If $m_C < 0$ then we still have stability, but if $m_C > 0$ then the equilibrium point corresponding to $J = 0$ is unstable, even with the control in place. It is only at the point where $m_C = 0$ that the control alters the stability of the equation.

Continuing on, we next look at the equation for $\dot{\Phi}$ and attempt to choose Ψ so as to stabilize this equation to the value $\Phi_d(J)$. As before, we assume that Ψ can be directly controlled and we set it to

$$\Psi_d(\Phi, J) = \Psi_c(\Phi^*) - k_2(\Phi - \Phi_d(J))$$

Finally, we look at $\dot{\Psi}$ and stabilize it to $\Psi_d(\Phi, J)$. A simple controller to achieve this is

$$u = -k_3(\Psi - \Psi_d(\Phi, J)).$$

Expanding Ψ_d and Φ_d, the resulting state feedback for the full system is given by

$$u = -k_3(\Psi - \Psi^*) - k_3k_2(\Phi - \Phi^*) - k_3k_2k_1J.$$

As noted above, this control renders the system stable when $m_C \leq 0$, including the point $m_C = 0$, where linear stability is lost. However, beyond the peak of the compressor characteristic, this control law cannot stabilize the unstalled equilibrium point $J = 0$.

2.3 Bifurcations and bifurcation control

As the last example illustrates, it is not always possible to stabilize a system about a desired operating point (e.g., when $m_C > 0$). In this section we show how to perform nonlinear control in a way that modifies the behavior of the system to be more beneficial without necessarily stabilizing the system.

Bifurcations

Consider a family of differential equations

$$\dot{x} = f(x, \mu), \qquad x \in \mathbb{R}^n, \qquad \mu \in \mathbb{R}^k, \tag{21}$$

where x is the state and μ is a set of parameters that describe the family of equations. The equilibrium solutions satisfy

$$f(x, \mu) = 0$$

and as μ is varied, the corresponding solutions $x_e(\mu)$ vary. We say that the system (21) has a *bifurcation* at $\mu = \mu^*$ if the flow of the system change quantitatively at μ^*. This can occur either due to a change in stability type or a change in the number of solutions at a given value of μ.
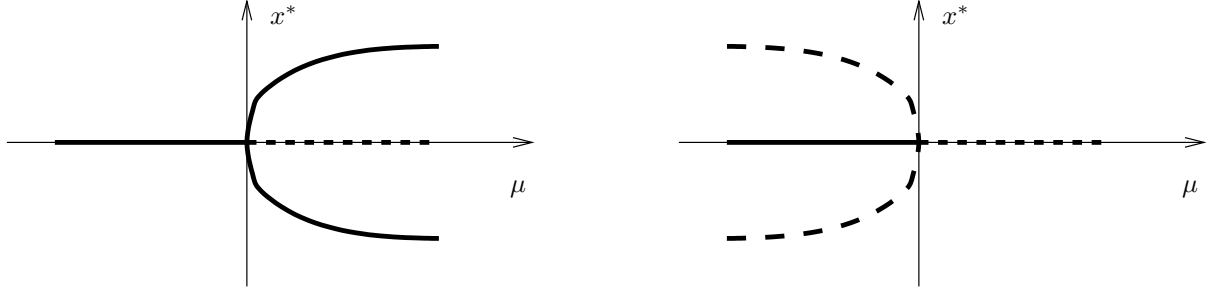
(a) supercritical pitchfork   (b) subcritical pitchfork

Figure 7: Pitchfork bifurcation: (a) subcritical and (b) supercritical.

Example 5. Simple exchange of stability

Consider the scalar dynamical system

$$\dot{x} = \mu x.$$

This system has a bifurcation at $\mu = 0$ since the stability of the system changes from asymptotically stable (for $\mu < 0$) to neutrally stable ($\mu = 0$) to unstable (for $\mu > 0$).

Example 6. Pitchfork bifurcation

Consider the scalar dynamical system

$$\dot{x} = \mu x - x^3.$$

The equilibrium values of x are plotted in Figure 7a, with solid lines representing stable equilibria and dashed lines representing unstable equilibria. As illustrated in the figure, the number and type of the solutions changes at $\mu = 0$ and hence we say there is a bifurcation at $\mu = 0$.

Note that the sign of the cubic term determines whether the bifurcation generates a stable branch (called a *supercritical* bifurcation and shown in Figure 7a) or a unstable branch (called a *subcritical* bifurcation and shown in Figure 7b).

Bifurcations provide a tool for studying how systems evolve as operating parameters change and are particularly useful in the study of stability of differential equations. To illustrate how bifurcations arise in the context of compression systems, we consider the 3 state Moore-Greitzer model introduced earlier.

Example 7. Bifurcation analysis of the MG-3 model

Consider again the special case given by a cubic compressor characteristic in the form of equation (20). As we have already seen, the $J^* = 0$ equilibrium point undergoes a bifurcation when $\frac{\partial \Psi_c(\Phi^*)}{\partial \Phi} = 0$ since the eigenvalue associated with J crosses into the right half plane.

However we can also analyze the stability of the *stalled* branch, given by

$$\frac{\partial \Psi_c(\Phi^*)}{\partial \Phi} + \frac{J^*}{8}\frac{\partial^3 \Psi_c}{\partial \Phi^3} = 0 \quad \Longrightarrow \quad J^* = 8\frac{\partial \Psi_c(\Phi^*)}{\partial \Phi}\bigg/\frac{J^*}{8}\frac{\partial^3 \Psi_c}{\partial \Phi^3}.$$

Note that this solution most be positive to make physical sense and hence J^* may not always exist. To complete the solution for this case, we must also have

$$\Psi_c(\Phi^*) - \Psi^* - \frac{J^*}{4}\frac{\partial^2 \Psi_c(\Phi^*)}{\partial \Phi^2} = 0 \quad \text{and} \quad \Phi^* = \Phi_T(\Psi^*).$$

18
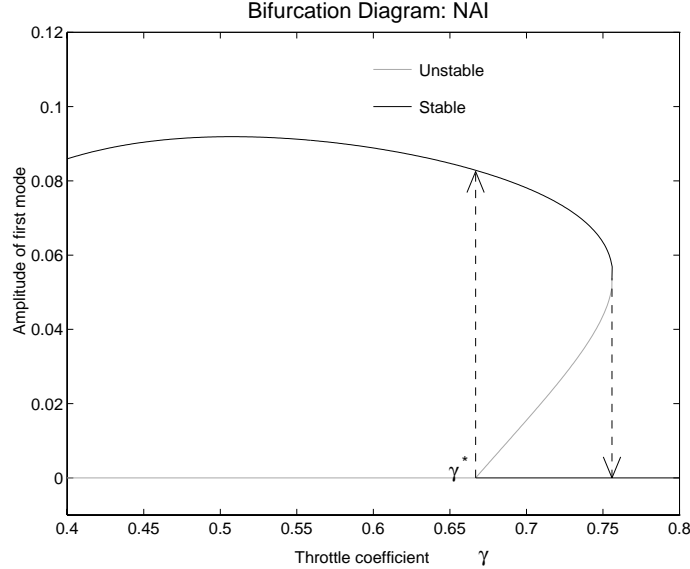
Figure 8: Bifurcation diagram for the MG-3 model.

A representative graph of J^* as a function of the bifurcation parameter γ is given in Figure 8, with a dark line indicating a stable equilibrium and a light line indicating an unstable equilibrium.

Several important features rotating stall are present in this example. First, note that locally Figure 8 looks like a subcritical pitchfork bifurcation, with only the top branch present (and the parameter varying in the opposite sense from the canonical pitchfork example). Thus, when we reach the critical value of γ where the slope of the compressor characteristic is zero, small perturbations in J grow and the system begins to stall ($J \neq 0$). Nonlinearities in the model stop the growth of the stall cell for J large and we eventually end up with a finite size stall cell (represented by the stable section of the upper branch). If at this point we increase γ, we remain on the upper (stalled) branch until we reach the *saddle-node* bifurcation, where we then drop back to the original unstalled operating point. This gives a *hysteresis loop* that corresponds to the well known hysteresis in rotating stall.

Control of bifurcations

Now consider a family of control systems

$$\dot{x} = f(x, u, \mu), \qquad x \in \mathbb{R}^n, \quad u \in \mathbb{R}^m, \quad \mu \in \mathbb{R}^k, \tag{22}$$

where u is the input to the system. We have seen in the previous sections that we can sometimes alter the stability of the system by choice of an appropriate feedback control, $u = \alpha(x)$. In this section we investigate how the control can be used to change the bifurcation characteristics of the system. As in the previous section, we rely on examples to illustrate the key points. A more detailed description of the use of feedback to control bifurcations can be found in the work of Abed and co-workers [23].

The simplest case of bifurcation control is when the system can be *stabilized* near the bifurcation point through the use of feedback. In this case, we can completely eliminate the bifurcation through feedback, as the following simple example shows.
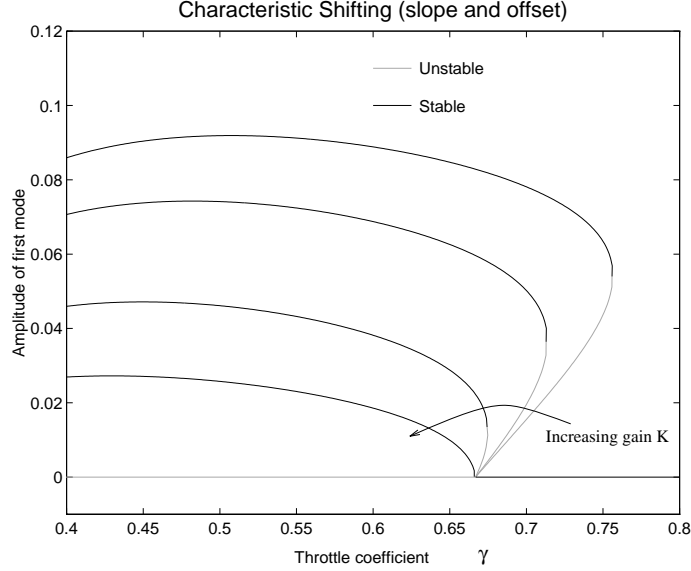
Figure 9: Relation of controller gain and behavior of bifurcation.

Example 8. Stabilization of the pitchfork bifurcation

Consider the subcritical pitchfork example from the previous section, with a simple additive control:

$$\dot{x} = \mu x + x^3 + u.$$

Choosing the control law $u = -kx$, we can stabilize the system at the nominal bifurcation point $\mu = 0$ since $\mu - k < 0$ at this point. Of course, this only shifts the bifurcation point and so k must be chosen larger than the maximum value of μ that can be achieved.

Alternatively, we could choose the control law $u = -kx^3$ with $k > 1$. This changes the sign of the cubic term and changes the pitchfork from a subcritical bifurcation to a supercritical bifurcation. The stability of the $x = 0$ equilibrium point is not changed, but the system operating point moves slowly away from zero after the bifurcation rather than growing without bound.

The more interesting case for consideration is when the control enters in such a way that it is not possible to stabilize the system (i.e., the linearization is unstabilizable at the bifurcation point). In this case, it might be possible to change the bifurcation behavior to a more benign case through the use of feedback. We illustrate this using the 3 state Moore-Greitzer model.

Example 9. Liaw-Abed Control of the MG-3 model

For stall control, Liaw and Abed [23] proposed a control law that modifies the throttle characteristic:

$$\Phi_T(\Psi, \gamma, u) = (\gamma + u)\sqrt{\Psi},$$
$$u = kJ.$$

This control law can be realized experimentally through the use of a bleed valve. For a large enough value of k, the nominally unstable branch of equilibrium solution created at $\gamma = \gamma^*$ "bends over" and eliminates the hysteresis loop, i.e. the subcritical nature of the transcritical bifurcation is changed to supercritical (Figure 9).

By substituting the stall control law and computing the quantity $\frac{dJ}{d\gamma}$ at the stall inception throttle coefficient γ^*, the minimum gain needed for this phenomenon to occur can be found by

asserting the condition that $\frac{dJ}{d\gamma}|_{\gamma=\gamma^*} < 0$. The expression for the minimum gain required for peak stabilization is given by

$$k_{\min} = -\frac{\Phi^* \Psi_c'''(\Phi^*)}{8\gamma^* \Psi^* \Psi_c''(\Phi^*)} - \frac{\gamma^* \Psi_c''(\Phi^*)}{8\Psi^*}, \tag{23}$$

which depends on the shape of the compressor characteristic. Since the second term is always non-negative around the peak, the larger the value of $\Psi_c'''(\Phi^*)$, the smaller $k_{\min}$. Roughly speaking, this amounts to a compressor characteristic which is more "filled out" to the left of the peak. This expression serves as one of the theoretical tools for predicting the bleed valve requirement needed for peak stabilization [38, 42].

Measurements at Compressor Face
of Unsteady Perturbations

⊗ ⊗ ⊗ ⊗ ⊗ ⊗ ⊗ ⊗

8 7 6 5 4 3 2 1   8 Sensors

Spatial Fourier Transform

3   2   1   0   Complex
                       Harmonic
                       Amplitudes

Control Law in Fourier Domain

3   2   1   0   Commanded
                       Actuation
                       Harmonics

Inverse Spatial Fourier Transform

12 11 10 9 8 7 6 5 4 3 2 1

Spatially Distributed Actuation in
Compressor, Jet Valves, or Vanes
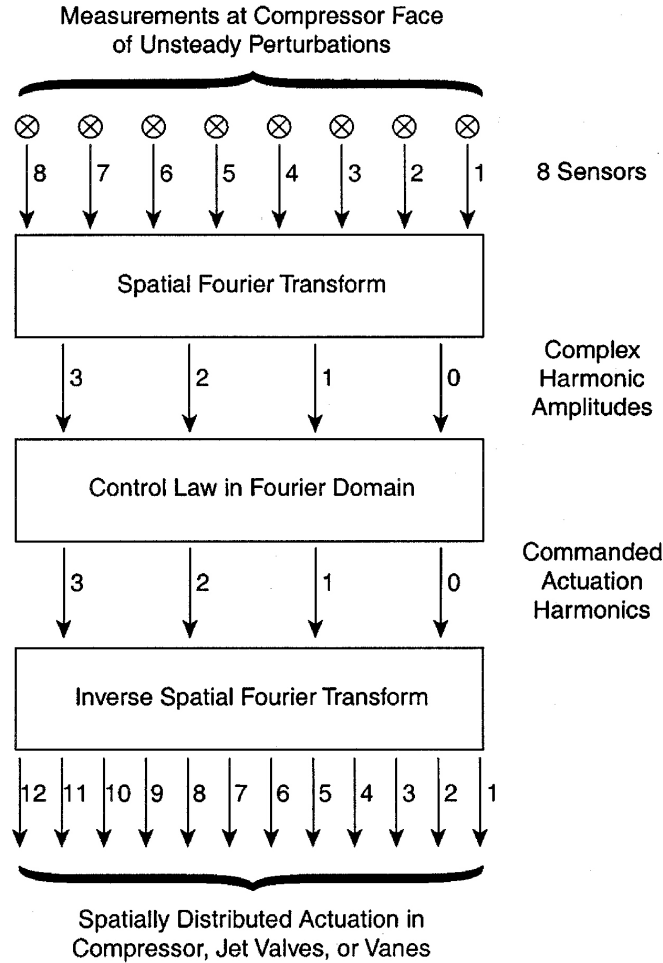
Figure 10: Architecture for modal control.

3   Modal Control of Compression Systems

One of the most common methods of controlling stall is through "modal" control. This type of control works for systems that are accurately described by long wavelength, modal inception of stall, as described in the course notes by Paduano. In this case, the circumferential modes of the flow perturbations can be taken as states of the dynamical system to be control and a feedback law can be designed to stabilize these states.

The basic architecture for modal control is illustrated in Figure 10. Roughly speaking, this architecture determines the magnitude and spatial location of each mode, applies a feedback control law in modal coordinates, and then maps these feedback into the actuator commands.

Modal control has been demonstrated using a variety of different actuators, including high frequency inlet guide vanes [30] and air injection [16, 39]. The specific control laws used for these are typically a gain proportional to the amplitude of the modal perturbation, combined with a spatial phase shift. The phase shift can be regarded as a mechanism for taking into account sensing and actuation delays, so that the eventual action of the control of the physics is properly timed to decrease the amplitude of the individual modes.

To analyze the effects of modal control, we consider the stabilization of the simple MG-3 modal

22
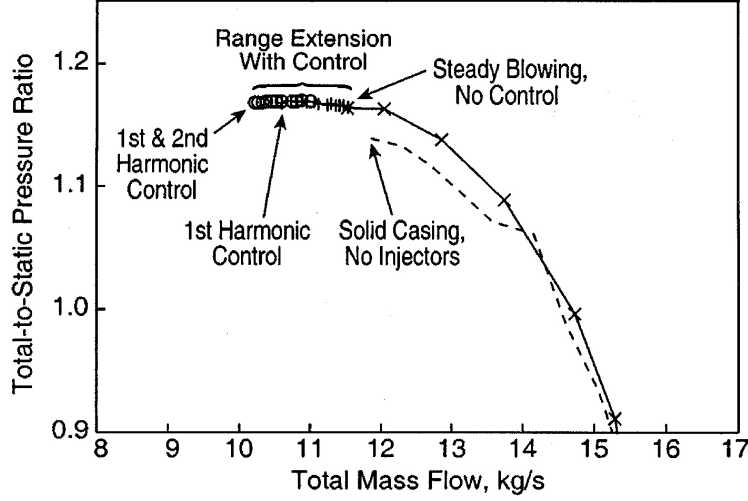
Figure 11: Range extension using modal control.

using 2D (spatially distributed) air injection. Paduano's course notes give a description of how this can be accurately incorporated in the model by taking into account changes in the compressor characteristic curve as well as momentum effects. For simplicity, we assume here that this actuation is represented by an additional term in the equation for J, which represents the square of the amplitude of the first mode:

$$
\begin{aligned}
\dot{\Phi} &= \frac{1}{l_c}\Big(\Psi_c(\Phi) - \Psi + \frac{J}{4}\frac{\partial^2 \Psi_c(\Phi)}{\partial \Phi^2}\Big) \\
\dot{\Psi} &= \frac{1}{4 l_c B^2}\big(\Phi - \Phi_T(\Psi, \gamma)\big) \\
\dot{J} &= \frac{2}{m + \mu} J\Big(\frac{\partial \Psi_c(\Phi)}{\partial \Phi} + \frac{J}{8}\frac{\partial^3 \Psi_c(\Phi)}{\partial \Phi^3} + u\Big).
\end{aligned}
\tag{24}
$$

It is easy to show using the techniques of the previous section that a control law of the form $u = kJ$ will extend the stability of the system beyond the nominal stall inception point. Indeed, the condition for stability of the stall mode is given by $k - m_C > 0$, where m_C is the slope of the compressor characteristic curve at the desired operating point. (The stability of the eigenvalue corresponding to surge is unchanged.)

Note that implicit in this formulation is that the modal control has been spatially locked to the phase of the first mode (so that we directly actuate the amplitude). Thus, although this appears to be a single control input (in modal coordinates), the implementation of this control action will require an arrange of actuators that are capable of modulating the amount of injected air in a spatially sinusoidally varying pattern that is aligned with the first mode flow perturbation.

This basic idea can be extended to multiple modes by applying independent controllers in modal coordinates. Typical modal control laws will make use of 8 pressure or flow sensors and 12 actuators. This allows control of up to three or four circumferential modes. The actuator bandwidths are a limiting factor in the effectiveness of the control and typically must be approximately 2.5 times the rotor frequency. Figure 11 shows the results of a modal control algorithm on a transonic compressor rig [31]. For this example, modulated air injection was used as the actuation mechanism, with a mean rate of mass injection of 1.5% of the mean compressor flow.

23

For high speed compressors, the compressibility effects become important and must be accounted for in the control design. A detailed discussion can be found in Weigl et al. [39].

It is also possible to make use of the ideas of modal feedback in *passive* control approaches. One such approach was given by Gysling and Greitzer [17], in which they used air injectors that had a "reed valve" mechanism that was sensitive to local pressure variations. This provided a direct mechanism to dynamically couple the flow perturbations of the rotating stall modes to the air injection, without electronic sensing or computation.
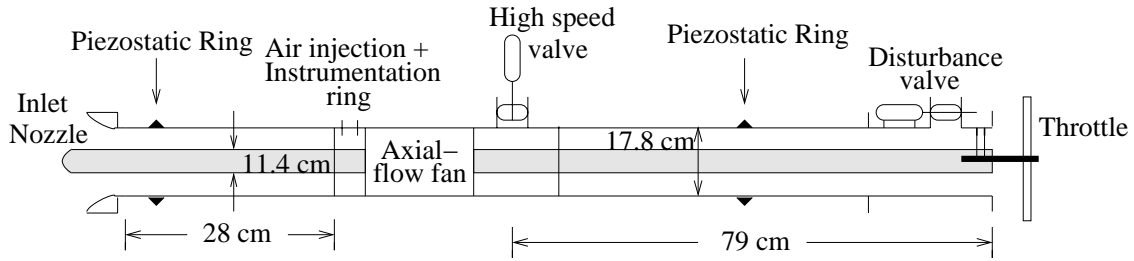
Figure 12: Experimental setup.

sensor ring (end view)   sensor ring (side view)
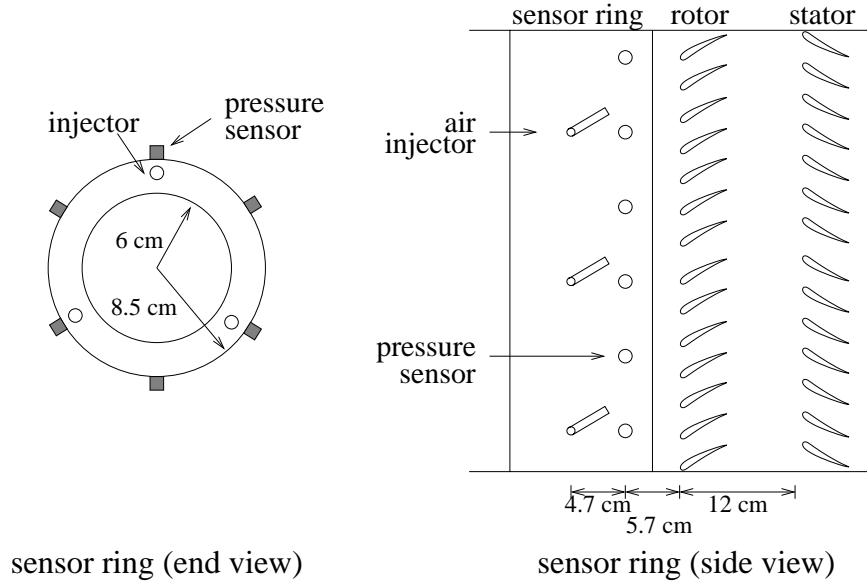
Figure 13: Sensor and injection actuator ring.

4 Nonlinear Control of Compression Systems

In this section we consider the use of nonlinear tools for analyzing and controlling rotating stall and surge. Throughout this section, we shall illustrate the various approaches as they apply to an experimental rig developed at Caltech. We begin with a description of this system.

4.1 Caltech Compressor Rig

The Caltech compressor rig is a single-stage, low-speed, axial flow compressor with sensing and actuation capabilities. Figure 12 shows a drawing of the rig and Figure 13 a magnified view of the sensor and injection actuator ring.

The compressor is an Able Corporation model 29680 low speed single stage axial compressor with 14 blades, a tip radius of 8.5 cm, and a hub radius of 6 cm. The blade stagger angle varies from $30°$ at the tip to $51.6°$ at the hub, and the rotor to stator distance is approximately 12 cm (1.4 rotor radii). Experiments are run with a rotor frequency of 100 Hz, giving a tip Mach number of 0.17. In the configuration shown in Figure 12, rotating stall is observed to occur with a frequency of approximately 67 Hz. With a plenum attached at the outlet (for compliance effects), surge occurs at approximately 1.8 Hz. Data taken for a stall transition event suggests that the stall cell grows

from the noise level to its fully developed size in approximately 30 msec (3 rotor revolutions). At the stall inception point, the velocity of the flow through the compressor is approximately 16 m/sec.

Six static pressure transducers with 1000 Hz bandwidth are evenly distributed along the annulus of the compressor at approximately 5.7 cm (1.1 rotor radii) from the rotor face. By performing a discrete Fourier transform on the signals from the transducers, the amplitude and phase of the first and second Fourier modes of the pressure perturbation of a nonaxisymmetric disturbance can be obtained. The difference between the pressure obtained from one static pressure transducer mounted at the piezostatic ring at the inlet and that from the piezostatic ring downstream near the outlet of the system is computed as the pressure rise across the compressor. For the velocity of the system, a hotwire anemometer is mounted approximately 13.4 cm (1.6 rotor radii) upstream of the rotor face. All of the sensor signals are filtered through a 4th order Bessel low pass filter with a cutoff frequency of 1000 Hz before the signal processing phase in the software.

A high speed and a low speed bleed valve are available on the Caltech rig. The high speed bleed valve, used primarily for stall control, has a magnitude saturation of 12% (corresponding to an area of 11.4 cm^2) of the flow at the stall inception point and is approximately 26 cm (3.1 rotor radii) downstream of the rotor. The low speed valve, used primarily for surge control and throttle disturbance generation, has a magnitude saturation of 30% of the flow of the system at the stall inception point and is estimated to have a small signal ($\pm 5°$ angle modulation) bandwidth of 50 Hz and a large signal ($\pm 90°$ angle modulation) bandwidth of 15 Hz.

The air injectors are on-off type injectors driven by solenoid valves. For applications on the Caltech compressor rig, the injectors are fed with a pressure source supplying air at a maximum pressure of 80 psig. The injectors are located at approximately 10.4 cm (1.2 rotor radii) upstream of the rotor. Due to significant losses across the solenoid valves and between the valves and the pressure source, the injector back pressure reading does not represent an accurate indication of the actual velocity of the injected air on the rotor face. Using a hotwire anemometer, the maximum velocity of the velocity profile produced by the injected air measured at a distance equivalent to the rotor-injector distance for 50 and 60 psig injector back pressure are measured to be approximately 30.2 and 33.8 m/sec respectively. At the stall inception point, each injector can add approximately 1.7% mass, 2.4% momentum, and 1.3% energy to the system when turned on continuously at 60 psig injector back pressure. The bandwidth associated with the injectors is approximately 200 Hz at 50% duty cycle. The angle of injection, injector back pressure, the axial location of the injectors, and the radial location of the injectors can all be varied.

One of the features of the experiment is the ability to use continuous air injection to modify the compressor characteristic curve for the system. This allows us to explore the role that the shape of the compressor characteristic plays in active control of stall and also allows us to emulate a range of compressors with a single experimental system.

4.2   System ID

Many of the nonlinear analysis techniques that we employ required knowledge of the compressor parameters and compressor characteristic curve. In this section, an identification algorithm proposed by Behnken [4] is briefly reviewed to illustrate how these can be obtained.

Due to the unstable nature of the portion of the compressor characteristic to the left of its peak, achievable stall-free performance of a given compressor has always been uncertain. Identification of the compressor characteristic and the parameters in the Moore-Greitzer model has been an ongoing research topic. The complexity of the identification process has evolved from an assumption

based on experience, namely a simplified Moore-Greitzer type cubic [15, 28] of the form

$$\Psi_c(\Phi) = \Psi_{c_0} + H\left[1 + \frac{3}{2}\left(\frac{\Phi}{W} - 1\right) - \frac{1}{2}\left(\frac{\Phi}{W} - 1\right)^3\right],$$

where Ψ_{c_0}, H, and W are fitting coefficients, to an iterative simulation-experiment matching procedure which results in piecewise continuous polynomials [24]. While the iterative approach gives quantitatively reliable stall inception results when used in simulations, a systematic method that reduces the uncertainty and effort, and increases the accuracy and precision of the identified parameters is extremely desirable. One such identification algorithm via a linear least squares fit of a modified version of the Moore-Greitzer equations using surge cycle data is proposed by Behnken [4].

Using modal decomposition and Galerkin projection, the Moore-Greitzer PDE can be projected onto the modes of interest. As an example, the one-mode Moore-Greitzer model (equation (14)) is repeated here in a slightly different form:

$$\dot{\Psi} = \frac{1}{4l_cB^2}(\Phi - \gamma\sqrt{\Psi})$$

$$\dot{\Phi} = \frac{1}{l_c}(\Psi_c(\Phi) - \Psi + \frac{A_1^2}{4}\frac{\partial^2\Psi_c(\Phi)}{\partial\Phi^2}) \tag{25}$$

$$\dot{A}_1 = \frac{1}{m+\mu}A_1(\frac{\partial\Psi_c(\Phi)}{\partial\Phi} + \frac{A_1^2}{8}\frac{\partial^3\Psi_c(\Phi)}{\partial\Phi^3}).$$

In this equation, A_1 represents the amplitude of stall (rather than the square amplitude, J).

The basic surge model is equation (25) with A_1 set to 0. The expanded surge model takes into account the amplitude of the rotating stall in the surge cycle without considering the corresponding time rate of change. Furthermore, for applications on data associated with *pressure* perturbation, a Taylor expansion can be used to express the stall amplitudes associated with pressure perturbation to those with flow perturbation. For instance (from [4]), the first mode associated with pressure perturbation $\hat{A}_1$ is given by

$$\hat{A}_1 = A_1\sqrt{\left[\Phi + \frac{1}{m+\mu}\left(\Psi_c'(\Phi) + \frac{A_1^2}{8}\Psi_c'''(\Phi)\right)\right]^2 + \dot{r_1}^2}.$$

To pose the problem in a linear least squares form, consider a polynomial description of $\Psi_c(\Phi)$ given by $\Psi_c(\Phi) = \sum_{i=0}^{N} a_i\Phi^i$ where N is an integer. The functional dependence of $\dot{\Phi}$ on $\hat{A}_i$ is neglected and terms higher than 2nd order in $\hat{A}_i$ truncated. For consideration of the first and second modes only, the equations can be written as the following:

$$\dot{\Phi} = \sum_{i=0}^{N}\hat{a}_i\Phi^i + c_0\Psi + d_1\hat{A}_1 + d_2\hat{A}_1\Phi + d_3\hat{A}_1^2 + d_4\hat{A}_1\hat{A}_2 + d_5\hat{A}_2 + d_6\hat{A}_2\Phi + d_7\hat{A}_2^2,$$

$$\dot{\Psi} = \frac{1}{4l_cB^2}(\Phi - \gamma\sqrt{\Psi}), \tag{26}$$

where $\hat{a}_i = a_i/l_c$, $b_1 = 1/4l_cB^2$, $b_2 = -\gamma/4l_cB^2$, and $c_0 = -1/l_c$. The algorithm uses surge cycle data from experiment and searches for coefficients that give the best fit to the expanded surge equations. A successful identification of the compressor characteristic is classified as one that gives a close fit to the time rate of change of the flow and pressure signals, and has a tight bound on the range of possible characteristics as a result of the linear least squares fit.

27
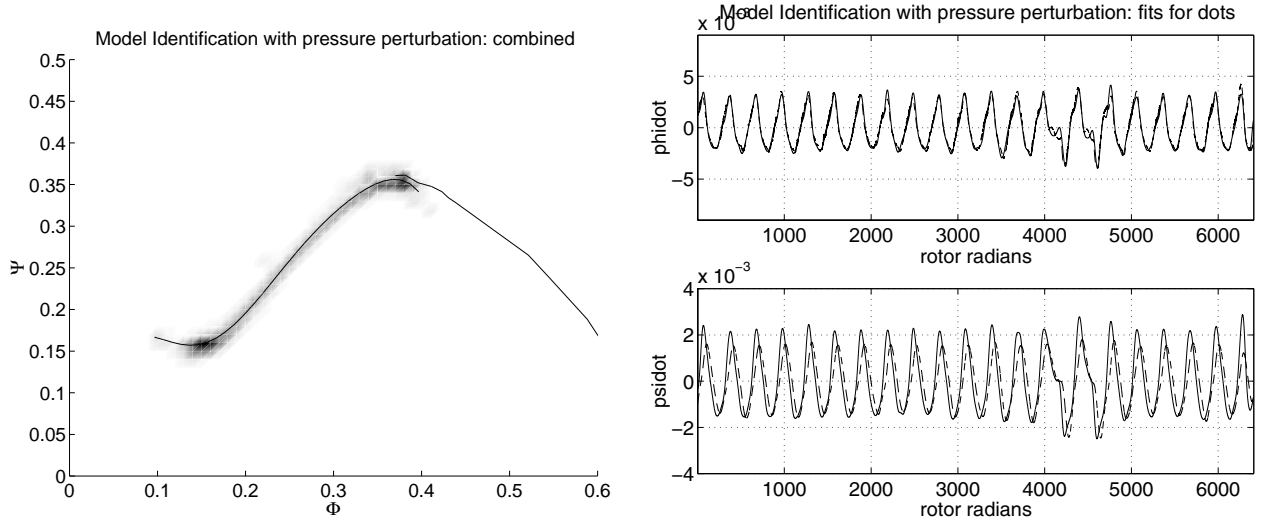
Figure 14: Identified compressor characteristic and estimated $\dot{\Phi}$ and $\dot{\Psi}$ using pressure perturbation; on the right plot, solid lines represent measured data and dashed estimated from fit.

To illustrate the method, surge cycle data was taken on the Caltech rig. Using the model described in equation (26), the resulting identified compressor characteristic and the estimated $\dot{\Phi}$ and $\dot{\Psi}$ are shown in Figure 14. The solid lines in the right plots represent the actual $\dot{\Phi}$ and $\dot{\Psi}$ time traces while the dashed lines the fitted counterparts. The shaded region in the left plot is a band formed by computing the compressor characteristic from the surge cycle data using the fitted values of the parameters. The tightness of this band and the close fit to the time traces indicate that the fit is good with respect to the underlying model.

4.3 Nonlinear control using bleed valves

One of the earliest nonlinear control laws to be proposed for stabilization of rotating stall was given by Liaw and Abed [23], who considered control using a downstream bleed valve. They demonstrated that by modulating the bleed proportionally to the square of the amplitude of the first mode of rotating stall, the normal bifurcation into stall could be transformed for a subcritical bifurcation to a supercritical one. The resulting closed loop dynamical system has no hysteresis loop, allowing operation much closer to the peak of the compressor characteristic.

Figure 15 shows the open- and closed-loop behavior of the Caltech compressor in the Φ-Ψ plane and the γ-J plane respectively, using the Liaw-Abed control law. The closed-loop behavior shows no hysteresis loop on Figure 15, as expected from the theory. As Figure 15 shows, after the bleed valve saturates, the system returns to the original stalled equilibria. The γ-J plot in Figure 15 is expected to show the same observation. The mismatch at low values of γ is due to the formation of the second mode of stall in the open-loop case. For the open-loop system, the second mode of rotating stall forms at a value of γ smaller than that for the formation of the first mode. At $\gamma = 0.45$ on Figure 15, the second mode forms and becomes dominant, and the amplitude of the first mode is decreased. Further decrease in γ leads to a further reduction in the amplitude of the first mode. At around $\gamma = 0.33$, the throttle is almost fully closed and the first mode becomes dominant again. In the closed-loop case, this phenomenon is not observed since the high speed bleed valve saturates and remains open. As a result, the main flow level is not low enough for the

28
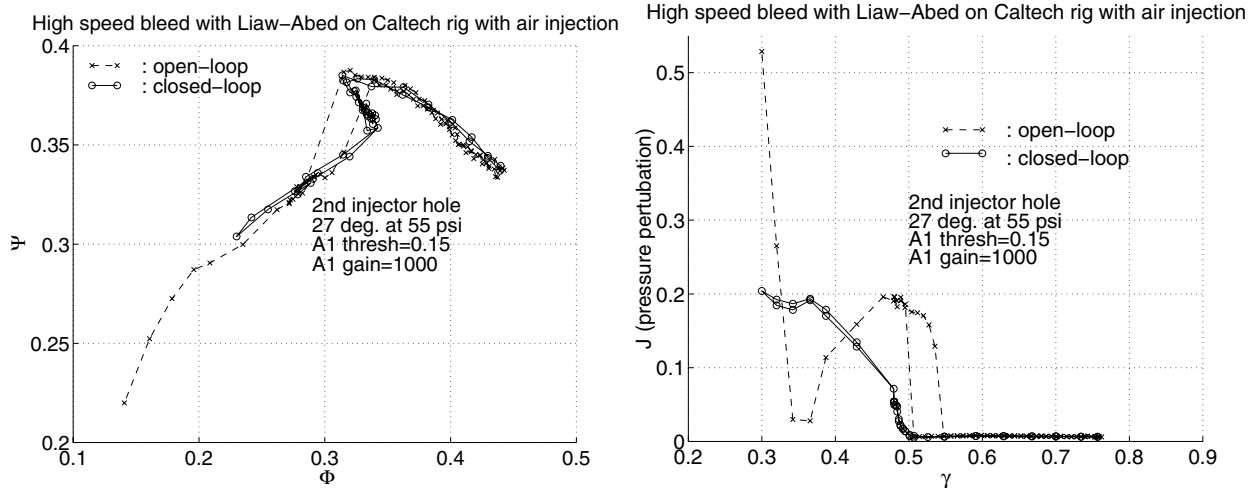
Figure 15: Open- and closed-loop behavior of system on Φ-Ψ plane for control with bleed valve and continuous air injection at 55 psig injector back pressure.

second mode of rotating stall to form.

A combined surge and stall control algorithm has implemented by using a high speed bleed valve for control of stall stall and a slow bleed valve (disturbance bleed) for surge. The surge controller is implemented with a proportional feedback on $\dot{\Phi}$. This control law is proposed by Badmus et al. [3]. The combined control law for rotating stall and surge takes the form

$$\Phi_T(\Psi) = (\gamma + K_{\mathrm{RS}}J + K_{\mathrm{S}}\dot{\Phi})\sqrt{\Psi},$$

where K_{RS} is the gain for rotating stall control and K_{S} that for surge control. Figure 16 shows plots of the dynamic response of the system. Control is initially turned off and the system is surging. Control is then activated at approximately 6000 rotor revolutions and the system is stable.

4.4 Nonlinear control using axisymmetric air injection

Control via bleed valves can described as a method of controlling the behavior of the compression system by modulating the throttle characteristic to change the criticality of the bifurcation. In a similar way, we can ask whether it is possible to change the behavior of the system by modulating the *compressor* characteristic. This requires a mechanism of modulating this curve, analogous to using the bleed valve to modulate the throttle characteristic. On the Caltech rig, we make use of unsteady air injection to accomplish this modulation.

In order to test the closed loop compressor characteristic shifting idea, a series of experiments were performed. We attempt to implement a close loop controller that modulates the compressor characteristic in a way that is proportional to the squared amplitude of the first mode amplitude of the rotating stall:

$$\Psi_c = \Psi_{c_{nom}} + KJ_1\Psi_{c_u}. \tag{27}$$

In order to achieve this proportional feedback on the amplitude of the stall cell magnitude, the duty cycle of the air injectors was varied. A carrier frequency of 100 Hz was used, with the duty cycle varying between 0–100% proportional to the amplitude of the static pressure perturbation amplitude. By varying the air injection parameters (back pressure, injection angle, etc), we can explore a variety of shifted compressor characteristics, Ψ_c. Two shifts were investigated, one with
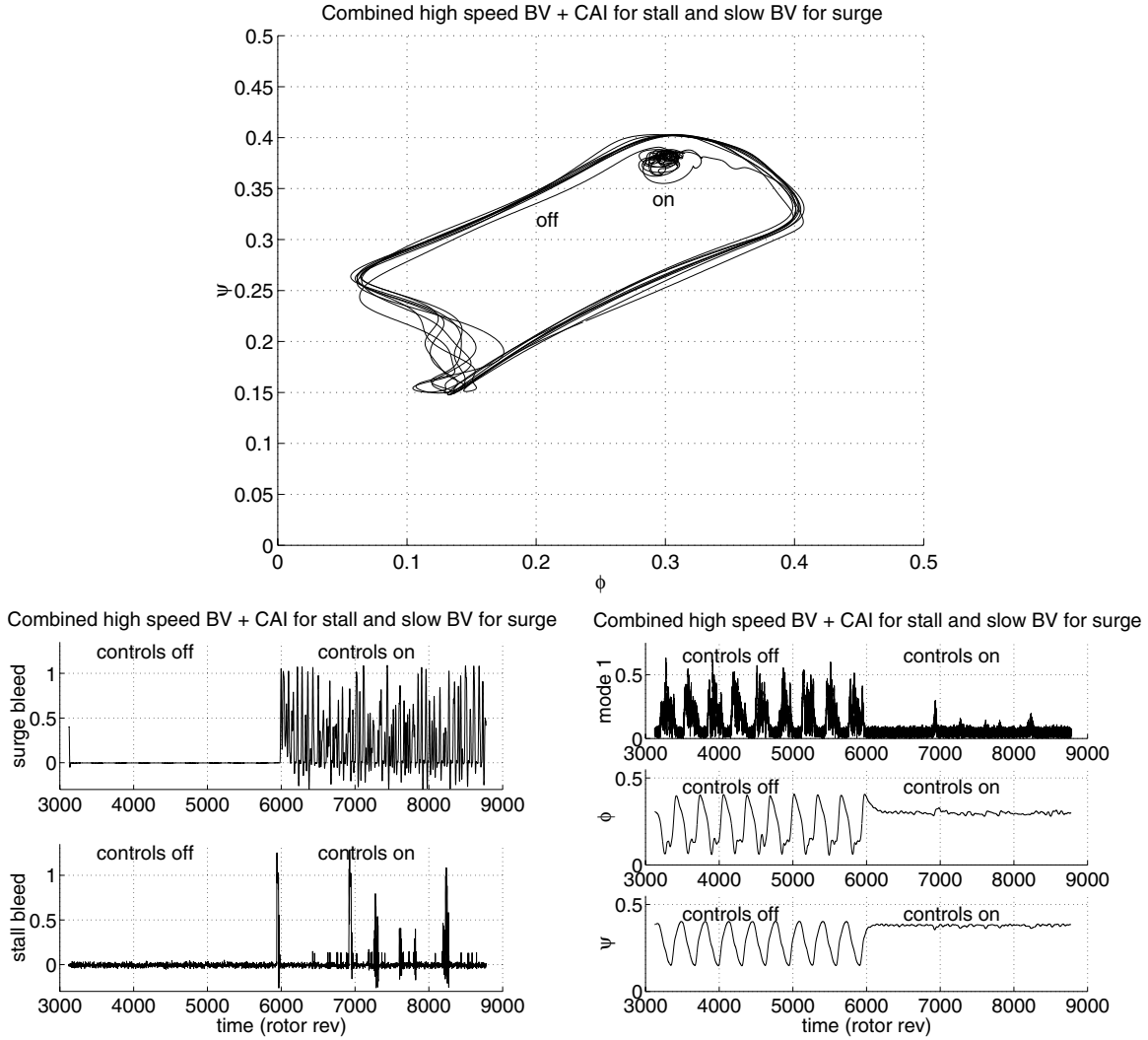
Figure 16: Combined stall control with high speed bleed and continuous air injection and surge control with slow bleed: control initially off and turned on at approximately 6000 rotor revolutions.

a rotating stall hysteresis region that did not overlap that of the uninjected case and one with a hysteresis region that did overlap.

Figure 17 shows the closed loop compressor characteristic obtained for the non-overlapping hysteresis region case (left of figure), along with an experimental bifurcation diagram (right of figure). The figure clearly shows that the entire nonzero equilibria branch is stable, and there is therefore no hysteresis region associated with rotating stall.

Figure 18 shows the closed loop compressor characteristic obtained for the overlapping hysteresis region case (left of figure), along with an experimental bifurcation diagram (right of figure). In this case, we see that there is still a hysteresis loop at the intersection of the two open loop curves. This effect is explained in more detail in [4].
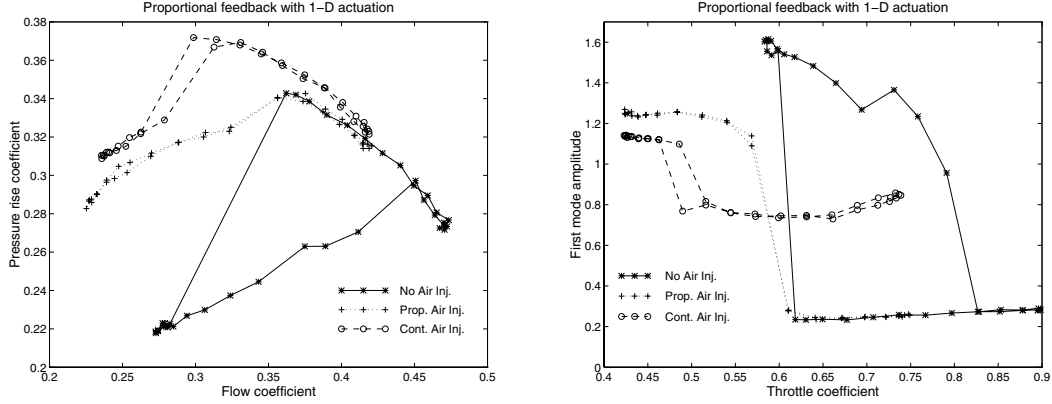
Figure 17: Closed loop compressor characteristic and bifurcation diagram, obtained with 1-D proportional feedback: non-overlapping hysteresis case.
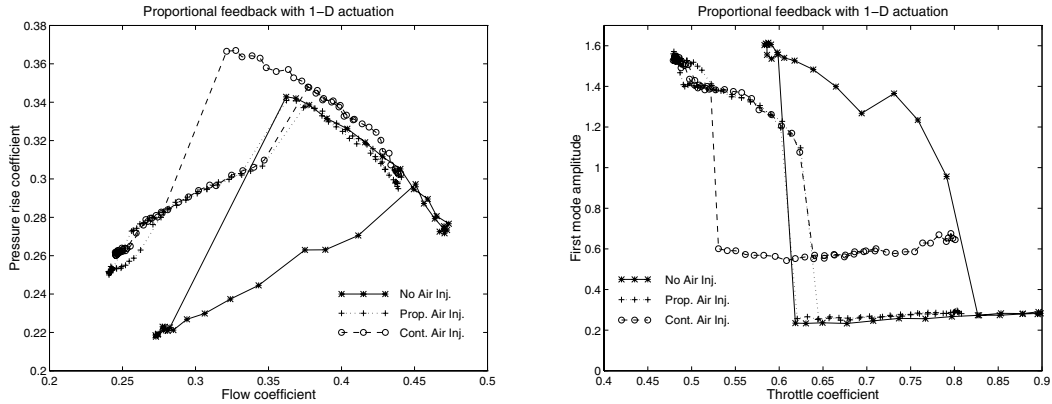
Figure 18: Closed loop compressor characteristic and bifurcation diagram obtained with 1-D proportional feedback: overlapping hysteresis case.

4.5   Nonlinear control using non-axisymmetric air injection

In this section, experimental results on the use of pulsed air injection to control rotating stall are presented. Unlikely the previous section, we use non-axisymmetric injection here, so that each air injector is independently controlled. However, we still make use of only three air injectors, so that the modal approaches described in Section 3 cannot be directly applied.

Control of stall

The basic strategy of this controller is to sense the location and magnitude of the peak of the first mode component of a circumferential pressure disturbance and inject air based on the location of this first mode relative to the positions of each air injector. It was shown in [4] that the second mode could be neglected with little effect.

The action of the controller is parameterized by the following variables:
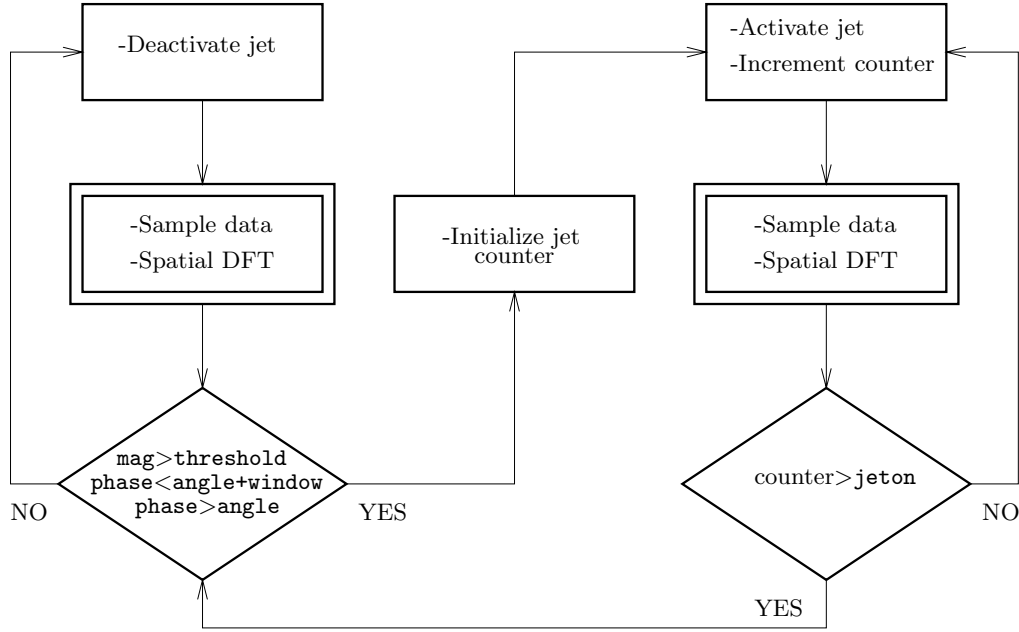
Figure 19: Control Algorithm. The above logic is repeated for each air injector. The double rectangle corresponds to the beginning of a servo-loop, which occurs at a rate of 2000 times per second. Figure courtesy of Raffaello D'Andrea.

`jeton`	minimum pulse width
`threshold`	threshold for stall detection
`window`	angle window for stall detection
`angle1`	activation angle for air injector 1
`angle2`	activation angle for air injector 2
`angle3`	activation angle for air injector 3,

and the algorithm itself is shown schematically in Figure 19. The flow chart can be interpreted as follows: each air injector is activated when the magnitude of the first mode is greater than `threshold` and the location of the peak of the first mode is within a pre-specified range of angular positions (as determined by `angle` and `window`); once an air injector is activated, it remains activated for `jeton` number of servo-loops, irrespective of the magnitude `mag` and location `phase` of the first mode. Note that `phase` and `mag` refer to the phase and magnitude of the first Fourier coefficient, not the physical location and value of the peak pressure disturbance at the compressor face. The higher circumferential modes effect the exact location, but the available pressure sensors only provide the location of the first two modes. In the case that the pressure disturbance is sinusoidal (which is a good approximation when fully stalled), `phase` and the physical location of the peak pressure disturbance differ only by a constant, which is due to delays in the data acquisition stage.

The closed loop compressor performance curve is shown in Figure 20 for the optimal choice of injector phasing and `jeton` = 15. The results shown to the left of the peak of the characteristic are time averaged values, since the controller is continuously rejecting stall disturbances in this region. Error bars are included to show the time variation of the circumferentially averaged flow

32
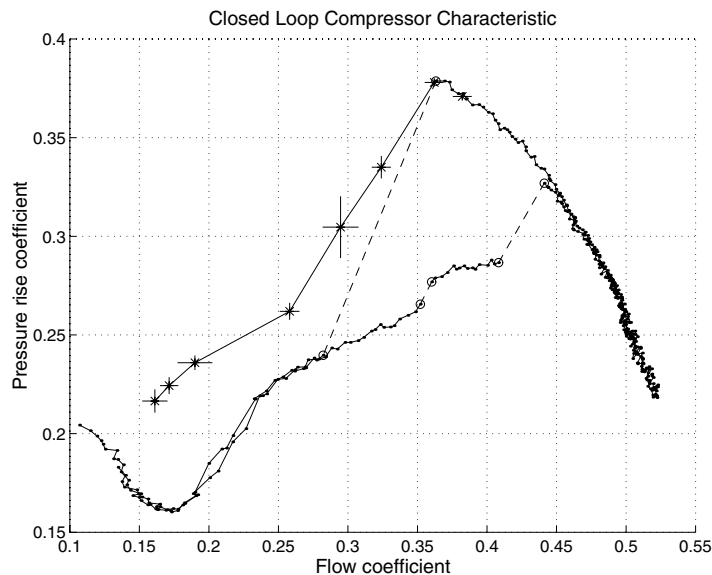
Figure 20: Closed loop compressor characteristic for `jeton` = 15, optimal controller. The asterisks correspond to time averaged data, while the solid lines interpolate these points. The pressure and flow variance are included for each data point as error bars. The open loop compressor characteristic is included for comparison purposes.

and the pressure rise coefficients at these unsteady operating points (this is because the system is continuously rejecting rotating stall disturbances in this region). The figure shows that hysteresis loop associated with rotating stall is eliminated by the pulsed air injection controller.

In addition to the closed loop compressor characteristic for the optimal controller presented above, the closed loop characteristic for a case where the placement of the air injectors resulted in non-overlapping hysteresis regions for the continuous air injection and the uninjected case was determined. Figure 21 shows the result of closed loop control in this case. The only difference that is apparent between two closed loop compressor characteristics is that the case with non-overlapping hysteresis regions has a less steep dropoff in pressure rise as the throttle is closed past the peak of the compressor characteristic. From these results it is clear that shifting the characteristic to the point where the hysteresis regions do not overlap does not provide significant benefit for this form of controller.

Figure 22 shows the transient behavior at two points (A and B) on the closed loop compressor characteristic shown in Figure 21. The figure shows the unsteadiness associated with operating the closed loop system to the left of the compressor characteristic peak (point B). Again, there are no significant differences between this case and the overlapping hysteresis case. The fact that non-overlapping hysteresis regions were not required to eliminate the hysteresis associated with rotating stall (this was not the case for the 1-D proportional controller presented in the previous section is a strong motivation to investigate this and other 2-D actuation schemes further.

Control of stall and surge

Several experiments were performed to determine the effect of the control algorithm when the rig was operated in a configuration with a large plenum attached, which made the resulting surge dynamics unstable. Data for the uncontrolled case is shown in the top four plots of Figure 23 for
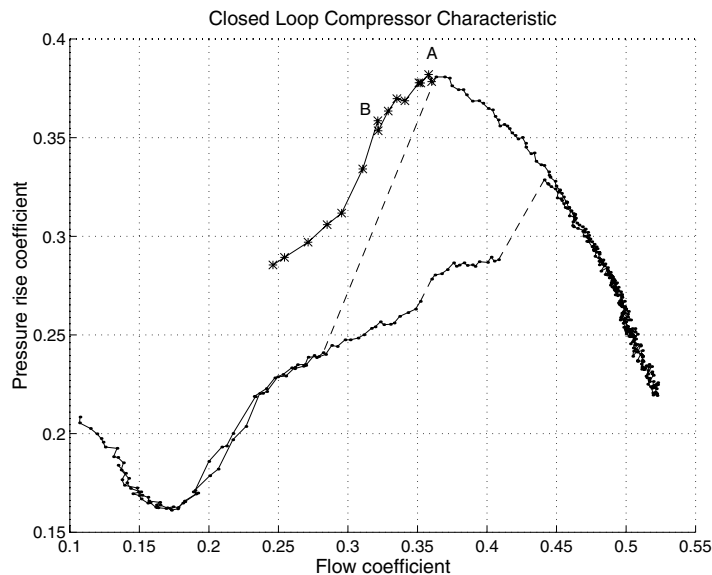
Figure 21: Closed loop performance characteristic for air injection geometric parameters which provide no overlap of the hysteresis regions.

reference.

The plots of the uncontrolled case show two different surge modes, one at 1.4 Hz and the other at 1.8 Hz (these two different surge modes are investigated further in [4]. The time traces for the first mode rotating stall clearly show that the compressor goes into stall during the low flow rate intervals and comes out of stall during the high flow rate intervals. The pressure rise coefficient versus flow coefficient plot clearly illustrates the two different surge limit cycles (note that the surge cycles are traversed in a counterclockwise direction).

The bottom four plots show the transient behavior of the compression system when the pulsed air injection controller for rotating stall is active. The plots show the response to a single throttle disturbance. As in the uncontrolled case, each pressure disturbance de-stabilized the system. Note that the controller had virtually no effect on the surge trajectory during the time the disturbance was present (in this 20 revolution time period, the trajectory is virtually the same as the one in the previous experiment). On the subsequent cycle the pressure and flow variations were substantially decreased and then eliminated. Experiments showed that by shortening the time duration of the pressure disturbance (while still keeping it large enough to cause the open loop system to go into surge), the pressure and flow variations during the first cycle were reduced. For short disturbances, the magnitude of the pressure and flow disturbances could be kept to within 30% of the nominal operating flow and pressure rise.

An explanation of why the control algorithm is successful at eliminating surge is based on the strong coupling between the surge and stall dynamics. Since the compressor begins to stall when the flow coefficient is decreasing, the stall controller can react to this aspect of the surge dynamics. When the system begins to stall, the control algorithm activates, and tries to eliminate the stalled condition. This has the effect of increasing the net flow rate through and pressure rise across the compressor when these states are low during a surge cycle. The control algorithm therefore provides positive damping to the surge dynamics.

4.6 Comparison of modal control versus nonlinear control

The techniques described in this chapter rely on nonlinear techniques to change the bifurcation behavior of rotating stall from a subcritical bifurcation to a supercritical bifurcation. The benefit of this change in bifurcation behavior is that the hysteresis loop is eliminated, potentially allowing the compressor to be operated closer to its peak in a robust fashion. However, the system still enters stalled operation past the peak of the compressor characteristic, even though the stall cell amplitude remains small.

In contrast, the modal controllers described in Section 3 operate by actually stabilizing the system beyond the peak. This means that no discernible stall is present and hence the engine designer can make use of the maximum pressure rise of the compressor. The amount of extension of the operation depends on the number of sensors and actuators (which determine the number of spatial modes that can be stabilized), the bandwidth of the actuators (typically bandwidths of 2—5 times the rotor frequency are required) and the actuator authority (magnitude limit).

Understanding which approach is more appropriate depends on the cost and weight of actuators and sensors, as well as the ability of the engine to operate in a stall condition (without hysteresis). A fairly detailed comparison of the performance tradeoffs between these various scenarios was carried out in [41].

Another important aspect of active control of compression systems is the affect of magnitude and rate limits. Work by Yeung [41] and Wang [37] has explored these effects and a detailed theory for predicting these limits has been developed. In particular, it was shown by Yeung that the *shape* of the compressor characteristic is a dominant factor in determining the bleed valve magnitude, rate, and bandwidth requirements. More information is available in [42].
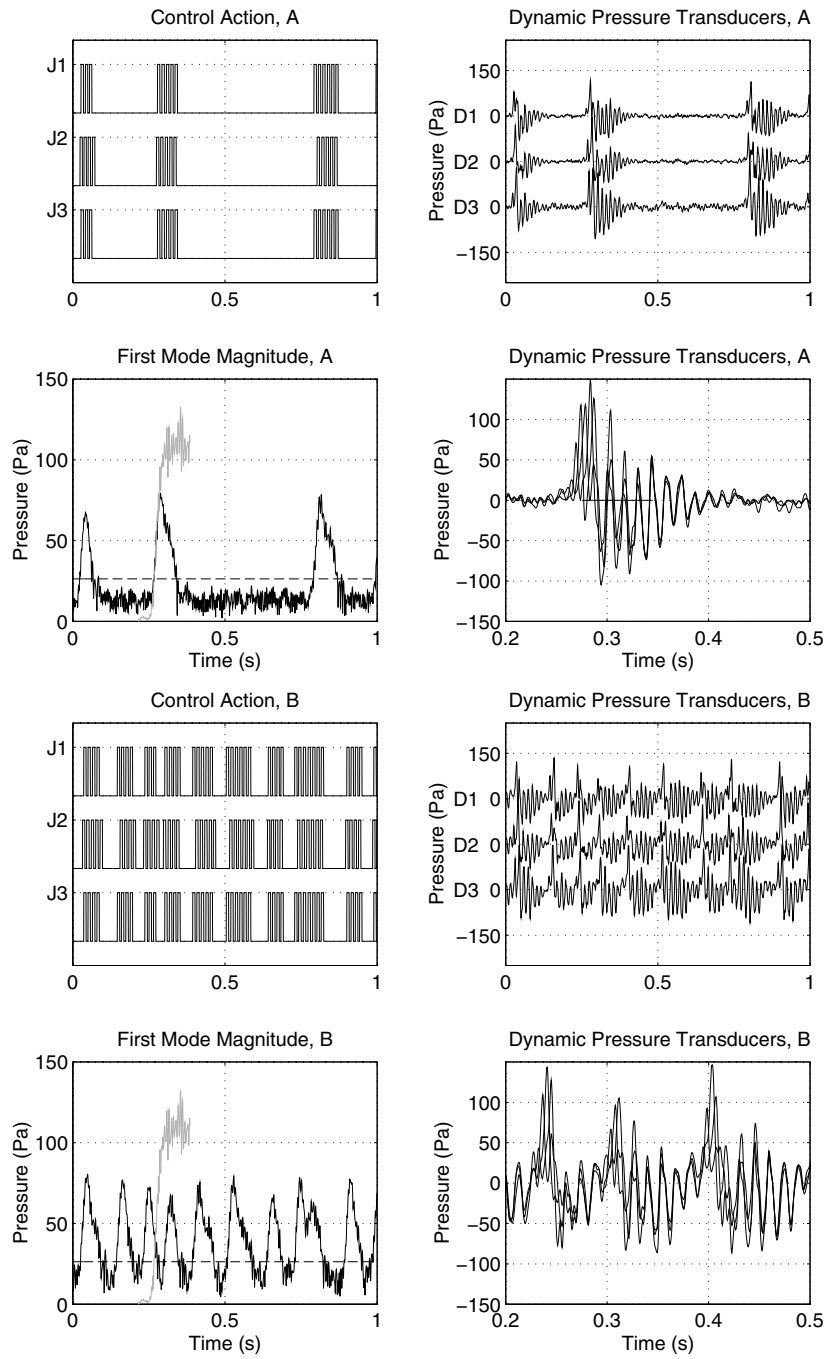
Figure 22: Comparison of controller performance for two different throttle settings. Points A and B refer to Figure 21. The first mode stall cell amplitude for the uncontrolled case is shown in gray.
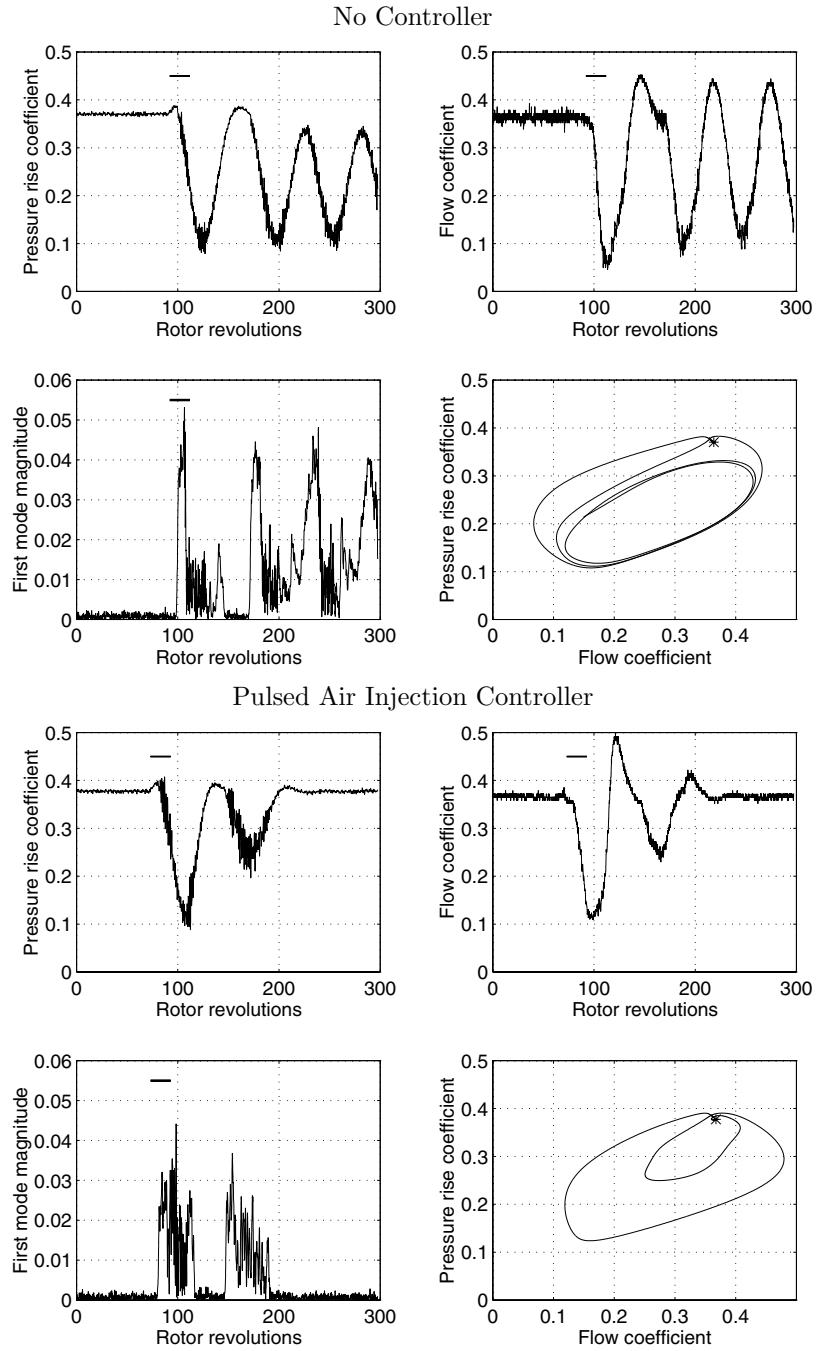
Figure 23: Effects of pulsed air injection controller on the surge dynamics. The top four plots correspond to no control action, and the bottom four plots correspond to pulsed air injection control. The horizontal line in the time trace plots corresponds to the throttle disturbance on time.

5   Summary

These notes have given a brief introduction to some of the key concepts and results in active control of compression systems. The main points of the notes can be summarized as follows:

- Benefits of active control: active control of compression systems can be used to extend the range of operation of a compressor, allowing fewer stages in a given engine design and leading to substantial fuel savings. Active control has been demonstrated in a variety of experiments, including full scale compression systems.

- Lyapunov stability analysis: Lyapunov stability theory can be used to prove stability of nonlinear systems and to construct stabilizers. Specific design methods include control Lyapunov functions and integrator backstepping.

- Bifurcation analysis and control: For systems that cannot be stabilized about a desired operating point, it is sometimes possible to change the bifurcation properties of the system. A specific example is changing a subcritical bifurcation to a supercritical bifurcation, allowing the instability to grow slowly in magnitude (as a function of a operating parameter).

- Modal control: By transforming the description of a system into modal coordinates, it is possible to directly stabilize the individual modes of a compression system. This requires an array of sensors and actuators of sufficient spatial density to stabilize the desired modes. Air injection and high-frequency inlet guide vanes are two actuation mechanisms that have been tested.

- Bifurcation control using axisymmetric actuation: Bleed valves or air injection can be used as an axisymmetric actuator to control stall by changing the bifurcation properties. This eliminates the hysteresis loop normally associated with rotating stall by "bending over" the bifurcation diagram.

- Bifurcation control using air injection: Air injectors can be used in a non-axisymmetric fashion to change the bifurcation behavior at the stall inception point. Non-axisymmetric actuation allows more control over the system behavior and appears better suited in the case when low amounts of actuator authority are needed.

These notes give only a basic introduction to some of the ideas that have been developed in the last year for active control of compression systems. More information is available on the web page for this course:

http://www.cds.caltech.edu/~murray/talks/vki-may01.html

References

[1] E. H. Abed, P. K. Houpt, and W. M. Hosny. Bifurcation analysis of surge and rotating stall in axial flow compressors. *Journal of Turbomachinery*, 115:817–824, October 1993.

[2] O. O. Badmus, S. Chowdhury, K. M. Eveker, and C. N. Nett. Control-oriented high-frequency turbomachinery modeling - single-stage compression system one-dimensional model. *Journal of Turbomachinery*, 117:47–61, January 1995.

[3] O. O. Badmus, C. N. Nett, and F. J. Schork. An integrated full-range surge control/rotating stall avoidance compressor control system. In *Proc. American Control Conference*, pages 3173–3180, 1991.

[4] R. L. Behnken. *Nonlinear Control and Modeling of Rotating Stall in an Axial Flow Compressor*. PhD thesis, California Institute of Technology, Mechanical Engineering, 1996.

[5] R. D'Andrea, R. L. Behnken, and R. M. Murray. Active control of rotating stall using pulsed air injection: A parametric study on a low-speed, axial flow compressor. In *Sensing, Actuation, and Control in Aeropropulsion; SPIE 1995 International Symposium on Aerospace/Defense Sensing and Dual-Use Photonics*, 1995.

[6] R. D'Andrea, R. L. Behnken, and R. M. Murray. Active control of an axial flow compressor via pulsed air injection. *Journal of Turbomachinery*, 119(4):742–752, 1998.

[7] I. J. Day. Active supression of rotating stall and surge in axial compressors. *Journal of Turbomachinery*, 115:40–47, 1993.

[8] I. J. Day. The fundamentals of stall and surge in axial compressors. In *von Karmon Institute for Fluid Dynamics, Lecture Series 1996-05*, 1996.

[9] H. W. Emmons, C. E. Pearson, and H. P. Grant. Compressor surge and stall propagation. *ASME Transactions*, 6:455–469, 1955.

[10] K. M. Eveker, D. L. Gysling, C. N. Nett, and O. P. Sharma. Integrated control of rotating stall and surge in aeroengines. In *Sensing, Actuation, and Control in Aeropropulsion; SPIE 1995 International Symposium on Aerospace/Defense Sensing and Dual-Use Photonics*, 1995.

[11] C. Freeman, A. G. Wilson, I. J. Day, and M. A. Swinbanks. Experiments in active control of stall on an aeroengine gas turbine. In *Proceedings of International Gas Turbine and Aeroengine Congress and Exhibition*, 1997. ASME 97-GT-280.

[12] G. B. Gilyard and J. S. Orme. Subsonic flight test evaluation of a performance seeking control algorithm on an f-15 airplane. In *Joint Propulsion Conference and Exhibit*, pages AIAA paper 92–3743, 1992.

[13] E. M. Greitzer. Surge and rotating stall in axial flow compressors—Parts I and II. *Journal of Engineering for Power*, pages 190–217, April 1976.

[14] E. M. Greitzer. The stability of pumping systems—the 1980 Freeman scholar lecture. *ASME Journal of Fluids Engineering*, 103:193–242, 1981.

[15] E. M. Greitzer and F. K. Moore. A theory of post-stall transients in axial compression systems—Part II: Application. *Journal of Turbomachinery*, 108:231–239, 1986.

[16] D. L. Gysling. *Dynamic Control of Rotating Stall in Axial Flow Compressors Using Aeromechanical Feedback*. PhD thesis, Department of Aeronautics and Astronautics, Massachusetts Institute of Technology, Cambridge, Massachusetts, 1993.

[17] D. L. Gysling and E. M. Greitzer. Dynamic control of rotating stall in axial-flow compressors using aeromechanical feedback. *Journal of Turbomachinery*, 117(3):307–319, 1995.

[18] J. M. Haynes, G. J. Hendricks, and A. H. Epstein. Active stabilization of rotating stall in a three-stage axial compressor. *Journal of Turbomachinery*, 116:226–239, 1994.

[19] G. J. Hendricks and D. L. Gysling. Theoretical study of sensor-actuator schemes for rotating stall control. *Journal of Propulsion and Power*, 10(1):101–109, 1994.

[20] H. K. Khalil. *Nonlinear Systems*. Macmillan Publishing Company, 1992.

[21] M. Krstic, D. Fontaine, P. V. Kokotovic, and J. D. Paduano. Useful nonlinearities and global stabilization of bifurcations in a model of jet engine surge and stall. *IEEE Transactions on Automatic Control*, 43(12):1739–1745, 1998.

[22] M. Krstić, I. Kanellakopoulos, and P. Kokotović. *Nonlinear and Adaptive Control Design*. Wiley, 1995.

[23] D. C. Liaw and E. H. Abed. Control of compressor stall inception: A bifurcation-theoretic approach. *Automatica*, 32(1):109–115, 1996.

[24] C. A. Mansoux, D. L. Gysling, J. D. Setiawan, and J. D. Paduano. Distributed nonlinear modeling and stability analysis of axial compressor stall and surge. In *Proc. American Control Conference*, pages 2305–2316, 1994.

[25] F. E. McCaughan. Application of bifurcation theory to axial flow compressor instability. *Journal of Turbomachinery*, 111:426–433, 1989.

[26] F. E. McCaughan. Bifurcation analysis of axial flow compressor stability. *SIAM Journal of Applied Mathematics*, 20(5):1232–1253, 1990.

[27] F. K. Moore. A theory of rotating stall in multistage axial compressors: Parts I, II, III. *Journal of Engineering for Gas Turbines and Power*, 106:313–336, 1984.

[28] F. K. Moore and E. M. Greitzer. A theory of post-stall transients in axial compression systems—Part I: Development of equations. *Journal of Turbomachinery*, 108:68–76, 1986.

[29] R. M. Murray, Z. Li, and S. S. Sastry. *A Mathematical Introduction to Robotic Manipulation*. CRC Press, 1994.

[30] J. D. Paduano, A. H. Epstein, L. Valavani, J. P. Longley, E. M. Greitzer, and G. R. Guenette. Active control of rotating stall in a low-speed axial compressor. *Journal of Turbomachinery*, 115:48–56, January 1993.

[31] J. D. Paduano, E. M. Greitzer, and A. H. Epstein. Compression systems stability and active control. *Annual Reviews in Fluid Mechanics*, 33:491–517, 2001.

[32] J. D. Paduano, L. Valavani, A. H. Epstein, E. M. Greitzer, and G. R. Guenette. Modeling for active control of rotating stall. *Automatica*, 30(9):1357–1373, 1994.

[33] S. S. Sastry and M. Bodson. *Adaptive Control: Stability, Convergence, and Robustness.* Prentice-Hall, 1989.

[34] R. H. Smith, J. D. Chisholm, and J. F. Stewart. Optimizing aircraft performance with adaptive, integrated flight/propulsion control. *Journal of Engineering for Gas Turbines and Power*, 113(87–94), 1991.

[35] E. D. Sontag. A Lyapunov-like characterization of asymptotic controllability. *SIAM Journal of Control and Optimization*, 21:462–471, 1983.

[36] M. Vidyasagar. *Nonlinear Systems Analysis.* Prentice-Hall, second edition edition, 1993.

[37] Y. Wang. *Effects of Actuator Limits in Bifurcation Control with Applications to Active Control of Fluid Instabilities in Turbomachinery.* PhD thesis, California Institute of Technology, Control and Dynamical Systems, 2000.

[38] Y. Wang, C. Yeung, and R. M. Murray. Bifurcation control of rotating stall with actuator magnitude and rate limits. *Automatica*, 2001. To appear.

[39] H. J. Weigl, J. D. Paduano, L. G. Frechette, A. H. Epstein, E. M. Greitzer, M. M. Bright, and A. J. Strazisar. Active stabilization of rotating stall in a transonic single state axial compressor. *Journal of Turbomachinery*, 120(4):625–636, 1997. 97-GT-411.

[40] S. Wiggins. *Introduction to Applied Nonlinear Dynamical Systems and Chaos.* Springer-Verlag, 1990.

[41] C.-H. Yeung. *Nonlinear Control of Rotating Stall and Surge with Axisymmetric Bleed and Air Injection on Axial Flow Compressors.* PhD thesis, California Institute of Technology, Chemical Engineering, 1996.

[42] C.-H. Yeung, Y. Wang, and R. M. Murray. Evaluation of bleed valve rate requirements in nonlinear control of rotating stall. *Journal of Propulsion and Power*, 15(5):781–791, 2000.

This page has been deliberately left blank

***

Page intentionnellement blanche

REPORT DOCUMENTATION PAGE

1. Recipient's Reference	2. Originator's References	3. Further Reference	4. Security Classification of Document
	RTO-EN-020 AC/323(AVT-083)TP/57	ISBN 92-837-1081-9	UNCLASSIFIED/ UNLIMITED

5. Originator	Research and Technology Organisation North Atlantic Treaty Organisation BP 25, F-92201 Neuilly-sur-Seine Cedex, France

6. Title	Active Control of Engine Dynamics

7. Presented at/sponsored by	the Applied Vehicle Technology Panel (AVT) and the von Kármán Institute for Fluid Dynamics (VKI) in Brussels, Belgium, 14-18 May 2001.

8. Author(s)/Editor(s)	9. Date
Multiple	November 2002

10. Author's/Editor's Address	11. Pages
Multiple	402

12. Distribution Statement	There are no restrictions on the distribution of this document. Information about the availability of this and other RTO unclassified publications is given on the back cover.

13. Keywords/Descriptors

Active control	Engine dynamics
Actuators	Engines diagnostics
Axial compression systems	Gas turbine engines
Combustion system dynamics	Passive control
Combustors	Reliability
Compression system dynamics	Requirements
Compressor instability	Robustness
Control equipment	Stability characteristics
Design constraints	State of the art reviews

14. Abstract

Active control can alleviate design constraints and improve the response to operational requirements in gas turbines. The Course presented the state-of-the-art including experimental, theoretical knowledge and practical information.

Topics treated: stability characteristics; active control approaches; robustness and fundamental limits; combustion systems processes; combustor dynamics; compression system dynamics models; diagnostics and control of compression instabilities; sensor and actuator architectures; R&D needs of future prospects.

The course has shown that for combustion systems, as well as in actuator and sensor technologies the active control approach is a viable option even at full scale with potential for aero engines and air breathing missiles.

This page has been deliberately left blank

_____

Page intentionnellement blanche

NATO's Research and Technology Organisation (RTO) holds limited quantities of some of its recent publications and those of the former AGARD (Advisory Group for Aerospace Research & Development of NATO), and these may be available for purchase in hard copy form. For more information, write or send a telefax to the address given above. **Please do not telephone**.

Further copies are sometimes available from the National Distribution Centres listed below. If you wish to receive all RTO publications, or just those relating to one or more specific RTO Panels, they may be willing to include you (or your organisation) in their distribution.

RTO and AGARD publications may be purchased from the Sales Agencies listed below, in photocopy or microfiche form. Original copies of some publications may be available from CASI.

NATIONAL DISTRIBUTION CENTRES

SALES AGENCIES

Requests for RTO or AGARD documents should include the word 'RTO' or 'AGARD', as appropriate, followed by the serial number (for example AGARD-AG-315). Collateral information such as title and publication date is desirable. Full bibliographical references and abstracts of RTO and AGARD publications are given in the following journals: